EXPERIMENTAL INVESTIGATION OF MULTIELEMENT AIRFOILS FOR LARGE-SCALE WIND TURBINES

BY

BRENT WILLIAM POMEROY

THESIS

Submitted in partial fulfillment of the requirements
for the degree of Master of Science in Aerospace Engineering
in the Graduate College of the
University of Illinois at Urbana-Champaign, 2012

Urbana, Illinois

Adviser:

Associate Professor Michael S. Selig

Abstract

Experimental results for high-lift multielement airfoils for application to megawatt-scale wind turbines are presented in this thesis. Two different airfoil configurations tested were designed for the inboard section of a 10 MW-scale wind turbine. The airfoil systems were designed as an airfoil system to replace a baseline airfoil that is 40.1% thick. A three-element system consisted of a main element and two flaps and a four-element system was tested with an additional strut. Experiments were performed with the ability to move two flaps to any location relative to a main element. Data were collected at a constant Reynolds number of 1.0 million. Tests were performed in the University of Illinois low turbulence subsonic wind tunnel with a chord length of approximately 1.5 feet (0.46 m) and a model span of approximately 2.8 feet (0.85 m). Results for the Reynolds number tested indicate that lift and drag do not always follow the same trends with respect to gap or overhang. In general, gap size should be no smaller than 2.0% system chord to avoid degradation in performance. In addition, a large overhang can adversely affect aerodynamic performance and lead to a loss of lift but also a reduction in drag. Consequently, it is important in the airfoil design process to identify the balance between aerodynamic efficiency and high lift configurations.

To the glory of God

Acknowledgments

The completion of my thesis would never have been possible without the love, support, and wisdom of many different individuals. I am deeply thankful for each and every one of those who have helped me climb the mountain.

First and foremost, thank you to my parents for raising me with a curious mind and giving me the passion to tackle the hardest challenges. You have both been a source of comfort, love, and support during my entire life. I'm not sure I can ever repay you. For my brother, Brian, I am also grateful. As a fellow aerospace engineering graduate student, it has been a blessing to follow in your footsteps. You have inspired me to seek answers and have instilled a strong passion for aerospace engineering deep in my heart. In addition, your love, support, and advice have all been appreciated.

I am blessed to have an incredible advisor, Dr. Michael S. Selig. You have taught me much during my tenure at Illinois. The aerodynamics knowledge which you have imparted into me is deeply appreciated. But I appreciate the life lessons and advice even more than the aerodynamic knowledge.

I never could have completed this research without the help of my fellow labmates. I acknowledge Greg Williamson and his aid of my research through CAD support and also tunnel assistance. To Adam Ragheb - your friendship is deeply appreciated and you have always helped me stay focused upon our shared long term dream in life. Rob Deters' wisdom and knowledge of all things grad school is also duly noted. For my fellow tunnel guys, Phil Ansell, and Jeff Diebold, I am also grateful. Phil, you have always helped me stay calm, cool and collected and have helped me keep my priorities in line. There are things far greater than either of us could ever imagine and we rejoice in this truth. Jeff, our incredibly deep friendship has kept me sane after many long hours in Talbot. I also appreciate the support of all my fellow APA labmates.

Support for my research has been provided by the National Science Foundation Graduate Research Fellowship Program and also GE Wind. The assistance of Christian Carroll, Stefan Herr, and Jonathan Luedke (all at GE Wind in Greenville, South Carolina) is acknowledged.

I am unbelievably indebted to Ken, David, and Shawn. Ken, you've inspired me to chase a dream I didn't even know I had and subsequently lit a fire deep in my soul. I learned much from you, and more than

just aerodynamics. David, I appreciate your wisdom and advice on all things life. You and I both know I never would have been here without your help and support during those formative years. And to Shawn, the one who believed in me when nobody else did. I'm not even sure you know how much you've changed my life for the better.

God has blessed me beyond my wildest imagination and I pray that all things I do may be for His glory and the glory of Christ's kingdom. All things I do, I do under and for you.

Table of Contents

List of Tables

List of Figures

Nomenclature

Symbols

A	=	cross-sectional area
C_l	=	2D coefficient of lift
C_d	=	2D coefficient of drag
C_m	=	2D pitching moment coefficient
c_n	=	individual chord of element n
c_{sys}	=	system chord length
D	=	drag per unit span
L	=	lift per unit span
M	=	pitching moment per unit span
q	=	dynamic pressure
P	=	pressure
P_∞	=	freestream pressure
P_0	=	stagnation pressure
Re	=	Reynolds number
S	=	model surface area
T	=	temperature
T_{amb}	=	ambient temperature
$\left(\frac{t}{c}\right)$	=	thickness-to-chord ratio
U_∞	=	freestream velocity
u	=	local streamwise velocity
x	=	Cartesian coordinate parallel to freestream flow
y	=	Cartesian coordinate orthogonal to freestream flow
α	=	angle of attack

δ_{main} = main element deflection angle

δ_n = absolute deflection angle of flap n

$\delta_{r,n}$ = relative deflection angle of flap n

ϵ = blockage correction

ϵ_{sb} = solid blockage correction

ϵ_{wb} = wake blockage correction

μ_{amb} = ambient dynamic viscosity

ρ_{amb} = ambient density

Δ = a difference between two quantities

Abbreviations

CC = closely coupled multielement airfoil configuration

CMM = coordinate measuring machine

FPS = flap positioning system

MFF = main-flap-flap multielement airfoil

$MFFS$ = main-flap-flap-strut multielement airfoil

MW = megawatt

$NASA$ = National Aeronautics and Space Administration

SFB = secondary force balance

$UIUC$ = University of Illinois at Urbana–Champaign

WS = well separated multielement airfoil configuration

Chapter 1

Introduction

There has been an increasing interest in wind turbine design and alternative energy in the United States within the last decade. As energy costs continue to rise and fossil fuel sources continue to dwindle, a sustainable energy solution for the United States must be developed. Wind energy is applicable on an industrial scale and is sustainable without significant government subsidies. As the global population continues to grow, electricity must be provided to billions of more individuals within the next few decades. Some of the regions of rapid population growth are not in a region where fossil fuels are readily available. Wind energy offers an alternative to burning fossil fuels.

1.1 Motivation

Wind turbine analysis and design has received increasing awareness in aerodynamic research over the last decade. Requirements for larger and more efficient wind turbines have required engineers to develop new designs for wind turbines. The power output of a wind turbine is proportional to the surface area of the blades while the weight of the wind turbine blade increases with the volume of the blade. This relationship is known as the squared-cubed law. Wind turbine manufacturers cannot simply scale up the size of a wind turbine to create more energy without solving structural complications. A multielement airfoil system can be designed to be structurally desirable while maintaining good aerodynamic performance. Consequently, a multielement airfoil system may be beneficial from a structural and aerodynamic performance when compared to a single element airfoil.

Conventional root sections of wind turbine blades have extremely thick and aerodynamically inefficient airfoils as the blade transitions from an airfoil shape into the circular hub. A strong and thick structure must exist at the root to support the aerodynamic loads as well as the weight of the blade. Thick airfoils are aerodynamically inefficient and are not as desirable as slender airfoils. The design trade-offs between a thin, aerodynamically efficient airfoil and a thick, strong structure are in conflict in the inboard 20% of the wind turbine. As the structure transitions to the circular hub, the structural requirements dominate

the aerodynamic efficiencies. There is a need for thick yet aerodynamically efficient airfoil near the root section of large scale wind turbines. One solution to solve the design challenge is the use of multielement airfoils. Multielement airfoils could be designed as a system of airfoils that replace one large and thick airfoil currently in use in the blade. The airfoil system could be designed to be thick enough to ensure structural integrity of the blade at the root.

The goal of research presented in this thesis was to experimentally test the aerodynamic performance of various multielement airfoil configurations for use in the root region of large-scale (10 MW) wind turbines. Multielement airfoil design is complex and aerodynamic performance is sensitive to geometric arrangement. Motivation for this project was driven by two primary factors, namely increased aerodynamic performance and improved structural integrity of the blade.

1.2 Previous Work

Multielement airfoil design is complex and aerodynamic performance is sensitive to geometric arrangement. Conflicts exist between structural requirements and aerodynamic performance [1]. A strong structure, contained in a thick airfoil, must exist at the root to support the aerodynamic loads as well as the weight of the blade. A thick airfoil can reduce aerodynamic performance when compared with a thinner airfoil. Blade design must incorporate the transition from an airfoil shape to a circle at the hub of the blade. Blending of the shapes typically occurs in the inboard 10% of the blade and airfoil shapes are primarily driven by structural considerations [2].

Experimental studies of multielement airfoils were first performed in the 1940s and were studied as part of the classic 2-D tests by Abbott and von Doenhoff [3] and supplemented by Jacobs, et al. [4]. As discussed by Smith in 1975 [5], numerous effects govern the flow around high-lift devices. Previous work studied multielement airfoil configurations for aircraft which are only required during takeoff and landing. Multielement airfoils on aircraft are typically stored in the main element during cruise and deployed during takeoff and landing. Wind turbine airfoils are mainly designed based on tip speed ratio at one angle of attack and can be point-designed as the flap does not need to retract into the main element as conventional aircraft do during cruise. Consequently, design and analysis efforts can be focused on the aerodynamics of the multielement airfoil configuration.

High lift aerodynamics are complex and flow fields can be complicated. Inverse airfoil design was used by Liebeck in 1976 to find the shape of a single element airfoil with the highest lift of any airfoil [6]. The Liebeck family of airfoils had a Stratford pressure recovery that avoided separation at one angle of attack.

Liebeck extended work to multielement airfoils and used the Jones inverse airfoil design code to design multielement airfoils [7]. Separation due to off the surface pressure recovery, as first discussed by Smith [5], can be eliminated by properly designing the main element of an airfoil system. Inverse multielement airfoil design can achieve an airfoil system that dumps flow at the trailing edge of the main element at a higher than freestream flow speed [5]. The ability to dump above freestream velocity reduces the adverse pressure gradient in the wake so the wake does not burst. Research presented by Klausmeyer and Lin indicates flap separation decreases as Reynolds number increases [8]. They also observed the flow over the flaps may be attached at higher angles but detached at lower angles due to complex pressure fields which are driven by the main element. High lift aerodynamics can dramatically change with Reynolds number and Mach number, as discussed by Valarezo, et al. [9]. Computational codes and turbulence models are continually being developed and refined to more accurately model all aspects of multielement aerodynamics. van Dam observed that accurate prediction of laminar separation bubbles is not yet possible with CFD simulations [10].

Numerous previous research projects have studied the effect of flap deflection on the aerodynamic performance of a multielement airfoil. The first tests were performed by Abbott and von Doenhoff [3]. Ashby performed computational and experimental 2-D tests on a two-element system with a lift enhancing tab in 1996 [11]. Lift enhancing tabs and Gurney flaps are sometimes desired as they can be easily retracted during cruise without complex mechanical devices. Ashby observed that a lift enhancing tab placed on the lower surface near to the trailing edge of the flap could increase C_l at a given alpha by up to 0.5. Large tabs can adversely effect the aerodynamics of the system and may greatly reduce L/D of the system. Myose, et al. studied a Gurney flap on a two element airfoil. Experiments indicated the Gurney flap increased $C_{l_{max}}$ and also increased C_d at a given α [12]. They also observed that the tab had a limited effect on multielement airfoils with a cove. Biber, et al. studied a two element slotted flap multielement airfoil system and concluded that an increase in flap deflection angle increases C_l at a given alpha but also reduces α_{stall} of the system [13]. Cerra and Katz performed inverse airfoil design for a thick high lift multielement airfoil system for use on a high altitude UAV [14]. The effect of flap deflection on C_l and C_d of the thick airfoil system is shown in Fig. 1.1. An increase in flap deflection yields a much stronger adverse pressure gradient on the main element and can also increase the suction peak over the flap [15].

Aerodynamics of high lift systems are sensitive to the location and size of the gap between elements. In general, a smaller gap accelerates the flow more rapidly while a large gap does not accelerate the flow as much. However, confluent boundary layers and complex wake interactions can adversely affect the performance of the system if the gap is too small [15]. A smaller gap increases the magnitude of the suction peak of the flap and may reduce drag compared to a larger gap configuration [14, 11]. Reduction in gap size can also

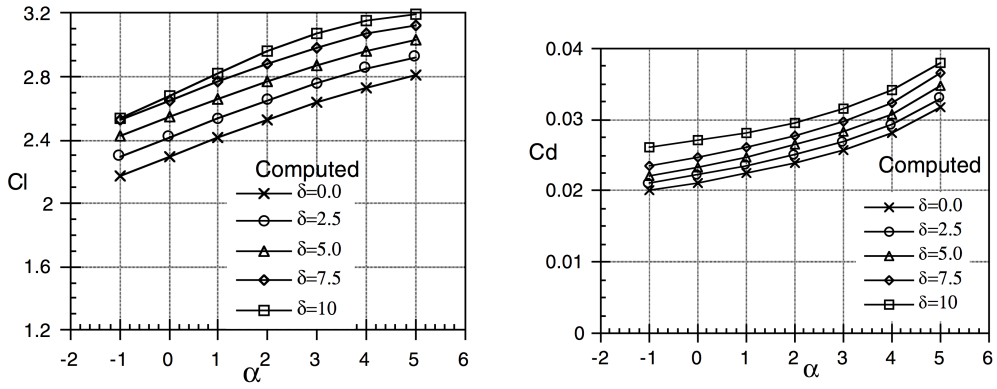

(a) Effect of flap deflection angle on lift coefficient ($Re = 1.0 \times 10^6$).

(b) Effect of flap deflection angle on drag coefficient ($Re = 1.0 \times 10^6$).

Figure 1.1: Computational results indicating effect of flap deflection on aerodynamic performance [14].

reduce or eliminate separation over the flap [15]. Small gaps may also be more sensitive to earlier stall than larger gap configurations [11]. Experimental tests indicate the best gap size is typically between 1.3% and 2.0% system chord [11, 16, 17]. Effect of the gap size is presented in Fig. 1.2, taken from Ashby [11]. Spaid concluded that a slat gap can accelerate the U/U_∞ to as high as 3.0 while flap gaps can accelerate U/U_∞ to values in excess of 2.0 [15]. Computational models have been developed which capture complex high-lift aerodynamics fairly well, though work is continuing on turbulence modeling to more accurately predict separation and complex wake interactions.

Performance as a result of the overhang of the flaps has not been studied in as much detail as the effect of the gap. A positive overhang corresponds to an element which is tucked under the previous element while a negative overhang indicates the leading edge of an element is aft of the trailing edge of the previous element. The location of the flap was first discussed by Smith in 1975 [5]. According to Lin, et al. [16],

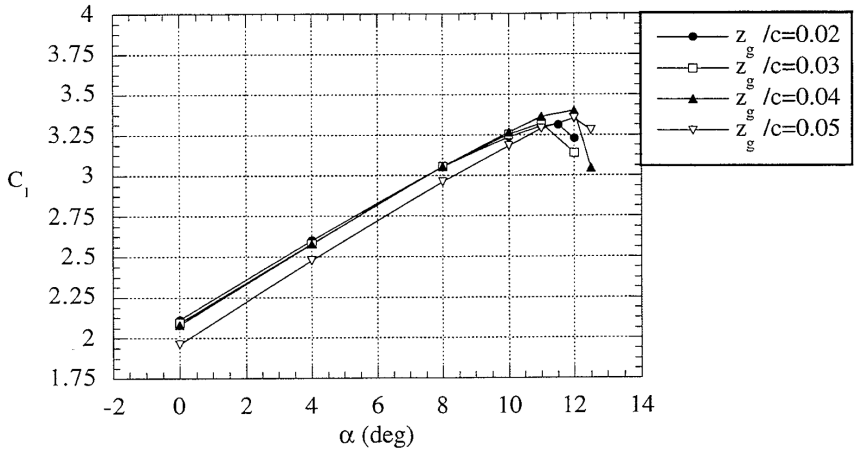

Figure 1.2: Experimental results indicating effect of gap size on aerodynamic performance [11].

the best overhang value is approximately -0.25%, which indicates the leading edge of the flap is behind the trailing edge of the previous element. If the overhang is too far behind the trailing edge, the flow will not be accelerated around the leading edge of the flap and the flap will not create as much lift as compared to a case with a smaller overhang [16]. Positive overhangs were studied by Coiro, et al., and results indicate the best overhang is between 2% and 3% [17]. The researchers did not study cases with a negative overhang. They also observed that an overhang that is too far forward will accelerate the flow over the lower surface of the previous element and cause a decrease in lift of the previous element.

Wake interactions off the surface of multielement airfoils can be highly complex, difficult to predict, and challenging to measure. Spreading and merging wakes shed from the different elements can have a strong effect on the pressure field and can also affect the value of $C_{l_{max}}$ [15, 18, 19]. In general, performance decreases if the wakes of the main element and the flaps interact in any manner while research indicates that the effect of the slat wake merging with the main element wake is minimal [15]. Experimental investigations by Nakayama, et al. indicate that the wake of the main element is the largest in momentum deficit and width [19]. The pressure field off the surface of the airfoil system is driven by the wake of the main element, the wake of the jet through the gaps, and the flap wake [19]. Merging flows and separation can dominate the flow field [18]. Research performed in NASA Langley's Low Turbulence Pressure Tunnel (LTPT) indicates that wake development and structure is highly dependent on Reynolds number of the flow [20]. Chin, et al. found that a lower Reynolds number can result in larger wakes and more off the surface flow reversal [20]. In addition, they found that a larger flap gap yields a smaller main element wake resulting in less wake reversal and less wake merging. It is difficult to accurately model complex and merging wakes. Results presented by Bucci, et al. indicate the multielement computational tool MSES calculates the wake trajectory reasonably well but does not predict the wake development accurately [21, 22, 23]. Some computational modeling researchers have had difficulty modeling the wake and the interacting shear layers of the multielement system [24, 25].

The low momentum wake of an upstream element can be adversely affected by the pressure gradients in the field of a downstream element. If the adverse pressure gradient is too great, the low momentum wake of the upstream element may experience an off-the-surface flow separation. This separation is known as wake bursting. Off-the-surface flow bursting has been a topic of interest since originally discussed in A.M.O. Smith's classic high lift aerodynamics paper [5]. Wake bursting effectively decambers the airfoil system and leads to a loss in lift [26, 27]. The burst wake is a region where static pressure P_0 drops and where the local mean velocity may approach zero or may even be negative [27, 28]. An experimental facility was constructed by Schneider, et al. to study the wake bursting phenomenon over multielement airfoils [29]. Experiments

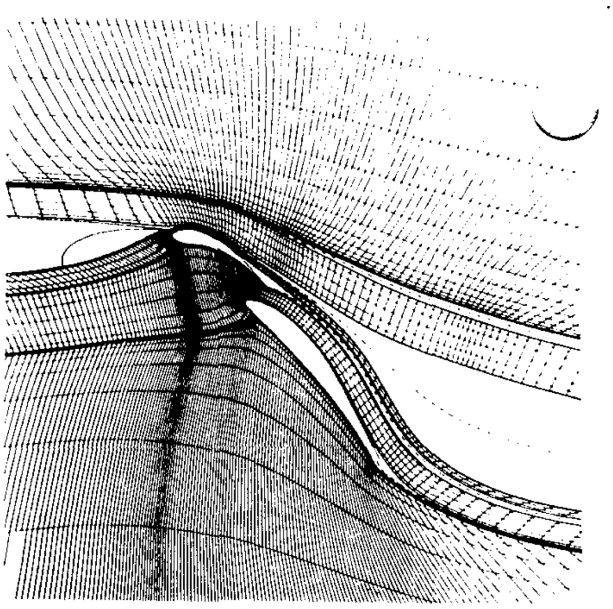

Figure 1.3: MSES streamline grid indicating main element wake bursting [22].

indicated the presence of two momentum deficit regions behind the multielement system; one was the wake of the airfoil system and the other was the burst wake. Results suggest a smaller gap can cause the wake of the main element to interact with the flap and maintain flow attachment instead of bursting and separating [29]. Additional tests by Schneider and Hoffenberg indicate the wakes in an adverse pressure gradient thicken and the momentum deficit grows as the adverse pressure gradient strengthens [30]. Moveable tunnel walls have also been used to impose a pressure gradient on the flow field, and results from these studies indicate that the wake thickness can grow by up to a factor of three when wake bursting was observed [26]. Tests in wind tunnels are influenced by the presence of wind tunnel walls and highly curved flow fields may lead to a separation of the flow off the side wall and might require wall suction to maintain flow attachment over the walls [28]. Wake bursting is predicted by Navier-Stokes computational tools and also viscous/inviscid flow field solvers [22, 31]. As discussed by Drela, the computational tool MSES can predict wake bursting in the inviscid grid region, as shown below in Fig. 1.3 [22].

Design of high lift multielement airfoils has been performed with various different methods. Ragheb, et al. used the inverse conformal mapping PROFOIL/MFOIL suite of programs to design high lift airfoils discussed in this thesis [32]. Inverse viscous Navier-Stokes optimization codes have been employed to optimize the multielement airfoil system for high lift [18, 33]. Different methods are desired for different reasons and an airfoil designer must choose the design method which fits the requirements for the scope of the project.

Research presented in this thesis was experimental in nature. Wind tunnel tests were performed on two different multielement airfoil configurations for application to the root section of megawatt-scale wind turbines. A three-element configuration consisting of a main element and two flaps was tested and a four-element system incorporating an additional strut was tested. Tests were performed in an effort to understand the relationship between gap, overhang, and relative deflection angles and the aerodynamic performance of the system.

Chapter 2

Experiment Design and Methodology

This chapter describes the setup for the experiments performed in this research project. The equipment and facility are discussed as well as a detailed description of two new systems which were manufactured for the tests. Baseline airfoil systems are highlighted and important parts of multielement airfoil geometry definition are presented. A short discussion of methods used to generate the test matrix is presented but the actual test matrix is presented in Chapter 3.

2.1 Facilities

Experiments conducted for this study were performed in the Aerodynamics Research Laboratory at the University of Illinois at Urbana–Champaign. The laboratory is divided into a control room, from where the data acquisition is monitored, and a large high bay room that contains two subsonic wind tunnels. A small model shop is adjacent to the control room. An overview of the lab is presented in Fig. 2.1.

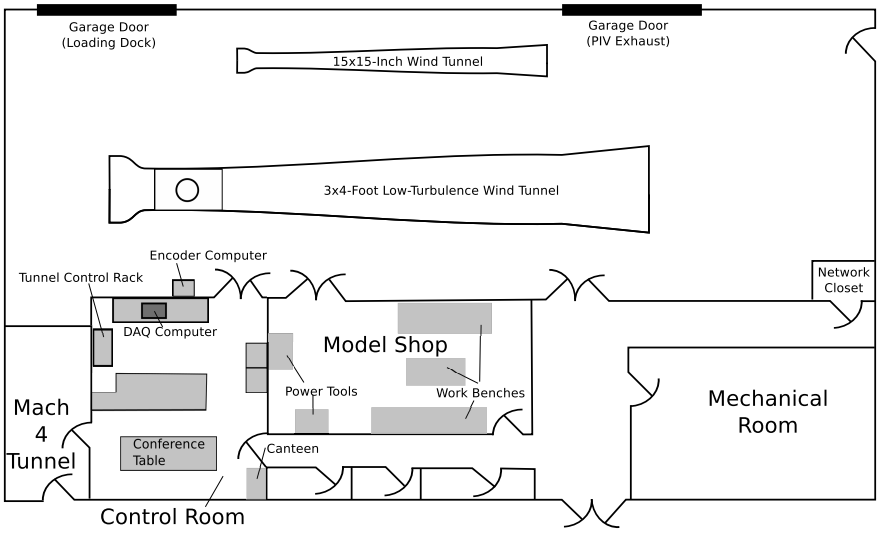

Figure 2.1: University of Illinois Aerodynamics Research Laboratory.

2.1.1 Wind Tunnel

Aerodynamic tests were executed using a subsonic, low-turbulence, open-return-type wind tunnel with a rectangular test section measuring 2.8 ft × 4.0 ft along a downstream distance of 8.0 ft. The downstream section of the test section is 0.5-in wider than the upstream end to account for boundary layer growth along the walls. The contraction ratio of the tunnel is 7.5:1. A schematic of the wind tunnel is displayed in Fig. 2.2. To ensure good flow quality, the air passes through a 4-in thick honeycomb mesh and also four stainless steel screens. Presence of these screens reduces the empty test section turbulence intensity to less than 0.1% at all operating speeds.

Tunnel speeds were set by a five-bladed metal fan driven by a 125-HP AC motor controlled by an ABB ACS 600 Low Voltage AC Drive. A maximum fan speed of 1,200 RPM creates an empty test section flow speed of approximately 165 mph or a maximum Reynolds number based on an 18-in chord of approximately 2×10^6. Reynolds number for the airfoil tests was calculated using the equation

$$Re_{system} = \frac{\rho_{amb} U_\infty c_{sys}}{\mu_{amb}} \tag{2.1}$$

Wind tunnel tests were performed at a given Reynolds number. The Reynolds number was computer-controlled to within 0.5% during all tests. Airspeed in the test section was determined by measuring the pressure difference (ΔP) between the settling section (P_{ss}) and the test section (P_{ts}). Measurements of ΔP were acquired using a DTC Initium differential pressure module system and also a Setra 239 differential pressure transducer. Four pressure taps downstream of the screens in the settling section were connected to a single tube to acquire an average pressure in the settling section. Steady and inviscid flow between the

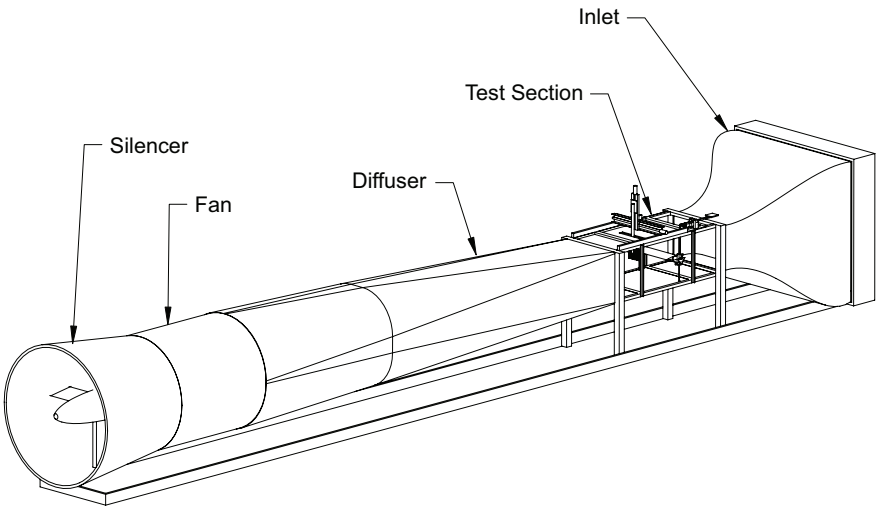

Figure 2.2: University of Illinois low turbulence wind tunnel.

settling section and test section were assumed. Calculations using the inviscid conservation of mass (Eq. 2.2) and Bernoulli's equation (Eq. 2.3) yield the test section velocity (Eq. 2.4).

$$A_{ss}U_{ss} = A_{ts}U_{ts} \tag{2.2}$$

$$\frac{1}{2}\rho U_{ts}^2 + P_{ts} = \frac{1}{2}\rho U_{ss}^2 + P_{ss} \tag{2.3}$$

$$U_{ts} = \sqrt{\frac{2(P_{ss} - P_{ts})}{\rho_{amb}\left(1 - \left(\frac{A_{ts}}{A_{ss}}\right)^2\right)}} \tag{2.4}$$

It is noted in Eq. 2.4 that A_{ts}/A_{ss} is the recripocal of the contraction area ratio. Density of the air was calculated assuming an ideal gas by the equation given by,

$$\rho_{amb} = \frac{P_{amb}}{RT_{amb}} \tag{2.5}$$

In Eq. 2.5, the variable R is the ideal gas constant for air, ambient temperature (T_{amb}) was measured using an Omega thermocouple located in the high bay, and ambient pressure (P_{amb}) was measured using a Setra 270 pressure transducer in the control room.

The dynamic pressure, q_∞, was calculated in the test section. Dynamic pressure is defined as

$$q_\infty = \frac{1}{2}\rho_\infty U_\infty^2 \tag{2.6}$$

where ρ_∞, the freestream density, is assumed to be ρ_{amb}. Application of incompressible conservation of mass, Eq. 2.2, and Bernoulli's equation, Eq. 2.3, yielded

$$q_\infty = \frac{1}{2}\rho_\infty U_{ts}^2 = \frac{P_{ss} - P_{ts}}{1 - \left(\frac{A_{ts}}{A_{ss}}\right)^2} \tag{2.7}$$

where the subscripts ts and ss correspond to the test section and settling section respectively.

2.1.2 Wind Tunnel Data Acquisition System

Software to control the tunnel and collect data for this test was written using National Instruments LabView programming language. The program incorporated a graphical user interface that allowed the user to perform various tasks and actions by clicking the display. Data were collected on a Dell Precision T3400 computer

with an 2.83 GHz Intel®quad-core CPU which ran the Windows XP 32-bit operating system. Commands sent to the three-component force balance, variable frequency drive, IDC drive, and Velmex controller were all sent via RS-232 serial communication. Wake pressure measurements were collected with the use of ethernet port communication to the DTC Initium device. Data collected from the three-component balance and secondary force balance were converted by use of a National Instruments analog to digital (A/D) board.

2.1.3 Main Wind Tunnel Force Balance

An external three-component force and moment balance was used to measure lift, drag, and pitching moment of the airfoil system. Fabrication of the balance was performed by Aerotech ATE Limited, of Heathfield, U.K.

The airfoil system was attached to the force balance with mounting brackets and measurements were taken using three load cells that measured forces and in the normal and axial directions as well as moment about center of the plate. Additional information regarding alignment of the balance and the balance coordinate system can be found in Noe [34]. Loads can be acquired in three different load ranges, including low, medium, and high, as shown below in Table 2.1. Proper setting of the balance was necessary to maximize accuracy without overloading the balance. The high range setting was used for all experiments presented in this report.

Each load cell had a full-scale voltage range of ±20 mv. Signals were low-pass filtered at 1 Hz and amplified to a full-scale voltage of ±5 V by use of a signal conditioner. Angle of attack, α, of the model was controlled with a mechanical turntable which was controllable to ±0.1 deg. Position was measured with a rotary optical encoder with a resolution of 0.001 deg. Balance load measurements were taken at a sample rate of 100 Hz for a period of 5 sec and were subsequently averaged.

External balance tares were measured at 1.0 deg increments for the angle-of-attack range tested. Voltage tares were acquired for each of the three components and the balance was subsequently rezeroed. Measurements taken during a run subtracted the previously measured tare voltage at the corresponding angle of attack. Voltage out of the signal conditioner (V_{0i}) was multiplied by a range ratio (RR_i) which yielded a

Table 2.1: Three-Component Balance Load Ranges

	High Range	Medium Range	Low Range
Normal Force	±450 lb	±225 lb	±90 lb
Axial Force	±90 lb	±55 lb	±18 lb
Pitching Moment	±45 ft-lb	±30 ft-lb	±15 ft-lb

Table 2.2: Three-Component Balance Range Ratios

	High Range	Medium Range	Low Range
Normal, RR_N	1	0.4944	0.2046
Axial, RR_A	1	0.6278	0.2173
Moment, RR_M	1	0.6755	0.3413

scaled voltage (V_i), as shown in Eq. 2.8. Values of the range ratio were determined from the load setting and are shown in Table 2.2.

$$V_i = V_{oi} \cdot RR_i \tag{2.8}$$

The resulting scaled voltages were evaluated in a second-order calibration matrix of the force balance shown in Eq. 2.9.

$$\begin{Bmatrix} F_N \\ F_A \\ M \end{Bmatrix} = \begin{bmatrix} 37.7 & 0.01359 & -0.2095 & 0.01094 & 0 & -0.000865 \\ -0.1607 & 8.3125 & -0.01638 & 0.007084 & 0 & 0.007660 \\ -0.01299 & -0.005521 & 1.247 & -0.002122 & 0 & 0.0001497 \end{bmatrix} \begin{Bmatrix} V_N \\ V_A \\ V_M \\ V_N^2 \\ V_A^2 \\ V_M^2 \end{Bmatrix} \tag{2.9}$$

Evaluation of the calibration matrix in Eq. 2.9 yielded normal force (F_N), axial force (F_A), and pitching moment about the center of the cruciform (M). These were subsequently reduced into lift (L), drag (D), and pitching moment about the quarter-chord of the system ($M_{c_{sys}/4}$). The variables x_{offset} and y_{offset} correspond to the distance the quarter-chord of the system is translated from the center of the cruciform.

$$L_{main} = F_N \cos\alpha - F_A \sin\alpha \tag{2.10a}$$

$$D_{main} = F_N \sin\alpha + F_A \cos\alpha \tag{2.10b}$$

$$M_{c_{sys}/4,main} = M + x_{offset} F_N + y_{offset} F_A \tag{2.10c}$$

It is noted that the forces and moments presented in Eq. 2.10(a–c) only correspond to forces and moments captured by the main balance and do not account for the secondary force balance.

2.1.4 Force and Moment Calculations

Forces and moments calculated by the main balance, presented in Eq. 2.10(a–c), were combined with loads captured from a secondary force balance (SFB). A discussion of the SFB is presented in Section 2.2. The difference between the lift vectors of the SFB and the main balance was determined to be no more than $\pm$ 0.024 deg, as discussed in Section 2.2. Values of x_{offset} and y_{offset} were equal for the top and bottom of the model. Total forces and moments for the model were calculated using

$$L_{tot} = L_{main} + L_{SFB} \tag{2.11a}$$

$$D_{tot} = D_{main} \tag{2.11b}$$

$$M_{c_{sys}/4,tot} = M_{c_{sys}/4,main} + L_{SFB} \cdot x_{offset} + L_{SFB} \cdot y_{offset} \tag{2.11c}$$

Non-dimensional coefficient of lift (C_l), coefficient of drag (C_d), and quarter-chord pitching moment coefficient ($C_{m,c_{sys}/4}$) were calculated by dividing the dimensional forces and moments by the freestream dynamic pressure (q_∞) and the model planform area (S). The pitching moment was also divided by the model chord (c). Drag data were measured and collected for the wind tunnel balance but results will not be presented in this report as wake profiles were used to calculate the drag of the model. Values of drag from the balance included the drag of the large flap support clamps which yielded higher drag than the wake survey system. Two-dimensional airfoil section coefficients were obtained from the standard equations given by

$$C_l = \frac{L_{tot}}{q_\infty S} \tag{2.12}$$

$$C_d = \frac{D_{tot}}{q_\infty S} \tag{2.13}$$

$$C_m = \frac{M_{tot,c_{sys}/4}}{q_\infty S c} \tag{2.14}$$

2.1.5 Wake Survey System

Drag measurements were taken using a wake rake traverse system. A set of 59 total pressure probes were installed in the wake rake, as seen in Fig. 2.3. The probes were manufactured from straight, thin-walled tubing with an 0.04-in outer diameter. The tubes were aligned parallel to the flow of air with the probe

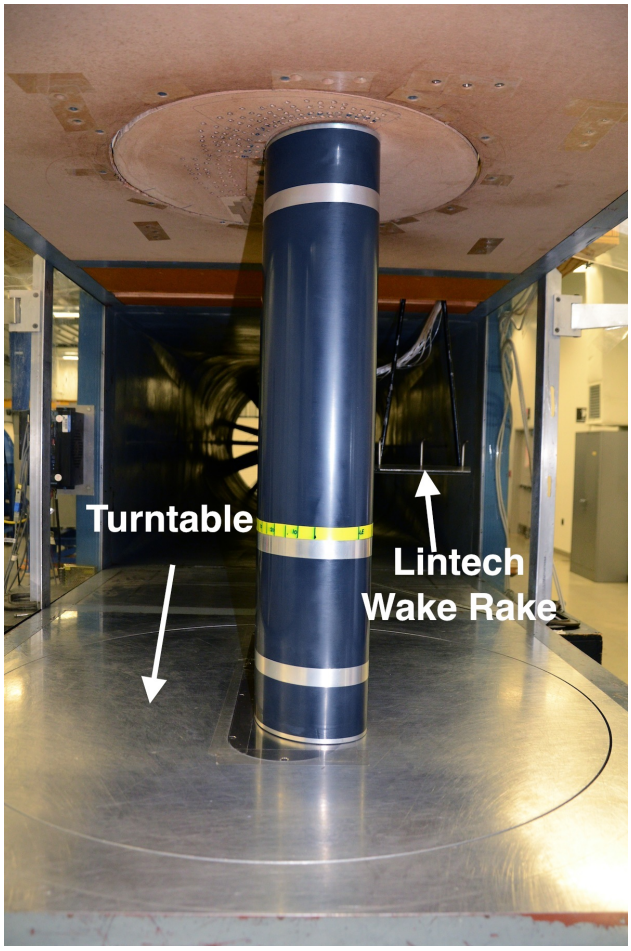

Figure 2.3: Location of Lintech wake rake relative to airfoil.

pointing upstream. Probes were used to measure pressure deficits generated by the model. The span of the wake rake was 9.75 in. The tubes were spaced at 0.27-in increment for the six outer probes and 0.135-in spacing in the middle of the rake wake. The two-axis wake raked moved in the spanwise and chordwise directions. Two Lintech traverse axis systems were controlled with an IDC S6962 Stepper Motor Drive. A box was constructed around the outside of the Lintech system to minimize air leaks into the tunnel. Wake measurements were taken using the DTC Initium system and two ± 0.35 psi pressure modules.

Wake profiles were taken for the full span of the tunnel in an effort to capture any secondary wake bursting that may occur off the surface of the airfoil system. A computer program was used to move the Lintech system to predefined spanwise locations where wake profiles were measured. The position of the wake rake was controllable to within ± 0.001 in.

2.1.6 Drag Calculation

Two-dimensional momentum deficit theory, as discussed by Jones [35] and Schlichting [36], was used to determine the drag of the airfoil by integrating across the wake. Momentum deficit theory integrates a wake profile to calculate a total momentum loss. A control-volume analysis representation is shown in Fig. 2.4.

A plane, noted by the subscript 1, perpendicular to U_∞ was assumed to exist far downstream of the airfoil model in which static pressure in the wake (P_w) was assumed to be equal to the freestream pressure (P_∞). The drag can be calculated by integrating the difference in velocities between the freestream and the velocity in the plane as shown by

$$D = \int \rho u_1 (U_\infty - u_1)\, dy_1 \tag{2.15}$$

A second plane is assumed to exist parallel to plane 1 but closer to the airfoil model. Wake rake measurements were taken in plane 2. Conservation of mass was applied in the differential form

$$u_1 dy_1 = u_2 dy_2 \tag{2.16}$$

Substitution of Eq. 2.16 into Eq. 2.15 yields the drag at plane 2 as

$$D = \int \rho u_w (U_\infty - u_1)\, dy \tag{2.17}$$

Total pressure in the freestream, wake plane, and plane 1 could be calculated by

$$P_\infty = \frac{1}{2}\rho u_\infty^2 = P_{0,\infty} \tag{2.18a}$$

$$P_\infty = \frac{1}{2}\rho u_1^2 = P_{0,1} \tag{2.18b}$$

$$P_\infty = \frac{1}{2}\rho u_w^2 = P_{0,w} \tag{2.18c}$$

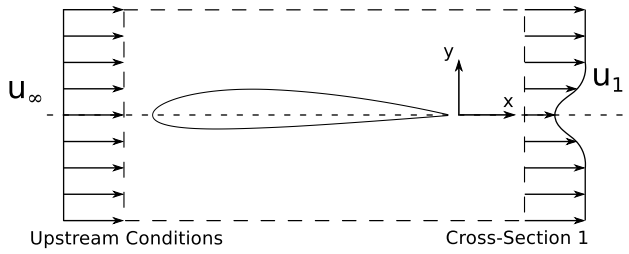

Figure 2.4: Control volume for the two-dimensional momentum deficit method.

It is assumed no pressure losses exist between plane 1 and the wake plane where $P_{0,1} = P_{0,w}$. Eqs. 2.18(a-c) can be solved in terms of the velocities U_∞, u_1, and u_w and substituted into Eq. 2.17 such that the drag per unit span was calculated as

$$D = 2 \int \sqrt{(P_{0,w} - P_w)} \left(\sqrt{(P_{0,\infty} - P_\infty)} - \sqrt{(P_{0,w} - P_\infty)} \right) dy \tag{2.19}$$

The assumption that $P_w = P_\infty$ and combination of Eq. 2.18 yielded

$$q_w = q_\infty - \left(P_{0,\infty} - P_{0,w} \right) \tag{2.20}$$

Equation 2.17 can be expressed in terms of dynamic pressure from Eq. 2.20 so the drag per unit span was

$$D = 2 \int \sqrt{q_\infty - (P_{0,\infty} - P_{0,w})} \left(\sqrt{q_\infty} - \sqrt{q_\infty - \left(P_{0,\infty} - P_{0,w} \right)} \right) dy \tag{2.21}$$

The drag equation expressed in Eq. 2.21 is preferred over the form expressed in Eq. 2.17 as the pressure difference $(P_{0,\infty} - P_{0,w})$ can be measured in the wake survey. Because pressure modules used to capture wake information were referenced to the ambient pressure, the ΔP value returned from the modules was $(P_{o,w} - P_{atm})$. Total pressure at the edge of the wake was assumed to be equal to the total pressure in the freestream, so the wake system measured the pressure difference $(P_{0,\infty} - P_{atm})$. The pressure difference between the freestream and the wake plane was shown to be =

$$P_{0,\infty} - P_{0,w} = \left(P_{0,\infty} - P_{atm} \right) - \left(P_{0,w} - P_{atm} \right) \tag{2.22}$$

A numerical trapezoidal integration scheme was used to evaluate Eq. 2.21. The incremental drag value between node i and $i+1$ was calculated by

$$\Delta D = \left[\sqrt{q_\infty - \left(P_{0,\infty} - P_{0,w_i} \right)} \left(\sqrt{q_\infty} - \sqrt{q_\infty - \left(P_{0,\infty} - P_{0,w_i} \right)} \right) + \right.$$
$$\left. \sqrt{q_\infty - \left(P_{0,\infty} - P_{0,w_{i+1}} \right)} \left(\sqrt{q_\infty} - \sqrt{q_\infty - \left(P_{0,\infty} - P_{0,w_{i+1}} \right)} \right) \right] \left(y_i - y_{i+1} \right) \tag{2.23}$$

The total drag per unit span was determined by summing all the incremental sectional drag values for the number of points collected n. It is noted that the value of n is greater than the number of probes as the wake rake collected three sets of data across the tunnel as the wake rake did not span the tunnel

$$D = \sum_{i=1}^{n_{nodes}} \Delta D_i \tag{2.24}$$

The coefficient of drag was calculated using the standard equation

$$C_d = \frac{D}{q_\infty c} \tag{2.25}$$

2.1.7 Tunnel Corrections

Aerodynamic performance data of airfoils in a finite volume wind tunnel is different than performance data of the airfoil in freestream. Wind tunnel walls interfere with the flow around the airfoil and corrections must be made to account for the effect of the finite test section. Corrections used in this research were based on those discussed by Barlow, Rae, and Pope [37].

Solid Blockage

Wind tunnel walls restrain the flow through the test section and the wind tunnel model reduces the area through which the flow can pass compared to freestream conditions. Simple application of Bernoulli's equation indicates that a decrease in cross-sectional area causes an increase in local velocity known as solid blockage (ϵ_{sb}). The magnitude of the solid blockage is a function of model thickness, the thickness distribution, model size, and angle of attack. Camber of the model does not affect solid blockage. Multiple methods have been developed to account for solid blockage which have been extensively discussed by Garner, et al. [38] Two-dimensional corrections developed by Thom were used in this research [39]. The solid blockage was corrected by

$$\epsilon_{sb} = \frac{K_1 \times (\text{model volume})}{A^{3/2}} \tag{2.26}$$

where K_1 is 0.52 for a model spanning the tunnel height as noted in Barlow, Rae, and Pope [37]. The cross-sectional area of the test section is denoted by A. Solid blockage effects the value of C_l, C_d, and C_m as discussed in Section 2.1.7.

Wake Blockage

Drag on the airfoil system creates a wake with a mean velocity lower than that of the freestream conditions. Application of the conservation of mass law suggests that the velocity outside the wake in a finite cross-section must be greater than the freestream condition to maintain flow continuity. Bernoulli's relationship suggests that the higher velocity flow outside the wake has a lower pressure than the freestream condition

which imposes a pressure gradient on the airfoil model. The pressure gradient on the model results in a velocity increase at the model. The value of wake blockage is a function of ratio of the wind tunnel model to the test section height c/h. Maskell [40] developed a correction based upon a mirror and estimated the wake blockage by using the equation

$$\epsilon_{wb} = \frac{c/h}{2} C_{d,\text{unc}} \tag{2.27}$$

Wake blockage also effects the value of C_l, C_d, and C_m as discussed in Sec. 2.1.7. The effect of both blockage parameters can be expressed as a total velocity increment(ϵ) where

$$\epsilon = \epsilon_{sb} + \epsilon_{wb} \tag{2.28}$$

Streamline Curvature

The wind tunnel floor and ceiling restricts the flow from developing the natural curvature of the streamlines and straightens the flow near the walls. Consequently, the airfoil appears to have more camber than the actual geometry. The increase in camber is approximately 1% for typical airfoil models. As a result of the artificial increase in camber, the values of C_l, C_m, and α are too large. Vortex theory discussed by Barlow, Rae, and Pope [37] suggest that data can be corrected with the streamline curvature correction, σ

$$\sigma = \frac{\pi^2}{48}\left(\frac{c}{h}\right)^2 \tag{2.29}$$

Correction Formulae

Two-dimensional corrections were applied to the measured wind tunnel data points. Corrections were applied for solid blockage, wake blockage, and streamline curvature as discussed in Barlow, Rae, and Pope [37]. The *unc* subscripit in this section corresponds to the uncorrected values while the *cor* subscript represents a corrected value. Corrections for α are dependent upon the streamline curvature such that

$$\alpha_{cor} = \alpha_{unc} + \frac{57.3\sigma}{2\pi}(C_{l,unc} + 4C_{m,unc}) \tag{2.30}$$

Lift must be corrected for streamline curvature and blockage effects where

$$C_{l,cor} = C_{l,unc}(1 - \sigma - 2\epsilon) \tag{2.31}$$

Quarter-chord pitching moment is corrected by streamline curvature and blockage so that

$$C_{m,cor} = C_{m_{\frac{1}{4}},unc}(1 - 2\epsilon) + \frac{1}{4}C_{l,cor} \tag{2.32}$$

Drag is corrected by incorporating the effects of solid blockage and wake blockage where

$$C_{d,cor} = C_{d,unc}(1 - 3\epsilon_{sb} - 2\epsilon_{wb}) \tag{2.33}$$

2.2 Secondary Force Balance

Maximum loads of the main wind tunnel balance are ±450 lb, as discussed in Section 2.1.3. High-lift airfoils operating at full tunnel Reynolds number of 1.85×10^6 may produce higher loads than the maximum rated load of the main balance. To ensure the main balance was not overloaded and to be able to test at higher Reynolds numbers, a secondary force balance (SFB) was designed and constructed for use in the wind tunnel.

A one-dimensional force balance was designed to capture only lift and was unconstrained in drag and pitching moment, as shown in Fig. 2.5. A high capacity THK SHS30 block and rail was used to constrain the system in the lift direction but allow it to freely slide in the drag direction. Moment was unconstrained through use of a rod-end bearing. Forces were captured using a bidirectional load cell, as discussed in Section 2.2.3. Data were taken at a sample rate of 200 Hz for 5 sec and then averaged over the sample time. Tare values were taken of the baseline load cell voltage each degree for which data was taken. Large crossmembers were constructed to span the wind tunnel and support the SFB system.

The SFB was attached to the top of the tunnel. During installation, the SFB system was squared with the front of the tunnel by measuring from each corner of the SFB to the tunnel centerline at the inlet. Measurements were determined to be accurate within ±0.024 deg. As shown in Fig. 2.5, the circular airfoil attachment spar was attached to a rod end bearing with a 1/2-13 bolt. The load cell was attached directly to the load cell bracket which was then connected to the block and rail.

Crossmembers and supporting hardware were assembled as a unit and installed on top of the tunnel. A box was constructed around the SFB to ensure that no air leaked into the wind tunnel through the ceiling. A plywood box was constructed and attached to the ceiling of the tunnel, as shown in Fig. 2.6. Edges of the box were sealed with a combination of silicone caulking, tape, and weather stripping. The top of the box was removable for access to the flap positioning system (FPS) on the top of the tunnel. A new ceiling for the wind tunnel was constructed to allow the SFB to properly attach to the model.

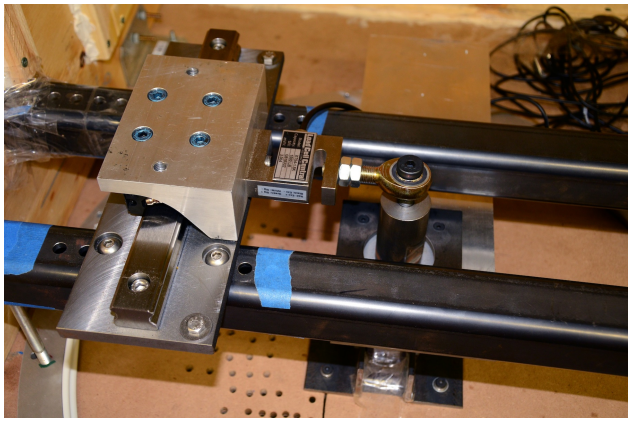

Figure 2.5: SFB system installed on top of the wind tunnel.

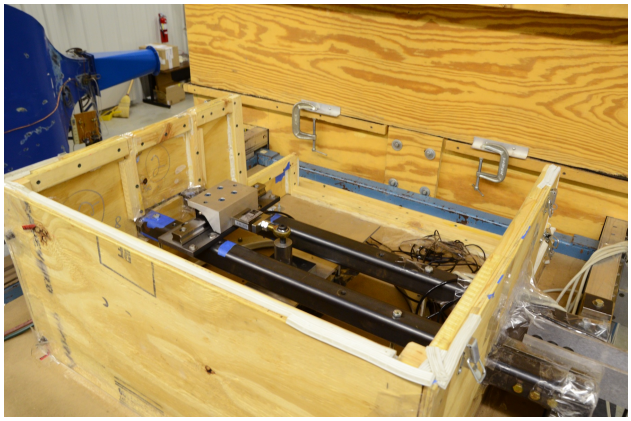

Figure 2.6: SFB and air containment box (with top removed).

Calibration of the SFB was performed by loading the bidirectional load cell with calibration (lifting weights) weights measured to an accuracy of ±0.05 lb. Eight weights were used for a maximum total load of approximately 350 lb. Weights were loaded into a box and hung from the load cell in tension, as shown in Fig. 2.7. The box was attached with an aircraft cable to the load cell with a large eyebolt as shown in Fig. 2.8.

Voltage values returned by the SFB load cell were in the range of ±10 mV. The signal was low-pass filtered at 1 Hz and amplified by a signal conditioner to a full-scale voltage of ±3 V. Load measurements were time-averaged for a period of 5 sec. SFB tares were measured at 1.0 deg increments for the angle-of-attack range tested. Voltage readings during the experiment were subtracted from the tare voltage and then compared with a linear least-squares regression fit over the calibration data to obtain a force. Force measured by the SFB consisted of a lift force and a moment-couple due to translation of the lift vector from the center of the cruciform.

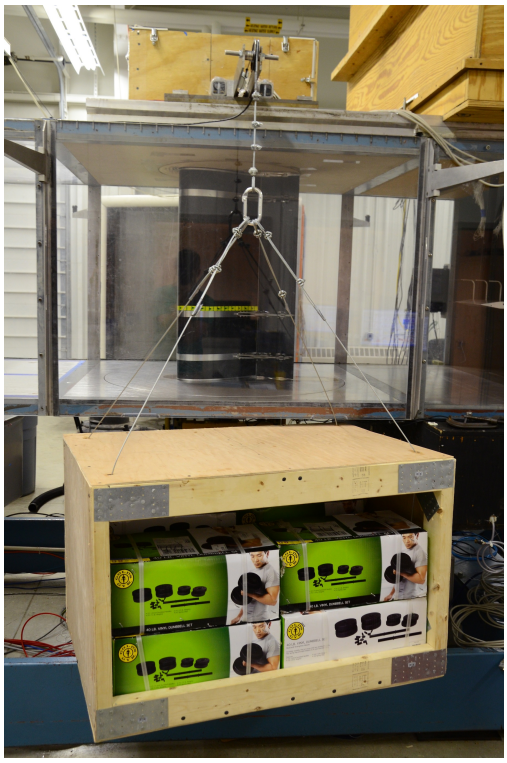

Figure 2.7: SFB in calibration configuration.

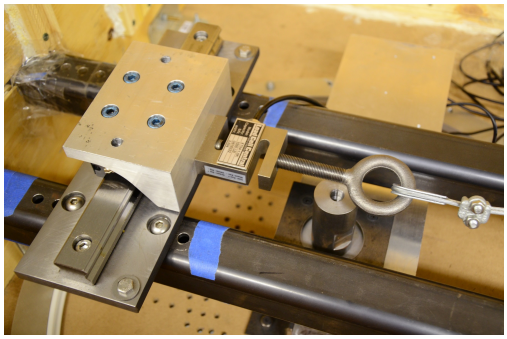

Figure 2.8: SFB calibration configuration attachment device.

2.2.1 SFB Validation

Tests were performed with the SFB and compared to previously-collected data with which the main tunnel balance was originally validated. Airfoil tests were performed with the S809 wind turbine airfoil designed by Somers [41]. The wind tunnel model, shown in Fig. 2.9, was mounted vertically in the tunnel. The chord of the model was 18 in, and mounting points existed on the top and the bottom of the model.

It is noted that several blemishes existed on the leading edge of the airfoil. Wake profiles were taken at least 6-in from these blemishes. Four profiles, spaced at 1-in increments, were captured for each angle

Figure 2.9: S809 airfoil used to validate secondary force balance.

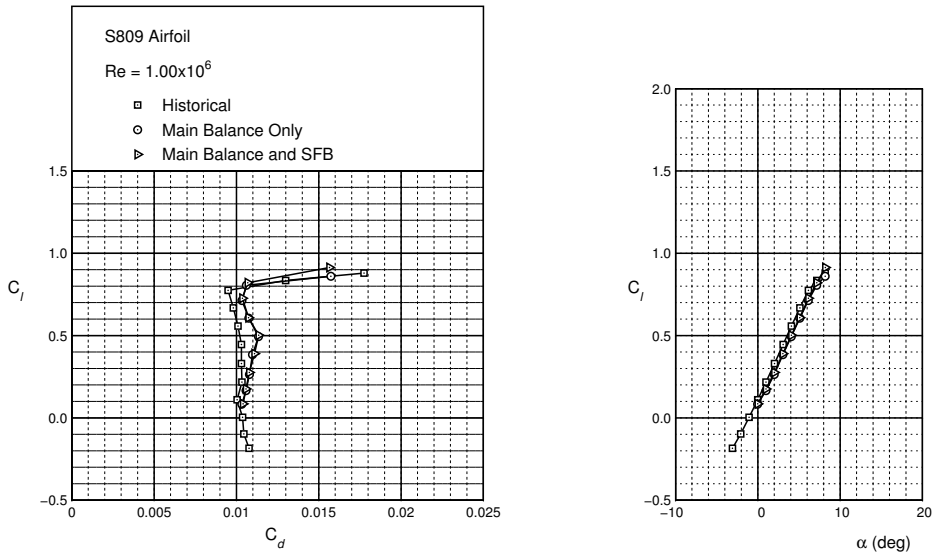

Figure 2.10: S809 airfoil and SFB validation at Re =1×10^6.

of attack. Data were collected using the main balance only as well as the SFB. Historical lift, drag, and moment data were compared against the new data sets at $Re = 1.00 \times 10^6$, 1.50×10^6, and 1.85×10^6, as shown in Fig. 2.10–2.12. The difference between the trials was within the acceptable range.

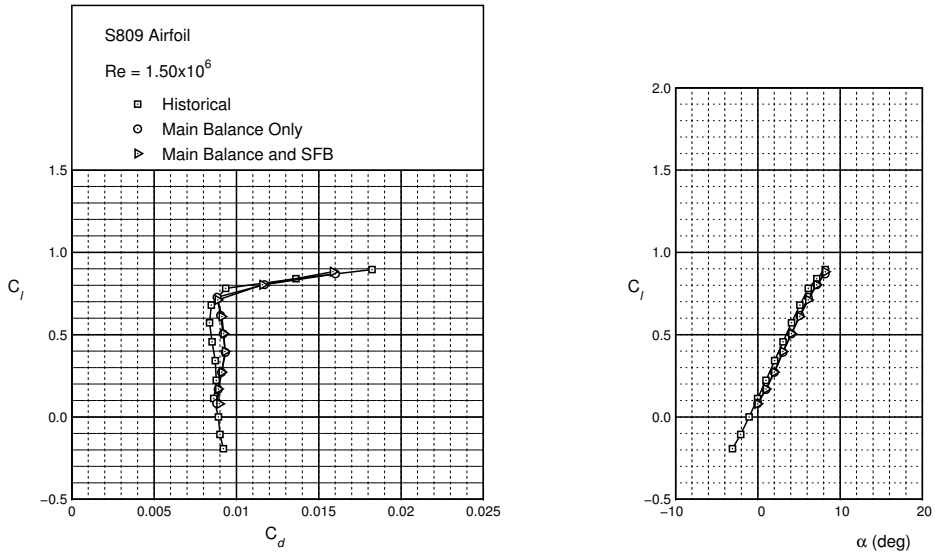

Figure 2.11: S809 airfoil and SFB validation at $Re = 1.5\times10^6$.

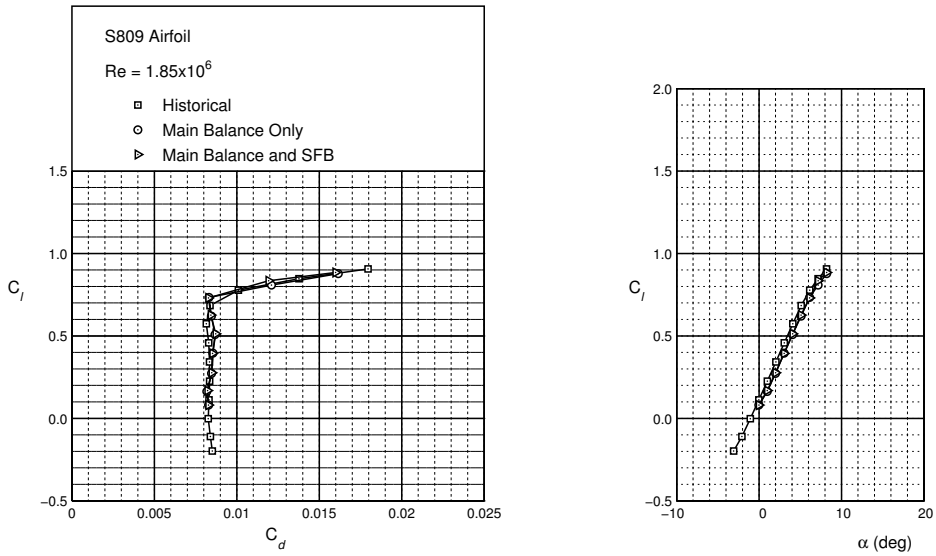

Figure 2.12: S809 airfoil and SFB validation at $Re = 1.85\times10^6$.

2.2.2 Assembly and Usage

The SFB was designed for use with future tests of high-lift airfoils. Airfoil-specific attachment spars will need to be manufactured to attach to the SFB. Two large crossmembers that span the tunnel supported the loads applied by the airfoils. The crossmembers were 48-in long and permanently attached to two support spacers. The spacers provide structural rigidity for the system. Care was taken to square the crossmembers with the support spacers. Spacers were secured to the crossmembers with four $^3/_8$-16 bolts. Red 271 Loctite was applied to the threads of the bolts.

The crossmember assembly was raised to the top of the wind tunnel with a low-capacity $^1/_4$ ton crane. One additional support spacer was added to each side of the SFB, as shown in Fig. 2.13. Spacers were added for this specific research to raise the traverses far enough off the tunnel ceiling; the additional spacers are not necessary for all models. Four $^3/_8$-16 holes were drilled and tapped in the aluminum support structure on the top of the wind tunnel. Four square plate clamps, one in each corner of the SFB, served as large washers. The entire attachment configuration is presented in Fig. 2.13.

Alignment of the SFB was important to ensure that the load cell was capturing forces in the lift direction. After the crossmember assembly was placed on top of the tunnel, it was squared up with the side of the tunnel. Measurements were taken from each upstream corner of the assembly to the center of the tunnel on the ceiling at the inlet to ensure the model was square. The error of angular offset due to measurement resolution was determined to be ± 0.024 deg. Noe discusses the alignment of the main tunnel balance [34].

Attachment of the airfoil models tested to the SFB was performed with a few adaption plates and clamps. An exploded view of the attachment assembly is presented in Fig. 2.14. The assembly contained

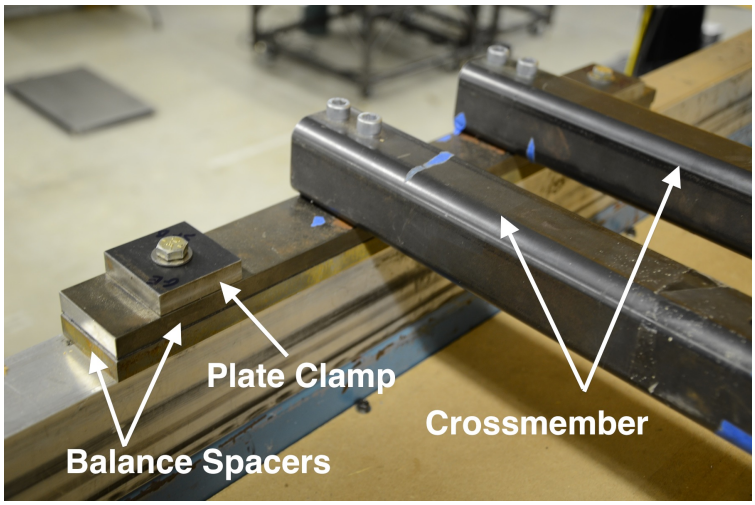

Figure 2.13: SFB attachment configuration.

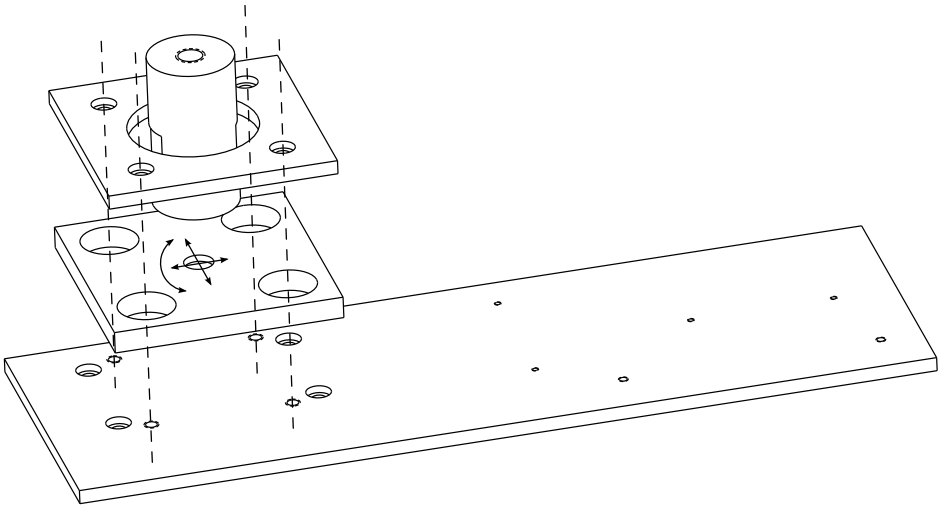

Figure 2.14: Exploded SFB attachment assembly.

a top extension plate, an adjustment place, a circular spar clamp, and a circular spar. The circular spar attached directly to an adjustment plate which had oversized holes placed in it. Four 1/4-20 bolts extended down from the circular spar clamp, through the oversized holes in the adjustment plate, and into four tapped holes in the top extension plate. Location of the adjustment plate was important to ensure that the circular spar at the top of the model was located at the center of rotation for the entire system. If the circular spar was not located at the center of rotation, the load cell may be damaged due to large forces placed on the load cell as the entire system rotated. As shown above in Fig. 2.5, a 1/2-13 bolt connects the rod end bearing to the circular spar. Two recessed flat surfaces on the circular spar allowed a crescent wrench to be used to tighten the spar onto the rest of the assembly.

2.2.3 Load Cell Selection

Load cells used in the SFB were chosen to accurately capture lift forces applied by the model and relieve lift forces applied to the main wind tunnel balance. Capacity of the load cell was selected to ensure that the SFB relieved some of the load from the main wind tunnel balance without overloading the load cell or the main wind tunnel balance. A 750-lb capacity XTS4-750 load cell, shown in Fig. 2.15, manufactured by Load Cell Central was chosen for use in the SFB. Validation trials presented in Section 2.2.1 verify that the use of the 750-lb capacity load cell was adequate for a range of Reynolds number from 1.0 $\times 10^6$ to 1.85 $\times 10^6$. High-lift airfoils tested by future researchers may require an alternate load cell.

The stiffness of the main wind tunnel balance was not known when the SFB was originally designed. To ensure that loads were balanced between the SFB and the main wind tunnel balance, a system was designed

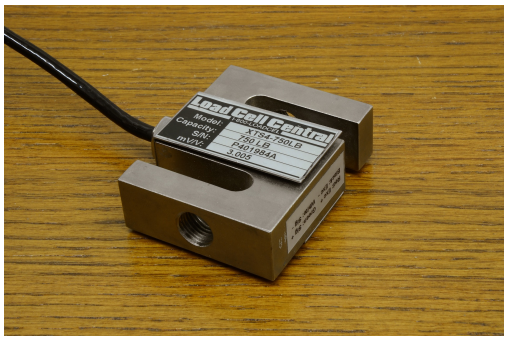

Figure 2.15: XTS4-750 load cell used to measure lift.

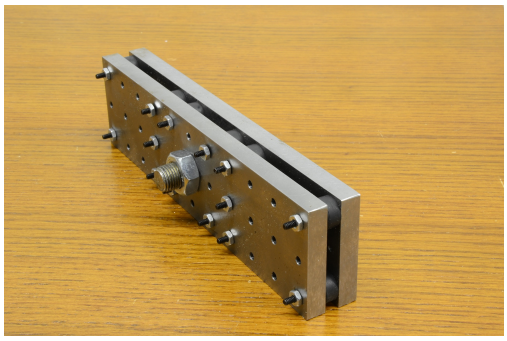

Figure 2.16: Bumper plate softening system.

to soften the SFB so more of the load would be carried by the main wind tunnel balance. The system, shown in Fig. 2.16, consisted of two metal plates and numerous rubber bumpers. Rubber bumpers were placed between two metal plates. Clearance holes were placed in the plate closest to the load cell while tapped holes were placed in the plate closest to the block and rail. A 4-40 nut secured the two plates and the rubber bumper together.

2.2.4 Requirements for Future Models

The SFB was designed and manufactured for ease of use in future research projects. As shown in Fig. 2.17, the span of the model must measure 33.50 in. If the model were longer, it would not fit inside the wind tunnel. If the model span was too short, tip effects would cause three-dimensionality in the flow field. Spars extended 4.21-in below the model and attached to the balance cruciform plate. A spar and adaption plug on the top of the model extended for 5 in. The plug on top of the spar was 0.375 in thick; the spar without the plug was 4.625-in long. The spar cap plug was attached to the top extension plate to which the traverses were attached. The assembly presented above in Fig. 2.14 attached to the top of the spar cap plug. An eyebolt was screwed into a 1/2-13 hole in the spar cap to provide a location to hoist the model. The main spar was placed behind the secondary spar in an effort to reduce pitching moment on the cruciform balance.

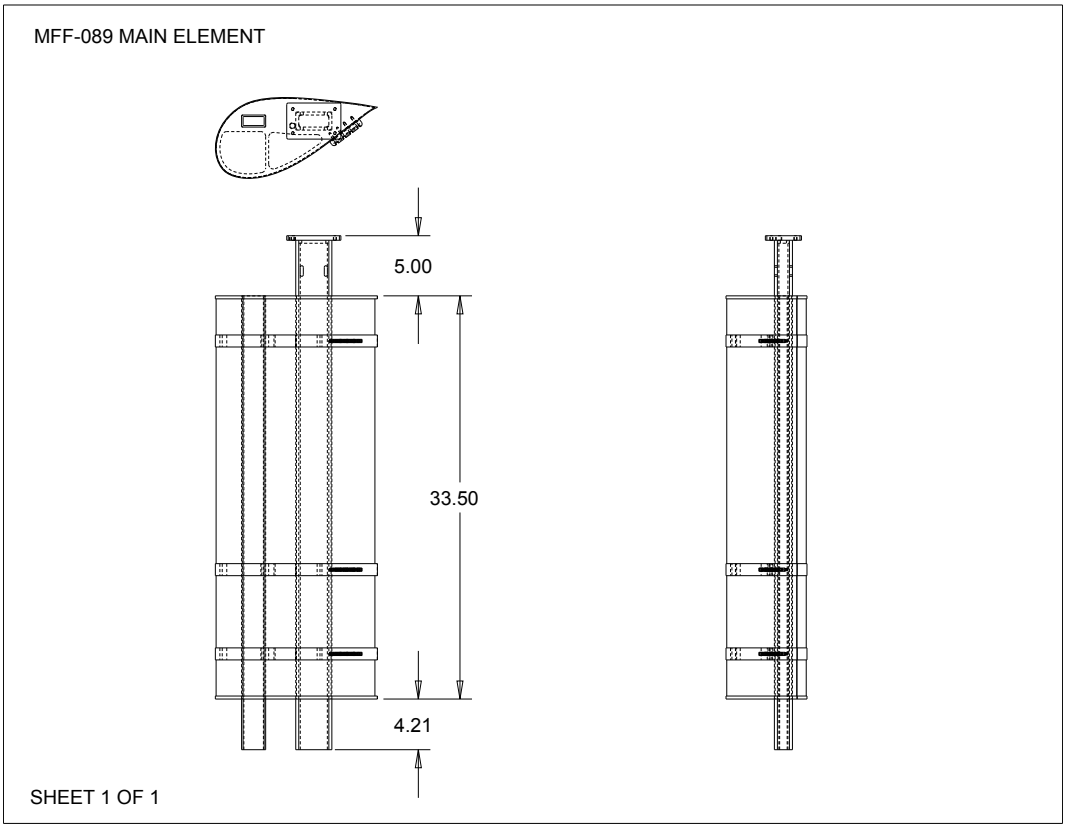

Figure 2.17: Schematic of MFF-089 main element used with SFB.

Future models need not have the main spar behind the secondary spar to use the secondary force balance as the SFB lines up with the center of rotation of the cruciform. The total span of the model was 33.5 in for all elements.

2.3 Flap Positioning System

The FPS was designed to accurately move flaps in three degrees of freedom. Each flap was able to independently traverse in the x_{tunnel} and y_{tunnel} directions as well as rotate in δ. Multielement aerodynamics are highly sensitive to the location of the flaps and a small difference in flap deflection can have large effects on the performance of the system. To minimize deflections and reduce spanwise dependency of flap location, traverses were attached to the model on the top and bottom of the tunnel. Two traverses, one per flap, were installed on the top of the wind tunnel and two traverses, one per flap, were installed on the bottom of the wind tunnel. A wood box was constructed to enclose the traverses on the top of the wind tunnel. The wind tunnel and traverse locations are shown below in Fig. 2.19. Multiple clamps attaching the main element to the flaps were also used.

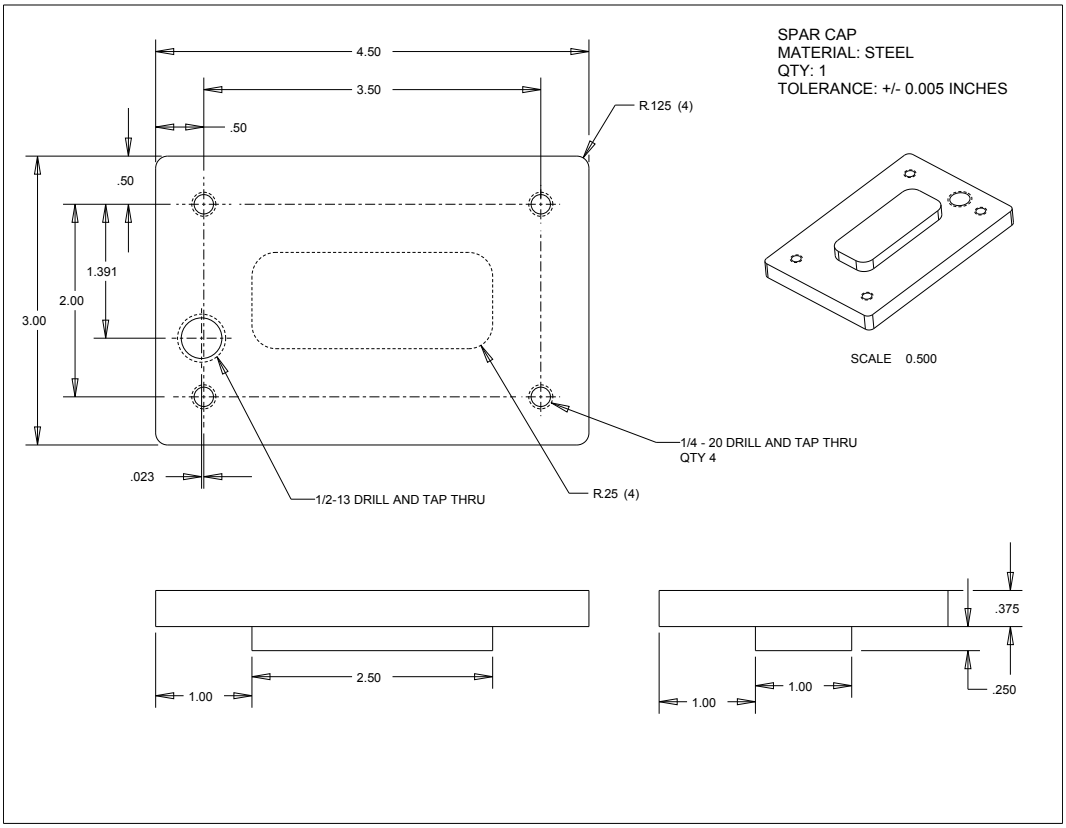

Figure 2.18: Schematic of MFF-089 spar cap plug.

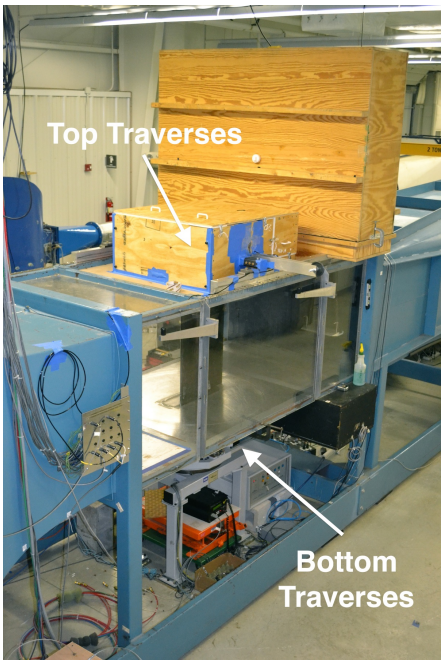

Figure 2.19: Location of traverses in wind tunnel.

2.3.1 Traverses

Four traverses were fabricated for use in the FPS. These four traverses, shown below in Fig. 2.20, consist of two pairs of top and bottom traverses. Each flap was supported by a traverse on the top and the bottom of the wind tunnel; these traverses were independent of each other. Traverses were installed on the top and on the bottom of the wind tunnel to reduce the amount of deflection of the flaps as multielement aerodynamics are very sensitive to small changes in flap placement. External dimensions of each traverse measured approximately 3.5-in wide, 3.5-in long, and 2.0-in tall. Size was minimized so the traverses could fit onto the existing wind tunnel balance. Each traverse consisted of multiple machined components, gears, and encoders. Each traverse is labeled with a number between one and four. The location of each traverse when installed in the wind tunnel is shown in Fig. 2.21.

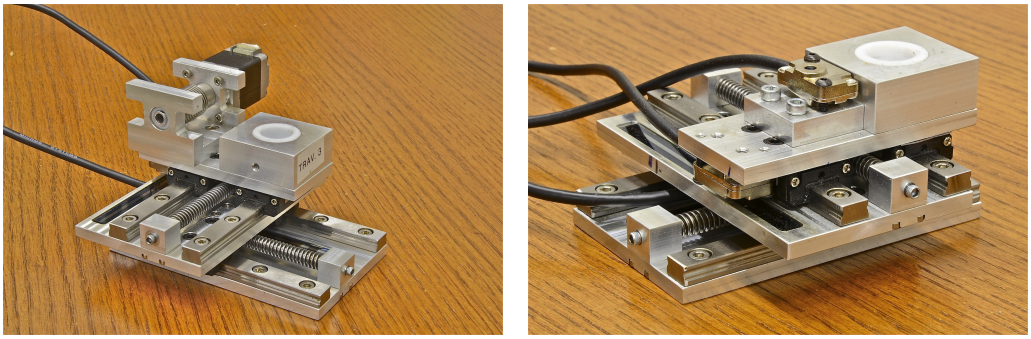

(a) (b)

Figure 2.20: Detailed flap positioning system (FPS) traverse pictures for (a) top and (b) bottom.

Figure 2.21: Location of four traverses in wind tunnel.

2.3.2 Traverse Design and Fabrication

Design of the traverses was performed in Pro/E Wildfire, a three-dimensional parametric modeling program developed by Parametric Technology Corporation. Parts were manufactured through use of a computer-controlled CNC mill or a computer-controlled water jet by Wagner Machine Company in Champaign, IL. As seen in Fig. 2.20, each traverse consisted of two primary layers. Each of these layers allowed the traverse to freely move in the x_{tunnel} and y_{tunnel} directions while the additional blocks and gear on top of the traverse controlled deflection angle of each flap. Supporting two-dimensional drawings for significant components are included in Appendix E.

Linear Motion

Linear movement of the system was accomplished through a combination of custom made components and commercially available products. The position of the traverse in the two linear directions was set by hand through use of a 0.050-in hex key which is inserted into a small 2-56 hex screw at the end of the traverse, as shown in Fig. 2.22. The hex screw was free to rotate in the worm mount, a small aluminum cube with a clearance hole in it (also visible in Fig. 2.22). This worm mount was mounted to a stationary plate which did not move. The hex screw screwed into a 1/4-20 Acme threaded precision rod. Hex screws were secured on both ends of the threaded rod with Loctite. A small rectangular worm collar, with a 1/4-20 internal threading, was attached to the bottom of the plate which was traversed. In this manner, the worm mounts were metric to a stationary plate and the worm collar was metric to the plate which was being moved. Thus, as the hex key was rotated, it rotated the threaded rod which was mounted in the threaded worm collar and moved the plate in a linear direction. The system slid on a pair of small SRS9M block and rail systems manufactured by THK. Numerous small ball bearings in each block allow for the system to slide smoothly. The position was monitored on the top and bottom of the wind tunnel through the use of Micro-E Mercury 1500-S optical encoders, which are discussed in Section 2.3.3. The linear systems on the top and the bottom traverses were identical. A side view of the entire traverse is presented in Fig. 2.23. The worm mounts, threaded rods, and encoders are clearly visible from this perspective.

Rotary Motion

Rotary position was controlled independently for each flap. Position was set by a program written in the National Instruments LabView programming language. Serial commands were sent via RS232-DB9 signal to a power junction box, as shown in Fig. 2.24. Power and signal were then sent via RS232-DB15 to a 2A-TTL bipolar controller manufactured by Excitron Corporation. A SM20-30 micro stepper motor,

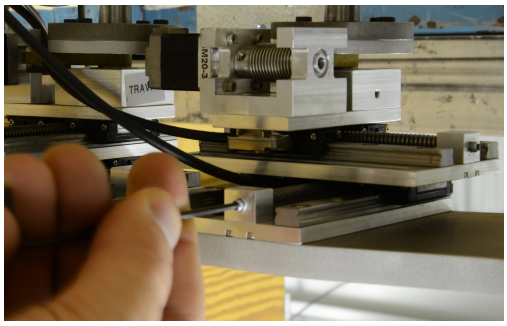

Figure 2.22: Changing linear position of the FPS.

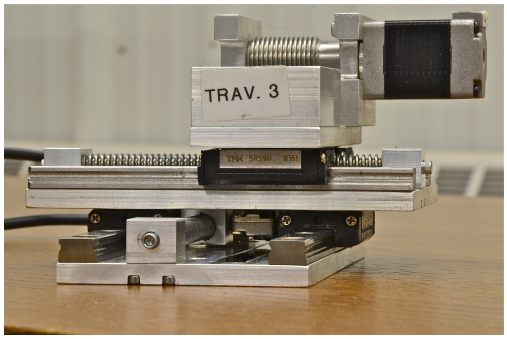

Figure 2.23: View of FPS showing worm drive assembly.

also manufactured by Excitron Corporation, was used to set the angle. The motors were installed on the traverses which were on the top of the wind tunnel. Each stepper motor was connected to a U-shaped mounting bracket. The drive shaft of the motor was connected to the inside of the worm drive collar, a long and thin aluminum annular cylinder that spanned the width of the motor mount to which a worm gear was attached; the S1D96Z-P064SS worm gear was manufactured by SDP/SI. A 40-deg sector of the SDP/SI gear S1C86Z-P064B180S was attached to the flap model and driven by the worm gear. Custom made teflon bushings rested between the motor shaft extension and the motor mount to reduce friction of the system. In an effort to reduce experimental uncertainty of flap angles, the worm gear fit tightly into motor mount block. Less than 0.050-in separated the inside edge of the motor mount and the worm. A horizontal cross section slice of the system is shown in Fig. 2.25. Similar to the linear traverses, position was monitored through use of a Micro-E Mercury 1500-S optical encoder which is discussed in further detail in Section 2.3.3.

2.3.3 Optical Encoders

Location of each degree of freedom in the FPS was determined through the use of multiple incremental digital optical encoders. A total of five encoders measured the location of each flap; three encoders attached to the traverse on the bottom of the tunnel and two encoders attached to the traverse on the top of the

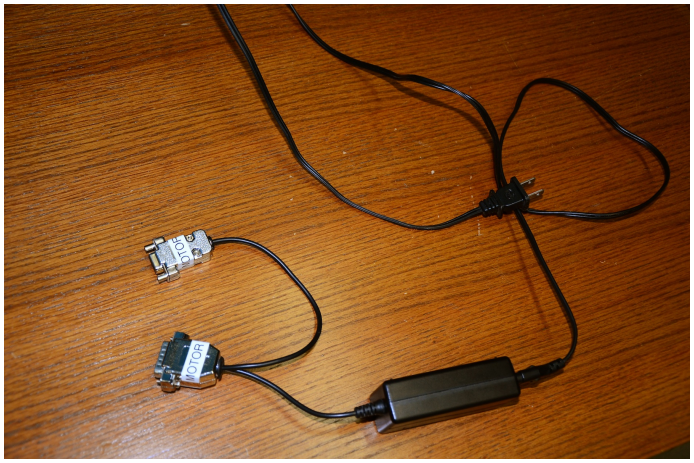

Figure 2.24: RS232-DB9 to RS232-DB15 (with power) for stepper motors.

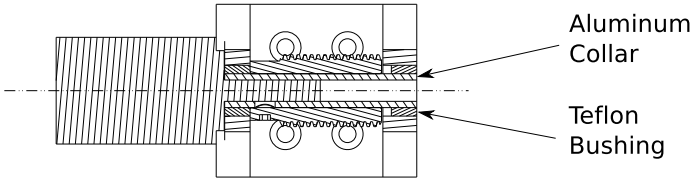

Figure 2.25: Cross section of angle of attack drive assembly.

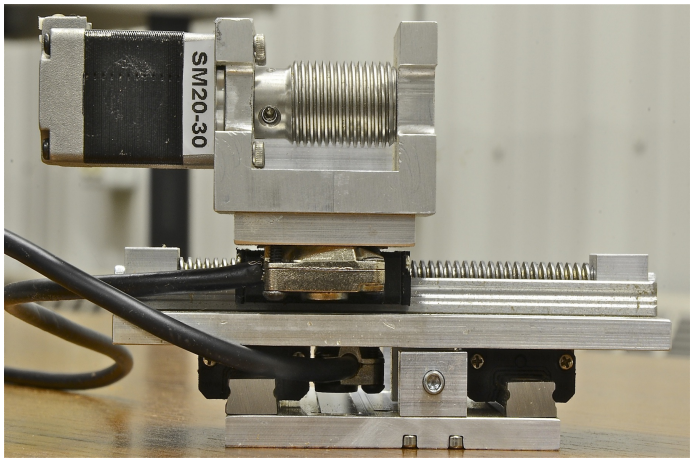

Figure 2.26: View of two encoders on FPS traverse.

tunnel. Linear position was measured on the top and the bottom of the tunnel and the angle was measured on the bottom of the tunnel. A total of ten Mercury 1500-S optical encoders manufactured by GSI Group (MicroE Systems) were used in all four traverses. Small encoders were used so satisfy the height constraint between the wind tunnel balance and wind tunnel floor. The space between the floor of the tunnel and tunnel balance was approximately 3 in. Two encoders can be seen in Fig. 2.26 with a black signal cable exiting each encoder head.

Eight L80A linear glass optical tapes with a resolution of 0.5 μm (1.97 $\times 10^{-5}$ in) and an accuracy of ± 3 μm (1.18×10^{-4} in) were used for the x_{tunnel} and y_{tunnel} directions. The angular alignment tolerance for the optical encoders was ± 2 deg (0.0349 radians) and the vertical displacement difference between the glass tape and the optical eye was $\pm$ 0.15 mm (5.91×10^{-3} in). Each encoder required a maximum of 40 mA at +5 V or 0 V. The encoders are transistor-transistor logic (TTL) capable. To ensure the optical eye was able to read the glass tape, a small slot was recessed into the aluminum plates which were stationary. Dimensions are given in the CAD of the system plate and x traverse plate which are in Appendix E. Tight tolerances on these slots ensured that the optical eye would be able to read the optical tape. The glass optical tapes were attached to each plate with a small portion of epoxy applied to the slot into which the tapes were fit and then inserting the glass optical tape into the slot. Care was taken to ensure the traverse tapes were level inside the slot; if the tape was not level, the proper vertical offset between the tape and the encoder eye would not be achieved.

A R5725-HC hub and rotary grating fixture, also manufactured by GSI Group (MicroE systems), with a resolution of 39.6 arc-seconds (0.011 deg and 32,768 counts per revolution) and an accuracy of $\pm$ 3.9 arc-seconds (0.0011 deg) was used to measure the rotary angles. To ensure proper vertical displacement between the rotary optical encoder and the rotary tape, a small encoder spacer was manufactured to raise the encoder up to the proper level to read the underside of the optical tape which was attached to a system which rested in the pillow block. Great care was taken to ensure the encoders were level as they were attached to the traverses. The standoff distance between the encoder eye and the optical tape was required to be 2.4 mm (0.0945 in) $\pm$0.015 mm (5.91×10^{-3} in) for the encoder to work properly. If the distance between the tape and the encoder is too large, the encoder will not tick with each grated line on the tape; alternatively, if the encoder is too close, the electronic eye will not be able to focus upon the tape and no signal will be returned. Proper alignment of the rotary optical tapes and linear optical tapes was verified with the use of an analog Mercury SS-AT 1500S-120 alignment tool manufactured by GSI Group (MicroE Systems), as shown below in Fig. 2.27. It is noted analog $\sin +$ and $\cos +$ signals were used by the alignment tool while all other signals were digital. The male pigtail from the encoder was plugged into the female pigtail extending from the alignment tool. The alignment tool checked for signal strength and signal quality which are both functions of vertical displacement, encoder yaw angle, and tape angle alignment. Signal quality was indicated by green, yellow, and red LED lights which corresponded to strong, weak, and unreadable signals respectively. Section 2.3.5 discusses the attachment of the flaps to the FPS in greater detail.

Optical tapes used in the FPS were sensitive to contamination by foreign debris and surface smudges. Debris such as dust and dirt inevitably settled on the surface of the linear optical encoders on the lower

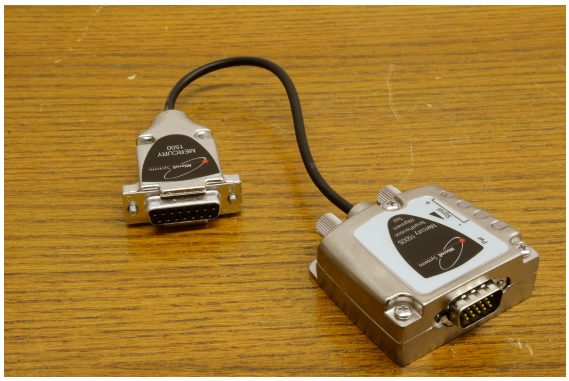

Figure 2.27: Mercury SS-AT 1500S-120 alignment tool.

traverses despite efforts to contain the traverses and keep them clean. The encoder head had difficulty reading the tick marks on the tape when foreign debris existed on the surface of the tape or when the surface was contaminated by a smudge such as a fingerprint. When the surface was dirty, the incremental distances read by the head would jump by as much as 0.3 in over a very short distance and this fault would be reflected in the Labview program used to monitor the position of the encoders. The magnitude of the distance would jump was not repeatable. In some instances, the interference would only occur while the traverse was moved in one direction. A lint-free glasses cleaning cloth and acetone were used to clean the surface of the optical tapes. The markings on the optical tapes were chromoly steel (CRMO) and were not scratched by the cloth.

The relative digital encoders were A-quad-B in differential. Four digital pulses were sent for each tick on the encoder tape; one tick for A+ up, one tick for A+ down, one tick for B+ up, and one tick for B+ down. The signals are shown below in Fig. 2.28. If A+ lead B+, as shown in Fig. 2.28(a), the value of Index+ was positive. Alternatively, if B+ lead A+, seen in Fig. 2.28(b), the value of Index+ was negative.

A zero-gate location on each optical tape, both rotary and linear, indicated the home position of each optical encoder. A Boolean value was sent from the encoder as the head passed over the zero-gate indicator. Cables were manufactured to allow use of the zero-gate Boolean, however functionality of this gate was not used in this research project because the location of the zero-gate on each tape was irrelevant. Position of each encoder was measured relative to the baseline airfoil position.

2.3.4 FPS Installation and Usage

The FPS was designed for ease of future use. While some supporting hardware may need to be manufactured, the overall system should be able to be used by future researchers. An adaption plate was manufactured to attach the FPS plates to the balance cruciform plate, as shown below in Fig. 2.29. Future models may require a different metric adaption plate than the one pictured. In addition, the traverses must be installed

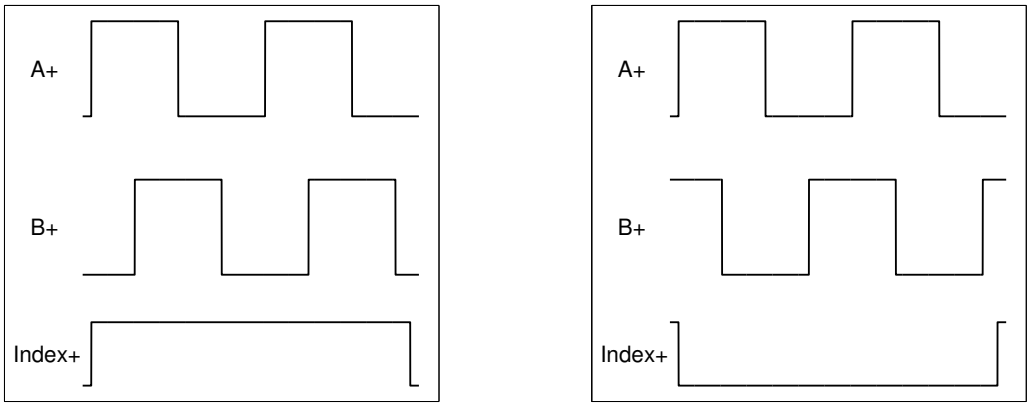

(a) (b)

Figure 2.28: A-quad-B differential signal (a) A+ leading B+ resulting in positive Index+ value and (b) B+ leading A+ resulting in negative Index+ value.

on the top of the tunnel. This hardware varies from model to model and new plates would most likely need to be manufactured for future models. For more information on design of future models, see Sec. 2.3.5. Electronic digital signals originated at the optical encoders and were transferred via RS422-DB15 to a series of breakout cables which were read by a digital counter card in the computer. A flowchart of the entire system is presented in Fig. 2.30.

Two National Instruments PCI-6602 digital counter DAQ cards were used to interface with the ten optical encoders. Five RS422-DB15 cables plugged into each DAQ card. The pinout for each DAQ card was the same and is presented in Fig. 2.31. A 68-pin connector was used to interface with the DAQ card. Each encoder required three pins including a source, a gate, and a direction (up/down).

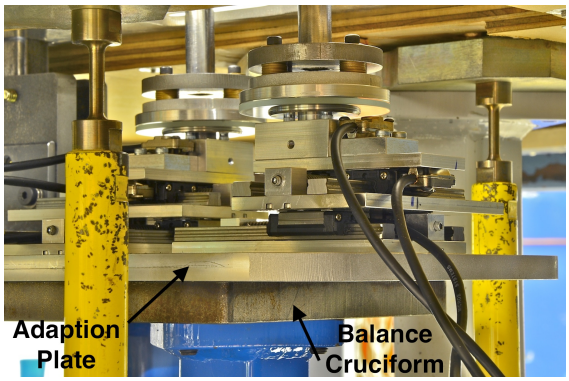

Figure 2.29: Balance cruciform plate, metric adaption plate, and traverses.

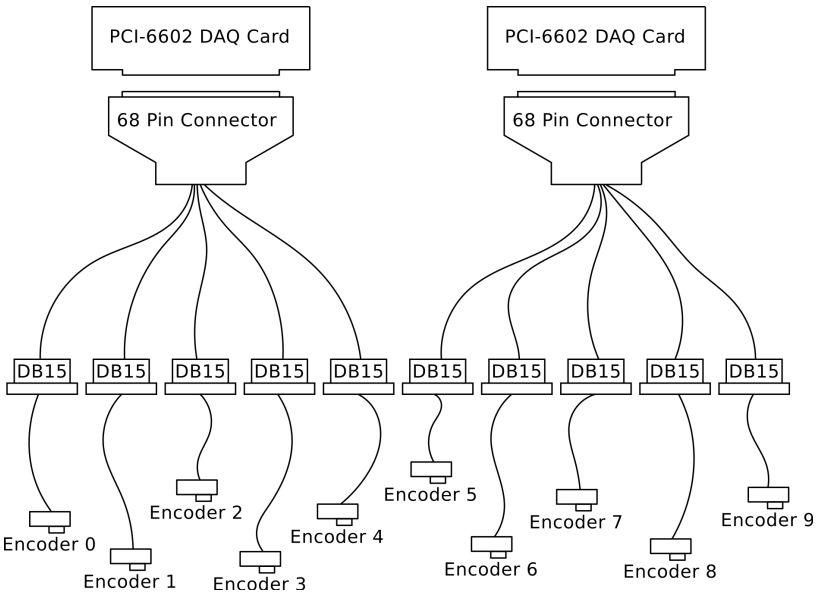

Figure 2.30: System flowchart for optical encoder attachment.

Custom manufactured adaption breakout cables, as pictured in Fig. 2.32, were used to convert the signal from 68-pin to five different RS422-DB15 pigtails, one for each encoder. Breakout cables were manufactured by GSI Group/Micro-E to interface with the PCI-6602 DAQ cards.

Software was written using the National Instruments Labview programming language to interface with the DAQ cards and the encoders. The location of each encoder was continuously monitored in dimensional coordinates (inches and degrees). Sample rate for all encoders in the PCI-6602 cards was set at 1 MHz. Each encoder could simultaneously move at 1 m/s without the DAQ card missing a line read by the encoder eye. Connection from the pigtails to each encoder was performed as presented in Table 2.3.

Table 2.3: Encoder Locations on FPS

Encoder Number	DAQ Card	Location
0	1	Bottom x_1
1	1	Bottom y_1
2	1	Top x_1
3	1	Top y_1
4	1	δ_1
0	2	Bottom x_2
1	2	Bottom y_2
2	2	Top x_2
3	2	Top y_2
4	2	δ_2

PFI31/SOURCE2	34	68	GND
GND	33	67	PFI30/GATE2
PFI28/OUT2	32	66	PFI29/UP_DOWN2
PFI27/SOURCE3	31	65	GND
GND	30	64	PFI26/GATE3
PFI24/OUT3	29	63	PFI25/UP_DOWN3
PFI23/SOURCE4	28	62	GND
GND	27	61	PFI22/GATE4
PFI20/OUT4	26	60	PFI21/UP_DOWN4
PFI19/SOURCE5	25	59	GND
GND	24	58	PFI18/GATE5
PFI16/OUT5	23	57	PFI17UP_DOWN5
PFI15/SOURCE6	22	56	Reserved
PFI14/GATE6	21	55	GND
GND	20	54	PFI13/UP_DOWN6
Reserved	19	53	PFI12/OUT6
GND	18	52	PFI11/SOURCE7
PFI9/UP_DOWN7	17	51	PFI10/GATE7
PFI8/OUT7	16	50	GND
PFI7/DIO7	15	49	GND
GND	14	48	PFI6/DIO6
PFI4/DIO4	13	47	PFI5/DIO5
PFI3/DIO3	12	46	GND
GND	11	45	PFI2/DIO2
PFI0/DIO0	10	44	PFI1/DIO1
PFI32/OUT1	9	43	Reserved
PFI34/GATE1	8	42	GND
PFI35/SOURCE1	7	41	GND
PFI33/UP_DOWN1	6	40	PFI37/UP_DOWN0
PFI36/OUT0	5	39	GND
Reserved	4	38	Reserved
PFI38/GATE0	3	37	Reserved
PFI39/SOURCE0	2	36	GND
+5V	1	35	Reserved

Figure 2.31: National Instruments PCI-6602 DAQ card pinout.

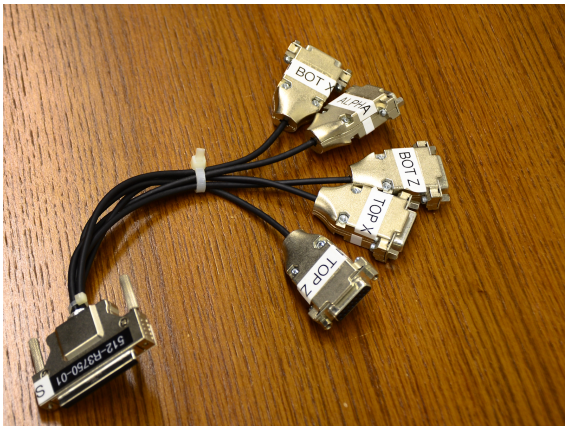

Figure 2.32: Custom manufactured optical encoder breakout cables.

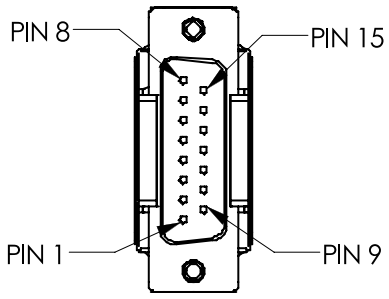

Pin	Function
1	Reserved
2	Reserved
3	Reserved
4	A- quadrature
5	A+ quadrature
6	Reserved
7	Sine+ (analog)
8	Cosine+ (analog)
9	B- quadrature
10	B+ quadrature
11	Reserved
12	+5 V DC
13	Ground
14	Index+
15	Index-

Figure 2.33: Mercury 1500S Optical Encoder DB15 pinout.

Each pigtail from the breakout cables was connected to a 25-ft long shielded RS422-DB15 cable. Each cable, ten in total, was securely fastened to a 2-m long pigtail which extended from each encoder head. The pinout for the optical encoder is shown in Fig. 2.33.

2.3.5 Requirements for Future Models

Future models are able to utilize the FPS. The CAD assembly drawings of flap one and flap two are presented in Appendix E. The total span of the flap was a critical distance. If the flap was too large, it would not fit in the wind tunnel whereas if it was too small, aerodynamic tip effects will cause the flow not to be two-dimensional. The distance between the top traverse and the bottom traverse was equally important. Supporting hardware on the top of the wind tunnel determined the location of the traverses above the ceiling. Traverses on the bottom of the tunnel were mounted to an adaption plate which was attached to the cruciform plate.

Each flap assembly consists of two airfoil attachment plates, a flap lower spar, a flap upper spar, and the flap itself. The airfoil attachment plates on the top and bottom of the flap are identical. Height of the airfoil upper spar was determined by the distance between the supporting hardware on top of the tunnel and the ceiling of the wind tunnel. Similarly, the lower spar length was determined based upon supporting CAD and the distance from the metric adaption plate to the wind tunnel floor. Unfortunately, CAD of the tunnel supplied to the researcher was incorrect; the actual distance from the balance cruciform to the bottom floor of the wind tunnel was 0.345-in larger than the previously supplied CAD. An adaption spacer

plate was manufactured and washers were stacked between the two spacer plates to lengthen the lower spar. The lower spar which was manufactured is shown in Fig. E.21 on page 316. A revised version of the CAD incorporating the 0.345-in offset is presented in Fig. E.22 on page 317. It is noted the proposed lower spar has never been manufactured.

2.4 Coordinate Systems

A pair of multielement airfoil systems, shown in Fig. 2.38, was designed and tested as a replacement airfoil system for an existing single element airfoil. A closely coupled airfoil system is presented in Fig. 2.34(a) and is comprised of a main element and two flaps while the well separated airfoil system, seen in Fig. 2.34(b), is comprised of a main element, two flaps, and a strut. Design of the multielement closely coupled and well separated airfoil system is discussed by Ragheb and Selig [32]. The strut in the well separated case adds structural integrity and bending stiffness for the entire blade. Representative I-beam spar caps would fit inside the main element and the strut of the well separated case while a representative I-beam would fit in the main element of the closely coupled system. Note the chord of the entire system is defined as unity as the main element and flaps were designed as a replacement airfoil system for a single element airfoil. The system was designed for one specific operating condition, and the flaps need not be stored in the main element as flaps are retracted in commercial airliners.

A system chord length of unity was defined for the baseline configuration and not for each configuration tested. Alternative tests which moved the flaps were analyzed as cases with chord lengths greater than or less than unity. The leading edge of the multielement system was not necessarily the leading edge of the main element. Flap deflections were defined and the trailing edge of the final flap was set on the system chord line of $y = 0$, as shown in Fig. 2.38 and defined as the trailing edge of the system (TE_{sys}). The leading edge of the system (LE_{sys}) was defined as the point furthest away from the trailing edge of the system and was set at the origin. The system angle of attack (α) was defined as the angle between the freestream velocity and the system chord line.

Three coordinate systems were used to define the airfoil configurations. The airfoil system can be described in absolute coordinates, relative coordinates, or experimental coordinates. Position of each element was constrained by three degrees of freedom in each coordinate system. Each coordinate system will now be discussed.

Absolute coordinates are provided for future researchers to easily replicate the configurations tested in this research project. The definition of this coordinate system is shown below in Fig. 2.35. The location in

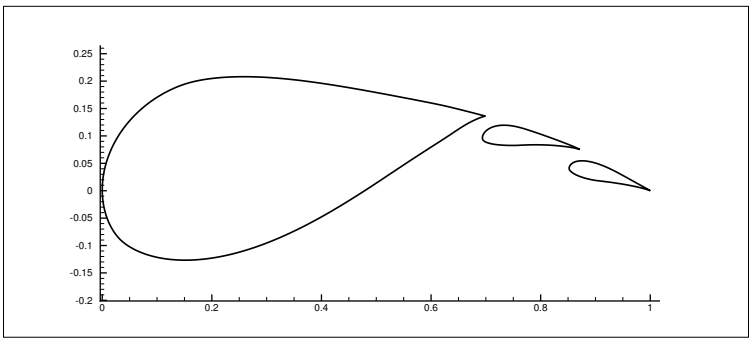

(a)

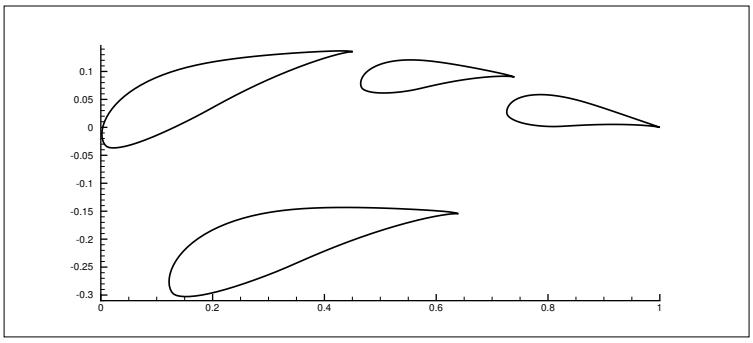

(b)

Figure 2.34: Multielement (a) closely coupled and (b) well separated airfoil systems designed for use in root section of wind turbines.

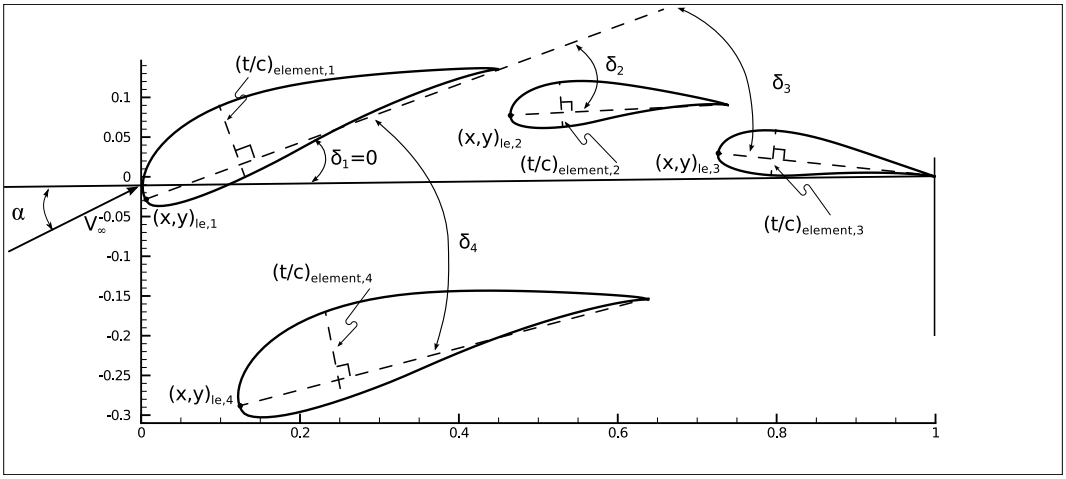

Figure 2.35: Absolute coordinate system for well separated airfoil tests.

space for each element is constrained by $x_{le,n}$ and $y_{le,n}$. The deflection of the main element (δ_1) was defined to be zero. The deflections angles of the flaps and strut (δ_2, δ_3, and δ_4) were defined from the chord line of each flap to the chord line of the main element.

The aerodynamic performance of the system is highly dependent on gap size and location as well as deflection angles between the elements. A relative coordinate system, shown below in Fig. 2.36, was used to

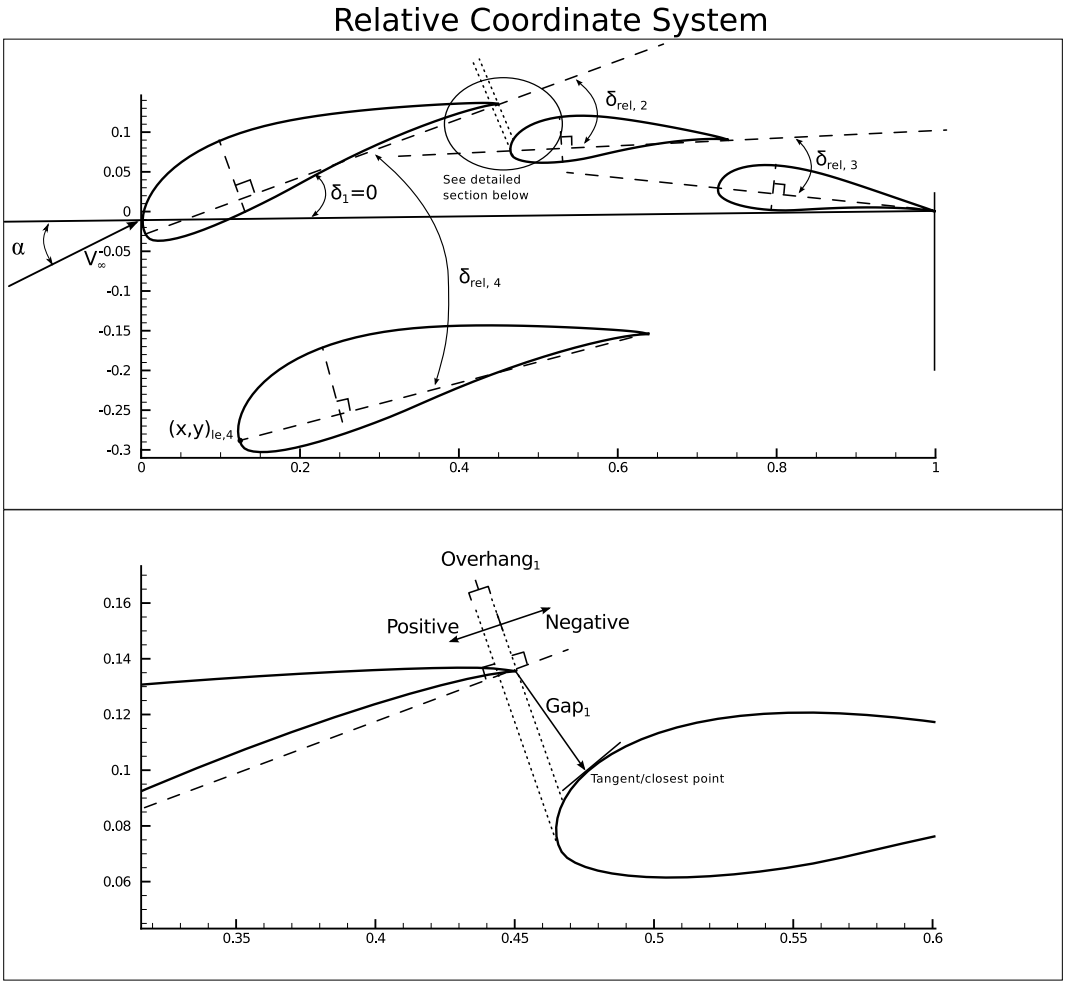

Figure 2.36: Relative coordinate system for well separated airfoil tests.

define the system by parameters which govern the flow. The deflection angle of the main element (δ_1) was declared as zero. Location of the flaps in space was constrained by gap size and overhang distance while the strut was defined by the location of the leading edge of the strut and a deflection angle relative to the main element. Gap size between elements (gap_n) was defined as the distance from the trailing edge of element n to the closest point on element $n+1$. Overhang distance ($overhang_n$) between element n and $n+1$ was defined as the distance from the leading edge of element $n+1$ to the trailing edge of n projected along the chord line of element n, as shown in the lower portion of Fig. 2.36. Positive overhang was towards the leading edge of the system while negative overhang was toward the trailing edge of the system. Relative deflection angles of the flaps ($\delta_{r,n}$) were defined as the angle between the chord line of element $n+1$ and the chord line of element n while deflection angle of the strut was measured relative to the main element. Positive deflection angle corresponded to a downward flap deflection. These coordinates are similar to those used by tests performed in NASA Langley's LTPT tunnel.

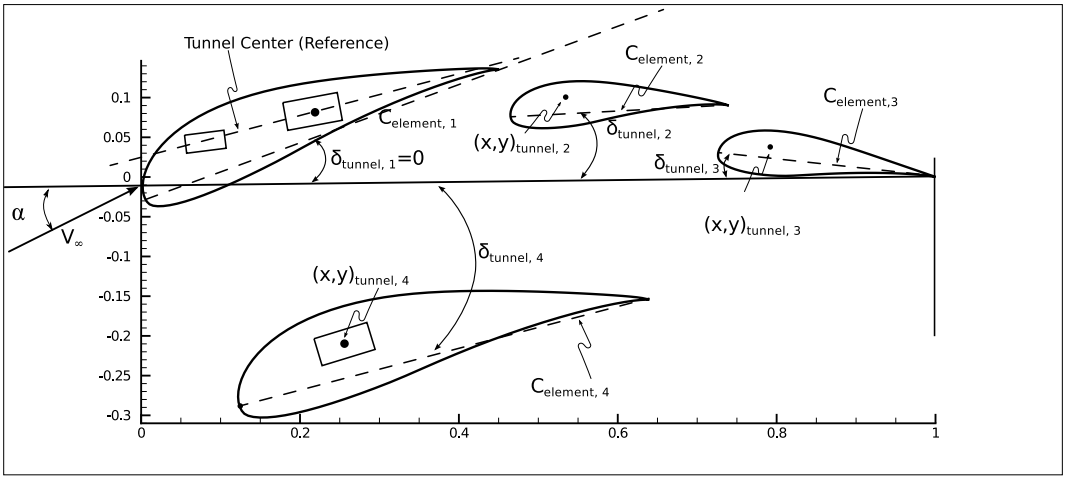

Figure 2.37: Experimental coordinate system for well separated airfoil tests.

Tests performed in the wind tunnel were conducted in the experimental coordinate system, shown in Fig. 2.37. The location of each element was defined based upon the location of the main spar of the element. The deflection angle of the main element relative to the freestream velocity, ($\delta_{tunnel,1}$) was defined as -18 deg for the closely coupled tests and -16.4 deg for the well separated test. It is noted the well separated model was mounted on the cruciform at a -9.85 deg angle relative to the cruciform plate. Offset angles were necessary for ease of installation in the tunnel and so the airfoil system could be tested using existing equipment. Consequently, the offset angles for the entire system δ_{offset} was -4.10 deg and -3.94 deg for the closely coupled and well separated tests respectively. The location of the main element was constrained in the x, y, and rotational directions by the mounting of the main spar to the center of the cruciform. The flap positions $(x, y)_{tunnel,n}$ were defined based on the spatial location of the spar. The rotation angle of element $n + 1$ was defined as the angle relative to element n.

2.5 Airfoil Models

Two multielement airfoil wind tunnel models were designed and fabricated for tests presented in this thesis. A closely coupled model, shown below in Fig. 2.38(a), and one well separated model, shown in Fig. 2.38(b), were manufactured. Design of the model was performed in PTC Pro/Engineer Wildfire 4.0, a commercially available parametric three-dimensional CAD package. Two-dimensional CAD drawings are presented in Appendix E.

(a) (b)

Figure 2.38: Multielement airfoil systems mounted for testing (a) closely coupled airfoil model and (b) well separated airfoil model.

Model Design and Fabrication

Three different elements were used for the closely coupled model and four elements were used for the well separated tests. The same flaps were used for each test. Each element was manufactured separately and the elements were attached to each other by three spanwise attachment brackets, shown in Fig. 2.39, to minimize the forces on the FPS traverses.

The main element core was constructed of foam, three steel support ribs, and two steel end caps. Two 1/4-in steel end caps were manufactured from stainless steel and were attached on each end of the model. Three steel ribs were spread out in the spanwise direction and provided a surface to which the mounting brackets could be attached. External dimensions of the end caps and interior ribs were CNC milled to a tolerance of 0.001 in. Foam cores were placed between the metal ribs to create the shape of the airfoil; a commercial vendor used a CNC hot wire to cut the profile of the cores. The foam cores were undercut by 1/16-in relative to the true airfoil profile. An epoxy resin filler was added to outer surface of the foam cores to create the true outline of the airfoil. Airfoil models were manufactured by Sean Cassidy, LLC located in Champaign, IL.

Figure 2.39: Mounting bracket used to connect the main element and two flaps for both models.

The main element for both models was supported by a main spar, which connected to the center of the cruciform plate, and a secondary spar to add structural integrity. Main spar dimensions for the closely coupled model measured 1.5-in by 3-in and the secondary spar measured 1-in by 2-in. The secondary spar was located 8.625-in upstream of the main spar. Spar integration in the well separated model was more challenging due to the smaller size of the main element. Measurements of the spars were 0.75-in by 1.5-in and 1.5-in by 3-in for the main and secondary spar respectively. The secondary spar is larger and is mounted at a 20-deg angle relative to the main spar to allow the spars to fit in the model. The main spar and the secondary spar were attached to the cruciform plate or the metric adaption plate with custom made mounting brackets.

As previously mentioned, the same two flaps were used for the closely coupled model and the well separated model. The flaps were made of 33 aluminum ribs that were 1-in thick. Flap cores were undercut by 0.030 in for the front portion of the airfoil and an epoxy filler was used to build the profiles up to the desired shape. The trailing edges were precision CNC milled to a tolerance of 0.001 in for ease of manufacturing the model. The ribs were stacked on top of each other and were held in location by two precision aluminum rods. One 0.5-in circular steel spar supported loads on the flap element. The spar was attached to the FPS, as described in Section 2.3.

A fourth element was designed and used in the well separated airfoil system. No other elements attached to the strut. The strut was manufactured with two 1/4-in aluminum end caps and one piece of foam that was placed between the two end caps. A single spar that measured 1-in by 2-in passed through the center of the model and was attached to the metric adaption plate on the bottom of the tunnel and onto the mounting plate on top of the tunnel.

Model Installation

The closely coupled model, the MFF-089 airfoil, was installed in the wind tunnel with a few additional machined components. The main spar was attached directly to the balance cruciform plate on the bottom of the tunnel with a standard set of mounting brackets. Two flap traverses were attached to a metric adaption plate which was attached to the cruciform plate, as shown in Fig. 2.40.

Connection of the well separated model, MFFS-026, to the main tunnel balance was different than the closely coupled model. A metric adaption plate was manufactured to which the entire airfoil system attached. As previously discussed, a 20-deg offset existed between the main spar and the secondary spar of the main element. Modified mounting brackets were manufactured for the main spar and the secondary spar of the main element. Custom manufactured mounting brackets were fabricated to attach the strut to the metric adaption plate. Supporting hardware and components are visible in Fig. 2.40.

Connection of the two models to the SFB was facilitated with multiple machined components, as pictured in Fig. 2.41. A rectangular metric extension plate was machined for the closely coupled model to which the two traverses and the main element were attached. A SFB spar was then attached to the metric adaption

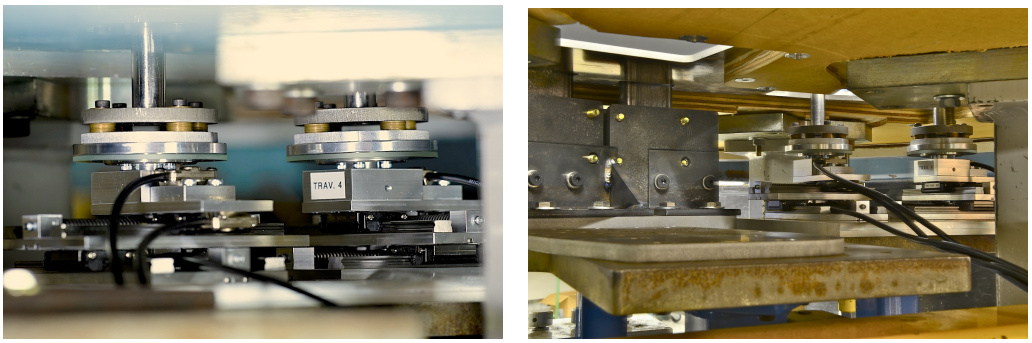

(a) (b)

Figure 2.40: Airfoils attached to main balance on bottom of wind tunnel for (a) closely coupled test and (b) well separated test.

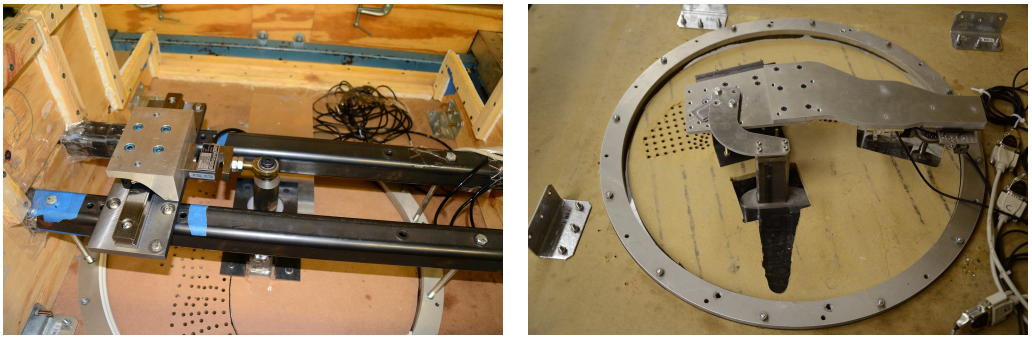

(a) (b)

Figure 2.41: Airfoils attached to SFB on top of wind tunnel for (a) closely coupled test and (b) well separated test.

plate, as discussed in Section 2.3. A zig-zag shaped plate was machined for the well separated airfoil system. The main element and the two traverses were connected to the plate, as shown in Fig. 2.41(b). Three L-brackets were used to connect the main element to the plug. This was done so the suction holes were not obstructed by the mounting bracket. The plug and suction system is discussed greater detail in Section 2.6.

Flap Alignment

As previously mentioned in Section 2.3, the flaps were positioned with the aid of incremental optical encoders. Flaps were positioned in the baseline, or home position, and the values of all ten optical encoders were set to zero. The home position of the two flaps was determined based off an alignment jig, shown in Fig. 2.42.

A 1/8-inch piece of aluminum was aligned with the profile of the main element. The flaps were then moved in the x and y directions until they fit snugly into the profile of the jig. Minor adjustments were made to x, y, and δ until the flaps were verified to be in the home position. Measurements with the jig were made on the bottom of the tunnel and the top of the tunnel. Repeatability studies indicated a linear repeatability of ± 0.01 in, or approximately 0.05% of the system chord, and a rotary repeatability of ± 0.1 deg.

2.6 Tunnel Modifications

A new floor was manufactured to be used with the well separated airfoil model. A new floor was constructed from wood so the spar of the strut could be placed through the floor. The floor was manufactured out of an existing solid floor that was used in a previous research project. Standard wood shop tools were used to

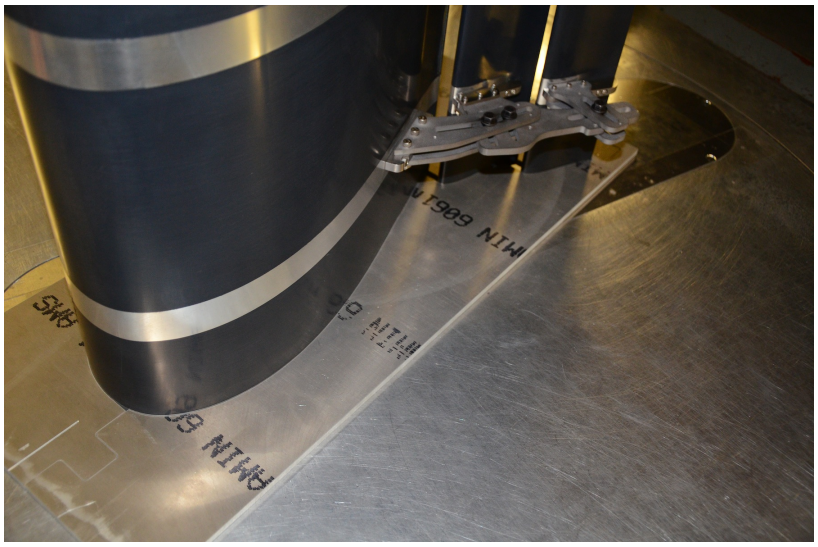

Figure 2.42: Jig used to align flaps in home position.

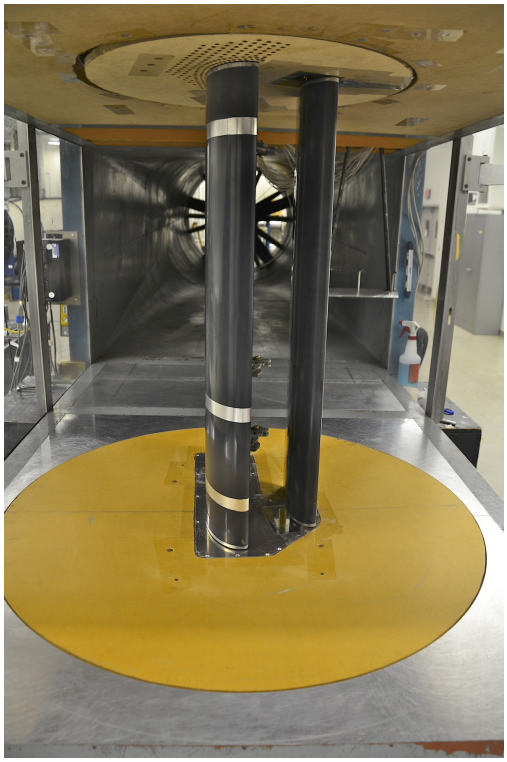

Figure 2.43: Well separated model with new floor.

create a hole for the main element and flap struts and a second hole was created for the strut spar to go through.

Preliminary results of the baseline closely coupled airfoil indicated aerodynamic performance did not change significantly with angle of attack. An investigation using surface oil flow visualization techniques was performed to examine the flow. Results suggested the presence of spanwise flow. In an effort to minimize the spanwise flow, the boundary layer was minimized. A new plug for the ceiling of the tunnel was manufactured out of MDF wood, and many holes were drilled into the plug, as shown in Fig. 2.44. Suction was applied using four 15-amp 120-volt Black and Decker LH4500 Leaf Hog blowers attached to the top of the SFB air containment box, previously discussed in Section 2.2, and this successfully minimized the boundary layer and reduced the amount of spanwise flow. Three-dimensional flow was localized to within 4-in of the wall as opposed to spanwise flow along the entire span of the model. Results of final flow visualization are presented in Section 3.2.4.

(a) (b)

Figure 2.44: Ceiling holes used to reduce boundary layer on ceiling for (a) closely coupled test and (b) well separated test.

2.7 Surface Flow Visualization

Fluorescent surface oil flow visualization techniques were applied to the airfoil models. Flow visualization was performed by first applying a very thin layer of 5W-30 motor oil to the surface of the airfoil model. An airbrush was then used to apply a fluorescent leak detector dye and mineral oil mixture to the surface of the model. Tests were performed at a Reynolds number of 1.0×10^6 and $\alpha = 9.9$ deg and 12.9 deg.

Surface oil visualization was performed similar to that discussed by Ansell [42]. A single strip of yellow electrical tape was applied to the surface of the main element which was marked with chordwise x/c coordinates 5% increments. The tape allowed the location of key flow features to be easily determined. Holes and gaps in the floor and ceiling of the wind tunnel were sealed with clear packing tape. This was done to ensure that no flow visualization oil leaked onto the traverses which may damage the optical tapes. The encoder tapes were sensitive to any type of foreign contaminant, as discussed in Section 2.3.3.

A coat of 10W-30 motor oil was applied to the surface of the airfoil model with a lint-free shop rag. A lint free rag was used to ensure no particulates were deposited on the surface of the model which would trip the flow from laminar to turbulent upstream of the laminar separation bubble. The oil was applied to reduce the surface sheer stress of the fluorescent mineral oil so the oil could easily flow downstream over the model. Excess motor oil was wiped away with a dry lint-free cloth. Four drops of Tracer TP34000601 UV florescent leak detection dye was added to a bottle of approximately 250 mL of standard mineral oil. Nitrogen gas regulated to about 30 psi was used to apply the mixture to the surface of the model with an airbrush while the tunnel was operating at 30 RPM. The tunnel was turned on so the fumes of the airbrush would be advected down the tunnel so as not to adversely effect the researchers. An airbrush was used to ensure the spray particles were small enough to not be dominated by the downward force of gravity and slide down the model. The entire surface of the model was sprayed with the fluorescent mineral oil mixture

so the surface resembled peach fuzz or the surface of an orange peel. Four black lights were used to fluoresce the dye on the model to ensure complete and even coverage of the model.

After application of the mineral oil mixture, the desired angle of attack of the model was set. The tunnel was then ramped up to the desired RPM for 3–5 minutes. After the proper time elapsed, the tunnel RPM was set to 30 RPM. Black lights were turned on and placed in the test section to minimize the glare reflecting from the surface of the model. Photographs were taken with a Nikon D7000 DSLR camera with a $f/3.5$-5.6 18-105 mm Nikkor lens. Images were captured in standard JPG format and later postprocessed using Adobe Photoshop Lightroom to enhance contrast of the surface oil flow. Photographs were taken at $f/7.1$ for an exposure time of 3 sec at an ISO of 800 to reduce image noise as well as increase clarity and sharpness in the photo. Focus was adjusted manually and proper image focus was ensured by using the LCD screen on the back of the camera. This was done by digitally zooming in on the yellow electrical tape and subsequently adjusting the focus until the written label was sharp and clear. The surface of the airfoil model was cleaned with standard glass cleaner after each run. The flow visualization process was repeated for each desired angle of attack.

Representative surface flow visualization on the upper surface of the system is shown in Fig. 2.45. Flow is from the right to the left. Movement of the oil on the surface is caused by the shear stress on the surface of the airfoil. Oil near the stagnation point of the airfoil system is in a region of high shear, so little oil remains in that region as the high-shear boundary layer has scoured much of the oil downstream. Regions of low shear are observed where the oil has not moved a significant amount. The oil accumulation line indicates the local shear stress is zero which corresponds to separated flow. Oil gathers at this point as there is no flow moving the oil downstream at this point. An oil accumulation line indicates a turbulent reattachment point or where flow has separated from the airfoil.

2.8 Test Matrix Generation

Configurations were generated by defining gaps, overhangs, and relative deflections for the proposed test case. An iterative program was used to locate each flap relative to the previous element. Experimental coordinates were determined from the final location of the flaps. An overview of the computational program will now be presented.

Unit chord airfoil profiles for each configuration were imported and subsequently scaled by user-defined scale factors. The leading edge of each airfoil was defined as (0,0) and the trailing edge coordinates for each unit chord airfoil were defined as (1,0). It is noted that an airfoil coordinate did not necessarily exist where

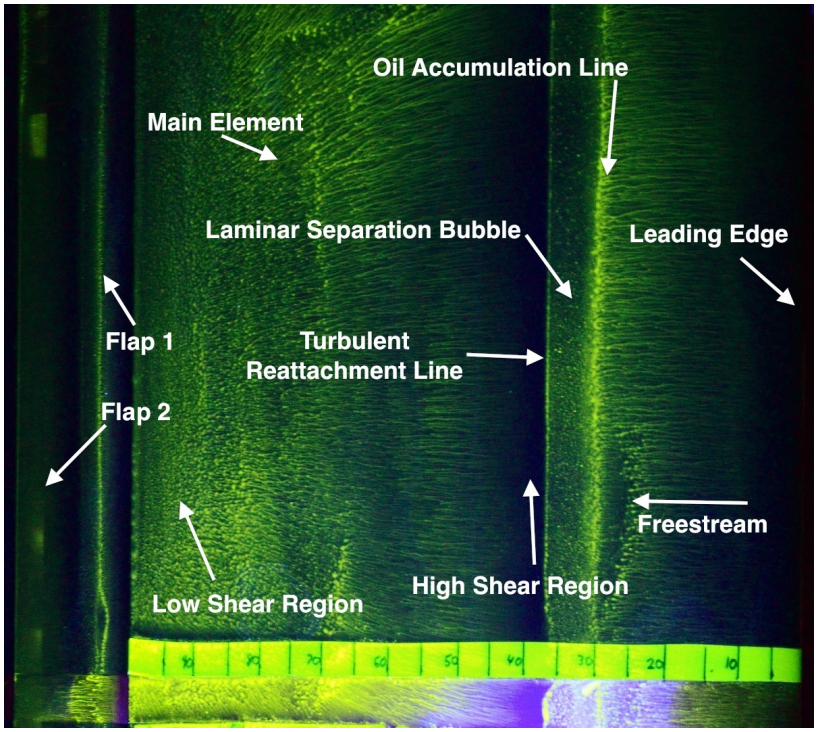

Figure 2.45: Representative flow visualization results with significant characteristics labeled.

the leading edge or trailing edge of the airfoil was defined. The computational process treated each element independently in the process.

Position of the first element was declared with a relative deflection angle relative to a static plane; the line used for configurations tested in this research was the plane through the middle of the wind tunnel. Coordinates of the scaled main element were rotated to the appropriate $\delta_{r,1}$ value. A horizontal offset was applied to the airfoil during the rotation about the leading edge. A correction was applied so the furthest point forward in the airfoil, the nose of the airfoil, was placed at the origin.

Elements two through n were declared based upon parameters relative to the previous element, $n-1$. Scaled coordinates of element n were rotated about the leading edge of the element and then the airfoil was adjusted so the nose of the airfoil was set at the trailing edge of element $n-1$. An overhang offset, projected along the chord line of element $n-1$ in the x and y directions, was applied to the element.

An iterative Newton-Rhapson scheme was employed to set the proper gap size between the trailing edge of element, $(x,y)_{TE_{n-1}}$ and the surface of element n. An initial guess of 0.7% chord was applied to all calculations. Analysis indicates an adequate choice of initial guess must be made to avoid the possibility of the process diverging. Distances of the initial gap size guess were projected normal to the chord line of the previous element to determine a Δx and Δy relative to the TE_{n-1} for the initial position while

maintaining the proper overhang value. Distance was calculated from $(x,y)_{TE_{n-1}}$ to all points on element n. The smallest distance between the surface of element n and $(x,y)_{TE_{n-1}}$ was referred to as point k. A 1000 point cubic spline was fit between $(x,y)_{k-10}$ and $(x,y)_{k+10}$. Gap size was calculated from $(x,y)_{TE_{n-1}}$ to the cubic spline. The difference in actual gap size to desired gap size was calculated and appropriate adjustments were made to the (x,y) coordinates of airfoil n until convergence was reached. Convergence for the gap size was satisfied for iteration j when

$$\epsilon = |gap_j - gap_{j-1}| < 1 \times 10^{-8} \tag{2.34}$$

Upon convergence, the entire multielement system was normalized to a system α of 0 deg and a unit chord. An iterative process was used to satisfy the two system geometry conditions. The trailing edge of the element furthest downstream was defined as $(x,y)_{te,system}$. The leading edge of the system was declared as the point furthest forward of the multielement system which lied on the x axis. It is noted that, while iterating, the proposed leading edge of the system changed with each iteration as the system was rotated and translated. The angle between the leading edge and trailing edge of the system and the multielement system was rotated about $(0,0)$ such that $(x,y)_{te,sys}$ was on the x axis. After rotation, a 1000 point cubic spline was fitted between $(x,y)_{k-10}$ and $(x,y)_{k+10}$ where k was the index of the coordinate furthest from the trailing edge of the system. The value of k changed with the iterative scheme and was not necessarily the leading edge of the system at iteration j. Upon convergence, though, coordinate k corresponded to the leading edge of the system. Offset values Δx and Δy were calculated such that coordinate k would lie on the origin. This process of system rotation and translation was repeated until convergence was reached. Convergence was satisfied when the trailing edge of the system and the system α between the proposed leading edge and trailing edge of the system were both less than 1×10^{-8}. At this point, the leading edge of the multielement airfoil system was defined as the point at $(0,0)$ and the system angle of attack, the angle between the leading edge and trailing edge of the system, was defined as 0 deg.

Chapter 3

Results and Discussion

Contents of this chapter include results and analysis of tests performed in the wind tunnel. Aerodynamic performance data are presented for the baseline configuration for both the closely coupled and well separated airfoil system. Values of C_l and C_d presented in this section were obtained from the force balance and wake rake respectively. Cross-configuration analysis results are presented to understand the effect of the relative deflection angle, gap, and overhang on the aerodynamic performance. In addition, flow visualization results are presented for the baseline closely coupled airfoil system.

3.1 Experimental Validation

Tests were performed with S809 check-standard airfoil with historical data to ensure the wind tunnel compared well to previously collected data. A check was executed at the beginning of the closely coupled and well separated trials. The S809 airfoil, originally constructed by Noe [34], was installed in the wind tunnel and data were collected using the three-component force balance. The drag polar and lift curve plots, shown in Fig. 3.1, showed excellent comparison to previously collected data at UIUC.

3.2 Closely Coupled Multielement Airfoil Tests

Data collected in the wind tunnel included quantitative and qualitative information. Quantitative data included aerodynamic performance parameters while qualitative data was focused upon flow visualization. Performance data were recorded and then standard wind tunnel corrections were applied as discussed in Section 2.1.7. Coordinates for the unit-chord airfoils that were tested are included in Appendix D. The main element was 14.0-in long, flap one measured 3.5 in, and the chord of flap two was 3.0 in. Chord length of the CC-1 configuration was 19.62-in.

Multielement airfoil configurations tested in the wind tunnel were all derivatives of the MFF-089 airfoil, designed by Ragheb, et al. [32]. The main-flap-flap multielement configurations tested in the tunnel were referred to closely coupled airfoil systems. The original configuration was named CC-1 (closely-coupled

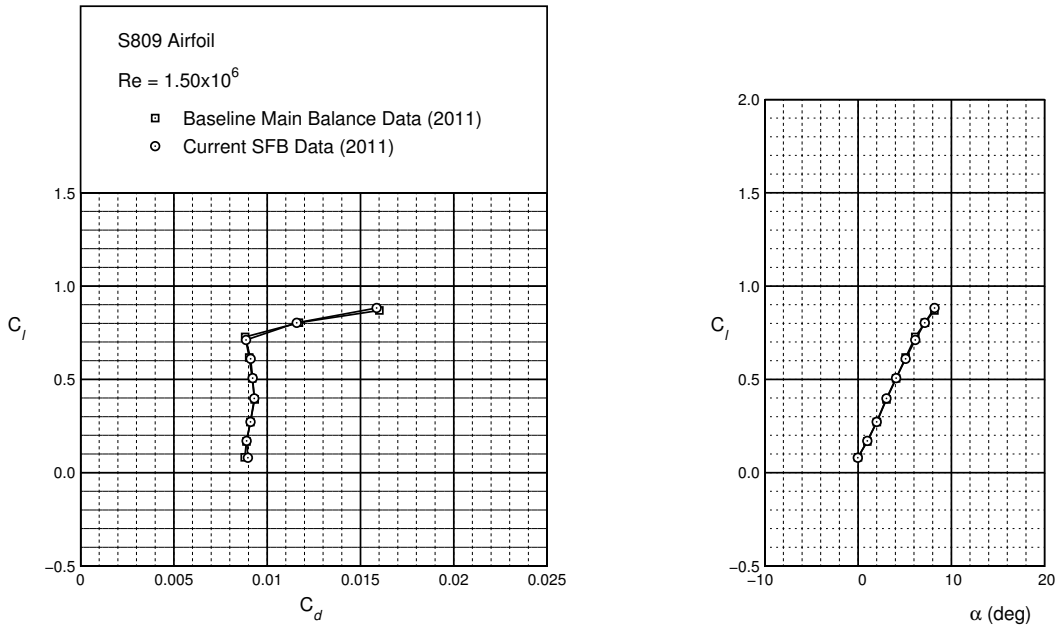

Figure 3.1: S809 airfoil validation at $Re = 1.5 \times 10^6$.

configuration). Different closely coupled configurations were tested with varying gap size, overhand distance, and relative deflection angles. A summary of all configurations tested is provided in Appendix A.

Aerodynamic performance data collected in the wind tunnel includes lift, drag, and system quarter chord pitching moment. Cross configuration results are discussed in this chapter. Individual drag polars and lift curves are presented in Appendix B. The tabulated data sets for each configuration tested are presented in Appendix C. All tests were performed at a Reynolds number of 1.0×10^6 and not at the full speed tunnel Reynolds number of 1.85×10^6 in an effort to reduce spanwise flow as discussed in Section 3.2.4.

Some configurations were tested more than once and were assigned a separate subtest letter. Subtest tests were performed for data repeatability and to replace invalid data sets. Closely coupled performance data were taken with the main wind tunnel balance and the secondary force balance. A 750-lb capacity load cell was used to measure lift applied to the secondary force balance.

3.2.1 Baseline Results

The CC-1 configuration was tested and analyzed and taken as a baseline configuration for all subsequent tests. Location of the flaps were declared by relative coordinates. Flap 1 was located such that $\delta_{r,2} = 21.40$, $overhang_2 = 0.0143$, and $gap_2 = 0.0228$. Flap 2, relative to flap one, was placed so $\delta_{r,3} = 9.03$, $overhang_3 = 0.0147$, and $gap_3 = 0.0201$. Baseline results are presented in Fig. 3.2. Data were collected from $\alpha = 9$ deg to $\alpha = 19$ deg to prevent damage to the wind tunnel balance caused by unsteady flow associated with stall.

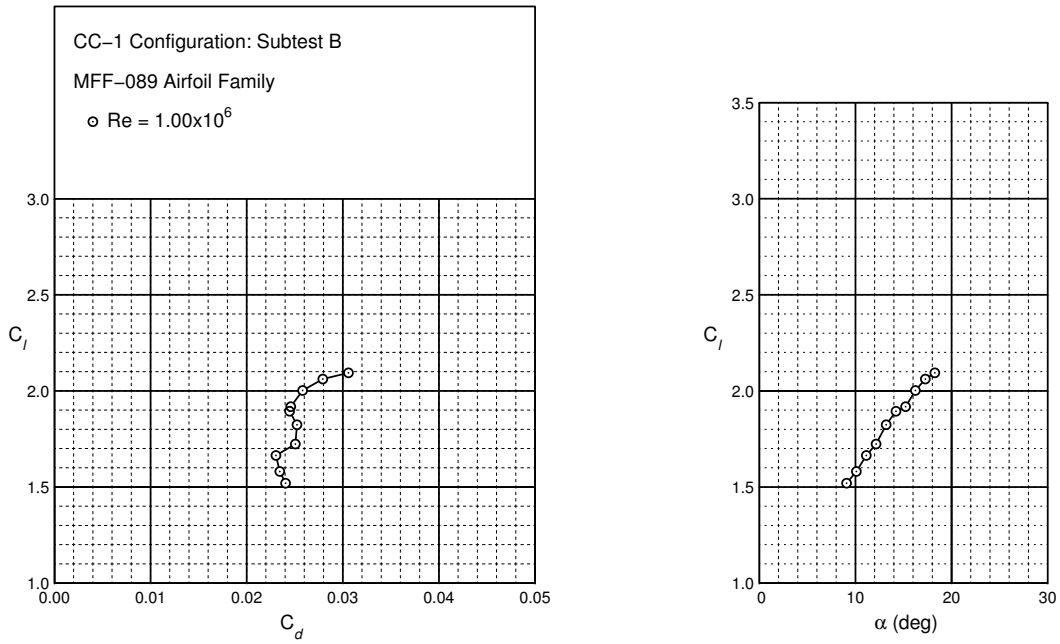

Figure 3.2: Baseline results of CC-1 configuration at $Re = 1.0 \times 10^6$.

The drag polar suggests a drag rise of approximately 20 counts at α of 12 deg relative to the drag value at α of 11 deg. This local drag rise may be attributed to flow phenomena any of the singular elements or a more complex multielement flow phenomena.

3.2.2 Test Matrix

Closely coupled configurations were generated in numerous different families. The baseline case was tested and referred to as the CC-1 configuration. In addition to the baseline, a family of tests corresponded to tests which isolated one or two of the relative airfoil coordinate parameters such as gap, overhang, or deflection angle. In this manner, the effect of the gap, overhang, or deflection angle could be isolated from all other parameters. A summary of the different families is presented in Table 3.1. In some tests, relative differences to the baseline were equal for Flap 1 and Flap 2. In these cases, the value of the corresponding spans the entire width of the parameter column. If a parameter was altered, it is presented in a form corresponding to $value_{min} : increment : value_{max}$. A detailed test matrix is presented in Appendix A. The effect of flap deflections were captured in Families 1-6. Flap deflection relative to the baseline configuration was constant for both flaps. Relationships between gap size and overhang distances were determined in Families 7-23.

Table 3.1: Closely Coupled Airfoil Test Matrix Families

Family	Configurations	$overhang_n$		gap_n		δ_n [deg]	
1	2:4	0.01434	0.01474	0.02283	0.02011	13	4 : 2 : 8
2	5:7	0.01434	0.01474	0.02283	0.02011	16	4 : 2 : 8
3	8:10	0.01434	0.01474	0.02283	0.02011	19	4 : 2 : 8
4	11:13	0.01434	0.01474	0.02283	0.02011	21	11 : 2 : 15
5	14:16	0.01434	0.01474	0.02283	0.02011	23	11 : 2 : 15
6	17:19	0.01434	0.01474	0.02283	0.02011	25	11 : 2 : 15
7	20:24	0.02684		0.01783 : 0.0025 : 0.02783		23	13
8	25:29	0.02184		0.01783 : 0.0025 : 0.02783		23	13
9	30:34	0.01684		0.01783 : 0.0025 : 0.02783		23	13
10	35:39	0.01184		0.01783 : 0.0025 : 0.02783		23	13
11	40:44	0.00684		0.01783 : 0.0025 : 0.02783		23	13
12	45:47	0.01		0.01	0.01 : 0.0025 : 0.015	23	13
13	48:50	0.01		0.0125	0.01 : 0.0025 : 0.015	23	13
14	51:53	0.01		0.015	0.01 : 0.0025 : 0.015	23	13
15	54:56	0.01	0.015	0.01	0.01 : 0.0025 : 0.015	23	13
16	57:59	0.01	0.015	0.0125	0.01 : 0.0025 : 0.015	23	13
17	60:62	0.01	0.015	0.015	0.01 : 0.0025 : 0.015	23	13
18	63:65	0.015	0.01	0.01	0.01 : 0.0025 : 0.015	23	13
19	66:68	0.015	0.01	0.0125	0.01 : 0.0025 : 0.015	23	13
20	69:71	0.015	0.01	0.015	0.01 : 0.0025 : 0.015	23	13
21	72:74	0.015	0.015	0.01	0.01 : 0.0025 : 0.015	23	13
22	75:77	0.015	0.015	0.0125	0.01 : 0.0025 : 0.015	23	13
23	78:80	0.015	0.015	0.015	0.01 : 0.0025 : 0.015	23	13

3.2.3 Cross-Configuration Analysis

Analysis of data was performed to understand the relationship between deflection angle, gap size, and overhang distance, and the aerodynamic performance. Data in this section are presented at a constant α

across all configurations. In this manner, the effect of the different parameters could be easily visualized and understood. Clear trends exist for some of the relationships. Lift at a constant α is denoted by $C_l|_\alpha$, drag is noted by $C_d|_\alpha$, and C_l/C_d is referred to as $C_l/C_d|_\alpha$.

Effect of flap deflection

As outlined in Section 3.2.2, the effect of flap deflection angle was studied in configurations CC-2 through CC-19. Relative deflection angles for each flap, $\delta_{rel,n}$, are defined in Fig. 2.36. Results in Fig. 3.3 indicate that an increase in deflection angle, for either flap, increased the lift coefficient of the airfoil system at a given angle of attack. Data suggest that the trend between relative deflection angle and $C_l|_\alpha$ is not necessarily linear. In addition, the relative change in $C_l|_\alpha$ with respect to deflection angle is not constant for all deflection angles. It is noted that the value of $C_l|_\alpha$ increases at a greater rate more for a given deflection angle at small deflection angles when compared with large deflection angles.

The relationship between relative deflection angle and drag was also determined and results are plotted in Fig. 3.4. In general, data suggest that drag increases as deflection angle δ increases, which is what was expected. It is noted that $C_d|_\alpha$ increases at a greater rate at lower deflection angles than at higher deflection angles. No clear trend exists between $C_d|_\alpha$ and $\delta_{r,2}$ at deflection angles greater than 11 deg. This trend may be due to stall or other off the surface aerodynamic phenomena such as wake bursting.

Finally, the relationship between aerodynamic efficiency C_l/C_d\$ and deflection angles was studied. Data presented in Fig. 3.5 suggest a relationship exists between δ and $C_l/C_d|_\alpha$ but it is not as strong as the relationship between lift or drag and deflection angle. Data indicate $C_l/C_d|_\alpha$ is affected more by a change in $\delta_{rel,2}$ than $\delta_{rel,1}$. This observation could be due to the fact that the deflections of the flaps were not finely tuned to the most desired deflection angle for the baseline configuration CC-1.

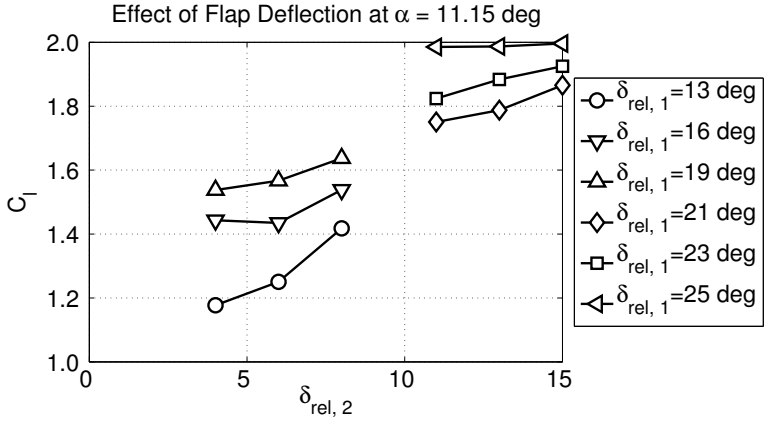

Figure 3.3: Effect of flap deflection on lift for closely coupled airfoil.

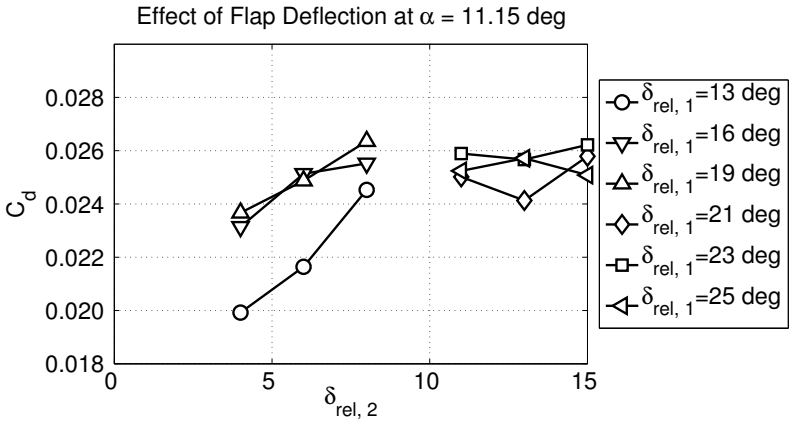

Figure 3.4: Effect of flap deflection on drag for closely coupled airfoil.

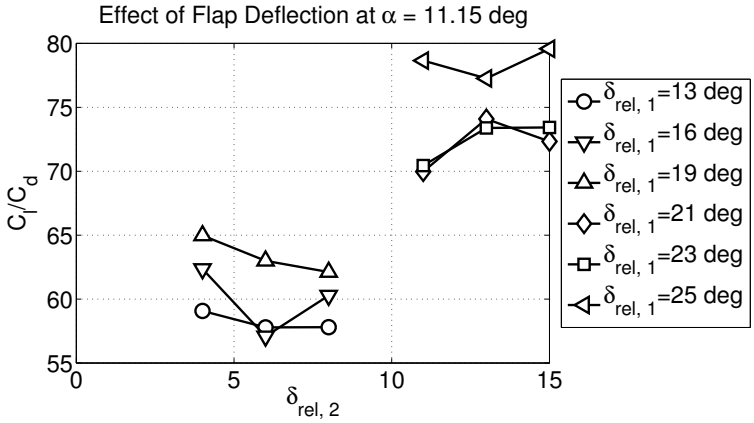

Figure 3.5: Effect of flap deflection on C_l/C_d for closely coupled airfoil.

Effect of gap size

Configurations were also generated in which gap sizes were varied while other parameters were held constant. Data presented in this subsection correspond to CC-40 through CC-44. All configurations summarized in this section were generated such that $overhang_1 = overhang_2 = 0.0068$. Results shown in Fig. 3.6 indicate that the gap size has a strong effect on the value of $C_l|_\alpha$ across all configurations. Data are plotted for three different angles of attack. Trends indicate that $C_l|_\alpha$ has a local maximum value between $gap_{1,2} = 0.020$ and $gap_{1,2} = 0.025$. Larger gap sizes do not accelerate the local flow through the gap as much as smaller gap sizes and, consequently, $C_l|_\alpha$ is smaller for larger gap sizes. However, gap sizes smaller than 2.0% of system chord indicate a sharp drop-off in $C_l|_\alpha$ which may be attributed to confluent boundary layers or other complex multielement flow phenomena.

The relationship between gap size and $C_d|_\alpha$ is presented in Fig. 3.7. An inverse linear relationship exists between gap size and $C_d|_\alpha$. Larger gap sizes create less drag than smaller gap sizes. The rate of drag increase

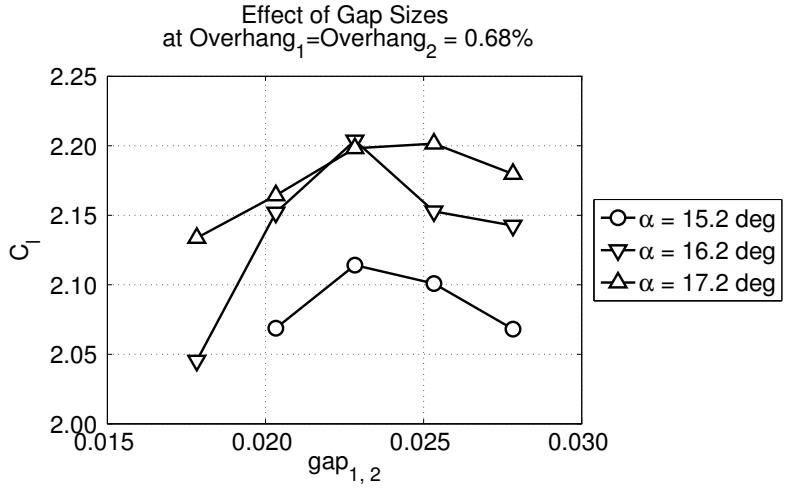

Figure 3.6: Effect of gap size on lift for closely coupled airfoil.

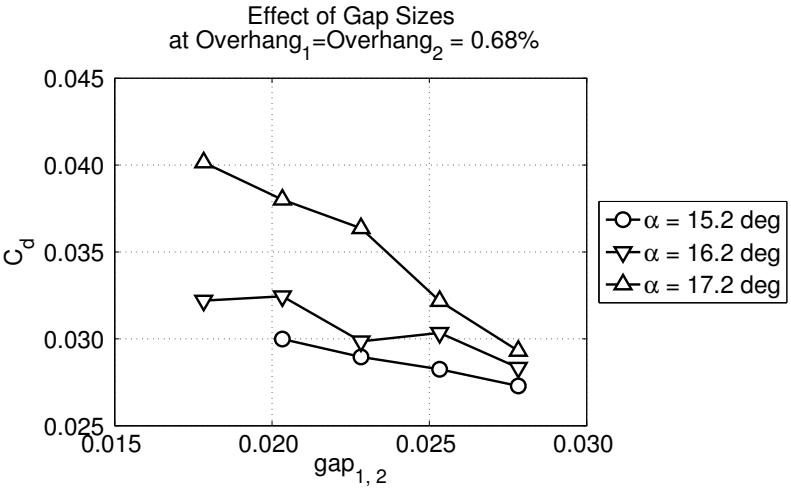

Figure 3.7: Effect of gap size on drag for closely coupled airfoil.

relative to gap size is not constant for all angles of attack. For cases where $\alpha = 15.2$ deg, the value of $C_d|_\alpha$ increases approximately 30% from $gap_{1,2} = 0.02783$ to $gap_{1,2} = 0.01783$. On the contrary, it is noted that the value of $C_d|_\alpha$ at $\alpha = 17.2$ deg increases approximately 12% from the largest gap size to the smallest gap size.

Results presented in Fig. 3.8 indicate a relationship exists between ${}^{C_l}/_{C_d}|_\alpha$ and gap size. A direct relationship exists between ${}^{C_l}/_{C_d}|_\alpha$ and gap size. As the gap size increases, the aerodynamic efficiency also increases. This trend is observed for all angles of attack. It is clear that the drag rise due to small gap size is dominant compared with the increase in lift near a gap size of 0.025. Data indicate the value of ${}^{C_l}/_{C_d}|_\alpha$ may increase as much as 35% from a gap size of 0.01783 to 0.02783.

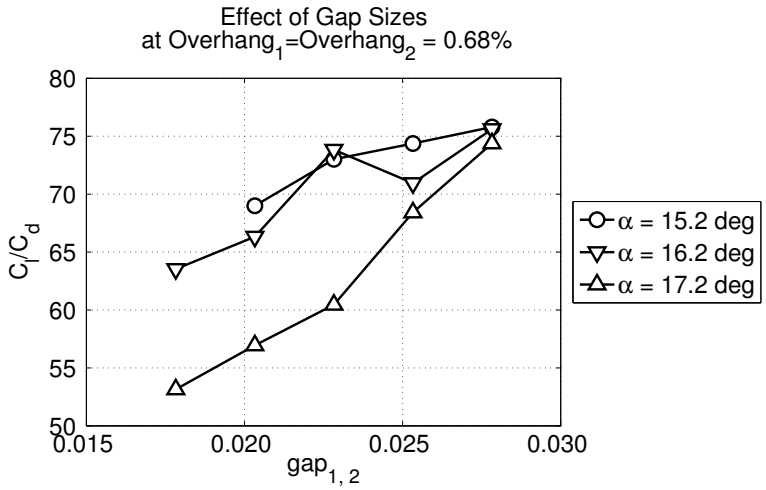

Figure 3.8: Effect of gap size on C_l/C_d for closely coupled airfoil.

Effect of overhang distance

Tests were also performed in an effort to determine the relationship between overhang distance and aerodynamic performance. Data presented in this subsection correspond to configurations CC-23, CC-28, CC-33, CC-38, and CC-43 which correspond to overhang distances between 0.00684 and 0.02684. All configurations had a constant $gap_1 = gap_2 = 0.0203$. As previously discussed in Section 2.4 and in Fig. 2.36, a positive overhang corresponds a configuration in which the leading edge of element n is upstream of the trailing edge of element $n-1$. By convention, element $n-1$ is the forward element and element n is the aft element. Comprehensive definitions are shown in Fig. 2.36 on page 41. The effect of overhang distance on the value of $C_l|_\alpha$ is presented in Fig. 3.9. In general, small overhang distances increase the value of $C_l|_\alpha$ relative to large overhang distances. A smaller overhang distance increases the value of $C_l|_\alpha$. A large overhang distance accelerates the flow over the lower surface of element $n-1$ and subsequently decreases the pressure differential between the upper surface and lower surface of element $n-1$. The reduction in pressure difference decreases the lift generated by element $n-1$. Data were not collected at overhangs less than 0.0203 in the closely coupled tests.

Overhang distance also affects the drag of the multielement airfoil system, as shown in Fig. 3.10. Data are plotted at four different α values. Data indicate that $C_d|_\alpha$ is minimized near an overhang distance of 0.01684, and it is noted that $C_d|_\alpha$ has a local maximum at an overhang value of 0.02184 at all angles of attack. The magnitude of the drag rise at an overhang distance of 0.02184 is as large as 0.01, or 30% relative to data at an overhang of 0.01684 or 0.02684. A local minimum in $C_d|_\alpha$ is observed at an overhang distance

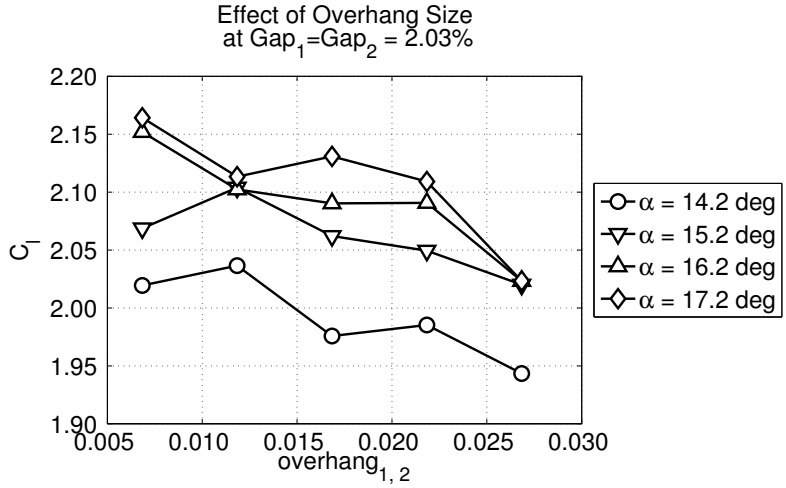

Figure 3.9: Effect of overhang distance on lift for closely coupled airfoil.

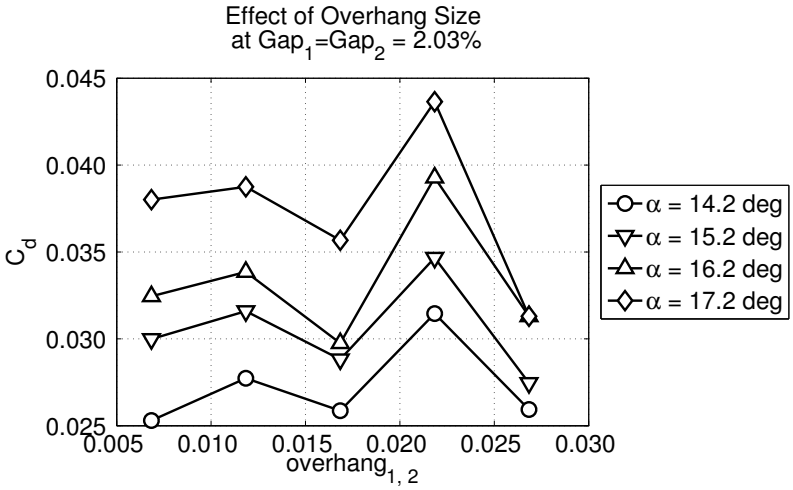

Figure 3.10: Effect of overhang distance on drag for closely coupled airfoil.

near 0.01684. The observed local minimums and maximums were observed at many different angles of attack for the configurations tested which captured the overhang effect.

Lift and drag were both affected by the overhang distance and the relationship between ${}^{C_l}/_{C_d}|_\alpha$, and overhang distance is presented in Fig. 3.11. In general, ${}^{C_l}/_{C_d}|_\alpha$ is not largely affected by the overhang distance. However, the drag rise at an overhang of 0.02184 causes a reduction in ${}^{C_l}/_{C_d}|_\alpha$. It is clear from Fig. 3.11 that the drag of the airfoil dominates the effect of the ${}^{C_l}/_{C_d}$ ratio.

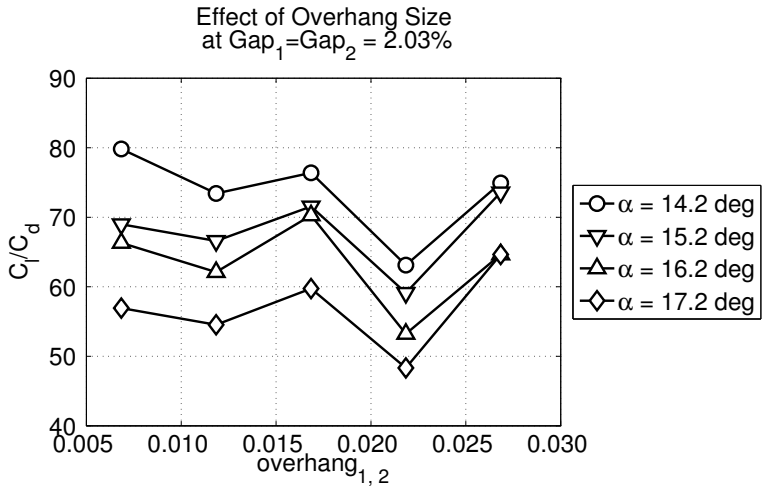

Figure 3.11: Effect of overhang distance on C_l/C_d for closely coupled airfoil.

3.2.4 Flow Visualization

Surface oil flow visualization was used as a tool in an effort to understand the aerodynamic flow in greater detail. The oil flow was used to examine the effect of the wind tunnel walls and the clamps upon the two-dimensionality of the flow.

CC-1 Flow Visualization

Flow visualization results of the CC-1 configuration at $\alpha = 9.9$ deg are shown in Fig. 3.12. Measurements presented on the yellow tape correspond to percent of chord based on the chord length of the main element only. Figure 3.12(a) depicts the upper surface and Fig. 3.12(b) shows the lower surface. As seen in Fig. 3.12(a), the leading edge is on the right side of the picture and the trailing edge is on the left. A laminar separation bubble begins to form at approximately 0.322 c_{main} and turbulent reattachment occurs at 0.39 c_{main}. A region of very high shear exists just downstream of the reattachment point. Results indicate that the flow was attached over the entire airfoil system as stagnation regions are not visible on the main element or on either flap. An oil accumulation line is visible on each flap which indicates the location of a laminar separation bubble.

Flow visualization on the lower surface, seen in Fig. 3.12(b), indicates a laminar separation bubble beginning at 0.27 c_{main} and turbulent reattachment at 0.40 c_{main}. A region of high shear exists from the turbulent reattachment line to approximately 0.49 c_{main}. Flow from 0.75 c_{main} to 0.93 c_{main} on the lower surface is very low shear. Separation is not indicated as there is no separation line indicated by an oil

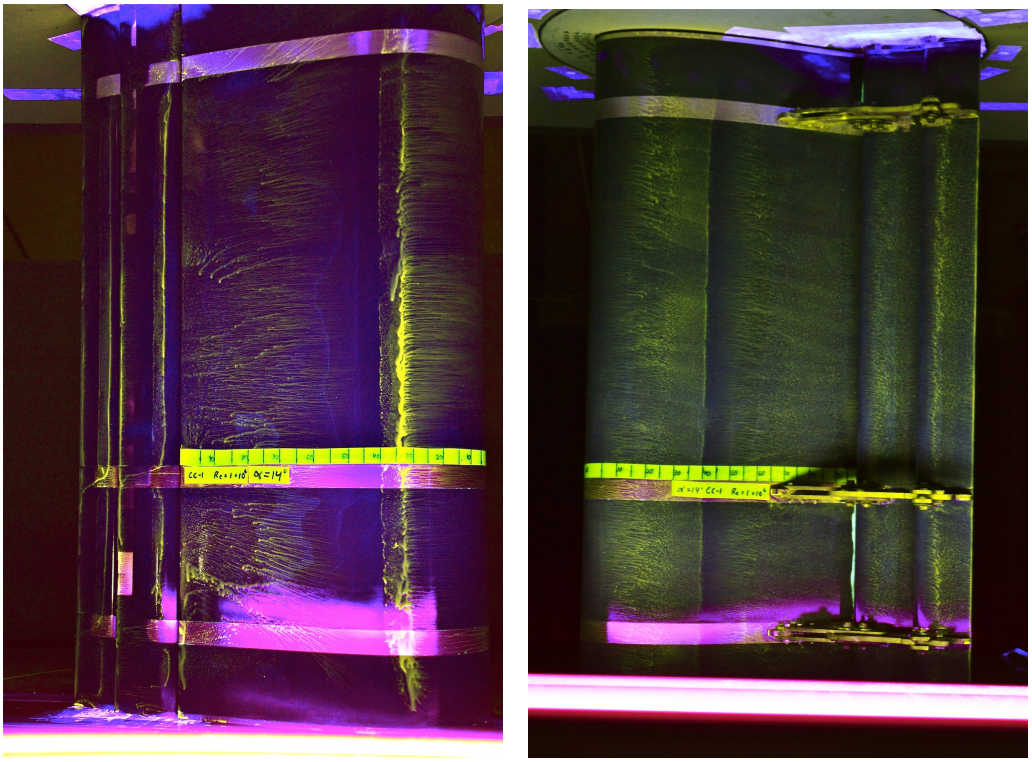

(a) (b)

Figure 3.12: Surface oil flow visualization of baseline configuration at $\alpha = 9.9$ deg and $Re = 1.0 \times 10^6$ on (a) upper surface and (b) lower surface.

accumulation line. The leading edge of Flap 1 and Flap 2 both show a region of high surface shear as minimal oil exists near the leading edge of either flap.

Surface oil flow visualization was also performed at $\alpha = 12.9$ deg, as shown in Fig. 3.13. The upper surface laminar separation bubble begins at approximately 0.30% c_{main}, slightly upstream when compared with $\alpha = 9.9$ deg, and a turbulent reattachment line is visible at 0.37 c_{main}. Size of the bubble at $\alpha = 12.9$ deg is smaller than the bubble at $\alpha = 9.9$ deg. The high shear region downstream of the laminar separation bubble is smaller at $\alpha = 12.9$ deg. It is noted that a region of low shear exists near the trailing edge of the main element on the upper and lower surface. Flow over the flaps is high shear as almost no oil is visible on the flap surfaces except at the laminar separation bubble and at the trailing edge.

The lower surface has a laminar separation bubble at 26% x/c_{main}, which is slightly upstream from $\alpha = 9.9$ deg. Turbulent reattachment occurs at 44% x/c_{main}, 4% x/c_{main} downstream compared to the $\alpha = 9.9$ deg. The high shear region on the lower surface is shorter than the high shear region downstream of the reattachment line on the upper surface. Flow approaching the trailing edge from 65% x/c_{main} to 93% x/c_{main} is very low shear. Low shear in this region indicates the local flow is slow and may be approaching separation. It is noted that the flow is significantly reenergized as it enters the gap between

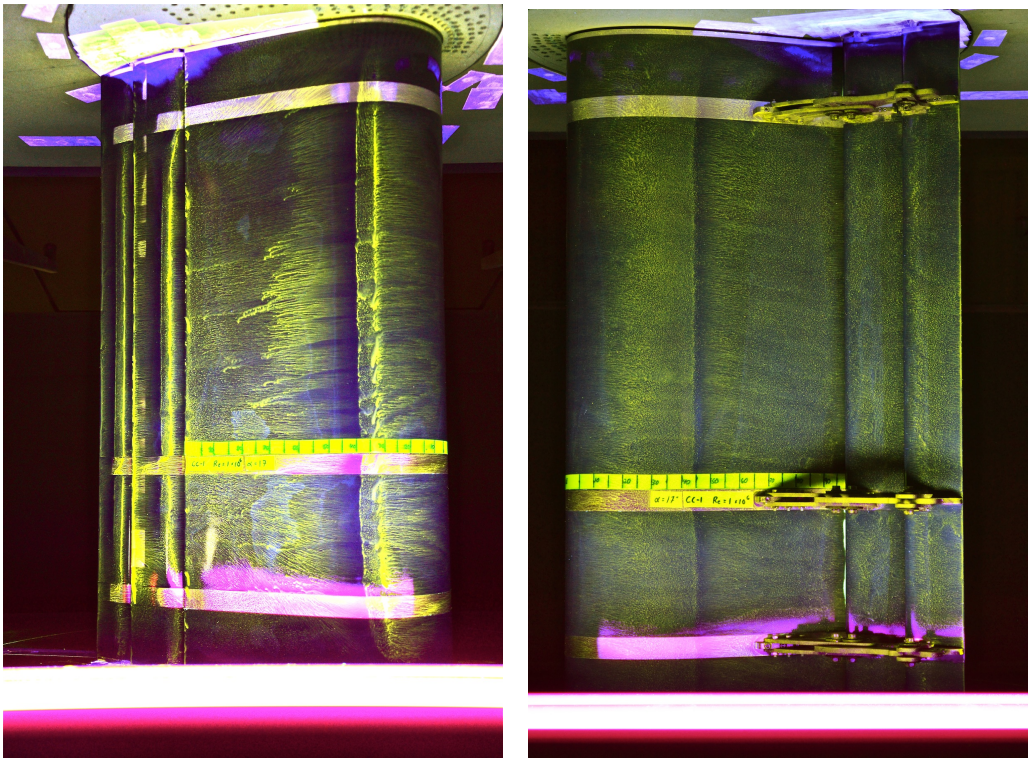

(a) (b)

Figure 3.13: Surface oil flow visualization of baseline configuration at $\alpha = 12.9$ deg and $Re = 1.0 \times 10^6$ on (a) upper surface and (b) lower surface.

the main element and the first flap. Flow over the lower surface of flap one and flap two indicate a region of very low shear as the surface oil has barely moved. The behavior at the leading edge of the two flaps is also noted and suggests a region of low shear, which is contrary to the high shear region at the leading edge of the two flaps at $\alpha = 9.9$ deg.

Effect of Clamps

Flow visualization techniques were applied to the CC-1 configuration with an emphasis on the flap clamps in an effort to understand the effect of the clamps on the flow characteristics. Results from a test at $\alpha = 12.9$ deg are shown in Fig. 3.14. A small region on the order of 2% x/c_{main} is disturbed upstream of the clamp mounting bracket, as shown in Fig. 3.14. Flow near the trailing edge underneath the main element flap clamp is also disturbed as three-dimensional flow is visible in this region. Three-dimensional flow was localized and did not interfere with flow more than 1-in away from the clamps. Overall, the effects of the clamps were determined to be minimal and did not significantly disturb the flow over the surface of the airfoil.

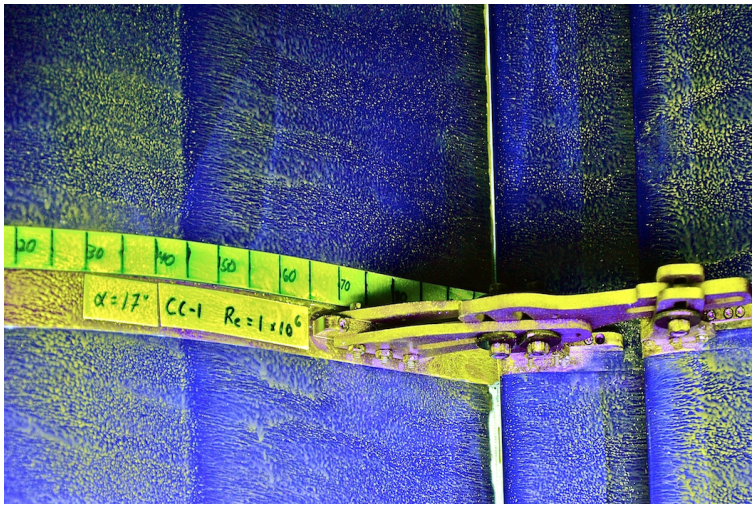

Figure 3.14: Surface oil flow visualization around clamps in CC-1 configuration at $\alpha = 13.9$ deg.

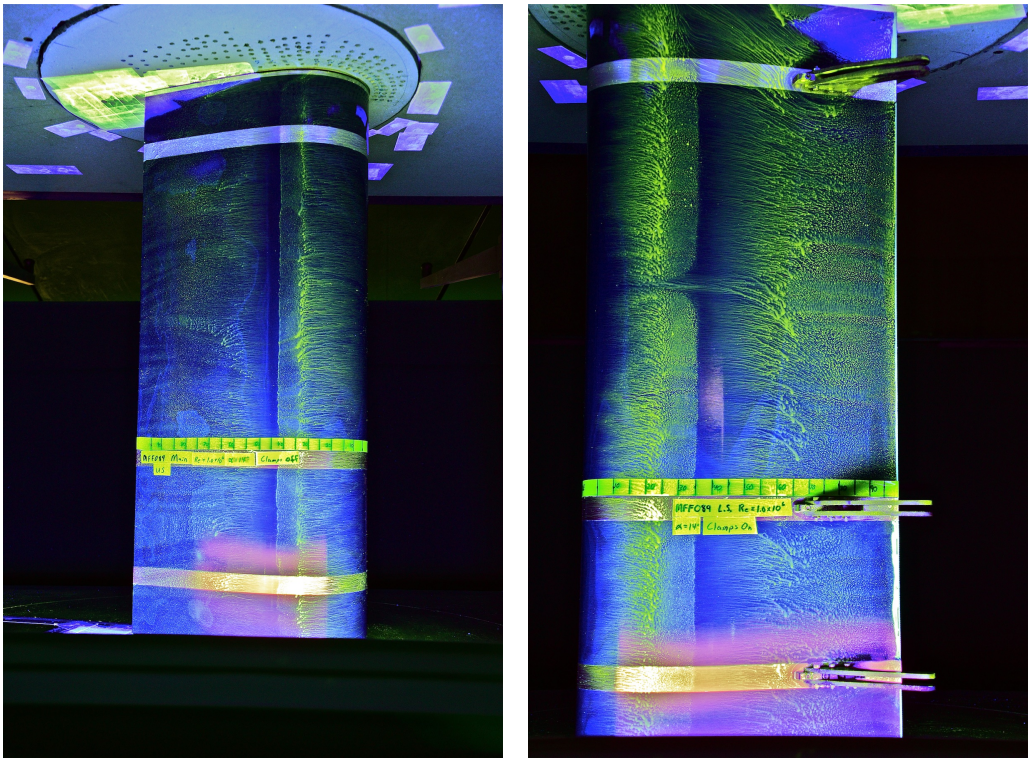

(a) (b)

Figure 3.15: Surface oil flow visualization of main element at $\alpha = 9.9$ deg and $Re = 1.0 \times 10^6$ on (a) upper surface and (b) lower surface.

Single element flow vizualization

Tests were performed on the MFF-089 main element only in an effort to understand the effect of the flaps on the entire system. Results, shown in Fig. 3.15, suggest that the absence of flaps adversely affects the aerodynamic performance. The flow over the upper surface downstream from $75\%x/c$ is extremely low shear.

This observation is contrary to the results with the flaps presented above in Fig. 3.15 where the region toward the trailing edge on the upper surface of the main element was relatively high shear. The lower surface is also a region of low shear which is similar to the results with the flaps. However, the flow is not reenergized as it approaches the trailing edge of the main element as there is no multielement effect as shown in Fig. 3.12. Results indicate the presence of low shear regions but separation was not observed.

Wall effects

Flow visualization indicated the tunnel floor and ceiling affected the flow over the multielement airfoil system. Results indicate that the walls reduced the two-dimensionality of the flow near the floor and ceiling, as shown in Fig. 3.16. Spanwise flow originated near the laminar separation bubble and disturbed approximately 4 inches of the flow. Results indicated that the intensity of the spanwise flow increased at large values of α at high Reynolds number. Spanwise flow was stronger at higher Reynolds number than at lower Reynolds numbers. Diagnostic tests were perform to establish the region in which the flow was minimally affected by the wind tunnel walls. The conclusion of these tests indicated that data would be collected at a Reynolds number no greater than 1.0×10^6 in an effort to minimize spanwise flow and to test large angles of attack. Large values of α were not affected at a Reynolds number of 1.0×10^6.

3.2.5 Data Challenges

Data collected for the closely coupled tests did not always exhibit the predicted behavior. Systematic problem solving and further investigation indicated that there were two fundamental challenges associated with the closely coupled family of airfoil tests. First, the airfoil system was extremely thick and conventional blockage corrections may or may not have accurately corrected for the solid blockage of the system. This observation was evidenced by a C_l vs. α curve which was approximately 15% less than the theoretical 2π. It is hypothesized that the thick airfoil model interacted with the walls and conventional tunnel corrections were not adequate for the tested airfoil. The reduced slope of the lift curve could be driven by the solid blockage correction or the dynamic pressure correction. Alternative blockage corrections developed by Garner [38], Glauert [43], Klunker [44], and Young [45] were applied to the data. These alternative corrections for solid blockage did not make a significant difference in the slope of the data. In addition, the correction for q, dynamic pressure, was examined. Some flow past the model was blocked by the thickness of the model and, consequently, the flow between the model and the wind tunnel walls was accelerated. Consequently, the value of q over the surface of the airfoil was larger than that measured in the freestream. Conventional methods outlined by Barlow, et al were applied to correct the value of q. However, the correction applied

to q may not be valid for thick airfoils. More research is needed to develop or verify corrections for thick airfoils.

A reduced C_l vs. α slope may also be attributed to wake bursting. While no definitive evidence of wake bursting was found during the wind tunnel experiments discussed in this thesis, research supporting the multielement project did suggest the presence of wake bursting. Two-dimensional CFD simulations were performed by Narsipur, et al. on the CC-1 configuration and they observed large stagnation regions off the surface of multielement system [31]. It is clear that more experiments and wake survey tests are needed to experimentally verify the presence of wake bursting.

In addition, the secondary force balance was found to be faulty after data were collected in the wind tunnel. Validation tests presented in Section 2.2.1 were performed with a low capacity (100-lb) load cell. Preliminary computational estimates indicated the closely coupled model may produce values of C_l in excess of 3.0 at a Reynolds number of 1.85 million and a high capacity (750-lb) load cell was attached to the secondary force balance. Previously discussed spanwise flow required tests to be performed at a lower Reynolds number of 1.0 million and the $C_{l,max}$ of the closely coupled airfoil was only approximately 2.1.

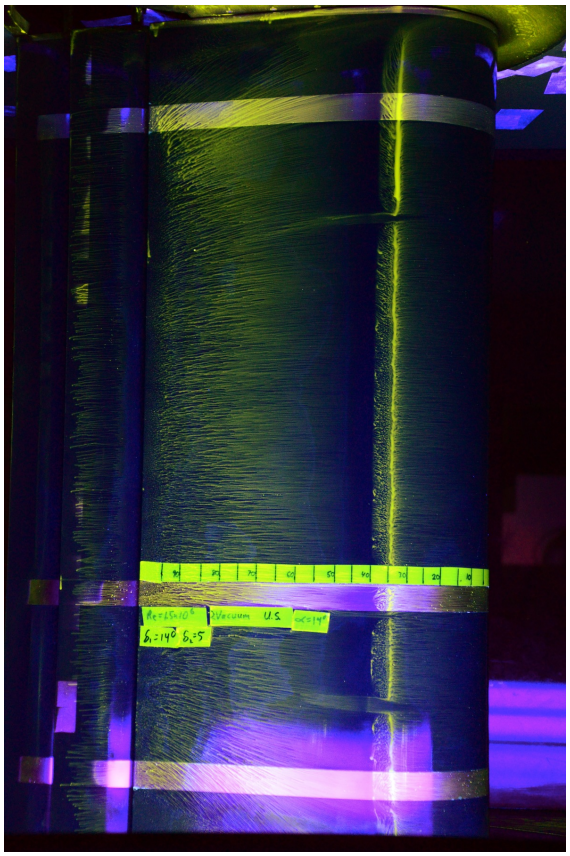

Figure 3.16: CC-1 configuration at $\alpha = 9.9$ deg and $Re = 1.0 \times 10^6$ with spanwise flow near walls.

The combination of the lower Reynolds number and lower lift than predicted yielded lift forces which were significantly less than what was predicted. As a result, the selected 750 lb capacity load cell was too large and a lower capacity load cell should have been chosen. The uncertainty values of the load cell were on the order of the values of the lift force applied to the secondary load cell. This uncertainty resulted in one or two data points in each polar which generated a local spike. Magnitude of the spike was not repeatable and the angle(s) at which the spike occurred was not repeatable. Measured values of C_l were as much as 0.15 higher or lower than the linear fit through the rest of the data. Consequently, statistical analysis was performed on all data sets, and a robust least squares regression fit was applied to each C_l vs. α curve and residuals were calculated for each data point relative to the robust least squares fit. Data points with a residual greater than 0.07 were removed from the data set.

3.3 Well Separated Multielement Airfoil Tests

Quantitative aerodynamic performance data were collected for the well separated family of airfoils. Flow visualization was not performed on any of the well separated configurations. Performance data were corrected for wind tunnel wall effects as noted in Section 2.1.7. A four-element system consisting of a main element, a strut, and two flaps was tested. The length of the main element was 11.5 in and the strut measured 7.8 in. Flaps used in the well separated family were the same as the closely coupled case and the flaps measured 3.5 in and 3.0 in for the first and second flap respectively. System chord length of the baseline configuration was 17.53 in. Unit chord coordinates of the four elements are supplied in Appendix D.

Well separated configurations tested in the wind tunnel were all related to the MFFS-026 airfoil system designed by Ragheb, et al. [32]. Different configurations of the main-flap-flap-strut multielement airfoil system were named well separated configurations. The baseline configuration was denoted by WS-1 (well separated). Many well separated configurations were generated by systematically varying gap size, overhang distance, strut deflection angle, and strut location. The full test matrix of all configurations tested is presented in Appendix A.

Data collected in the wind tunnel included C_l, C_d, and C_m. The effects of different relative coordinate parameters are discussed in this chapter and individual drag polars are presented in Appendix B. Tabulated data for each configuration tested are supplied in Appendix C. It is noted that all tests were performed at a Reynolds number of 0.975×10^6. A faulty thermocouple caused tests to be performed at a Reynolds number of 0.975×10^6 as opposed to 1×10^6 at which the closely coupled tests were performed.

Multiple tests of the same test are differentiated by a subtest label. It is noted that well separated data were taken with only the main wind tunnel balance and the secondary force balance (SFB) was not used.

3.3.1 Baseline Results

Tests were performed on the baseline WS-1 configuration and the measured drag polar and lift curve are presented in Fig. 3.17. The WS-1 system produced less lift than the baseline CC-1 configuration plotted in Fig. 3.2. The value of $C_{l,max}$ is 1.72 at $\alpha = 13$ deg. Wake profiles suggest the flow over the entire system is detached at $\alpha = 0$ deg. The three-element cascade airfoil systems attaches at an angle of $\alpha = 1$ deg while the strut flow did not attach until $\alpha = 6$ deg. A large drop in C_d is noted where the flow over the strut attached at $\alpha = 5.5$ deg. Stall characteristics are gradual and gentle which suggest a thin airfoil stall or a trailing edge stall. The linear region of the $C_l - \alpha$ curve extends from an α of 1 deg through 11 deg.

3.3.2 Test Matrix

Methods used to choose and generate the test matrix were similar to procedures used for the closely coupled tests, as discussed in Section 3.2.2. The baseline configuration was referred to as the WS-1 configuration. Configurations studied for the well separated airfoil tests captured the independent effect of multielement

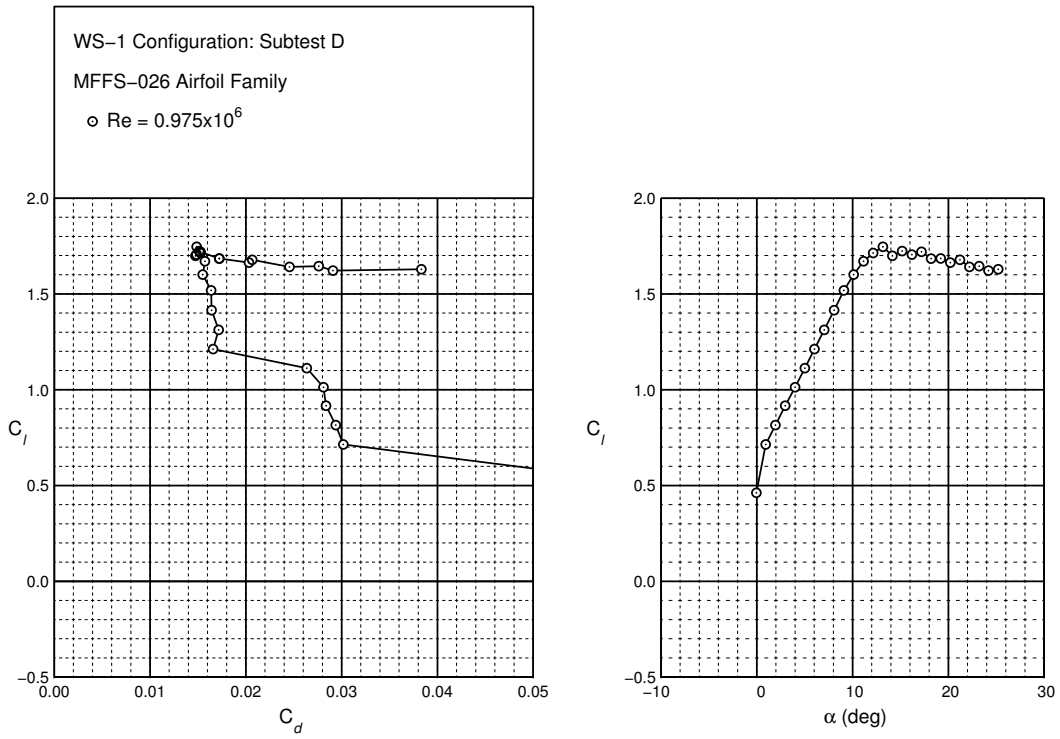

Figure 3.17: Baseline results of WS-1 configuration at $Re = 0.975 \times 10^6$.

effects with emphasis on gap size and overhang distance. A summary of the families of configurations tested is presented in Table 3.2. A more detailed table with more significant digits is presented in Appendix A. Some significant digits have been truncated in Table 3.2 to save space. It is noted that configurations 11 and 12 are included in two different families. Each family consisted of a single parameter which was altered. Notation in Table 3.2 is the same as notation used in Table 3.1 in which a range of values is denoted by $value_{min} : increment : value_{max}$. Tests performed in Family 1 and Family 2 measured the effect of overhang distance at two different gap sizes. Family 3 captured the effect of strut deflection angle on the aerodynamic performance of the system. Performance of the system as a function of gap size was captured in Family 7 and 8 while the location of the strut was tested in Families 8 through 13. The focus of Family 8 was to study the effect of the gap size if the strut was not in its home position. Data collected in Families 9 through 13 (supplemented by data in Families 2, 4, and 8) studied the effect of the strut location on the aerodynamic performance.

Table 3.2: Well Separated Airfoil Test Matrix Families

Family	Configurations	$overhang_n$	gap_n	δ_n [deg]		x_{strut}	y_{strut}	δ_{strut}
1	2, 3:2:13	-0.010:0.005:0.020	0.030	17.1	13	0.172	-0.268	-6.5
2	4:2:14	-0.005:0.005:0.020	0.025	17.1	13	0.172	-0.268	-6.5
3	15:20	-0.005:0.005:0.020	0.025	17.1	13	0.182	-0.286	-16.5
4	21:23	0:0.005:0.010	0.025	17.1	13	0.158	-0.212	-6.5
5	24:27	-0.005:0.005:0.010	0.025	17.1	13	0.185	-0.323	-6.5
6	28:31	-0.005:0.005:0.010	0.025	17.1	13	0.240	-0.310	-6.5
7	11:12 32:35	0.015	0.01:0.005:0.035	17.1	13	0.172	-0.268	-6.5
8	36:41	0.015	0.01:0.005:0.035	17.1	13	0.185	-0.323	-6.5
9	42	0.010	0.025	17.1	13	0.214	-0.199	-6.5
10	43	0.010	0.025	17.1	13	0.103	-0.225	-6.5
11	44	0.010	0.025	17.1	13	0.116	-0.281	-6.5
12	45	0.010	0.025	17.1	13	0.227	-0.254	-6.5
13	46	0.010	0.025	17.1	13	0.164	-0.247	-6.5

3.3.3 Cross-Configuration Analysis

Data from the carefully constructed test matrix was analyzed to understand the relationship between each independent parameter and the aerodynamic performance. Tests were performed in an effort to understand the effect of gap size, overhang distance, and strut location on the aerodynamic performance of the airfoil system. Gap and overhang distances were changed using the flap positioning system discussed in Section 2.3 and configurations were generated by methods outlined in Section 2.8. The strut was moved to eight different positions denoted by $(x, y)_{le,strut}$. The deflection angle δ_{strut} was also independently changed.

Effect of gap size

As shown in Fig. 3.18, the gap size of the two flaps affects the lift of the entire multielement system. A peak in the C_l vs *gap* curve is observed at a gap size of 0.020, which is similar to the best size for the closely coupled system which was 0.025. The rate of decrease of C_l is greater at small gaps than the rate of decay at larger gaps.

Drag is also affected by the size of the gap between the different elements and results are plotted in Fig. 3.19. A local minimum in drag is observed at a gap size of 0.015 which is a slightly smaller gap size than the gap size with maximum lift. Drag is reduced by approximately 5% relative to the drag at a gap size of 0.020. Data at small a gap size of 0.010 suggest a drag rise at small gap sizes which may be driven by interacting boundary layers and wakes.

Aerodynamic efficiency, ${}^{C_l}/_{C_d}|_\alpha$, as a function of gap size is plotted in Fig. 3.20. A maximum in the lift-to-drag-ratio is observed at a gap size of 0.015, which is the gap size with minimum drag. The lift-to-drag ratio at the gap size with maximum lift (0.020) is 78.2, a 4.6% reduction relative to the point with maximum ${}^{C_l}/_{C_d}|_\alpha$. A reduction in ${}^{C_l}/_{C_d}|_\alpha$ is observed at small gap sizes which is primarily driven by a reduction in lift.

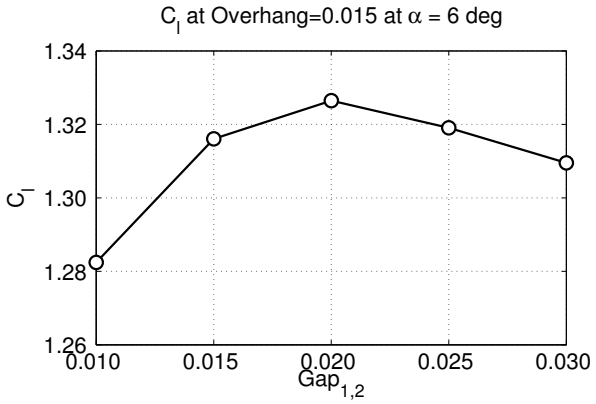

Figure 3.18: Effect of gap size on lift for well separated airfoil.

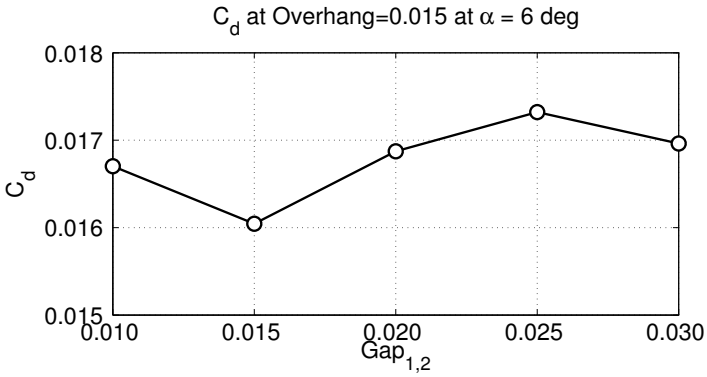

Figure 3.19: Effect of gap size on drag for well separated airfoil.

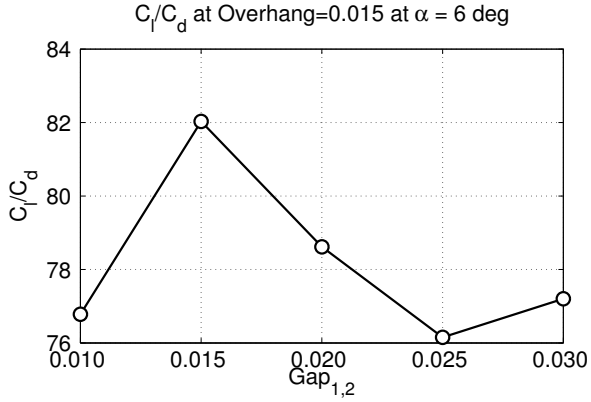

Figure 3.20: Effect of gap size on $^{C_l}/_{C_d}$ for well separated airfoil.

Effect of overhang distance

Tests were performed to isolate the effect of the overhang distance on the aerodynamic performance and results are presented in Fig. 3.21-3.23. Lift as a function of overhang is presented in Fig. 3.21. The relationship is more complex than that of the gap effect on the lift. A maximum value of C_l is observed at an overhang distance of -0.005. As noted in Fig. 2.4, a negative overhang is a distance in which the leading edge of element n is forward of the trailing edge of element $n-1$. Positive overhang distances adversely affect the lift produced by the system.

Drag of the multielement airfoil system is also a function of the overhang distance and results are shown in Fig. 3.22. Data suggest that larger positive overhangs have less drag than those with smaller positive, or even negative, overhang distances. A drag reduction of 5.6% exists at an overhang distance of 0.015 compared with an overhang distance of 0. A sharp drag reduction is observed between 0.005 and 0.010.

Lift-to-drag ratio as a function of overhang distance is plotted in Fig. 3.23. The $^{C_l}/_{C_d}|_\alpha$ value at the overhang with maximum lift is 75.0 while the $^{C_l}/_{C_d}|_\alpha$in the low drag region is as high as 77.7. Additionally,

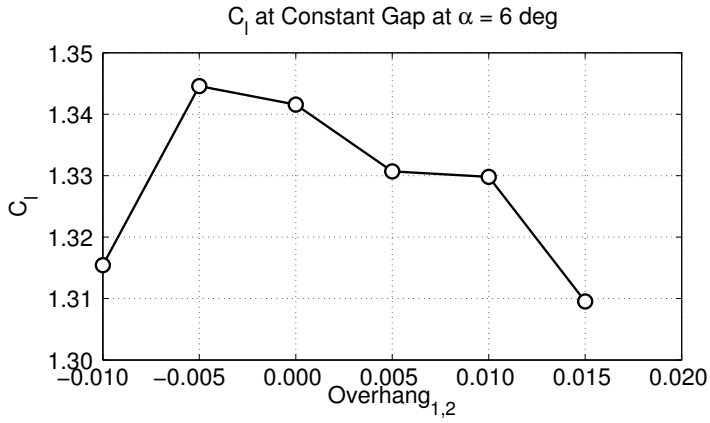

Figure 3.21: Effect of overhang distance on lift for well separated airfoil.

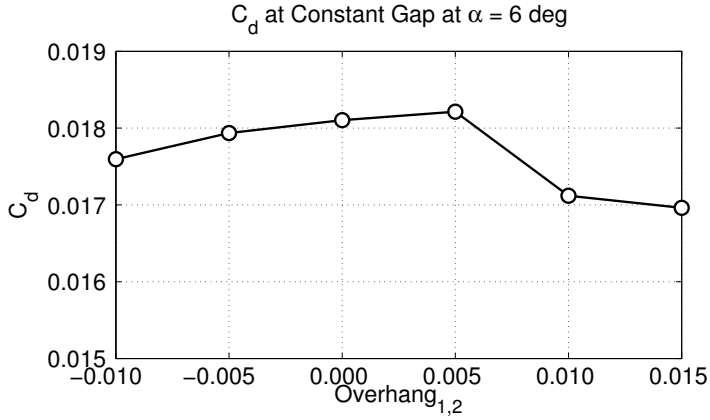

Figure 3.22: Effect of overhang distance on drag for well separated airfoil.

the lift-to-drag ratio is locally minimized at an overhang of 0.005 which is the value with the highest drag. Data suggest the effect of the low drag values has a greater effect on the aerodynamic efficiency than the benefit of increased lift.

Effect of strut deflection angle

Data were collected with the gap and overhang at a constant value while the strut deflection angle was independently varied. Baseline deflection of the strut was -6.5 deg and it could be deflected ± 10 deg in the baseline $x - y$ position. Strut deflections were not possible in any other $x - y$ position. The strut was designed to act as a fairing and not as a lifting element. More details on the design are discussed by Ragheb, et al [32]. Data presented in Fig. 3.24–3.26 are presented at three angles at $\alpha = 7$ deg and $\alpha = 8$ deg. Lift as a function of strut deflection angle is presented in Fig. 3.24. Lift is increased for positive strut deflections as the strut transitions from a curved non-lifting fairing to a lifting element. In addition, the lift decreases as

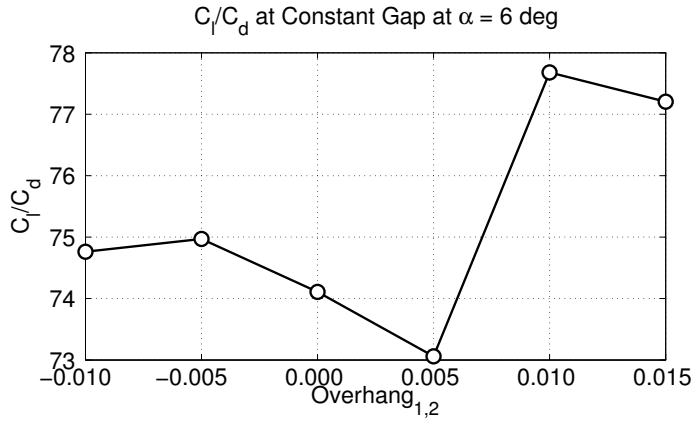

Figure 3.23: Effect of overhang distance on C_l/C_d for well separated airfoil.

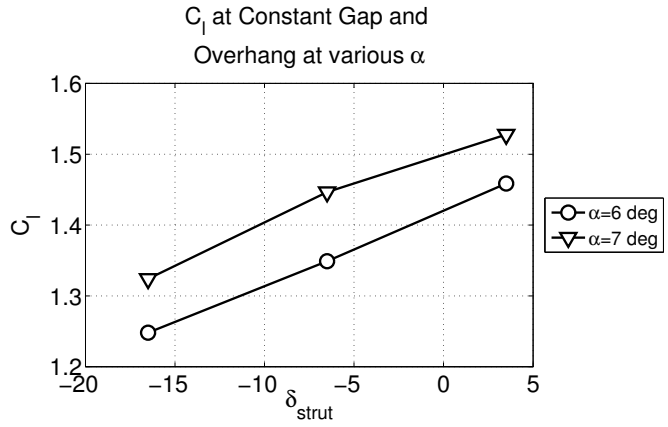

Figure 3.24: Effect of δ_{strut} on lift for well separated airfoil.

the strut deflection decreases because the strut produces negative lift. The rate of change of lift with respect to deflection angle is nearly constant for a positive deflection angle compared to a negative deflection angle.

Deflection of the strut also affects the drag of the multielement airfoil system, as noted in Fig. 3.25. A negative strut deflection angle causes the drag to triple relative to the baseline case, as noted for the cases with $\delta_{strut} = -16.5$ deg. This drag rise could be a result of flow separation over the lower surface of the strut or multielement aerodynamic effects caused by the strut on the rest of the airfoil system. Drag remains nearly constant for positive strut deflection angles.

The combined effect of the strut deflection angle on the aerodynamic efficiency of the system is presented in Fig. 3.26. Negative deflection angles, due to the large drag rise and negatively lifting strut, drastically decrease the value of $C_l/C_d|_\alpha$ relative to the baseline case. A positively deflected generates slightly more lift than the baseline case for approximately the same drag value which translates into a small $C_l/C_d|_\alpha$ increase at a positive strut deflection relative to the baseline case.

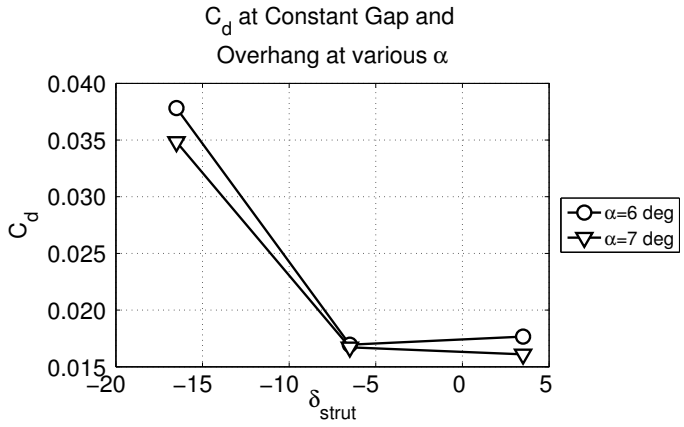

Figure 3.25: Effect of δ_{strut} on drag for well separated airfoil.

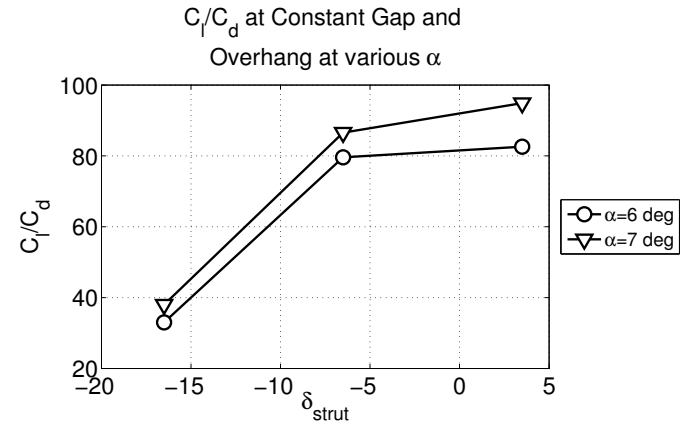

Figure 3.26: Effect of δ_{strut} on C_l/C_d for well separated airfoil.

Effect of strut location

The experimental configuration allowed the strut to be moved to eight separate locations and collect data at each location. Movement was permitted in a direction normal and/or tangential to the main element chord at a distance of 5.7% system chord. Movement was possible in any combination of up/down and forward/back except forward and down as the wind tunnel balance support leg would have interfered with the strut spar. As shown in Fig. 3.27, the location of the strut has an effect on the C_l of the system. The strut was able to be moved in a direction normal or tangential to the main element chord line. The label of $Strut_{ud}$ corresponds to the location of the strut in the direction normal to the chord of the main element (up/down) while $Strut_{fore/aft}$ is the distance the strut has been moved tangential to the main element chord line. Lift is the highest when the strut is in the baseline position and is reduced in all other seven locations. No clear trend exists between cases at a constant up/down location.

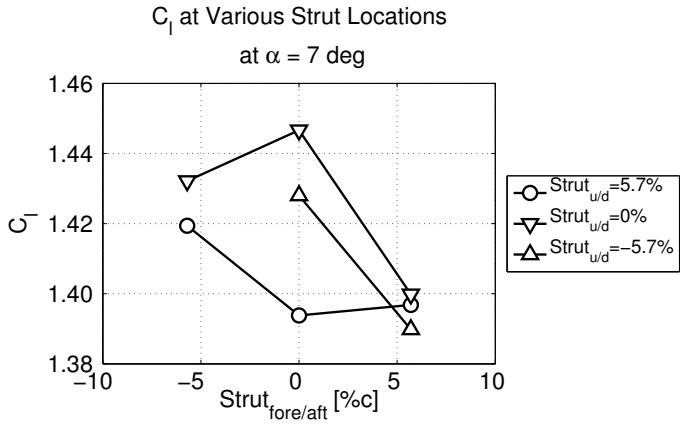

Figure 3.27: Effect of strut location on lift for well separated airfoil.

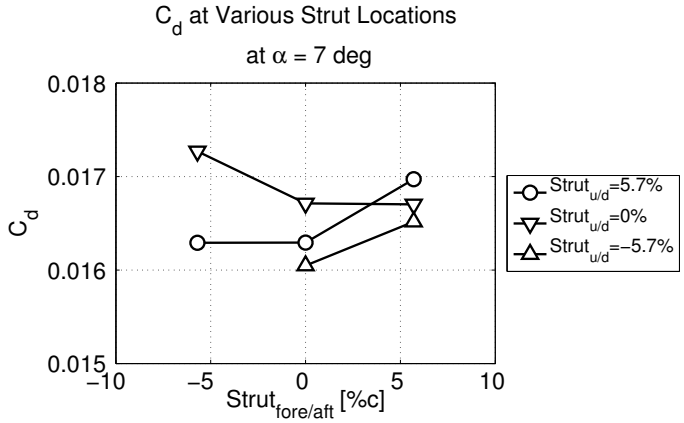

Figure 3.28: Effect of strut location on drag for well separated airfoil.

Additionally, the drag values of the eight different strut location cases are presented in Fig. 3.28. Drag is reduced for cases in which the strut is moved away from the main element (moved down). In general, drag is the smallest value for a given main element chord normal location when the fore/aft location is 0.

Finally, the ${}^{C_l}/_{C_d}|_\alpha$ of the airfoil system as a function of strut location is presented in Fig. 3.29. The ${}^{C_l}/_{C_d}|_\alpha$, based on the data collected, is maximized when the strut is in the baseline fore/aft location and moved away from the main element of the system. The lift to-drag-ratio in the baseline case is 2.9% less than the best observed case.

Coupled effect of strut deflection angle and overhang distance

The combined effect of δ_{strut} and overhang distance was captured and results are presented in Fig. 3.30–3.32. Airfoil configurations were tested at a strut deflection of -6.5 deg (the baseline deflection angle) and at -16.5 deg. A range of overhang distances varied from -0.005 to 0.02 c_{system}. All tests were performed

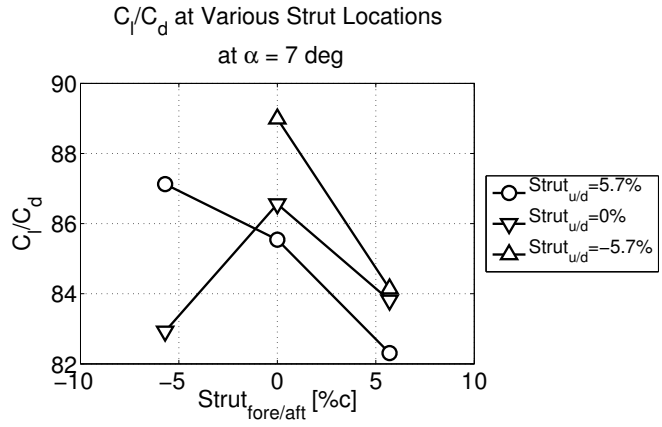

Figure 3.29: Effect of strut location on C_l/C_d for well separated airfoil.

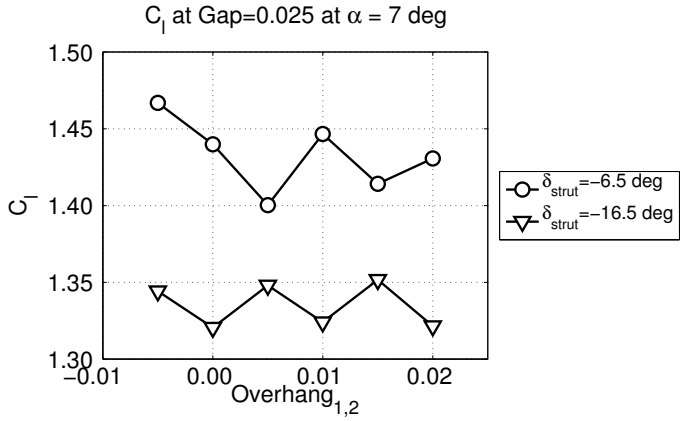

Figure 3.30: Effect of strut deflection angle and overhang distance on lift for well separated airfoil.

at a constant gap size of 0.025. The combined effect on lift is plotted in Fig. 3.30. The effect of the strut deflection angle on C_l is larger than the effect of the overhang distance. As previously observed in Fig. 3.21, overhang distance has a minimal effect on the lift of the multielement airfoil system.

Drag as a function of strut deflection angle and overhang distance is plotted in Fig. 3.31. The deflection angle of the strut affects the drag of the multielement system more than the overhang distance and drag values at a negative deflection angle are more than twice as high as the baseline deflection case. A positive overhang may reduce the drag of the system compared to a negative overhang distance.

Aerodynamic efficiency at various strut deflection angles and overhang distances is plotted in Fig. 3.32. It is noted that the overhang distance has a minimal affect on the value of $C_l/C_d|_\alpha$. The strut deflection angle greatly affects the value of $C_l/C_d|_\alpha$. This reduction aerodynamic efficiency is primarily driven by the drag rise at the reduced deflection angle.

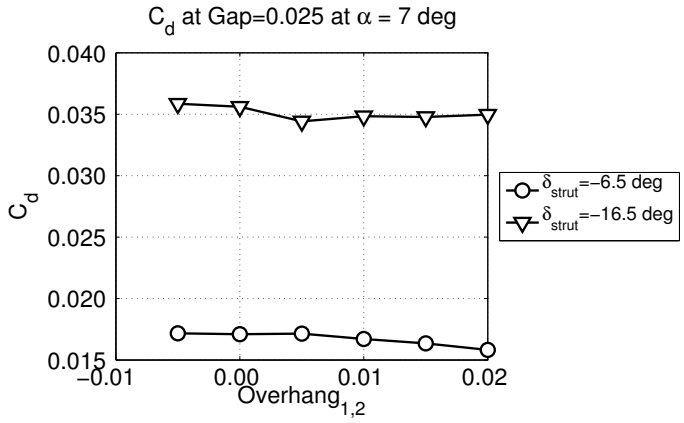

Figure 3.31: Effect of strut deflection angle and overhang distance on drag for well separated airfoil.

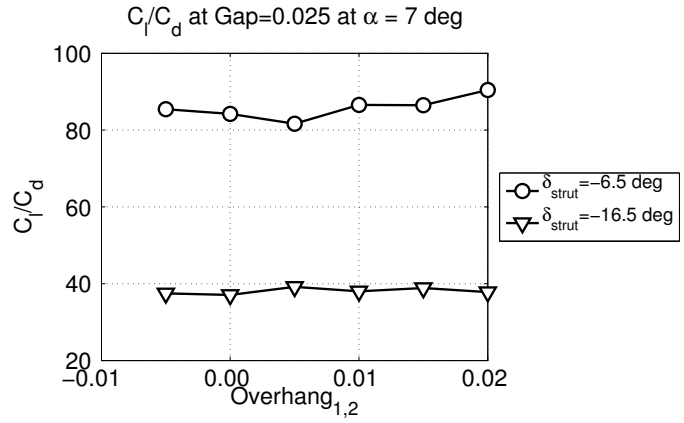

Figure 3.32: Effect of strut deflection angle and overhang distance on C_l/C_d for well separated airfoil.

Coupled effect of strut location and gap size

The joint effect of gap size and strut position was also captured and results are plotted in Fig. 3.33–3.35. Cases were generated at a constant overhang distance of 0.015 and a gap size from 0.01 to 0.035. The strut was place in the baseline position and also moved away from the main element chord line. Movement of the strut is discussed in greater detail in Section 2.5. The coupled effect of lift is presented in Fig. 3.33. In general, lift decreases for gap sizes less than 0.02 and a local maximum is observed at 0.02. The lift of the system decreases for gap sizes between 0.02 and 0.03 but increases at at gap size of 0.035 relative to the lift at a gap size of 0.03. Data were not collected at gap sizes greater than 0.035.

Figure 3.34 plots the effect of strut location and gap size on the drag of the system. Both parameters affect the drag and the relationship between the two parameters is not clear. Drag for the baseline configuration is minimized at a gap size of 0.015 and maximized at a gap size of 0.025, as presented in Fig. 3.19. However,

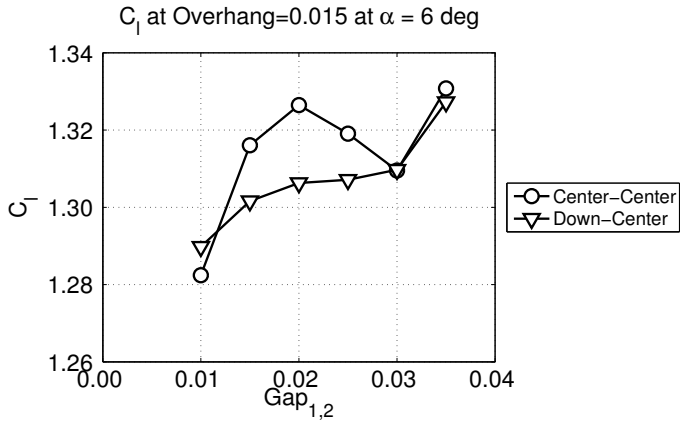

Figure 3.33: Effect of strut location and gap size on lift for well separated airfoil.

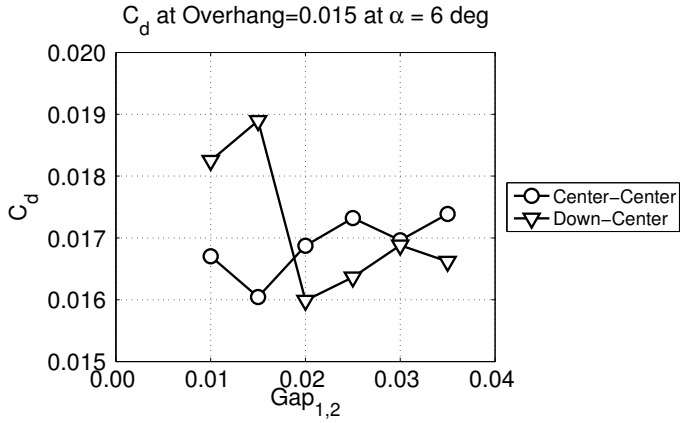

Figure 3.34: Effect of strut location and gap size on drag for well separated airfoil.

drag for the case in which the strut was moved down is minimized at a gap size of 0.02 and maximized at a gap size of 0.015.

The combined aerodynamic efficiency as a function of strut location and gap size is presented in Fig. 3.35. As previously discussed, the relationship between strut location and aerodynamic performance is not clear. A maximum of $C_l/C_d|_\alpha$ is observed between 0.015 and 0.02 for both locations of the strut. A sharp reduction in lift-to-drag ratio is observed for gap sizes slightly smaller than where the maximum was observed.

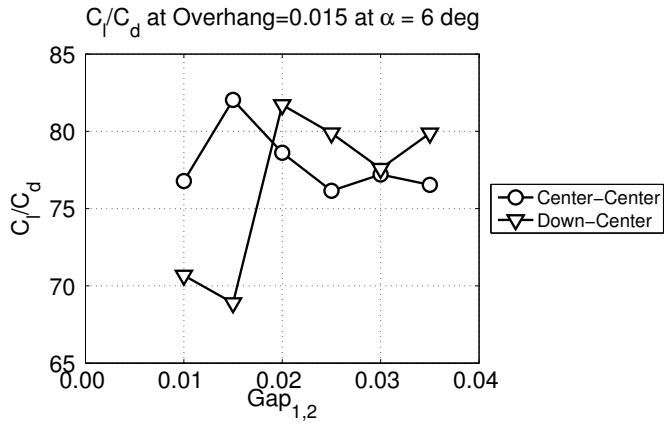

Figure 3.35: Effect of strut location and gap size on C_l/C_d for well separated airfoil.

Chapter 4

Summary, Conclusions, and Future Work

4.1 Summary

Experimental research discussed in this thesis was performed at the University of Illinois at Urbana-Champaign from August 2010 through April 2012. Two multielement airfoil systems were the focus of the investigation; the closely coupled model was comprised of a main element and two flaps while the well separated model contained a main element, two flaps, and a strut. The systems were designed by other researchers for application in the root section of large (10-MW) scale wind turbines. Wind tunnel tests were performed in the UIUC 3×4 ft low-speed, low-turbulence wind tunnel at a Reynolds number based on system chord length of approximately 1.0×10^6. A high lift secondary force balance was designed, validated, and implemented on the wind tunnel. The SFB can be used for future tests of high lift airfoils. In addition, a flap positioning system was designed, manufactured, and implemented to accurately move flaps to precise locations. The FPS can be used by future researchers for flaps, slats, or any application requiring precisely located airfoil elements. Design of the two multielement models was performed by the researchers, and the models were constructed and tested in the wind tunnel. Data were collected using a three-component force balance. Wake profiles were captured and drag was calculated by integrating across the wake of the multielement system.

Test matrices for the two tests were carefully constructed to capture the independent effect of parameters which govern multielement airfoil aerodynamics. The gap, overhang, relative deflection angles, and strut locations were all independently varied to capture the effect of each parameter. Some tests altered more than one parameter in an effort to understand the relationship between the different parameters.

4.2 Conclusions

1. Multielement aerodynamics are complex and are driven by the location of the elements relative to the previous element. The effect of gap size, overhang distance, and relative deflection angle are all coupled, and it is difficult to obtain one "best" location for the flaps.

2. A smaller gap size, in general, creates more lift. Results indicate the gap size with the highest lift is between 2.0% and 2.5% system chord. A sharp decrease in lift is observed for small gap sizes. Decrease in lift at large gap sizes is more forgiving than that at small gap sizes.

3. Drag is minimized near a gap size of 1.5% system chord and affects the value of C_l/C_d more than the lift of the system. Data suggest the best gap size, based on aerodynamic efficiency, is approximately 1.5% system chord.

4. Lift is minimally affected by the overhang distance. Data suggest that lift is locally maximized near an overhang distance of approximately -0.5%. In general, the difference in lift at many different overhang values was less than 2%.

5. Drag of positive overhang values is less than that of negative overhang values—the opposite effect of lift. Drag is minimized locally near an overhang distance of 1% to 1.5% system chord. The C_l/C_d value of the system is affected by the drag values more than the lift values, which is the same relationship observed in the gap size.

6. Performance of the well separated model is, in general, decreased when the strut element is moved to any position other than the baseline (as designed) position. This trend is observed if the strut to an alternative x-y location or if the deflection angle of the strut is changed.

7. Complex wake interactions can adversely affect the performance of the airfoil system.

4.3 Future Work

There are numerous methods in which work presented in this thesis can be expanded in the future to further understand the multielement effects of thick airfoils. It is clear that a deeper understanding of the governing flowfield is required for the closely coupled model. A wake survey system could be implemented to map the local velocity of the flowfield and data of the unsteady wake bursting phenomena could be taken with a multi-component hot wire or a split film. In addition, the location of the flaps could be independently changed to understand the effect of the various parameters on the aerodynamic performance of the entire multielement

system. One proposed method is to study the relationship between the boundary layer thickness and the gap size. More research is also needed to understand the effect of the strut on the aerodynamics of the system. Data collected with pressure taps on the model could help understand the relationship between the C_p curves and the aerodynamic performance.

Appendix A

Test Matrix

A summary of configurations tested are presented in this appendix. Coordinates are presented in relative coordinates and absolute coordinates for both the closely coupled and well separated family of tests. A discussion of the different coordinate systems is presented in Section 2.4 on page 39. Configurations for the closely coupled airfoil system are discussed in Section 3.2.2 on page 54. Details of the well separated configurations are presented in Section 3.3.2 on page 68.

Table A.1: Closely Coupled Test Matrix (Relative Coordinates).

Configuration	$\delta_{r,2}$ [deg]	$overhang_2$ [$\%c_{sys}$]	gap_2 [$\%c_{sys}$]	$\delta_{r,3}$ [deg]	$overhang_3$ [$\%c_{sys}$]	gap_3 [$\%c_{sys}$]
CC-1	21.40	0.01434	0.02283	9.03	0.01474	0.02011
CC-2	13.00	0.01434	0.02283	4.00	0.01474	0.02011
CC-3	13.00	0.01434	0.02283	6.00	0.01474	0.02011
CC-4	13.00	0.01434	0.02283	8.00	0.01474	0.02011
CC-5	16.00	0.01434	0.02283	4.00	0.01474	0.02011
CC-6	16.00	0.01434	0.02283	6.00	0.01474	0.02011
CC-7	16.00	0.01434	0.02283	8.00	0.01474	0.02011
CC-8	19.00	0.01434	0.02283	4.00	0.01474	0.02011
CC-9	19.00	0.01434	0.02283	6.00	0.01474	0.02011
CC-10	19.00	0.01434	0.02283	8.00	0.01474	0.02011
CC-11	21.00	0.01434	0.02283	11.00	0.01474	0.02011
CC-12	21.00	0.01434	0.02283	13.00	0.01474	0.02011
CC-13	21.00	0.01434	0.02283	15.00	0.01474	0.02011
CC-14	23.00	0.01434	0.02283	11.00	0.01474	0.02011
CC-15	23.00	0.01434	0.02283	13.00	0.01474	0.02011
CC-16	23.00	0.01434	0.02283	15.00	0.01474	0.02011
CC-17	25.00	0.01434	0.02283	11.00	0.01474	0.02011
CC-18	25.00	0.01434	0.02283	13.00	0.01474	0.02011
CC-19	25.00	0.01434	0.02283	15.00	0.01474	0.02011
CC-20	23.00	0.02684	0.02783	13.00	0.02684	0.02783
CC-21	23.00	0.02684	0.02533	13.00	0.02684	0.02533
CC-22	23.00	0.02684	0.02283	13.00	0.02684	0.02283
CC-23	23.00	0.02684	0.02033	13.00	0.02684	0.02033
CC-24	23.00	0.02684	0.01783	13.00	0.02684	0.01783
CC-25	23.00	0.02184	0.02783	13.00	0.02184	0.02783
CC-26	23.00	0.02184	0.02533	13.00	0.02184	0.02533
CC-27	23.00	0.02184	0.02283	13.00	0.02184	0.02283
CC-28	23.00	0.02184	0.02033	13.00	0.02184	0.02033
CC-29	23.00	0.02184	0.01783	13.00	0.02184	0.01783
CC-30	23.00	0.01684	0.02783	13.00	0.01684	0.02783
CC-31	23.00	0.01684	0.02533	13.00	0.01684	0.02533
CC-32	23.00	0.01684	0.02283	13.00	0.01684	0.02283
CC-33	23.00	0.01684	0.02033	13.00	0.01684	0.02033
CC-34	23.00	0.01684	0.01783	13.00	0.01684	0.01783
CC-35	23.00	0.01184	0.02783	13.00	0.01184	0.02783
CC-36	23.00	0.01184	0.02533	13.00	0.01184	0.02533
CC-37	23.00	0.01184	0.02283	13.00	0.01184	0.02283
CC-38	23.00	0.01184	0.02033	13.00	0.01184	0.02033
CC-39	23.00	0.01184	0.01783	13.00	0.01184	0.01783
CC-40	23.00	0.00684	0.02783	13.00	0.00684	0.02783
CC-41	23.00	0.00684	0.02533	13.00	0.00684	0.02533
CC-42	23.00	0.00684	0.02283	13.00	0.00684	0.02283

Continued on next page

Table A.1 – continued from previous page

Configuration	$\delta_{r,2}$ [deg]	$overhang_2$ [$\%c_{sys}$]	gap_2 [$\%c_{sys}$]	$\delta_{r,3}$ [deg]	$overhang_3$ [$\%c_{sys}$]	gap_3 [$\%c_{sys}$]
CC-43	23.00	0.00684	0.02033	13.00	0.00684	0.02033
CC-44	23.00	0.00684	0.01783	13.00	0.00684	0.01783
CC-45	23.00	0.01000	0.01000	13.00	0.01000	0.01000
CC-46	23.00	0.01000	0.01000	13.00	0.01000	0.01250
CC-47	23.00	0.01000	0.01000	13.00	0.01000	0.01500
CC-48	23.00	0.01000	0.01250	13.00	0.01000	0.01000
CC-49	23.00	0.01000	0.01250	13.00	0.01000	0.01250
CC-50	23.00	0.01000	0.01250	13.00	0.01000	0.01500
CC-51	23.00	0.01000	0.01500	13.00	0.01000	0.01000
CC-52	23.00	0.01000	0.01500	13.00	0.01000	0.01250
CC-53	23.00	0.01000	0.01500	13.00	0.01000	0.01500
CC-54	23.00	0.01000	0.01000	13.00	0.01500	0.01000
CC-55	23.00	0.01000	0.01000	13.00	0.01500	0.01250
CC-56	23.00	0.01000	0.01000	13.00	0.01500	0.01500
CC-57	23.00	0.01000	0.01250	13.00	0.01500	0.01000
CC-58	23.00	0.01000	0.01250	13.00	0.01500	0.01250
CC-59	23.00	0.01000	0.01250	13.00	0.01500	0.01500
CC-60	23.00	0.01000	0.01500	13.00	0.01500	0.01000
CC-61	23.00	0.01000	0.01500	13.00	0.01500	0.01250
CC-62	23.00	0.01000	0.01500	13.00	0.01500	0.01500
CC-63	23.00	0.01500	0.01000	13.00	0.01000	0.01000
CC-64	23.00	0.01500	0.01000	13.00	0.01000	0.01250
CC-65	23.00	0.01500	0.01000	13.00	0.01000	0.01500
CC-66	23.00	0.01500	0.01250	13.00	0.01000	0.01000
CC-67	23.00	0.01500	0.01250	13.00	0.01000	0.01250
CC-68	23.00	0.01500	0.01250	13.00	0.01000	0.01500
CC-69	23.00	0.01500	0.01500	13.00	0.01000	0.01000
CC-70	23.00	0.01500	0.01500	13.00	0.01000	0.01250
CC-71	23.00	0.01500	0.01500	13.00	0.01000	0.01500
CC-72	23.00	0.01500	0.01000	13.00	0.01500	0.01000
CC-73	23.00	0.01500	0.01000	13.00	0.01500	0.01250
CC-74	23.00	0.01500	0.01000	13.00	0.01500	0.01500
CC-75	23.00	0.01500	0.01250	13.00	0.01500	0.01000
CC-76	23.00	0.01500	0.01250	13.00	0.01500	0.01250
CC-77	23.00	0.01500	0.01250	13.00	0.01500	0.01500
CC-78	23.00	0.01500	0.01500	13.00	0.01500	0.01000
CC-79	23.00	0.01500	0.01500	13.00	0.01500	0.01250
CC-80	23.00	0.01500	0.01500	13.00	0.01500	0.01500

Table A.2: Closely Coupled Test Matrix (Absolute Coordinates).

Configuration	$x_{LE,1}$ [$\%c_{sys}$]	$y_{LE,1}$ [$\%c_{sys}$]	δ_1 [deg]	$x_{LE,2}$ [$\%c_{sys}$]	$y_{LE,2}$ [$\%c_{sys}$]	δ_2 [deg]	$x_{LE,3}$ [$\%c_{sys}$]	$y_{LE,3}$ [$\%c_{sys}$]	δ_3 [deg]
CC−1	0.00436	−0.03677	−13.90	0.69132	0.09754	−7.46	0.85328	0.04393	−16.51
CC−2	0.00436	−0.03677	−36.00	0.69210	0.09429	−1.67	0.85775	0.06244	11.39
CC−3	0.00436	−0.03677	−36.00	0.69210	0.09429	−1.67	0.85774	0.06321	13.39
CC−4	0.00436	−0.03677	−36.00	0.69210	0.09429	−1.67	0.85773	0.06395	15.39
CC−5	0.00436	−0.03677	−36.00	0.69180	0.09550	1.33	0.85632	0.05520	14.39
CC−6	0.00436	−0.03677	−36.00	0.69180	0.09550	1.33	0.85634	0.05595	16.39
CC−7	0.00436	−0.03677	−36.00	0.69180	0.09550	1.33	0.85637	0.05667	18.39
CC−8	0.00436	−0.03677	−36.00	0.69152	0.09665	4.33	0.85460	0.04796	17.39
CC−9	0.00436	−0.03677	−36.00	0.69152	0.09665	4.33	0.85467	0.04870	19.39
CC−10	0.00436	−0.03677	−36.00	0.69152	0.09665	4.33	0.85473	0.04940	21.39
CC−11	0.00436	−0.03677	−36.00	0.69134	0.09739	6.33	0.85360	0.04555	26.39
CC−12	0.00436	−0.03677	−36.00	0.69134	0.09739	6.33	0.85368	0.04618	28.39
CC−13	0.00436	−0.03677	−36.00	0.69134	0.09739	6.33	0.85376	0.04678	30.39
CC−14	0.00436	−0.03677	−36.00	0.69116	0.09810	8.33	0.85225	0.04069	28.39
CC−15	0.00436	−0.03677	−36.00	0.69116	0.09810	8.33	0.85235	0.04130	30.39
CC−16	0.00436	−0.03677	−36.00	0.69116	0.09810	8.33	0.85245	0.04189	32.39
CC−17	0.00436	−0.03677	−36.00	0.69099	0.09879	10.33	0.85077	0.03583	30.39
CC−18	0.00436	−0.03677	−36.00	0.69099	0.09879	10.33	0.85089	0.03643	32.39
CC−19	0.00436	−0.03677	−36.00	0.69099	0.09879	10.33	0.85100	0.03701	34.39
CC−20	0.00436	−0.03677	−36.00	0.68049	0.08920	8.33	0.83194	0.02473	30.39
CC−21	0.00436	−0.03677	−36.00	0.67988	0.09162	8.33	0.83174	0.02964	30.39
CC−22	0.00436	−0.03677	−36.00	0.67928	0.09405	8.33	0.83153	0.03454	30.39
CC−23	0.00436	−0.03677	−36.00	0.67868	0.09648	8.33	0.83133	0.03945	30.39
CC−24	0.00436	−0.03677	−36.00	0.67808	0.09891	8.33	0.83112	0.04435	30.39
CC−25	0.00436	−0.03677	−36.00	0.68530	0.09054	8.33	0.84025	0.02590	30.39
CC−26	0.00436	−0.03677	−36.00	0.68470	0.09297	8.33	0.84005	0.03082	30.39
CC−27	0.00436	−0.03677	−36.00	0.68410	0.09540	8.33	0.83984	0.03575	30.39
CC−28	0.00436	−0.03677	−36.00	0.68350	0.09784	8.33	0.83964	0.04067	30.39
CC−29	0.00436	−0.03677	−36.00	0.68290	0.10027	8.33	0.83944	0.04560	30.39
CC−30	0.00436	−0.03677	−36.00	0.69004	0.09221	8.33	0.84851	0.02756	30.39
CC−31	0.00436	−0.03677	−36.00	0.68944	0.09466	8.33	0.84830	0.03252	30.39
CC−32	0.00436	−0.03677	−36.00	0.68883	0.09711	8.33	0.84810	0.03748	30.39
CC−33	0.00436	−0.03677	−36.00	0.68822	0.09956	8.33	0.84789	0.04245	30.39
CC−34	0.00436	−0.03677	−36.00	0.68761	0.10201	8.33	0.84769	0.04743	30.39
CC−35	0.00436	−0.03677	−36.00	0.69469	0.09423	8.33	0.85670	0.02976	30.39
CC−36	0.00436	−0.03677	−36.00	0.69408	0.09671	8.33	0.85649	0.03478	30.39
CC−37	0.00436	−0.03677	−36.00	0.69346	0.09920	8.33	0.85628	0.03981	30.39
CC−38	0.00436	−0.03677	−36.00	0.69285	0.10169	8.33	0.85607	0.04485	30.39
CC−39	0.00436	−0.03677	−36.00	0.69223	0.10419	8.33	0.85586	0.04991	30.39
CC−40	0.00436	−0.03677	−36.00	0.69924	0.09665	8.33	0.86483	0.03254	30.39
CC−41	0.00436	−0.03677	−36.00	0.69862	0.09918	8.33	0.86461	0.03766	30.39
CC−42	0.00436	−0.03677	−36.00	0.69799	0.10173	8.33	0.86440	0.04280	30.39

Continued on next page

Table A.2 – continued from previous page

Configuration	$x_{LE,1}$ [$\%c_{sys}$]	$y_{LE,1}$ [$\%c_{sys}$]	δ_1 [deg]	$x_{LE,2}$ [$\%c_{sys}$]	$y_{LE,2}$ [$\%c_{sys}$]	δ_2 [deg]	$x_{LE,3}$ [$\%c_{sys}$]	$y_{LE,3}$ [$\%c_{sys}$]	δ_3 [deg]
CC−43	0.00436	−0.03677	−36.00	0.69735	0.10429	8.33	0.86418	0.04796	30.39
CC−44	0.00436	−0.03677	−36.00	0.69672	0.10686	8.33	0.86396	0.05315	30.39
CC−45	0.00436	−0.03677	−36.00	0.69192	0.11307	8.33	0.85819	0.06716	30.39
CC−46	0.00436	−0.03677	−36.00	0.69192	0.11307	8.33	0.85777	0.06452	30.39
CC−47	0.00436	−0.03677	−36.00	0.69192	0.11307	8.33	0.85735	0.06191	30.39
CC−48	0.00436	−0.03677	−36.00	0.69256	0.11052	8.33	0.85882	0.06460	30.39
CC−49	0.00436	−0.03677	−36.00	0.69256	0.11052	8.33	0.85840	0.06197	30.39
CC−50	0.00436	−0.03677	−36.00	0.69256	0.11052	8.33	0.85798	0.05935	30.39
CC−51	0.00436	−0.03677	−36.00	0.69319	0.10797	8.33	0.85945	0.06206	30.39
CC−52	0.00436	−0.03677	−36.00	0.69319	0.10797	8.33	0.85903	0.05942	30.39
CC−53	0.00436	−0.03677	−36.00	0.69319	0.10797	8.33	0.85861	0.05681	30.39
CC−54	0.00436	−0.03677	−36.00	0.69192	0.11307	8.33	0.85458	0.06657	30.39
CC−55	0.00436	−0.03677	−36.00	0.69192	0.11307	8.33	0.85417	0.06401	30.39
CC−56	0.00436	−0.03677	−36.00	0.69192	0.11307	8.33	0.85376	0.06145	30.39
CC−57	0.00436	−0.03677	−36.00	0.69256	0.11052	8.33	0.85521	0.06401	30.39
CC−58	0.00436	−0.03677	−36.00	0.69256	0.11052	8.33	0.85480	0.06145	30.39
CC−59	0.00436	−0.03677	−36.00	0.69256	0.11052	8.33	0.85440	0.05890	30.39
CC−60	0.00436	−0.03677	−36.00	0.69319	0.10797	8.33	0.85584	0.06146	30.39
CC−61	0.00436	−0.03677	−36.00	0.69319	0.10797	8.33	0.85543	0.05890	30.39
CC−62	0.00436	−0.03677	−36.00	0.69319	0.10797	8.33	0.85502	0.05635	30.39
CC−63	0.00436	−0.03677	−36.00	0.68741	0.11051	8.33	0.85367	0.06460	30.39
CC−64	0.00436	−0.03677	−36.00	0.68741	0.11051	8.33	0.85325	0.06197	30.39
CC−65	0.00436	−0.03677	−36.00	0.68741	0.11051	8.33	0.85283	0.05935	30.39
CC−66	0.00436	−0.03677	−36.00	0.68802	0.10803	8.33	0.85429	0.06212	30.39
CC−67	0.00436	−0.03677	−36.00	0.68802	0.10803	8.33	0.85386	0.05948	30.39
CC−68	0.00436	−0.03677	−36.00	0.68802	0.10803	8.33	0.85345	0.05687	30.39
CC−69	0.00436	−0.03677	−36.00	0.68863	0.10556	8.33	0.85490	0.05964	30.39
CC−70	0.00436	−0.03677	−36.00	0.68863	0.10556	8.33	0.85448	0.05701	30.39
CC−71	0.00436	−0.03677	−36.00	0.68863	0.10556	8.33	0.85406	0.05439	30.39
CC−72	0.00436	−0.03677	−36.00	0.68741	0.11051	8.33	0.85006	0.06401	30.39
CC−73	0.00436	−0.03677	−36.00	0.68741	0.11051	8.33	0.84965	0.06145	30.39
CC−74	0.00436	−0.03677	−36.00	0.68741	0.11051	8.33	0.84924	0.05889	30.39
CC−75	0.00436	−0.03677	−36.00	0.68802	0.10803	8.33	0.85067	0.06153	30.39
CC−76	0.00436	−0.03677	−36.00	0.68802	0.10803	8.33	0.85027	0.05896	30.39
CC−77	0.00436	−0.03677	−36.00	0.68802	0.10803	8.33	0.84986	0.05641	30.39
CC−78	0.00436	−0.03677	−36.00	0.68863	0.10556	8.33	0.85129	0.05905	30.39
CC−79	0.00436	−0.03677	−36.00	0.68863	0.10556	8.33	0.85088	0.05649	30.39
CC−80	0.00436	−0.03677	−36.00	0.68863	0.10556	8.33	0.85047	0.05394	30.39

Table A.3: Well Separated Test Matrix (Relative Coordinates).

Configuration	$\delta_{r,2}$ [deg]	$overhang_2$ [$\%c_{sys}$]	gap_2 [$\%c_{sys}$]	$\delta_{r,3}$ [deg]	$overhang_3$ [$\%c_{sys}$]	gap_3 [$\%c_{sys}$]	$x_{LE,strut}$ [$\%c_{sys}$]	$y_{LE,strut}$ [$\%c_{sys}$]	δ_{strut} [deg]
WS-1	17.15	0.02168	0.03028	8.74	-0.00816	0.03031	0.17155	-0.26819	-6.50
WS-2	17.14	-0.01000	0.03000	13.00	-0.01000	0.03000	0.17148	-0.26762	-6.50
WS-3	17.14	-0.00500	0.03000	13.00	-0.00500	0.03000	0.17148	-0.26762	-6.50
WS-4	17.14	-0.00500	0.02500	13.00	-0.00500	0.02500	0.17148	-0.26762	-6.50
WS-5	17.14	0.00000	0.03000	13.00	0.00000	0.03000	0.17148	-0.26762	-6.50
WS-6	17.14	0.00000	0.02500	13.00	0.00000	0.02500	0.17148	-0.26762	-6.50
WS-7	17.14	0.00500	0.03000	13.00	0.00500	0.03000	0.17148	-0.26762	-6.50
WS-8	17.14	0.00500	0.02500	13.00	0.00500	0.02500	0.17148	-0.26762	-6.50
WS-9	17.14	0.01000	0.03000	13.00	0.01000	0.03000	0.17148	-0.26762	-6.50
WS-10	17.14	0.01000	0.02500	13.00	0.01000	0.02500	0.17148	-0.26762	-6.50
WS-11	17.14	0.01500	0.03000	13.00	0.01500	0.03000	0.17148	-0.26762	-6.50
WS-12	17.14	0.01500	0.02500	13.00	0.01500	0.02500	0.17148	-0.26762	-6.50
WS-13	17.14	0.02000	0.03000	13.00	0.02000	0.03000	0.17148	-0.26762	-6.50
WS-14	17.14	0.02000	0.02500	13.00	0.02000	0.02500	0.17148	-0.26762	-6.50
WS-15	17.14	0.02000	0.02500	13.00	0.02000	0.02500	0.18199	-0.28629	-16.50
WS-16	17.14	0.01500	0.02500	13.00	0.01500	0.02500	0.18199	-0.28629	-16.50
WS-17	17.14	0.01000	0.02500	13.00	0.01000	0.02500	0.18199	-0.28629	-16.50
WS-18	17.14	0.00500	0.02500	13.00	0.00500	0.02500	0.18199	-0.28629	-16.50
WS-19	17.14	0.00000	0.02500	13.00	0.00000	0.02500	0.18199	-0.28629	-16.50
WS-20	17.14	-0.00500	0.02500	13.00	-0.00500	0.02500	0.18199	-0.28629	-16.50
WS-21	17.14	0.01000	0.02500	13.00	0.01000	0.02500	0.15846	-0.21210	-6.50
WS-22	17.14	0.00500	0.02500	13.00	0.00500	0.02500	0.15846	-0.21210	-6.50
WS-23	17.14	0.00000	0.02500	13.00	0.00000	0.02500	0.15846	-0.21210	-6.50
WS-24	17.14	0.01000	0.02500	13.00	0.01000	0.02500	0.18450	-0.32314	-6.50
WS-25	17.14	0.00500	0.02500	13.00	0.00500	0.02500	0.18450	-0.32314	-6.50
WS-26	17.14	0.00000	0.02500	13.00	0.00000	0.02500	0.18450	-0.32314	-6.50
WS-27	17.14	-0.00500	0.02500	13.00	-0.00500	0.02500	0.18450	-0.32314	-6.50
WS-28	17.14	0.01000	0.02500	13.00	0.01000	0.02500	0.24002	-0.31012	-6.50
WS-29	17.14	0.00500	0.02500	13.00	0.00500	0.02500	0.24002	-0.31012	-6.50
WS-30	17.14	0.00000	0.02500	13.00	0.00000	0.02500	0.24002	-0.31012	-6.50
WS-31	17.14	-0.00500	0.02500	13.00	-0.00500	0.02500	0.24002	-0.31012	-6.50
WS-32	17.14	0.01500	0.01000	13.00	0.01500	0.01000	0.17148	-0.26762	-6.50
WS-33	17.14	0.01500	0.01500	13.00	0.01500	0.01500	0.17148	-0.26762	-6.50
WS-34	17.14	0.01500	0.02000	13.00	0.01500	0.02000	0.17148	-0.26762	-6.50
WS-35	17.14	0.01500	0.03500	13.00	0.01500	0.03500	0.17148	-0.26762	-6.50
WS-36	17.14	0.01500	0.01000	13.00	0.01500	0.01000	0.18450	-0.32314	-6.50
WS-37	17.14	0.01500	0.01500	13.00	0.01500	0.01500	0.18450	-0.32314	-6.50
WS-38	17.14	0.01500	0.02000	13.00	0.01500	0.02000	0.18450	-0.32314	-6.50
WS-39	17.14	0.01500	0.02500	13.00	0.01500	0.02500	0.18450	-0.32314	-6.50
WS-40	17.14	0.01500	0.03000	13.00	0.01500	0.03000	0.18450	-0.32314	-6.50
WS-41	17.14	0.01500	0.03500	13.00	0.01500	0.03500	0.18450	-0.32314	-6.50
WS-42	17.14	0.01000	0.02500	13.00	0.01000	0.02500	0.21398	-0.19908	-6.50

Continued on next page

Table A.3 – continued from previous page

Configuration	$\delta_{r,2}$ [deg]	$overhang_2$ [$\%c_{sys}$]	gap_2 [$\%c_{sys}$]	$\delta_{r,3}$ [deg]	$overhang_3$ [$\%c_{sys}$]	gap_3 [$\%c_{sys}$]	$x_{LE,strut}$ [$\%c_{sys}$]	$y_{LE,strut}$ [$\%c_{sys}$]	δ_{strut} [deg]
WS-43	17.14	0.01000	0.02500	13.00	0.01000	0.02500	0.10294	-0.22512	-6.50
WS-44	17.14	0.01000	0.02500	13.00	0.01000	0.02500	0.11596	-0.28064	-6.50
WS-45	17.14	0.01000	0.02500	13.00	0.01000	0.02500	0.22700	-0.25460	-6.50
WS-46	17.14	0.01000	0.02500	13.00	0.01000	0.02500	0.16437	-0.24740	3.50

Table A.4: Well Separated Test Matrix (Absolute Coordinates).

Configuration	$x_{LE,1}$ [$\%c_{sys}$]	$y_{LE,1}$ [$\%c_{sys}$]	δ_1 [deg]	$x_{LE,2}$ [$\%c_{sys}$]	$y_{LE,2}$ [$\%c_{sys}$]	δ_2 [deg]	$x_{LE,3}$ [$\%c_{sys}$]	$y_{LE,3}$ [$\%c_{sys}$]	δ_3 [deg]	$x_{LE,strut}$ [$\%c_{sys}$]	$y_{LE,strut}$ [$\%c_{sys}$]	δ_{strut} [deg]
WS-1	0.00125	-0.01244	-12.60	0.62888	0.08912	17.15	0.83220	0.03828	25.89	0.17155	-0.26819	-6.50
WS-2	0.00125	-0.01244	-16.37	0.65709	0.10756	17.19	0.86212	0.05897	30.19	0.17148	-0.26762	-6.50
WS-3	0.00125	-0.01244	-16.37	0.65293	0.10339	17.19	0.85368	0.05279	30.19	0.17148	-0.26762	-6.50
WS-4	0.00125	-0.01244	-16.37	0.65161	0.10903	17.19	0.85275	0.06408	30.19	0.17148	-0.26762	-6.50
WS-5	0.00125	-0.01244	-16.37	0.64863	0.09983	17.19	0.84513	0.04764	30.19	0.17148	-0.26762	-6.50
WS-6	0.00125	-0.01244	-16.37	0.64738	0.10519	17.19	0.84426	0.05842	30.19	0.17148	-0.26762	-6.50
WS-7	0.00125	-0.01244	-16.37	0.64421	0.09679	17.19	0.83649	0.04338	30.19	0.17148	-0.26762	-6.50
WS-8	0.00125	-0.01244	-16.37	0.64299	0.10197	17.19	0.83564	0.05382	30.19	0.17148	-0.26762	-6.50
WS-9	0.00125	-0.01244	-16.37	0.63969	0.09417	17.19	0.82777	0.03984	30.19	0.17148	-0.26762	-6.50
WS-10	0.00125	-0.01244	-16.37	0.63850	0.09922	17.19	0.82695	0.05007	30.19	0.17148	-0.26762	-6.50
WS-11	0.00125	-0.01244	-16.37	0.63508	0.09192	17.19	0.81898	0.03697	30.19	0.17148	-0.26762	-6.50
WS-12	0.00125	-0.01244	-16.37	0.63391	0.09690	17.19	0.81817	0.04704	30.19	0.17148	-0.26762	-6.50
WS-13	0.00125	-0.01244	-16.37	0.63040	0.08998	17.19	0.81013	0.03462	30.19	0.17148	-0.26762	-6.50
WS-14	0.00125	-0.01244	-16.37	0.62925	0.09489	17.19	0.80933	0.04457	30.19	0.17148	-0.26762	-6.50
WS-15	0.00125	-0.01244	-16.37	0.62925	0.09489	17.19	0.80933	0.04457	30.19	0.18199	-0.28629	-16.50
WS-16	0.00125	-0.01244	-16.37	0.63391	0.09690	17.19	0.81817	0.04704	30.19	0.18199	-0.28629	-16.50
WS-17	0.00125	-0.01244	-16.37	0.63850	0.09922	17.19	0.82695	0.05007	30.19	0.18199	-0.28629	-16.50
WS-18	0.00125	-0.01244	-16.37	0.64299	0.10197	17.19	0.83564	0.05382	30.19	0.18199	-0.28629	-16.50
WS-19	0.00125	-0.01244	-16.37	0.64738	0.10519	17.19	0.84426	0.05842	30.19	0.18199	-0.28629	-16.50
WS-20	0.00125	-0.01244	-16.37	0.65161	0.10903	17.19	0.85275	0.06408	30.19	0.18199	-0.28629	-16.50
WS-21	0.00125	-0.01244	-16.37	0.63850	0.09922	17.19	0.82695	0.05007	30.19	0.15846	-0.21210	-6.50
WS-22	0.00125	-0.01244	-16.37	0.64299	0.10197	17.19	0.83564	0.05382	30.19	0.15846	-0.21210	-6.50
WS-23	0.00125	-0.01244	-16.37	0.64738	0.10519	17.19	0.84426	0.05842	30.19	0.15846	-0.21210	-6.50
WS-24	0.00125	-0.01244	-16.37	0.63850	0.09922	17.19	0.82695	0.05007	30.19	0.18450	-0.32314	-6.50
WS-25	0.00125	-0.01244	-16.37	0.64299	0.10197	17.19	0.83564	0.05382	30.19	0.18450	-0.32314	-6.50
WS-26	0.00125	-0.01244	-16.37	0.64738	0.10519	17.19	0.84426	0.05842	30.19	0.18450	-0.32314	-6.50
WS-27	0.00125	-0.01244	-16.37	0.65161	0.10903	17.19	0.85275	0.06408	30.19	0.18450	-0.32314	-6.50
WS-28	0.00125	-0.01244	-16.37	0.63850	0.09922	17.19	0.82695	0.05007	30.19	0.24002	-0.31012	-6.50
WS-29	0.00125	-0.01244	-16.37	0.64299	0.10197	17.19	0.83564	0.05382	30.19	0.24002	-0.31012	-6.50
WS-30	0.00125	-0.01244	-16.37	0.64738	0.10519	17.19	0.84426	0.05842	30.19	0.24002	-0.31012	-6.50
WS-31	0.00125	-0.01244	-16.37	0.65161	0.10903	17.19	0.85275	0.06408	30.19	0.24002	-0.31012	-6.50
WS-32	0.00125	-0.01244	-16.37	0.63040	0.11188	17.19	0.81573	0.07740	30.19	0.17148	-0.26762	-6.50
WS-33	0.00125	-0.01244	-16.37	0.63157	0.10687	17.19	0.81654	0.06723	30.19	0.17148	-0.26762	-6.50
WS-34	0.00125	-0.01244	-16.37	0.63275	0.10187	17.19	0.81736	0.05711	30.19	0.17148	-0.26762	-6.50
WS-35	0.00125	-0.01244	-16.37	0.63624	0.08697	17.19	0.81979	0.02694	30.19	0.17148	-0.26762	-6.50
WS-36	0.00125	-0.01244	-16.37	0.63040	0.11188	17.19	0.81573	0.07740	30.19	0.18450	-0.32314	-6.50
WS-37	0.00125	-0.01244	-16.37	0.63157	0.10687	17.19	0.81654	0.06723	30.19	0.18450	-0.32314	-6.50
WS-38	0.00125	-0.01244	-16.37	0.63275	0.10187	17.19	0.81736	0.05711	30.19	0.18450	-0.32314	-6.50
WS-39	0.00125	-0.01244	-16.37	0.63391	0.09690	17.19	0.81817	0.04704	30.19	0.18450	-0.32314	-6.50
WS-40	0.00125	-0.01244	-16.37	0.63508	0.09192	17.19	0.81898	0.03697	30.19	0.18450	-0.32314	-6.50
WS-41	0.00125	-0.01244	-16.37	0.63624	0.08697	17.19	0.81979	0.02694	30.19	0.18450	-0.32314	-6.50
WS-42	0.00125	-0.01244	-16.37	0.63850	0.09922	17.19	0.82695	0.05007	30.19	0.21398	-0.19908	-6.50

Continued on next page

Table A.4 −− continued from previous page

Configuration	$x_{LE,1}$ [$\%c_{sys}$]	$y_{LE,1}$ [$\%c_{sys}$]	δ_1 [deg]	$x_{LE,2}$ [$\%c_{sys}$]	$y_{LE,2}$ [$\%c_{sys}$]	δ_2 [deg]	$x_{LE,3}$ [$\%c_{sys}$]	$y_{LE,3}$ [$\%c_{sys}$]	δ_3 [deg]	$x_{LE,strut}$ [$\%c_{sys}$]	$y_{LE,strut}$ [$\%c_{sys}$]	δ_{strut} [deg]
WS-43	0.00125	-0.01244	-16.37	0.63850	0.09922	17.19	0.82695	0.05007	30.19	0.10294	-0.22512	-6.50
WS-44	0.00125	-0.01244	-16.37	0.63850	0.09922	17.19	0.82695	0.05007	30.19	0.11596	-0.28064	-6.50
WS-45	0.00125	-0.01244	-16.37	0.63850	0.09922	17.19	0.82695	0.05007	30.19	0.22700	-0.25460	-6.50
WS-46	0.00125	-0.01244	-16.37	0.63850	0.09922	17.19	0.82695	0.05007	30.19	0.16437	-0.24740	3.50

Appendix B

Performance Plots

Performance data for the closely coupled and well separated configurations are presented in this appendix. Some configurations were tested more than once, and the different subtests are denoted by a letter and labeled on the performance plots appropriately.

Closely Coupled Performance Data

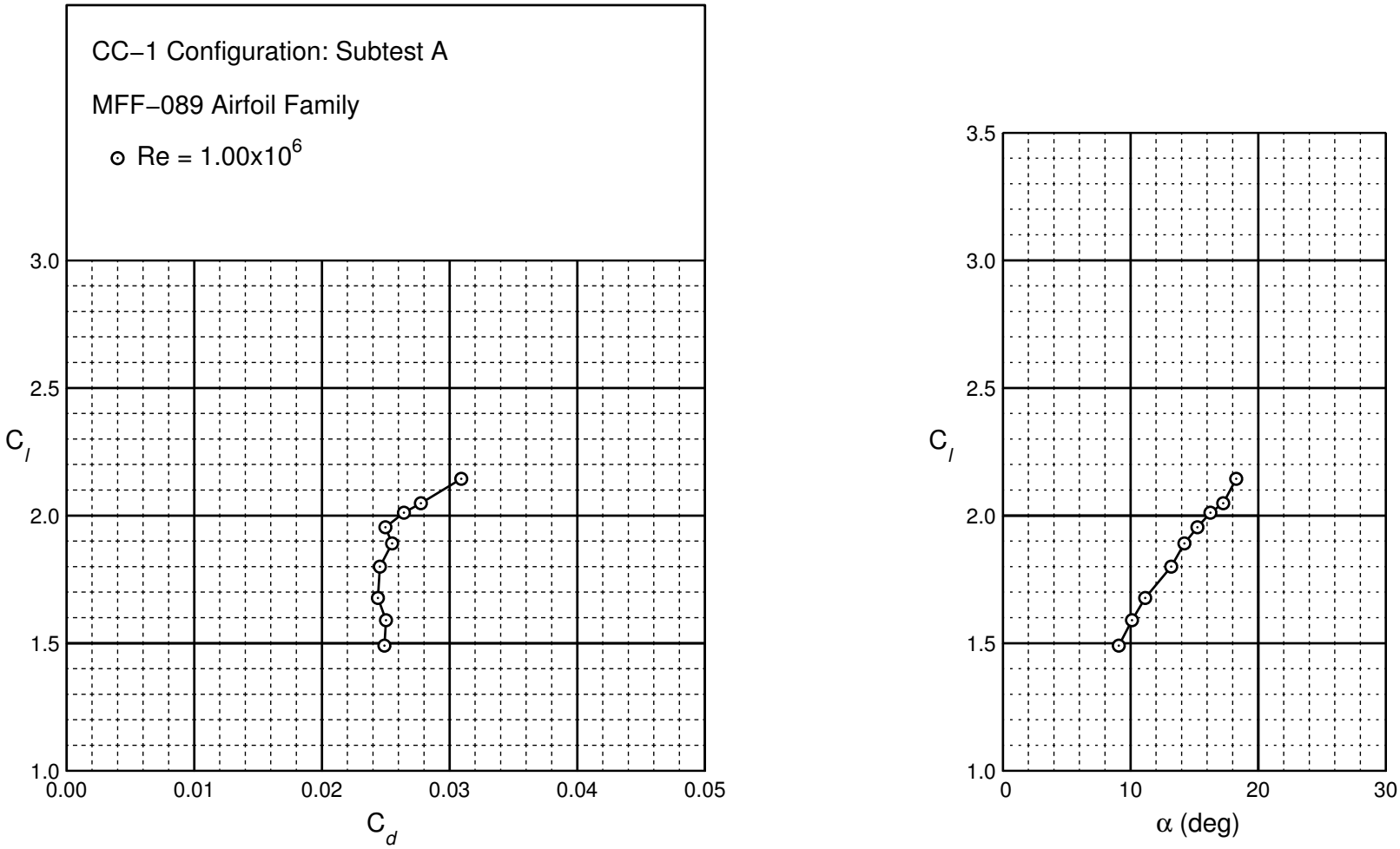

Figure B.1: CC-1 performance at $Re = 1.0 \times 10^6$.

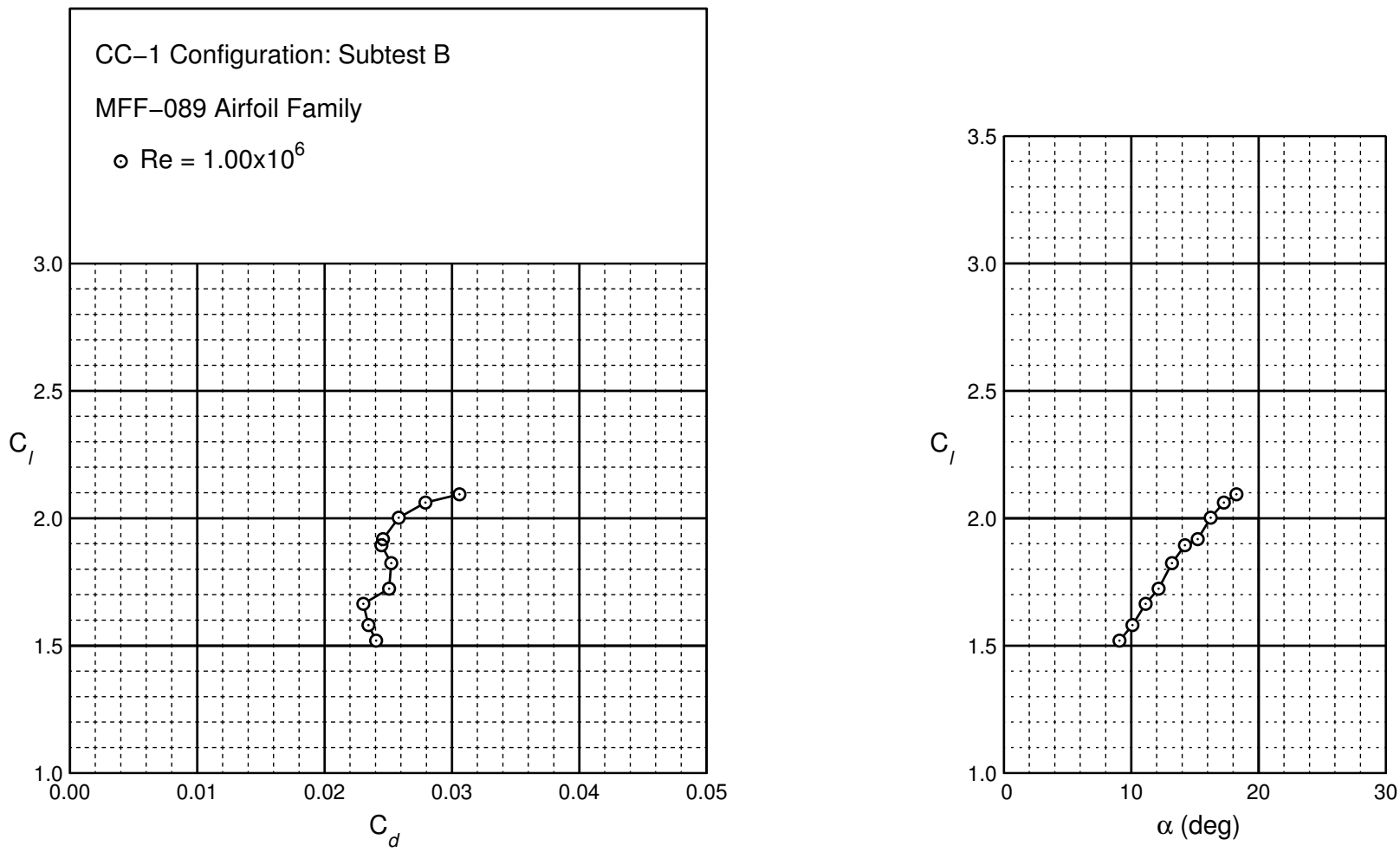

Figure B.2: CC-1 performance at $Re = 1.0 \times 10^6$.

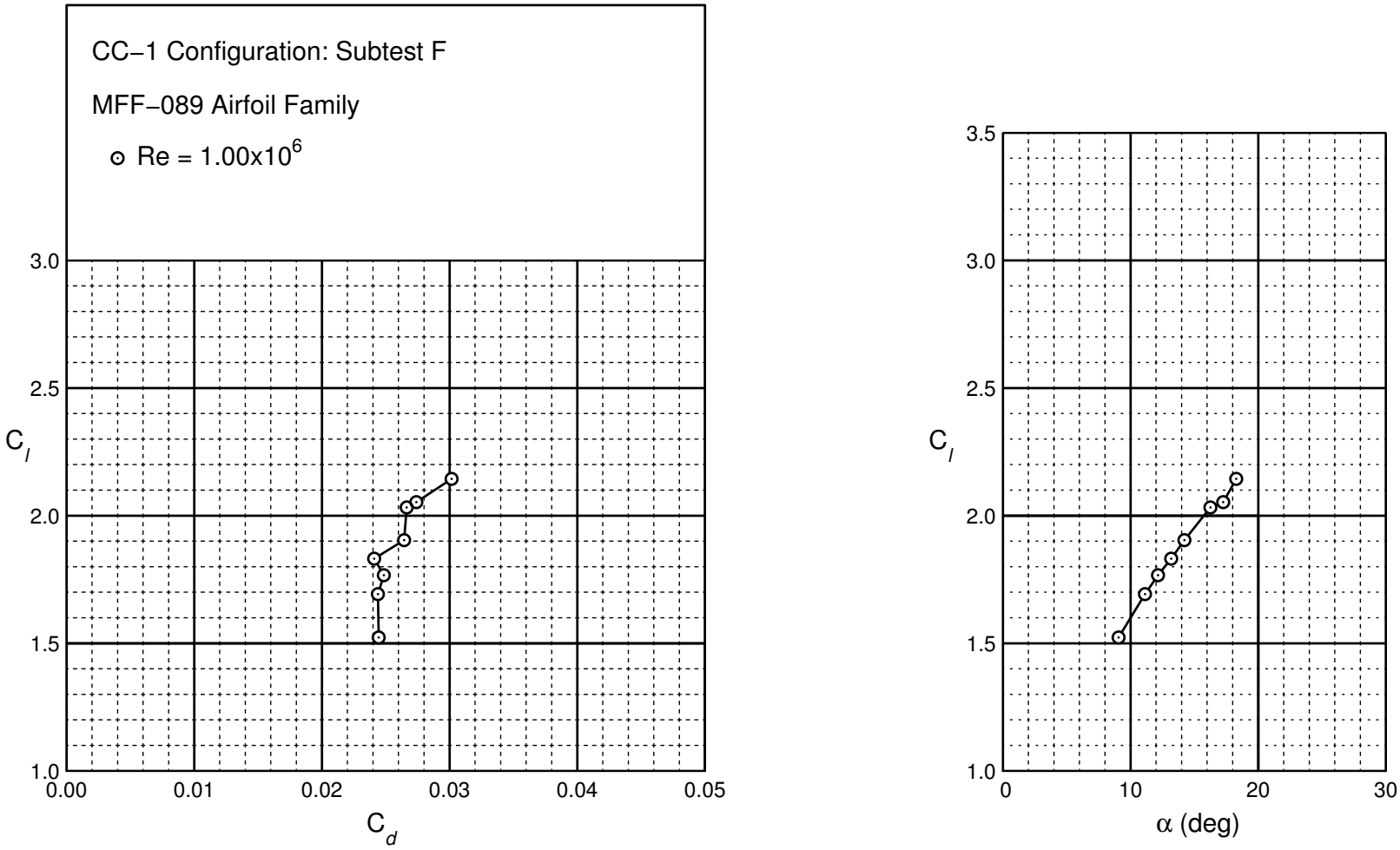

Figure B.3: CC-1 performance at $Re = 1.0 \times 10^6$.

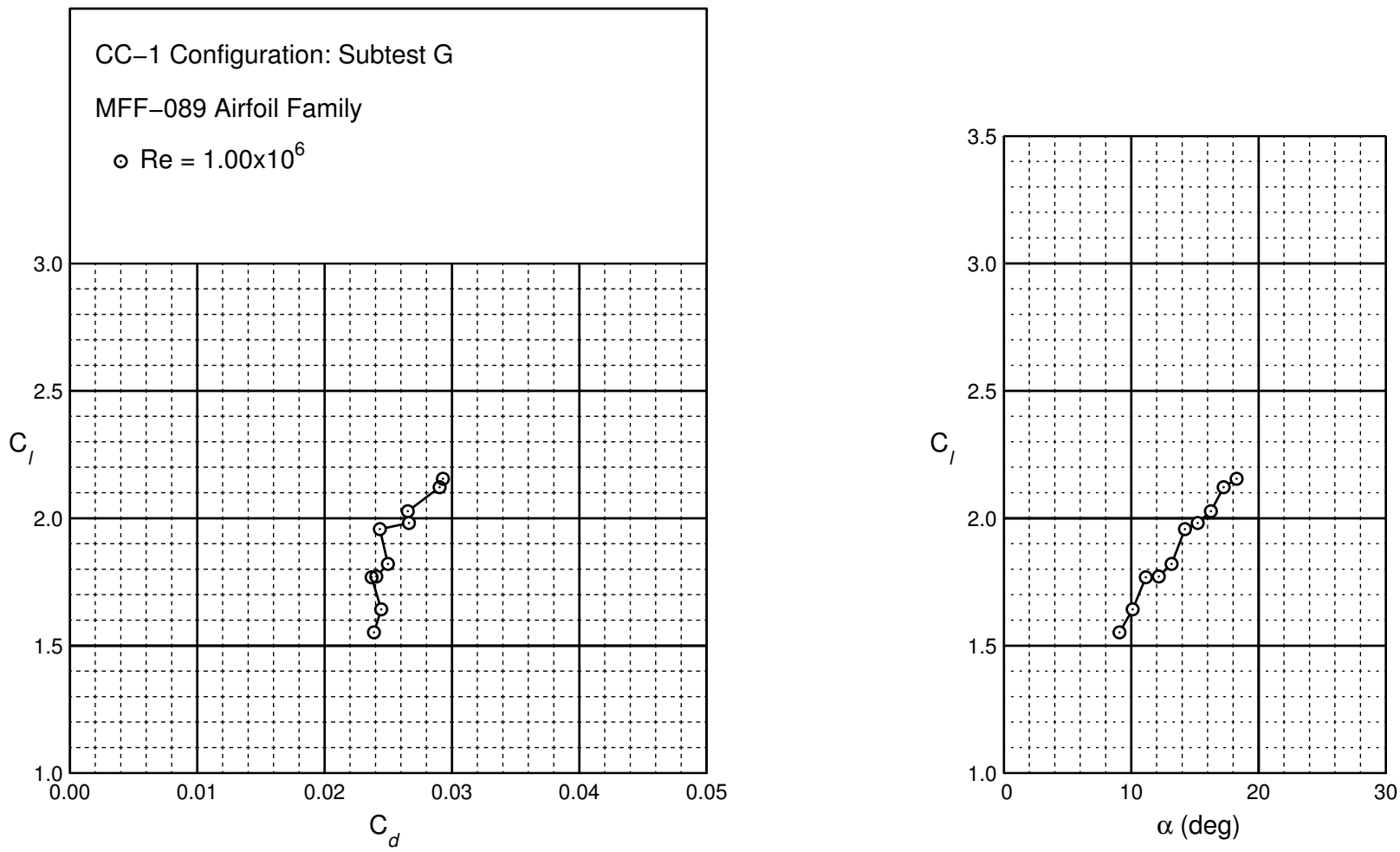

Figure B.4: CC-1 performance at $Re = 1.0 \times 10^6$.

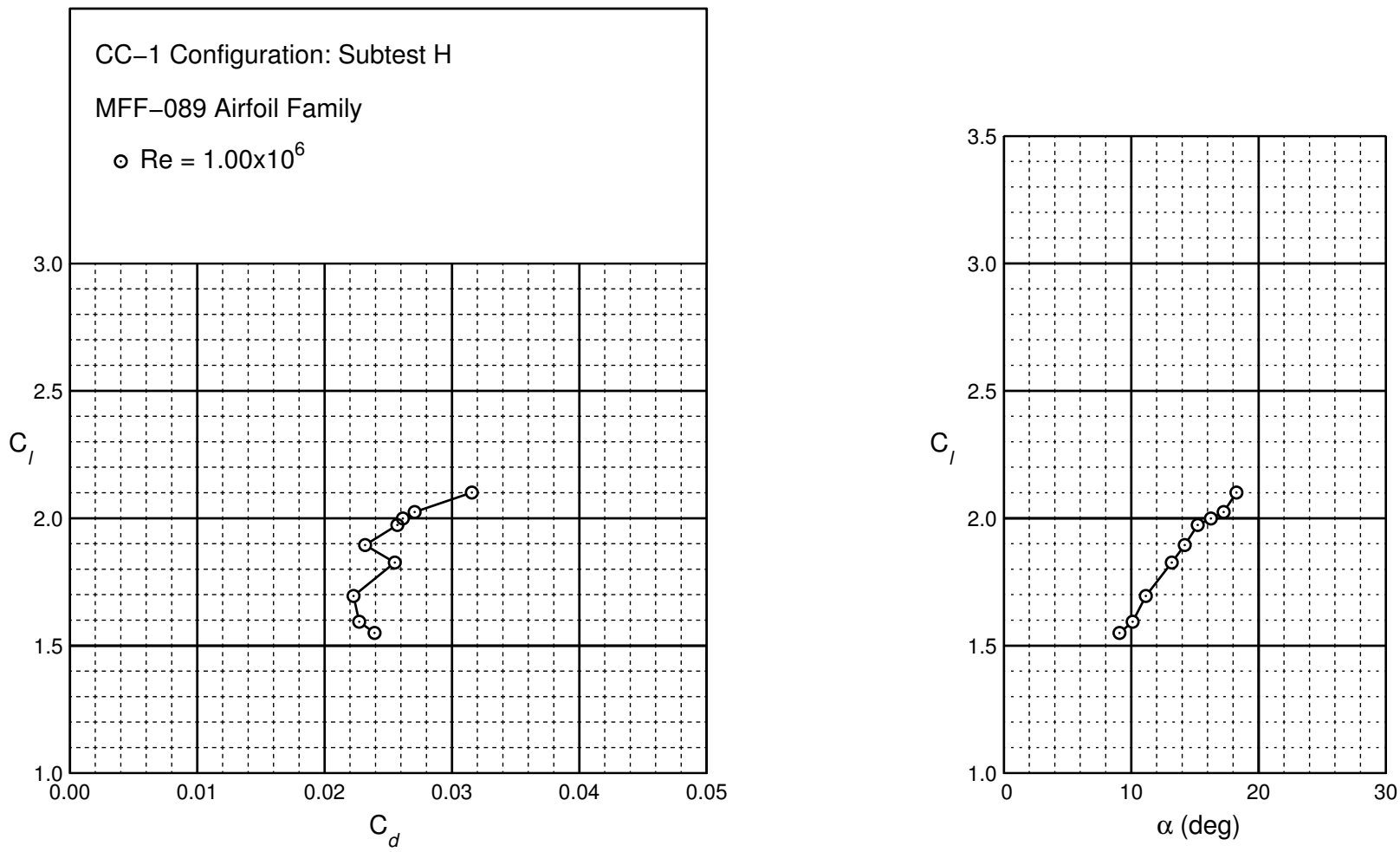

Figure B.5: CC-1 performance at $Re = 1.0 \times 10^6$.

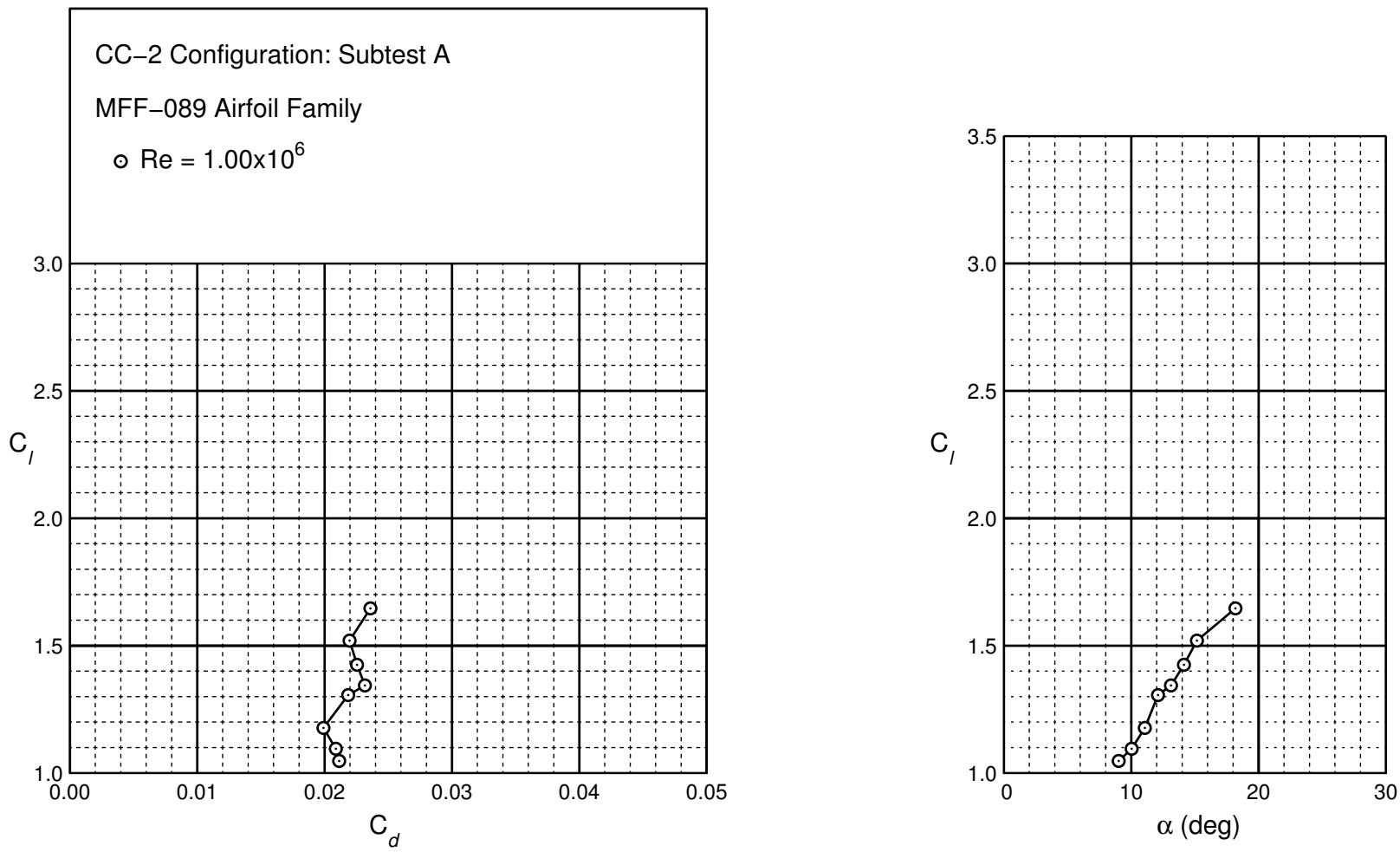

Figure B.6: CC-2 performance at $Re = 1.0 \times 10^6$.

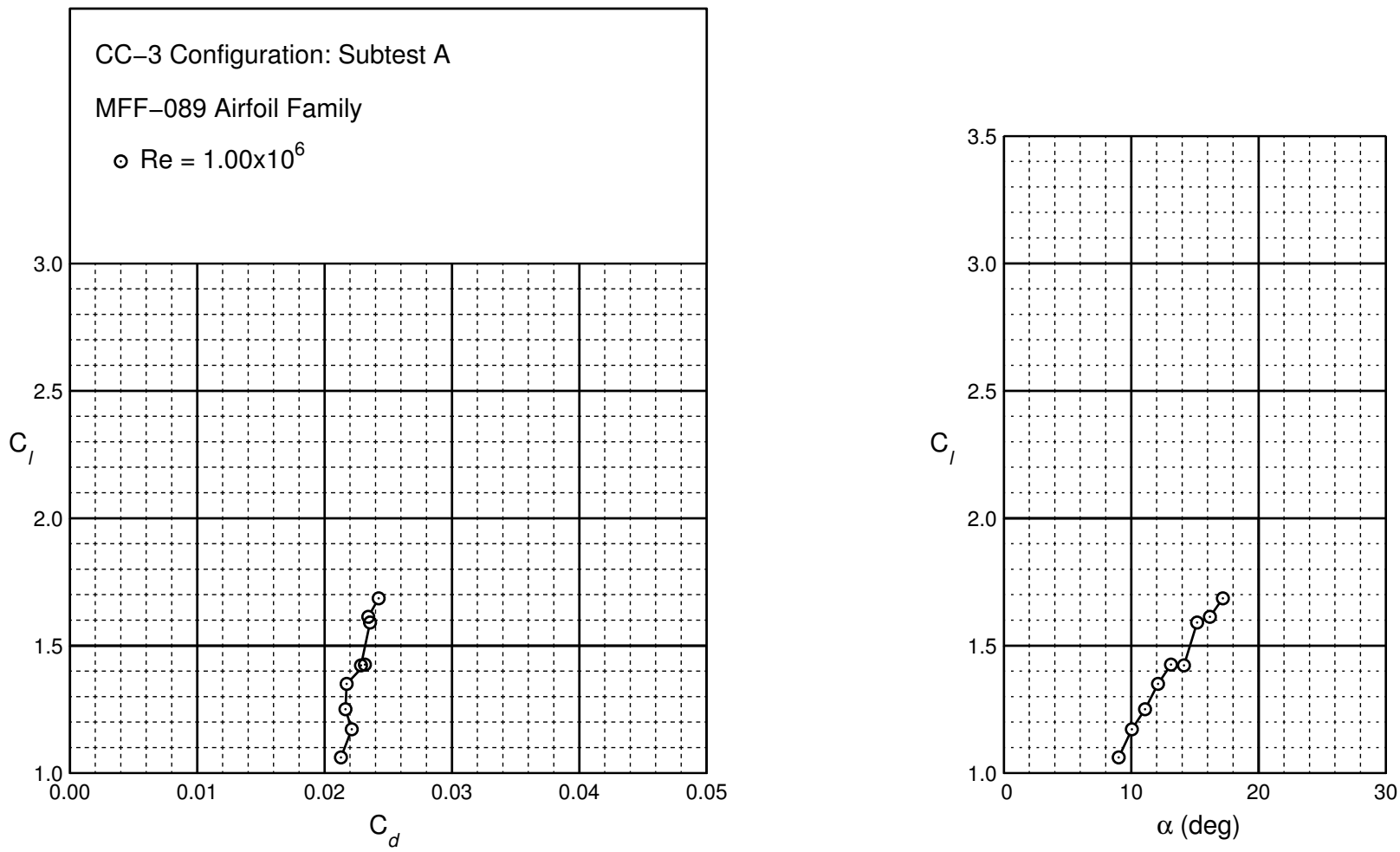

Figure B.7: CC-3 performance at $Re = 1.0 \times 10^6$.

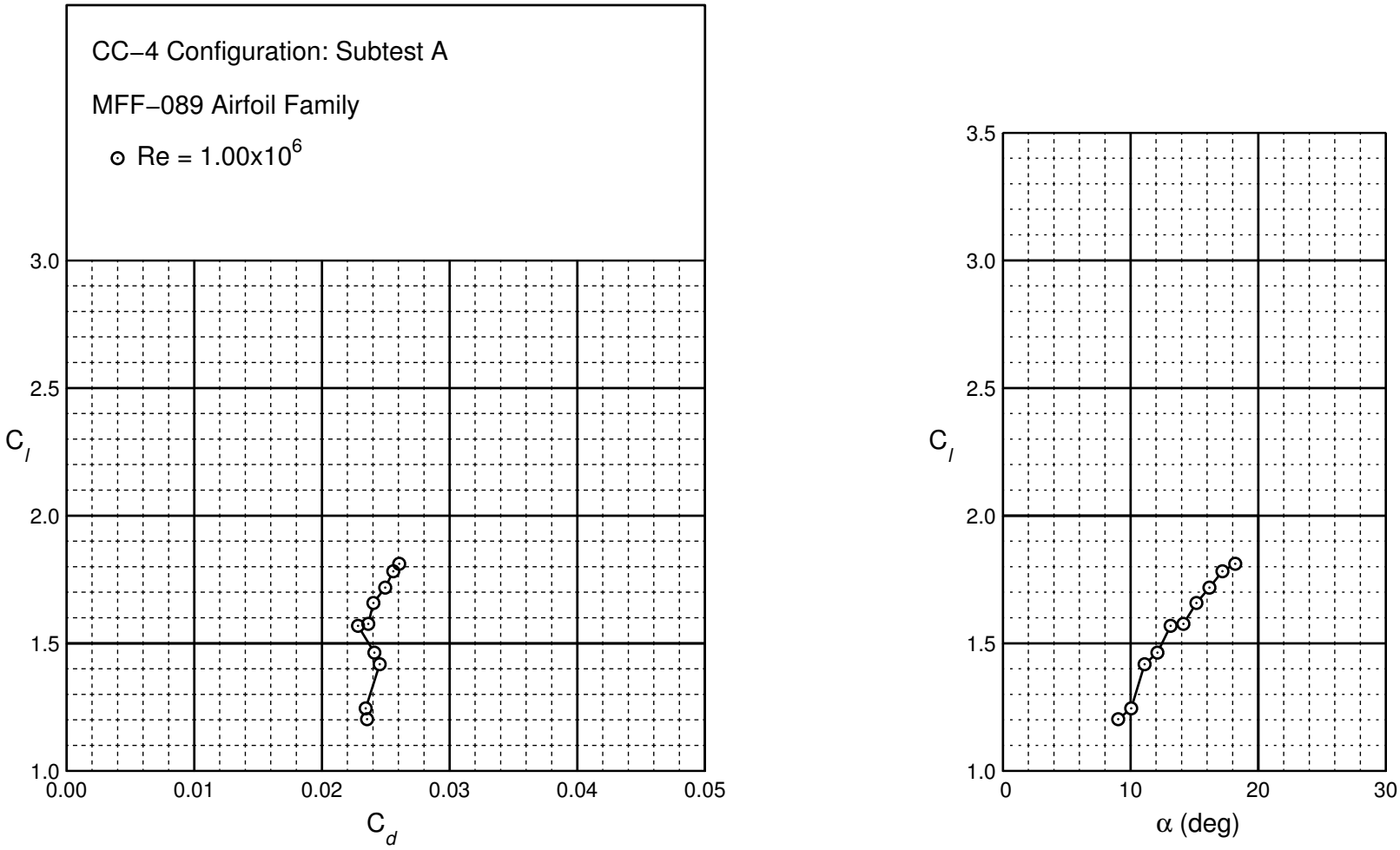

Figure B.8: CC-4 performance at $Re = 1.0 \times 10^6$.

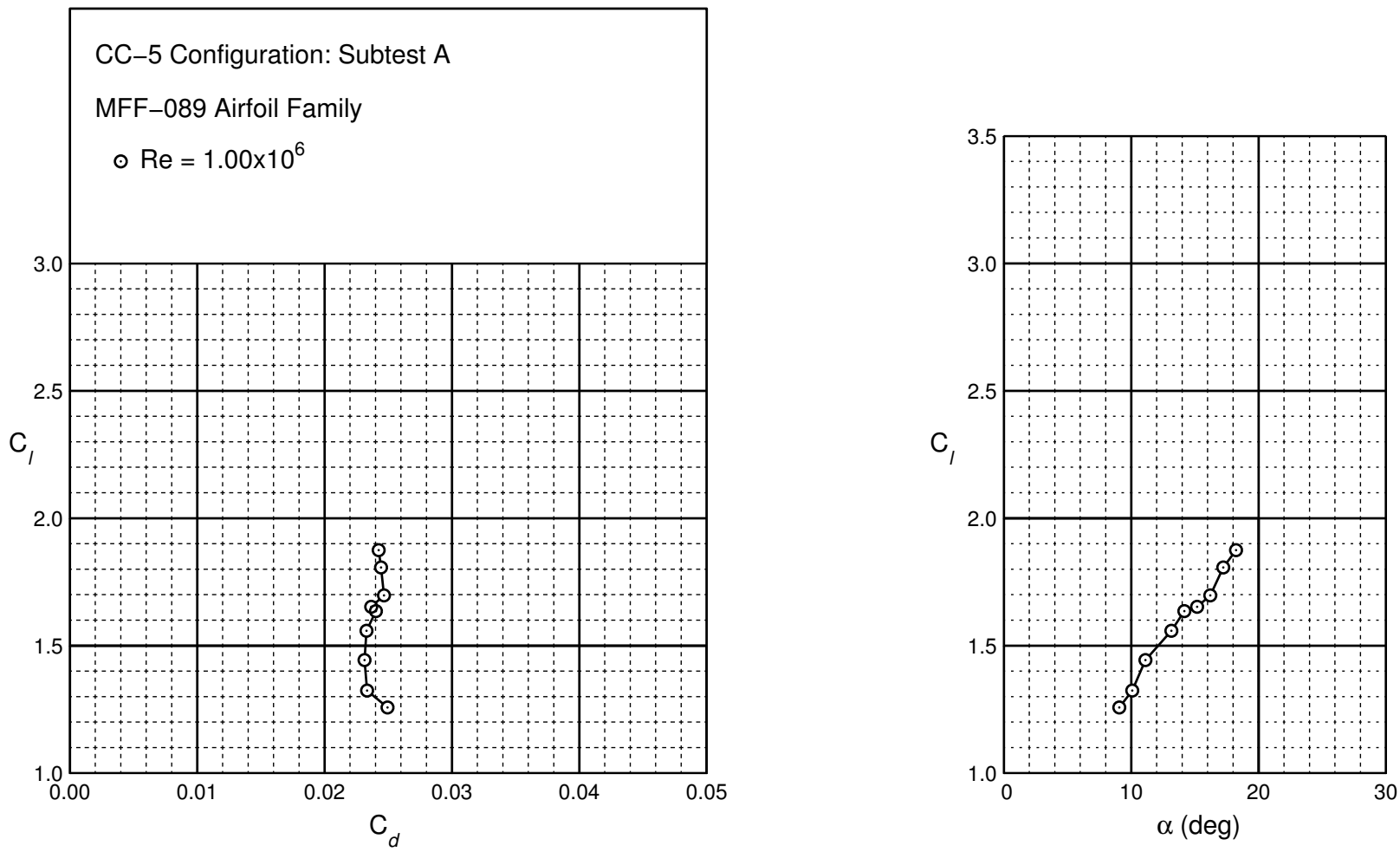

Figure B.9: CC-5 performance at $Re = 1.0 \times 10^6$.

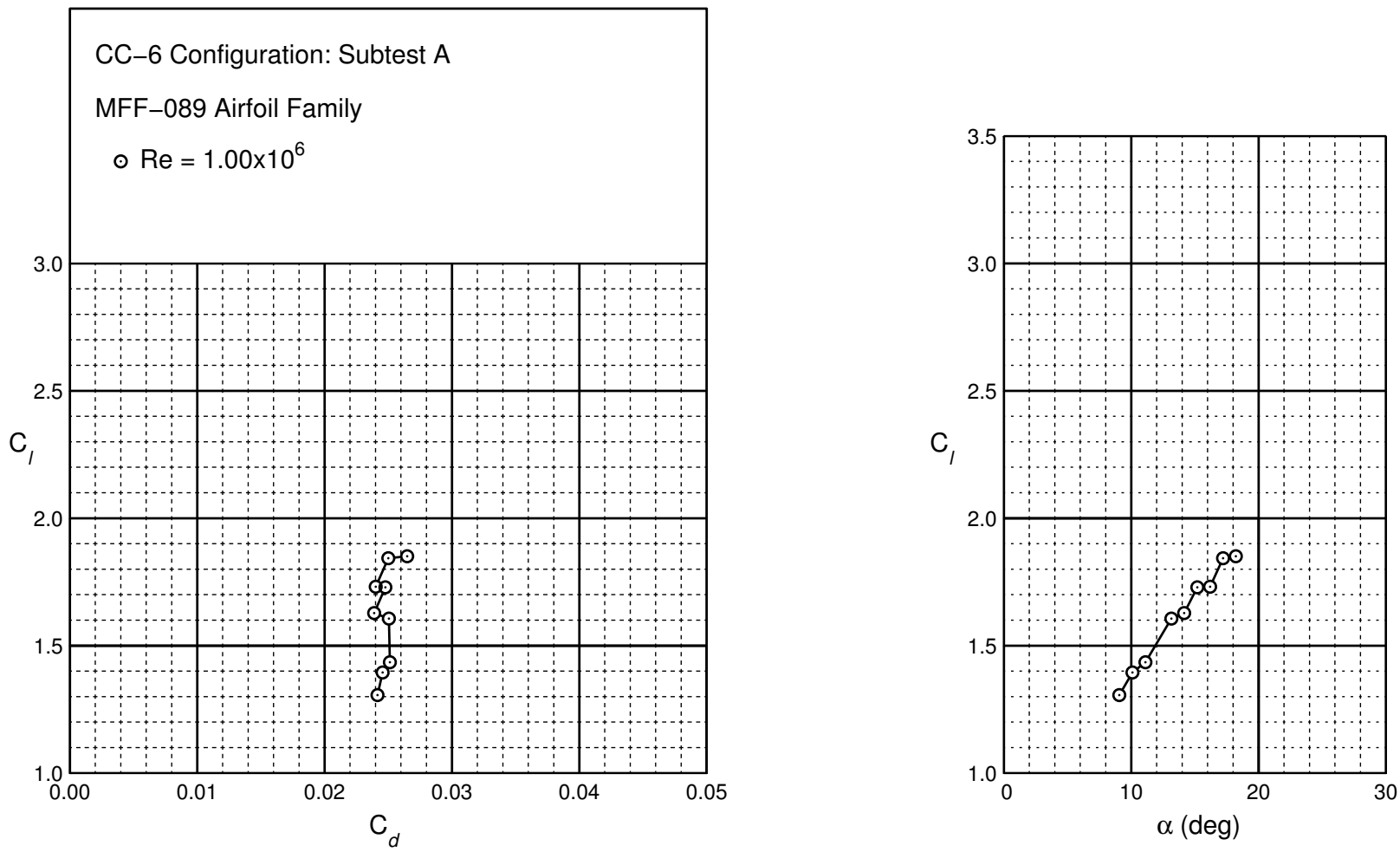

Figure B.10: CC-6 performance at $Re = 1.0 \times 10^6$.

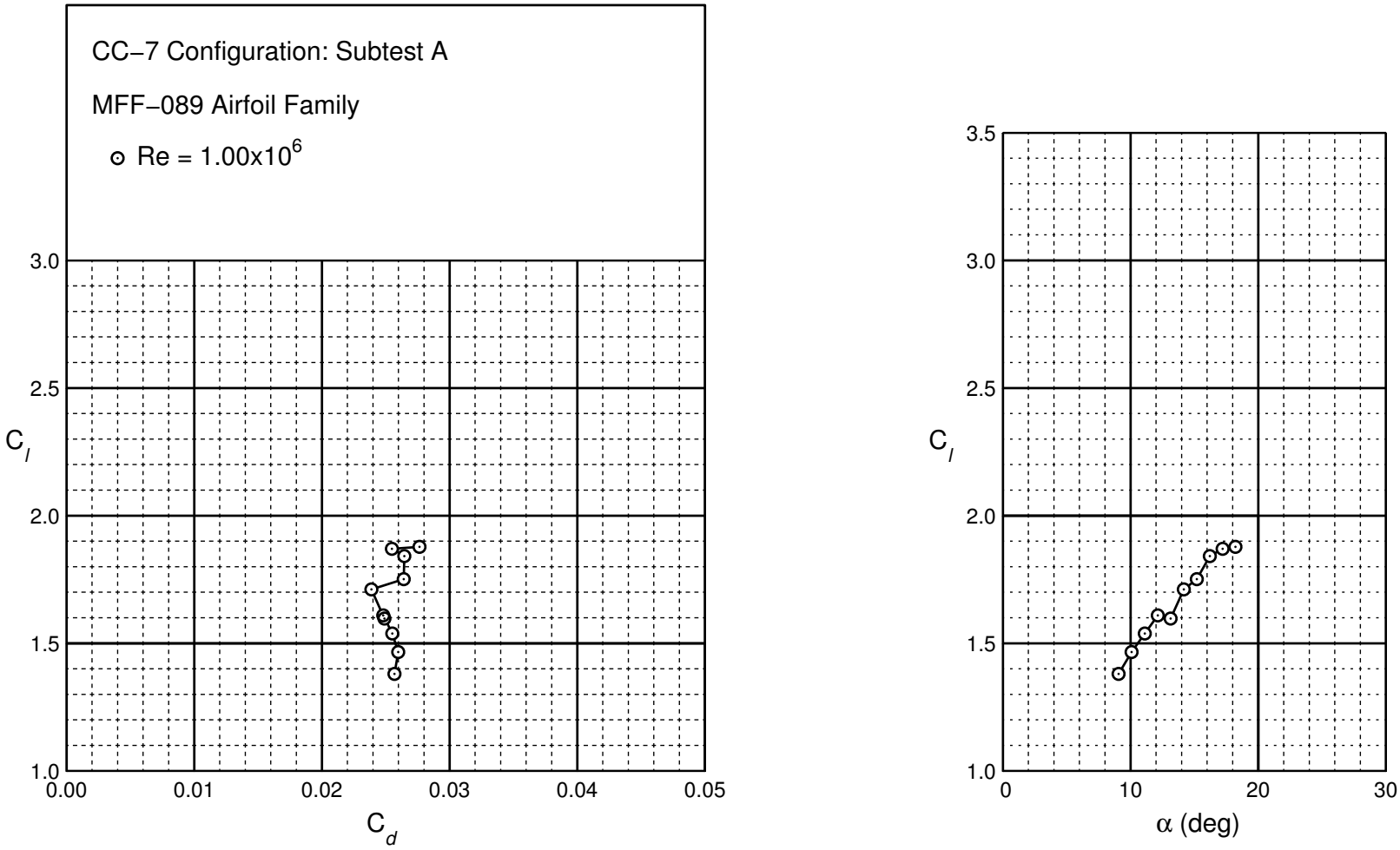

Figure B.11: CC-7 performance at $Re = 1.0 \times 10^6$.

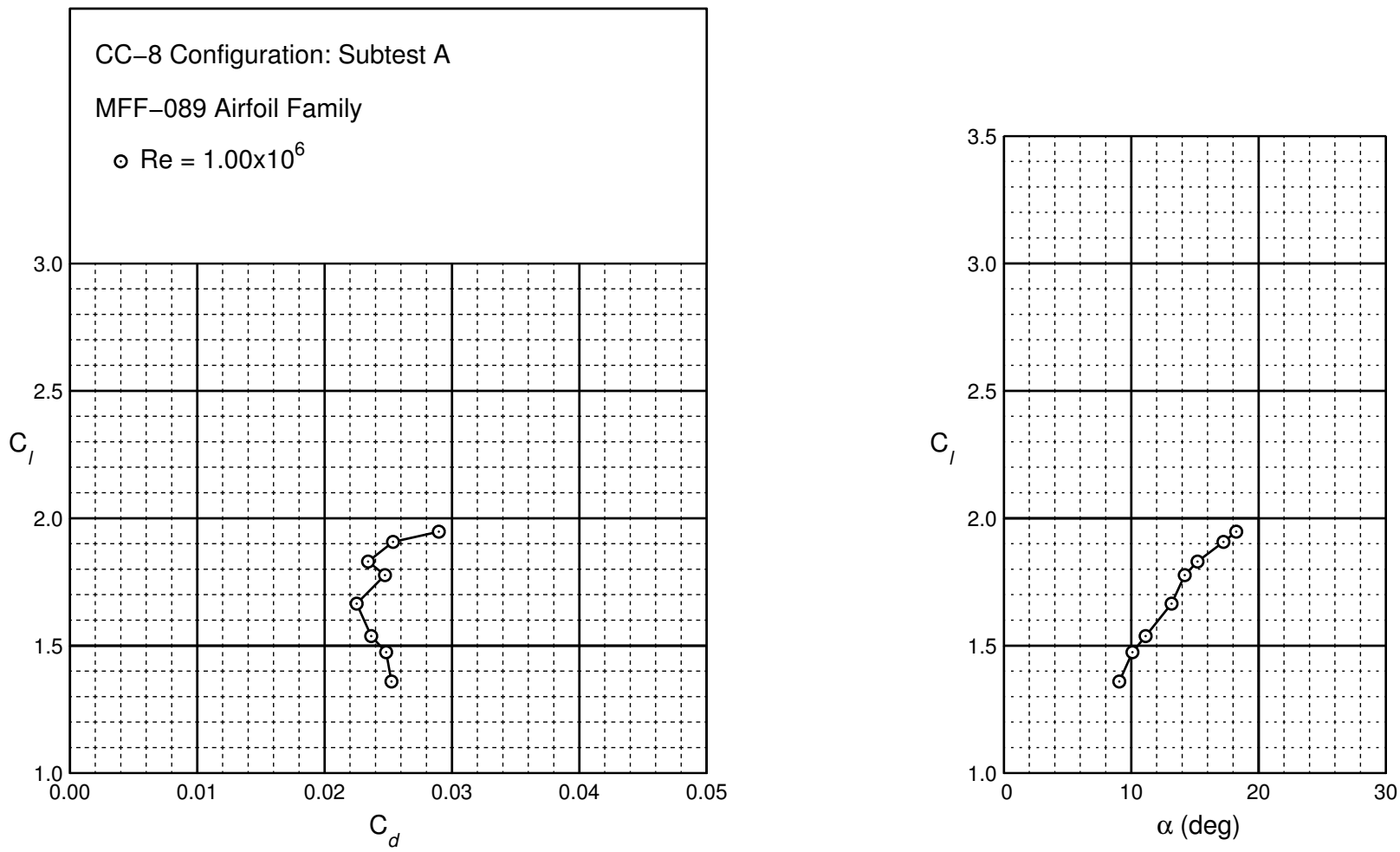

Figure B.12: CC-8 performance at $Re = 1.0 \times 10^6$.

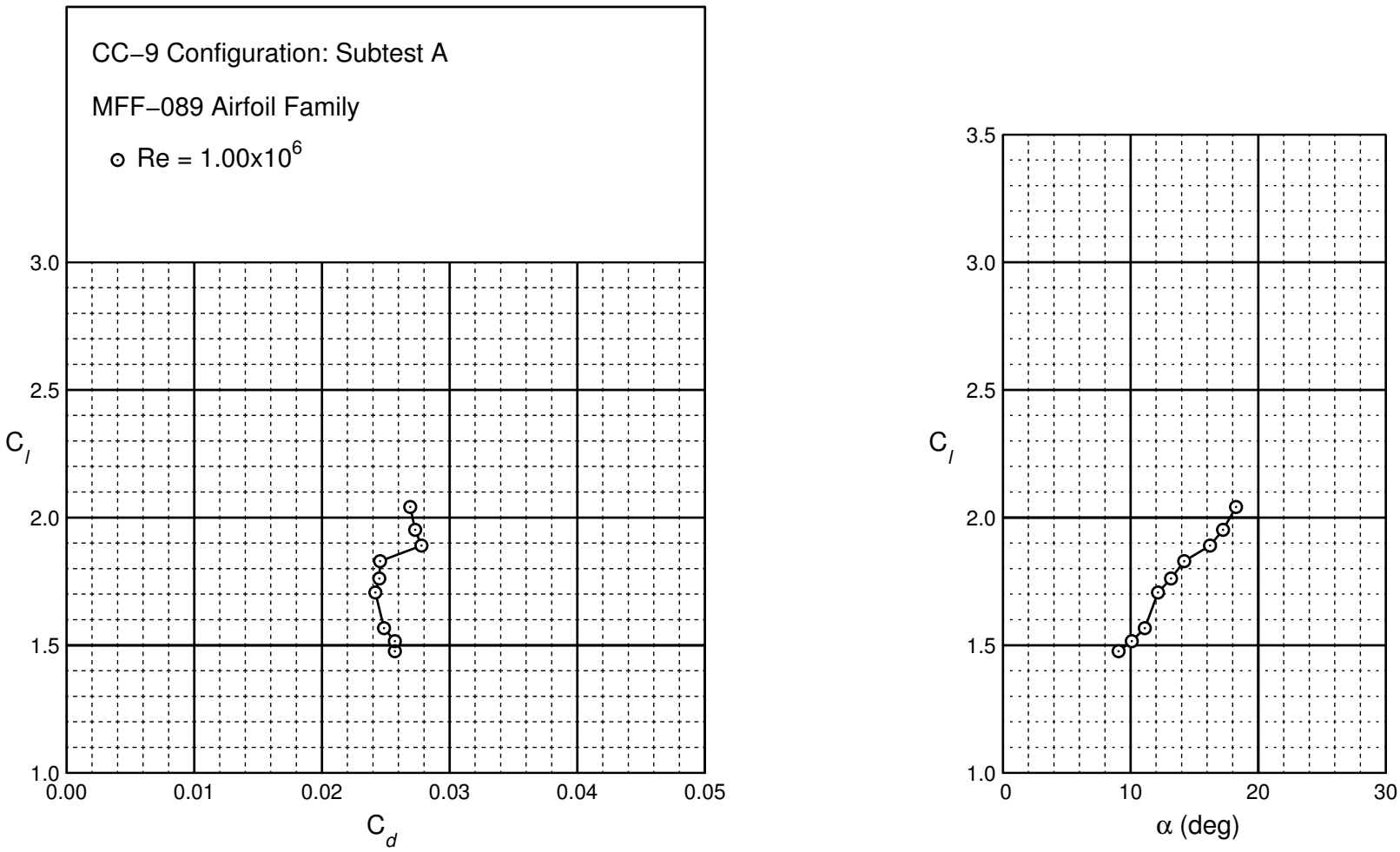

Figure B.13: CC-9 performance at $Re = 1.0 \times 10^6$.

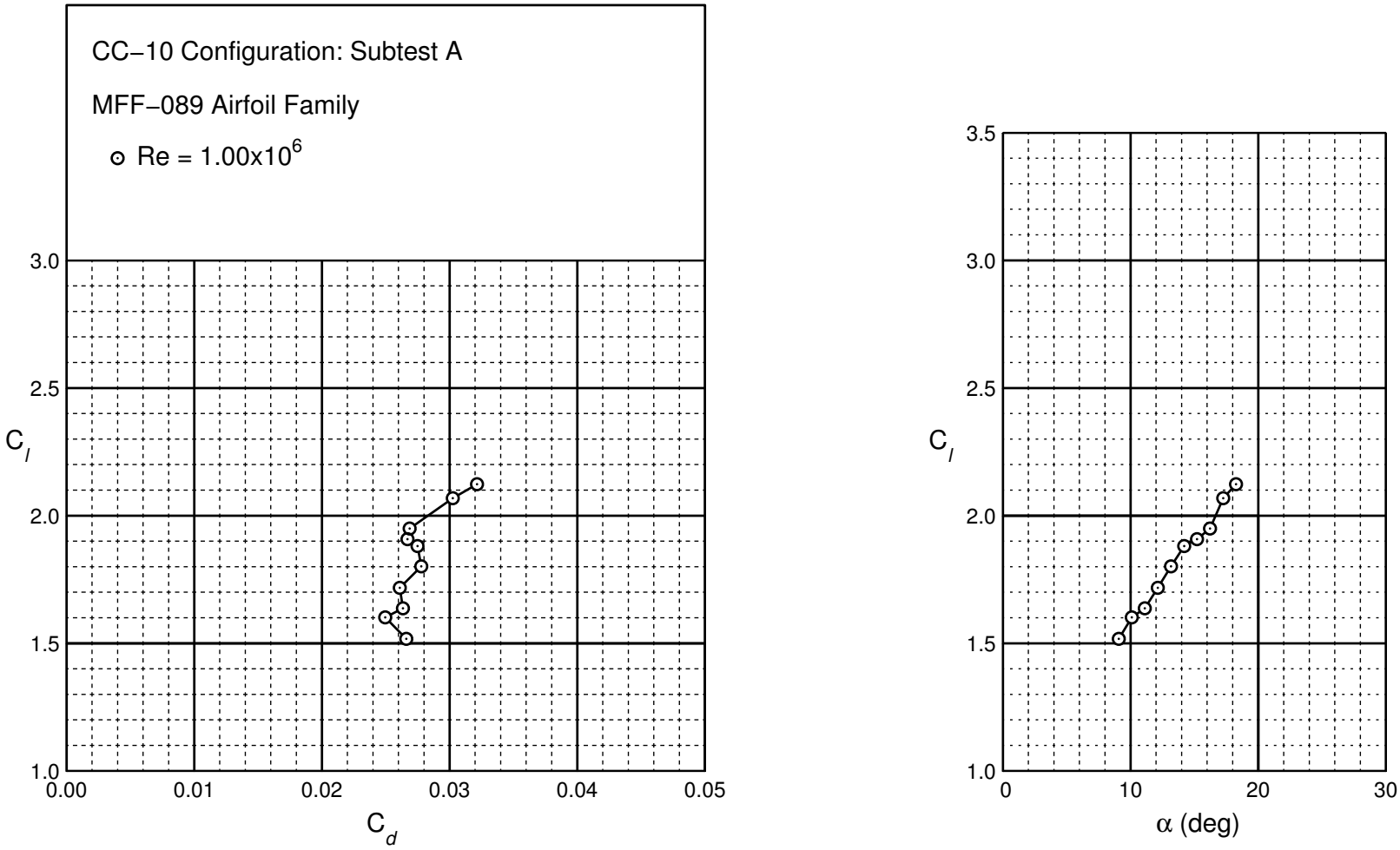

Figure B.14: CC-10 performance at $Re = 1.0 \times 10^6$.

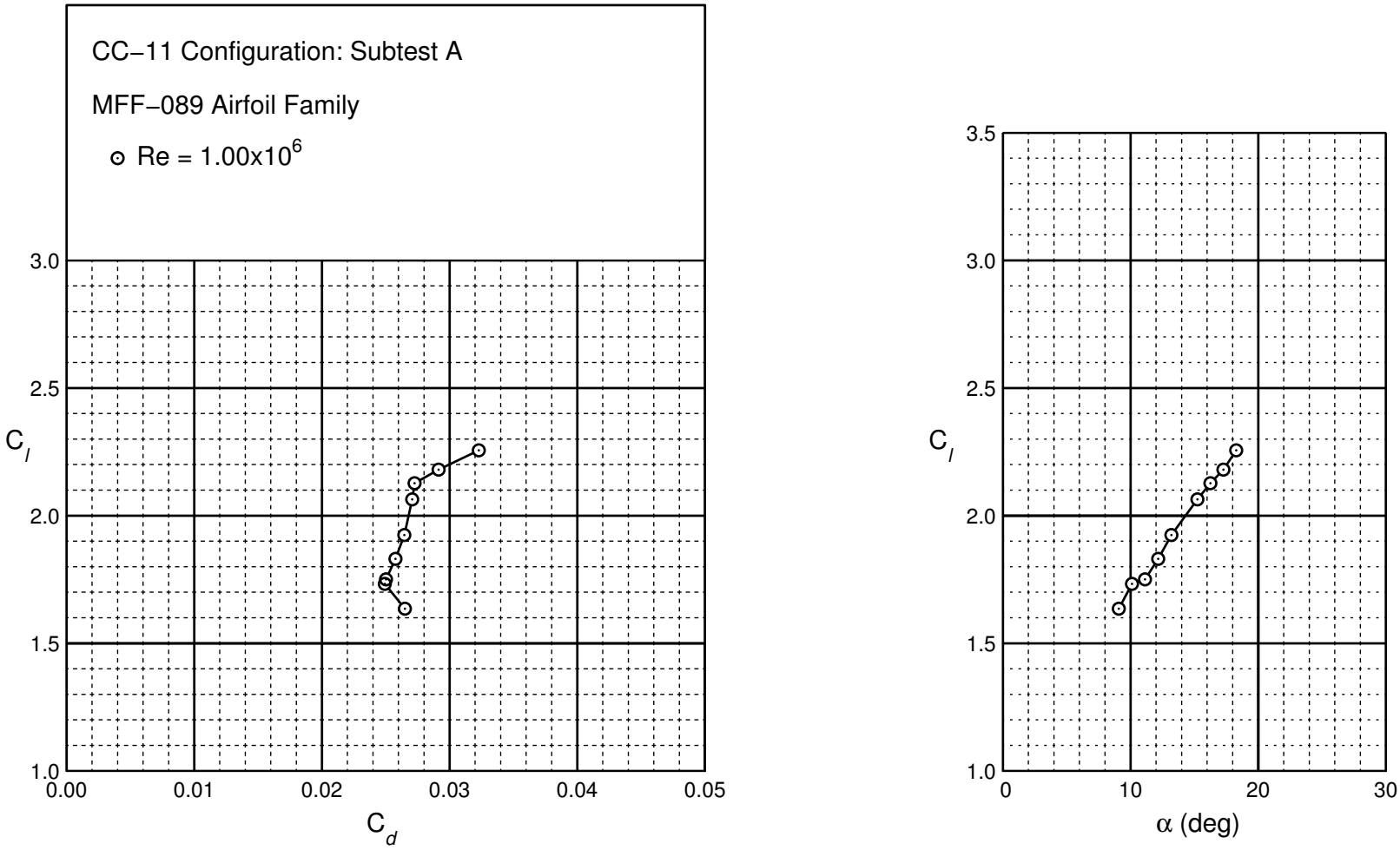

Figure B.15: CC-11 performance at $Re = 1.0 \times 10^6$.

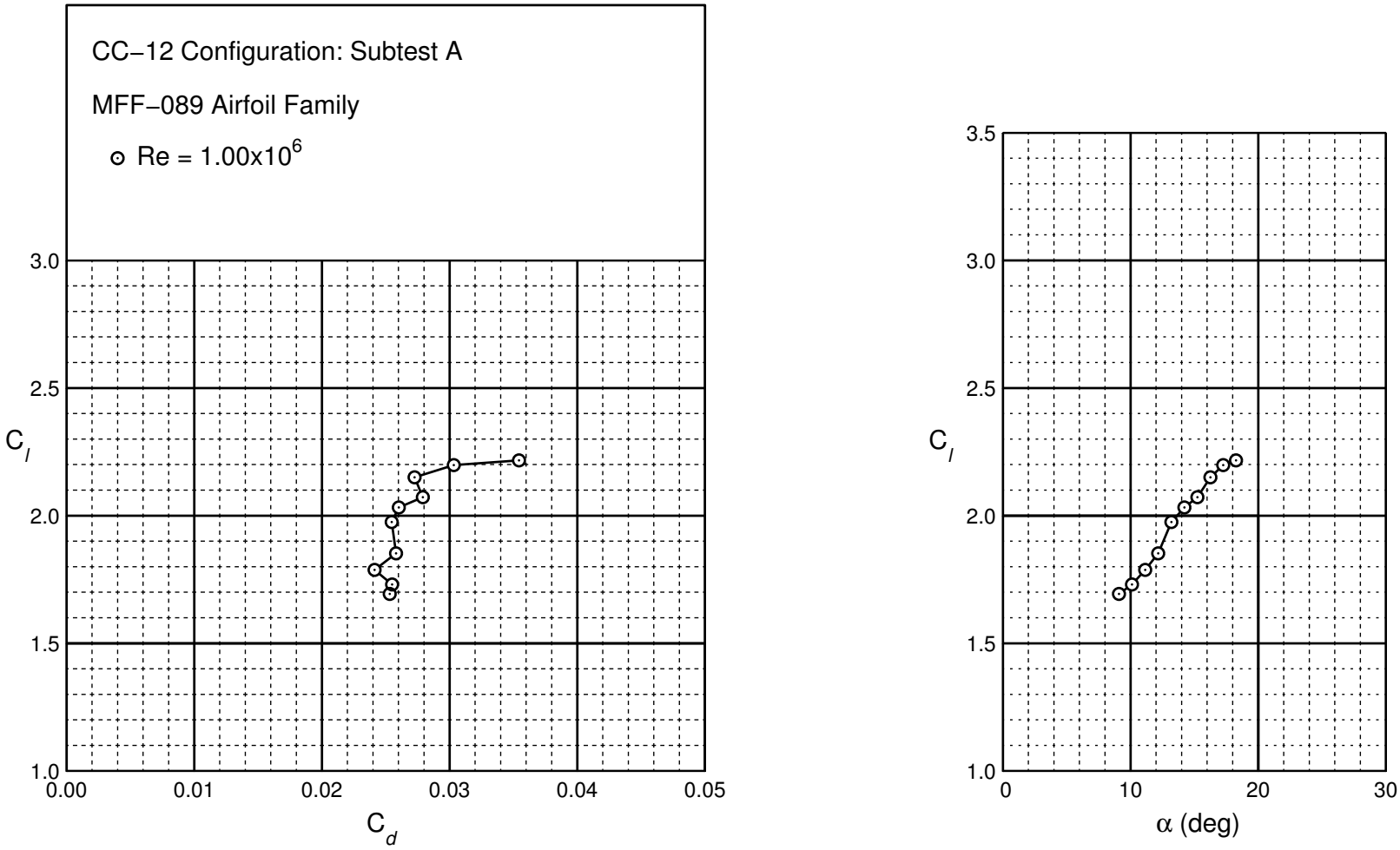

Figure B.16: CC-12 performance at $Re = 1.0 \times 10^6$.

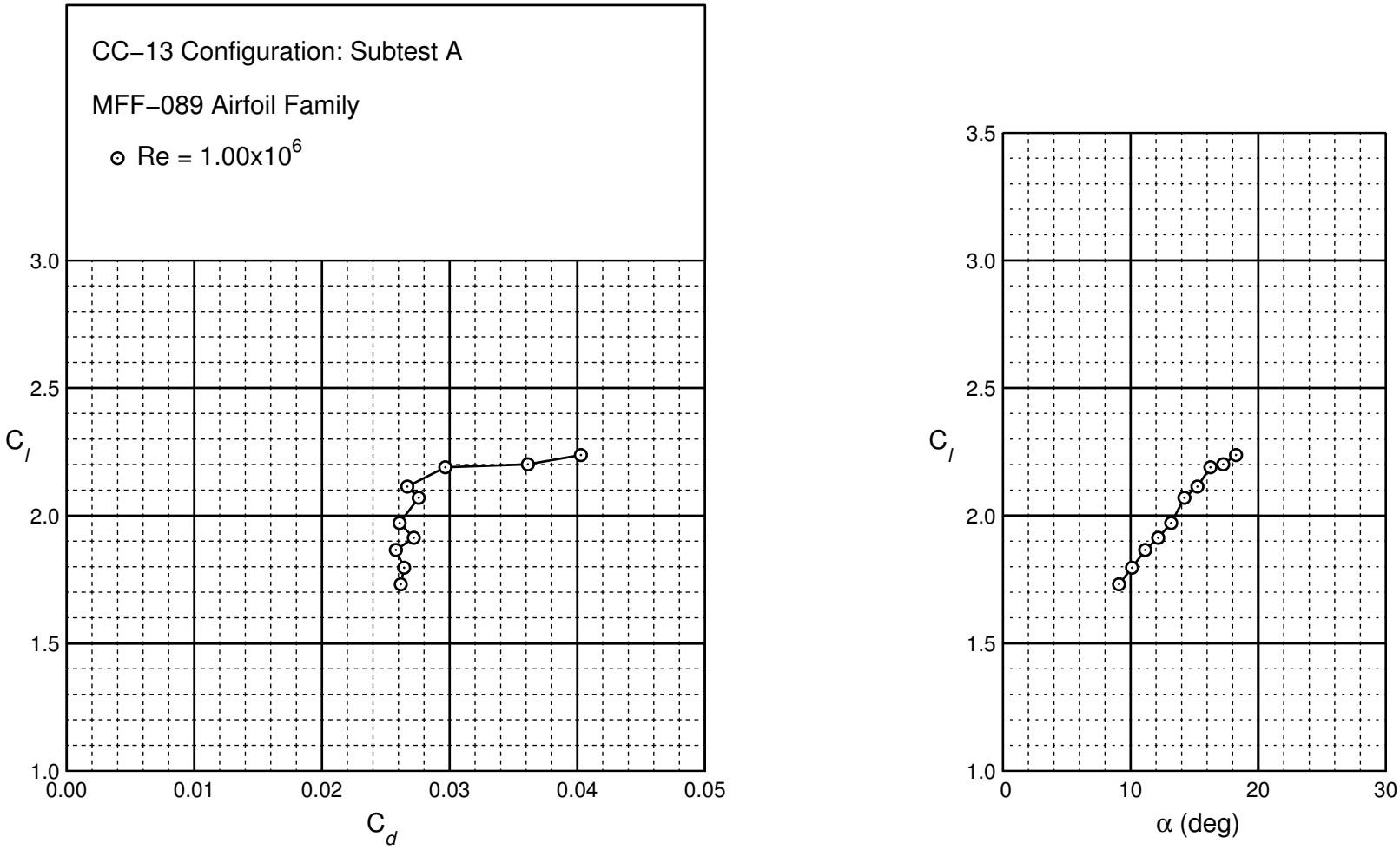

Figure B.17: CC-13 performance at $Re = 1.0 \times 10^6$.

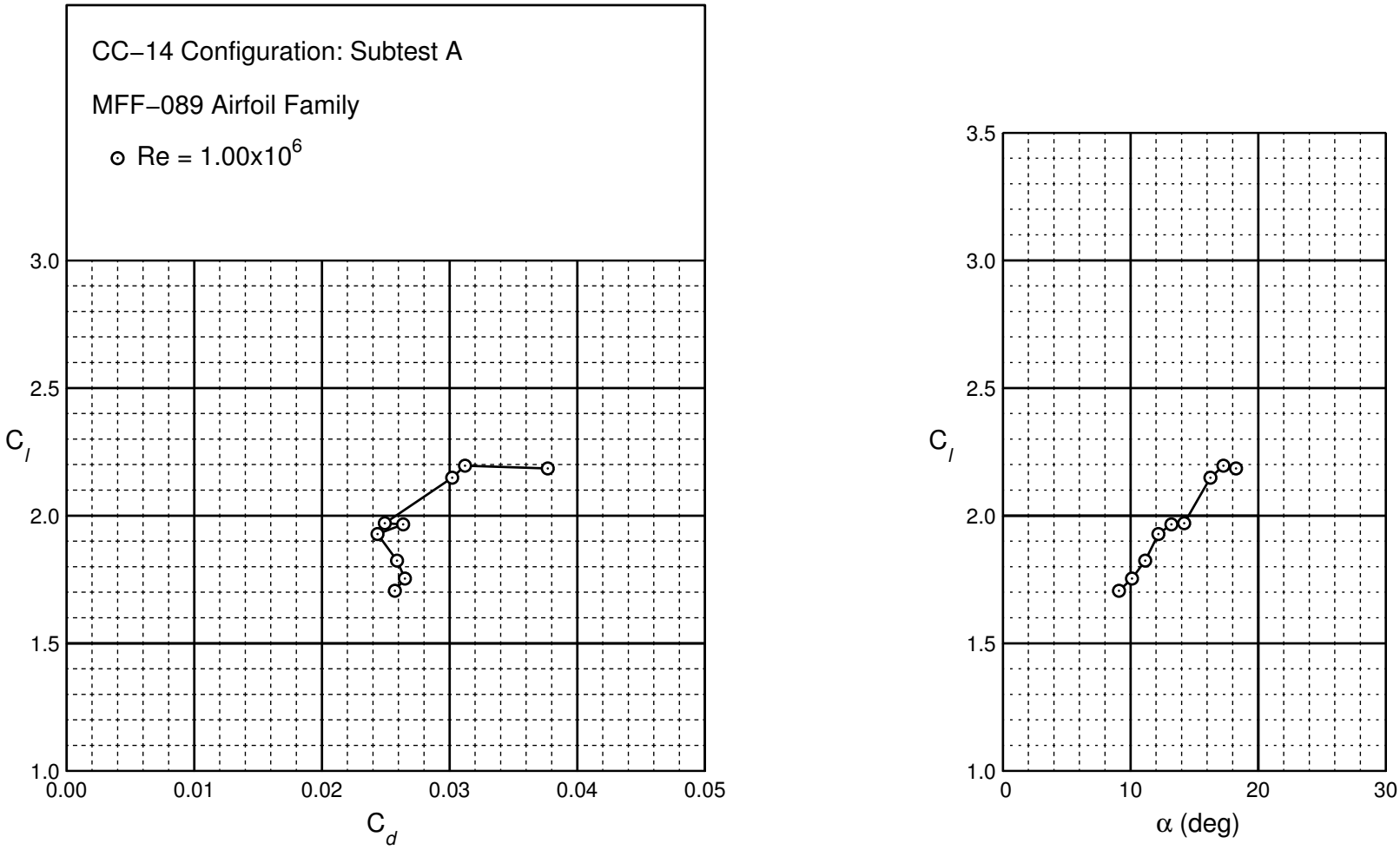

Figure B.18: CC-14 performance at $Re = 1.0 \times 10^6$.

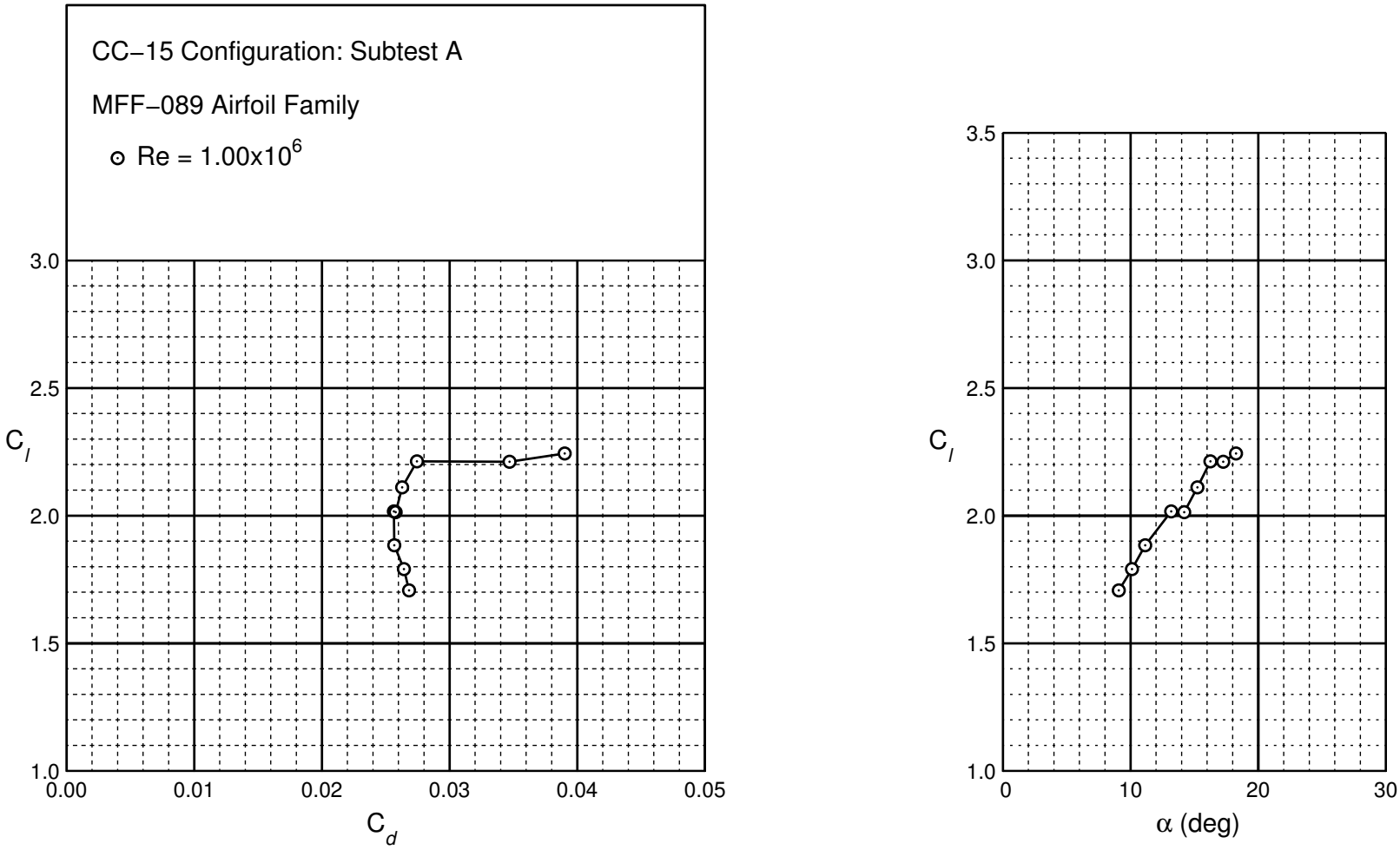

Figure B.19: CC-15 performance at $Re = 1.0 \times 10^6$.

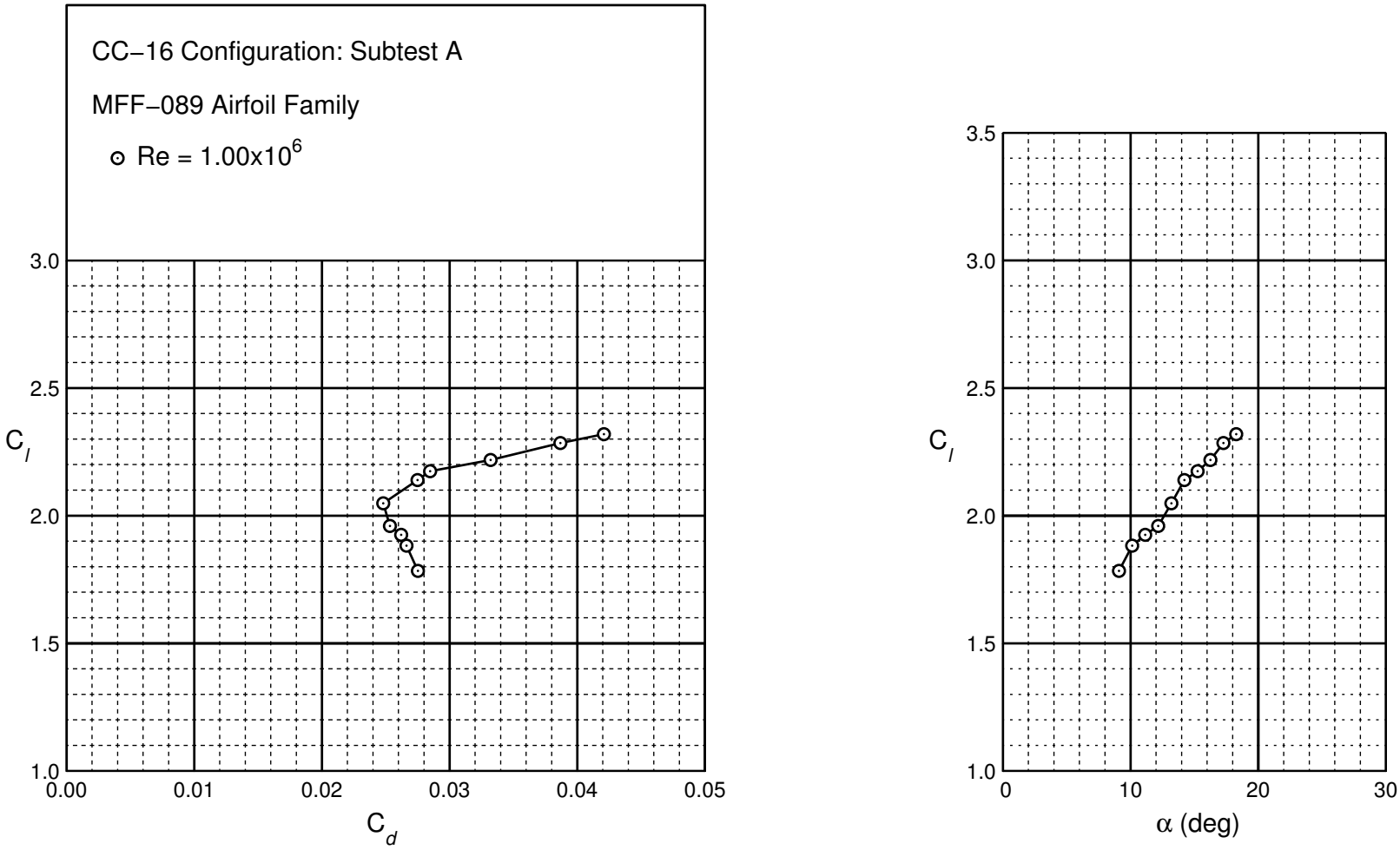

Figure B.20: CC-16 performance at $Re = 1.0 \times 10^6$.

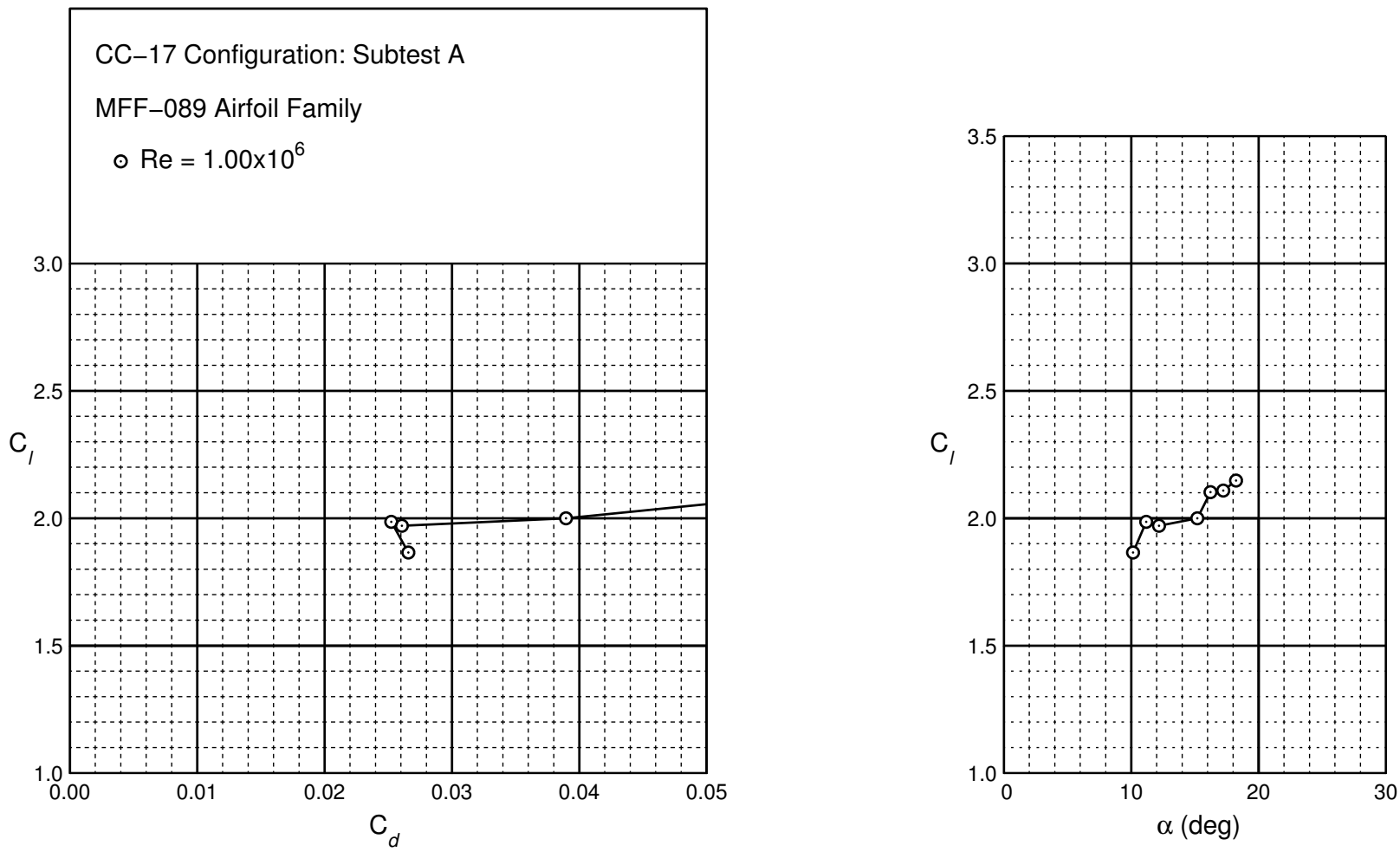

Figure B.21: CC-17 performance at $Re = 1.0 \times 10^6$.

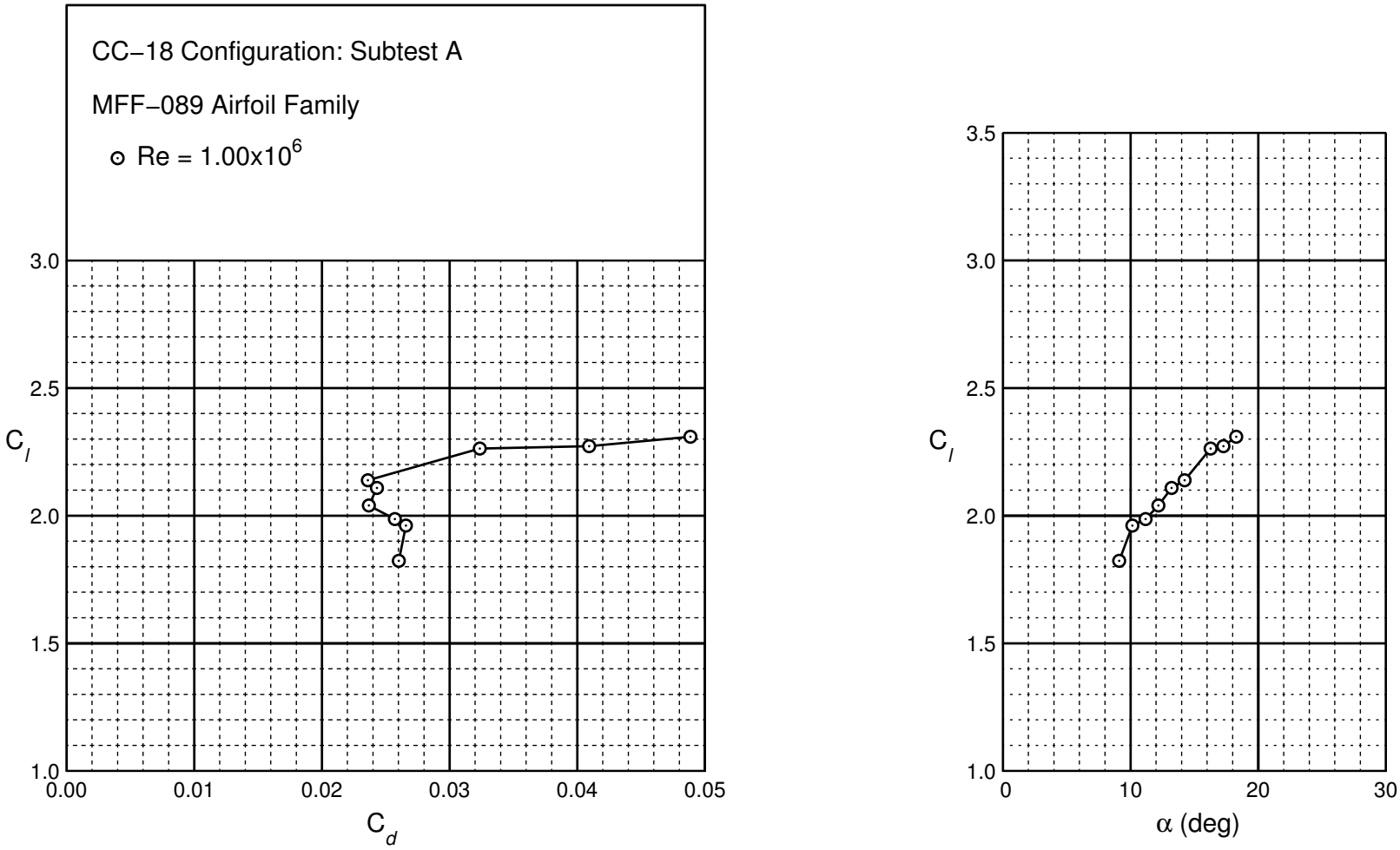

Figure B.22: CC-18 performance at $Re = 1.0 \times 10^6$.

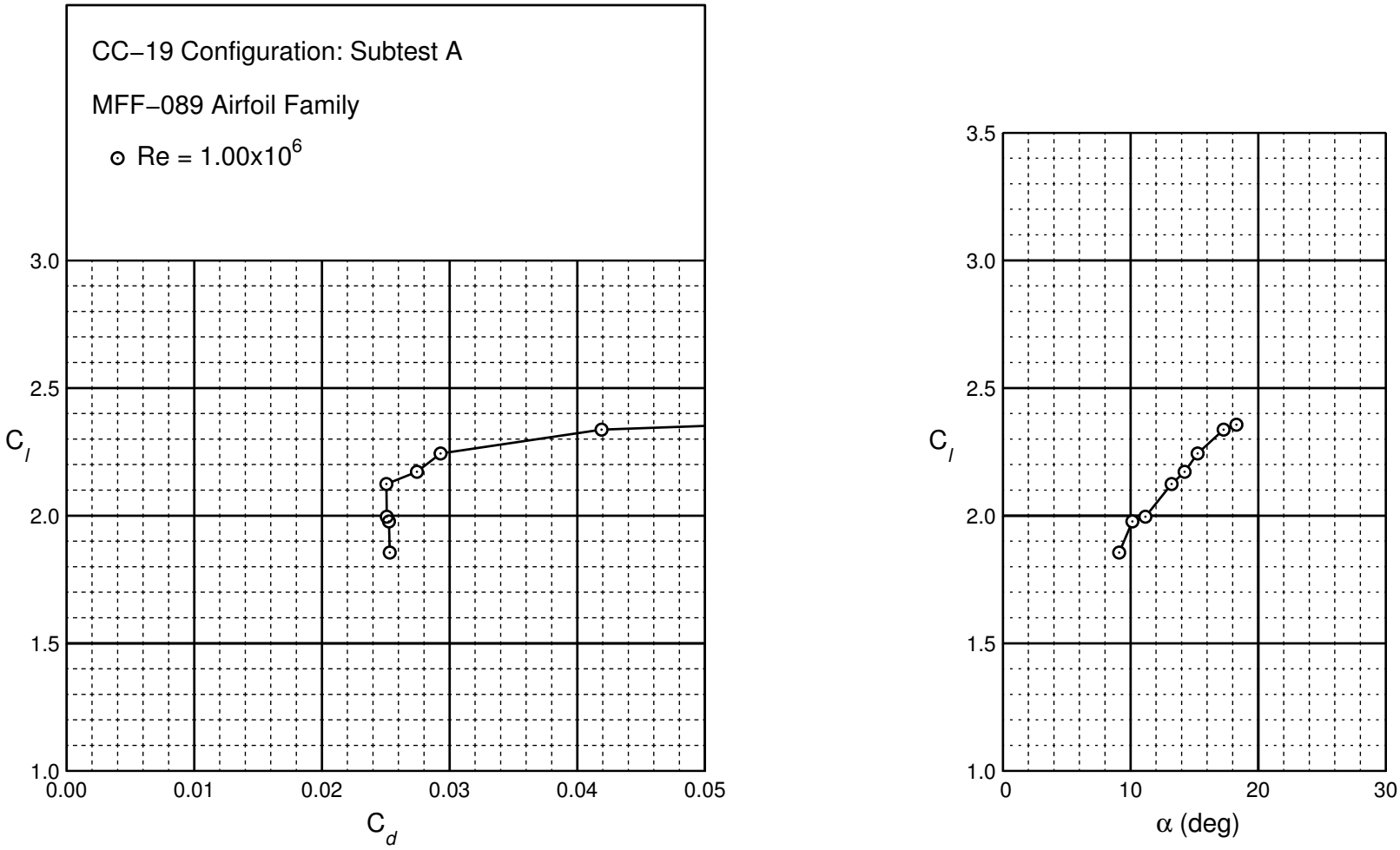

Figure B.23: CC-19 performance at $Re = 1.0 \times 10^6$.

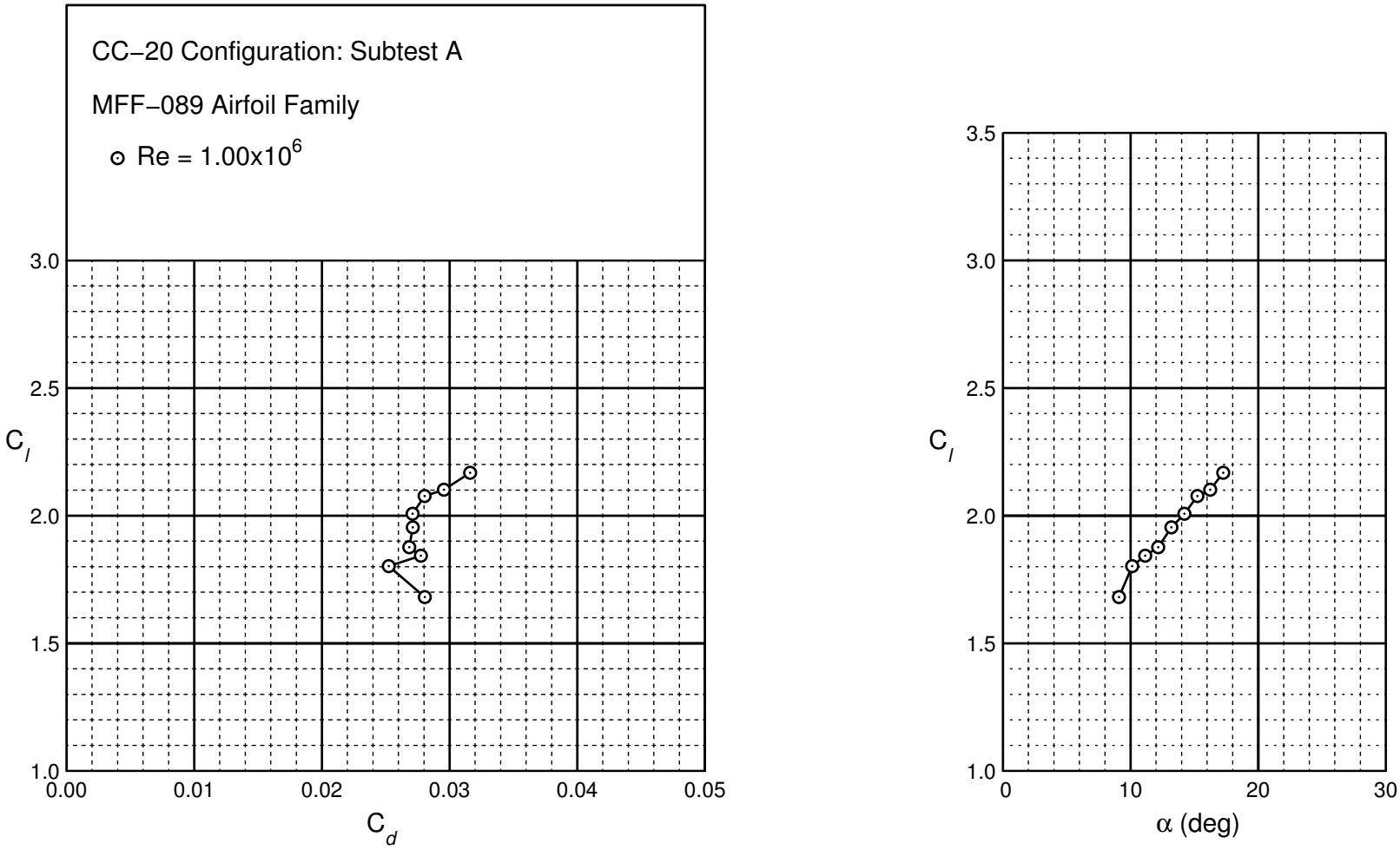

Figure B.24: CC-20 performance at $Re = 1.0 \times 10^6$.

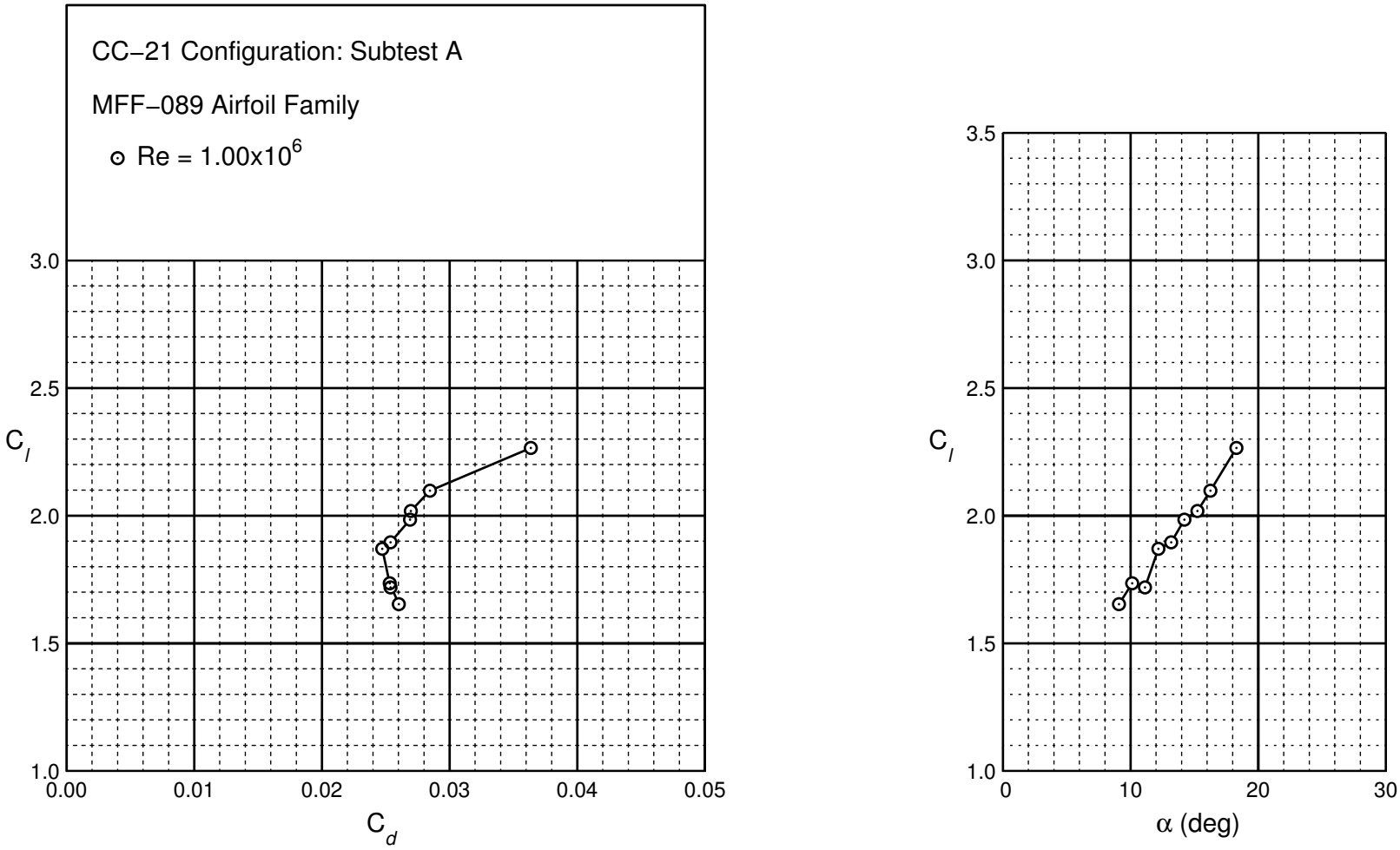

Figure B.25: CC-21 performance at $Re = 1.0 \times 10^6$.

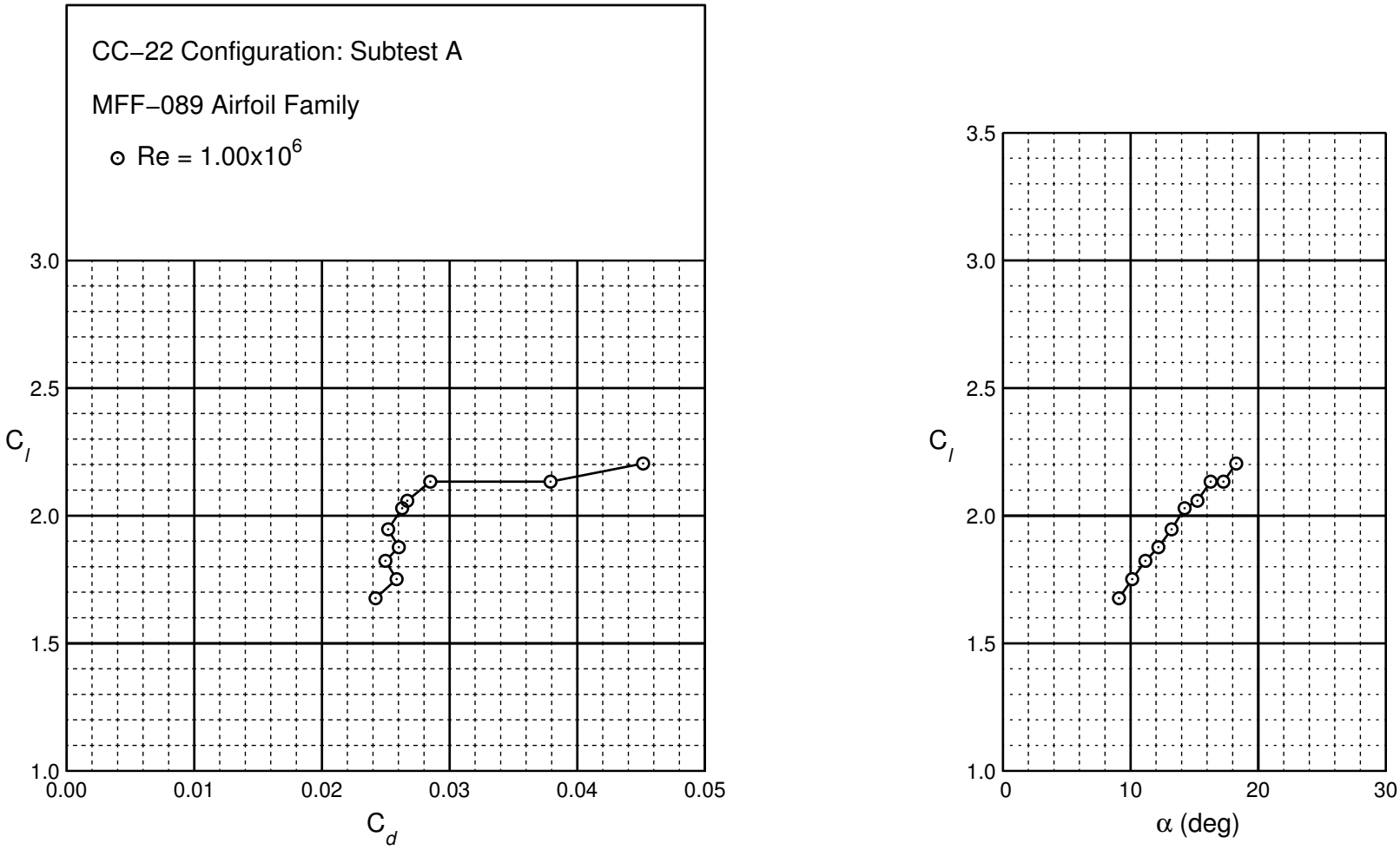

Figure B.26: CC-22 performance at $Re = 1.0 \times 10^6$.

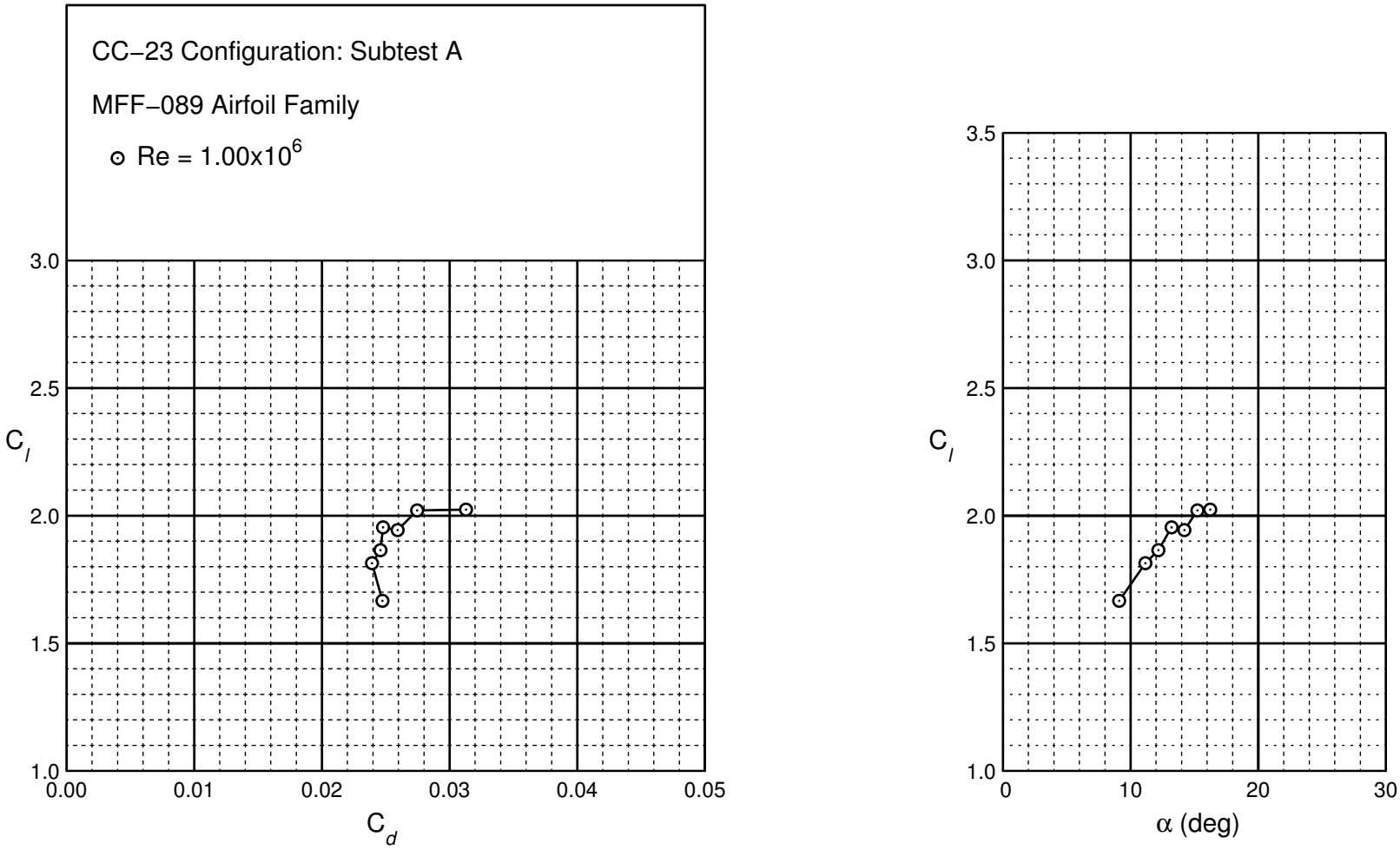

Figure B.27: CC-23 performance at $Re = 1.0 \times 10^6$.

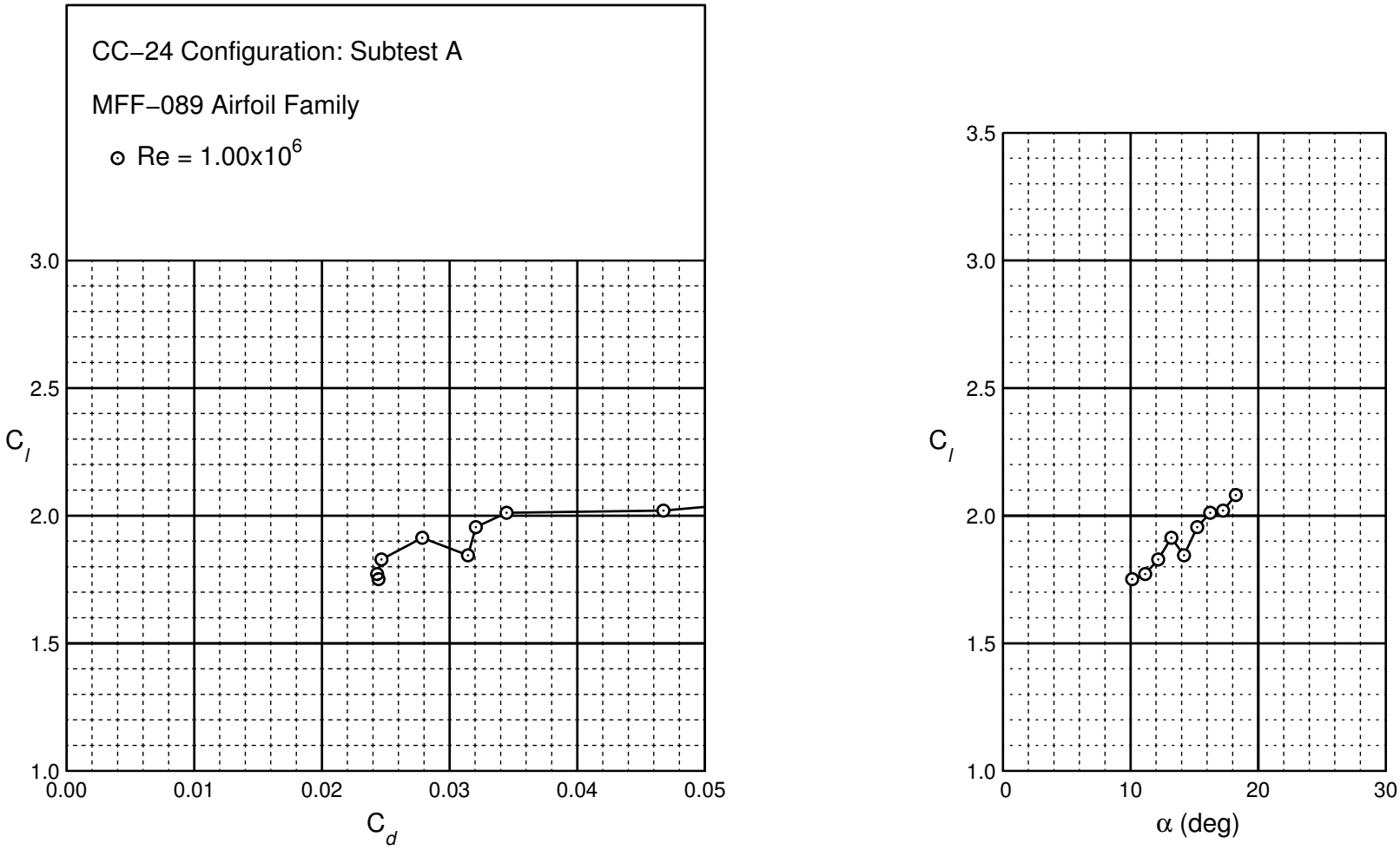

Figure B.28: CC-24 performance at $Re = 1.0 \times 10^6$.

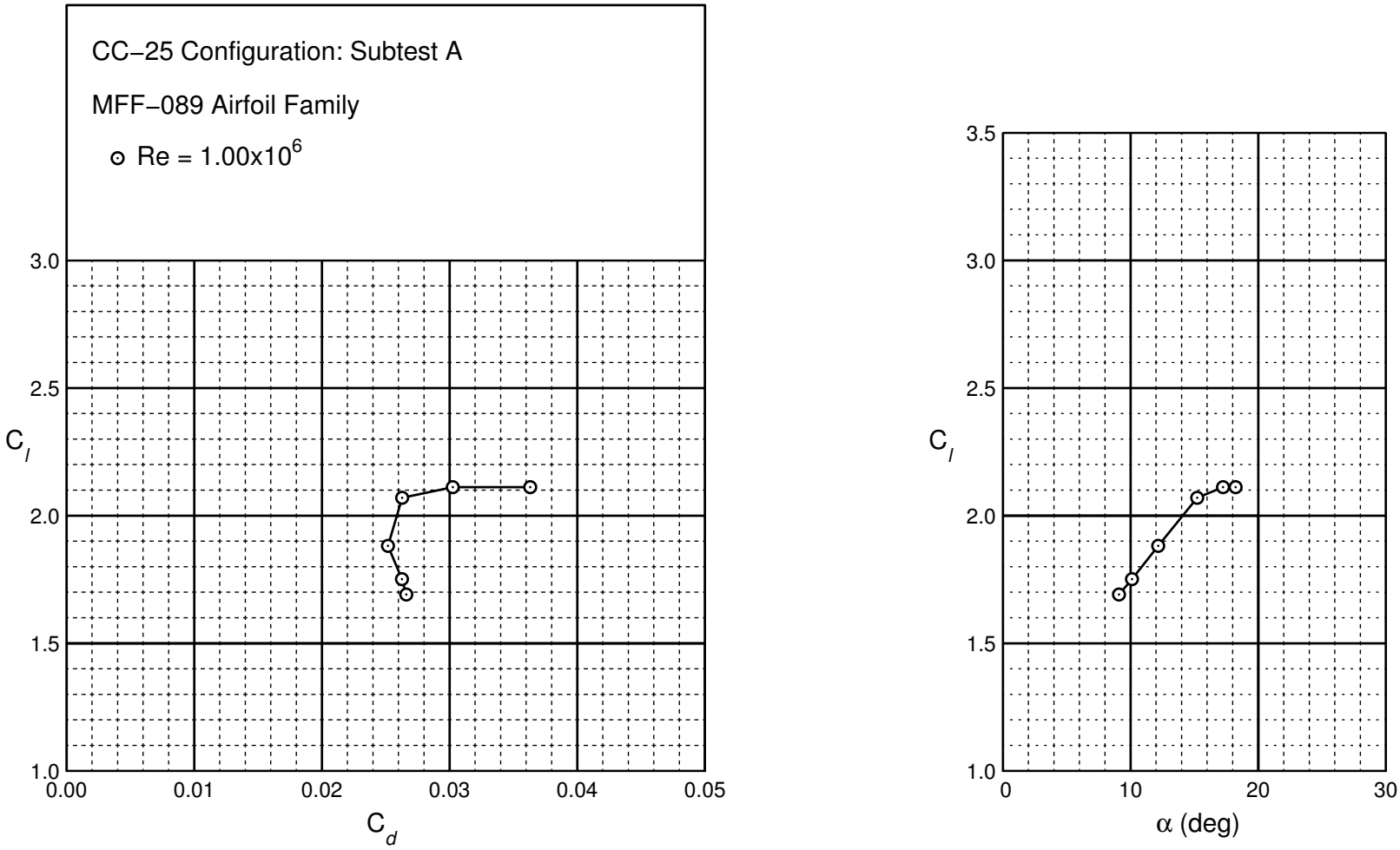

Figure B.29: CC-25 performance at $Re = 1.0 \times 10^6$.

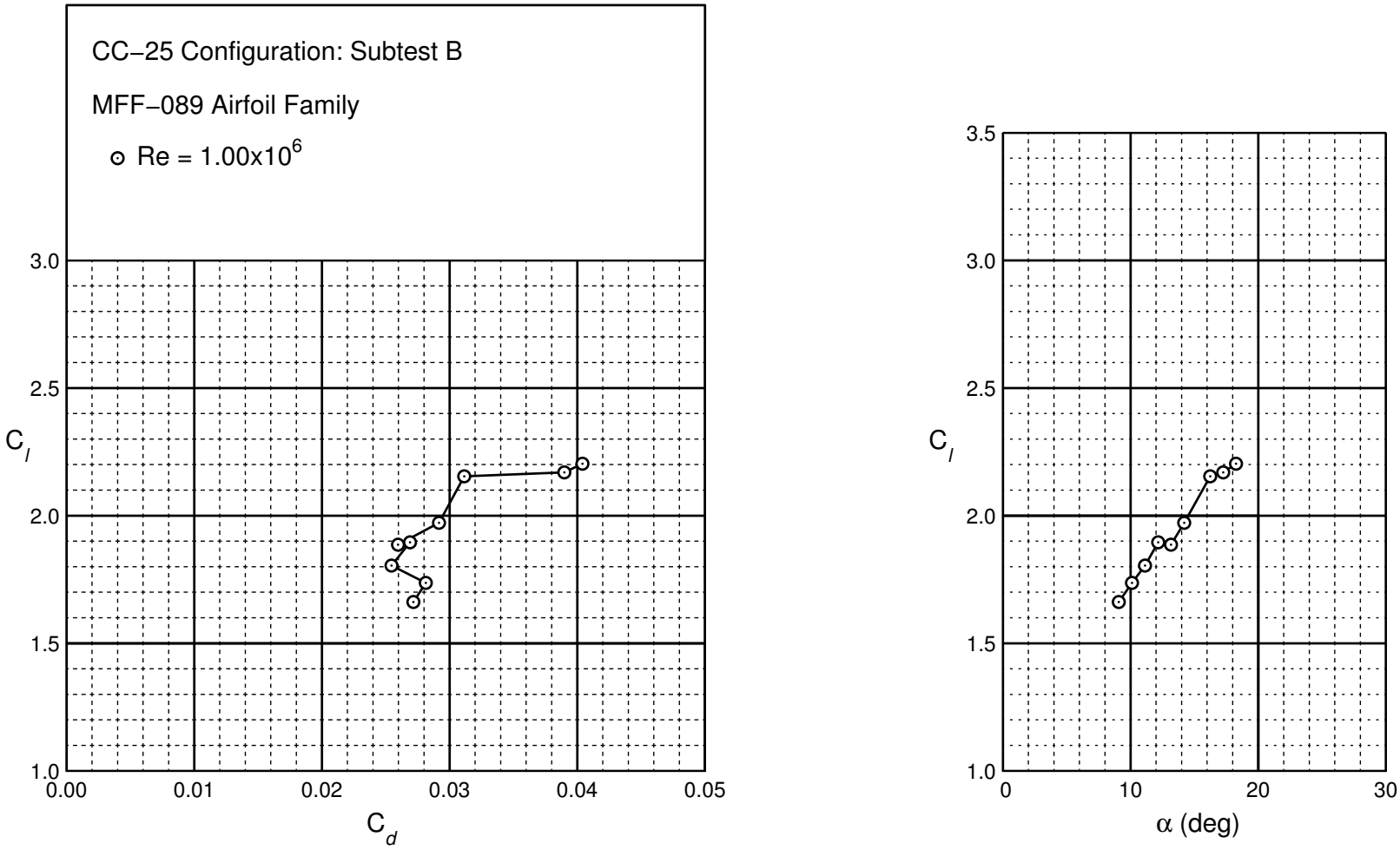

Figure B.30: CC-25 performance at $Re = 1.0 \times 10^6$.

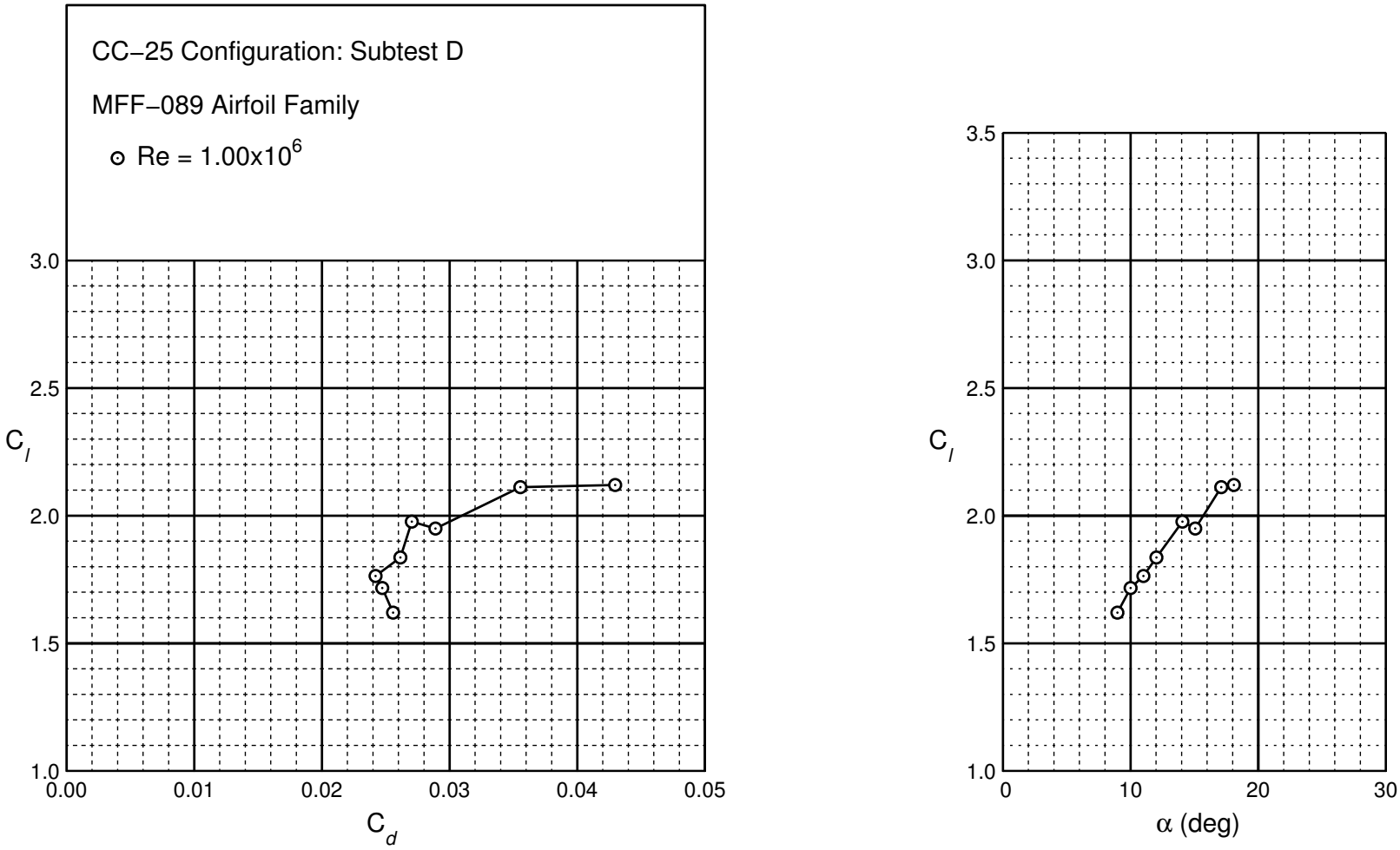

Figure B.31: CC-25 performance at $Re = 1.0 \times 10^6$.

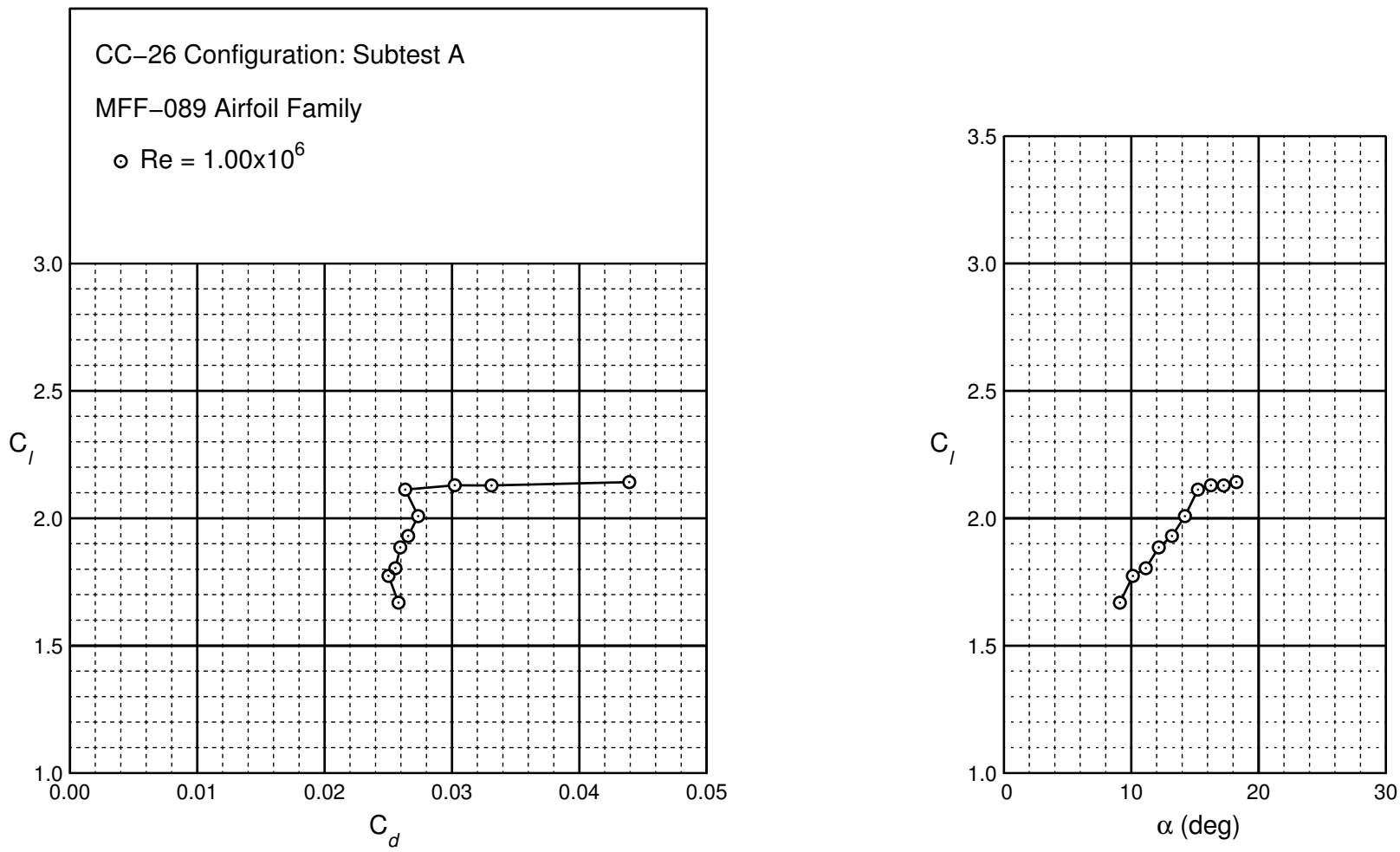

Figure B.32: CC-26 performance at $Re = 1.0 \times 10^6$.

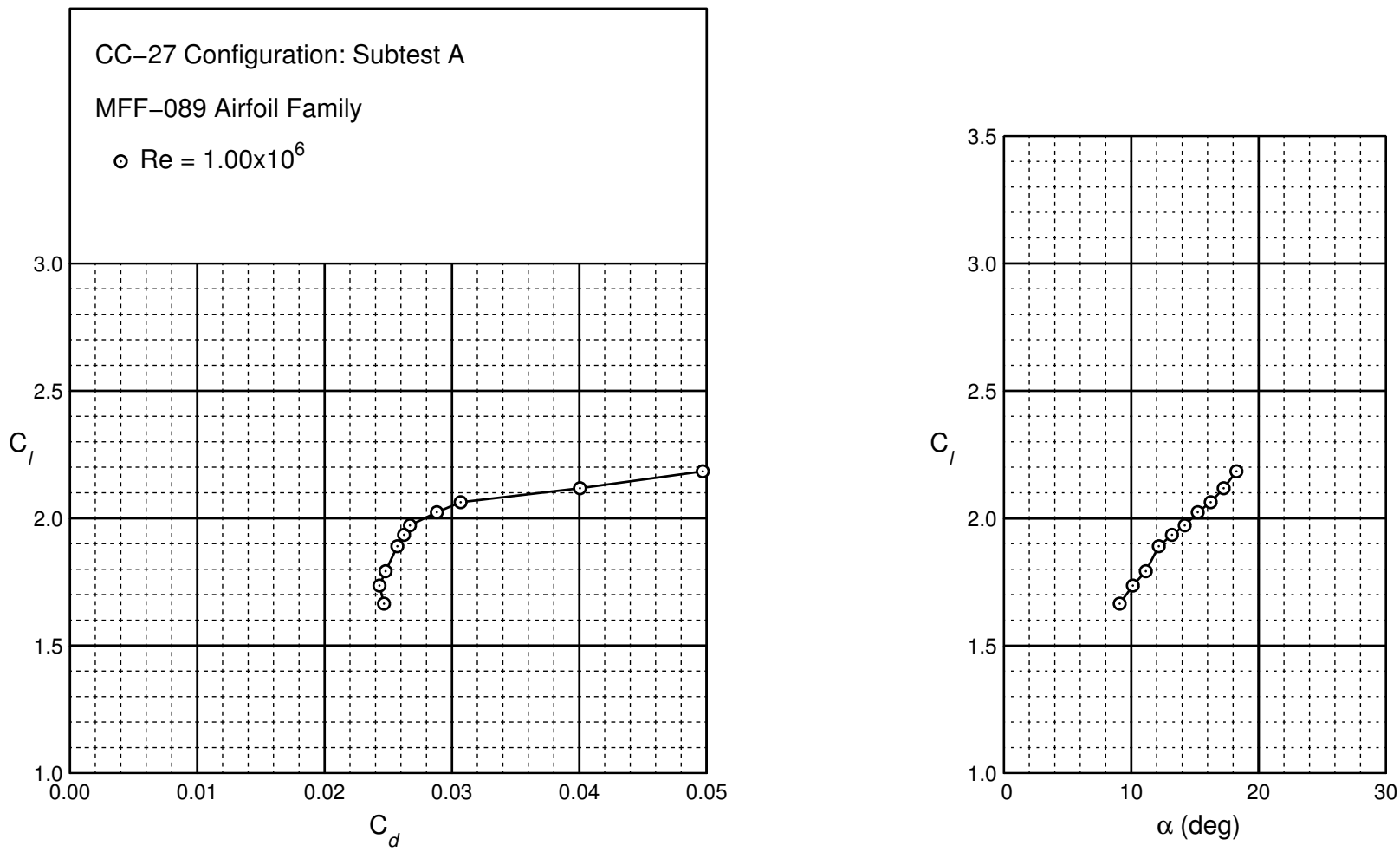

Figure B.33: CC-27 performance at $Re = 1.0 \times 10^6$.

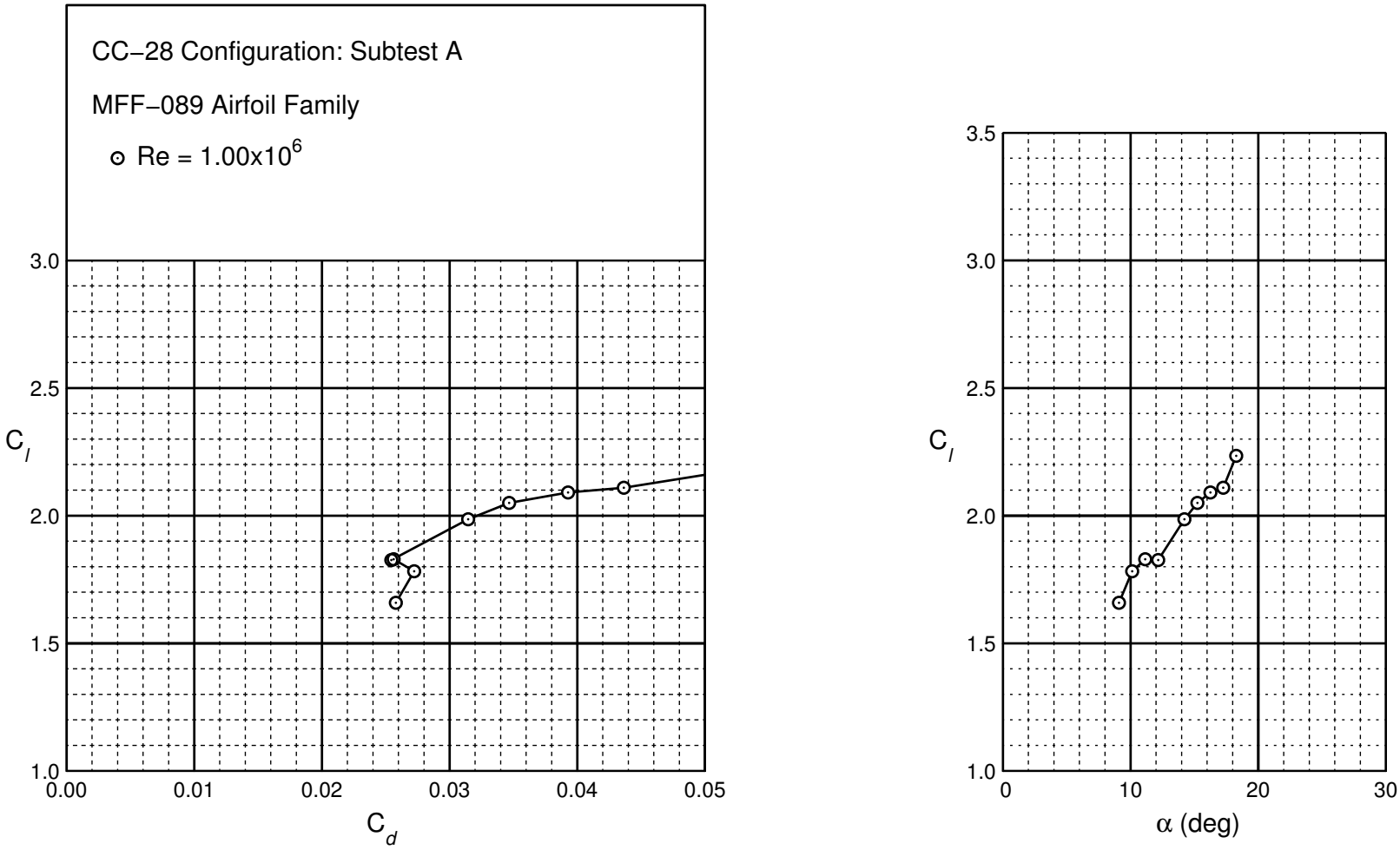

Figure B.34: CC-28 performance at $Re = 1.0 \times 10^6$.

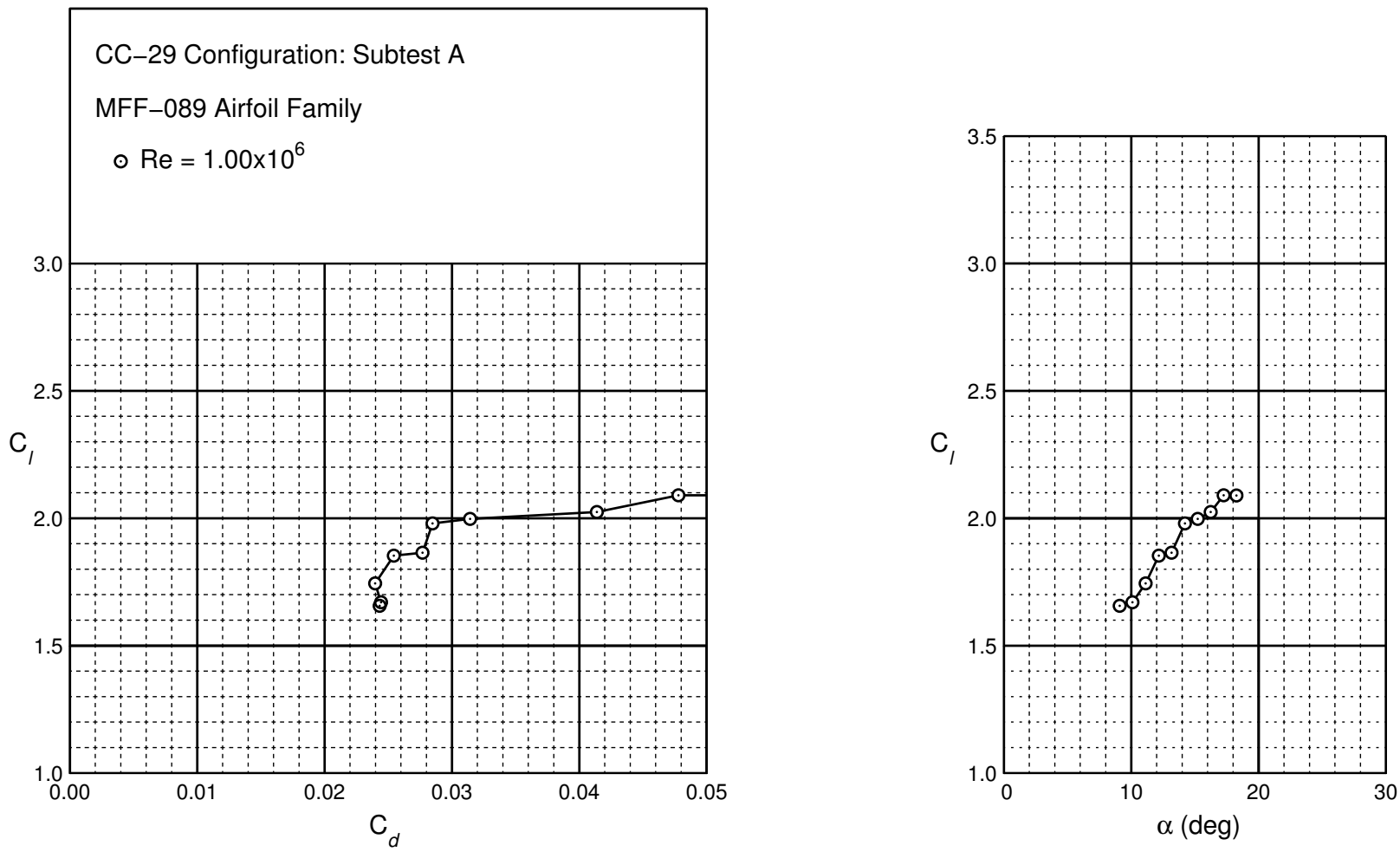

Figure B.35: CC-29 performance at $Re = 1.0 \times 10^6$.

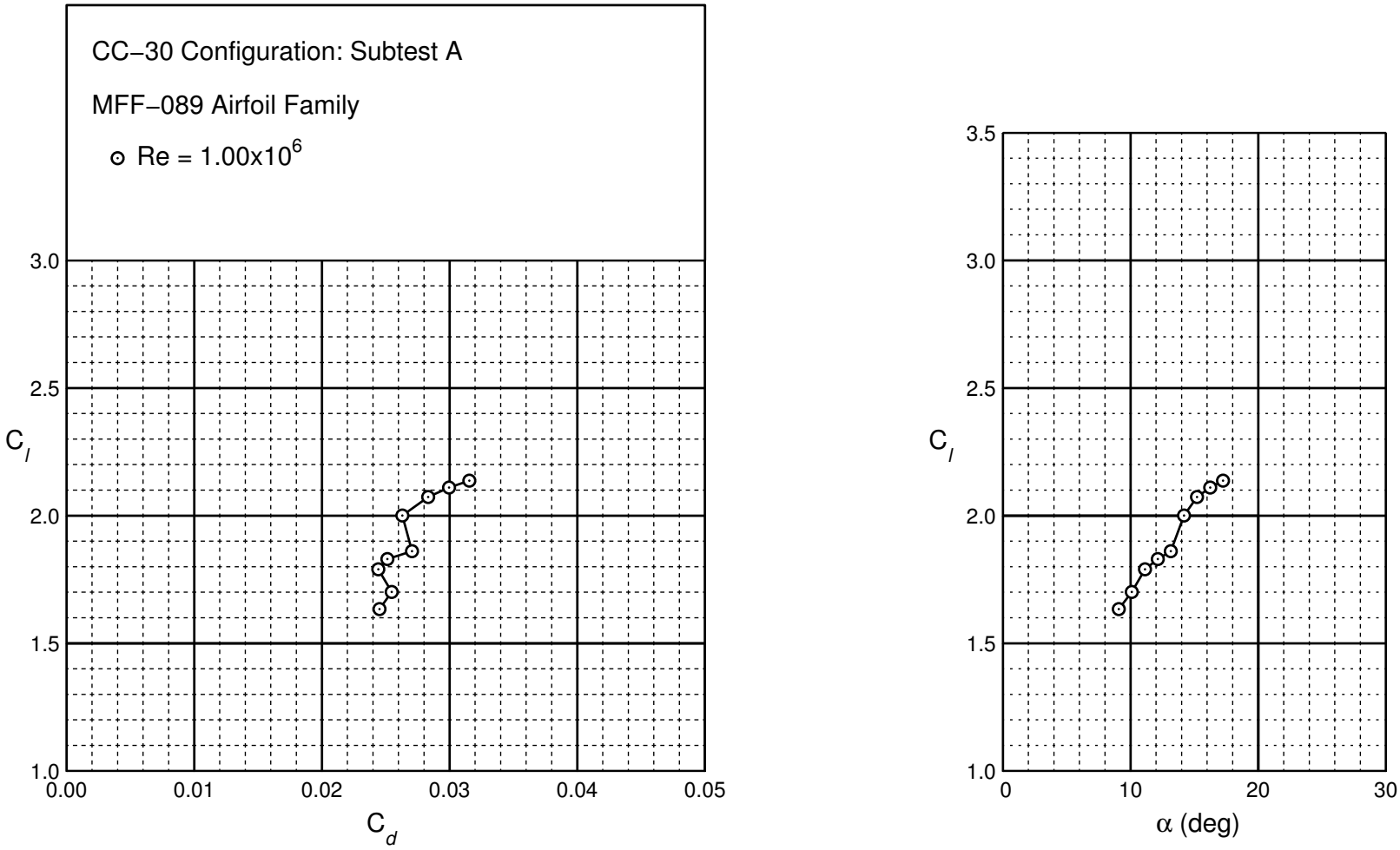

Figure B.36: CC-30 performance at $Re = 1.0 \times 10^6$.

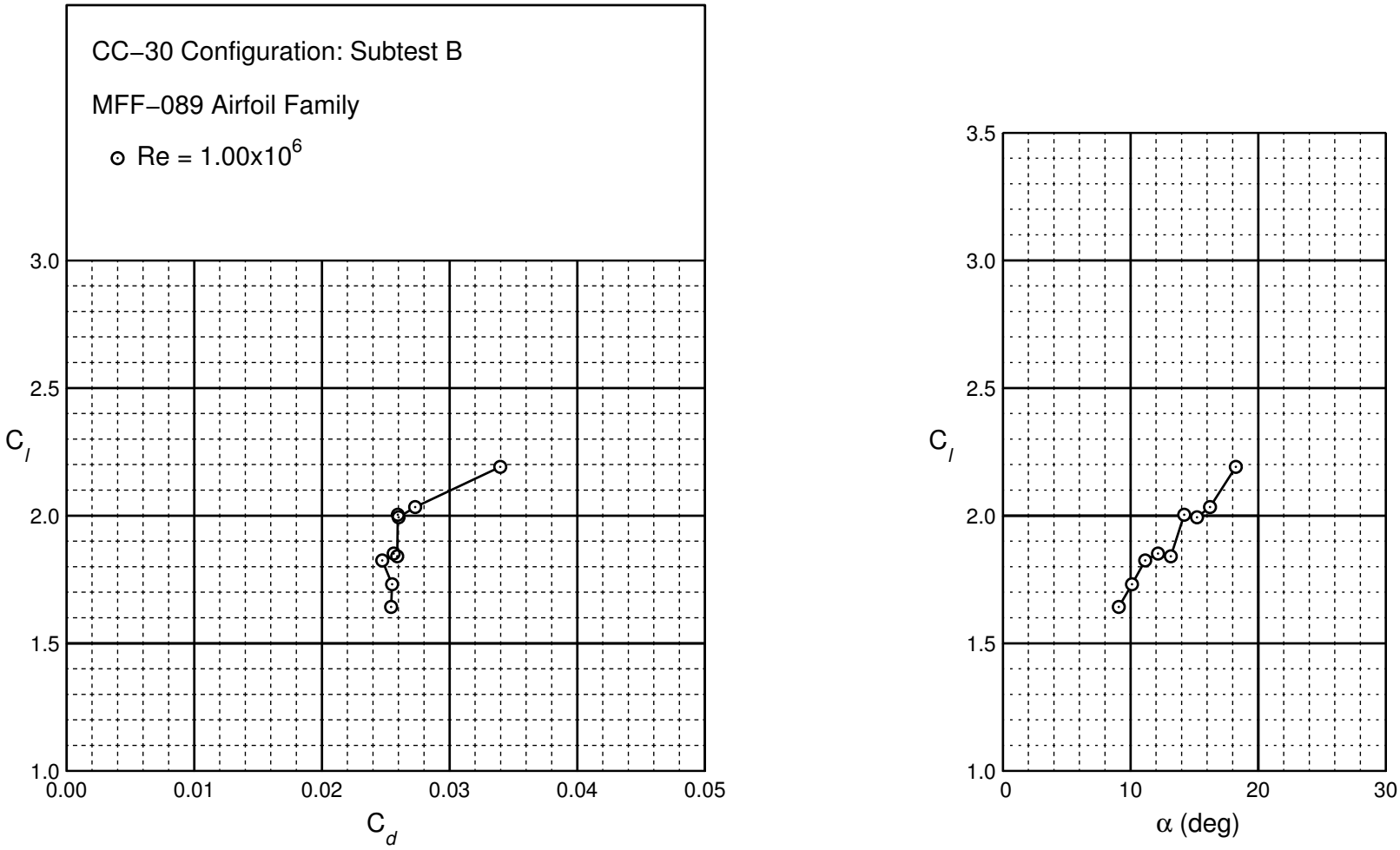

Figure B.37: CC-30 performance at $Re = 1.0 \times 10^6$.

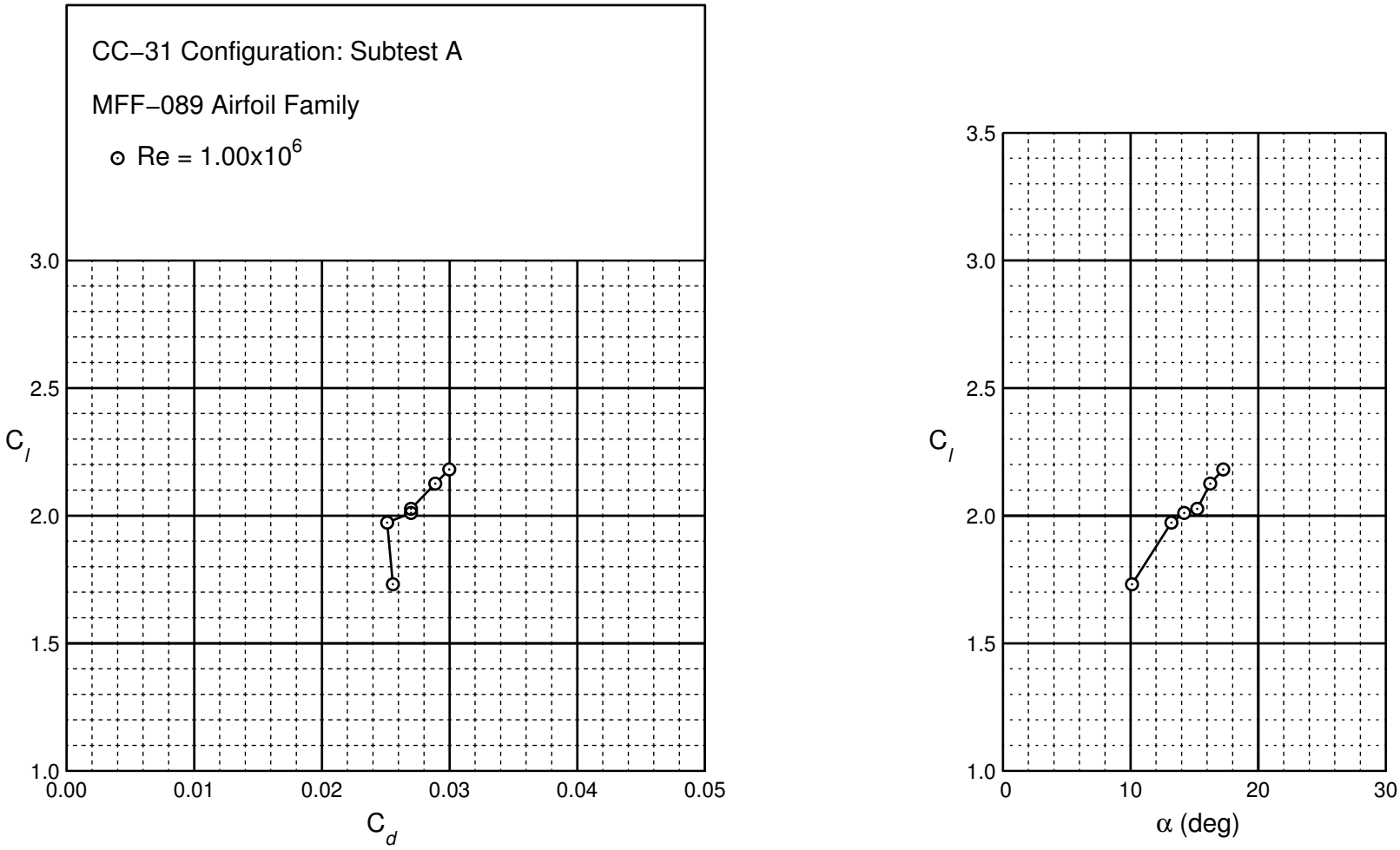

Figure B.38: CC-31 performance at $Re = 1.0 \times 10^6$.

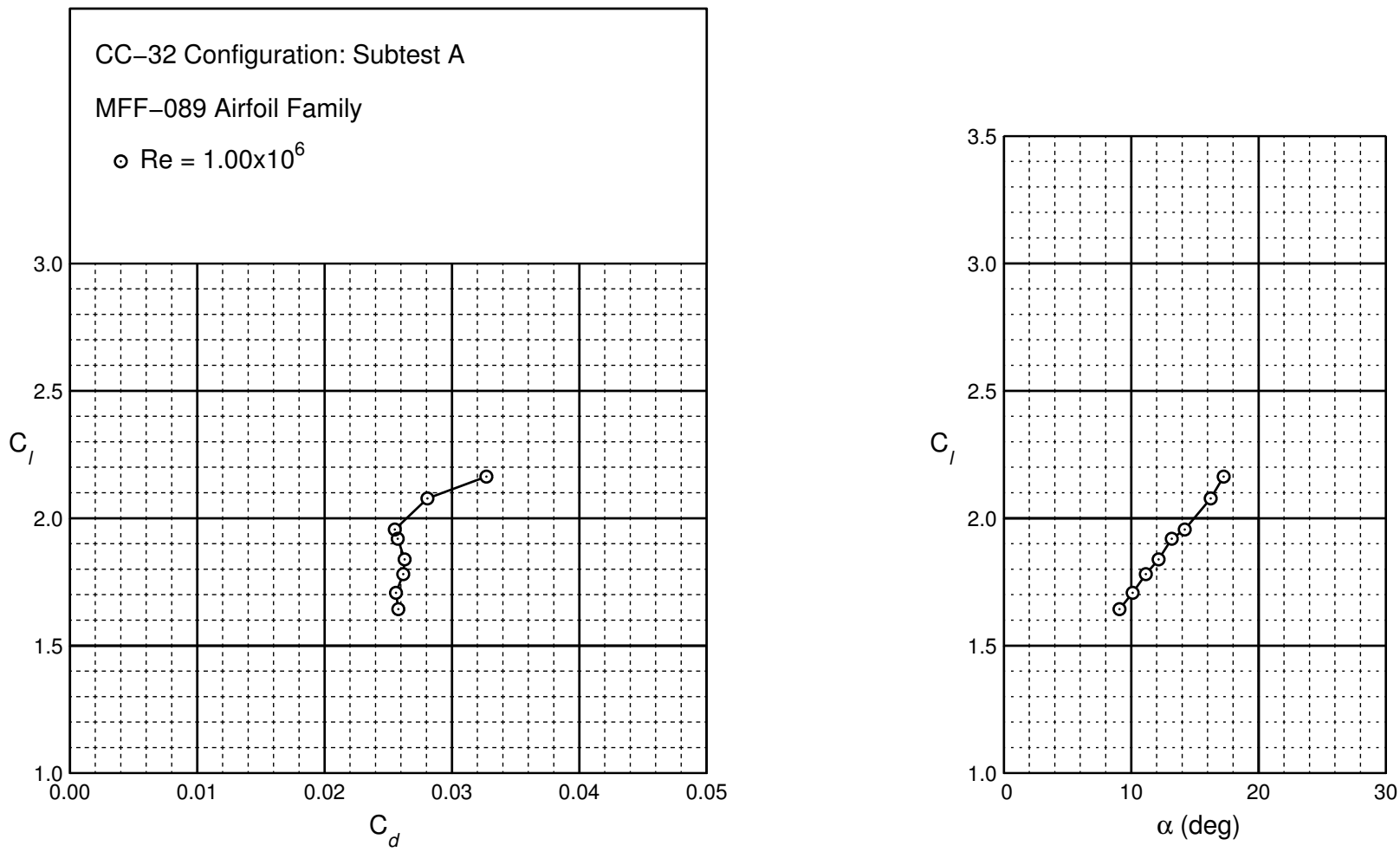

Figure B.39: CC-32 performance at $Re = 1.0 \times 10^6$.

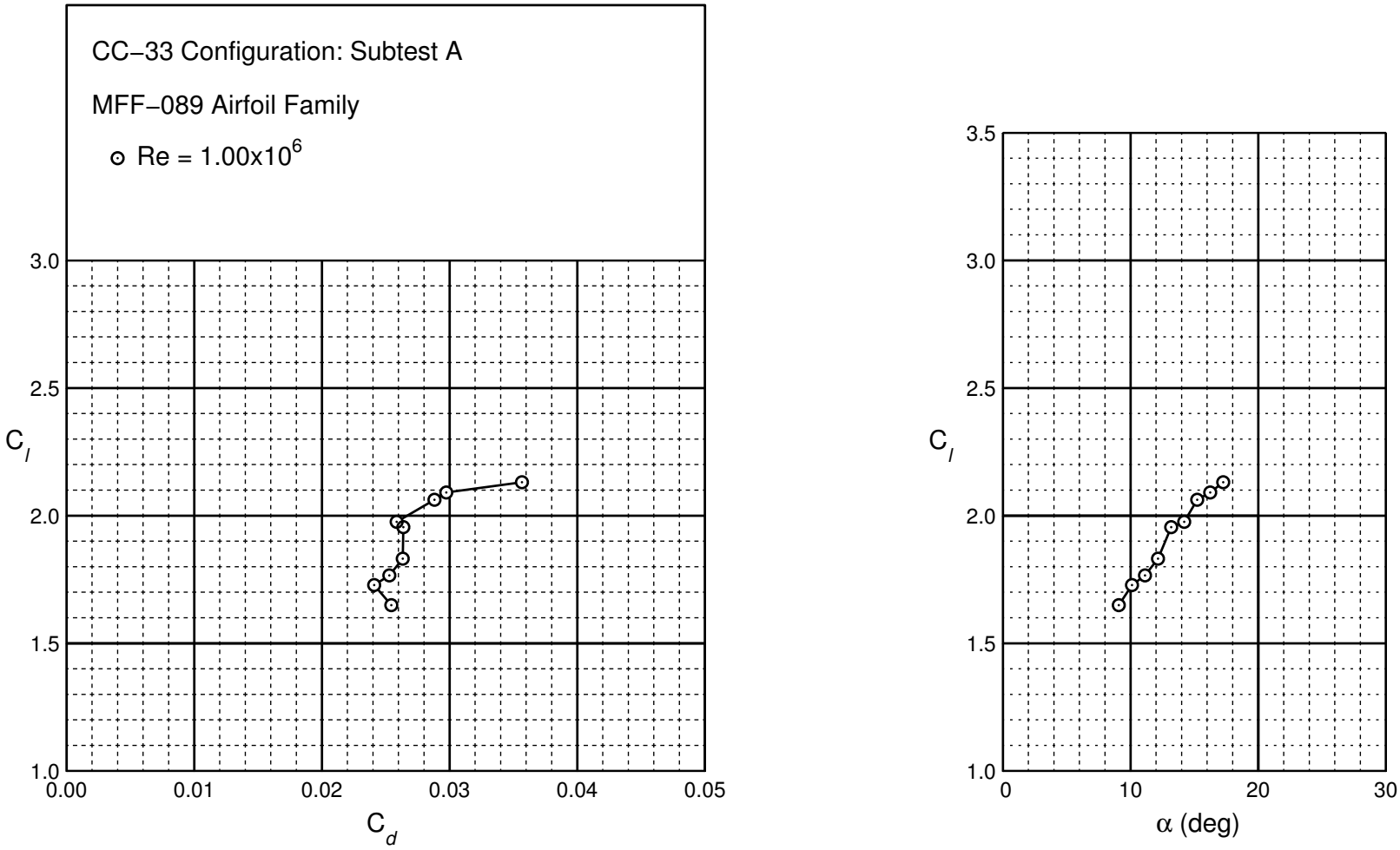

Figure B.40: CC-33 performance at $Re = 1.0 \times 10^6$.

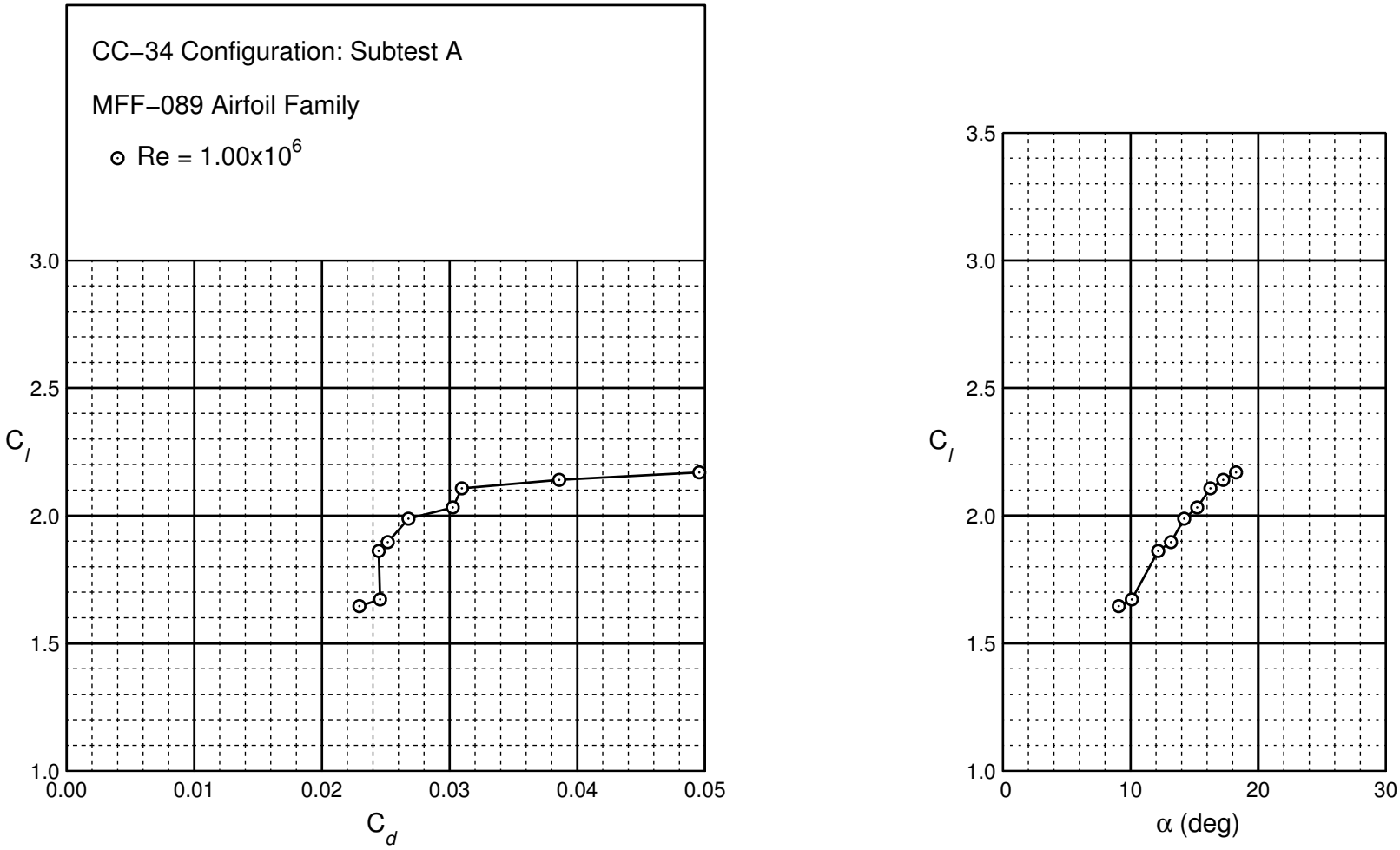

Figure B.41: CC-34 performance at $Re = 1.0 \times 10^6$.

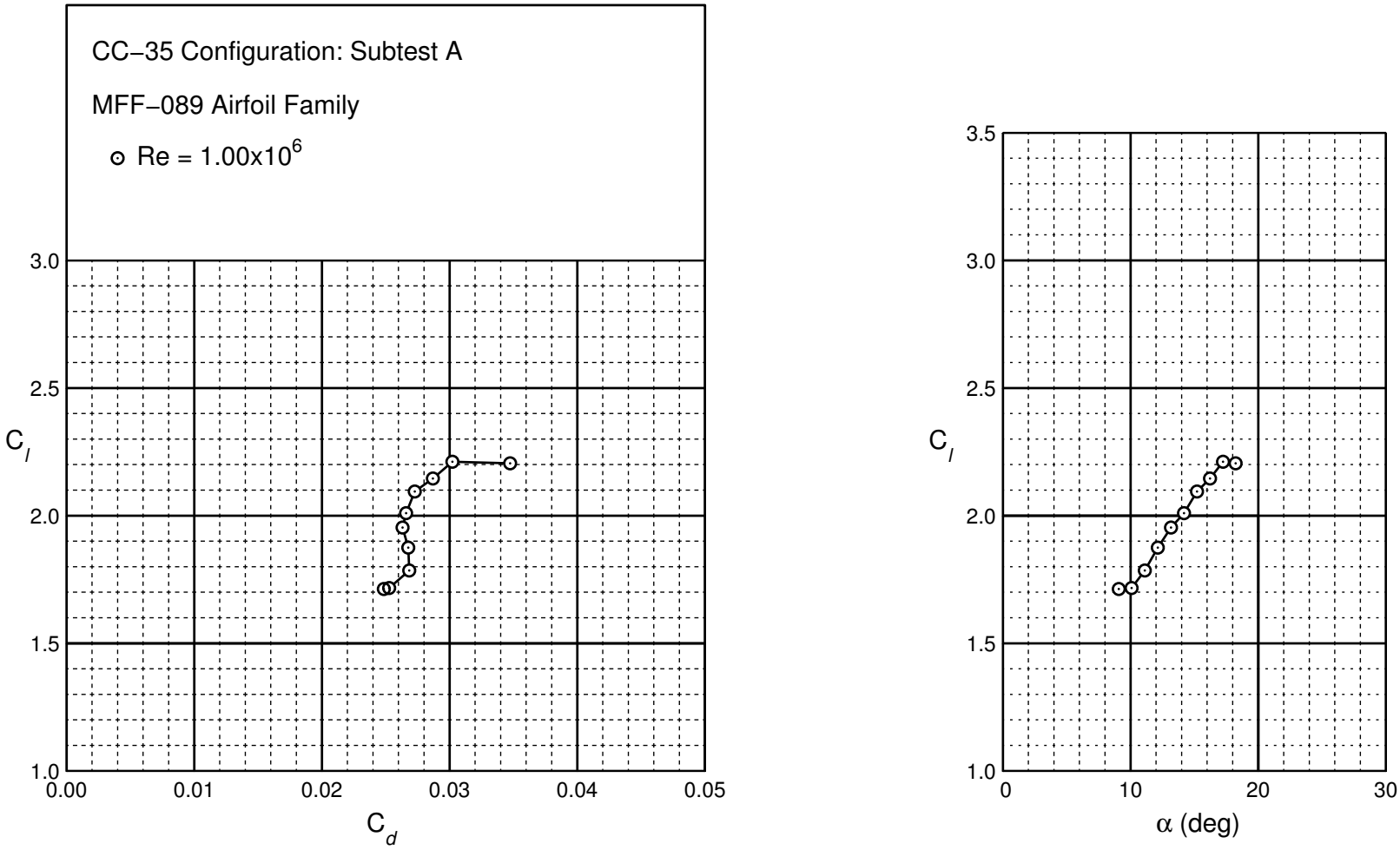

Figure B.42: CC-35 performance at $Re = 1.0 \times 10^6$.

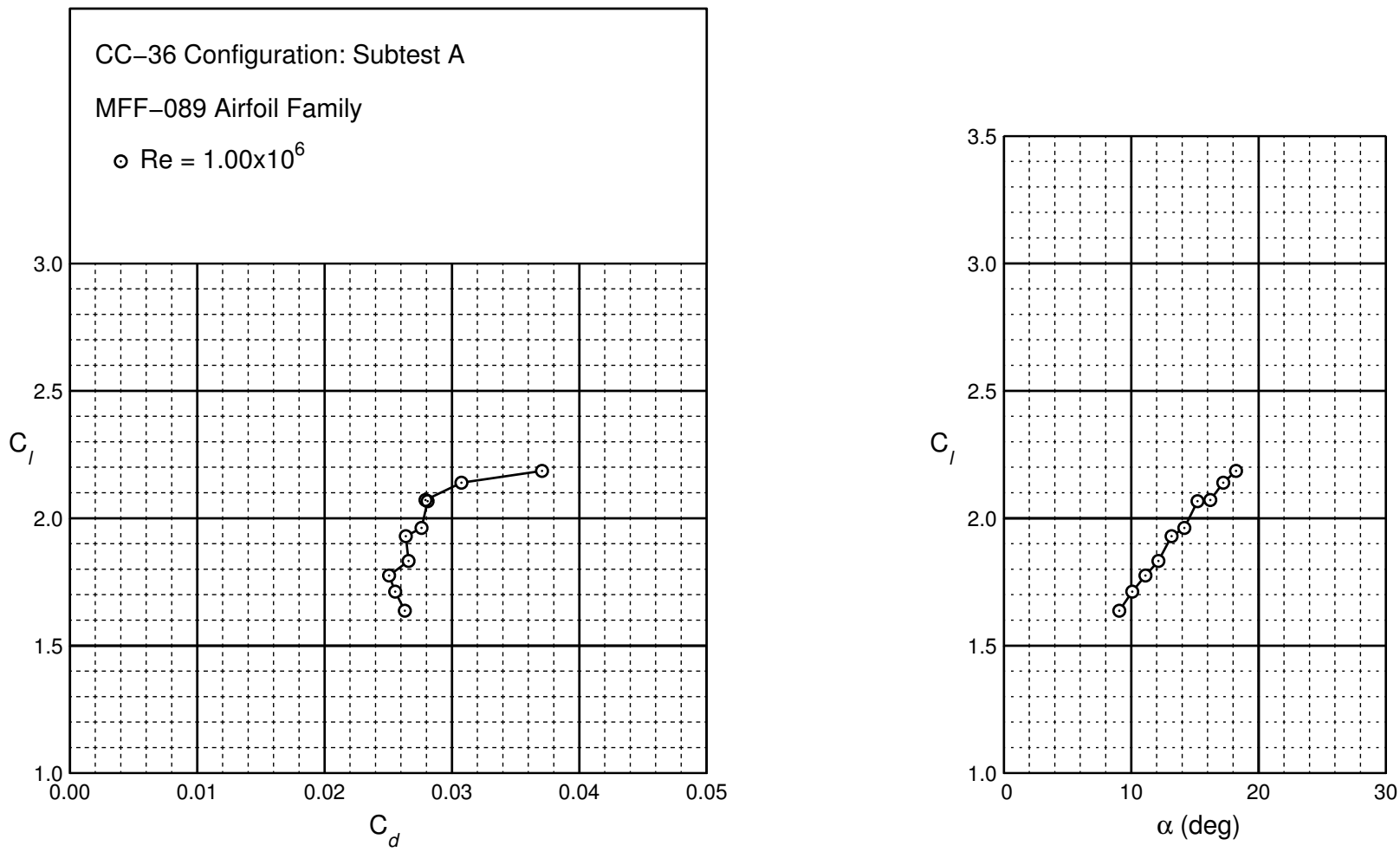

Figure B.43: CC-36 performance at $Re = 1.0 \times 10^6$.

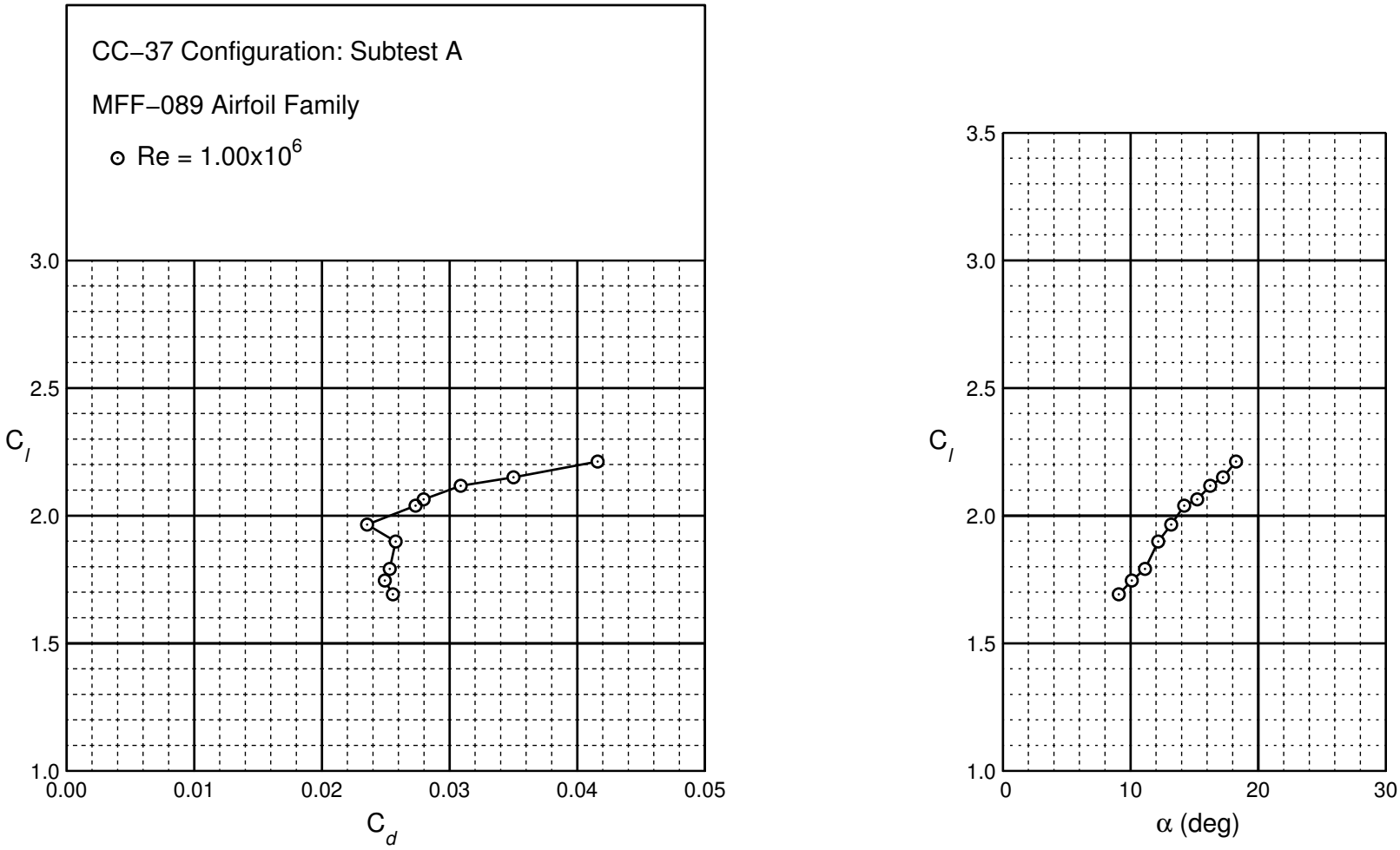

Figure B.44: CC-37 performance at $Re = 1.0 \times 10^6$.

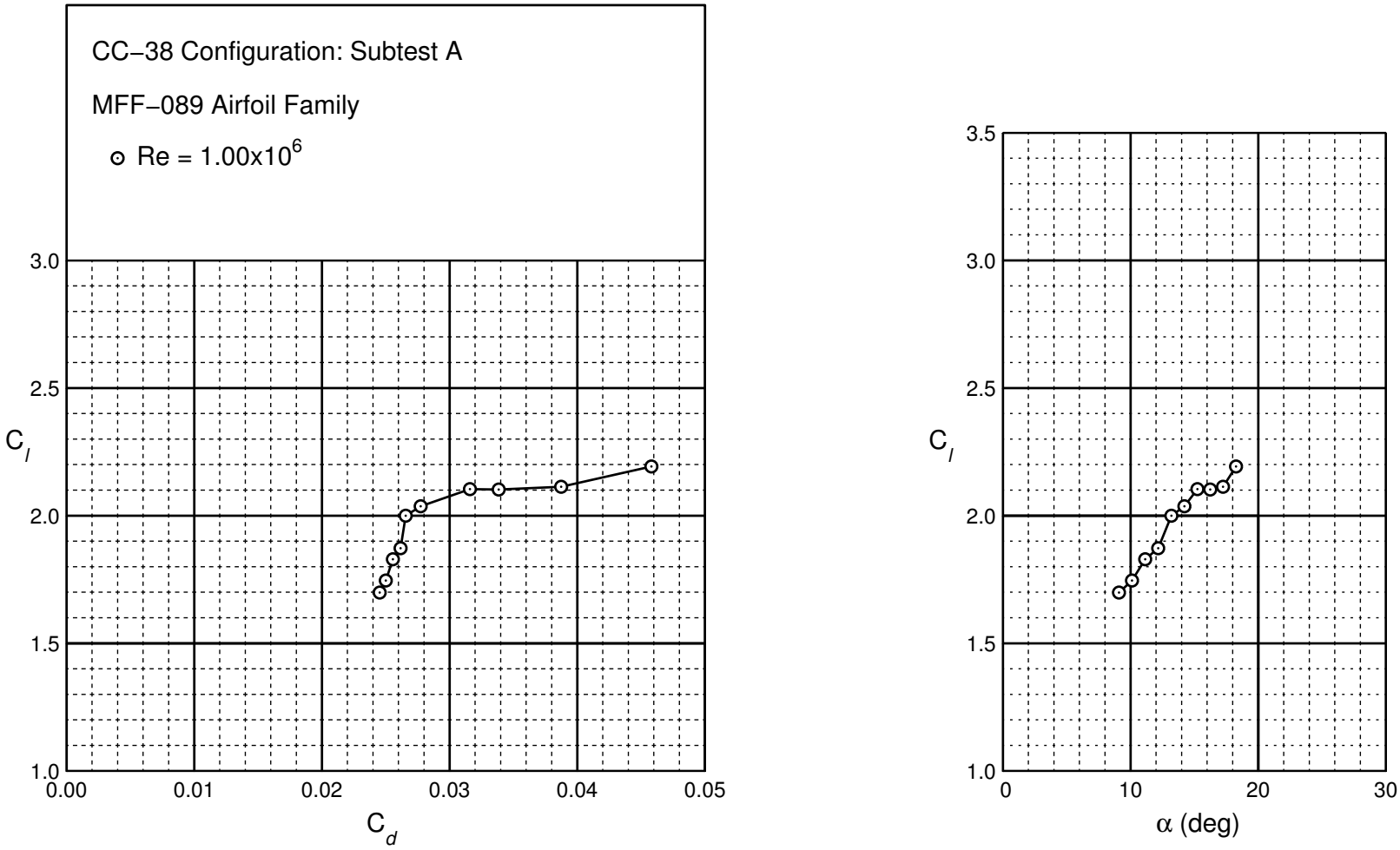

Figure B.45: CC-38 performance at $Re = 1.0 \times 10^6$.

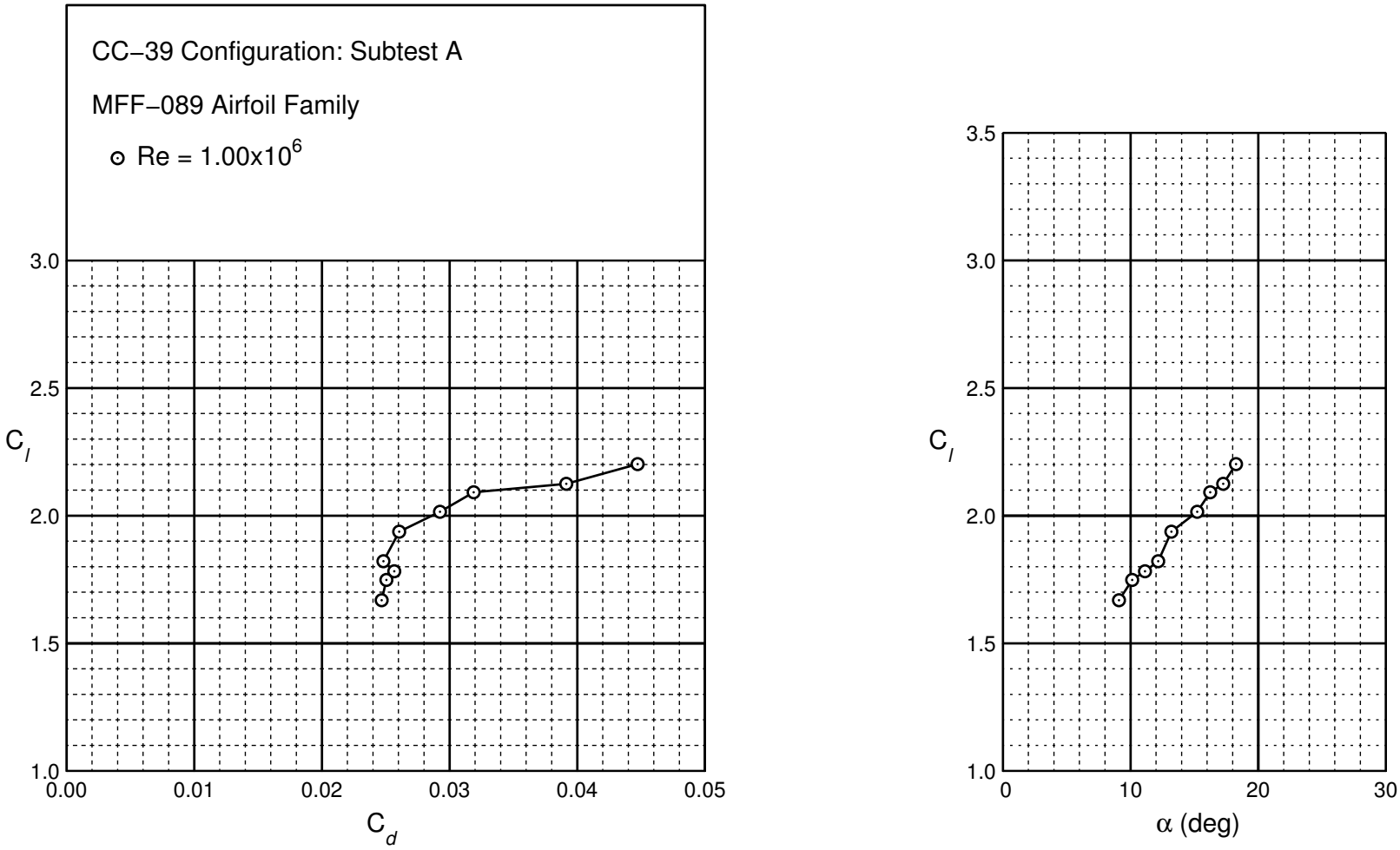

Figure B.46: CC-39 performance at $Re = 1.0 \times 10^6$.

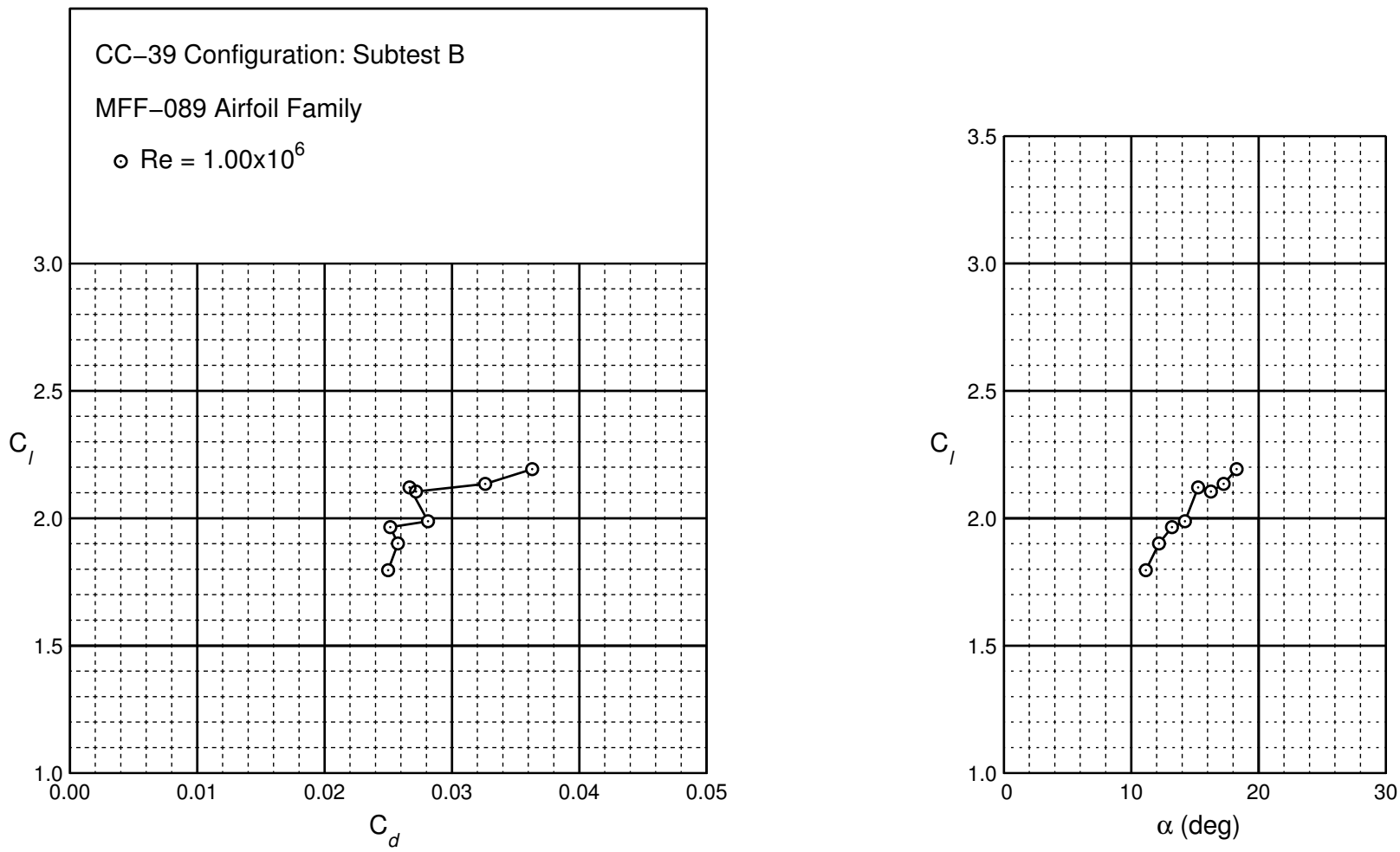

Figure B.47: CC-39 performance at $Re = 1.0 \times 10^6$.

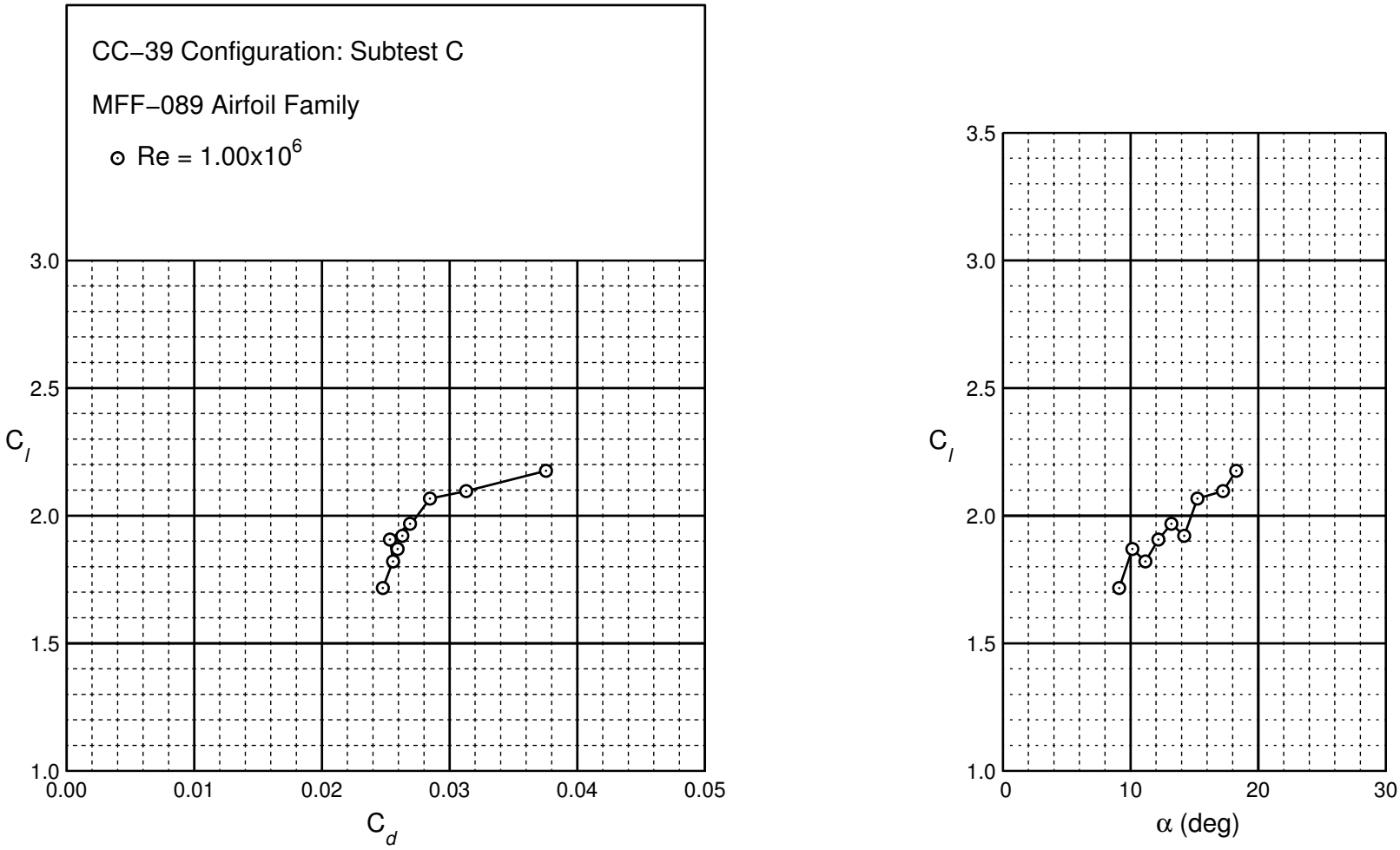

Figure B.48: CC-39 performance at $Re = 1.0 \times 10^6$.

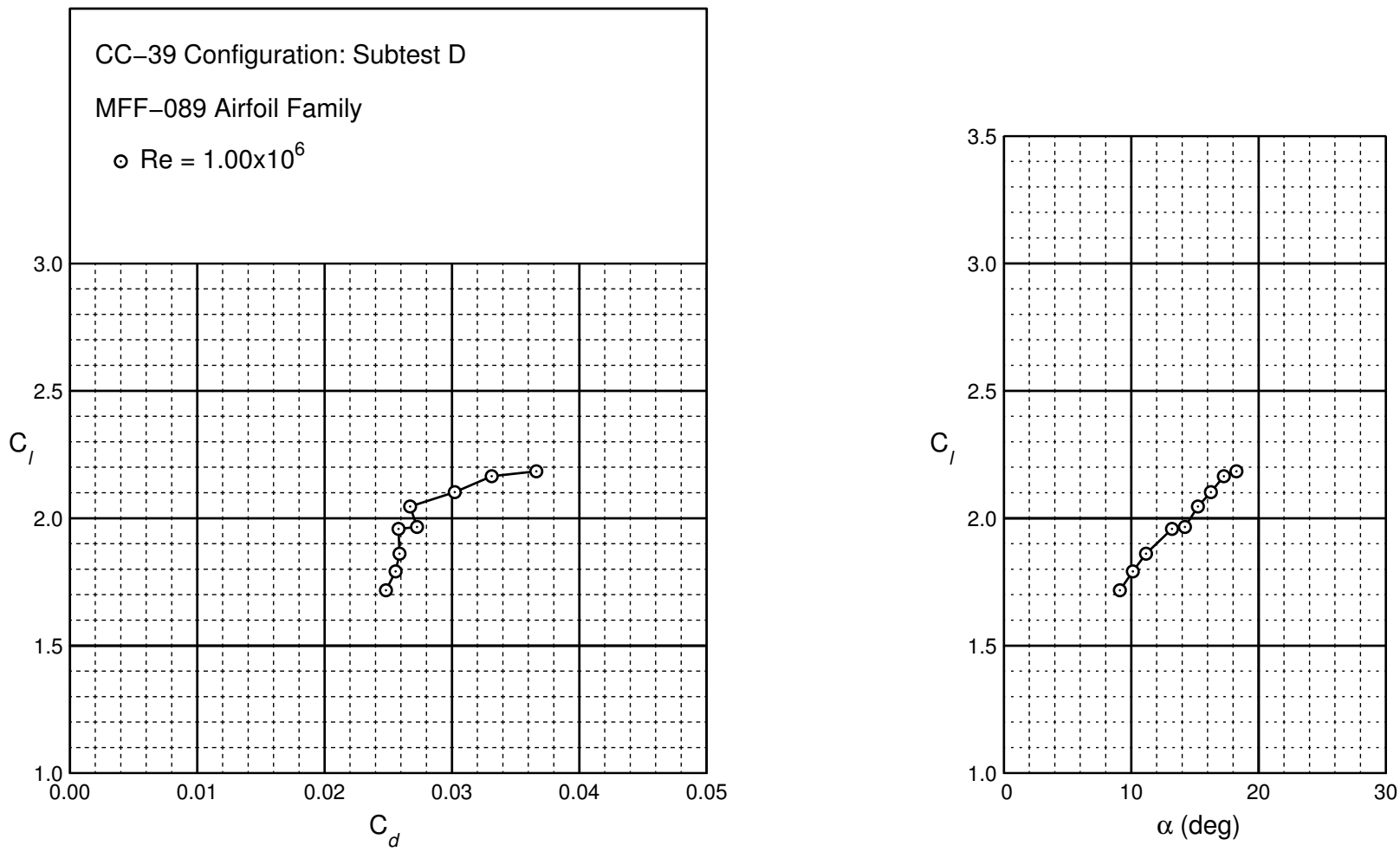

Figure B.49: CC-39 performance at $Re = 1.0 \times 10^6$.

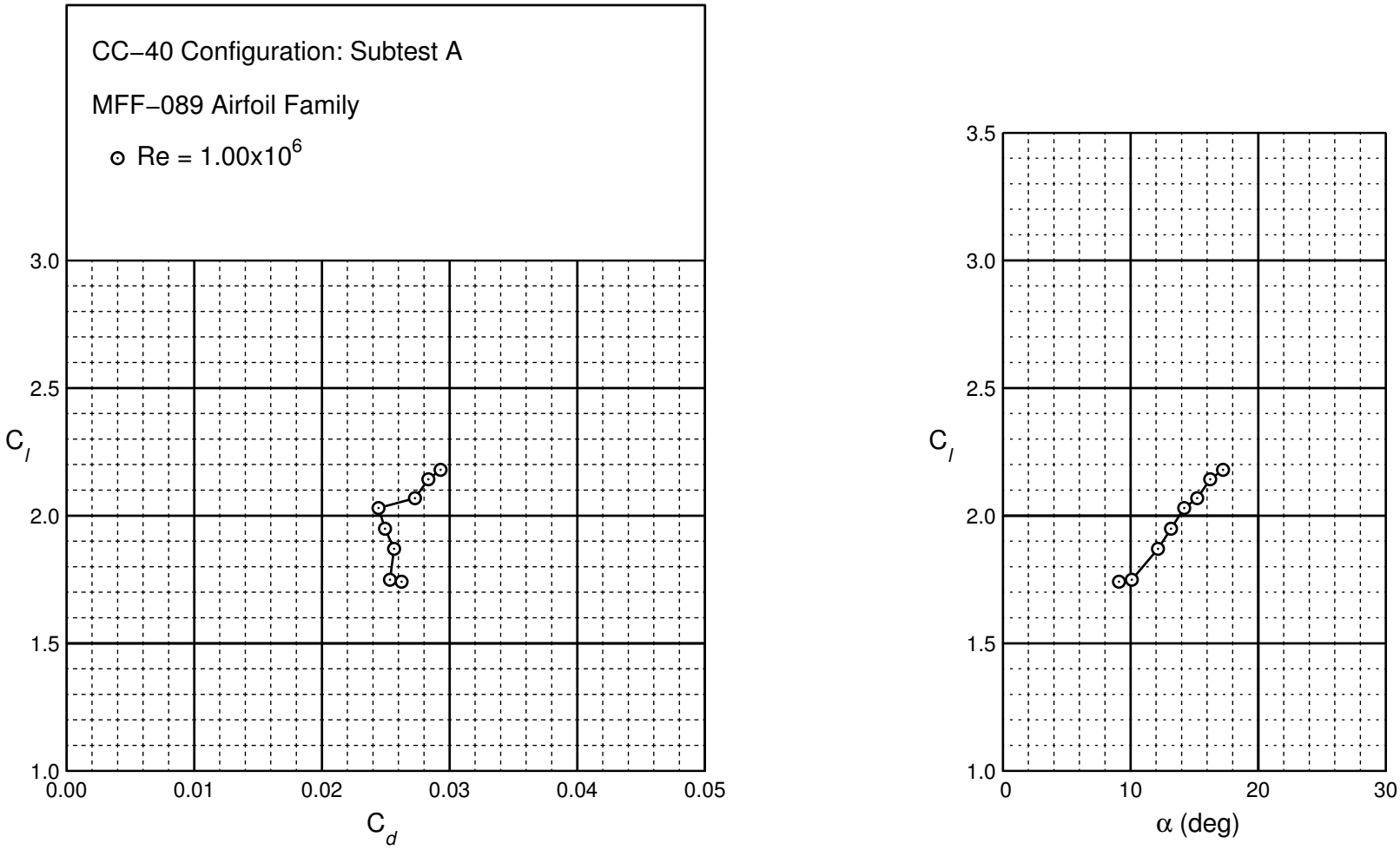

Figure B.50: CC-40 performance at $Re = 1.0 \times 10^6$.

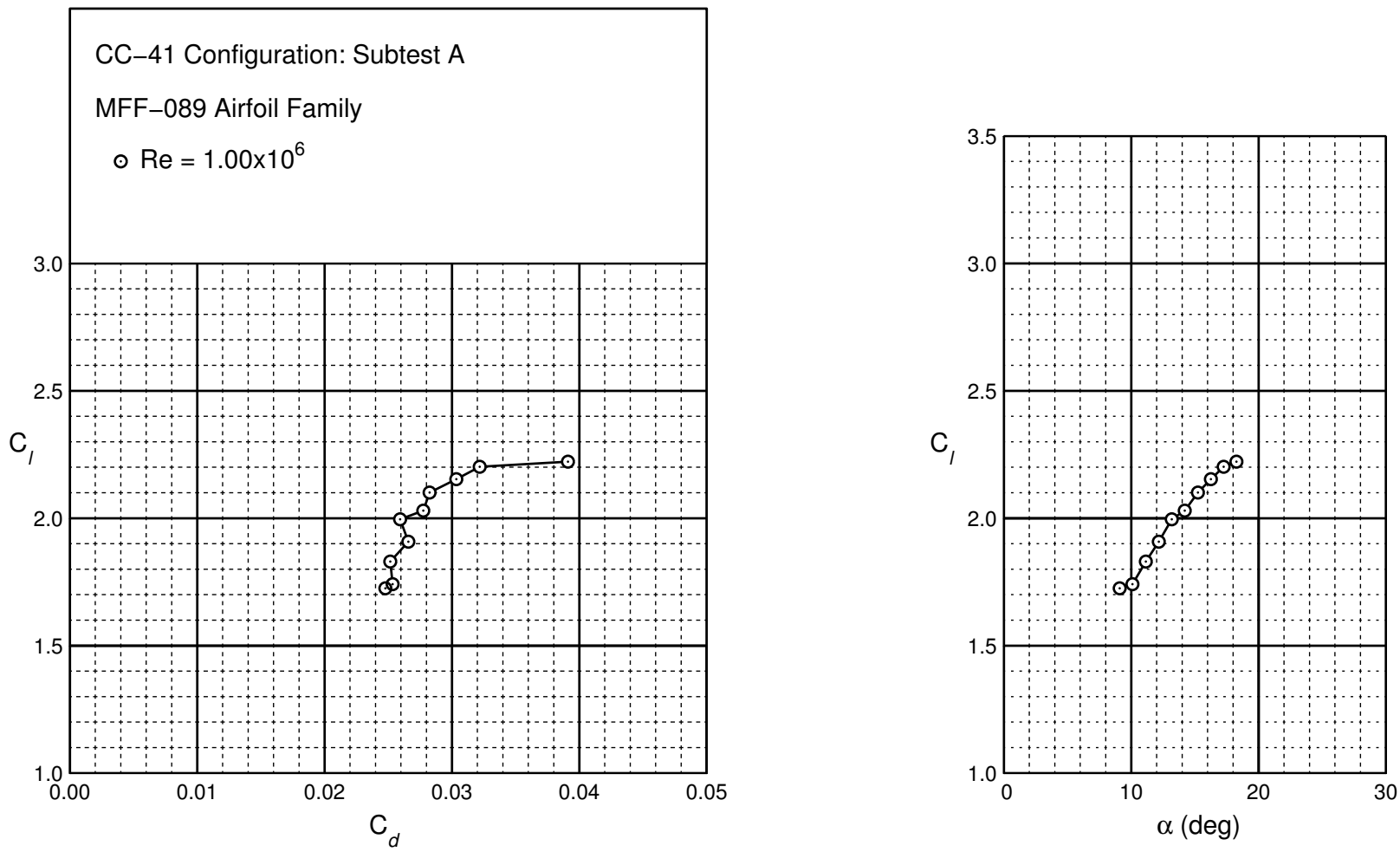

Figure B.51: CC-41 performance at $Re = 1.0 \times 10^6$.

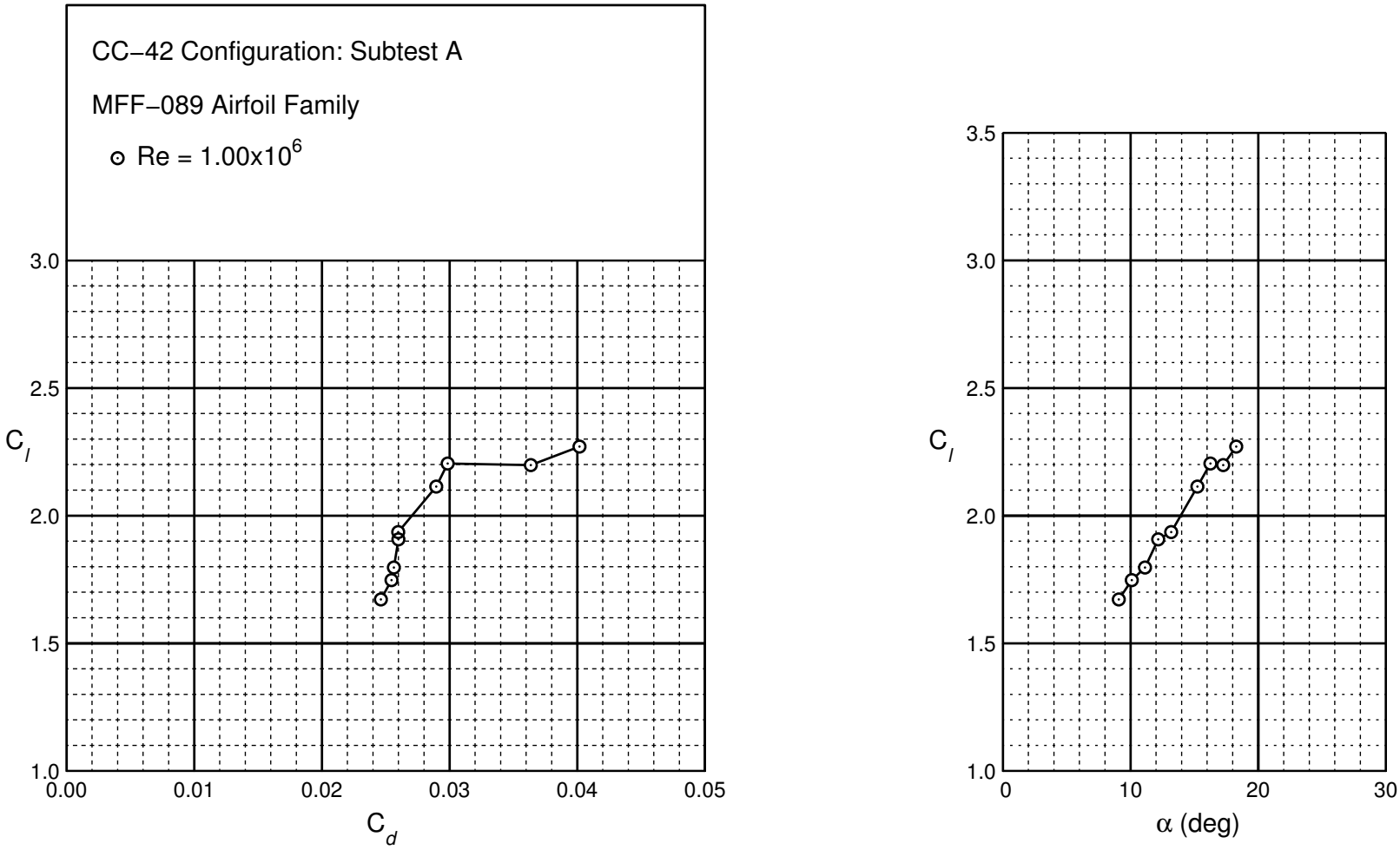

Figure B.52: CC-42 performance at $Re = 1.0 \times 10^6$.

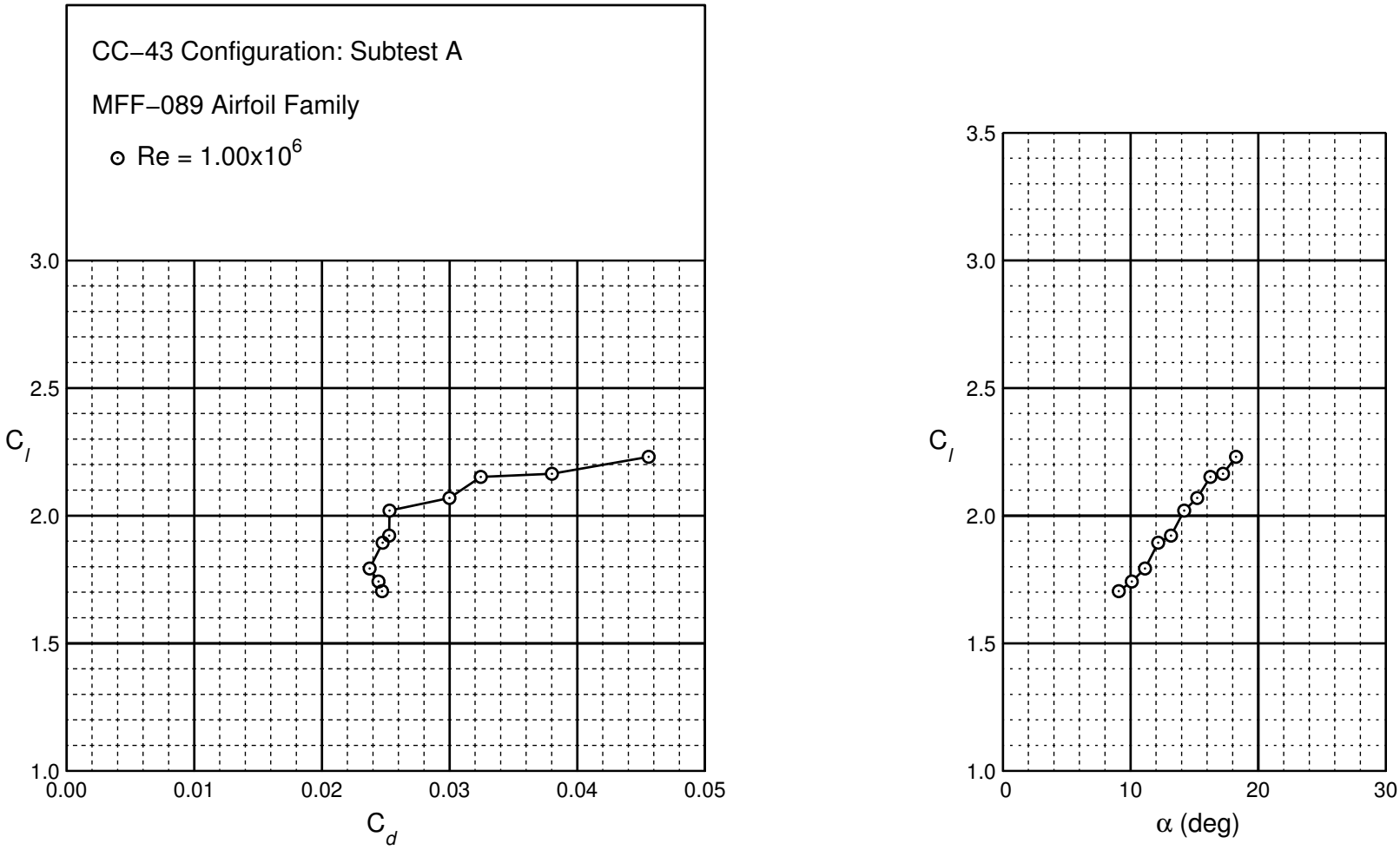

Figure B.53: CC-43 performance at $Re = 1.0 \times 10^6$.

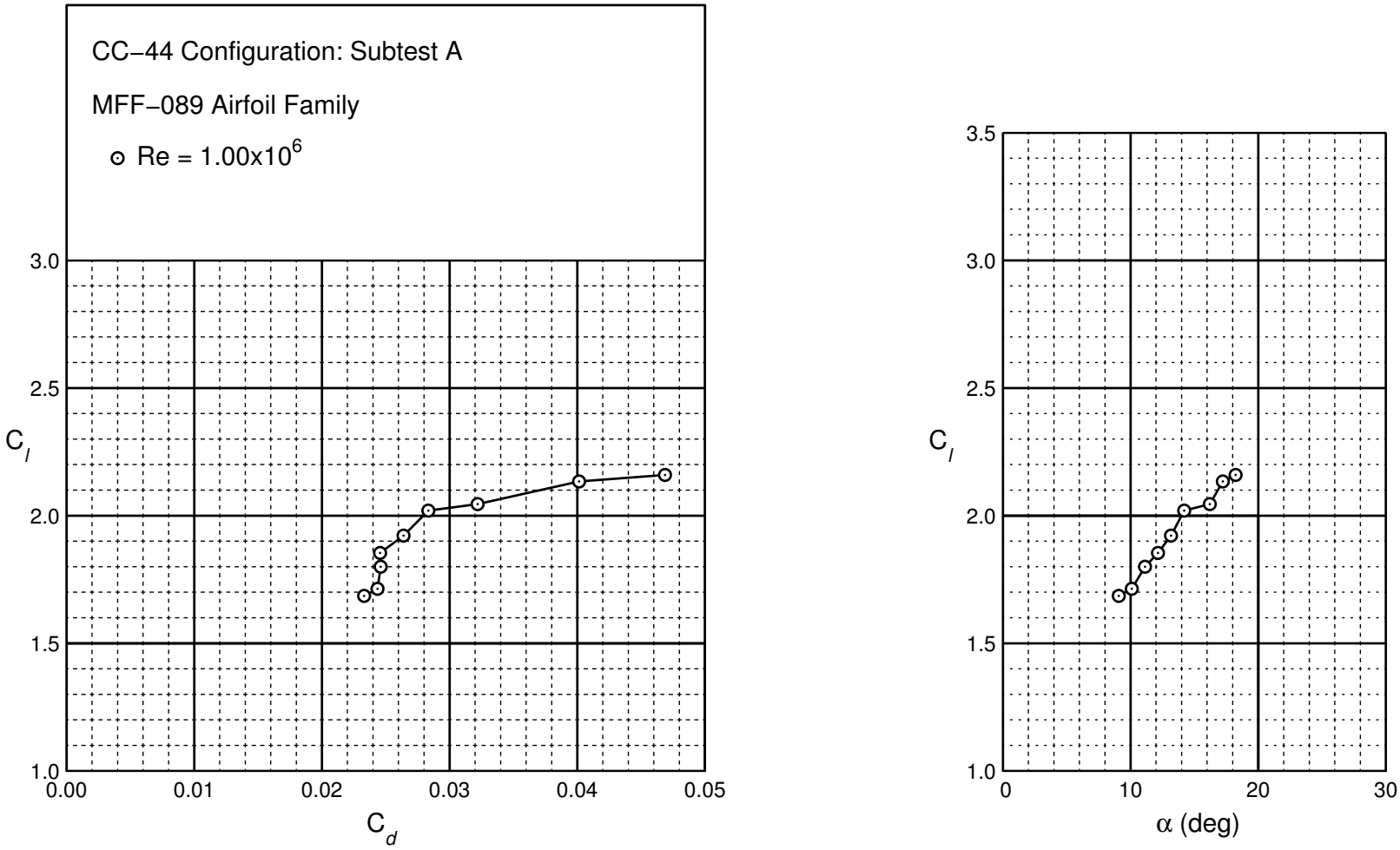

Figure B.54: CC-44 performance at $Re = 1.0 \times 10^6$.

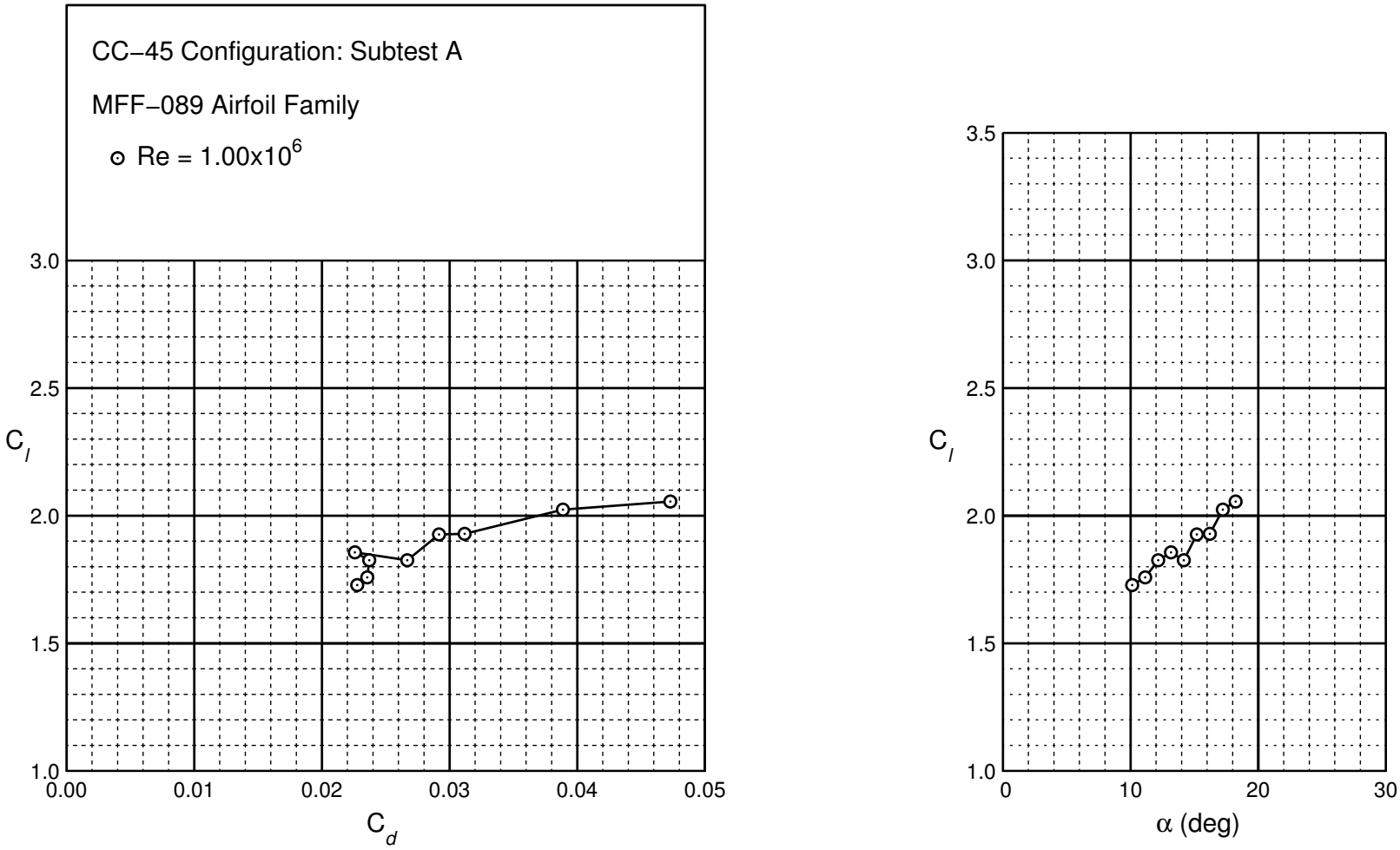

Figure B.55: CC-45 performance at $Re = 1.0 \times 10^6$.

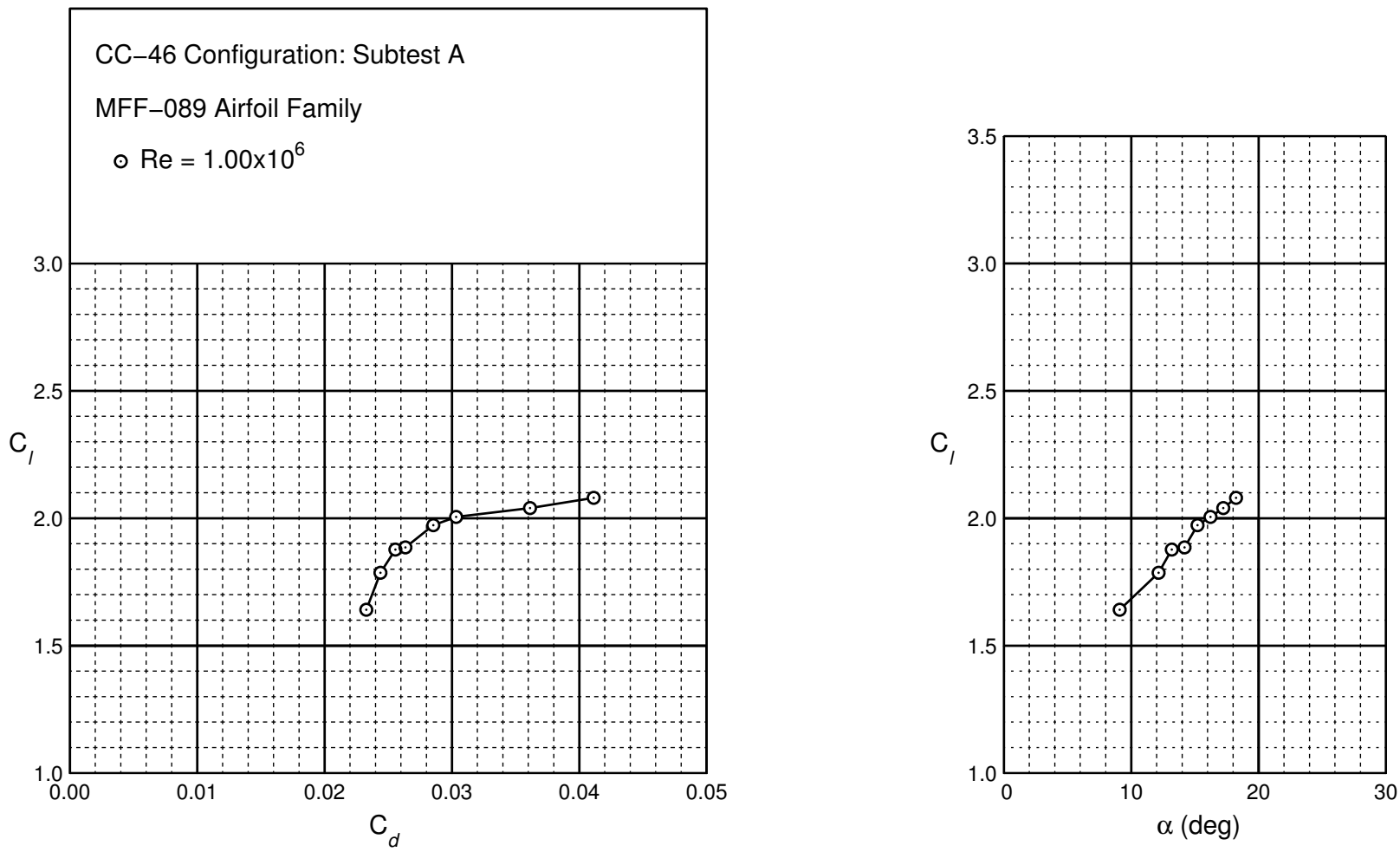

Figure B.56: CC-46 performance at $Re = 1.0 \times 10^6$.

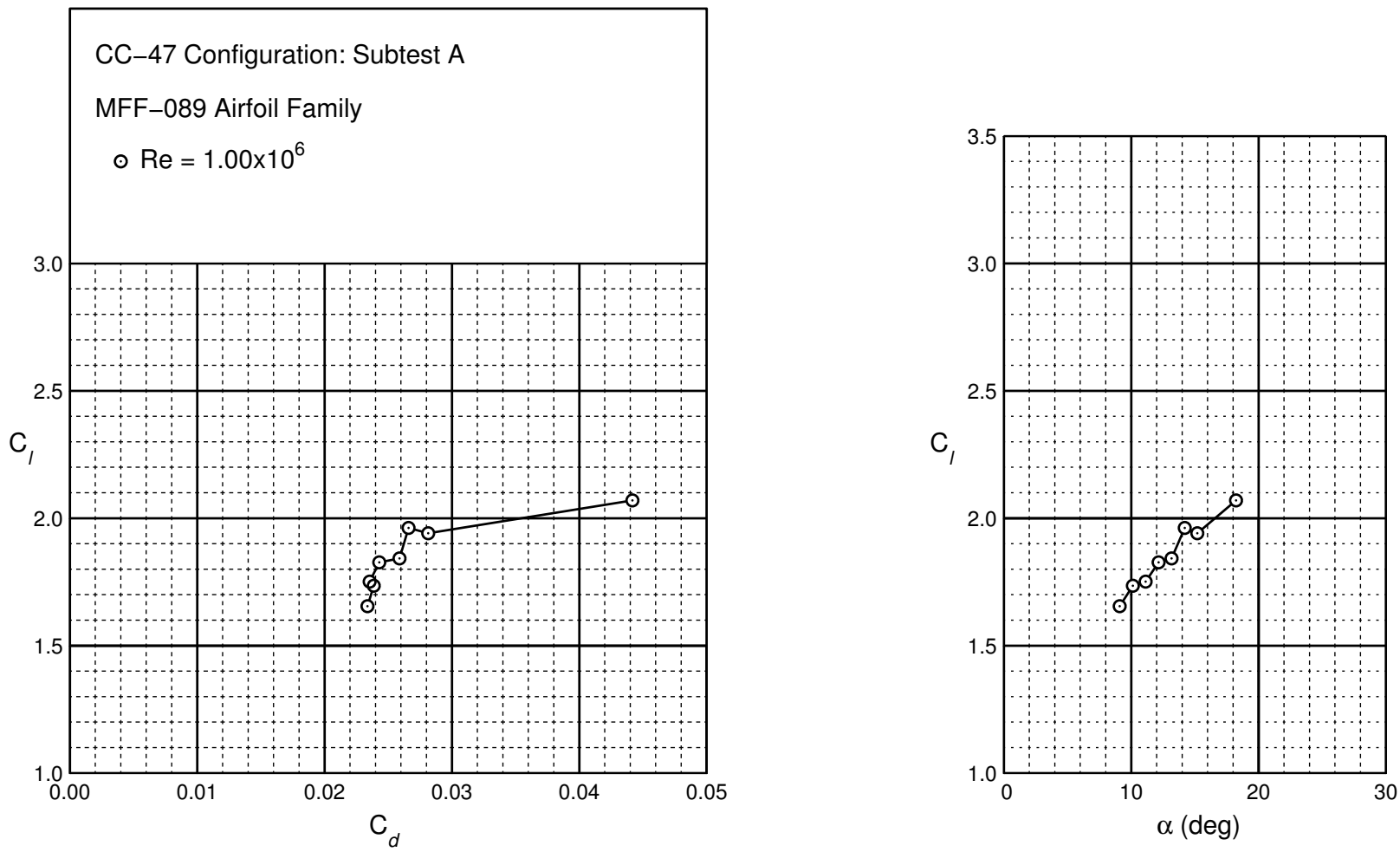

Figure B.57: CC-47 performance at $Re = 1.0 \times 10^6$.

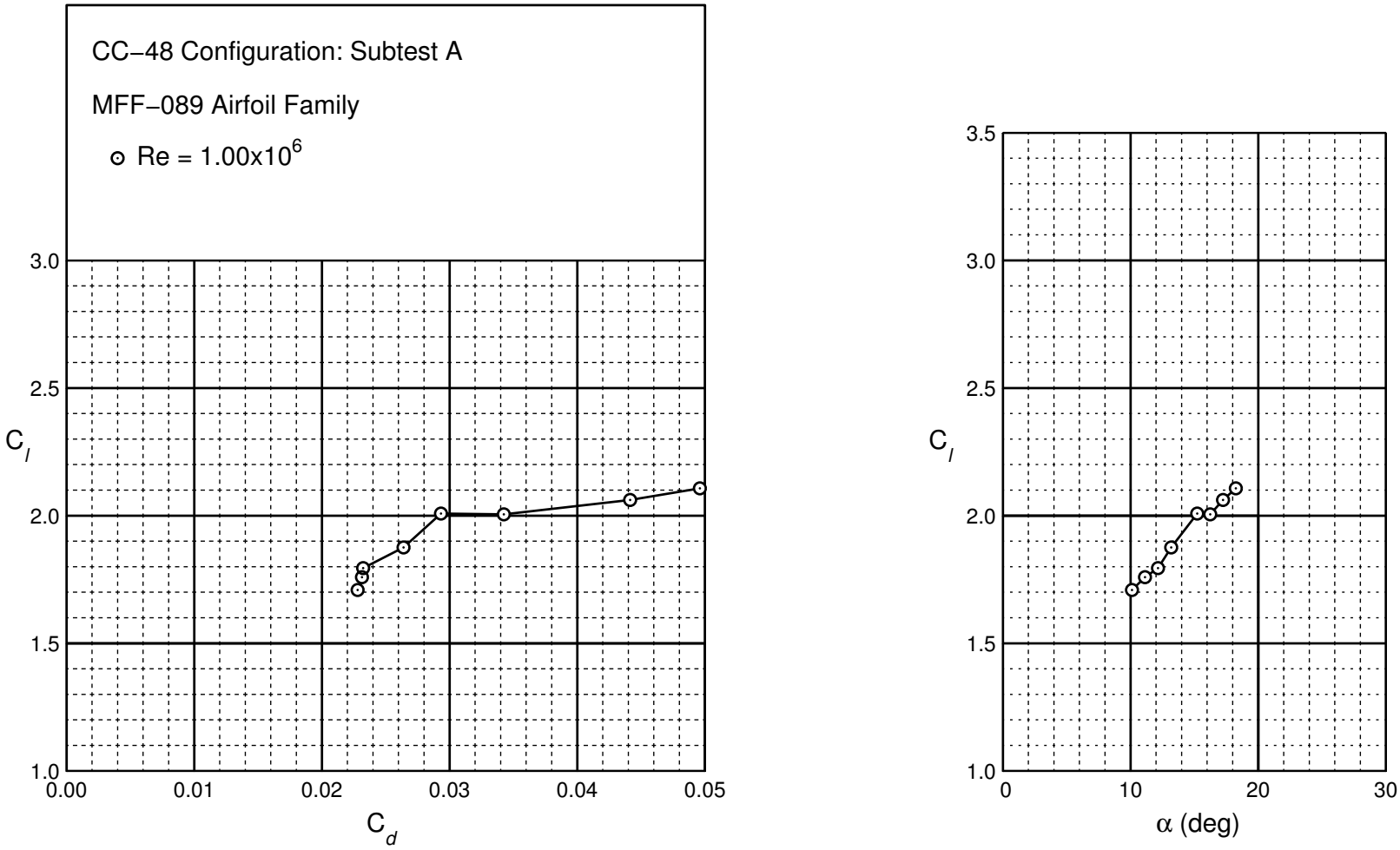

Figure B.58: CC-48 performance at $Re = 1.0 \times 10^6$.

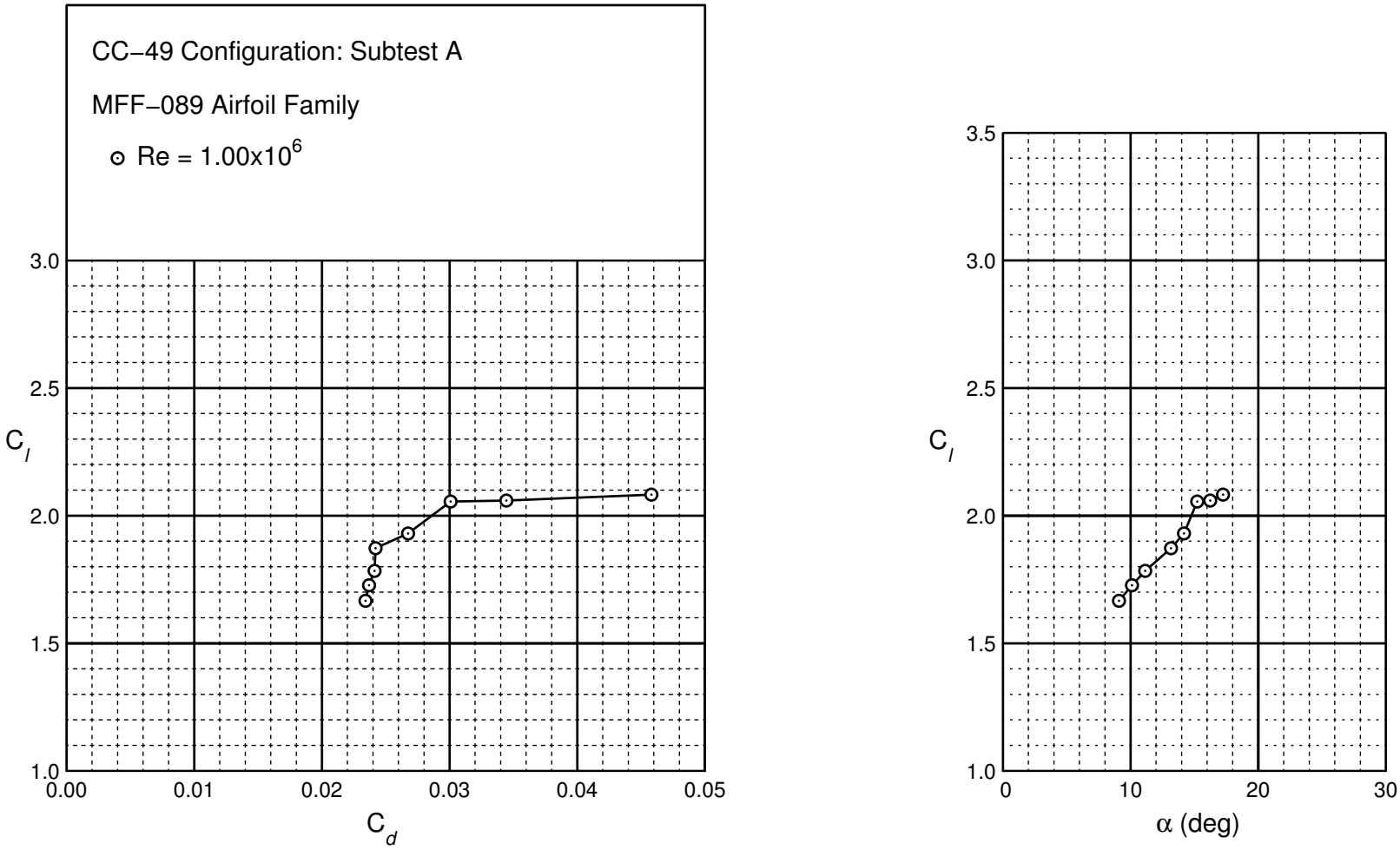

Figure B.59: CC-49 performance at $Re = 1.0 \times 10^6$.

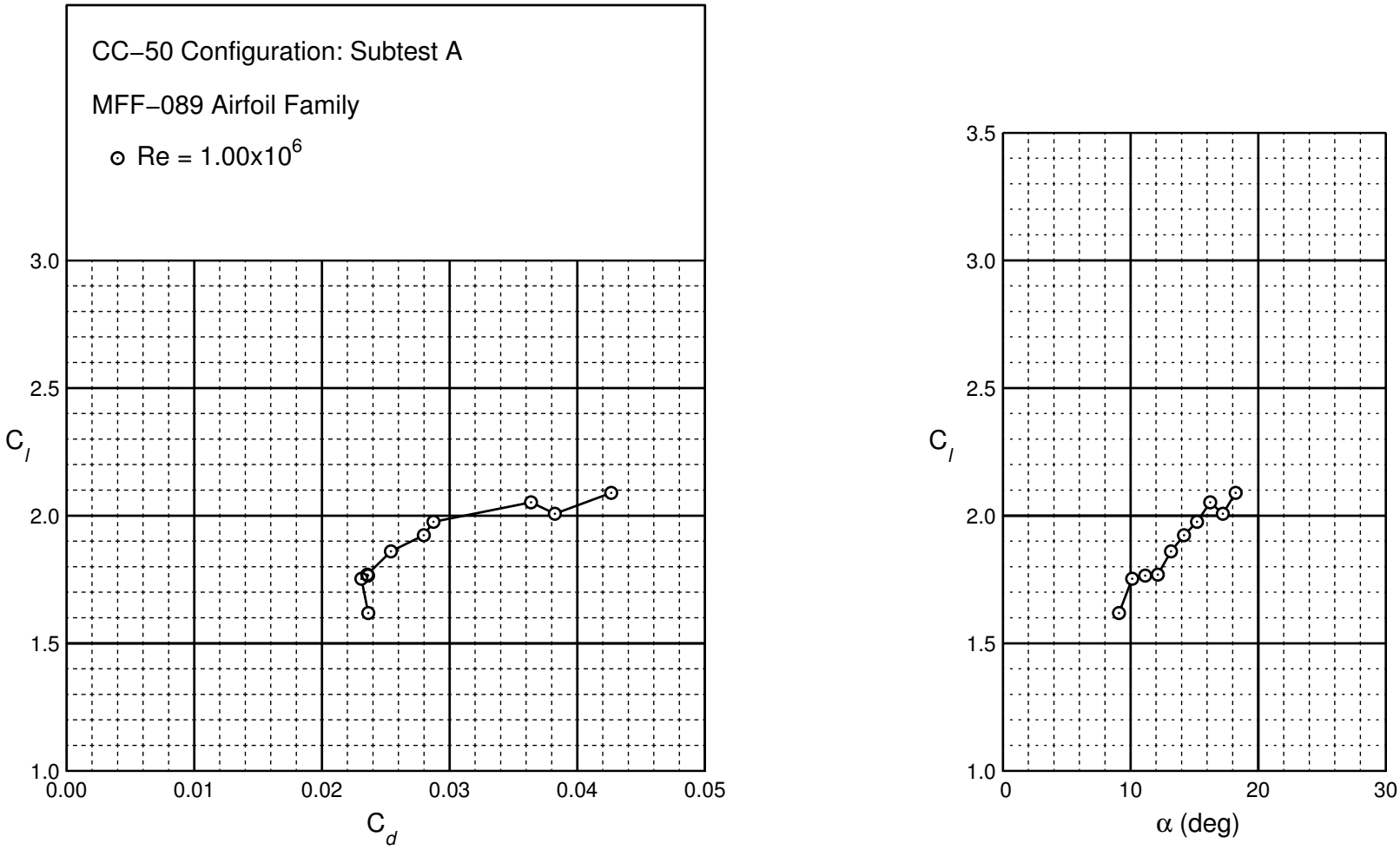

Figure B.60: CC-50 performance at $Re = 1.0 \times 10^6$.

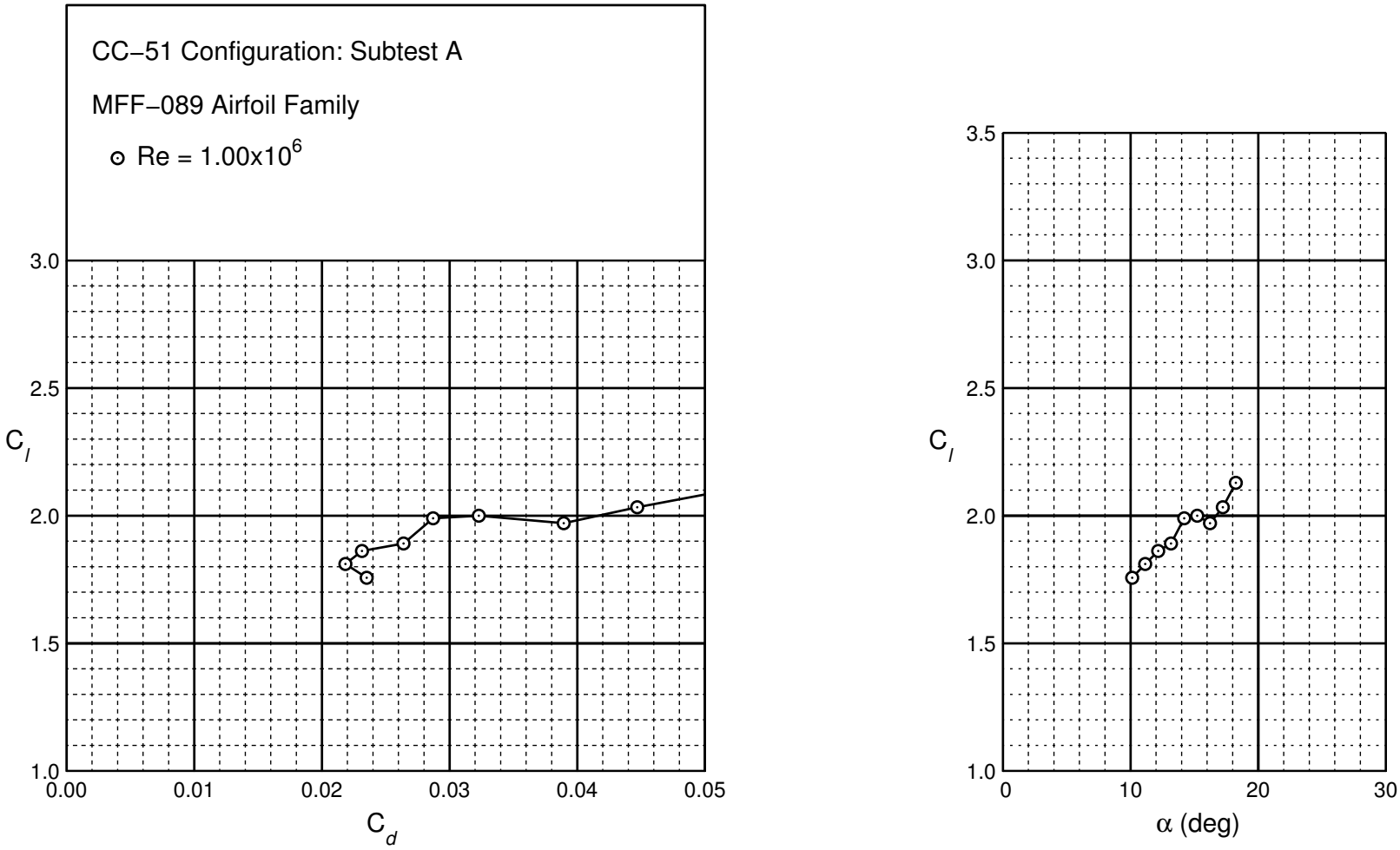

Figure B.61: CC-51 performance at $Re = 1.0 \times 10^6$.

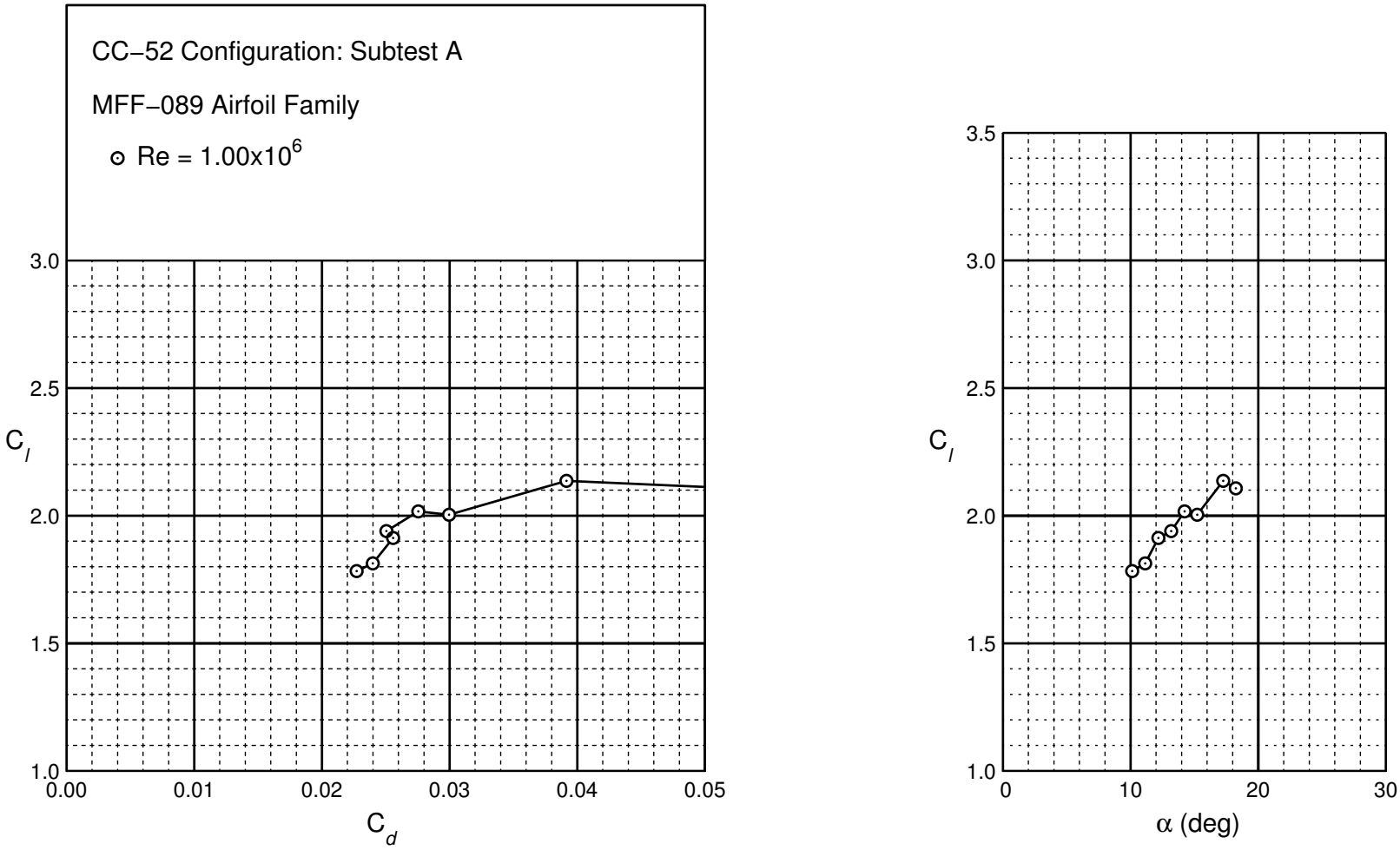

Figure B.62: CC-52 performance at $Re = 1.0 \times 10^6$.

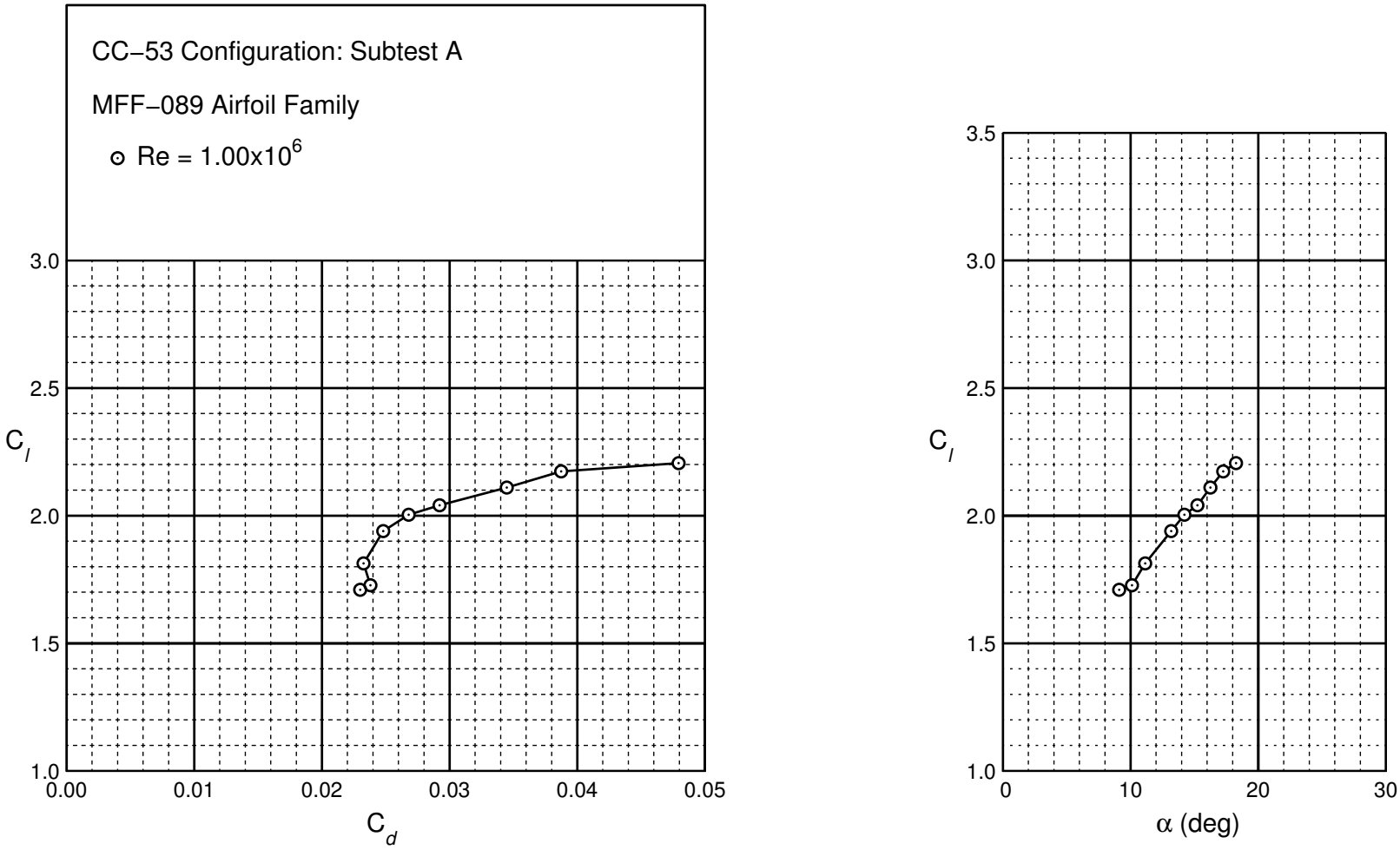

Figure B.63: CC-53 performance at $Re = 1.0 \times 10^6$.

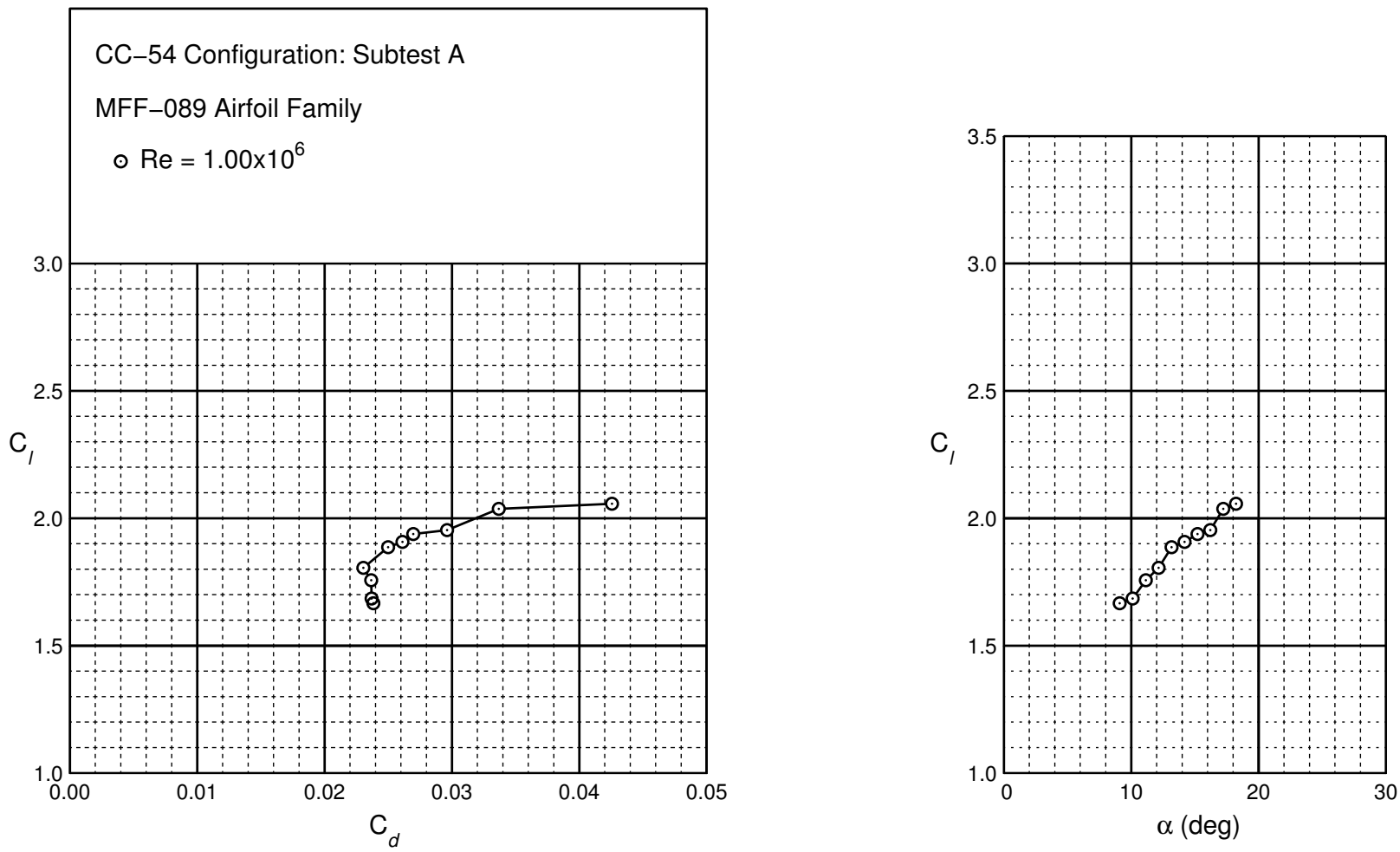

Figure B.64: CC-54 performance at $Re = 1.0 \times 10^6$.

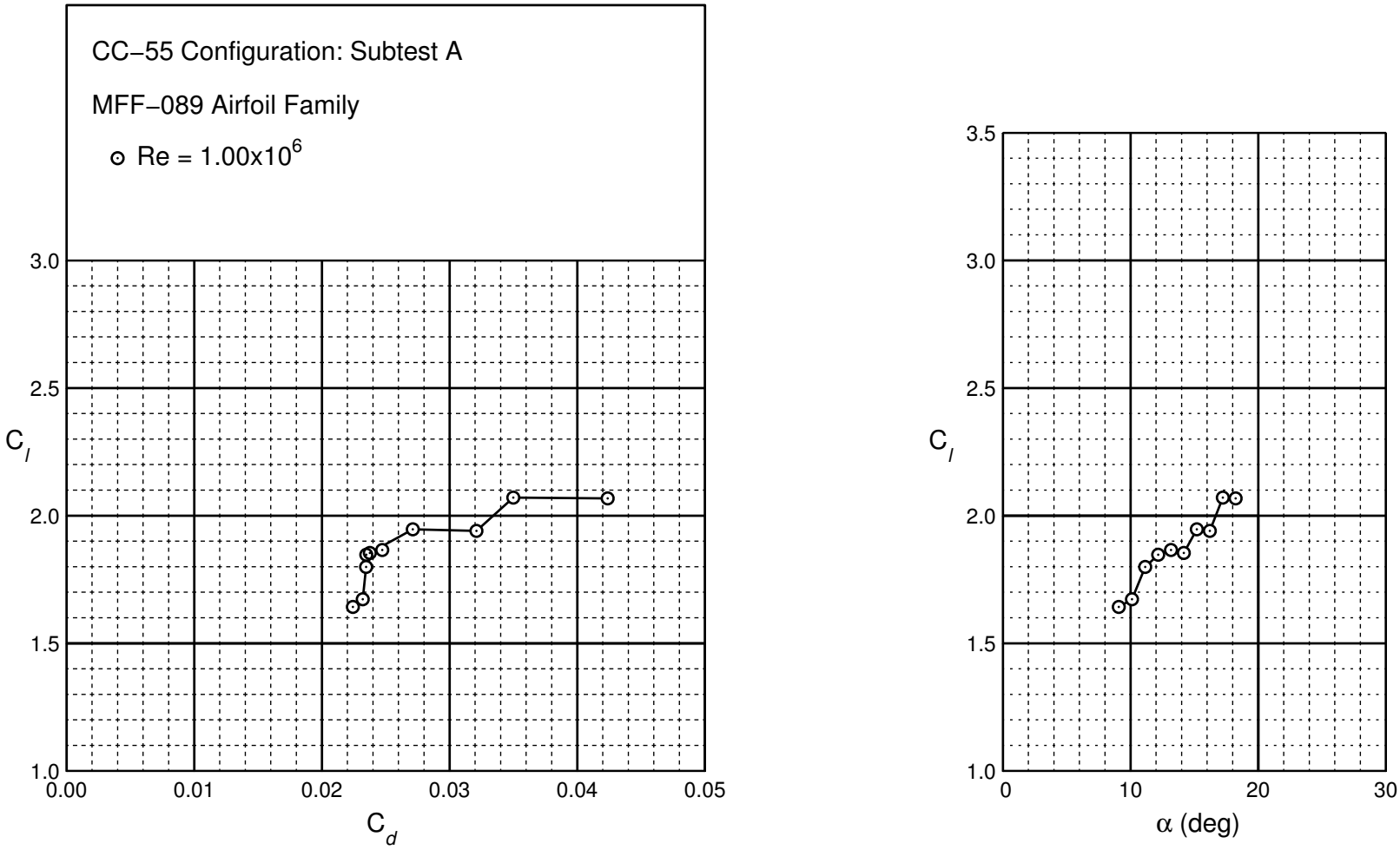

Figure B.65: CC-55 performance at $Re = 1.0 \times 10^6$.

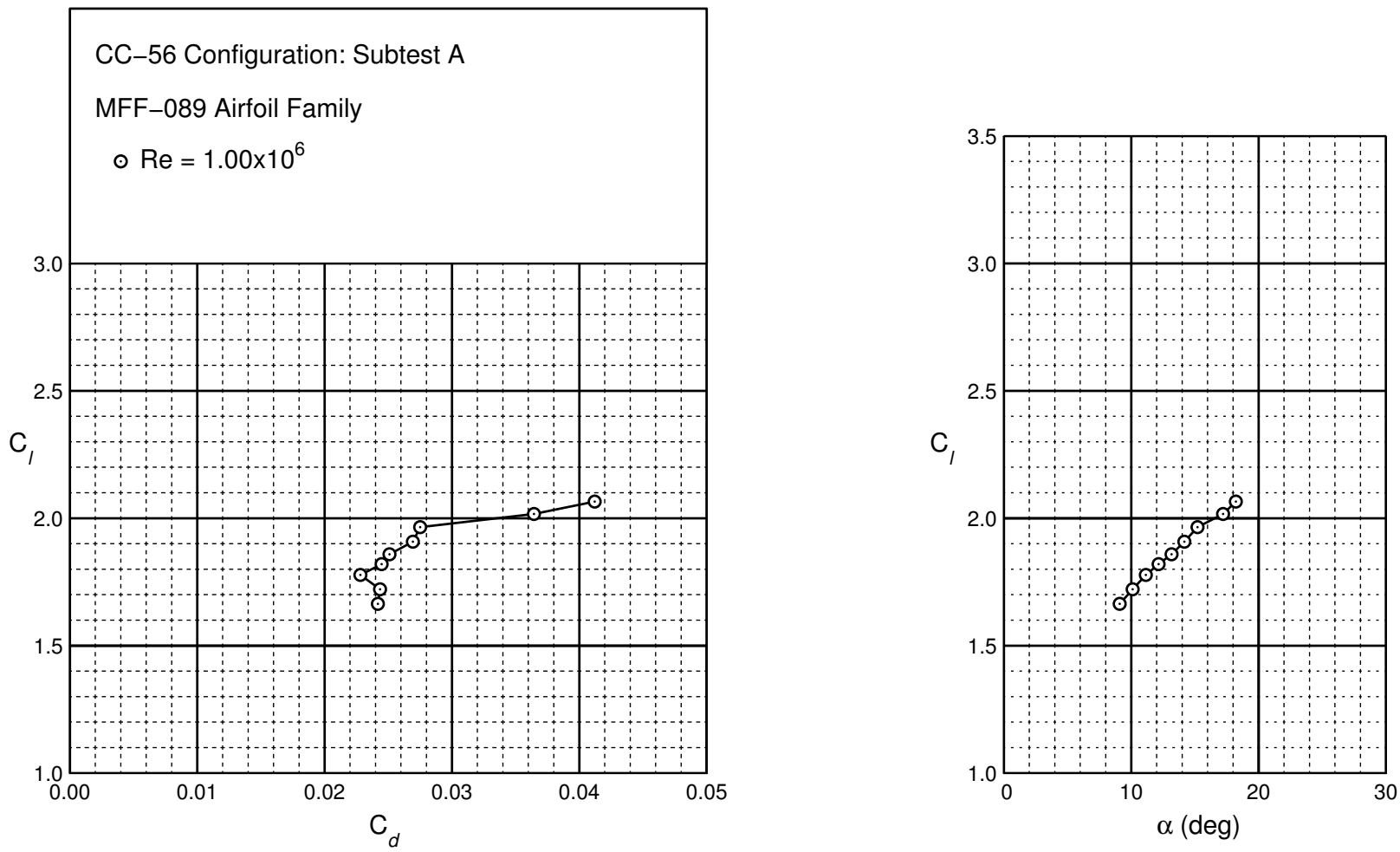

Figure B.66: CC-56 performance at $Re = 1.0 \times 10^6$.

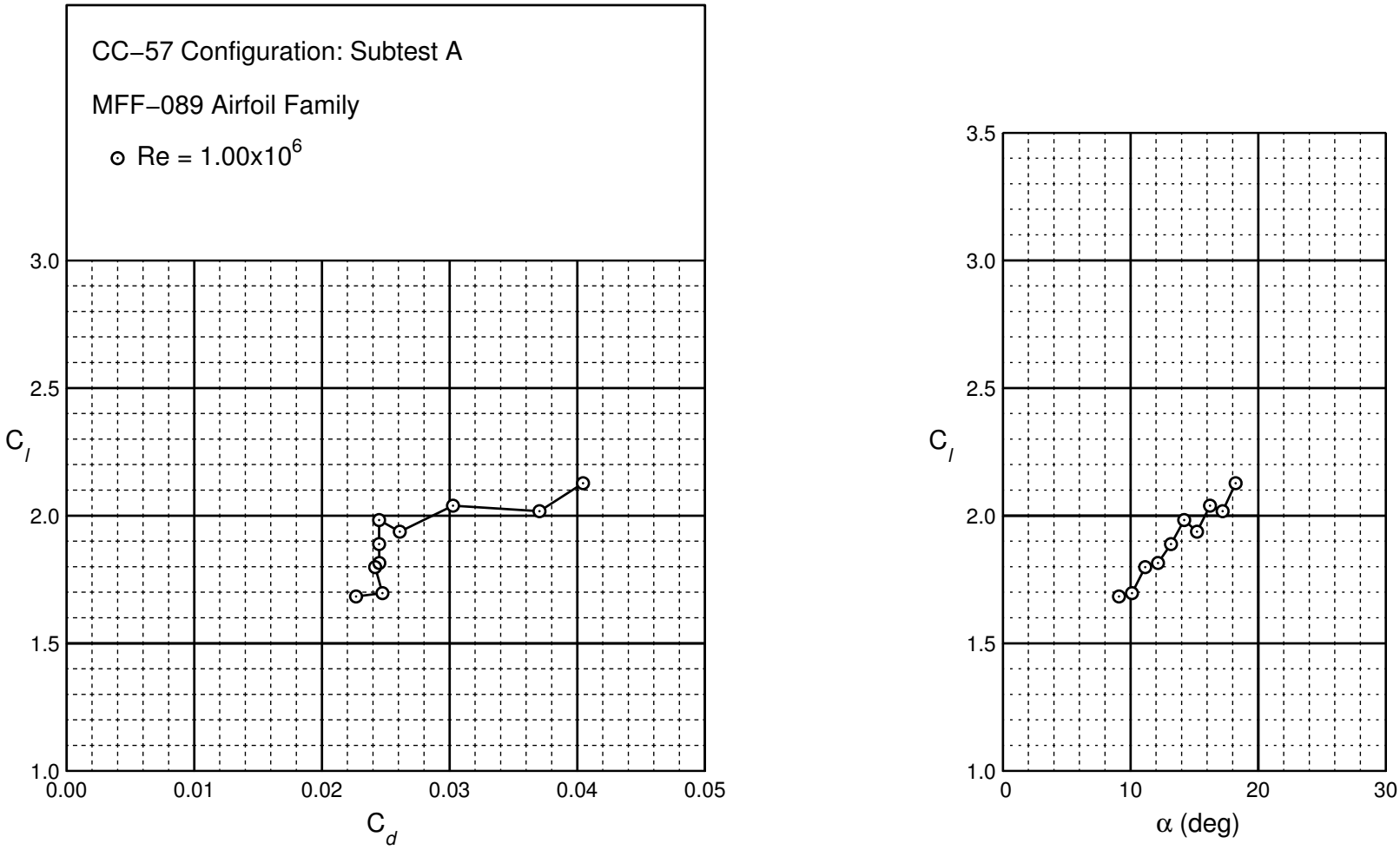

Figure B.67: CC-57 performance at $Re = 1.0 \times 10^6$.

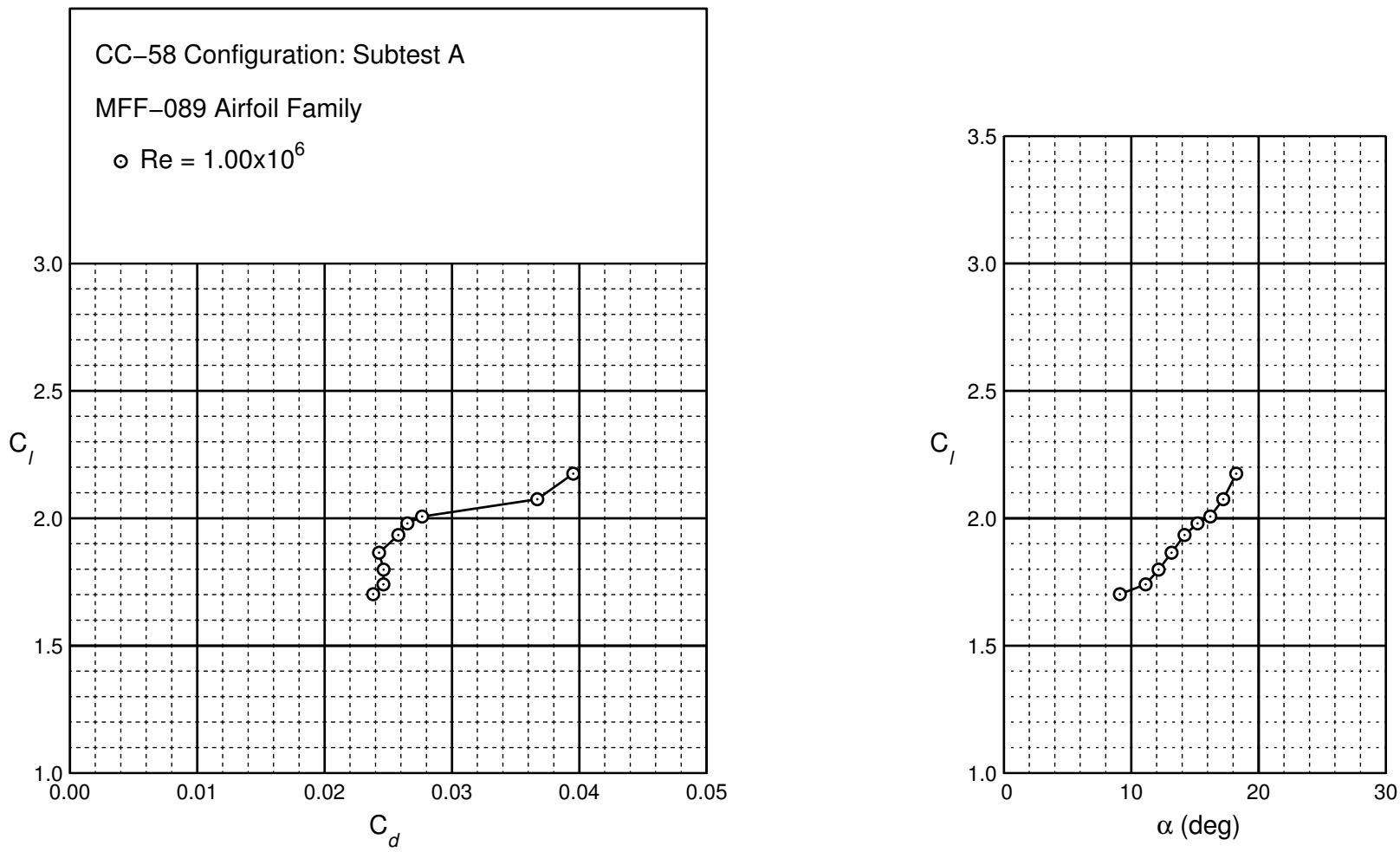

Figure B.68: CC-58 performance at $Re = 1.0 \times 10^6$.

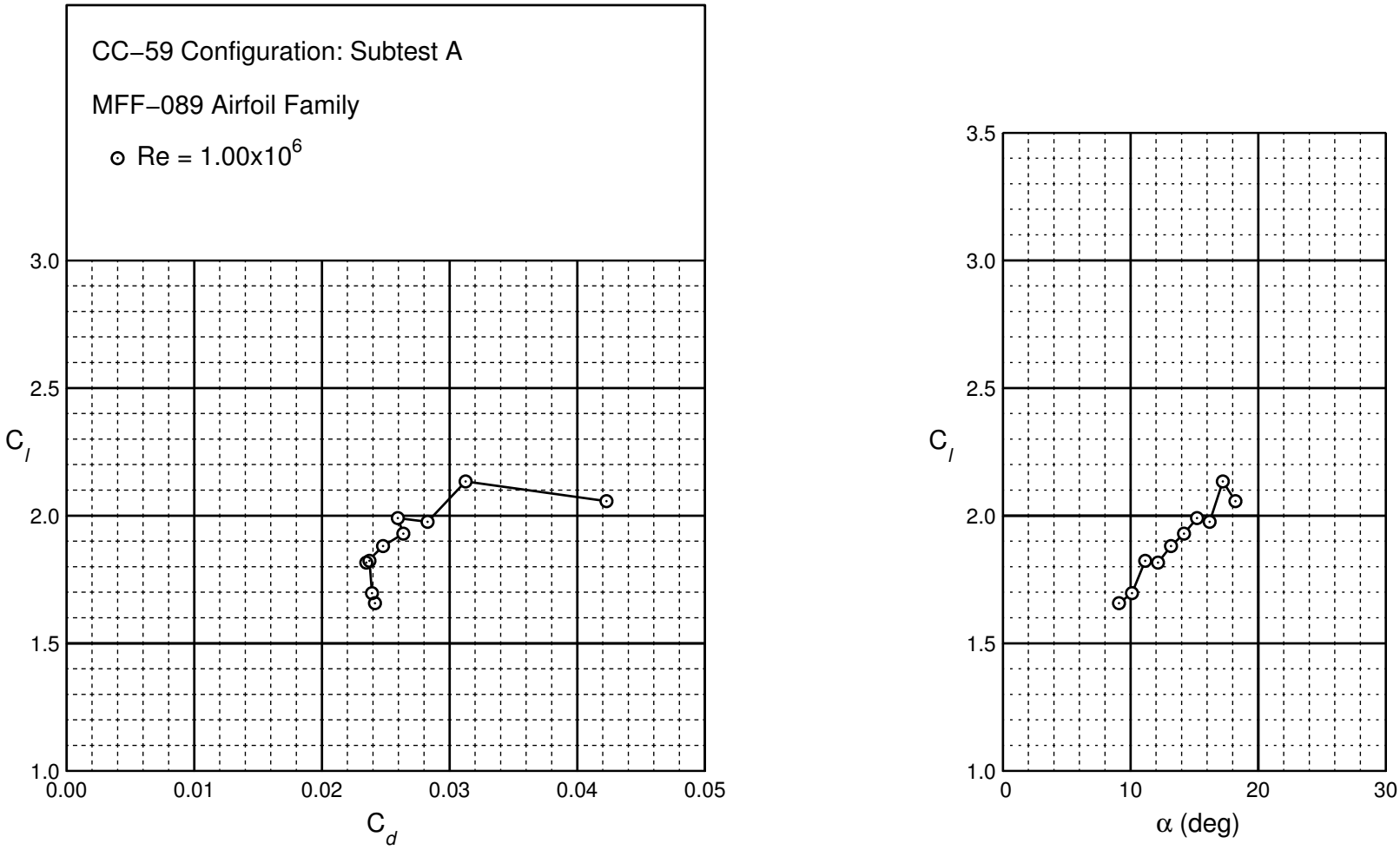

Figure B.69: CC-59 performance at $Re = 1.0 \times 10^6$.

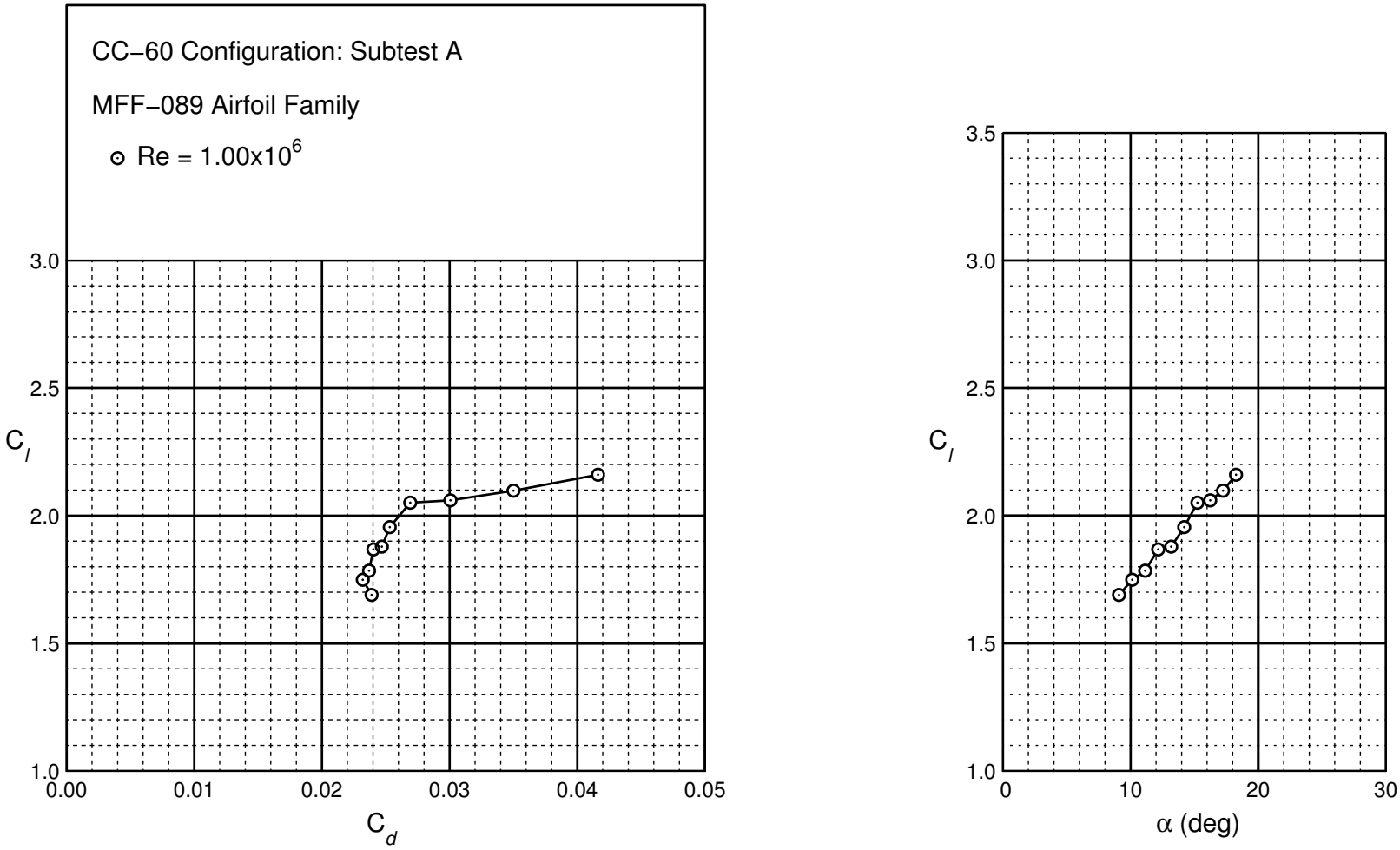

Figure B.70: CC-60 performance at $Re = 1.0 \times 10^6$.

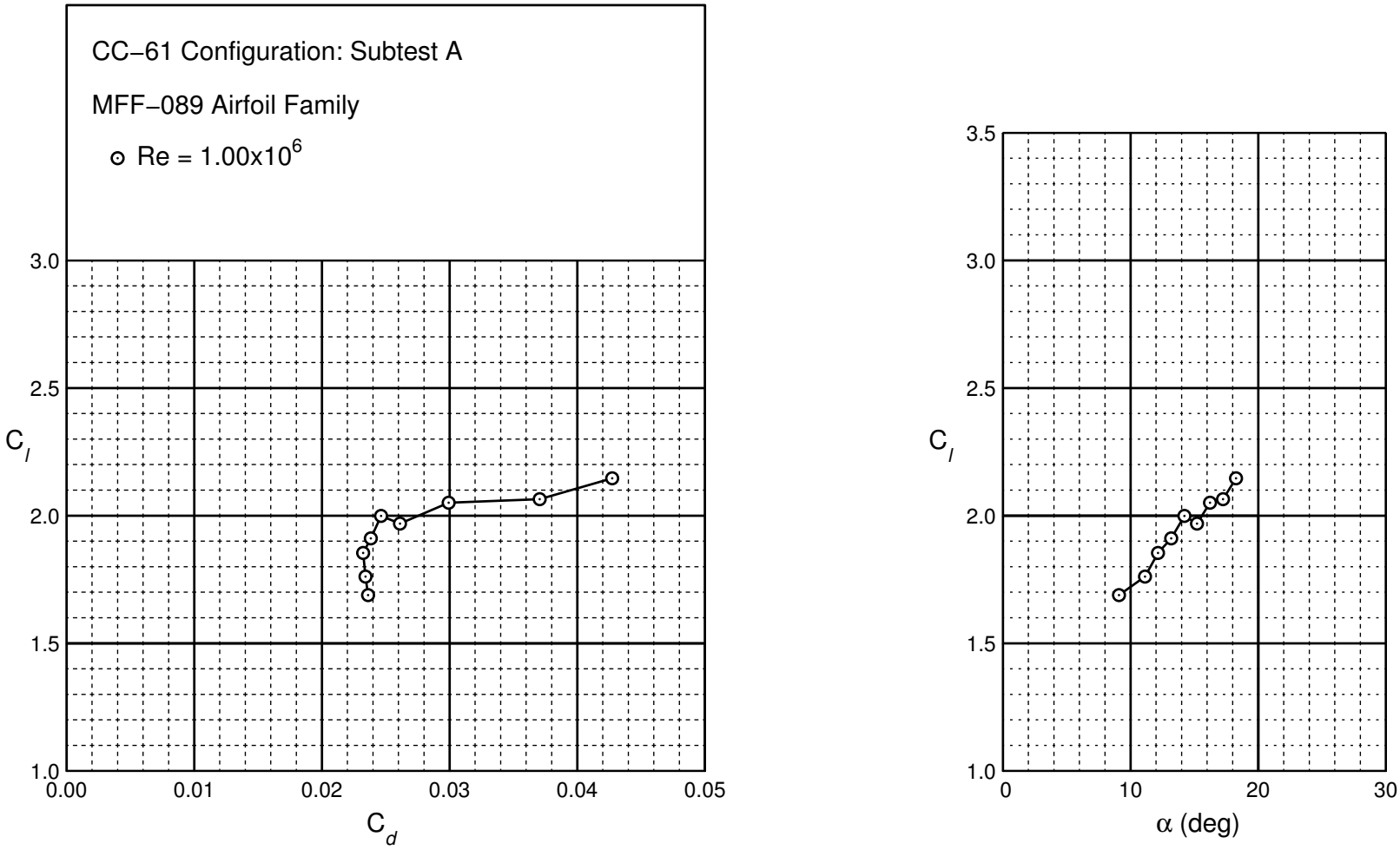

Figure B.71: CC-61 performance at $Re = 1.0 \times 10^6$.

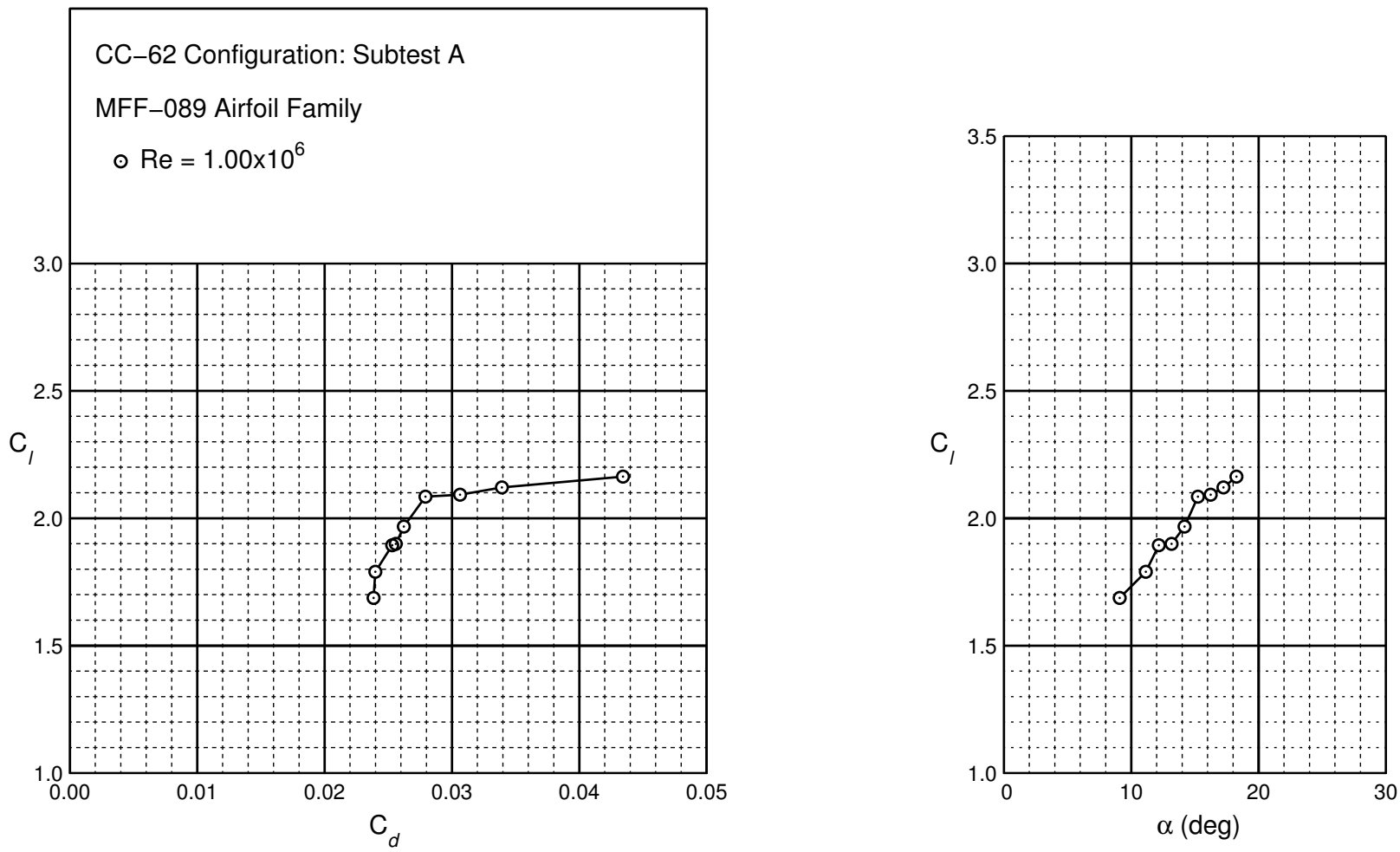

Figure B.72: CC-62 performance at $Re = 1.0 \times 10^6$.

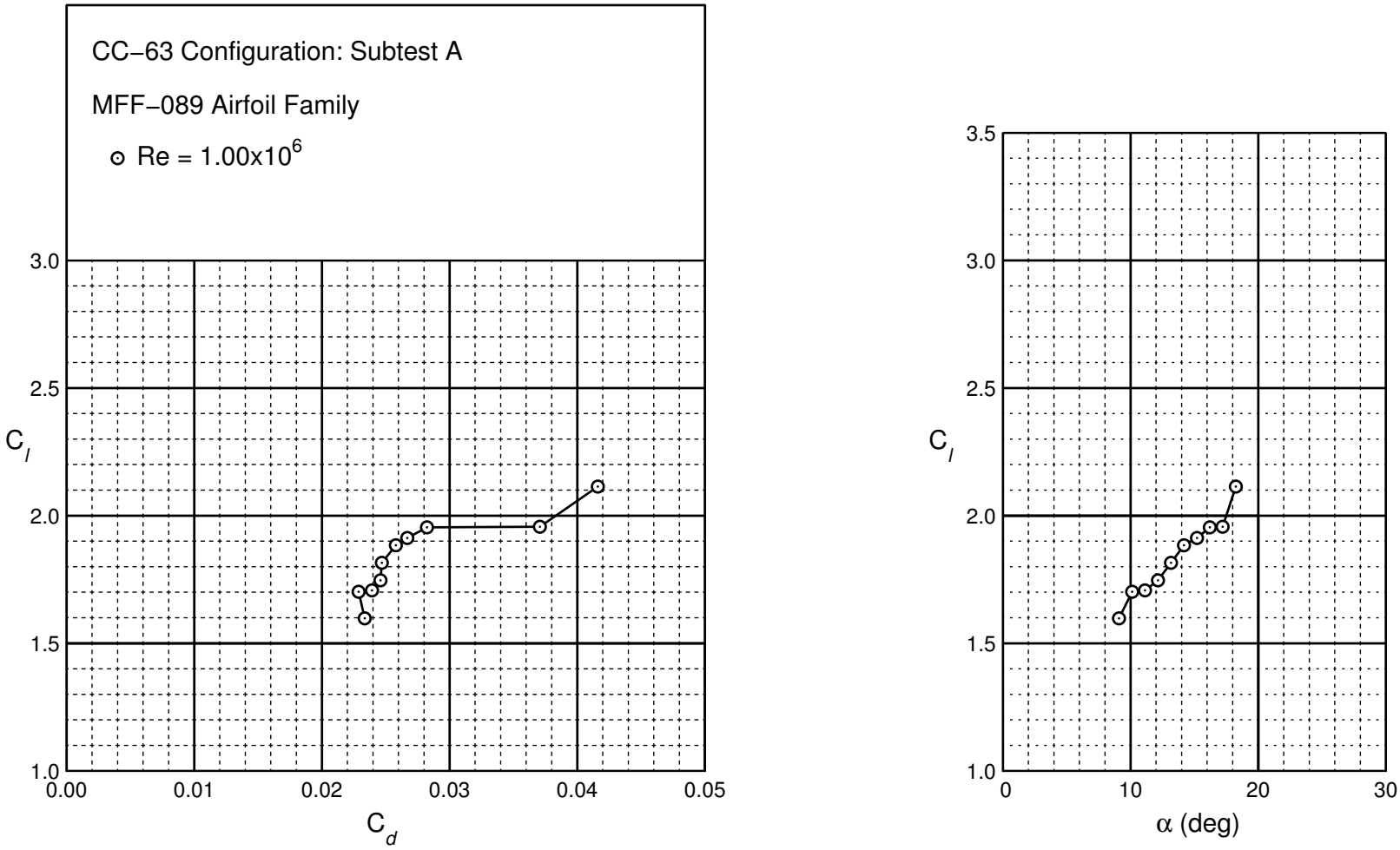

Figure B.73: CC-63 performance at $Re = 1.0 \times 10^6$.

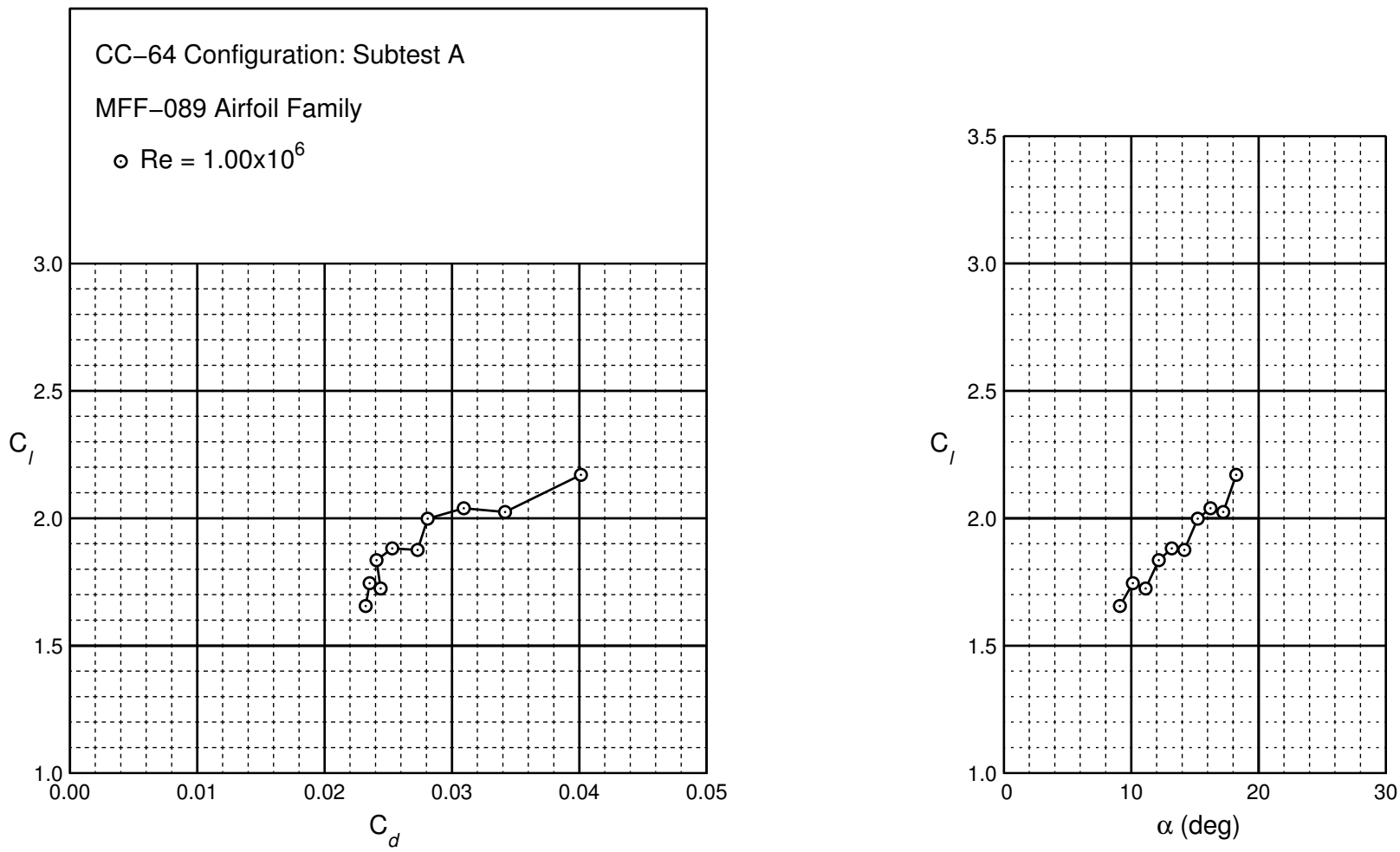

Figure B.74: CC-64 performance at $Re = 1.0 \times 10^6$.

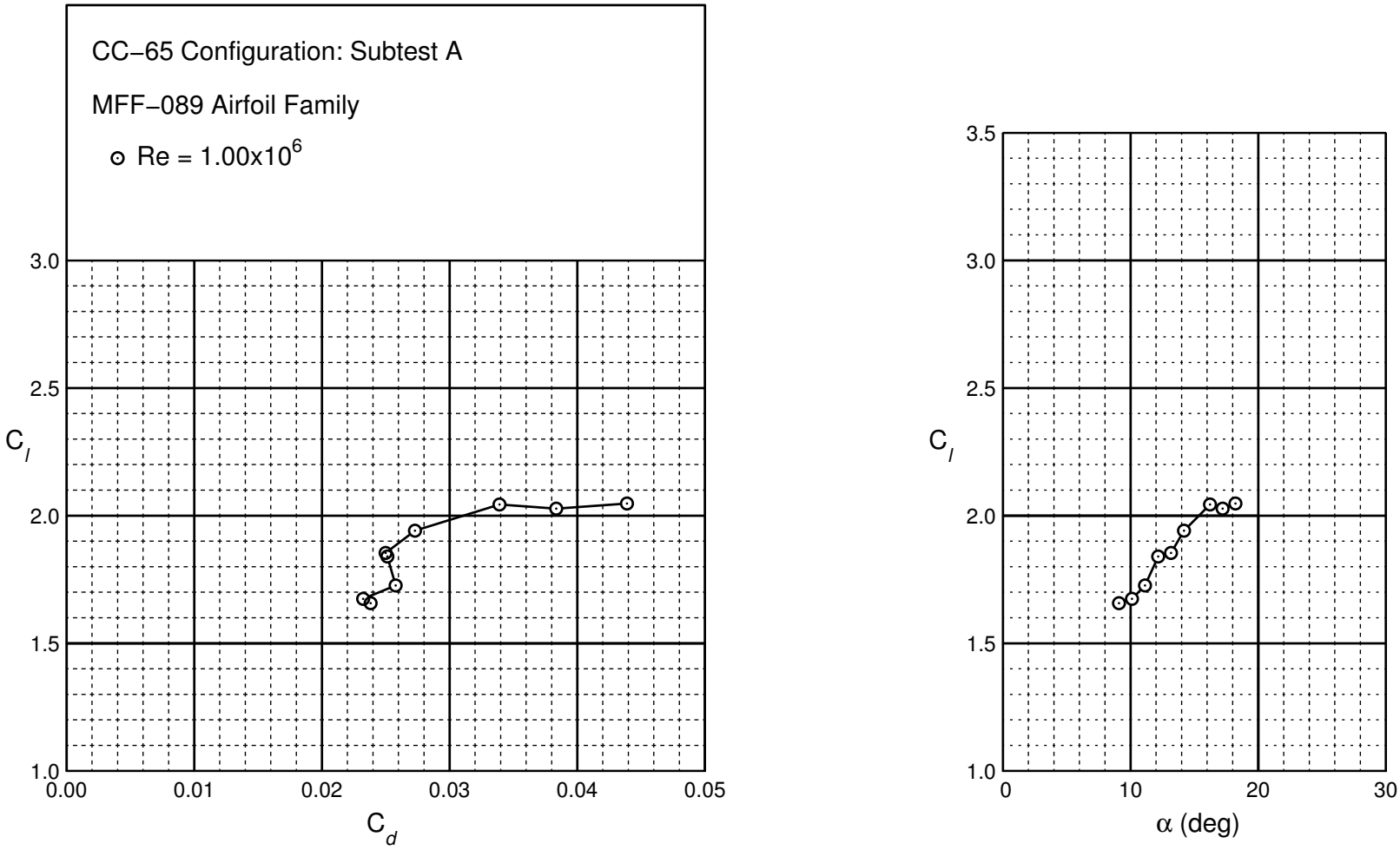

Figure B.75: CC-65 performance at $Re = 1.0 \times 10^6$.

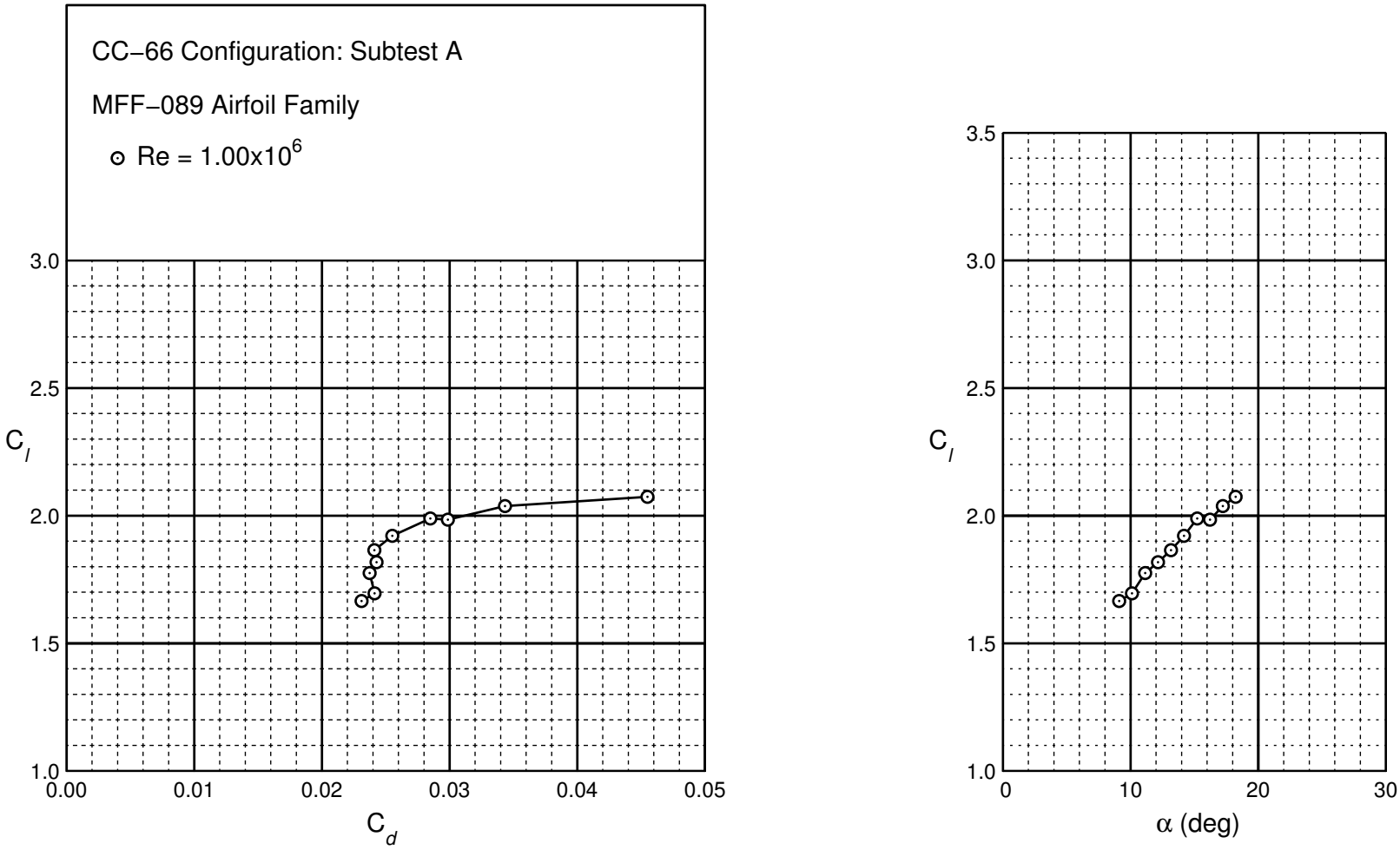

Figure B.76: CC-66 performance at $Re = 1.0 \times 10^6$.

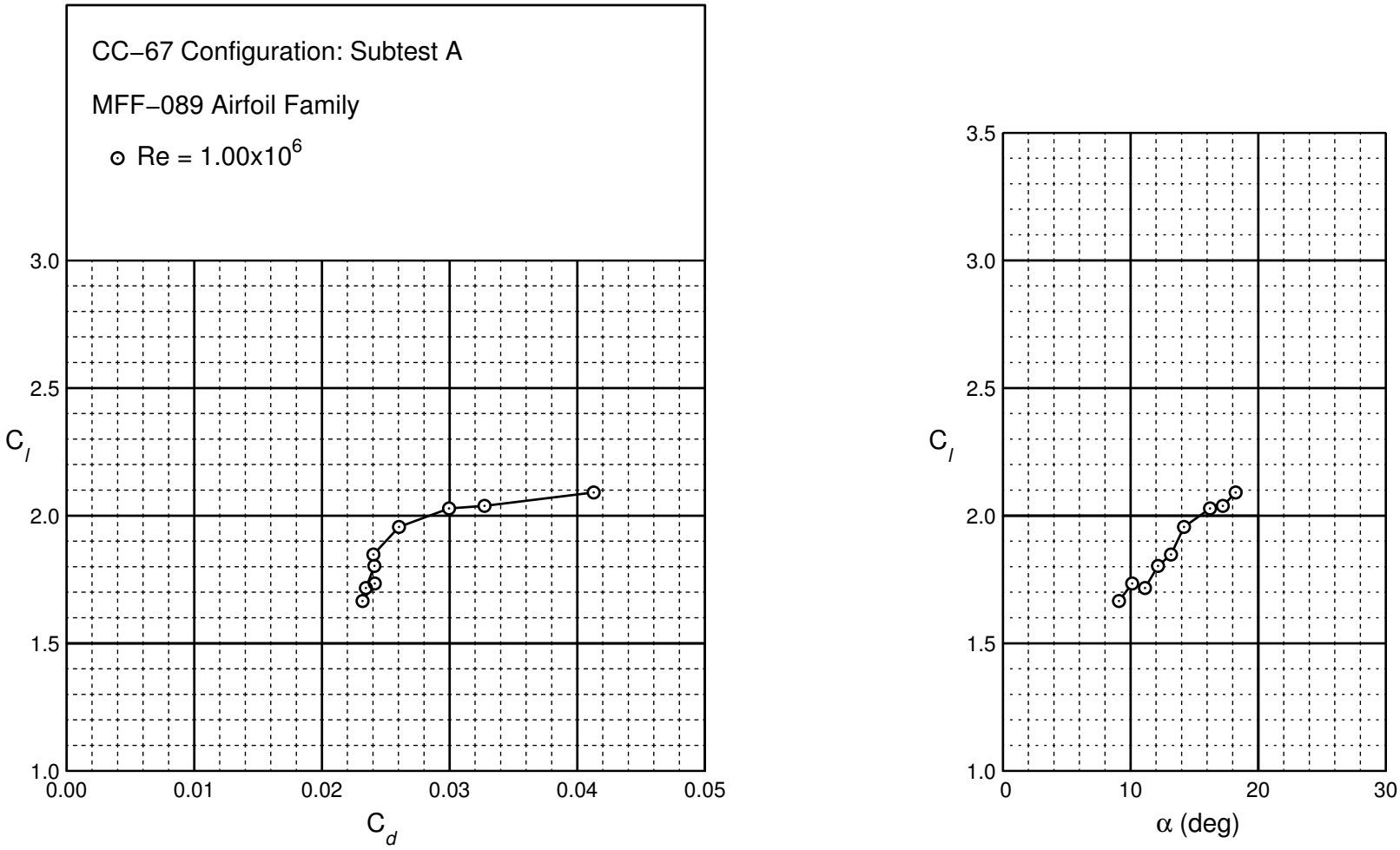

Figure B.77: CC-67 performance at $Re = 1.0 \times 10^6$.

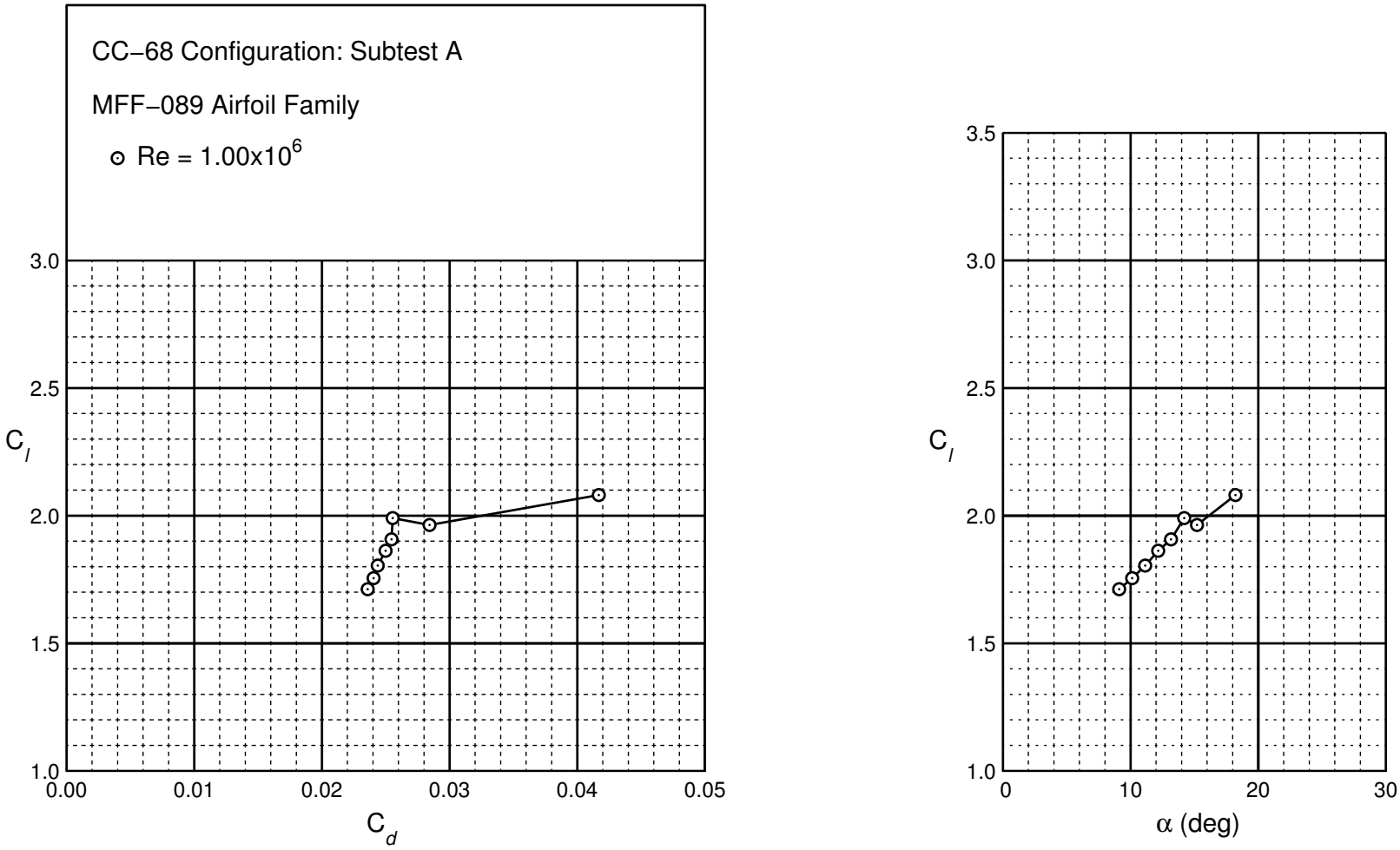

Figure B.78: CC-68 performance at $Re = 1.0 \times 10^6$.

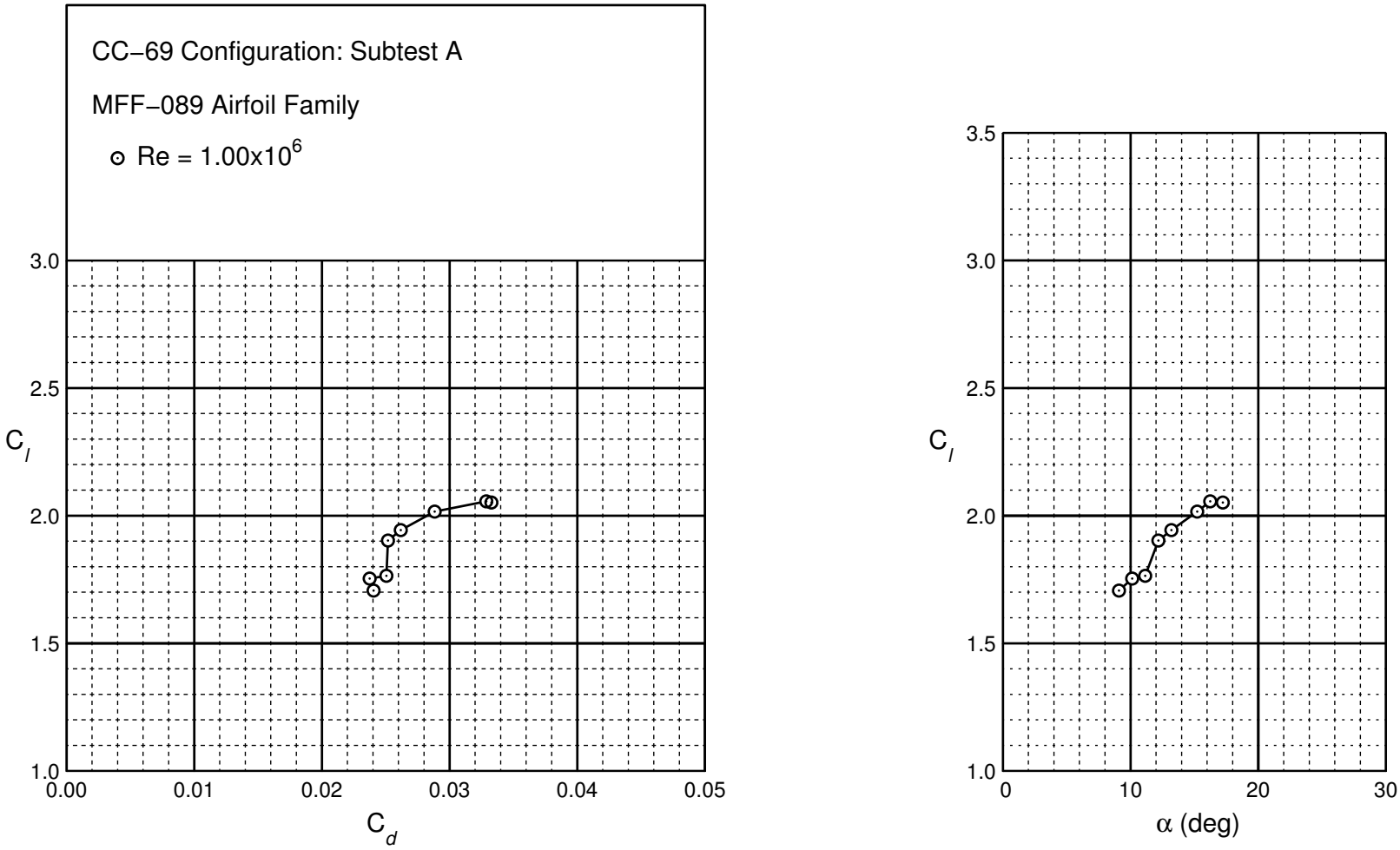

Figure B.79: CC-69 performance at $Re = 1.0 \times 10^6$.

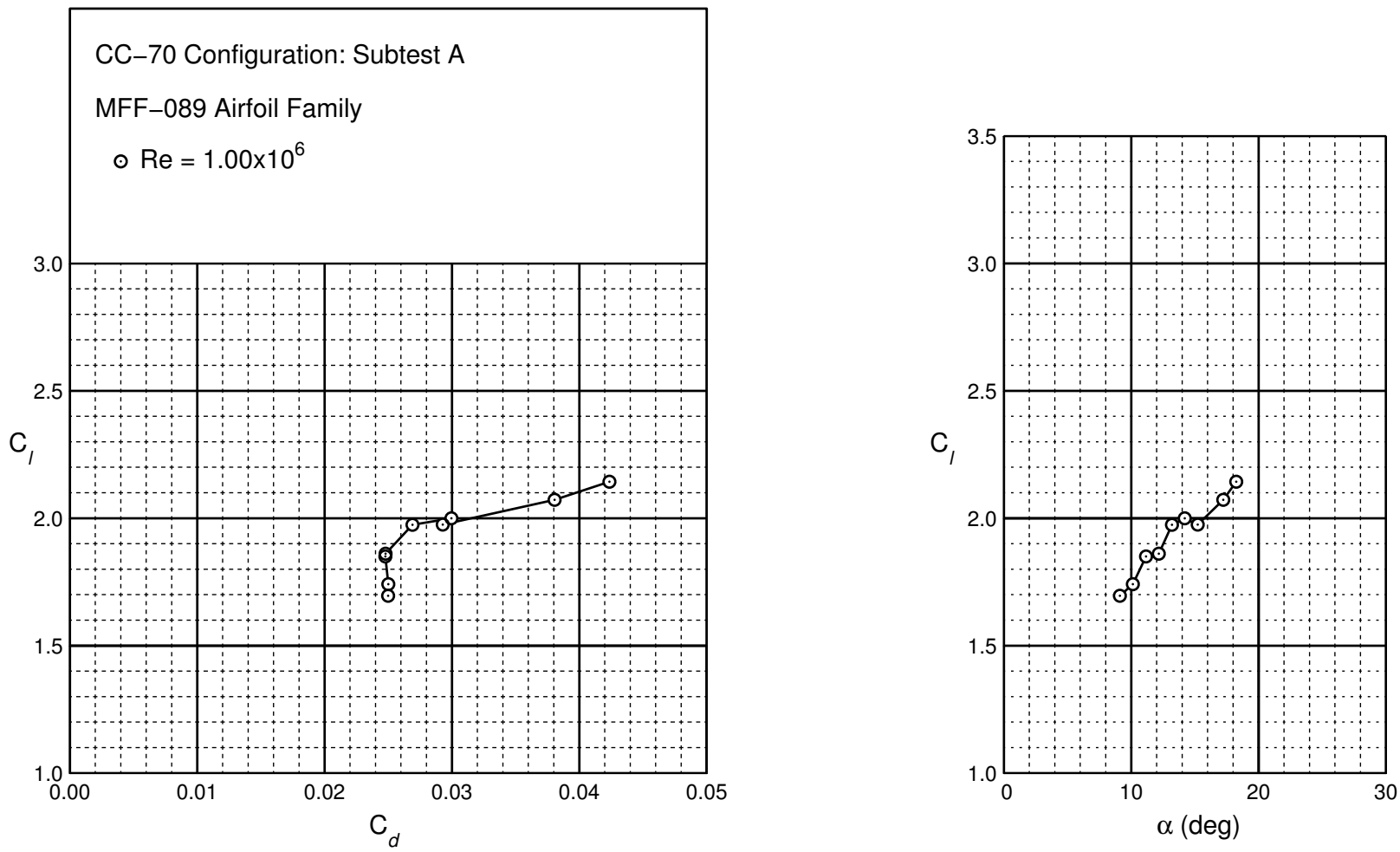

Figure B.80: CC-70 performance at $Re = 1.0 \times 10^6$.

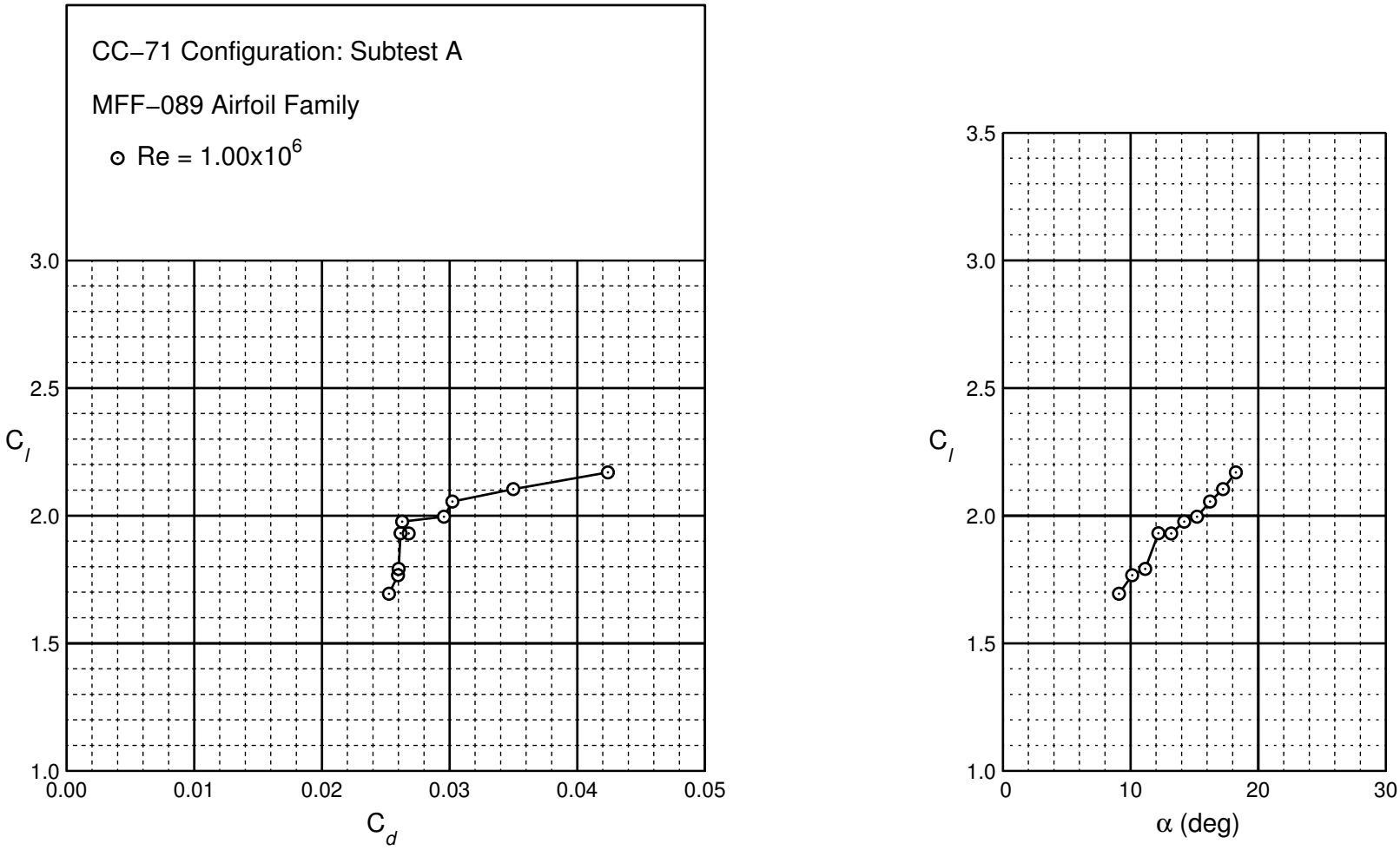

Figure B.81: CC-71 performance at $Re = 1.0 \times 10^6$.

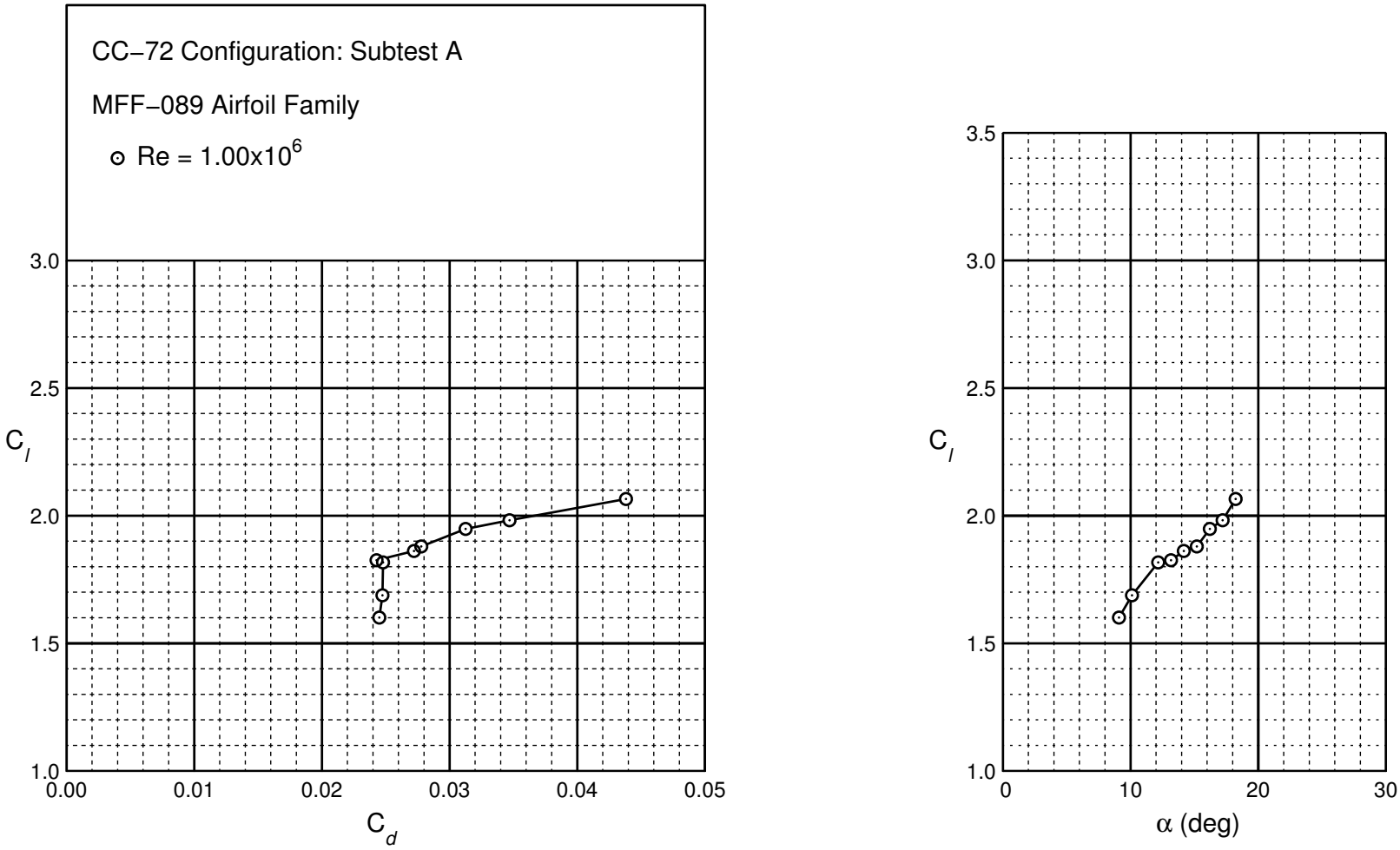

Figure B.82: CC-72 performance at $Re = 1.0 \times 10^6$.

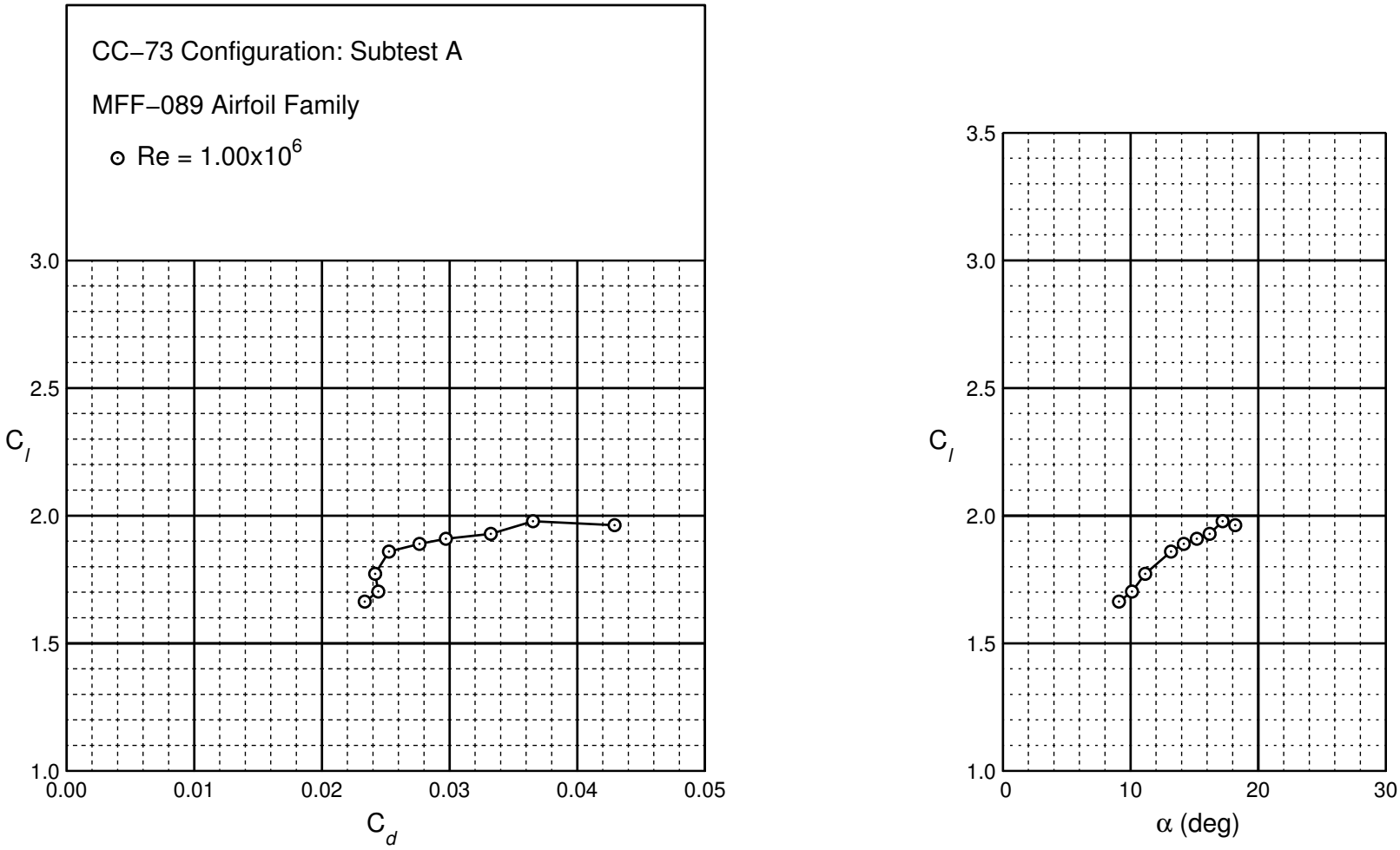

Figure B.83: CC-73 performance at $Re = 1.0 \times 10^6$.

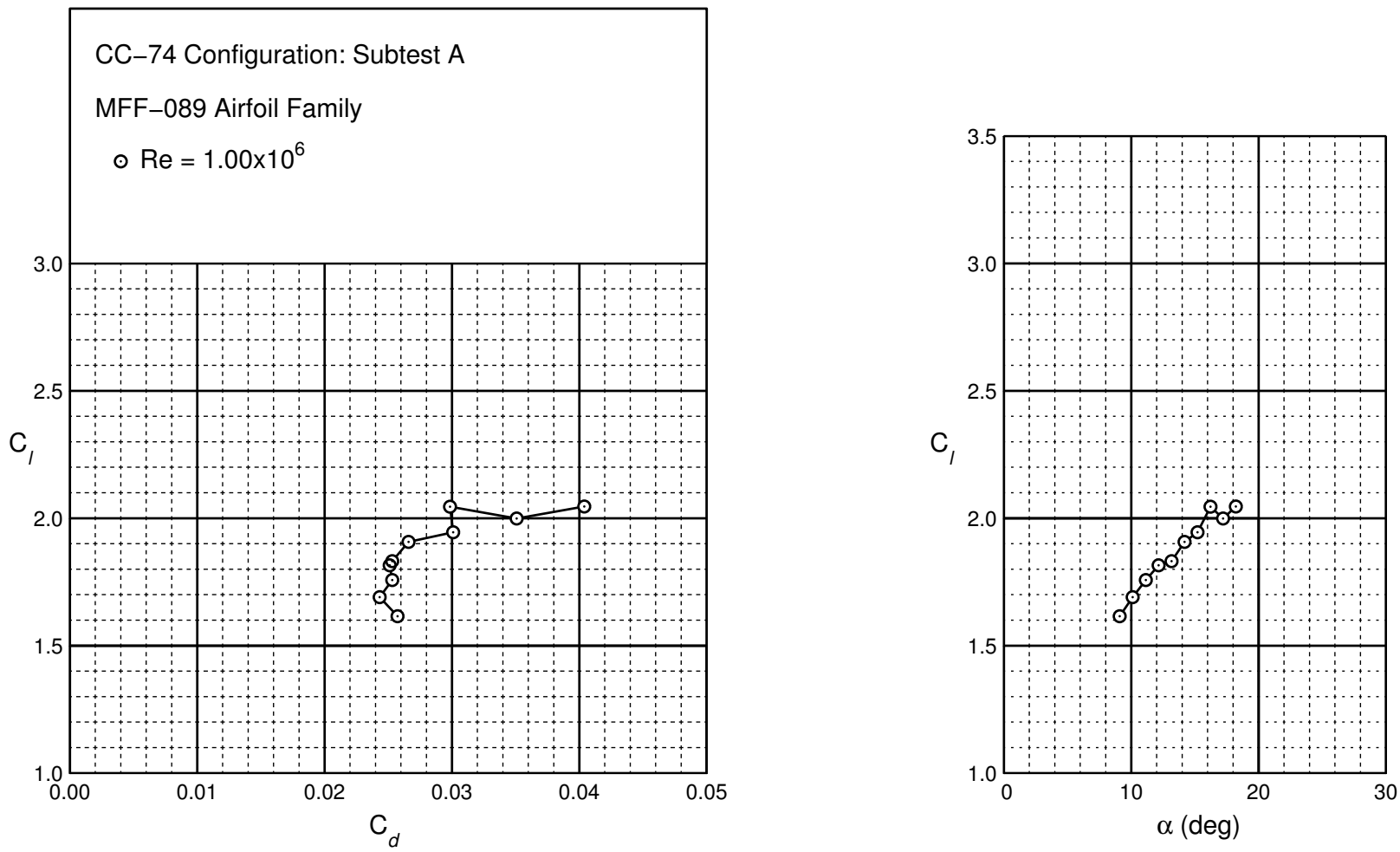

Figure B.84: CC-74 performance at $Re = 1.0 \times 10^6$.

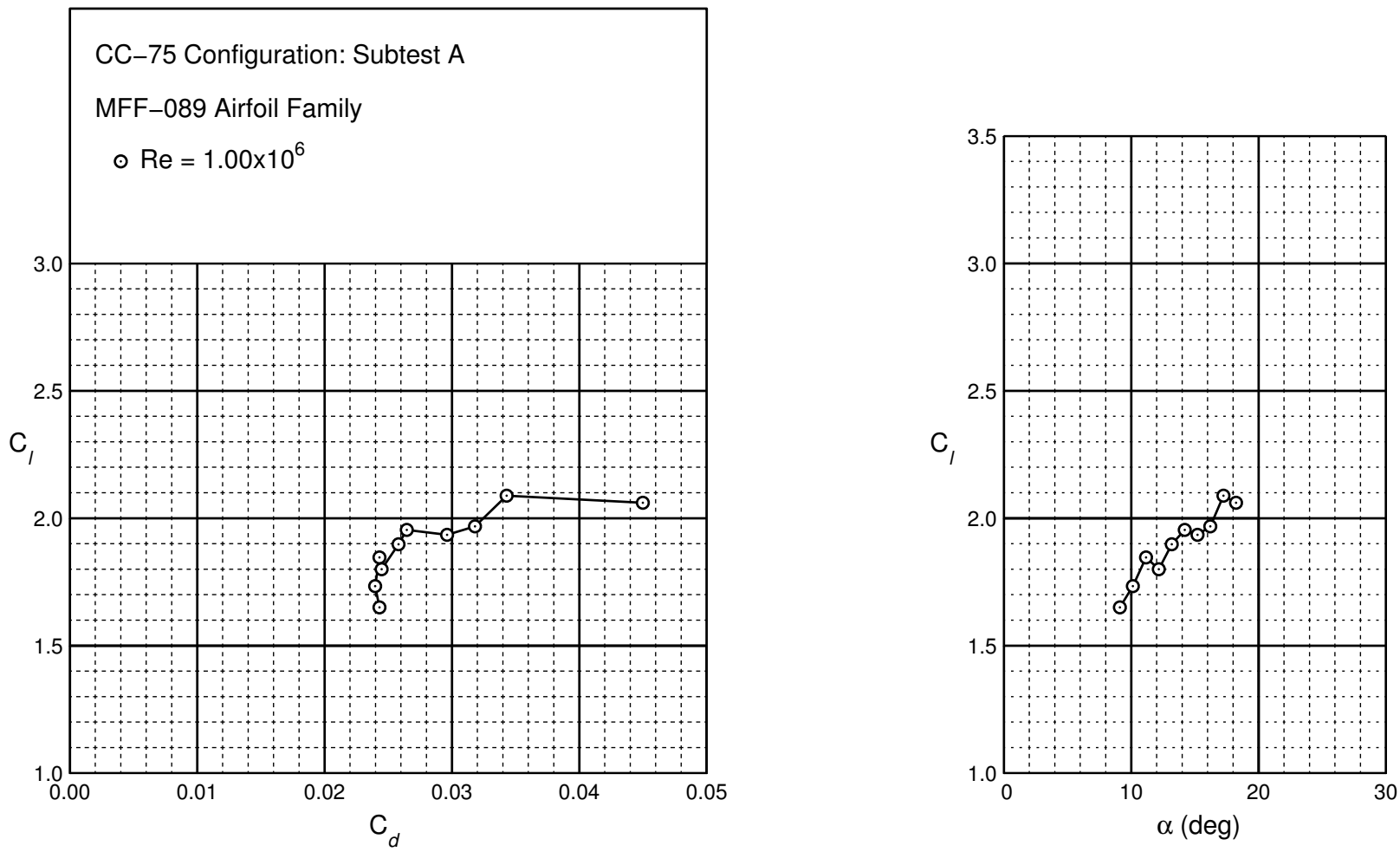

Figure B.85: CC-75 performance at $Re = 1.0 \times 10^6$.

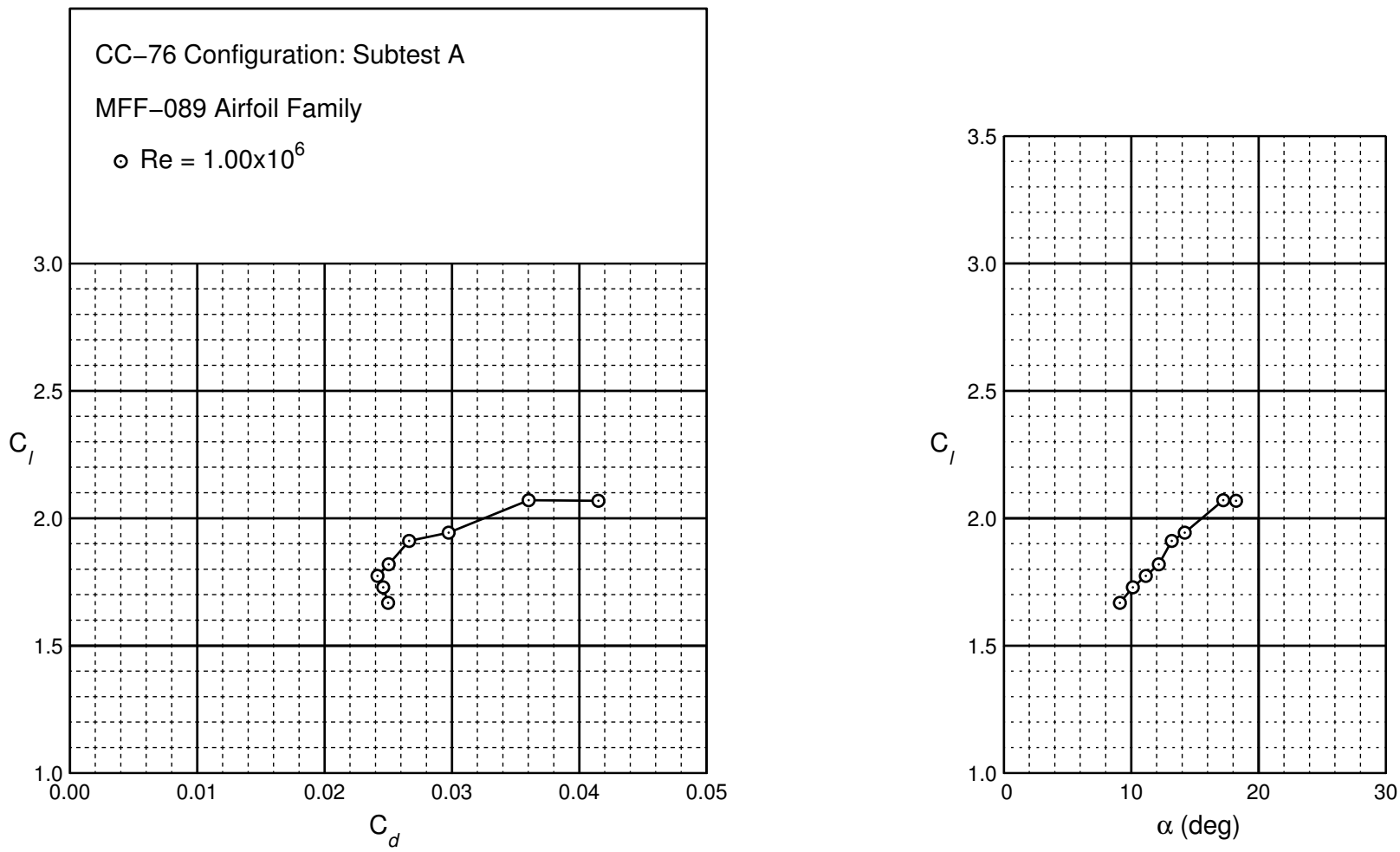

Figure B.86: CC-76 performance at $Re = 1.0 \times 10^6$.

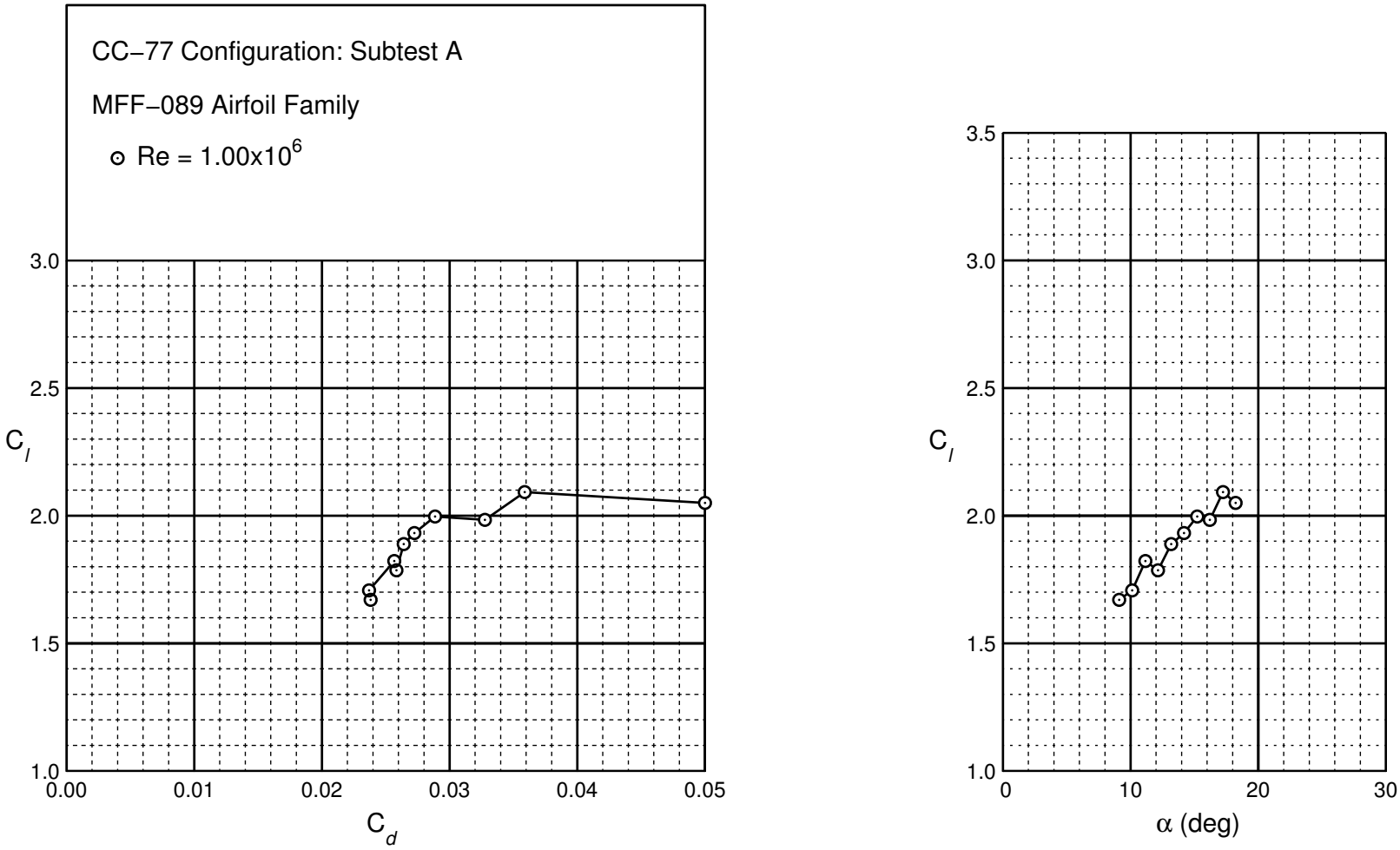

Figure B.87: CC-77 performance at $Re = 1.0 \times 10^6$.

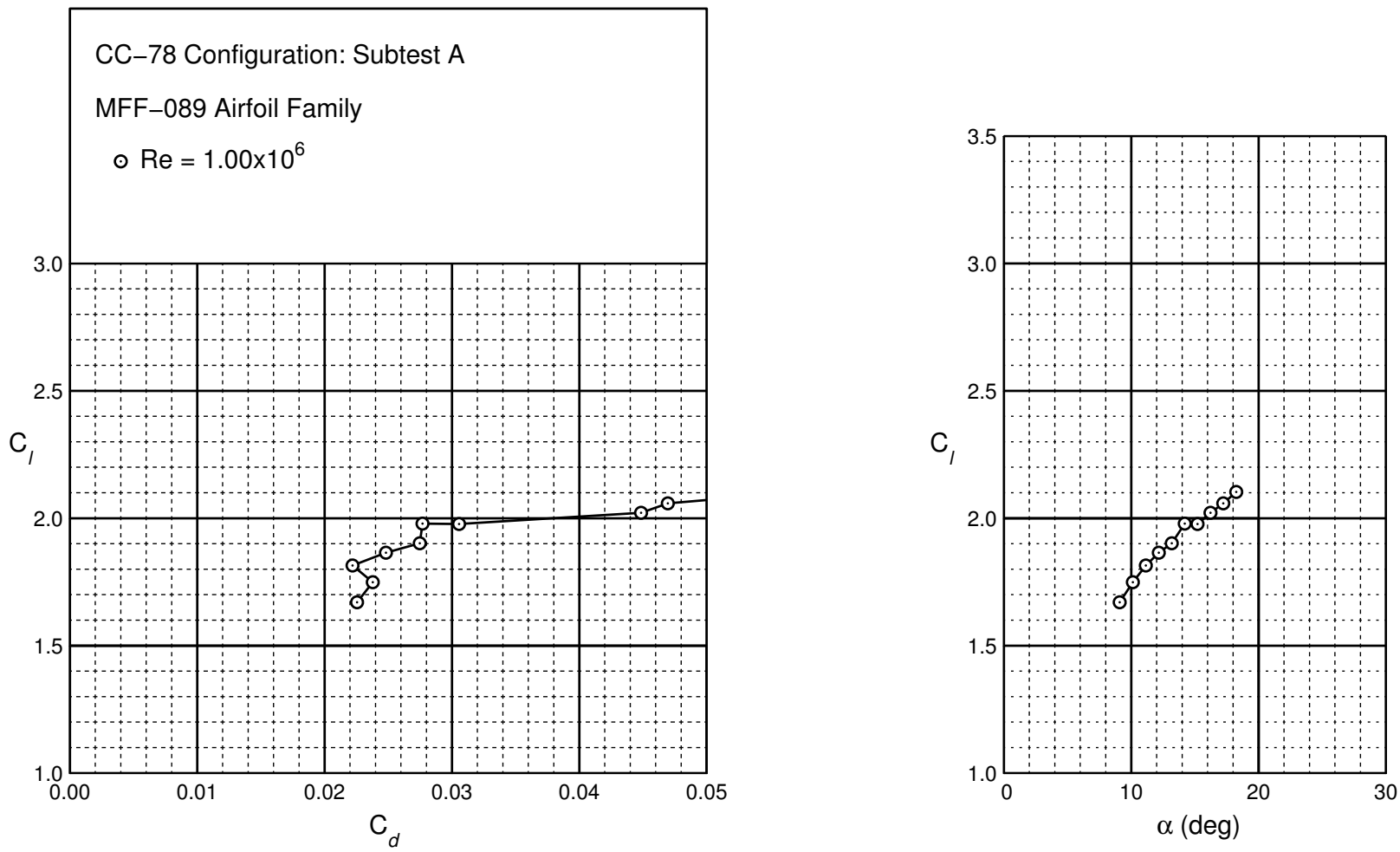

Figure B.88: CC-78 performance at $Re = 1.0 \times 10^6$.

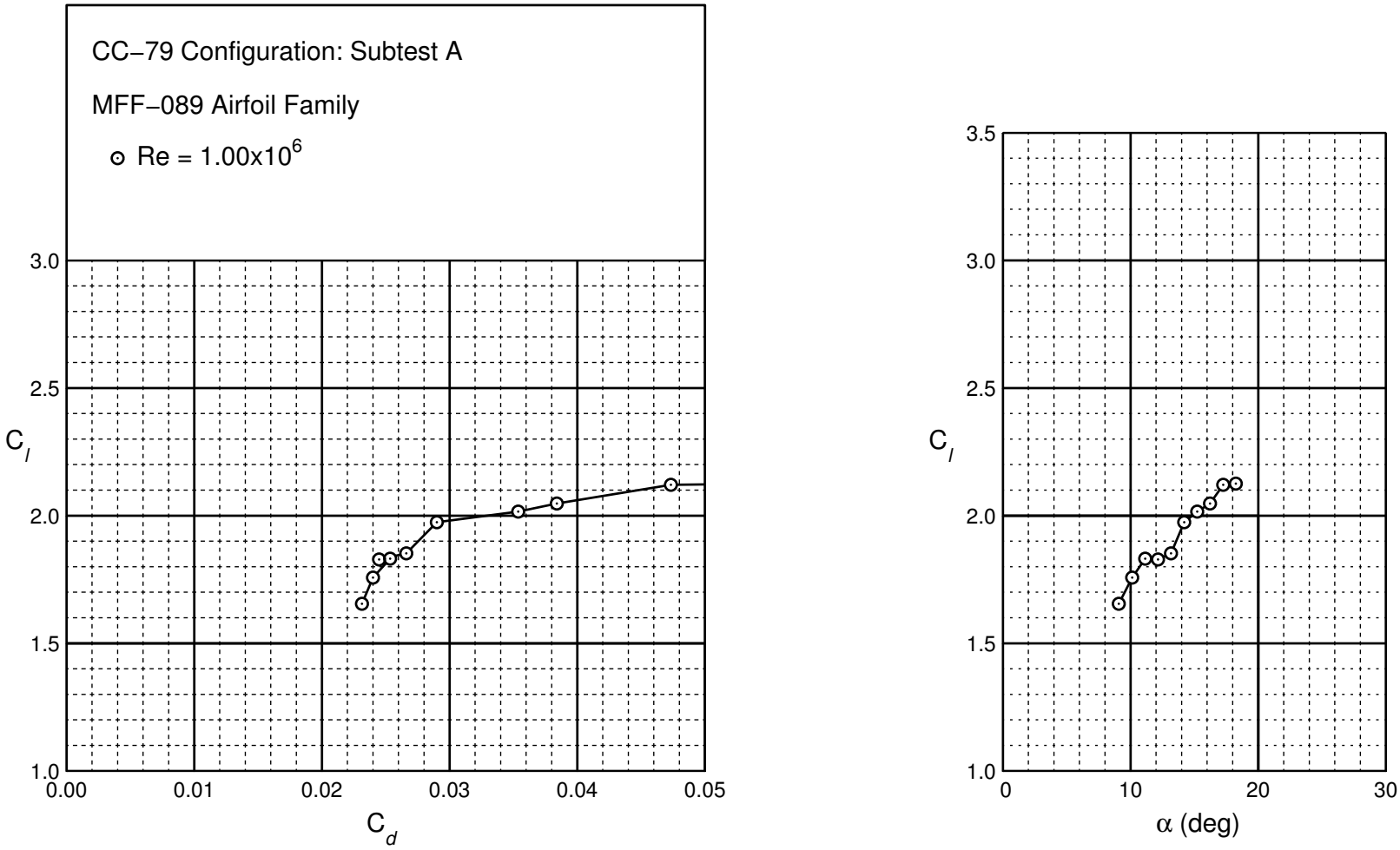

Figure B.89: CC-79 performance at $Re = 1.0 \times 10^6$.

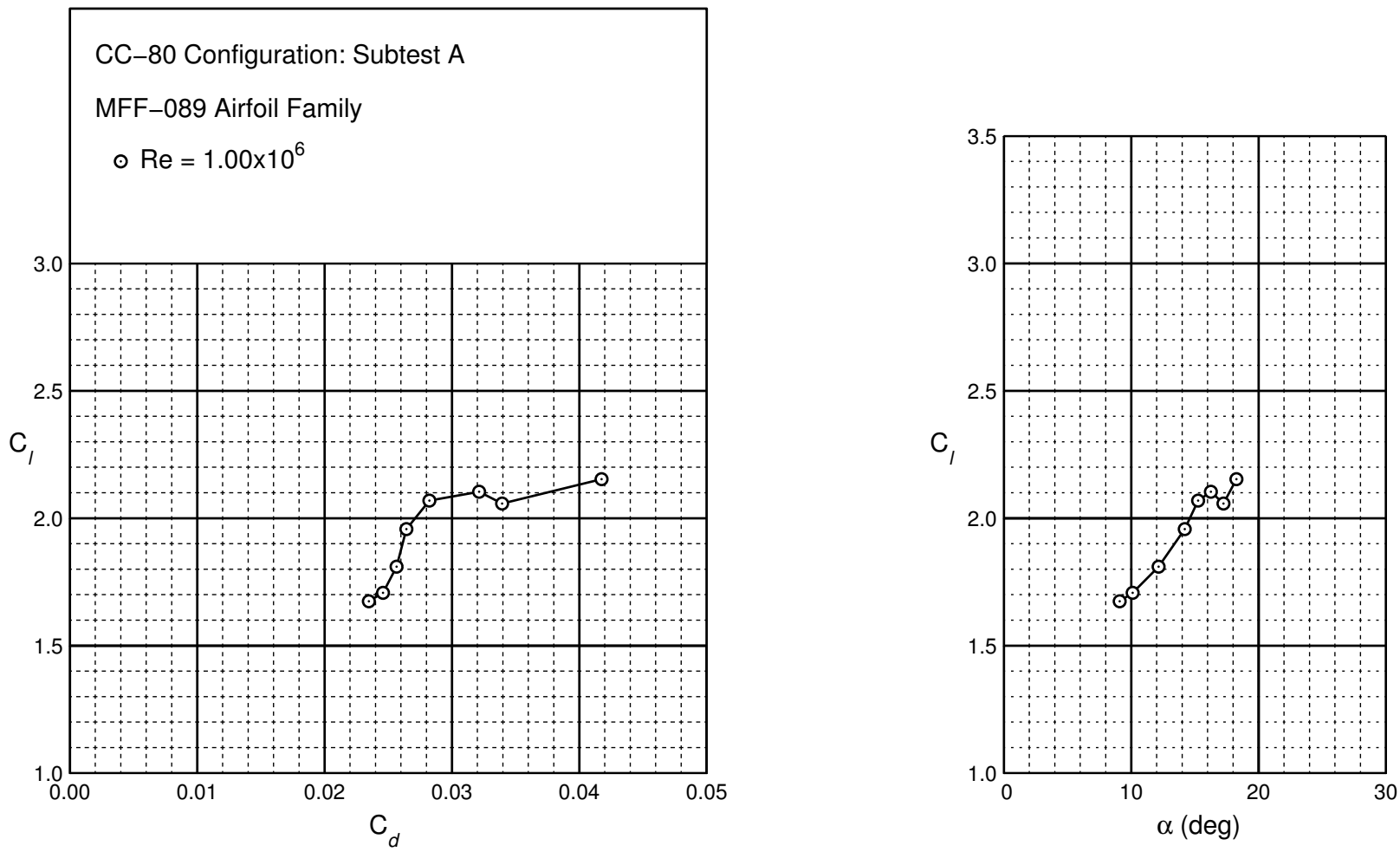

Figure B.90: CC-80 performance at $Re = 1.0 \times 10^6$.

Well Separated Performance Data

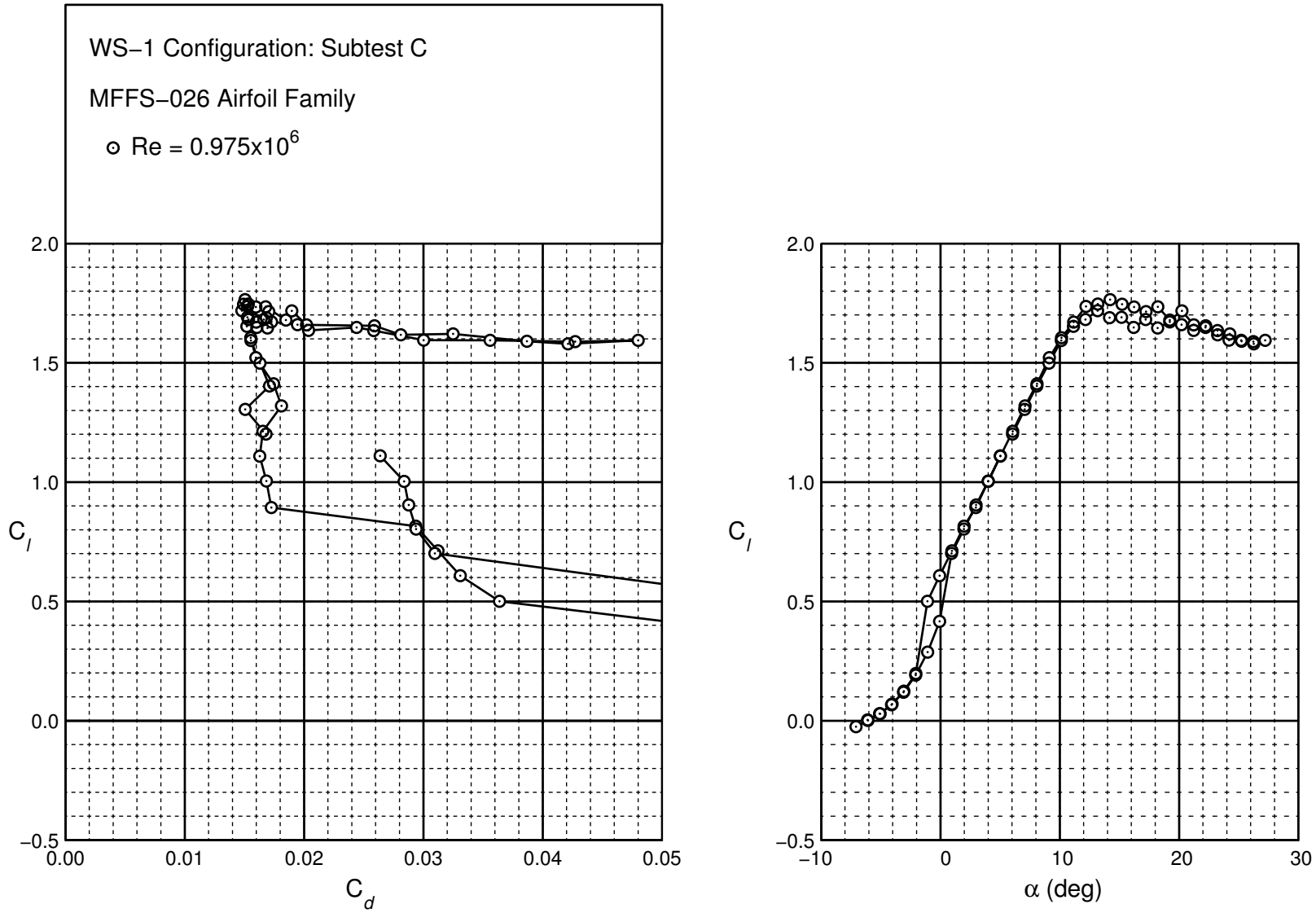

Figure B.91: WS-1 performance at $Re = 0.975 \times 10^6$.

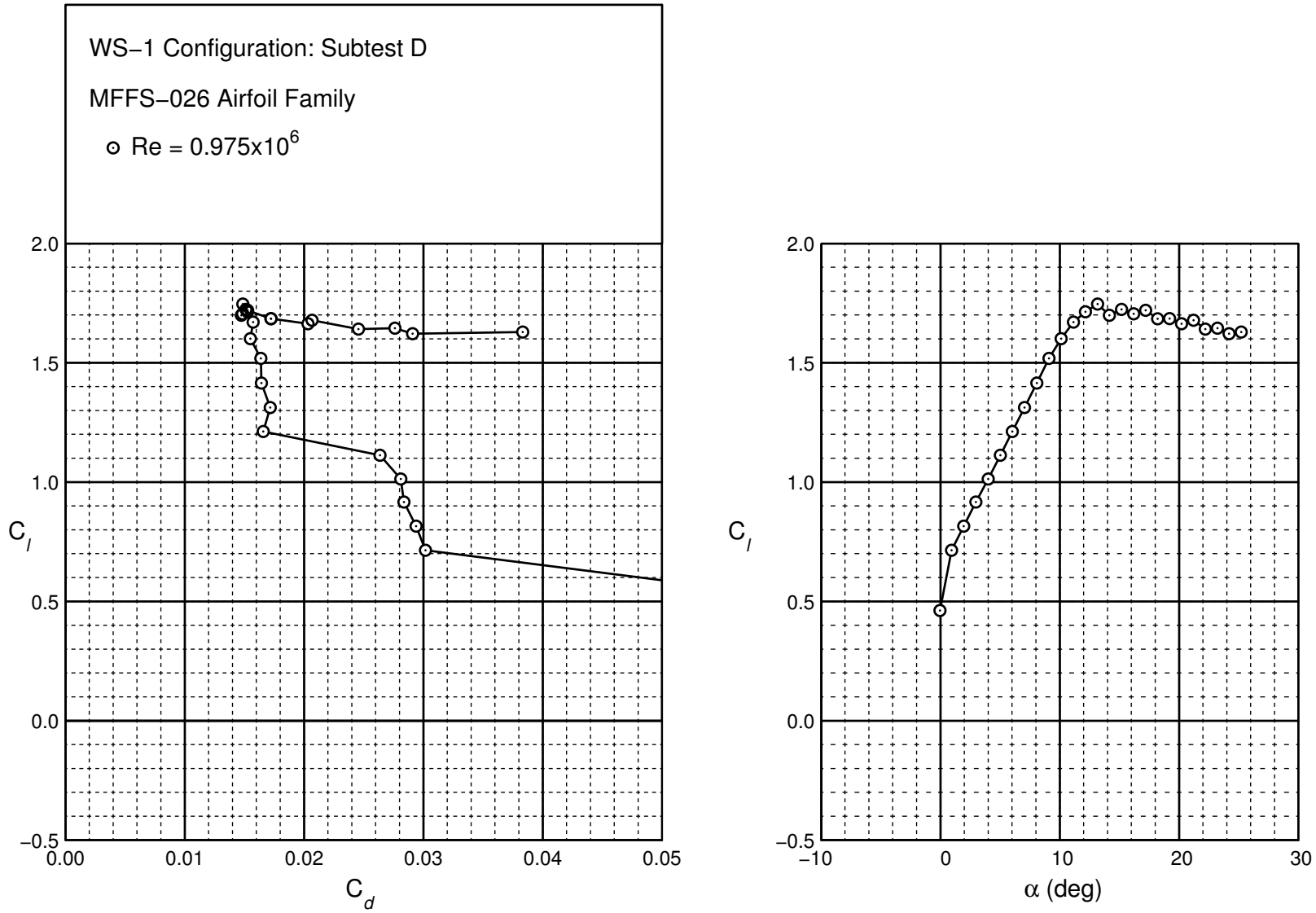

Figure B.92: WS-1 performance at $Re = 0.975 \times 10^6$.

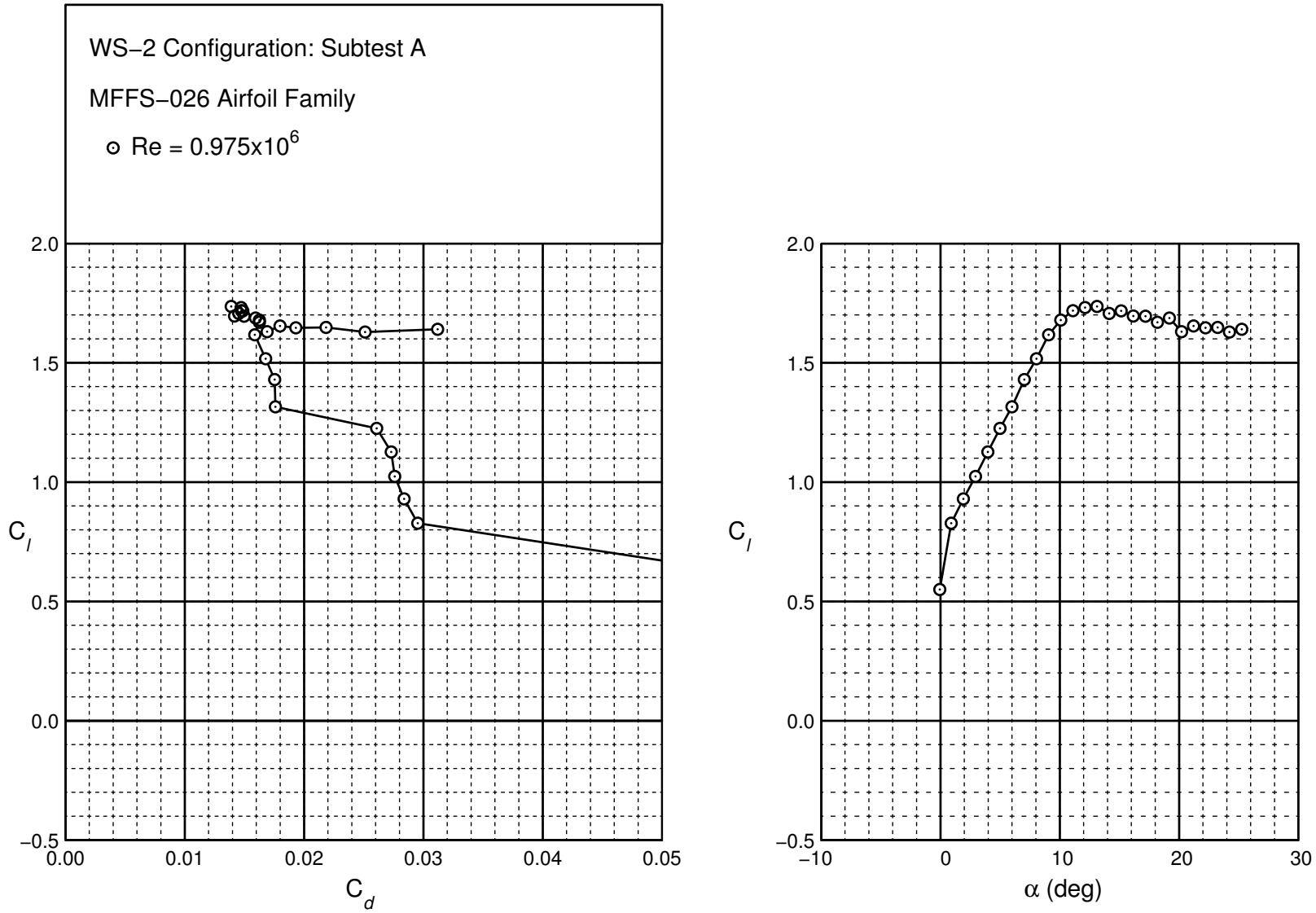

Figure B.93: WS-2 performance at $Re = 0.975 \times 10^6$.

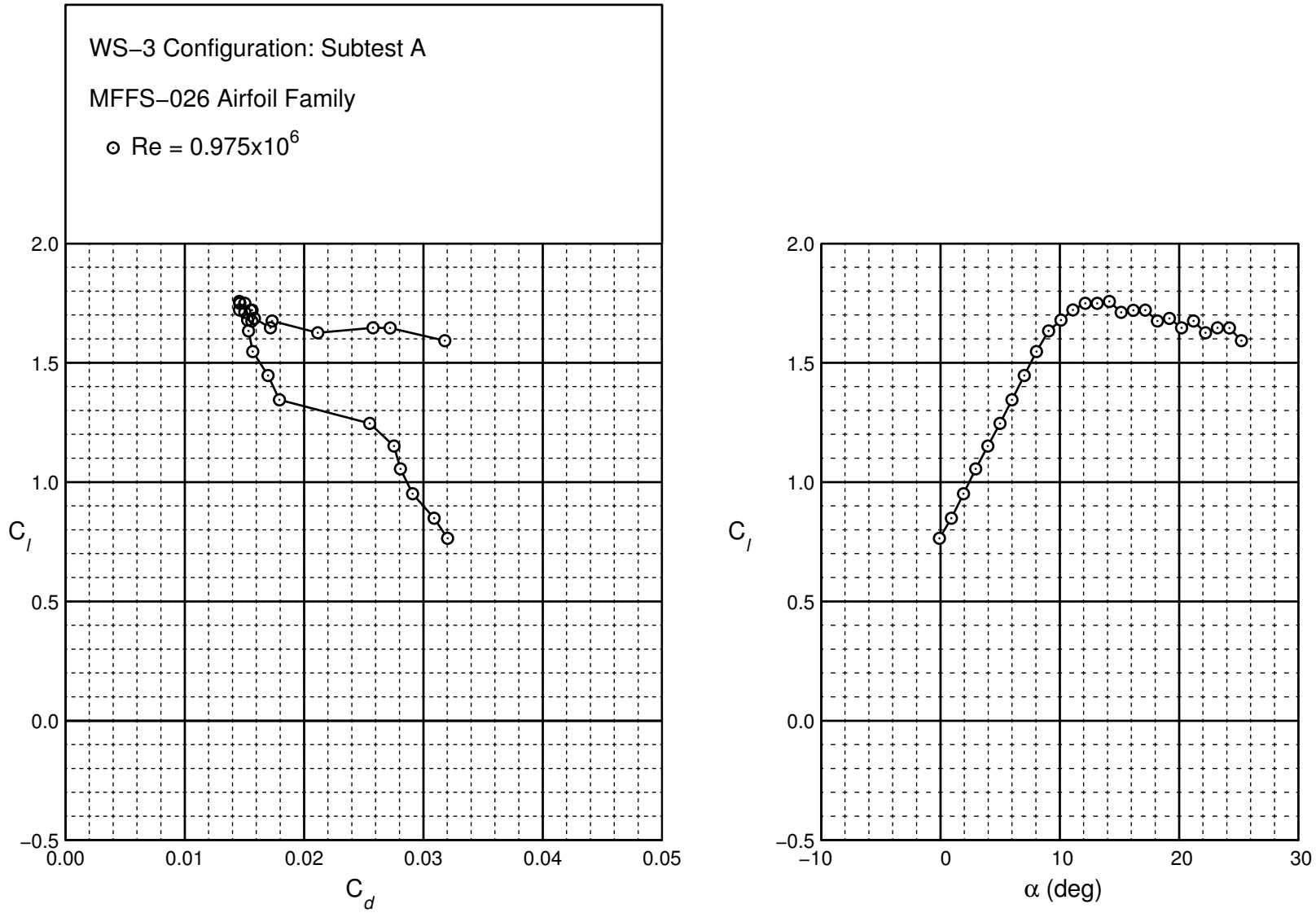

Figure B.94: WS-3 performance at $Re = 0.975 \times 10^6$.

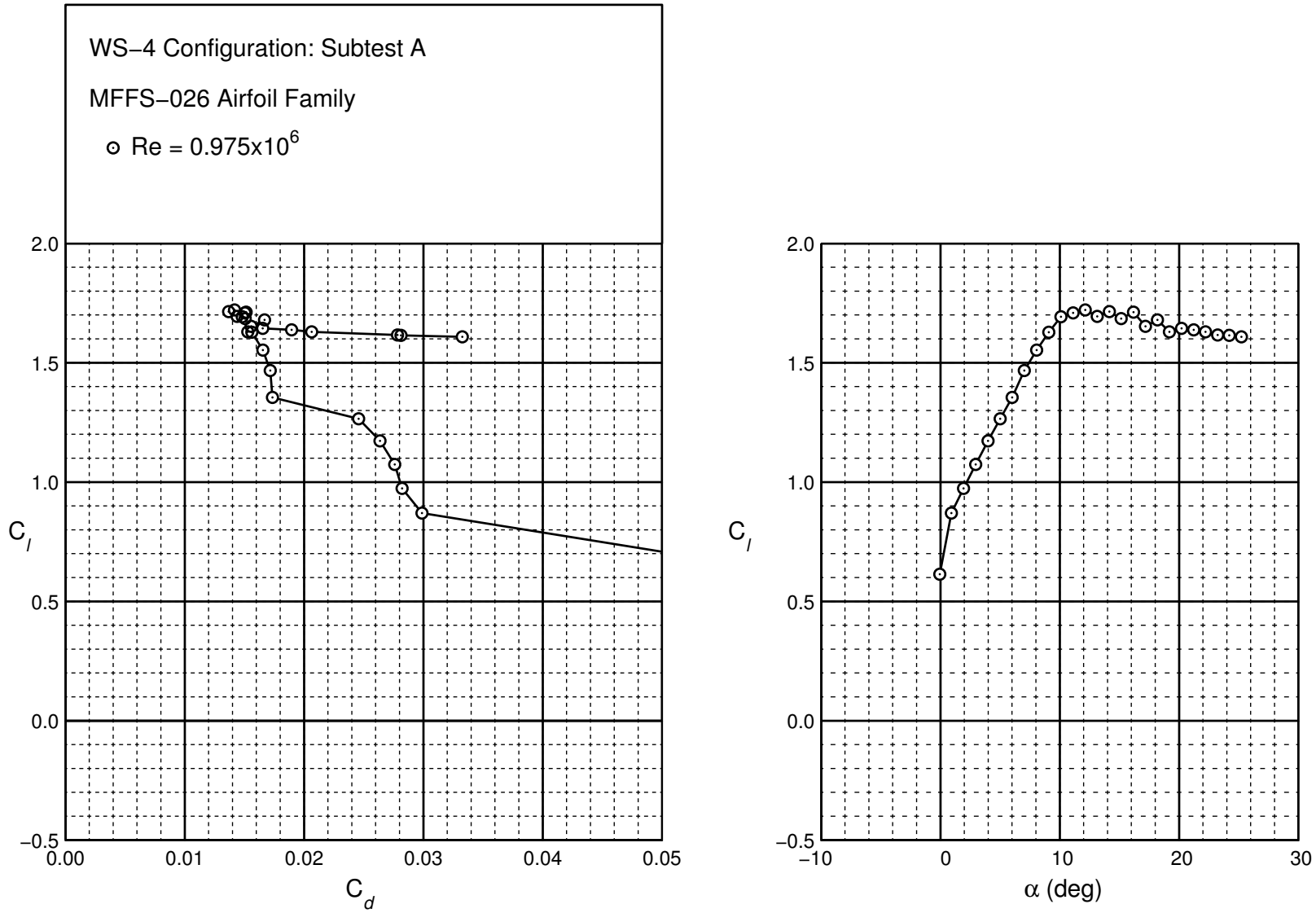

Figure B.95: WS-4 performance at $Re = 0.975 \times 10^6$.

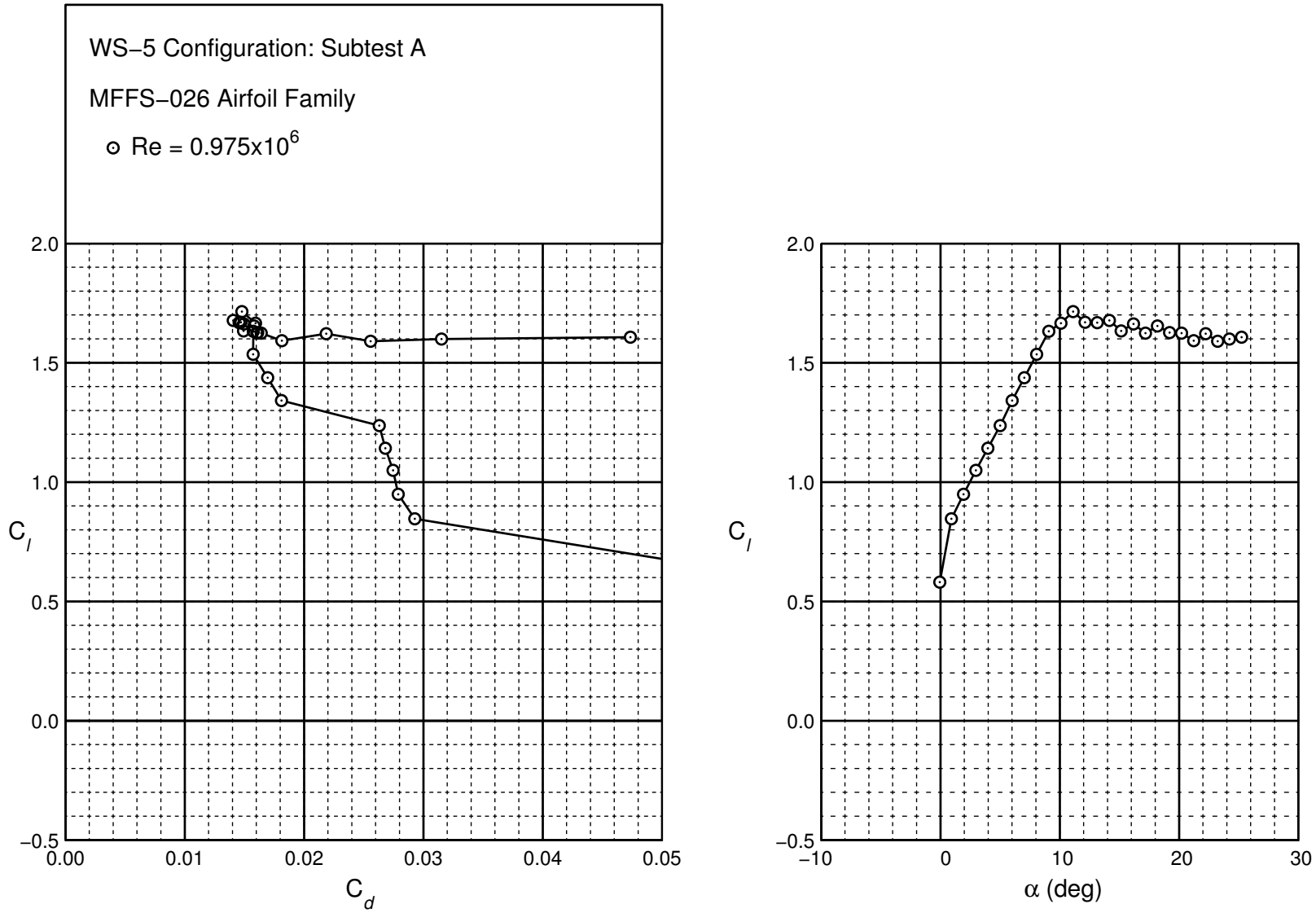

Figure B.96: WS-5 performance at $Re = 0.975 \times 10^6$.

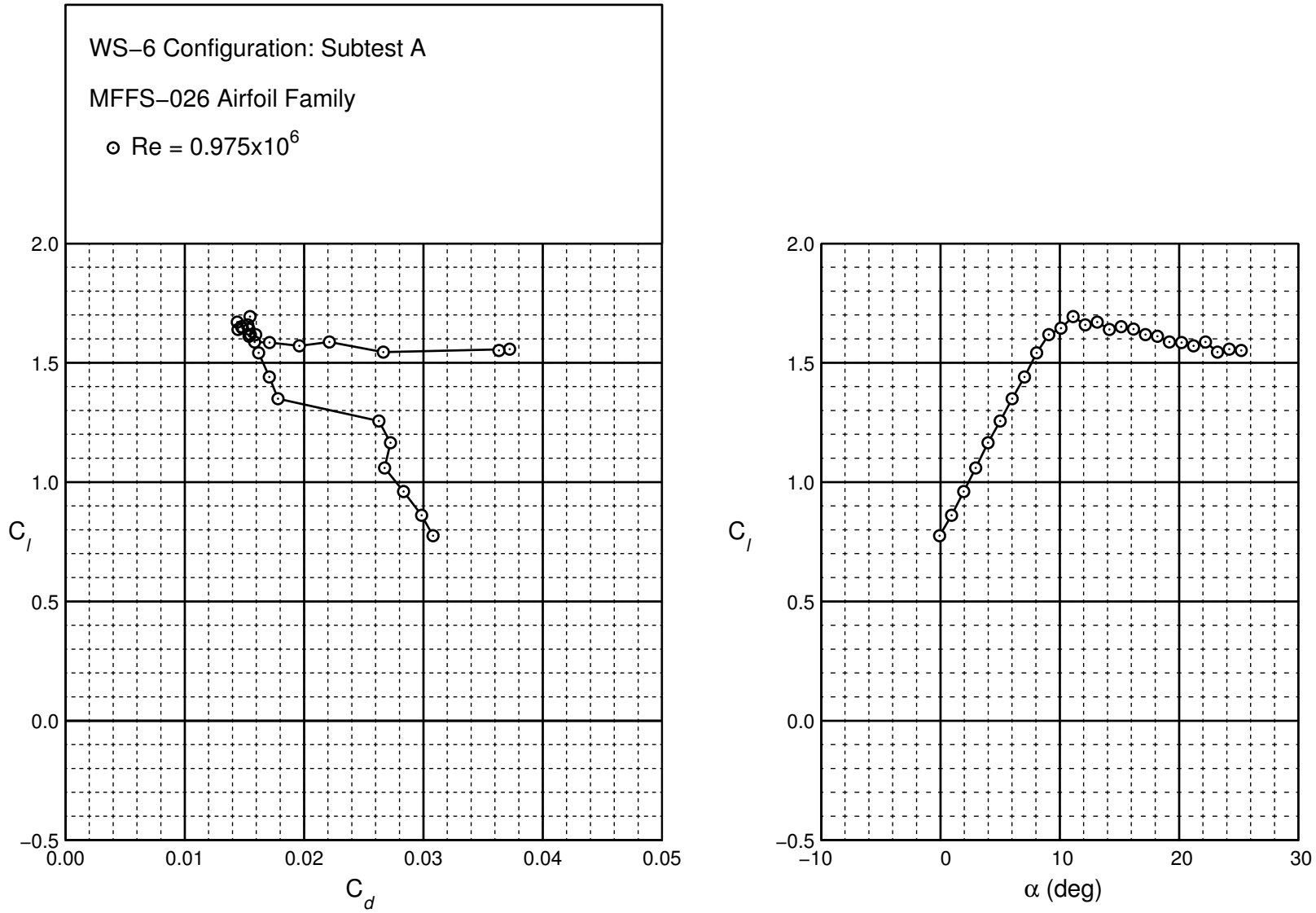

Figure B.97: WS-6 performance at $Re = 0.975 \times 10^6$.

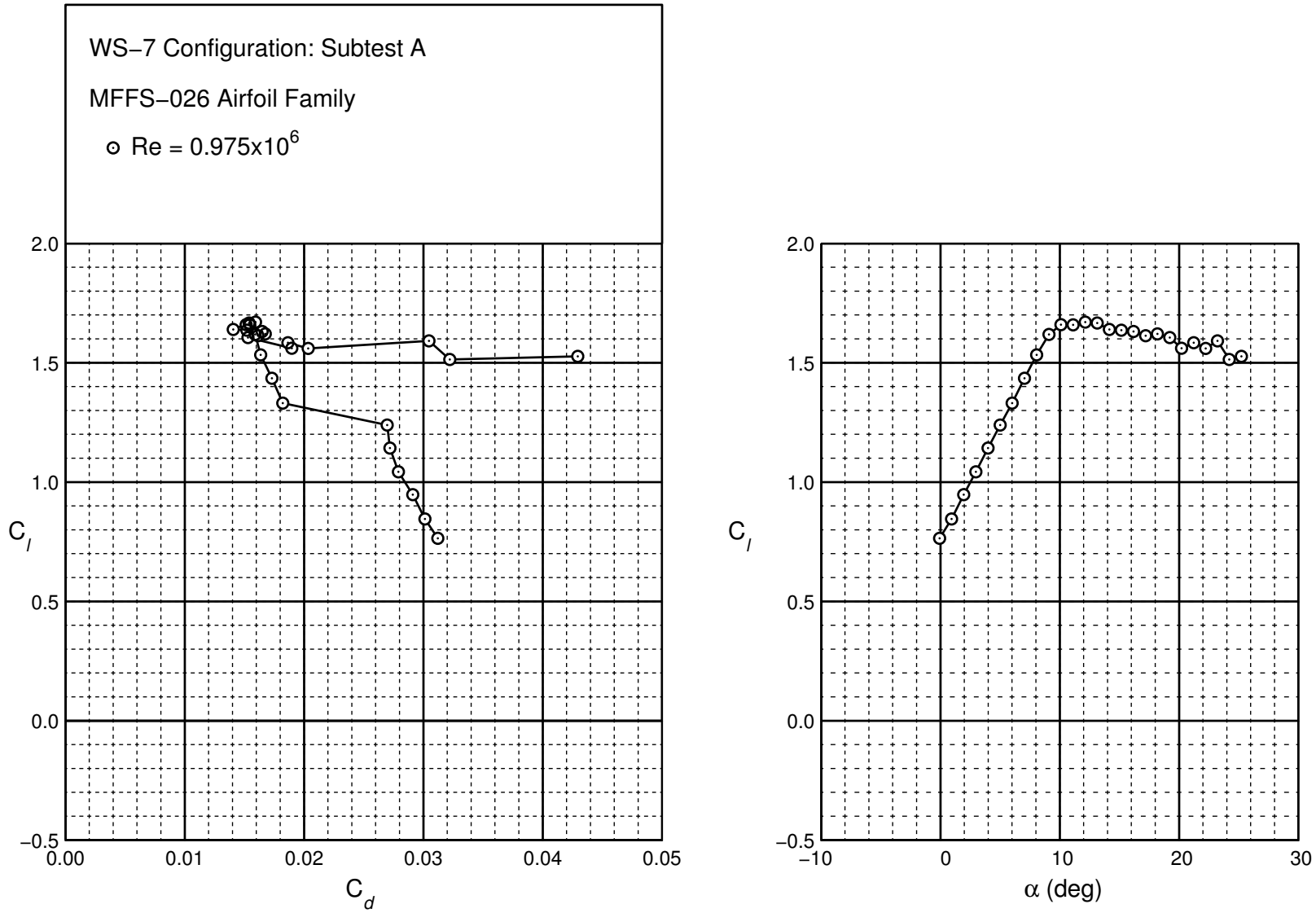

Figure B.98: WS-7 performance at $Re = 0.975 \times 10^6$.

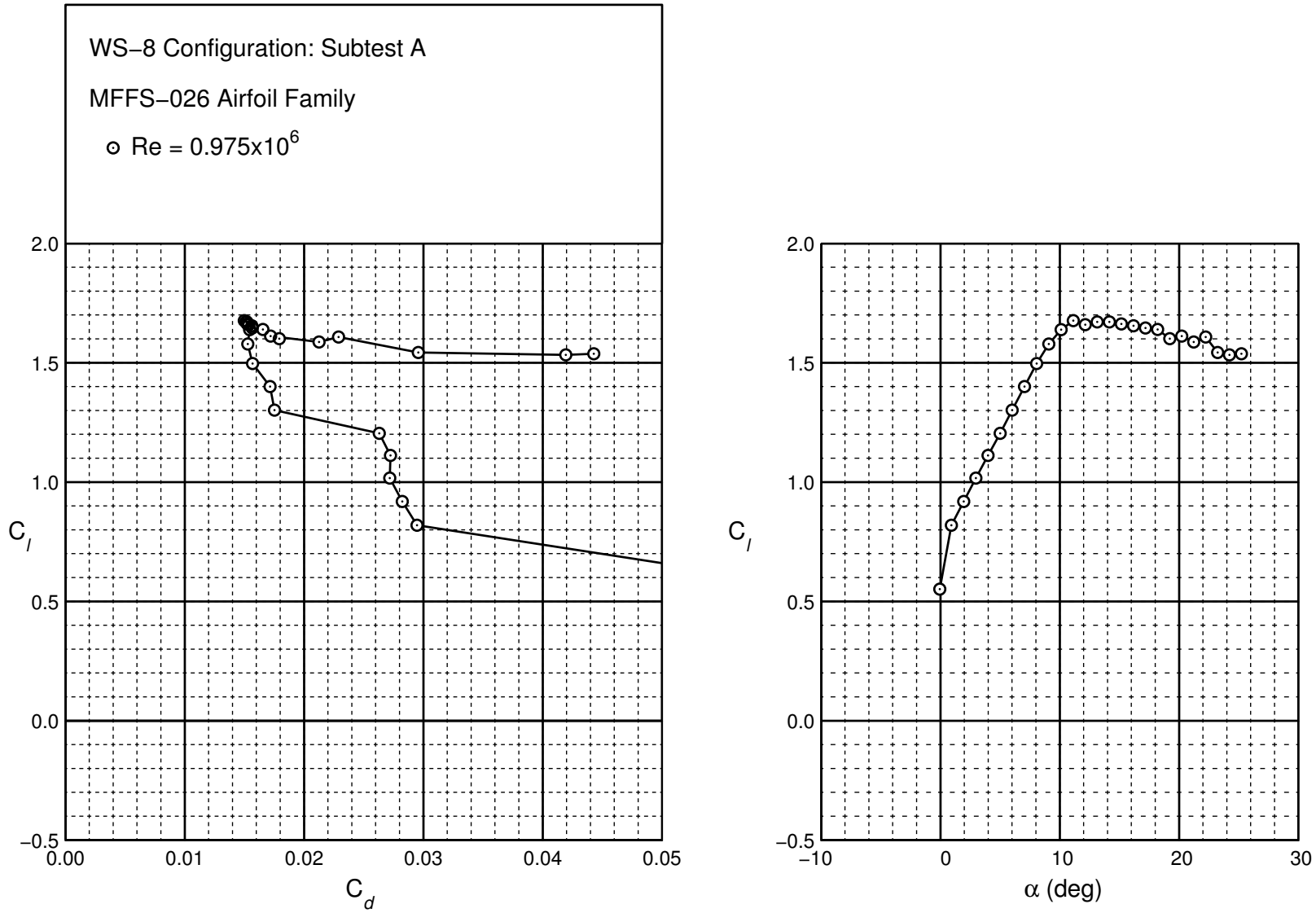

Figure B.99: WS-8 performance at $Re = 0.975 \times 10^6$.

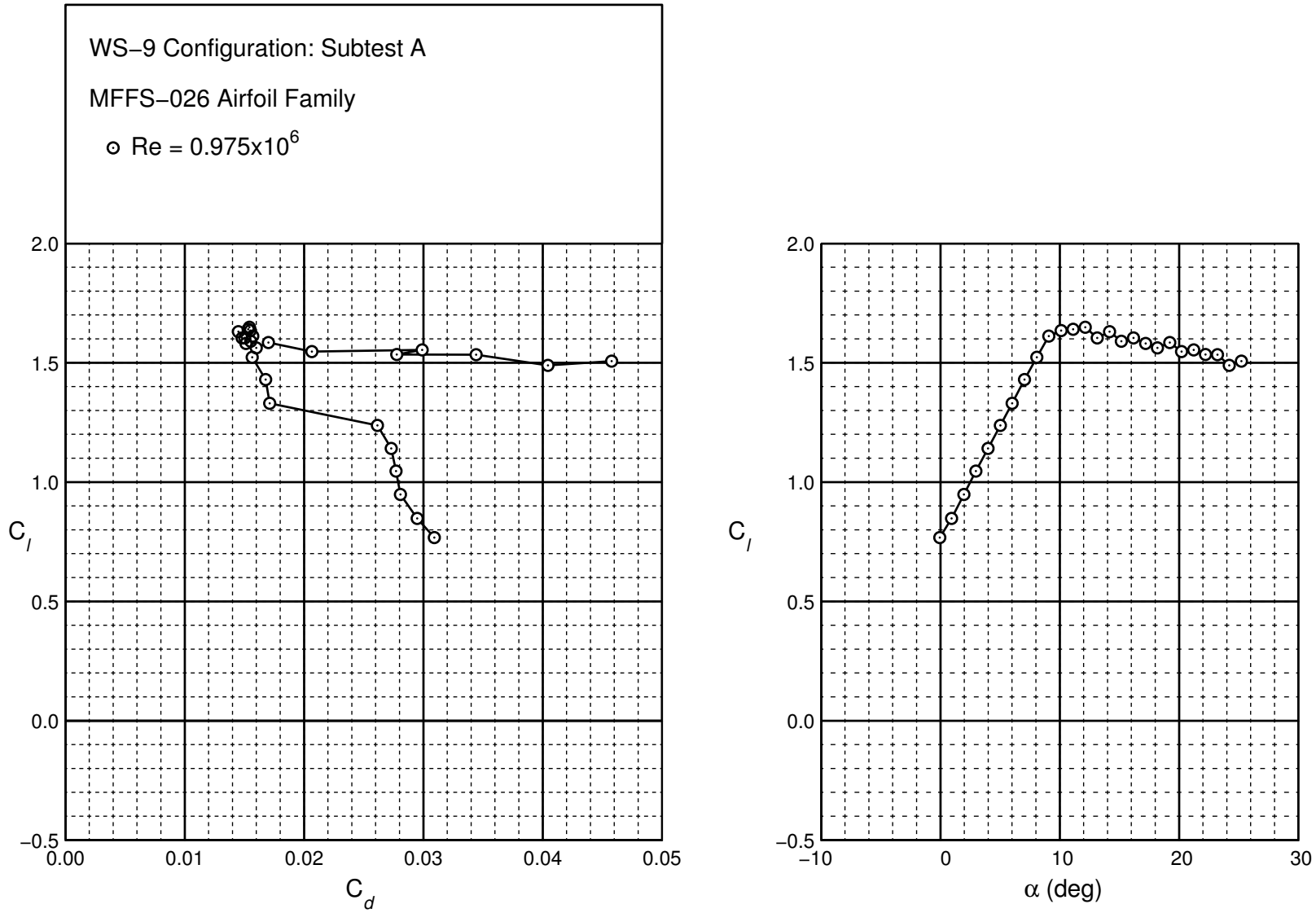

Figure B.100: WS-9 performance at $Re = 0.975 \times 10^6$.

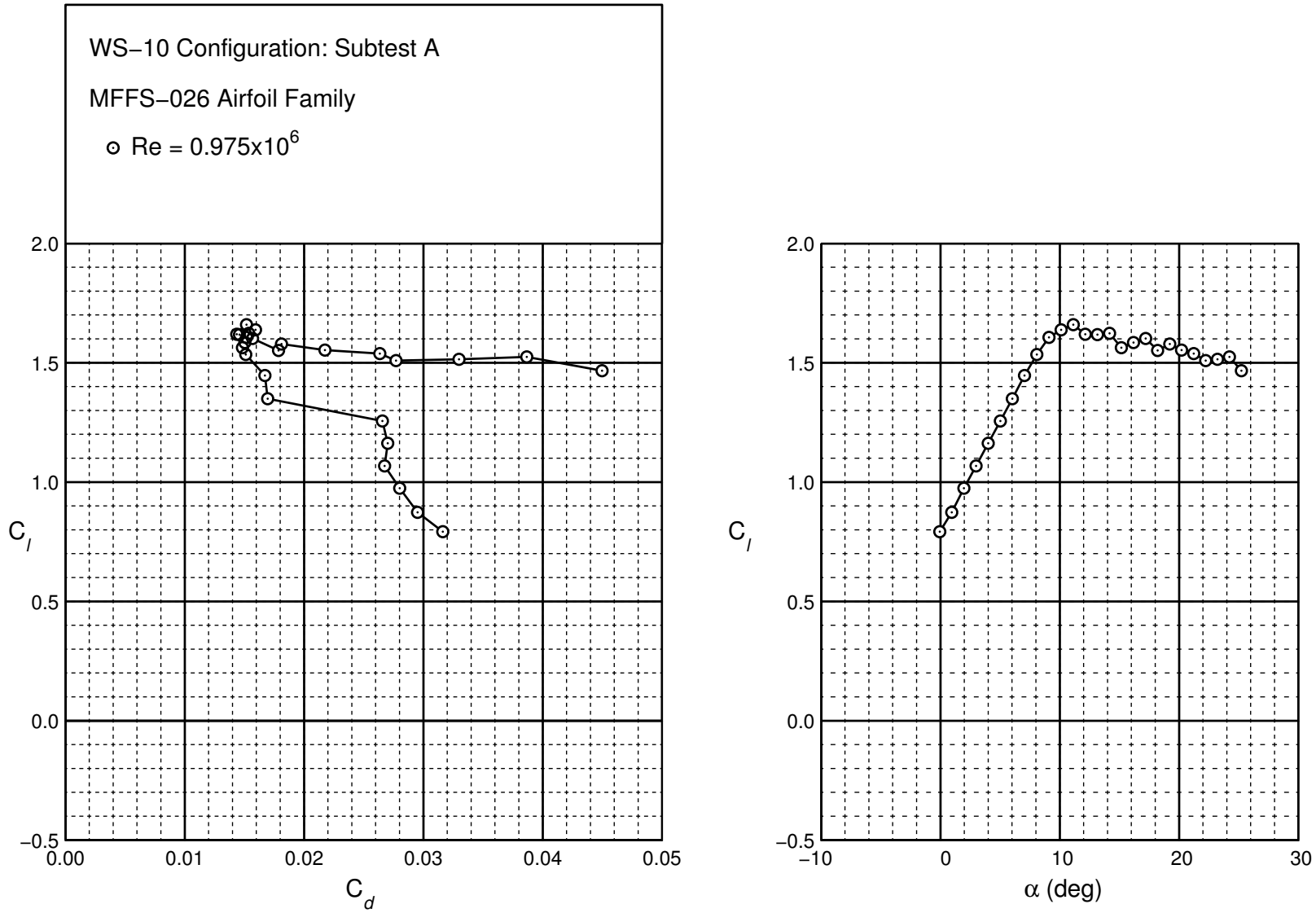

Figure B.101: WS-10 performance at $Re = 0.975 \times 10^6$.

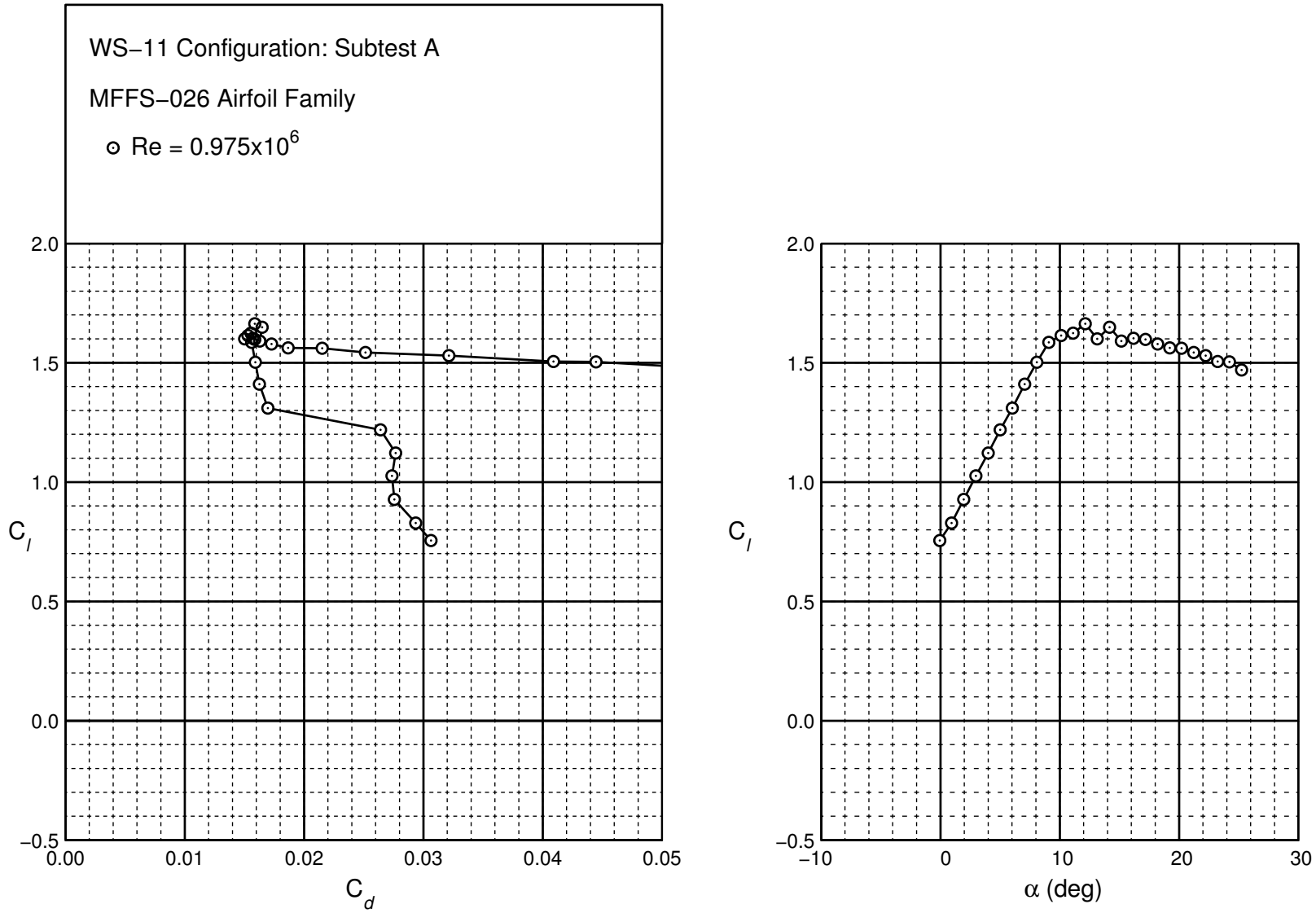

Figure B.102: WS-11 performance at $Re = 0.975 \times 10^6$.

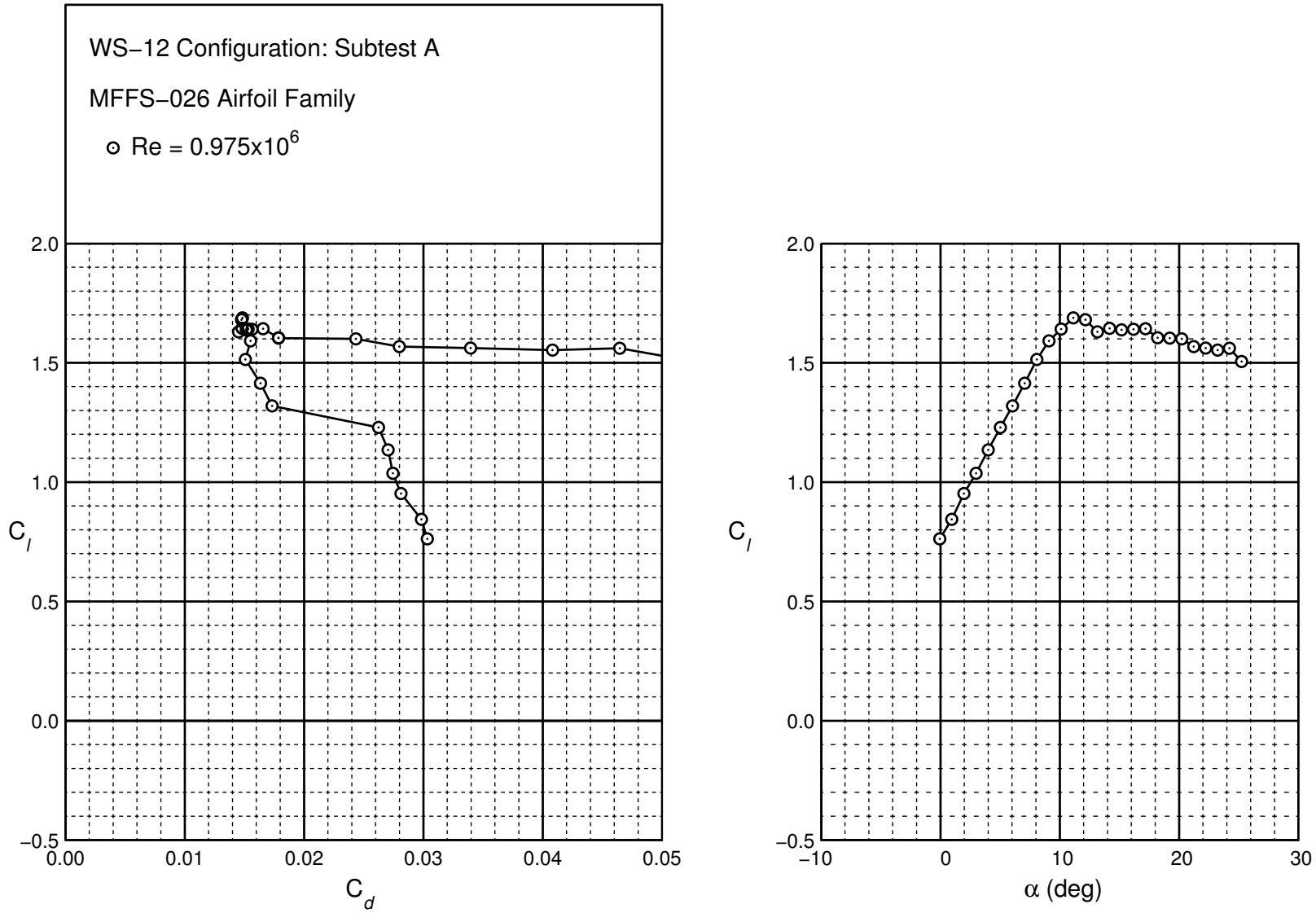

Figure B.103: WS-12 performance at $Re = 0.975 \times 10^6$.

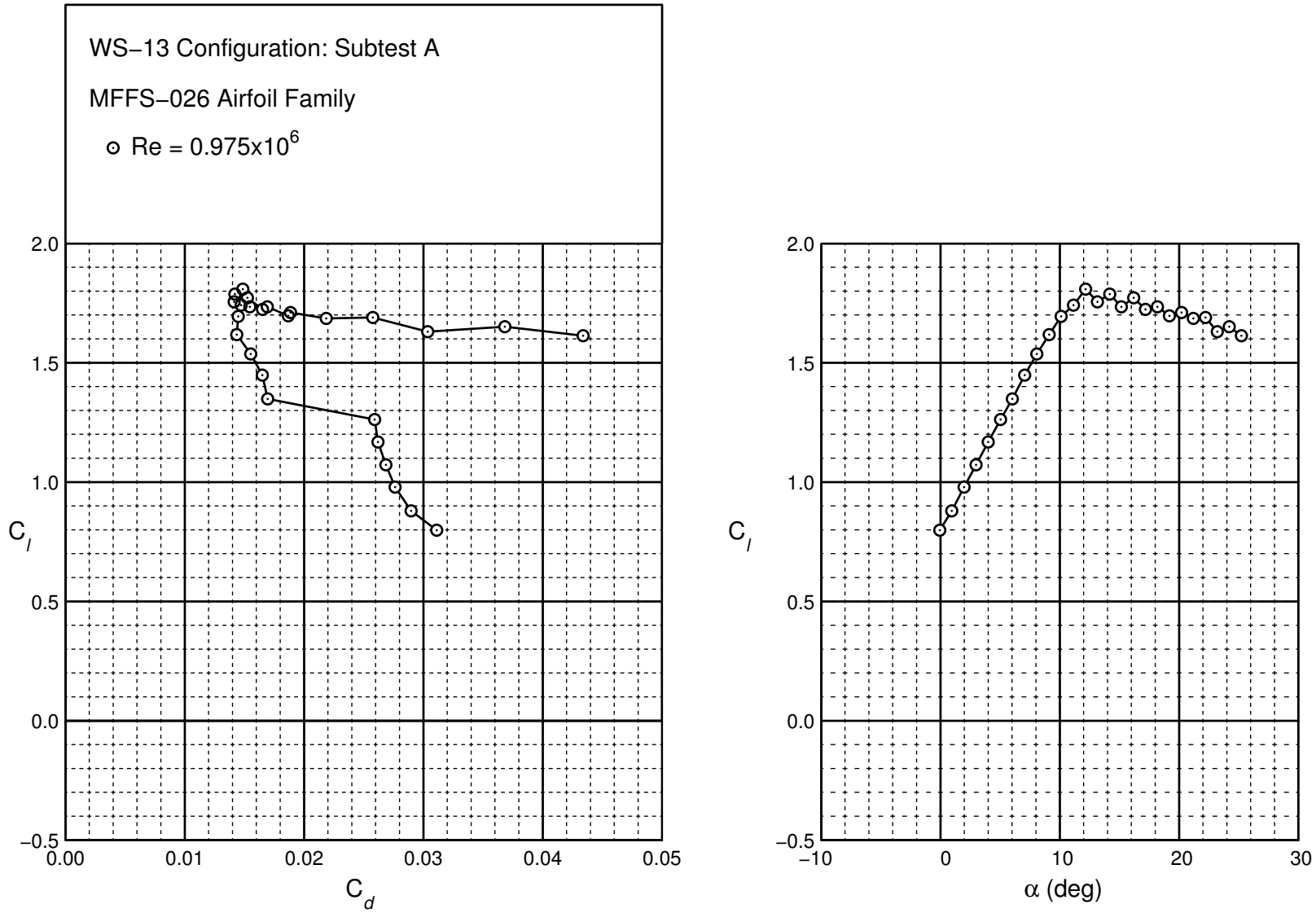

Figure B.104: WS-13 performance at $Re = 0.975 \times 10^6$.

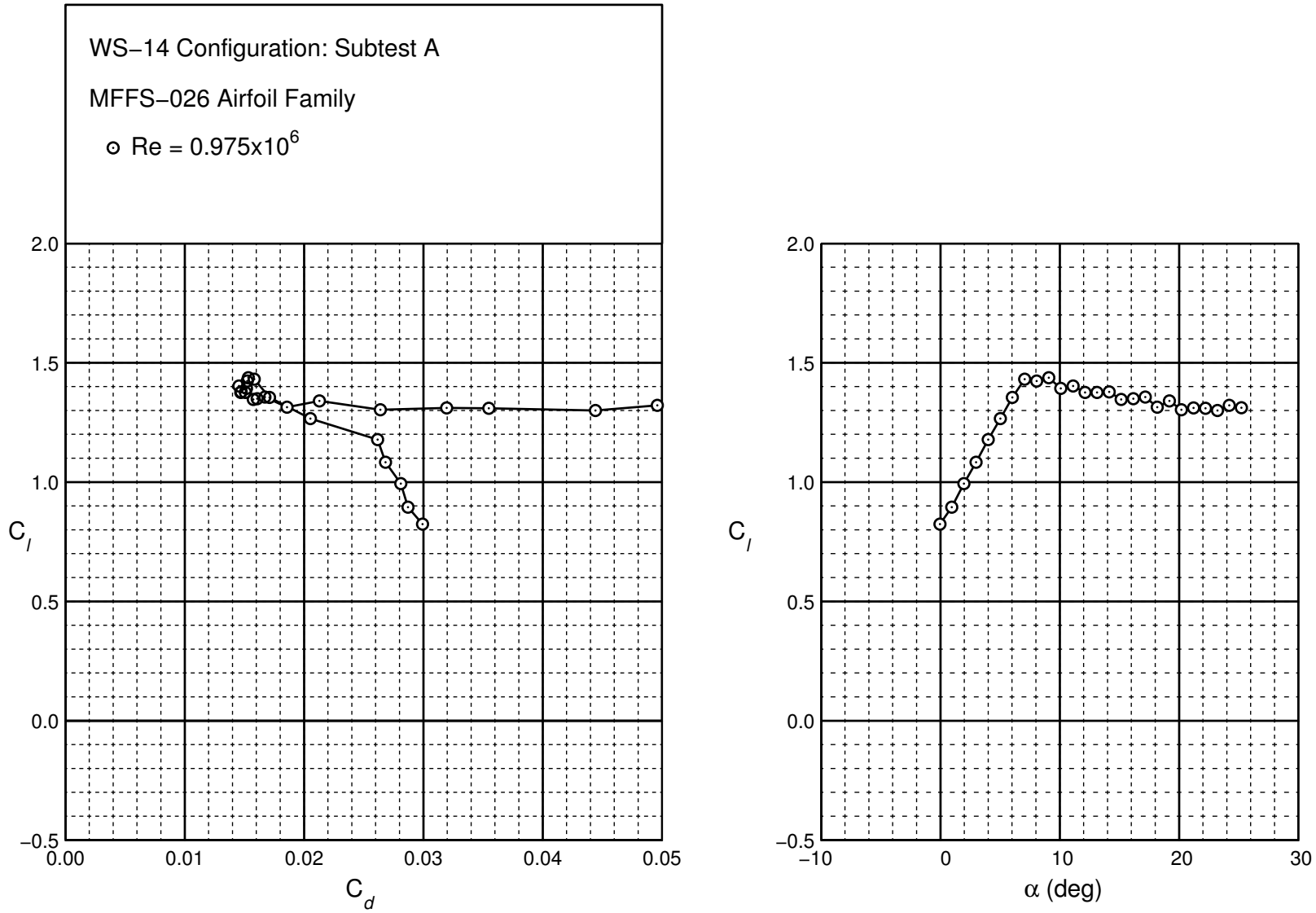

Figure B.105: WS-14 performance at $Re = 0.975 \times 10^6$.

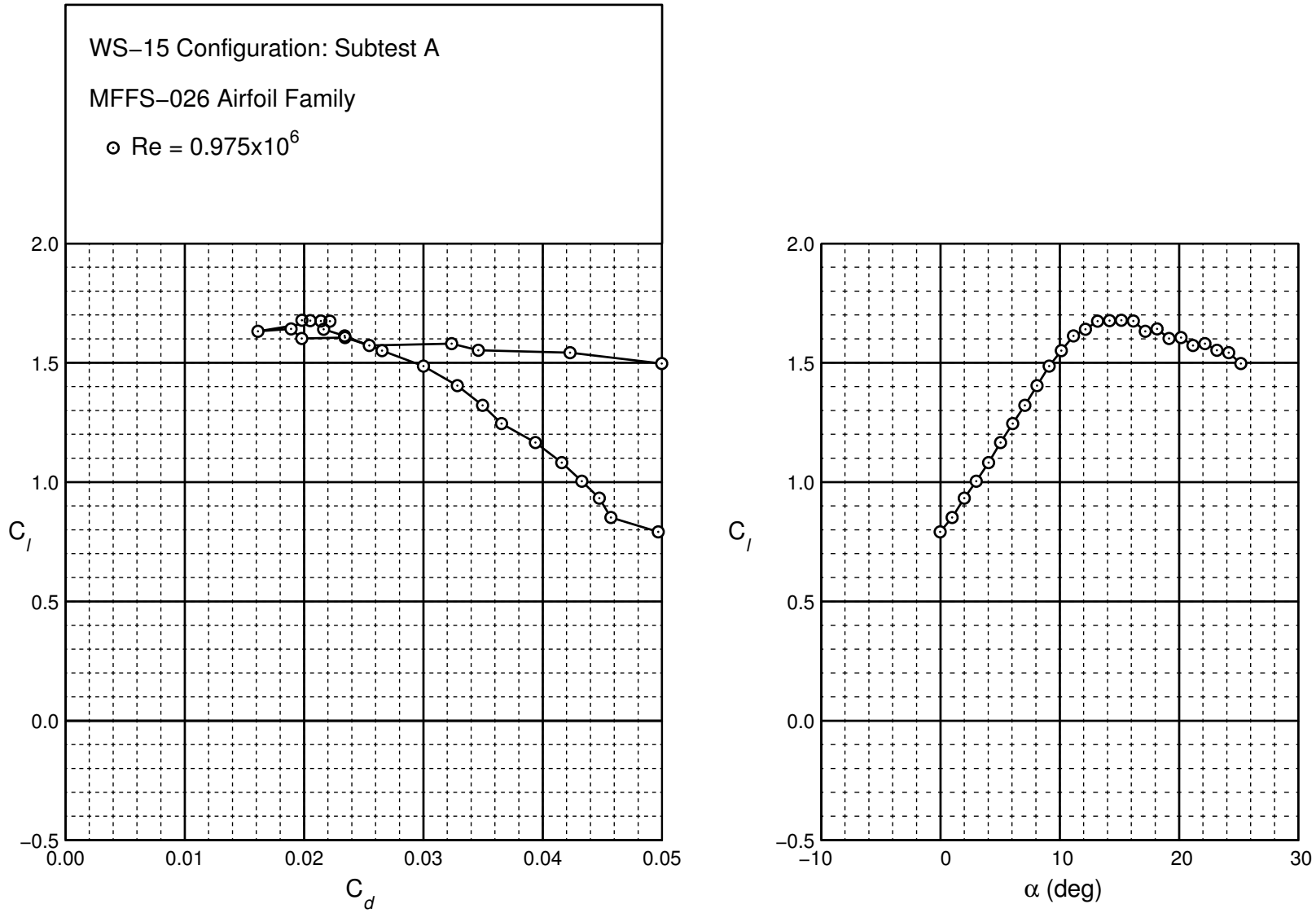

Figure B.106: WS-15 performance at $Re = 0.975 \times 10^6$.

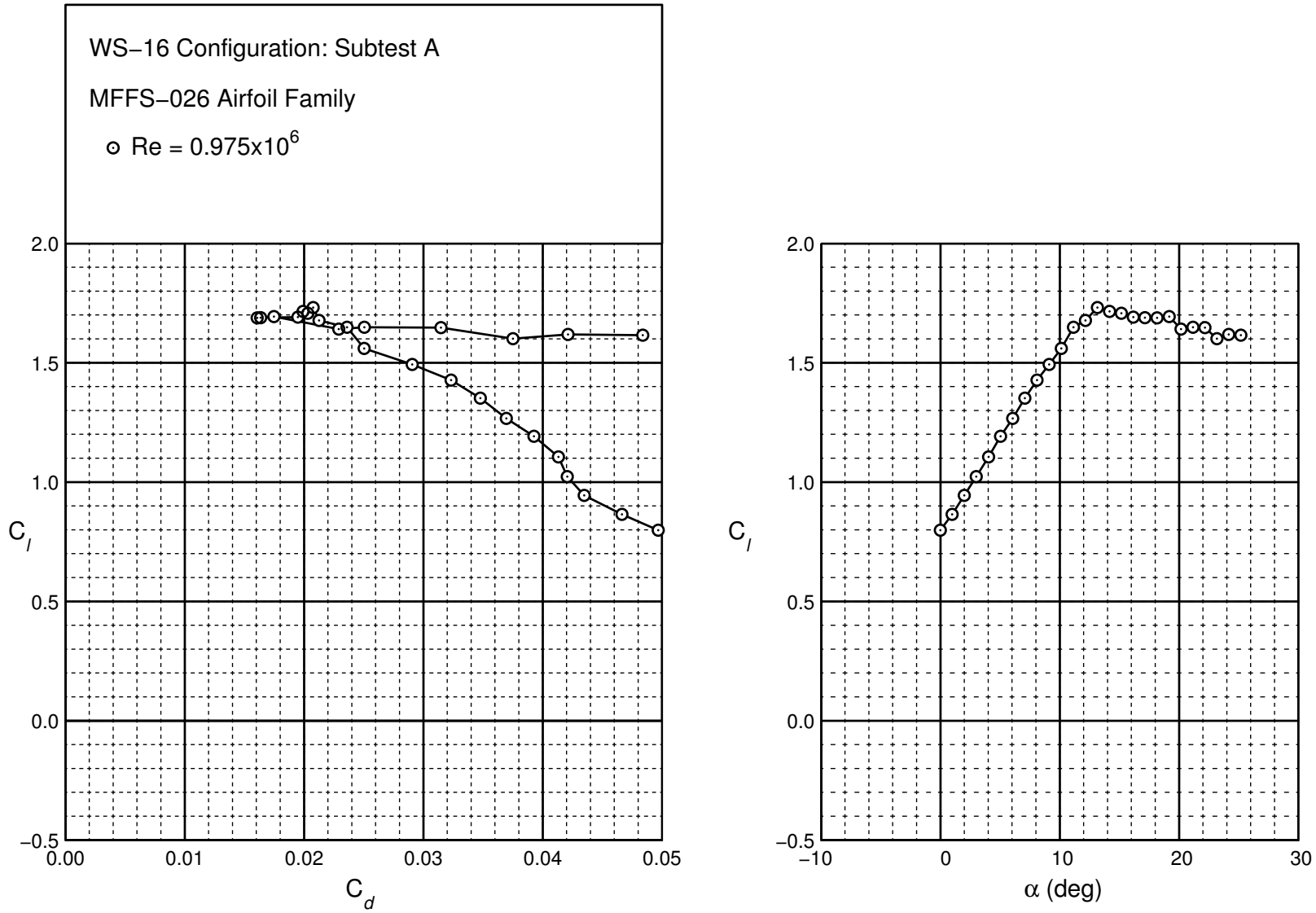

Figure B.107: WS-16 performance at $Re = 0.975 \times 10^6$.

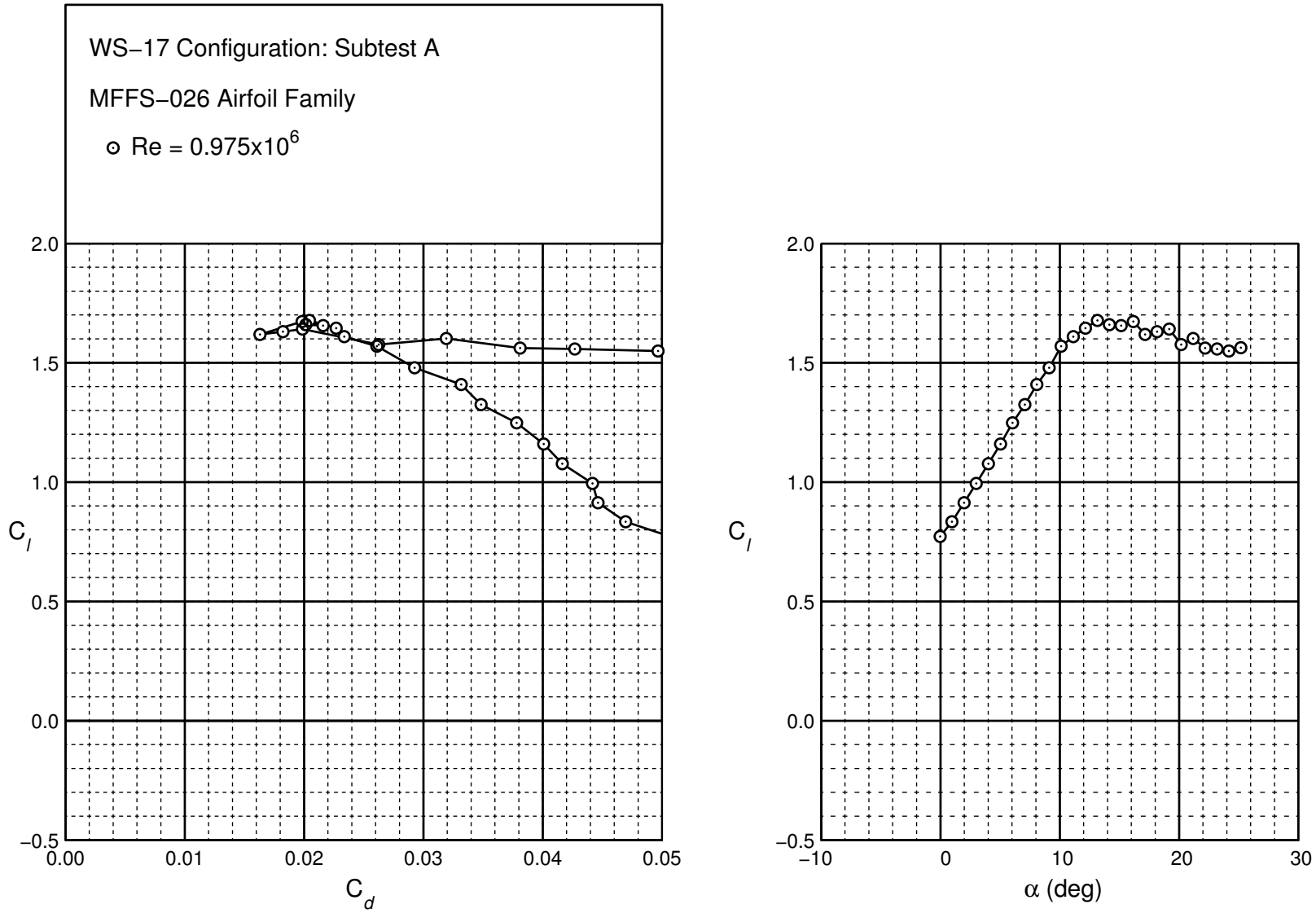

Figure B.108: WS-17 performance at $Re = 0.975 \times 10^6$.

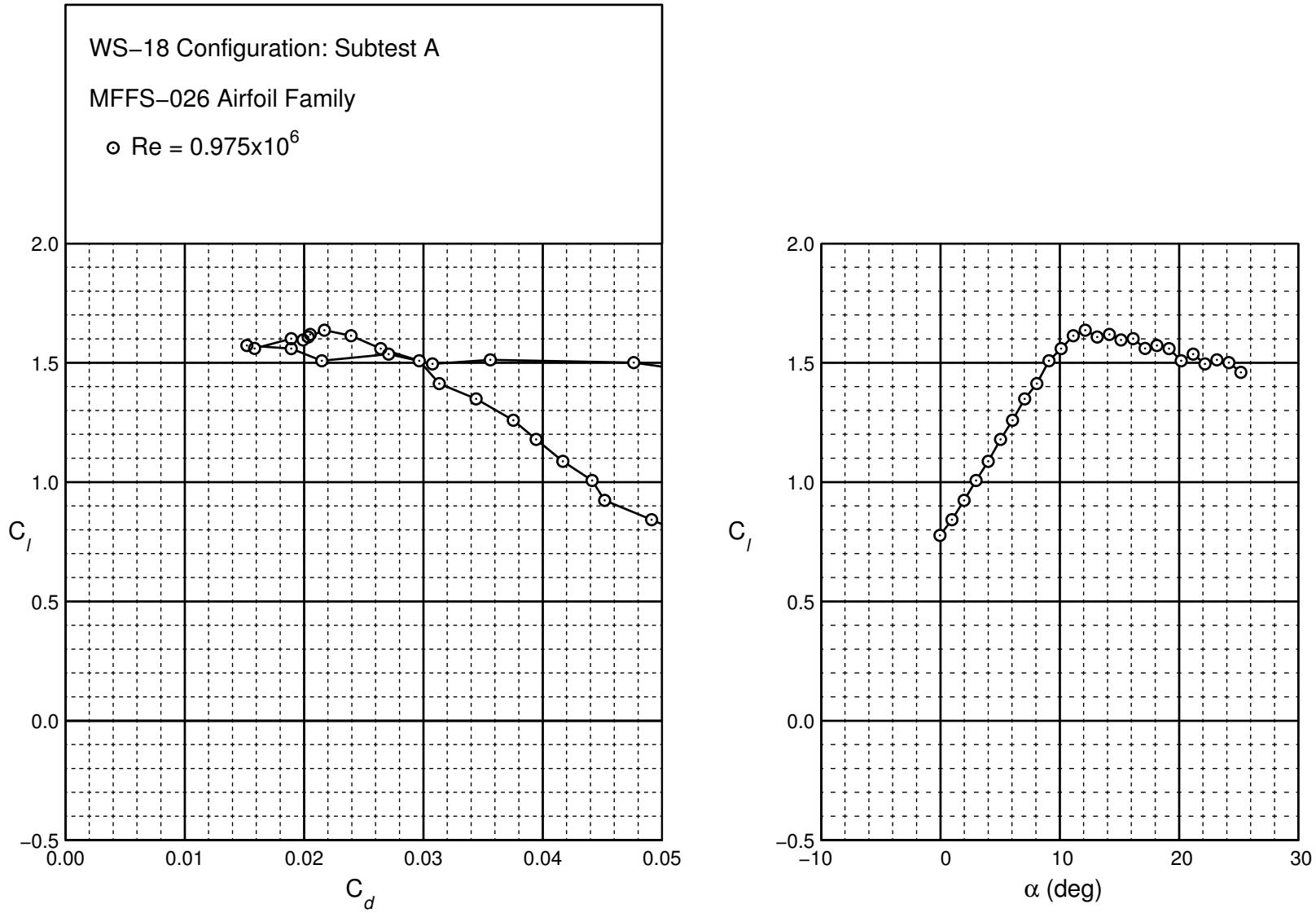

Figure B.109: WS-18 performance at $Re = 0.975 \times 10^6$.

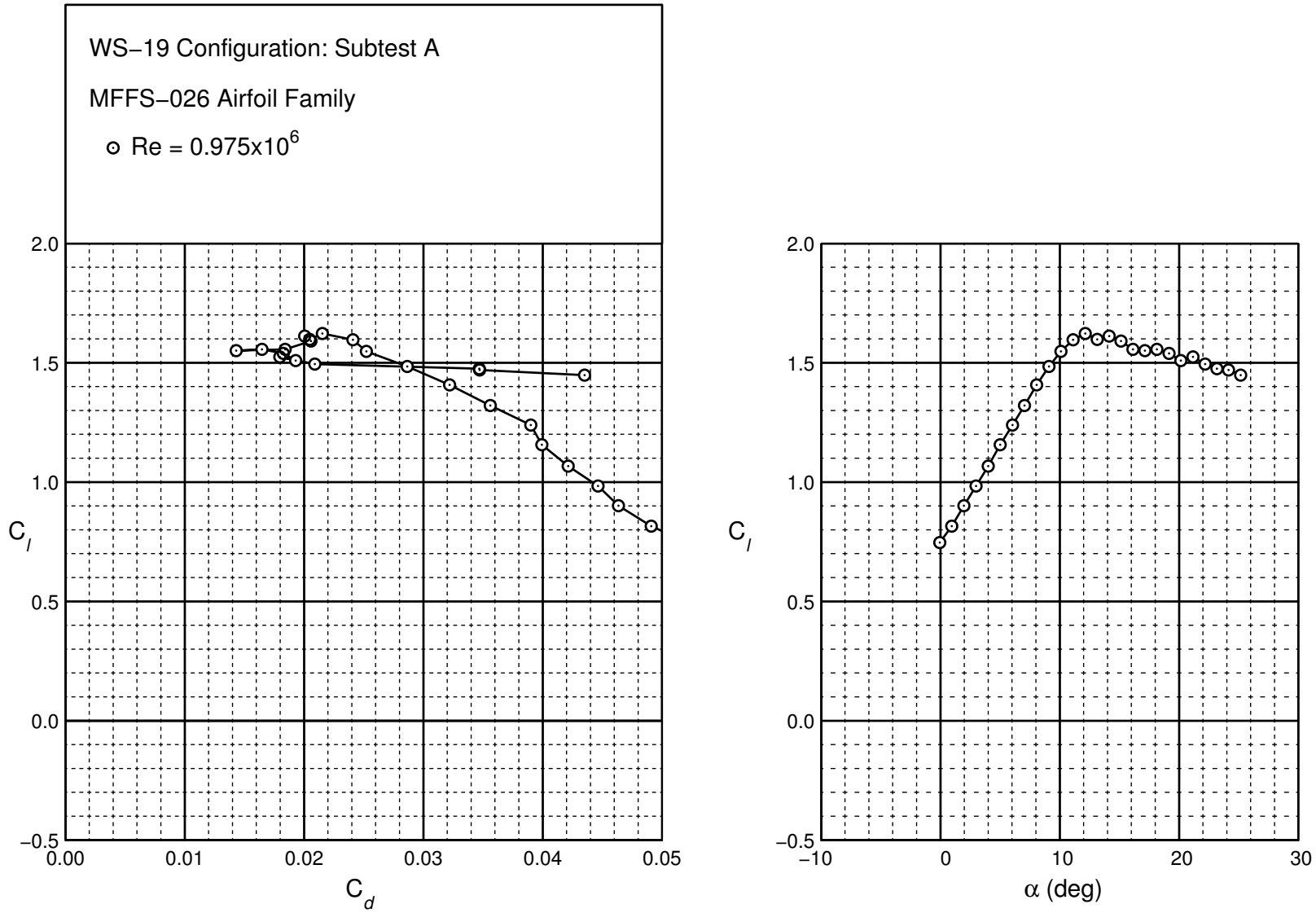

Figure B.110: WS-19 performance at $Re = 0.975 \times 10^6$.

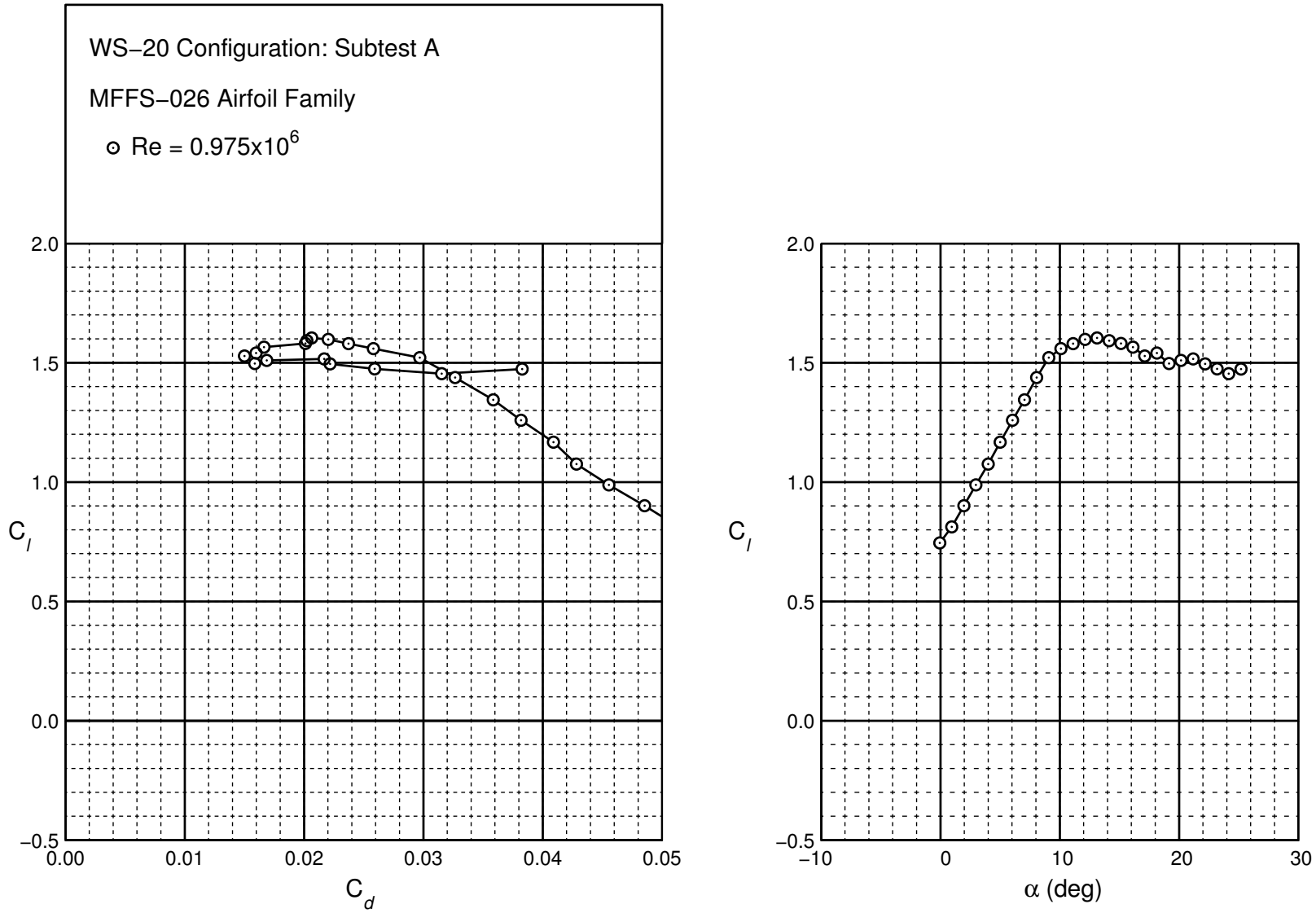

Figure B.111: WS-20 performance at $Re = 0.975 \times 10^6$.

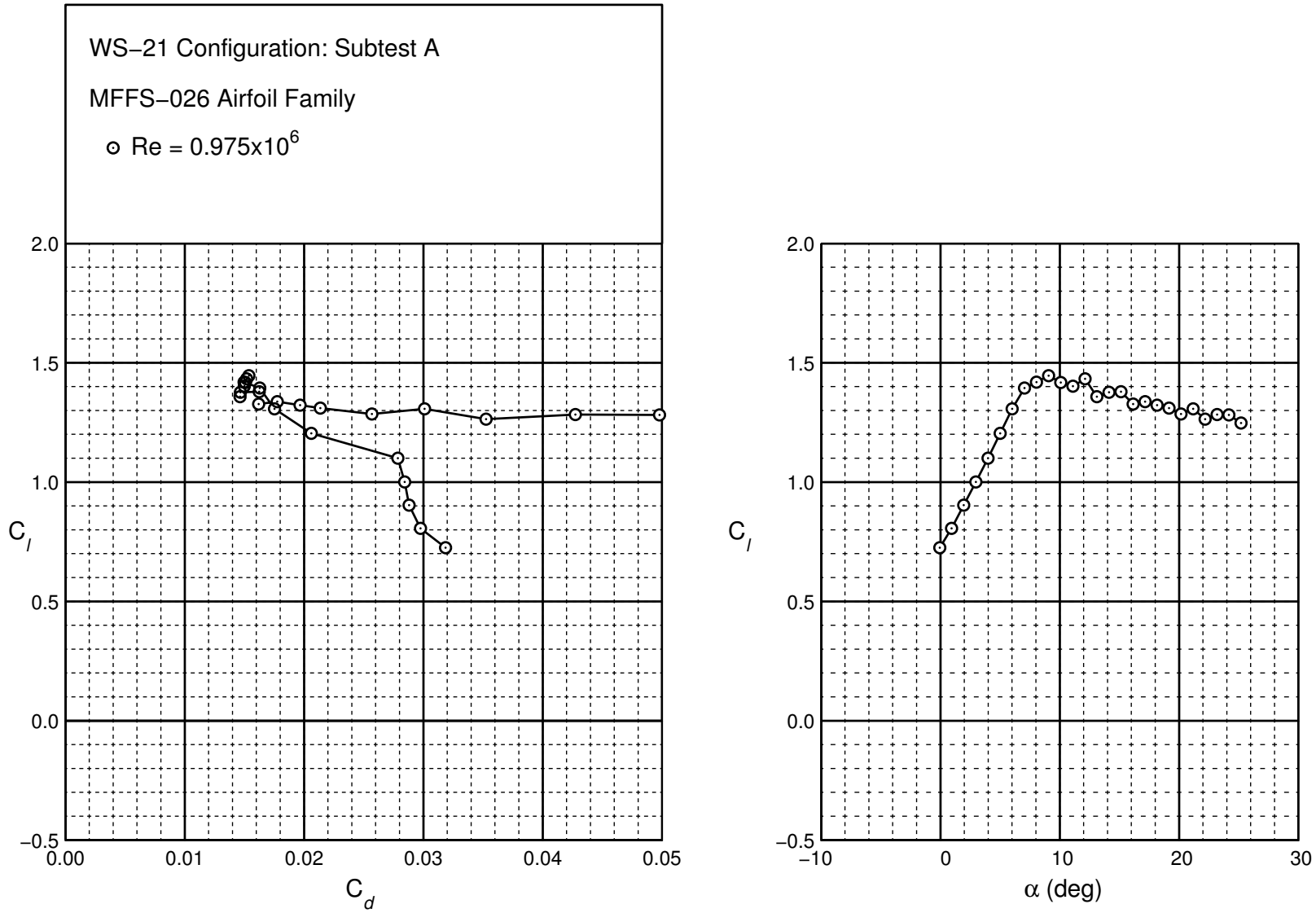

Figure B.112: WS-21 performance at $Re = 0.975 \times 10^6$.

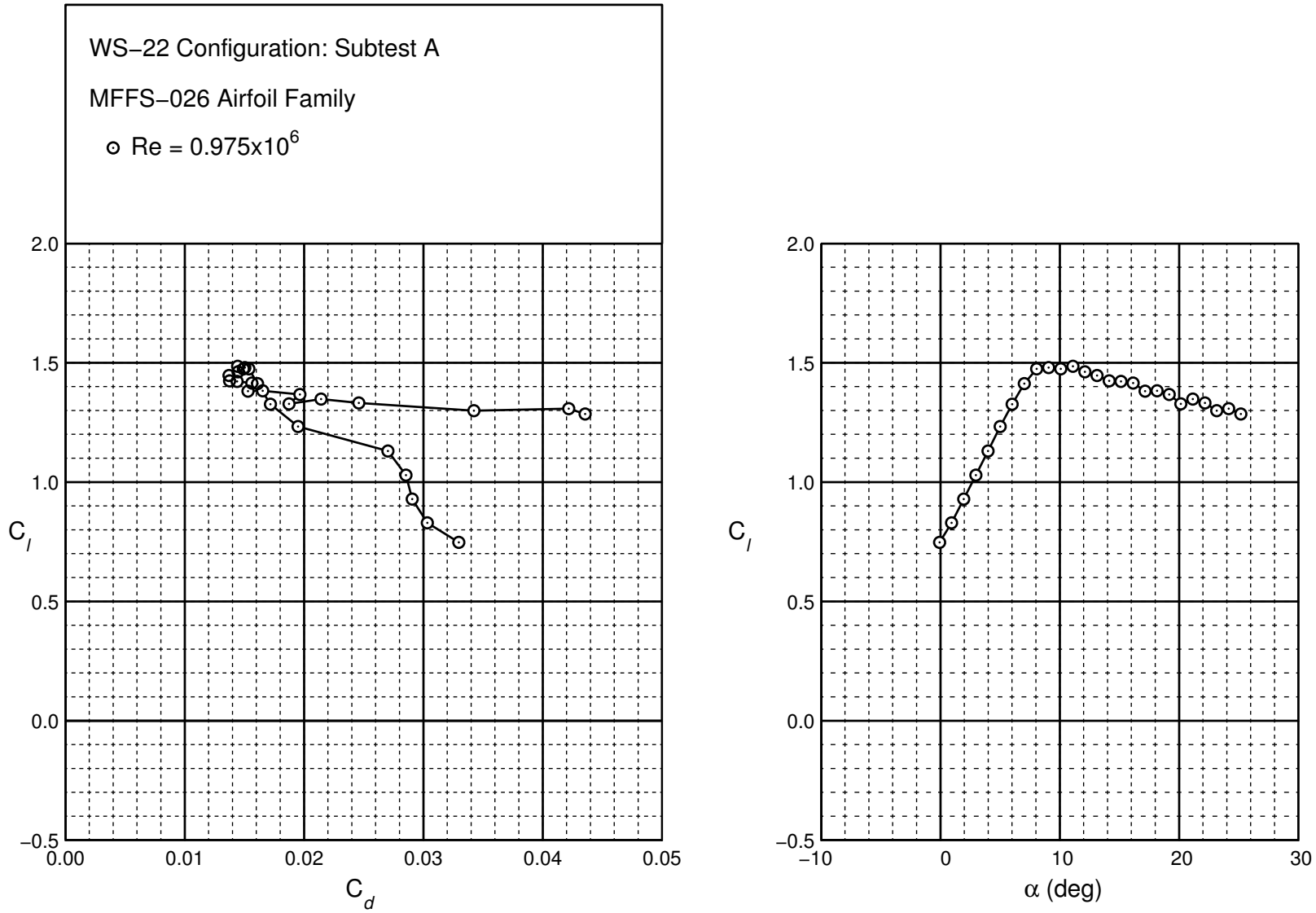

Figure B.113: WS-22 performance at $Re = 0.975 \times 10^6$.

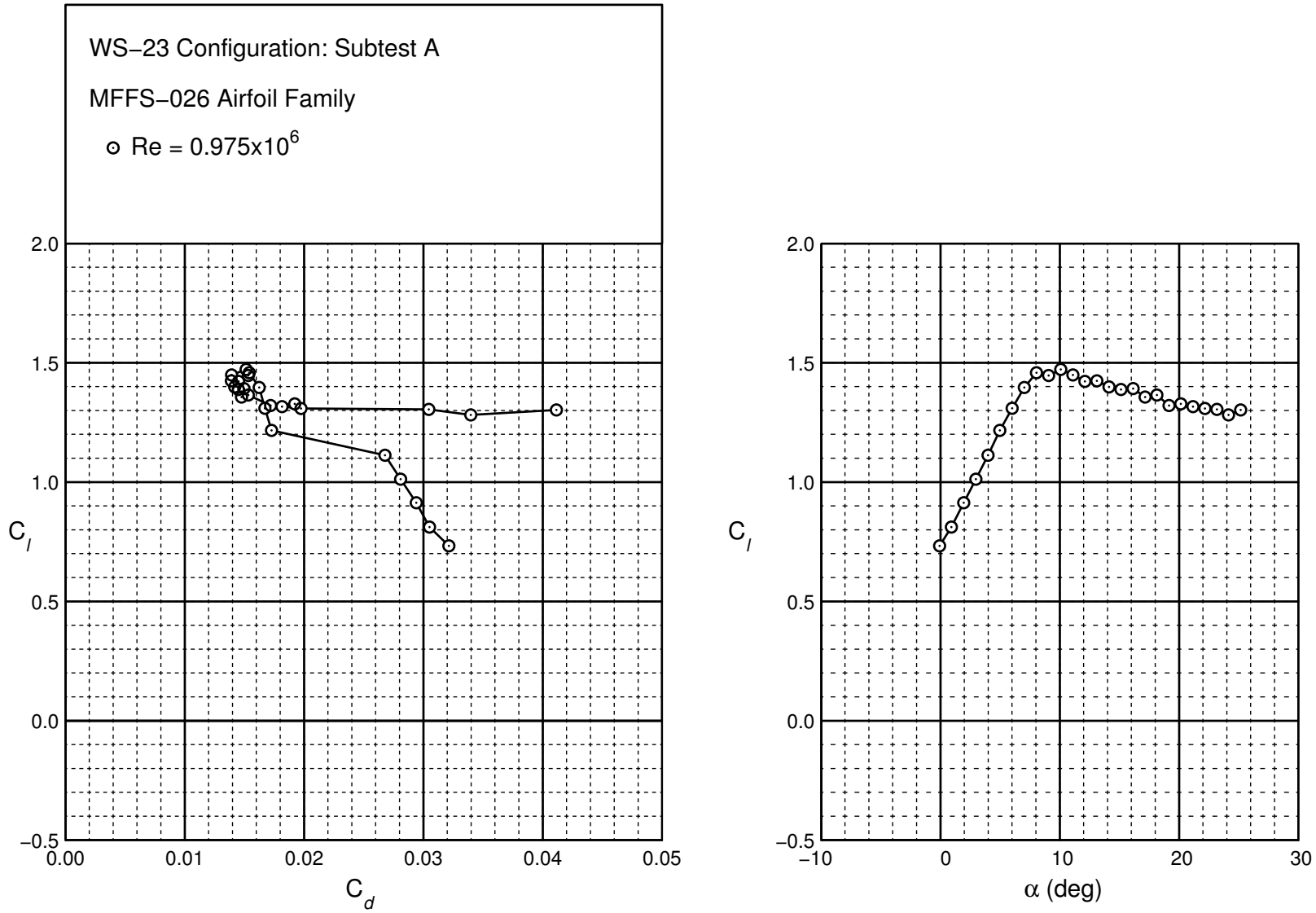

Figure B.114: WS-23 performance at $Re = 0.975 \times 10^6$.

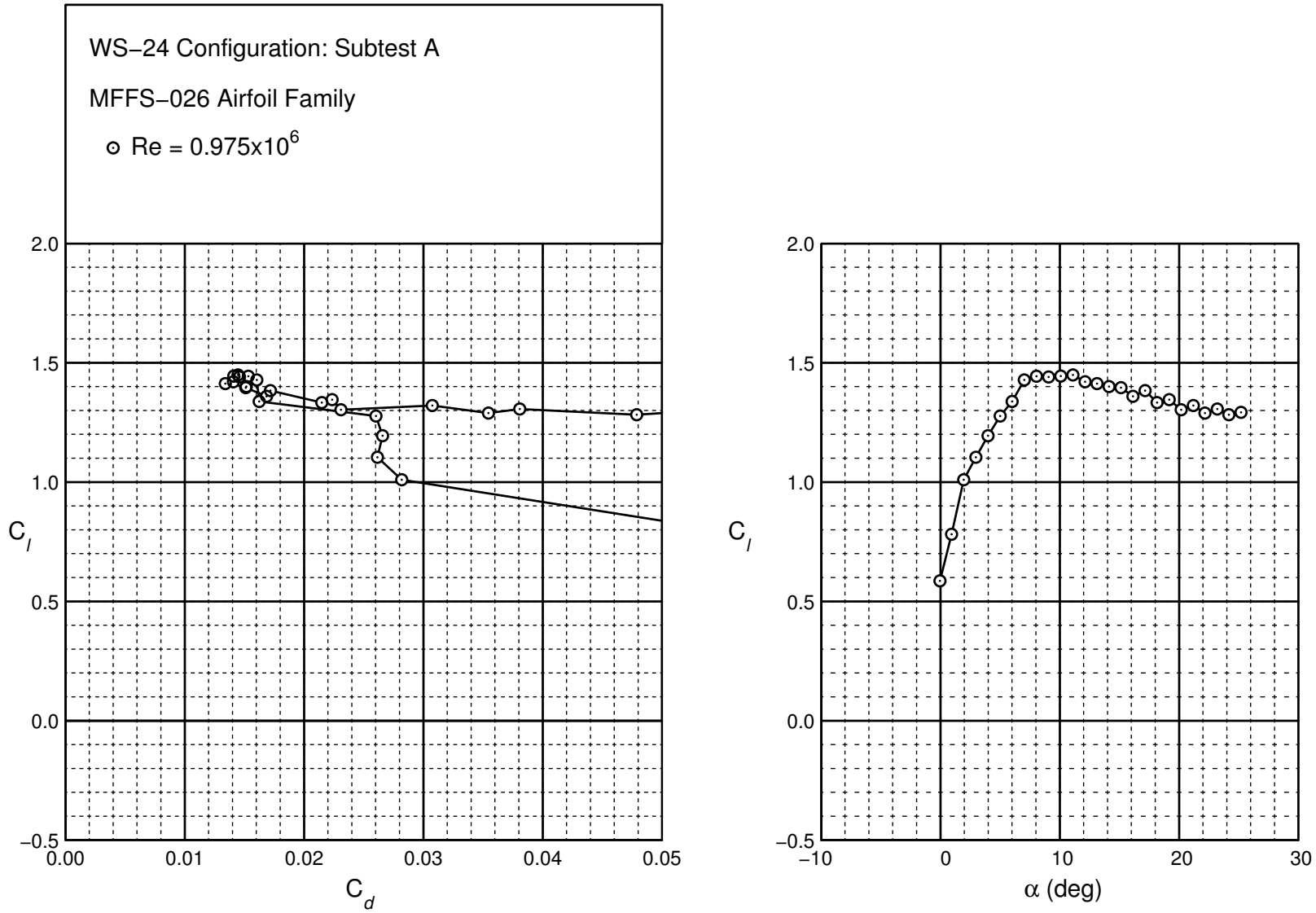

Figure B.115: WS-24 performance at $Re = 0.975 \times 10^6$.

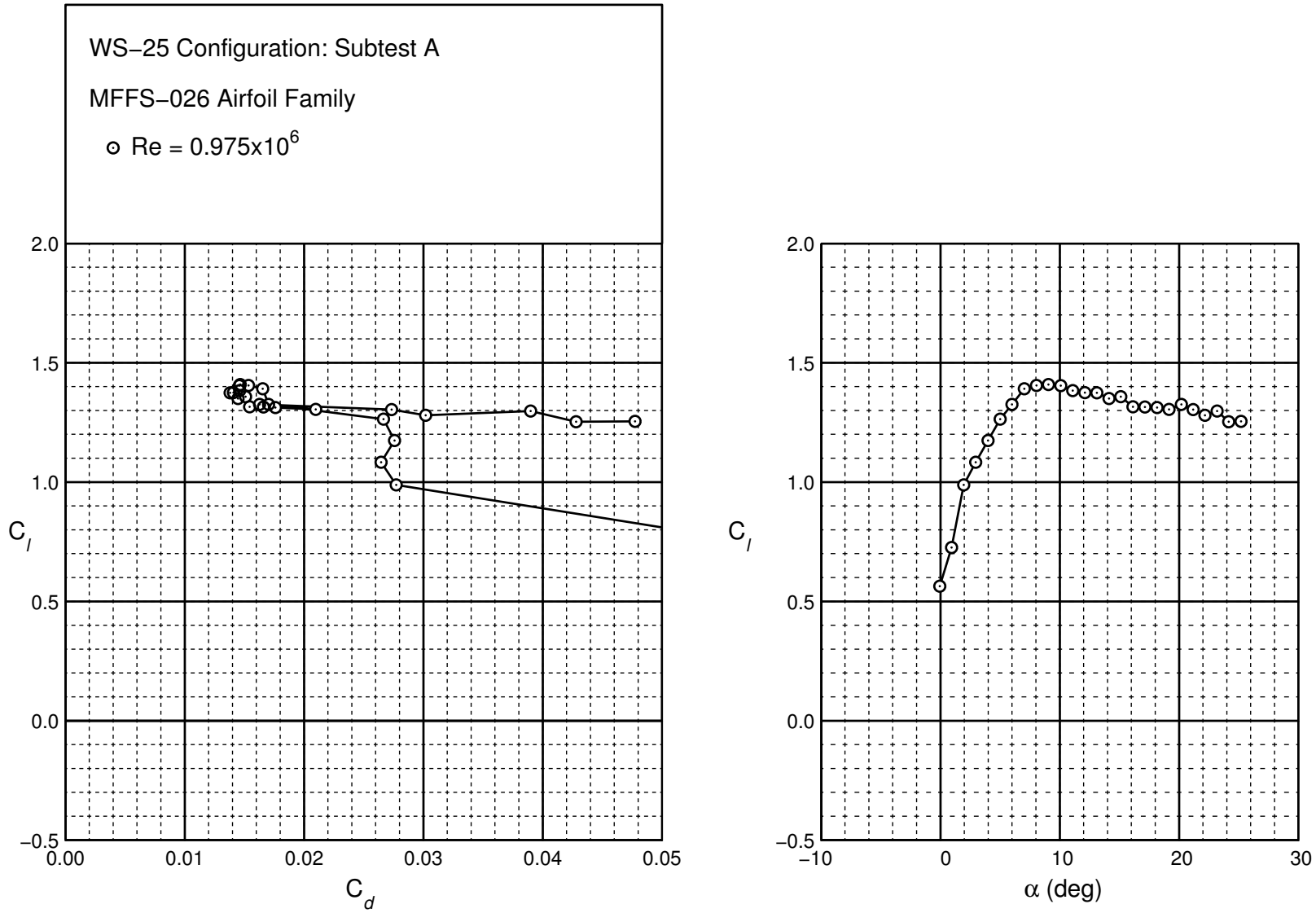

Figure B.116: WS-25 performance at $Re = 0.975 \times 10^6$.

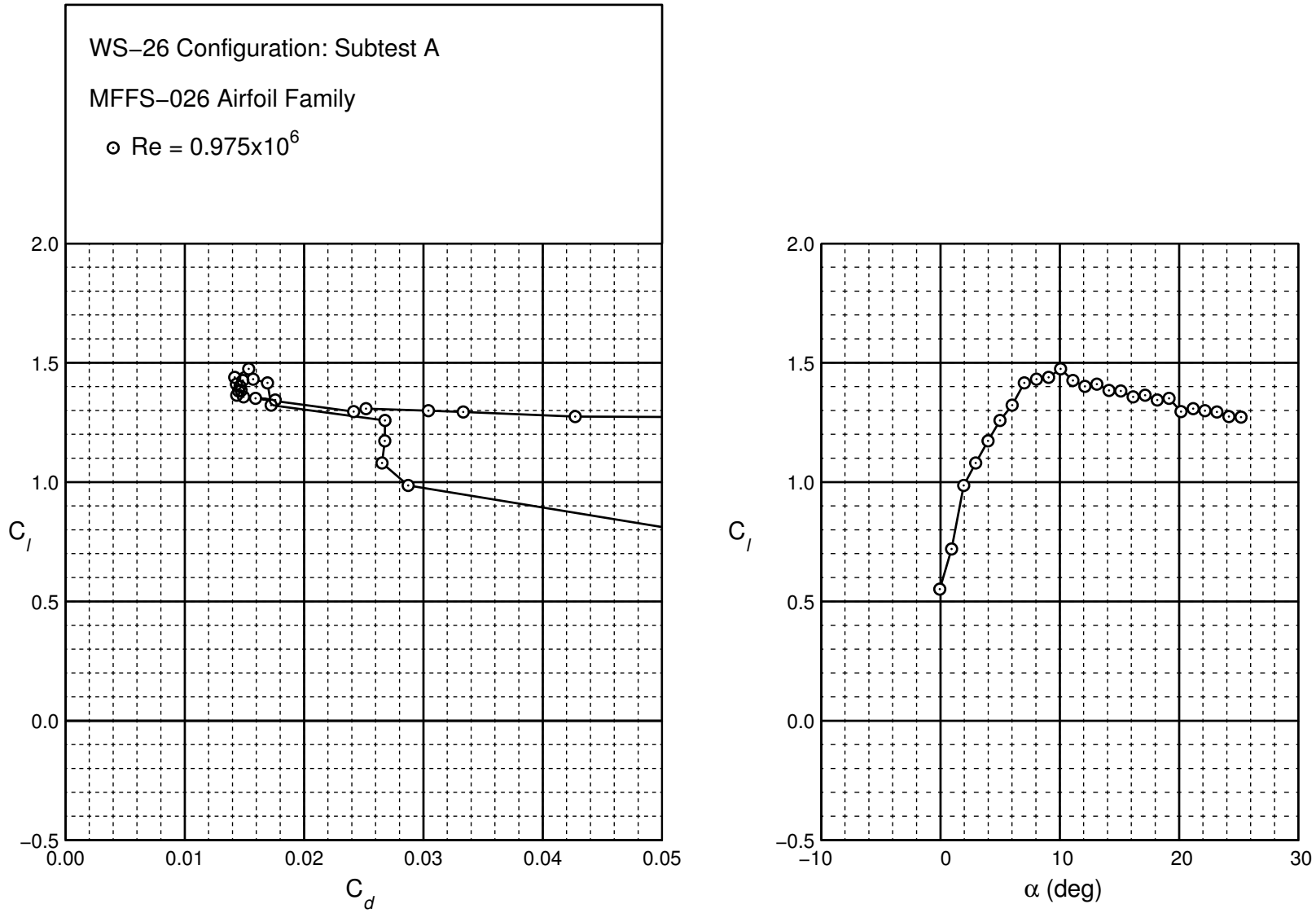

Figure B.117: WS-26 performance at $Re = 0.975 \times 10^6$.

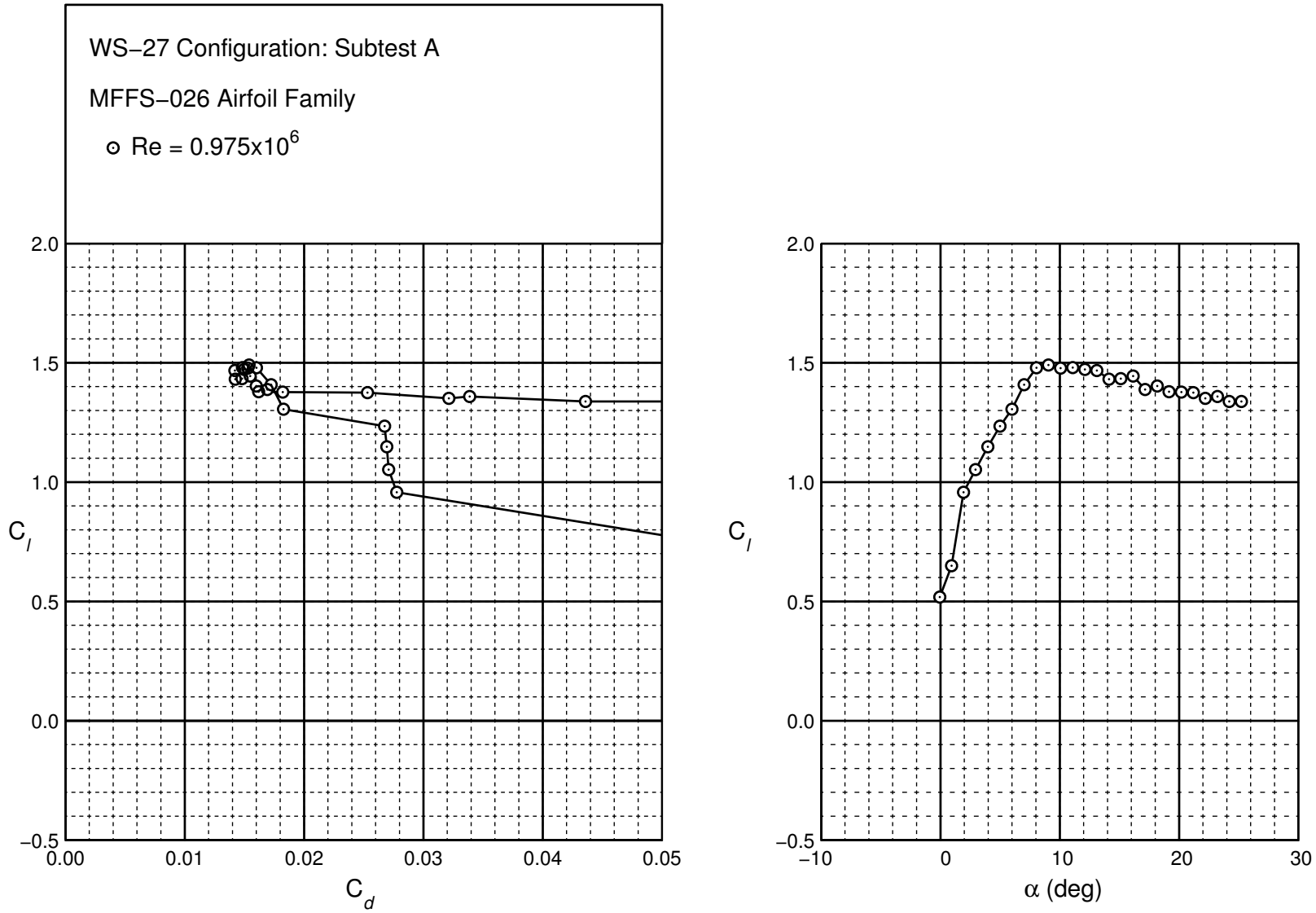

Figure B.118: WS-27 performance at $Re = 0.975 \times 10^6$.

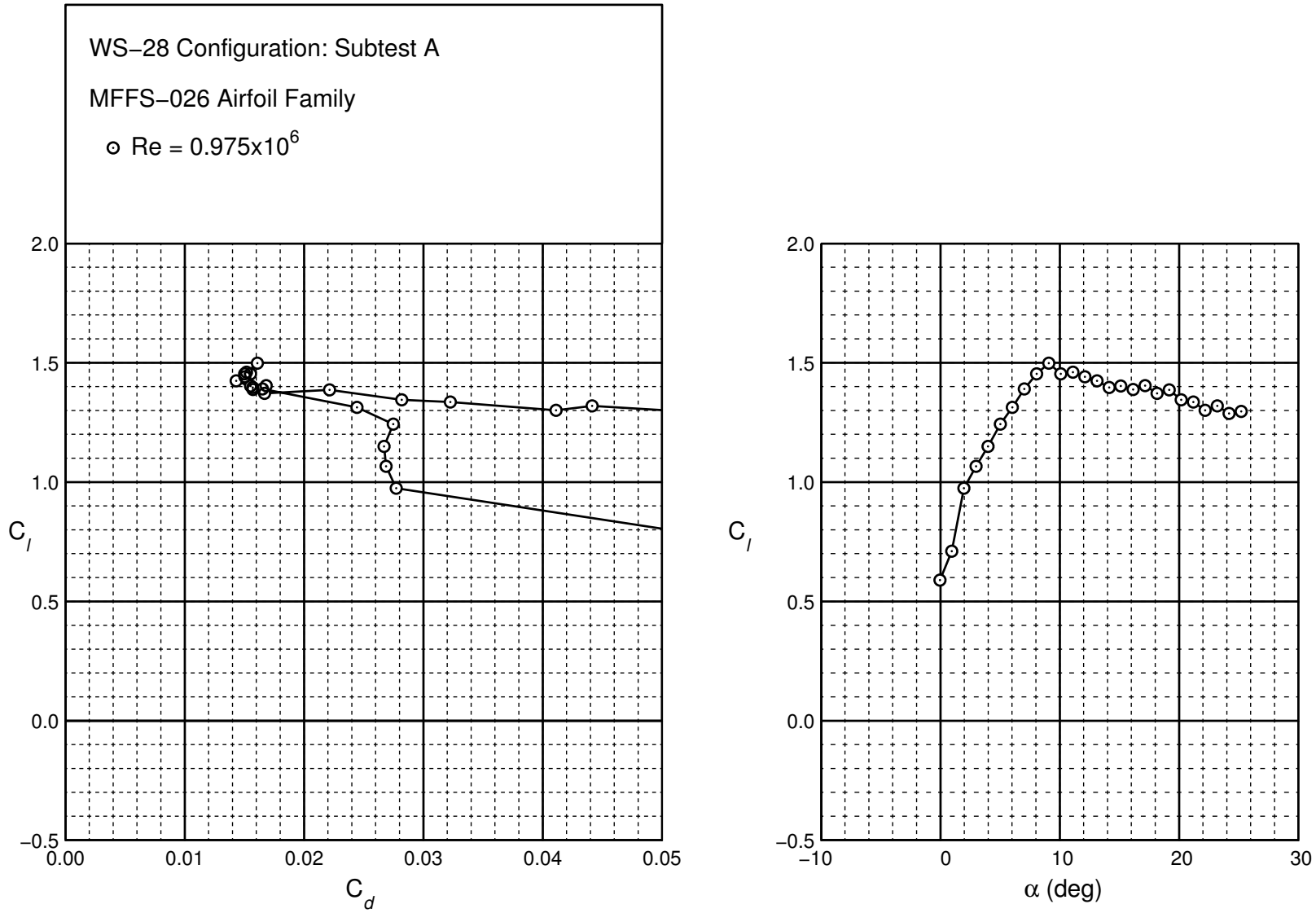

Figure B.119: WS-28 performance at $Re = 0.975 \times 10^6$.

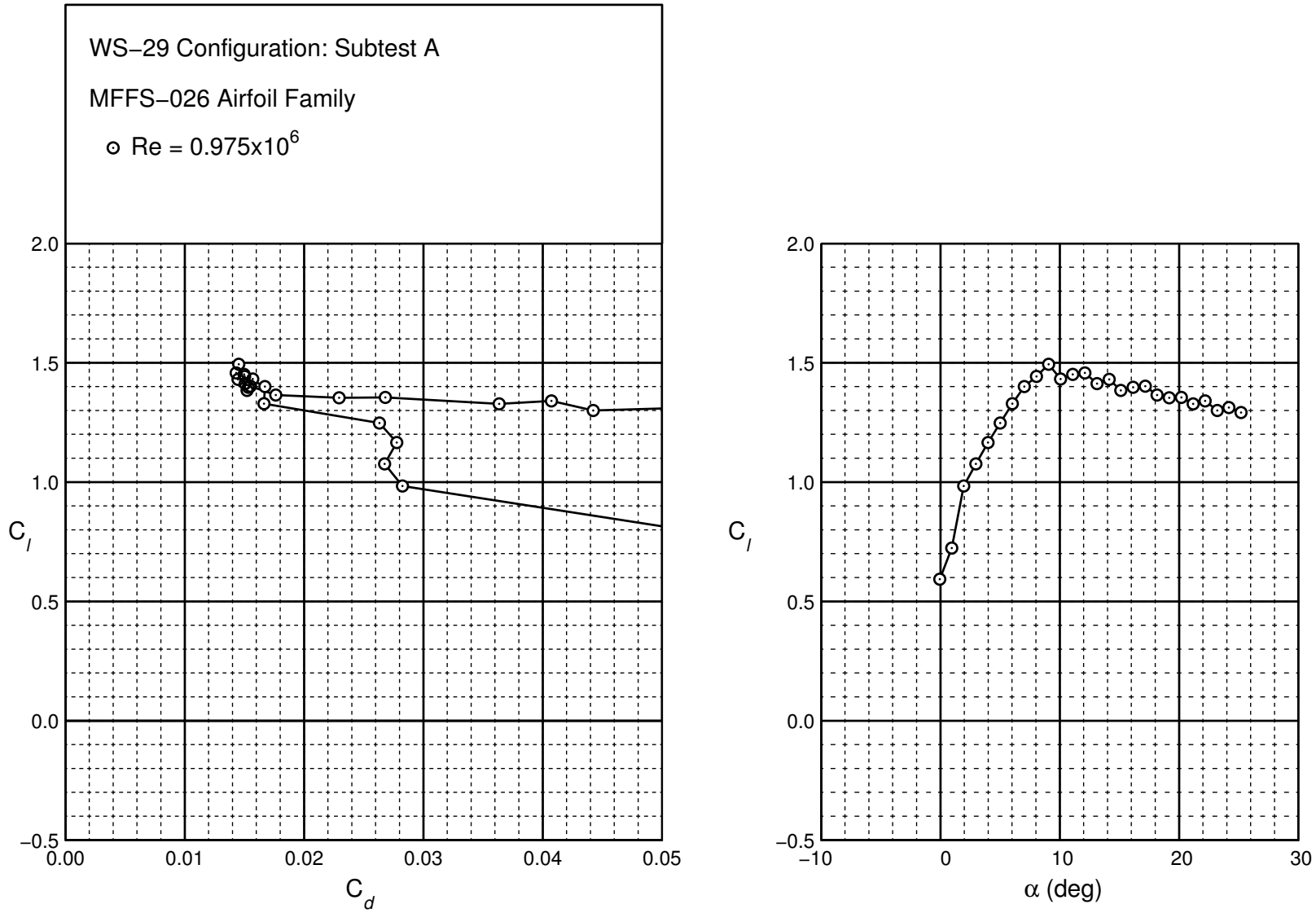

Figure B.120: WS-29 performance at $Re = 0.975 \times 10^6$.

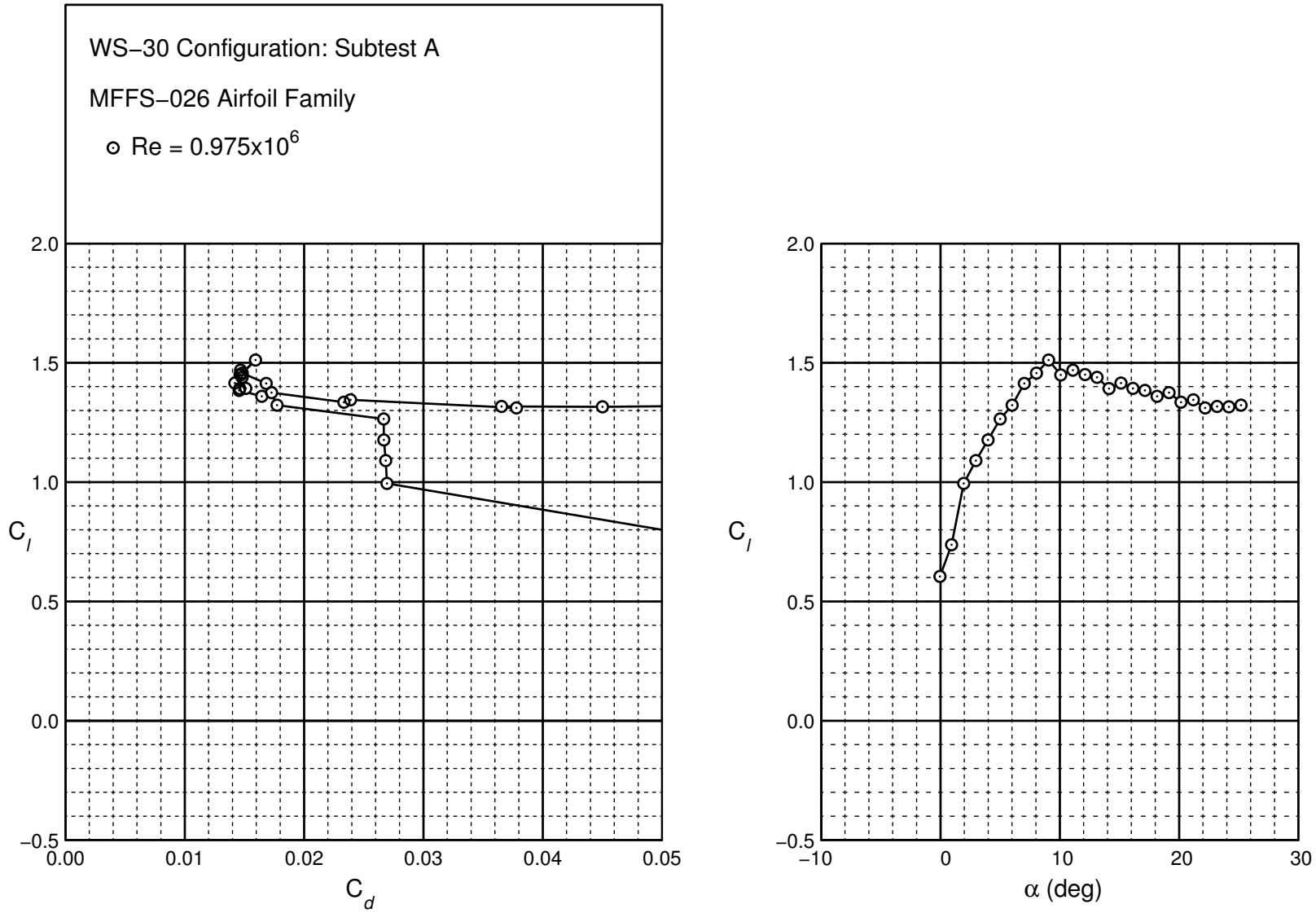

Figure B.121: WS-30 performance at $Re = 0.975 \times 10^6$.

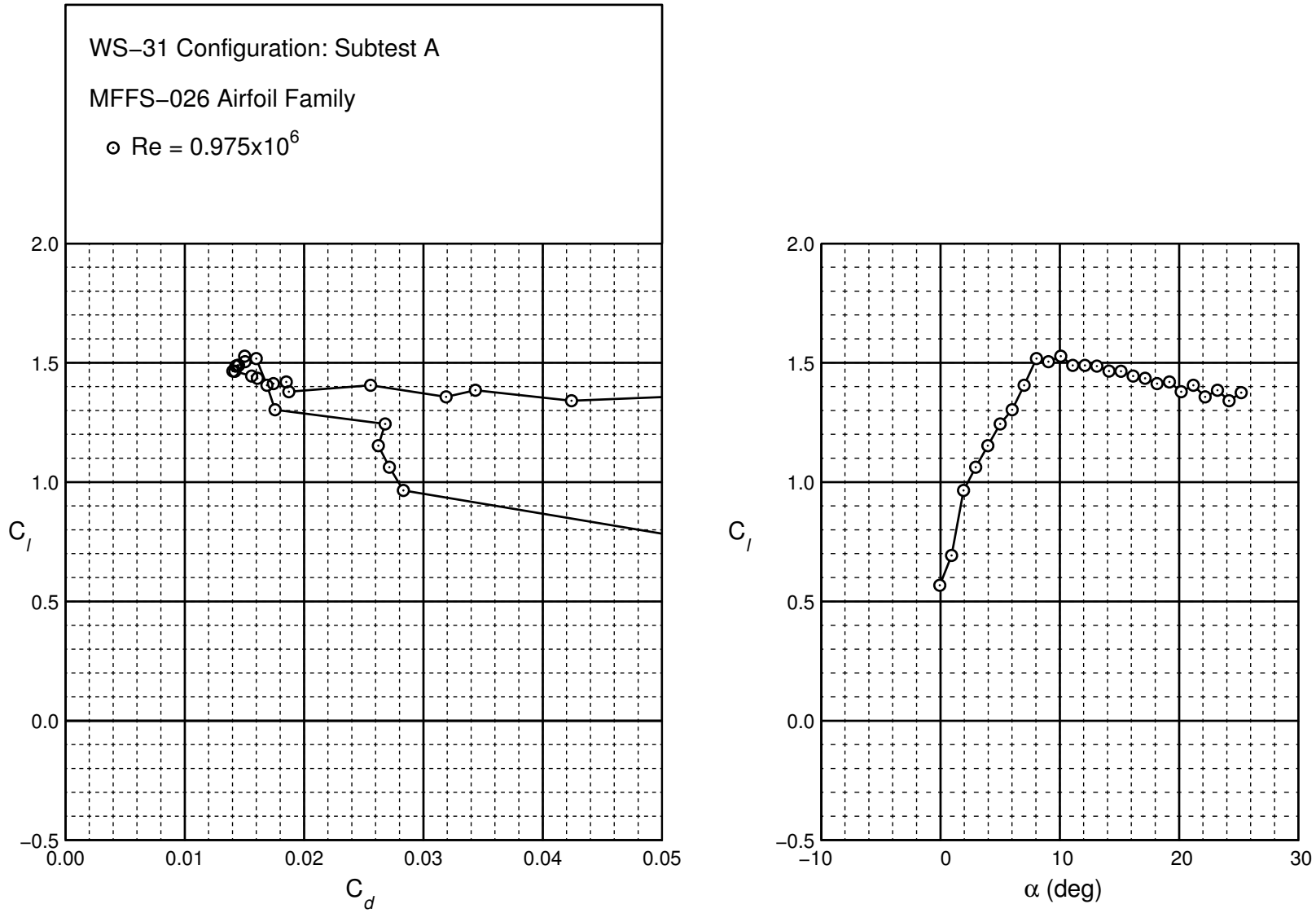

Figure B.122: WS-31 performance at $Re = 0.975 \times 10^6$.

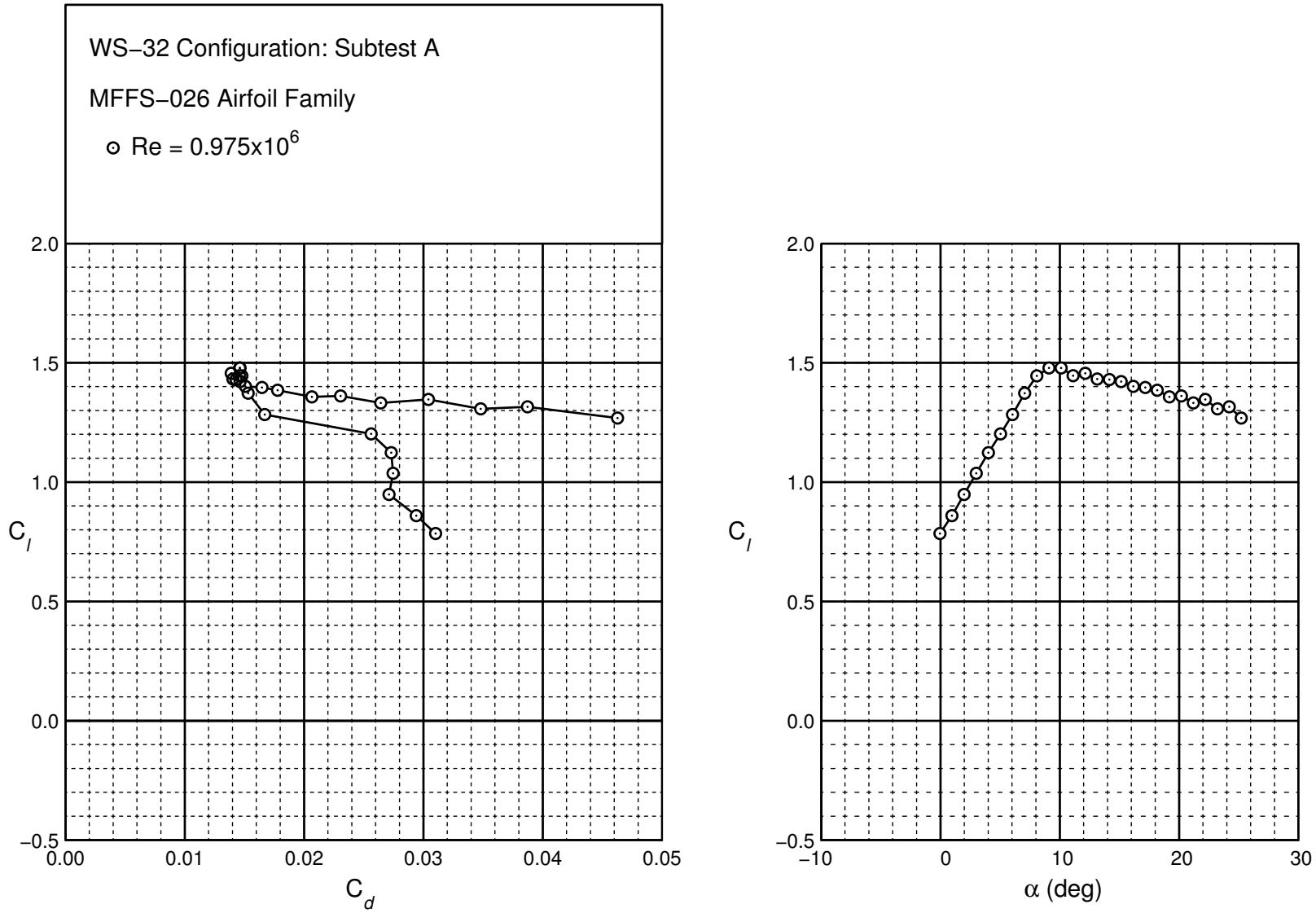

Figure B.123: WS-32 performance at $Re = 0.975 \times 10^6$.

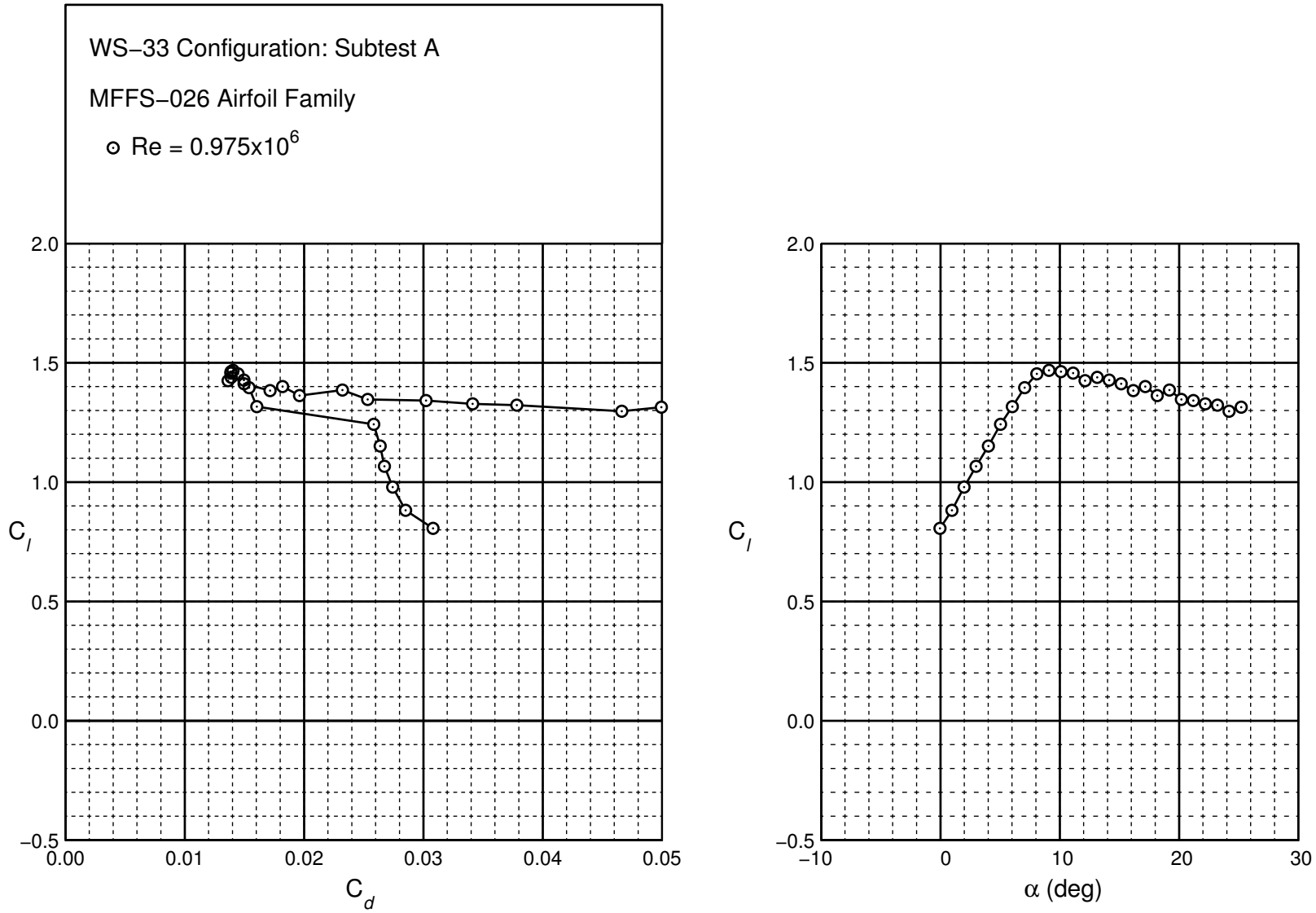

Figure B.124: WS-33 performance at $Re = 0.975 \times 10^6$.

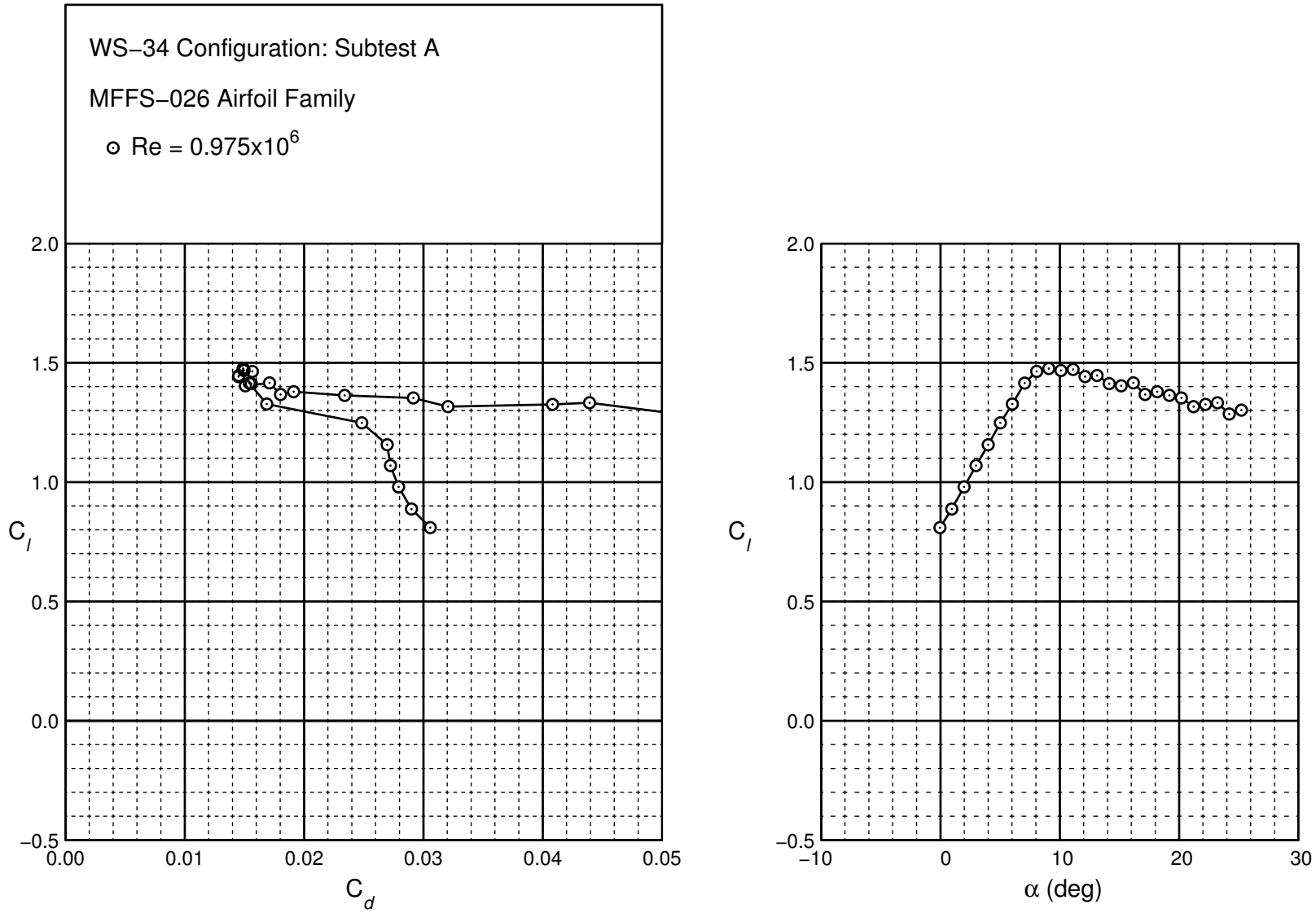

Figure B.125: WS-34 performance at $Re = 0.975 \times 10^6$.

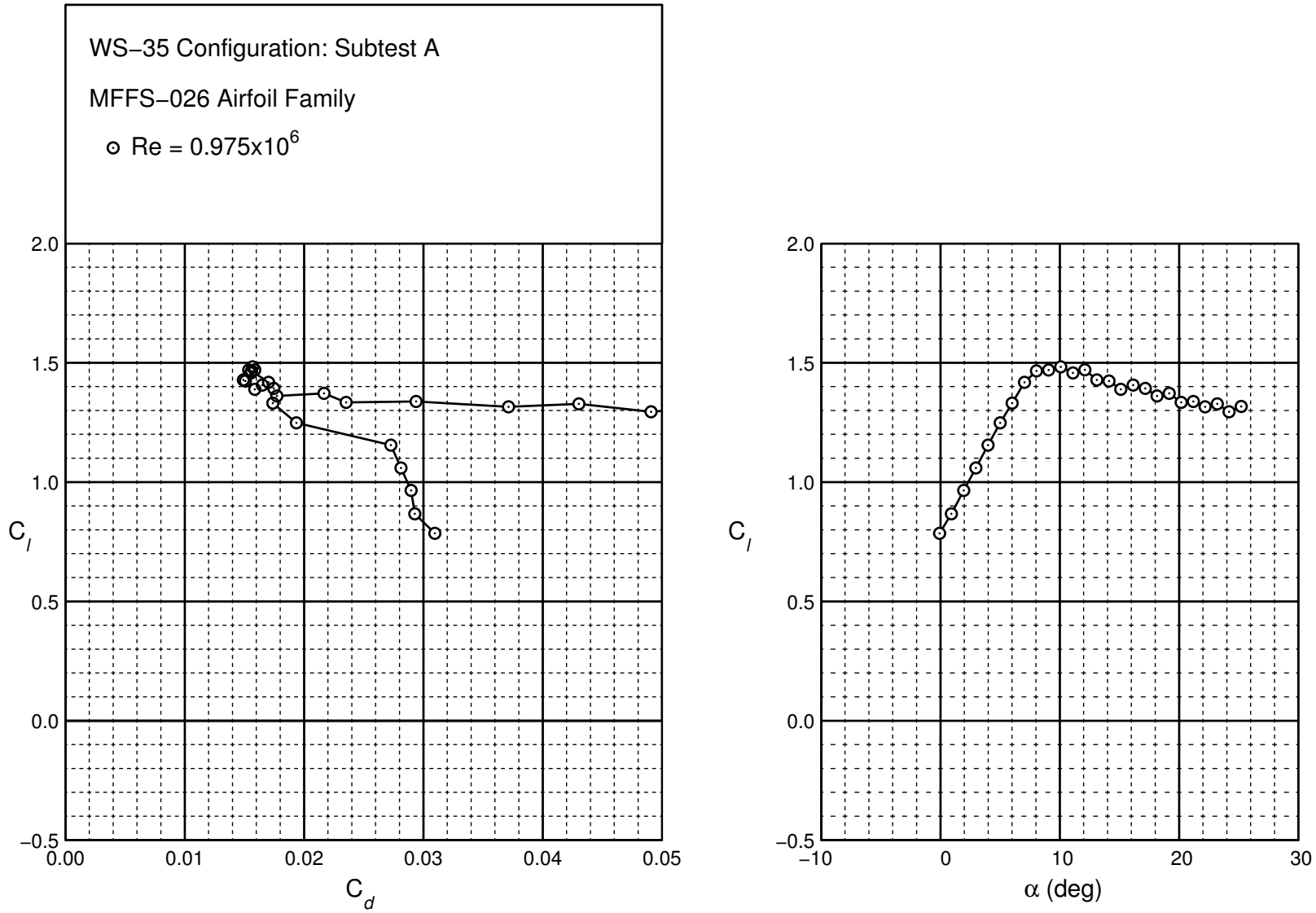

Figure B.126: WS-35 performance at $Re = 0.975 \times 10^6$.

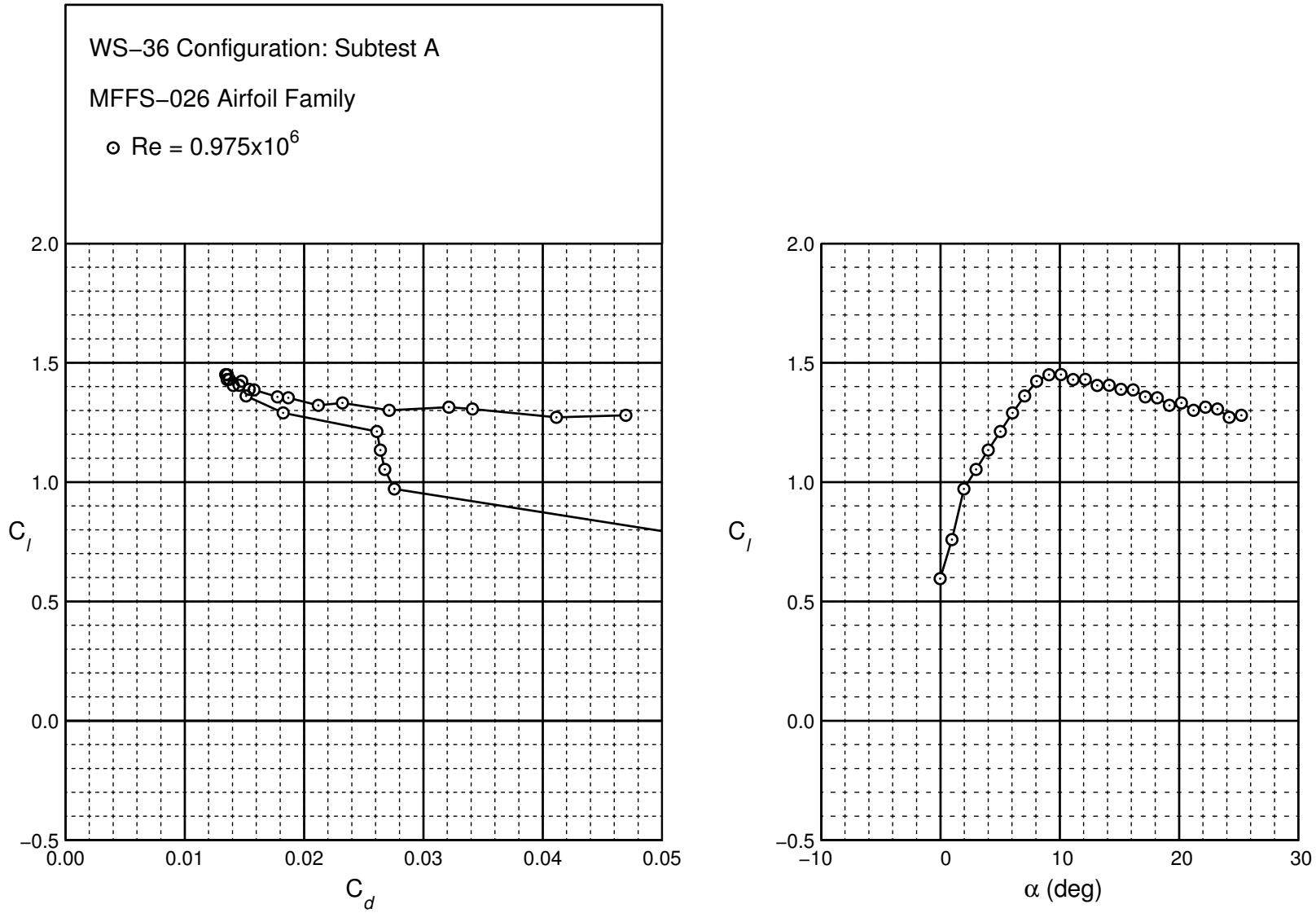

Figure B.127: WS-36 performance at $Re = 0.975 \times 10^6$.

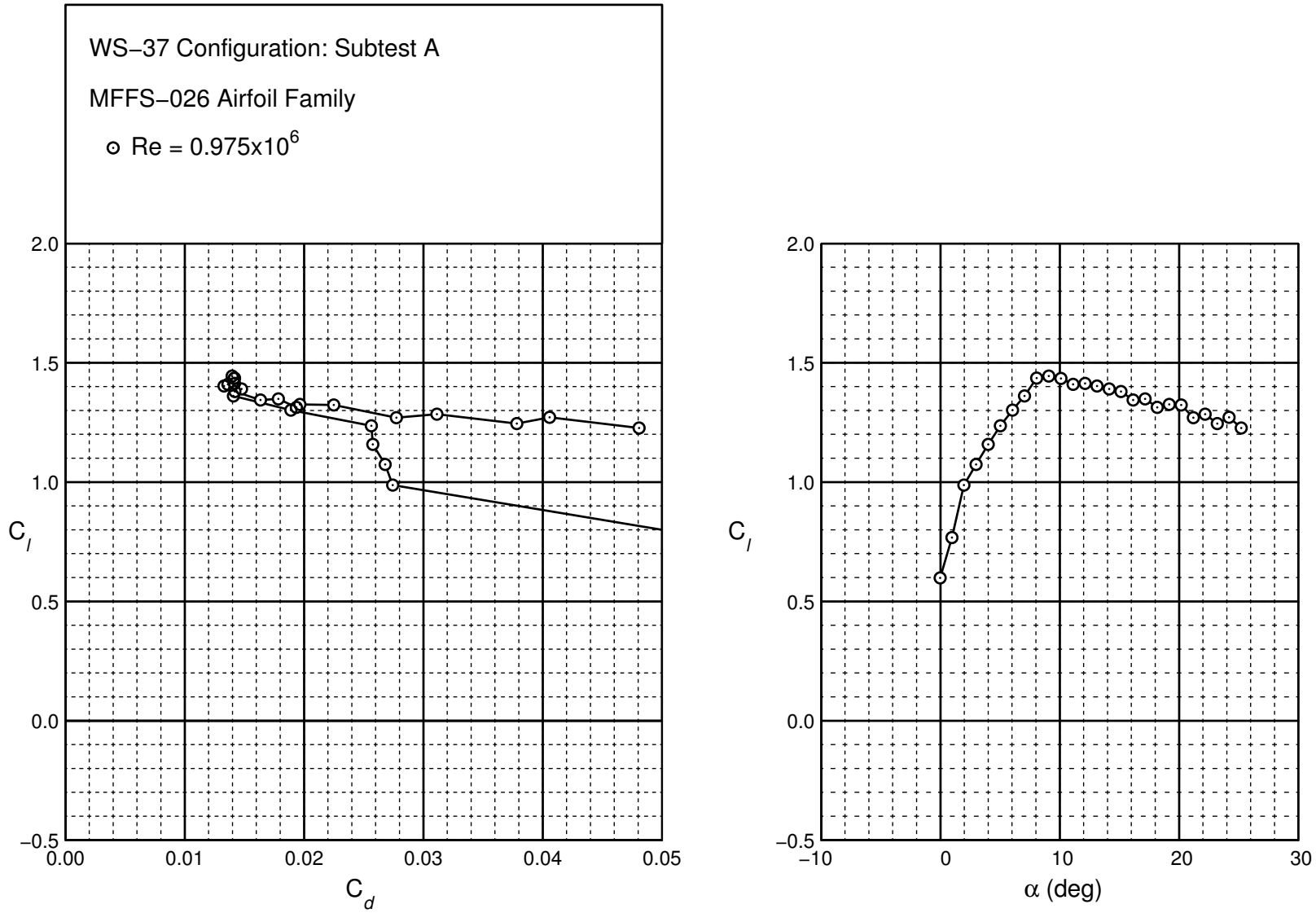

Figure B.128: WS-37 performance at $Re = 0.975 \times 10^6$.

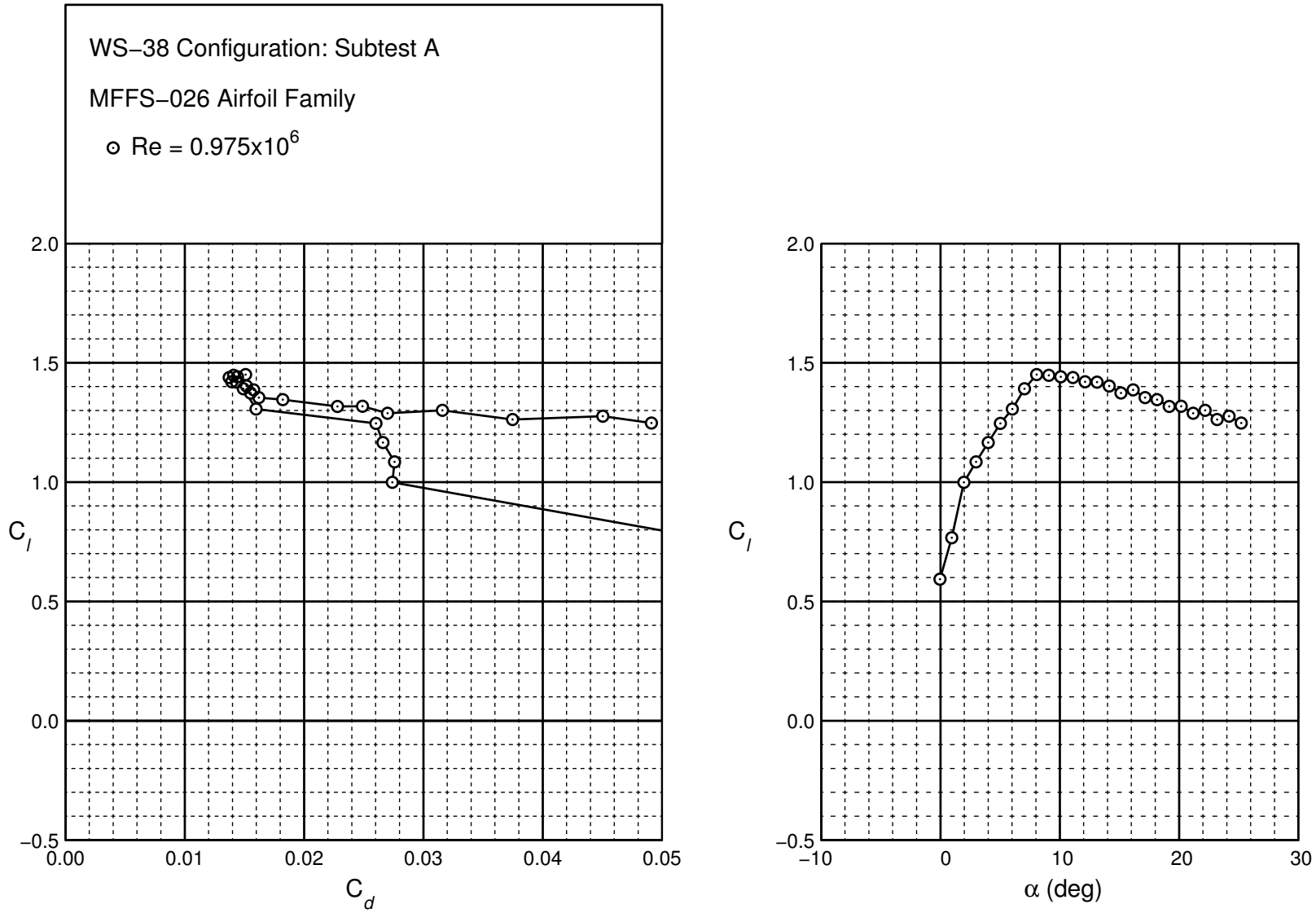

Figure B.129: WS-38 performance at $Re = 0.975 \times 10^6$.

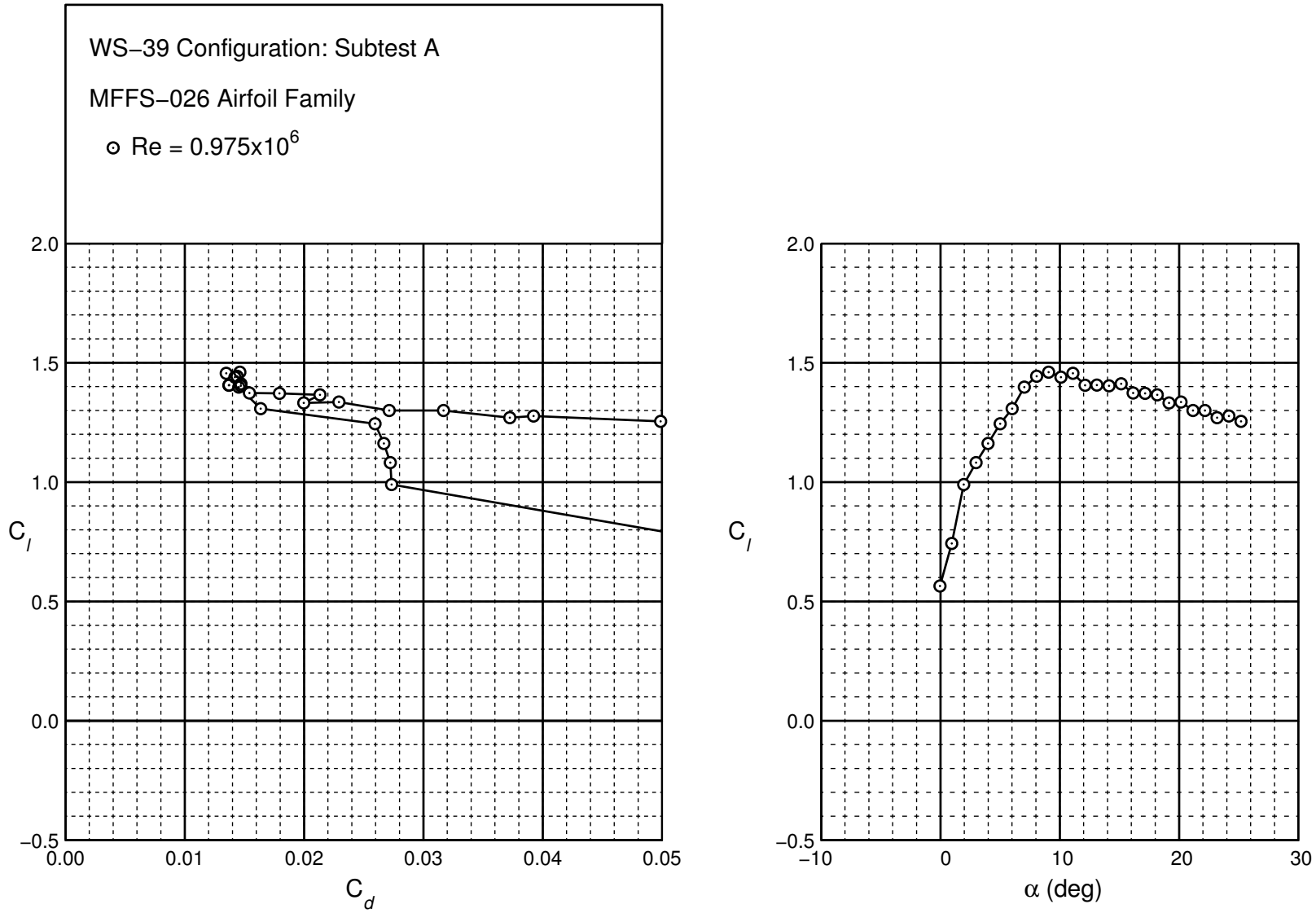

Figure B.130: WS-39 performance at $Re = 0.975 \times 10^6$.

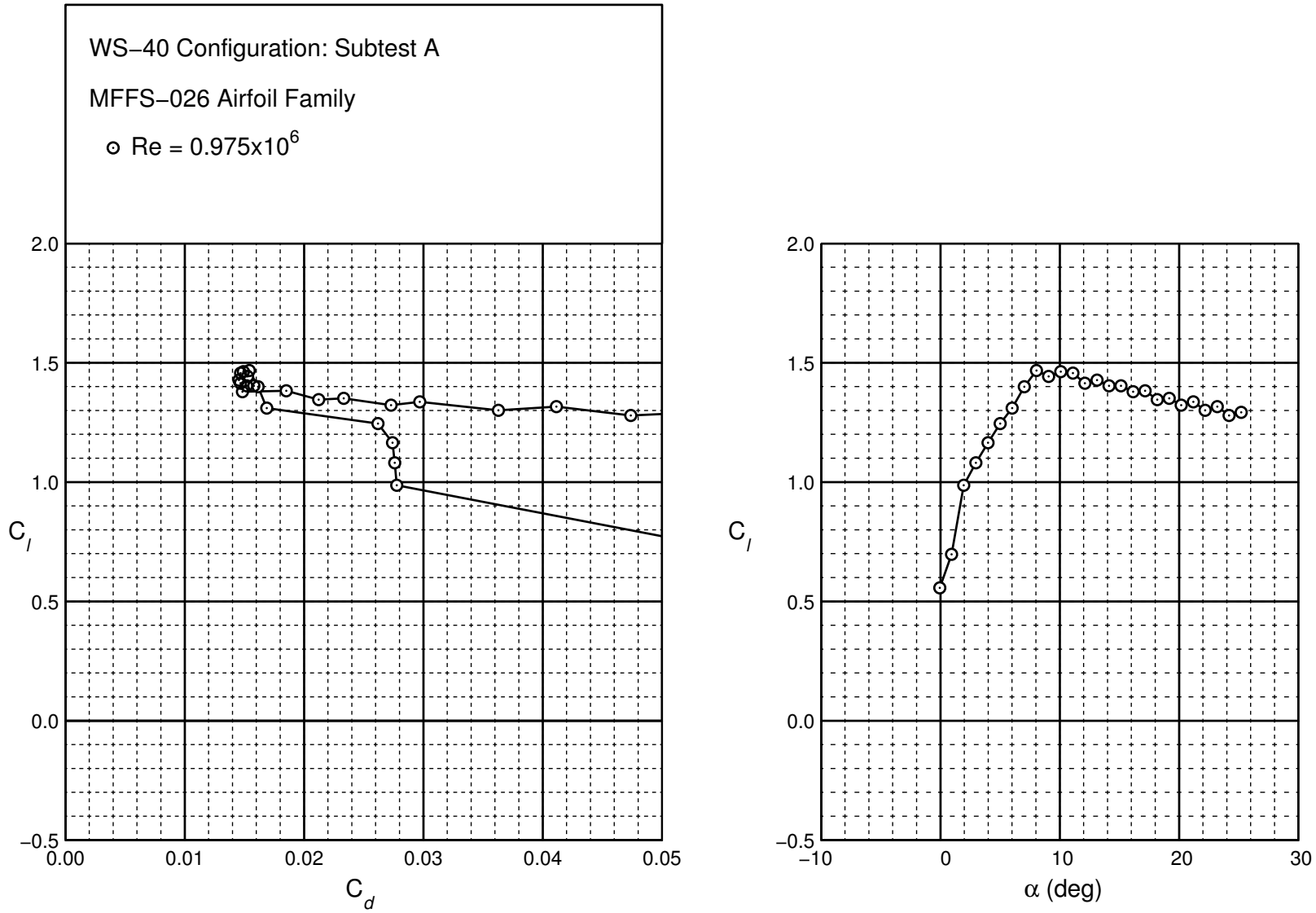

Figure B.131: WS-40 performance at $Re = 0.975 \times 10^6$.

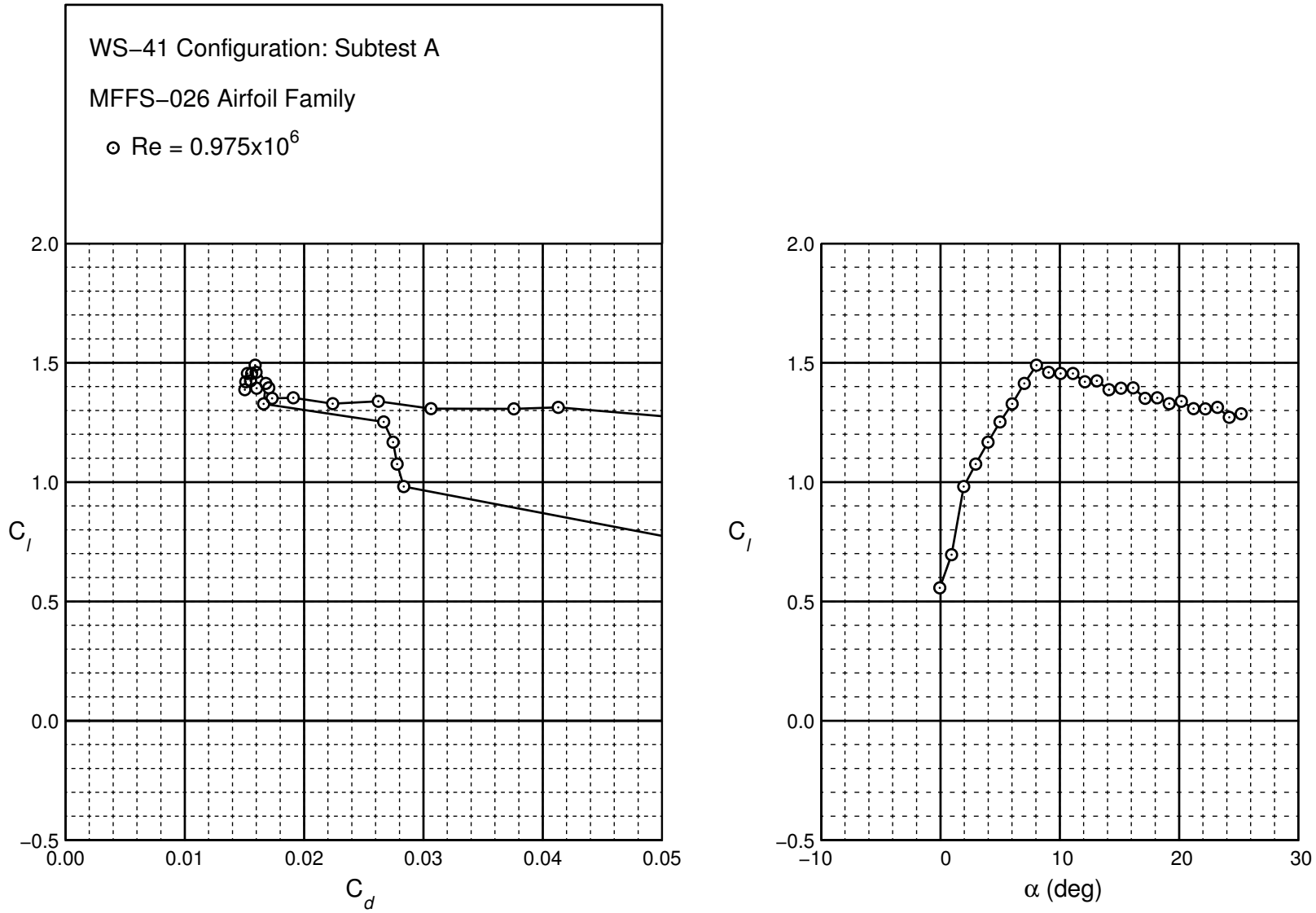

Figure B.132: WS-41 performance at $Re = 0.975 \times 10^6$.

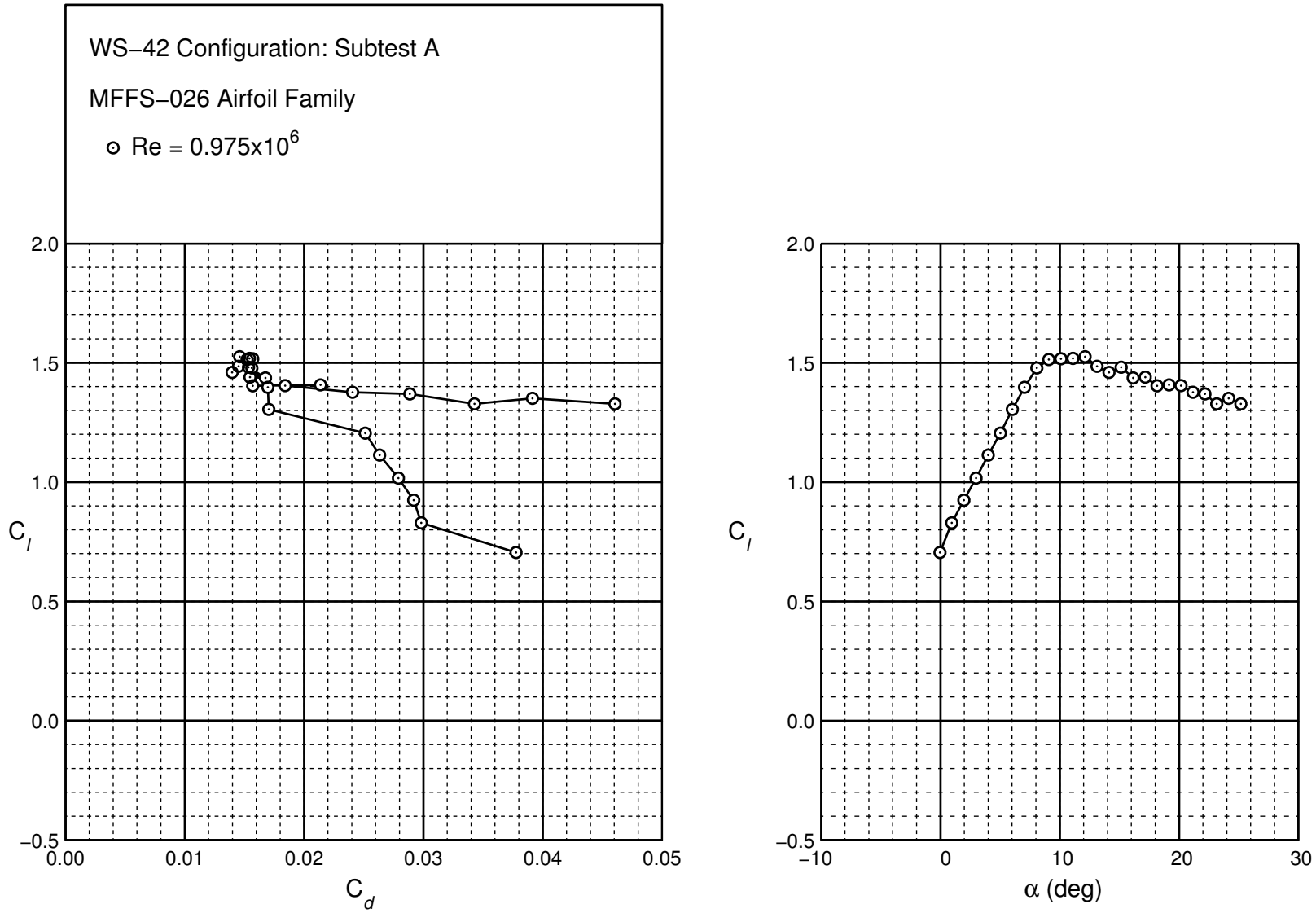

Figure B.133: WS-42 performance at $Re = 0.975 \times 10^6$.

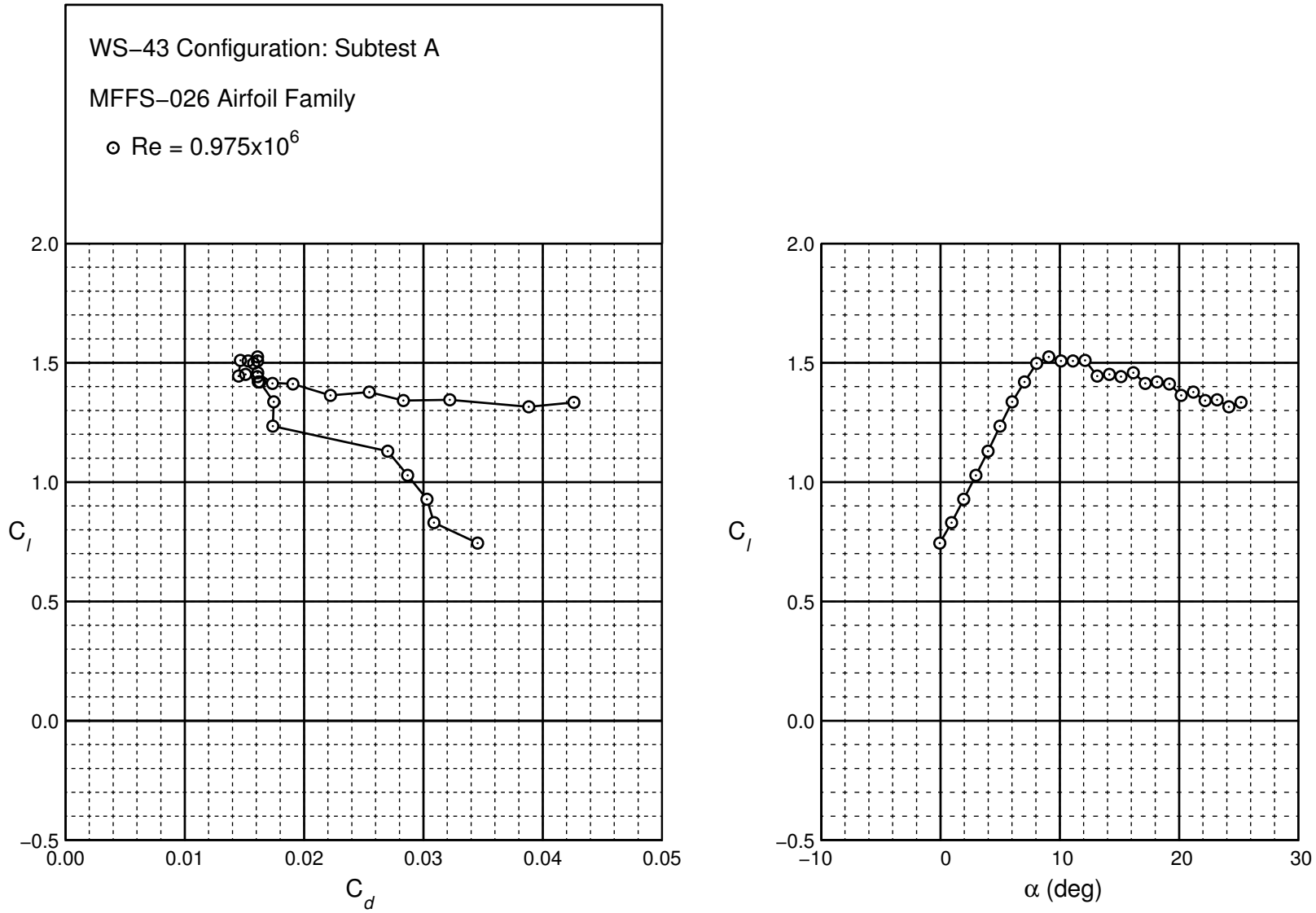

Figure B.134: WS-43 performance at $Re = 0.975 \times 10^6$.

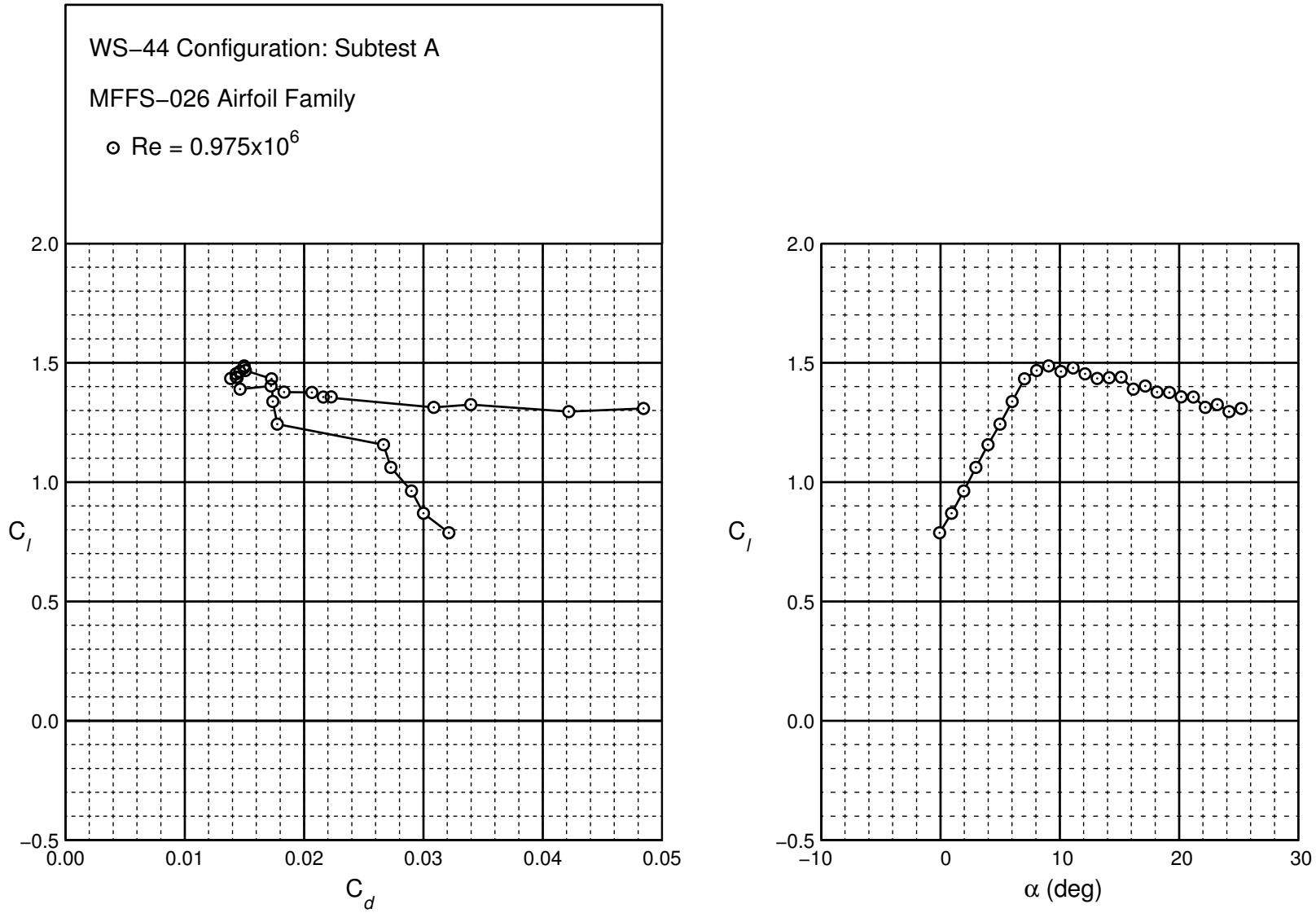

Figure B.135: WS-44 performance at $Re = 0.975 \times 10^6$.

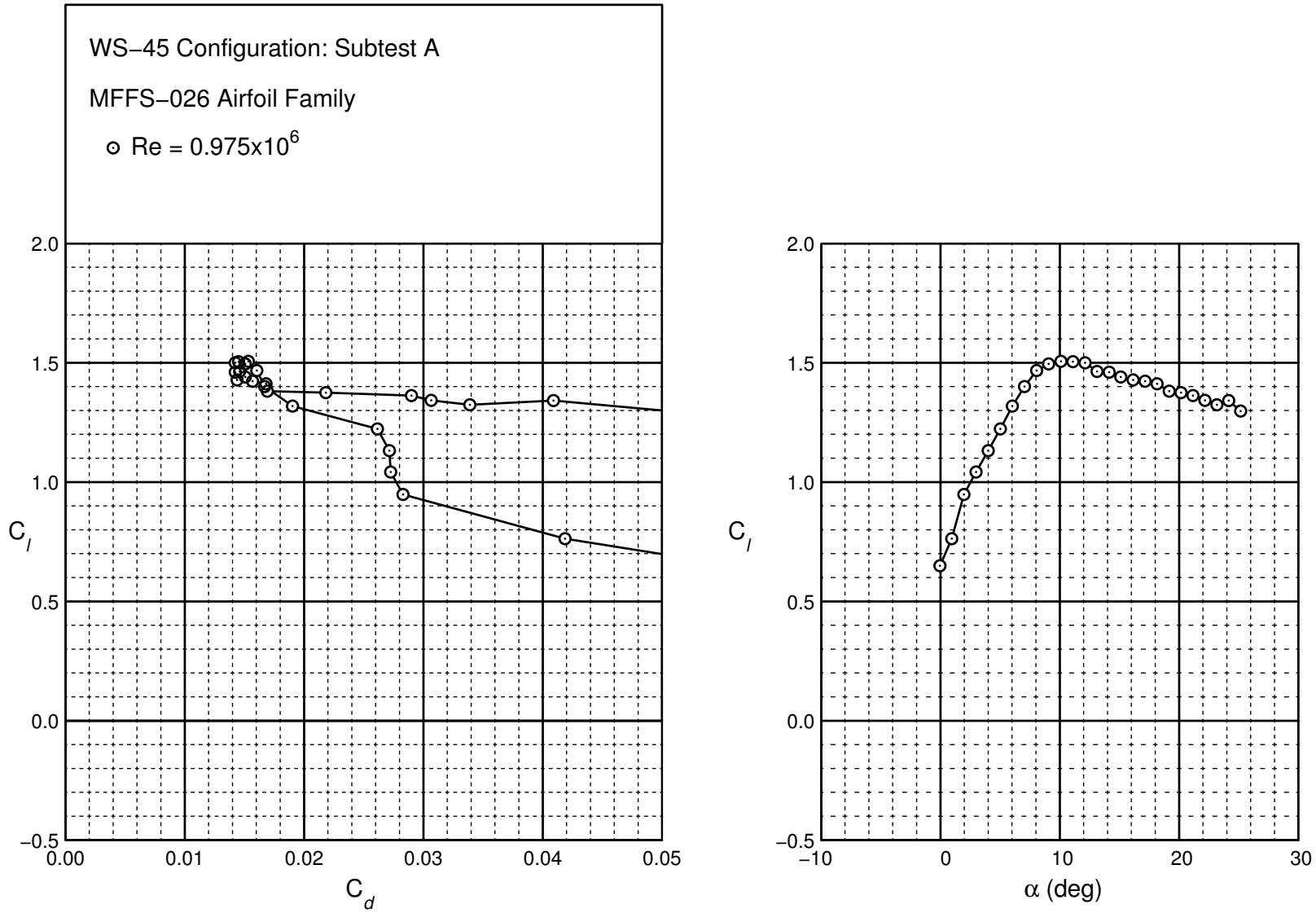

Figure B.136: WS-45 performance at $Re = 0.975 \times 10^6$.

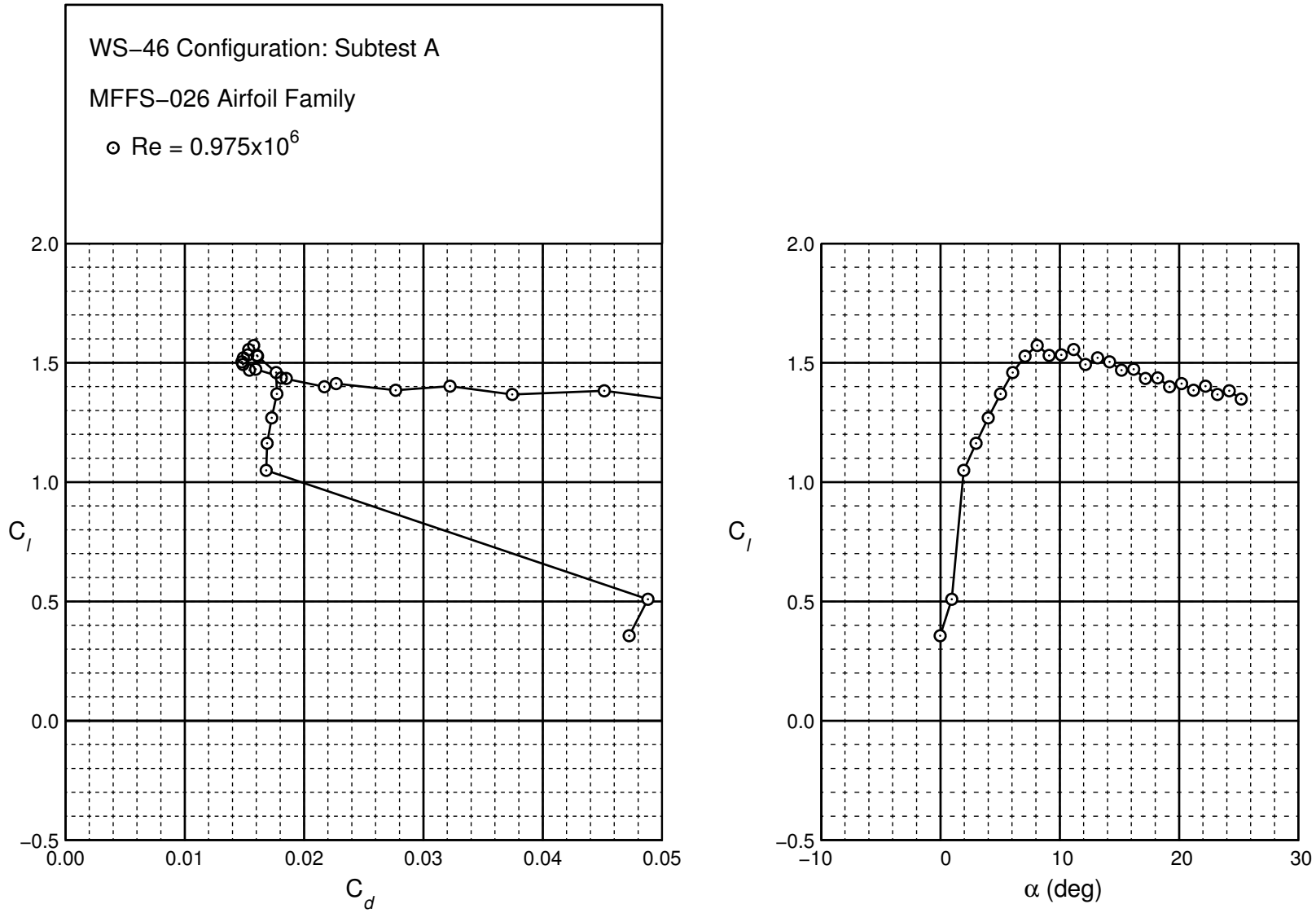

Figure B.137: WS-46 performance at $Re = 0.975 \times 10^6$.

Appendix C

Data Tables

Tabulated performance data are presented in this appendix. Data are presented for the closely coupled and well separated configurations. Data in these tables have been corrected for wind tunnel effects.

Tabulated Closely Coupled Performance Data Tables

Configuration CC-1
Subtest A
Run 1674BP
Fig. B.1

α	C_l	$C_{d,wake}$	$C_{m,c_{sys}/4}$
9.1	1.49	0.02490	-0.2240
10.1	1.59	0.02502	-0.2262
11.1	1.68	0.02440	-0.2269
13.2	1.80	0.02454	-0.2227
14.2	1.89	0.02551	-0.2253
15.2	1.95	0.02498	-0.2252
16.3	2.01	0.02642	-0.2264
17.3	2.05	0.02776	-0.2249
18.3	2.14	0.03092	-0.2311

Configuration CC-1
Subtest B
Run 1675BP
Fig. B.2

α	C_l	$C_{d,wake}$	$C_{m,c_{sys}/4}$
9.1	1.52	0.02405	-0.2252
10.1	1.58	0.02345	-0.2258
11.1	1.66	0.02305	-0.2265
12.2	1.72	0.02507	-0.2239
13.2	1.82	0.02524	-0.2249
14.2	1.89	0.02447	-0.2260
15.2	1.92	0.02459	-0.2238
16.2	2.00	0.02583	-0.2246
17.3	2.06	0.02792	-0.2243
18.3	2.09	0.03060	-0.2254

Configuration CC-1
Subtest F
Run 1762BP
Fig. B.3

α	C_l	$C_{d,wake}$	$C_{m,c_{sys}/4}$
9.1	1.52	0.02445	-0.2271
11.1	1.69	0.02439	-0.2319
12.2	1.77	0.02485	-0.2319
13.2	1.83	0.02409	-0.2333
14.2	1.90	0.02645	-0.2336
16.3	2.03	0.02664	-0.2359
17.3	2.05	0.02740	-0.2315
18.3	2.14	0.03017	-0.2350

Configuration CC-1
Subtest G
Run 1763BP
Fig. B.4

α	C_l	$C_{d,wake}$	$C_{m,c_{sys}/4}$
9.1	1.55	0.02388	-0.2294
10.1	1.64	0.02445	-0.2322
11.2	1.77	0.02370	-0.2376
12.2	1.77	0.02406	-0.2329
13.2	1.82	0.02498	-0.2315
14.2	1.96	0.02434	-0.2389
15.2	1.98	0.02663	-0.2363
16.3	2.03	0.02654	-0.2356
17.3	2.12	0.02904	-0.2384
18.3	2.15	0.02929	-0.2352

Configuration CC-1
Subtest H
Run 1764BP
Fig. B.5

α	C_l	$C_{d,wake}$	$C_{m,c_{sys}/4}$
9.1	1.55	0.02392	-0.2281
10.1	1.59	0.02272	-0.2281
11.1	1.69	0.02228	-0.2315
13.2	1.83	0.02551	-0.2313
14.2	1.89	0.02318	-0.2308
15.2	1.97	0.02572	-0.2327
16.2	2.00	0.02614	-0.2311
17.3	2.02	0.02707	-0.2306
18.3	2.10	0.03157	-0.2346

Configuration CC-2
Subtest A
Run 1676BP
Fig. B.6

α	C_l	$C_{d,wake}$	$C_{m,c_{sys}/4}$
9.0	1.05	0.02115	-0.1540
10.0	1.10	0.02089	-0.1545
11.1	1.18	0.01992	-0.1563
12.1	1.31	0.02186	-0.1606
13.1	1.34	0.02317	-0.1591
14.1	1.42	0.02256	-0.1643
15.2	1.52	0.02197	-0.1685
18.2	1.65	0.02360	-0.1740

Configuration CC-3
Subtest A
Run 1677BP
Fig. B.7

α	C_l	$C_{d,wake}$	$C_{m,c_{sys}/4}$
9.0	1.06	0.02130	-0.1620
10.1	1.17	0.02213	-0.1660
11.1	1.25	0.02164	-0.1669
12.1	1.35	0.02174	-0.1701
13.1	1.43	0.02317	-0.1727
14.1	1.42	0.02287	-0.1672
15.2	1.59	0.02357	-0.1777
16.2	1.61	0.02344	-0.1808
17.2	1.69	0.02425	-0.1843

Configuration CC-4
Subtest A
Run 1678BP
Fig. B.8

α	C_l	$C_{d,wake}$	$C_{m,c_{sys}/4}$
9.0	1.20	0.02353	-0.1870
10.0	1.24	0.02344	-0.1857
11.1	1.42	0.02453	-0.1943
12.1	1.46	0.02411	-0.1968
13.1	1.57	0.02284	-0.2011
14.1	1.58	0.02363	-0.1992
15.2	1.66	0.02404	-0.2034
16.2	1.72	0.02496	-0.2057
17.2	1.78	0.02559	-0.2091
18.2	1.81	0.02605	-0.2110

Configuration CC-5
Subtest A
Run 1679BP
Fig. B.9

α	C_l	$C_{d,wake}$	$C_{m,c_{sys}/4}$
9.1	1.26	0.02495	-0.1799
10.1	1.32	0.02334	-0.1807
11.1	1.44	0.02314	-0.1852
13.2	1.56	0.02329	-0.1879
14.2	1.64	0.02404	-0.1901
15.2	1.65	0.02366	-0.1919
16.2	1.70	0.02467	-0.1867
17.2	1.81	0.02444	-0.1958
18.2	1.87	0.02424	-0.1991

Configuration CC-6
Subtest A
Run 1680BP
Fig. B.10

α	C_l	$C_{d,wake}$	$C_{m,c_{sys}/4}$
9.1	1.31	0.02415	-0.1878
10.1	1.39	0.02457	-0.1907
11.1	1.43	0.02513	-0.1895
13.2	1.61	0.02505	-0.1971
14.2	1.63	0.02390	-0.1985
15.2	1.73	0.02478	-0.1986
16.2	1.73	0.02402	-0.2012
17.2	1.84	0.02500	-0.2116
18.2	1.85	0.02648	-0.2023

Configuration CC-7
Subtest A
Run 1681BP
Fig. B.11

α	C_l	$C_{d,wake}$	$C_{m,c_{sys}/4}$
9.1	1.38	0.02568	-0.2040
10.1	1.47	0.02598	-0.2058
11.1	1.54	0.02552	-0.2079
12.1	1.61	0.02480	-0.2125
13.1	1.60	0.02490	-0.2079
14.2	1.71	0.02389	-0.2093
15.2	1.75	0.02641	-0.2113
16.2	1.84	0.02645	-0.2169
17.2	1.87	0.02549	-0.2190
18.2	1.88	0.02765	-0.2167

Configuration CC-8
Subtest A
Run 1682BP
Fig. B.12

α	C_l	$C_{d,wake}$	$C_{m,c_{sys}/4}$
9.1	1.36	0.02526	-0.1984
10.1	1.47	0.02484	-0.2044
11.1	1.54	0.02367	-0.2071
13.2	1.67	0.02253	-0.2047
14.2	1.78	0.02475	-0.2085
15.2	1.83	0.02342	-0.2083
17.2	1.91	0.02537	-0.2078
18.2	1.95	0.02898	-0.2062

Configuration CC-9
Subtest A
Run 1683BP
Fig. B.13

α	C_l	$C_{d,wake}$	$C_{m,c_{sys}/4}$
9.1	1.48	0.02571	-0.2203
10.1	1.52	0.02572	-0.2197
11.1	1.57	0.02487	-0.2191
12.2	1.71	0.02419	-0.2238
13.2	1.76	0.02449	-0.2213
14.2	1.83	0.02456	-0.2224
16.2	1.89	0.02780	-0.2178
17.2	1.95	0.02731	-0.2184
18.3	2.04	0.02693	-0.2235

Configuration CC-10
Subtest A
Run 1684BP
Fig. B.14

α	C_l	$C_{d,wake}$	$C_{m,c_{sys}/4}$
9.1	1.52	0.02661	-0.2293
10.1	1.60	0.02496	-0.2346
11.1	1.64	0.02635	-0.2322
12.1	1.72	0.02610	-0.2315
13.2	1.80	0.02778	-0.2323
14.2	1.88	0.02748	-0.2331
15.2	1.91	0.02671	-0.2305
16.2	1.95	0.02688	-0.2316
17.3	2.07	0.03026	-0.2350
18.3	2.12	0.03215	-0.2402

Configuration CC-11
Subtest A
Run 1685BP
Fig. B.15

α	C_l	$C_{d,wake}$	$C_{m,c_{sys}/4}$
9.1	1.64	0.02651	-0.2533
10.1	1.73	0.02493	-0.2545
11.1	1.75	0.02502	-0.2508
12.2	1.83	0.02576	-0.2487
13.2	1.92	0.02646	-0.2510
15.2	2.06	0.02707	-0.2511
16.3	2.13	0.02726	-0.2536
17.3	2.18	0.02915	-0.2540
18.3	2.26	0.03229	-0.2590

Configuration CC-12
Subtest A
Run 1686BP
Fig. B.16

α	C_l	$C_{d,wake}$	$C_{m,c_{sys}/4}$
9.1	1.69	0.02532	-0.2618
10.1	1.73	0.02551	-0.2592
11.1	1.79	0.02413	-0.2566
12.2	1.85	0.02581	-0.2549
13.2	1.98	0.02547	-0.2590
14.2	2.03	0.02603	-0.2586
15.2	2.07	0.02790	-0.2563
16.3	2.15	0.02726	-0.2587
17.3	2.20	0.03033	-0.2591
18.3	2.22	0.03544	-0.2573

Configuration CC-13
Subtest A
Run 1687BP
Fig. B.17

α	C_l	$C_{d,wake}$	$C_{m,c_{sys}/4}$
9.1	1.73	0.02618	-0.2718
10.1	1.80	0.02645	-0.2709
11.2	1.87	0.02579	-0.2694
12.2	1.91	0.02720	-0.2663
13.2	1.97	0.02609	-0.2635
14.2	2.07	0.02758	-0.2659
15.2	2.11	0.02669	-0.2646
16.3	2.19	0.02967	-0.2665
17.3	2.20	0.03613	-0.2639
18.3	2.24	0.04029	-0.2646

Configuration CC-14
Subtest A
Run 1688BP
Fig. B.18

α	C_l	$C_{d,wake}$	$C_{m,c_{sys}/4}$
9.1	1.71	0.02572	-0.2635
10.1	1.75	0.02651	-0.2607
11.2	1.82	0.02589	-0.2604
12.2	1.93	0.02437	-0.2610
13.2	1.97	0.02637	-0.2571
14.2	1.97	0.02493	-0.2540
16.3	2.15	0.03021	-0.2582
17.3	2.20	0.03122	-0.2582
18.3	2.18	0.03770	-0.2540

Configuration CC-15
Subtest A
Run 1689BP
Fig. B.19

α	C_l	$C_{d,wake}$	$C_{m,c_{sys}/4}$
9.1	1.71	0.02682	-0.2704
10.1	1.79	0.02643	-0.2736
11.2	1.88	0.02567	-0.2751
13.2	2.02	0.02564	-0.2706
14.2	2.01	0.02578	-0.2631
15.2	2.11	0.02628	-0.2684
16.3	2.21	0.02744	-0.2712
17.3	2.21	0.03470	-0.2676
18.3	2.24	0.03902	-0.2654

Configuration CC-16
Subtest A
Run 1690BP
Fig. B.20

α	C_l	$C_{d,wake}$	$C_{m,c_{sys}/4}$
9.1	1.78	0.02752	-0.2808
10.1	1.88	0.02662	-0.2823
11.2	1.92	0.02622	-0.2827
12.2	1.96	0.02533	-0.2741
13.2	2.05	0.02481	-0.2750
14.2	2.14	0.02750	-0.2773
15.2	2.17	0.02848	-0.2737
16.3	2.22	0.03322	-0.2754
17.3	2.28	0.03868	-0.2785
18.3	2.32	0.04209	-0.2758

Configuration CC-17
Subtest A
Run 1691BP
Fig. B.21

α	C_l	$C_{d,wake}$	$C_{m,c_{sys}/4}$
10.1	1.87	0.02658	-0.2712
11.2	1.99	0.02524	-0.2744
12.2	1.97	0.02607	-0.2670
15.2	2.00	0.03896	-0.2734
16.2	2.10	0.05957	-0.2773
17.2	2.11	0.07915	-0.2701
18.2	2.15	0.10068	-0.2674

Configuration CC-18
Subtest A
Run 1692BP
Fig. B.22

α	C_l	$C_{d,wake}$	$C_{m,c_{sys}/4}$
9.1	1.82	0.02603	-0.2794
10.2	1.96	0.02658	-0.2837
11.2	1.99	0.02572	-0.2793
12.2	2.04	0.02368	-0.2772
13.2	2.11	0.02432	-0.2767
14.2	2.14	0.02361	-0.2764
16.3	2.26	0.03237	-0.2725
17.3	2.27	0.04093	-0.2714
18.3	2.31	0.04886	-0.2697

Configuration CC-19
Subtest A
Run 1693BP
Fig. B.23

α	C_l	$C_{d,wake}$	$C_{m,c_{sys}/4}$
9.1	1.86	0.02532	-0.2854
10.1	1.98	0.02526	-0.2921
11.2	2.00	0.02508	-0.2849
13.2	2.12	0.02505	-0.2796
14.2	2.17	0.02745	-0.2819
15.3	2.24	0.02930	-0.2819
17.3	2.34	0.04191	-0.2790
18.3	2.36	0.05233	-0.2779

Configuration CC-20
Subtest A
Run 1694BP
Fig. B.24

α	C_l	$C_{d,wake}$	$C_{m,c_{sys}/4}$
9.1	1.68	0.02806	-0.2569
10.1	1.80	0.02524	-0.2615
11.2	1.84	0.02775	-0.2597
12.2	1.88	0.02685	-0.2568
13.2	1.95	0.02713	-0.2565
14.2	2.01	0.02711	-0.2558
15.2	2.08	0.02805	-0.2561
16.2	2.10	0.02956	-0.2569
17.3	2.17	0.03162	-0.2565

Configuration CC-21
Subtest A
Run 1695BP
Fig. B.25

α	C_l	$C_{d,wake}$	$C_{m,c_{sys}/4}$
9.1	1.65	0.02603	-0.2482
10.1	1.73	0.02532	-0.2504
11.1	1.72	0.02538	-0.2439
12.2	1.87	0.02474	-0.2483
13.2	1.90	0.02538	-0.2446
14.2	1.98	0.02691	-0.2465
15.2	2.02	0.02697	-0.2446
16.3	2.10	0.02846	-0.2485
18.3	2.26	0.03636	-0.2521

Configuration CC-22
Subtest A
Run 1696BP
Fig. B.26

α	C_l	$C_{d,wake}$	$C_{m,c_{sys}/4}$
9.1	1.68	0.02421	-0.2481
10.1	1.75	0.02586	-0.2487
11.2	1.82	0.02498	-0.2476
12.2	1.88	0.02603	-0.2450
13.2	1.95	0.02519	-0.2438
14.2	2.03	0.02629	-0.2442
15.2	2.06	0.02668	-0.2446
16.3	2.13	0.02850	-0.2450
17.3	2.13	0.03791	-0.2434
18.3	2.20	0.04516	-0.2444

Configuration CC-23
Subtest A
Run 1697BP
Fig. B.27

α	C_l	$C_{d,wake}$	$C_{m,c_{sys}/4}$
9.1	1.67	0.02475	-0.2436
11.2	1.81	0.02393	-0.2458
12.2	1.86	0.02459	-0.2445
13.2	1.95	0.02479	-0.2409
14.2	1.94	0.02593	-0.2419
15.2	2.02	0.02746	-0.2404
16.2	2.02	0.03130	-0.2393

Configuration CC-24
Subtest A
Run 1698BP
Fig. B.28

α	C_l	$C_{d,wake}$	$C_{m,c_{sys}/4}$
10.1	1.75	0.02443	-0.2453
11.2	1.77	0.02432	-0.2419
12.2	1.83	0.02467	-0.2415
13.2	1.91	0.02786	-0.2427
14.2	1.84	0.03144	-0.2338
15.2	1.96	0.03206	-0.2361
16.2	2.01	0.03446	-0.2377
17.2	2.02	0.04675	-0.2354
18.3	2.08	0.06054	-0.2368

Configuration CC-25
Subtest A
Run 1699BP
Fig. B.29

α	C_l	$C_{d,wake}$	$C_{m,c_{sys}/4}$
9.1	1.69	0.02661	-0.2615
10.1	1.75	0.02627	-0.2612
12.2	1.88	0.02518	-0.2602
15.2	2.07	0.02629	-0.2606
17.2	2.11	0.03026	-0.2586
18.2	2.11	0.03631	-0.2567

Configuration CC-25
Subtest B
Run 1700BP
Fig. B.30

α	C_l	$C_{d,wake}$	$C_{m,c_{sys}/4}$
9.1	1.66	0.02717	-0.2596
10.1	1.74	0.02814	-0.2606
11.1	1.80	0.02545	-0.2614
12.2	1.90	0.02691	-0.2619
13.2	1.89	0.02596	-0.2554
14.2	1.97	0.02917	-0.2586
16.2	2.15	0.03114	-0.2658
17.3	2.17	0.03898	-0.2619
18.3	2.20	0.04040	-0.2633

Configuration CC-25
Subtest D
Run 1702BP
Fig. B.31

α	C_l	$C_{d,wake}$	$C_{m,c_{sys}/4}$
9.0	1.62	0.02558	-0.3326
10.0	1.72	0.02474	-0.3400
11.0	1.76	0.02421	-0.3416
12.0	1.84	0.02615	-0.3454
14.1	1.98	0.02705	-0.3560
15.1	1.95	0.02890	-0.3528
17.1	2.11	0.03555	-0.3627
18.1	2.12	0.04297	-0.3666

Configuration CC-26
Subtest A
Run 1703BP
Fig. B.32

α	C_l	$C_{d,wake}$	$C_{m,c_{sys}/4}$
9.1	1.67	0.02581	-0.2493
10.1	1.77	0.02502	-0.2536
11.2	1.80	0.02556	-0.2513
12.2	1.89	0.02595	-0.2524
13.2	1.93	0.02657	-0.2508
14.2	2.01	0.02735	-0.2532
15.2	2.11	0.02634	-0.2579
16.3	2.13	0.03022	-0.2567
17.3	2.13	0.03311	-0.2531
18.3	2.14	0.04393	-0.2518

Configuration CC-27
Subtest A
Run 1704BP
Fig. B.33

α	C_l	$C_{d,wake}$	$C_{m,c_{sys}/4}$
9.1	1.66	0.02467	-0.2523
10.1	1.74	0.02432	-0.2527
11.1	1.79	0.02479	-0.2520
12.2	1.89	0.02572	-0.2528
13.2	1.93	0.02624	-0.2522
14.2	1.97	0.02670	-0.2518
15.2	2.02	0.02882	-0.2521
16.2	2.06	0.03069	-0.2522
17.3	2.12	0.04006	-0.2528
18.3	2.18	0.04970	-0.2573

Configuration CC-28
Subtest A
Run 1705BP
Fig. B.34

α	C_l	$C_{d,wake}$	$C_{m,c_{sys}/4}$
9.1	1.66	0.02579	-0.2517
10.1	1.78	0.02723	-0.2569
11.2	1.83	0.02562	-0.2567
12.2	1.83	0.02543	-0.2481
14.2	1.99	0.03145	-0.2488
15.2	2.05	0.03467	-0.2478
16.3	2.09	0.03928	-0.2487
17.3	2.11	0.04365	-0.2471
18.3	2.23	0.05916	-0.2585

Configuration CC-29
Subtest A
Run 1706BP
Fig. B.35

α	C_l	$C_{d,wake}$	$C_{m,c_{sys}/4}$
9.1	1.66	0.02433	-0.2497
10.1	1.67	0.02444	-0.2466
11.1	1.74	0.02397	-0.2475
12.2	1.85	0.02544	-0.2491
13.2	1.86	0.02770	-0.2446
14.2	1.98	0.02848	-0.2477
15.2	2.00	0.03143	-0.2466
16.2	2.02	0.04138	-0.2426
17.3	2.09	0.04779	-0.2433
18.3	2.09	0.06625	-0.2431

Configuration CC-30
Subtest A
Run 1707BP
Fig. B.36

α	C_l	$C_{d,wake}$	$C_{m,c_{sys}/4}$
9.1	1.63	0.02451	-0.2620
10.1	1.70	0.02547	-0.2634
11.1	1.79	0.02441	-0.2654
12.1	1.83	0.02513	-0.2646
13.2	1.86	0.02705	-0.2614
14.2	2.00	0.02630	-0.2675
15.2	2.07	0.02833	-0.2681
16.2	2.11	0.02996	-0.2682
17.2	2.14	0.03155	-0.2667

Configuration CC-30
Subtest B
Run 1708BP
Fig. B.37

α	C_l	$C_{d,wake}$	$C_{m,c_{sys}/4}$
9.1	1.64	0.02543	-0.2596
10.1	1.73	0.02551	-0.2617
11.1	1.82	0.02473	-0.2651
12.2	1.85	0.02563	-0.2616
13.2	1.84	0.02591	-0.2561
14.2	2.00	0.02596	-0.2622
15.2	1.99	0.02601	-0.2584
16.2	2.03	0.02731	-0.2588
18.3	2.19	0.03398	-0.2649

Configuration CC-31
Subtest A
Run 1709BP
Fig. B.38

α	C_l	$C_{d,wake}$	$C_{m,c_{sys}/4}$
10.1	1.73	0.02556	-0.2589
13.2	1.97	0.02512	-0.2622
14.2	2.01	0.02698	-0.2612
15.2	2.03	0.02699	-0.2570
16.2	2.13	0.02888	-0.2616
17.3	2.18	0.02998	-0.2630

Configuration CC-32
Subtest A
Run 1710BP
Fig. B.39

α	C_l	$C_{d,wake}$	$C_{m,c_{sys}/4}$
9.1	1.64	0.02579	-0.2556
10.1	1.71	0.02560	-0.2555
11.1	1.78	0.02617	-0.2574
12.2	1.84	0.02628	-0.2552
13.2	1.92	0.02575	-0.2559
14.2	1.96	0.02551	-0.2529
16.2	2.08	0.02808	-0.2570
17.3	2.16	0.03272	-0.2584

Configuration CC-33
Subtest A
Run 1711BP
Fig. B.40

α	C_l	$C_{d,wake}$	$C_{m,c_{sys}/4}$
9.1	1.65	0.02544	-0.2575
10.1	1.73	0.02410	-0.2591
11.1	1.77	0.02528	-0.2578
12.2	1.83	0.02633	-0.2562
13.2	1.95	0.02639	-0.2580
14.2	1.98	0.02586	-0.2547
15.2	2.06	0.02882	-0.2567
16.2	2.09	0.02975	-0.2554
17.3	2.13	0.03567	-0.2538

Configuration CC-34
Subtest A
Run 1712BP
Fig. B.41

α	C_l	$C_{d,wake}$	$C_{m,c_{sys}/4}$
9.1	1.65	0.02294	-0.2555
10.1	1.67	0.02456	-0.2538
12.2	1.86	0.02445	-0.2557
13.2	1.90	0.02516	-0.2539
14.2	1.99	0.02678	-0.2559
15.2	2.03	0.03025	-0.2543
16.3	2.11	0.03097	-0.2514
17.3	2.14	0.03858	-0.2520
18.3	2.17	0.04957	-0.2536

Configuration CC-35
Subtest A
Run 1713BP
Fig. B.42

α	C_l	$C_{d,wake}$	$C_{m,c_{sys}/4}$
9.1	1.71	0.02485	-0.2786
10.1	1.72	0.02527	-0.2744
11.1	1.79	0.02685	-0.2750
12.1	1.87	0.02677	-0.2764
13.2	1.95	0.02632	-0.2781
14.2	2.01	0.02659	-0.2764
15.2	2.09	0.02728	-0.2781
16.2	2.15	0.02870	-0.2801
17.2	2.21	0.03022	-0.2818
18.2	2.20	0.03474	-0.2791

Configuration CC-36
Subtest A
Run 1714BP
Fig. B.43

α	C_l	$C_{d,wake}$	$C_{m,c_{sys}/4}$
9.1	1.64	0.02631	-0.2685
10.1	1.71	0.02555	-0.2709
11.1	1.77	0.02507	-0.2707
12.1	1.83	0.02660	-0.2709
13.2	1.93	0.02638	-0.2719
14.2	1.96	0.02762	-0.2695
15.2	2.07	0.02810	-0.2717
16.2	2.07	0.02792	-0.2703
17.2	2.14	0.03075	-0.2715
18.2	2.19	0.03707	-0.2734

Configuration CC-37
Subtest A
Run 1715BP
Fig. B.44

α	C_l	$C_{d,wake}$	$C_{m,c_{sys}/4}$
9.1	1.69	0.02556	-0.2681
10.1	1.75	0.02493	-0.2685
11.1	1.79	0.02532	-0.2677
12.2	1.90	0.02577	-0.2682
13.2	1.96	0.02354	-0.2672
14.2	2.04	0.02734	-0.2669
15.2	2.06	0.02797	-0.2640
16.2	2.12	0.03087	-0.2630
17.2	2.15	0.03500	-0.2637
18.3	2.21	0.04160	-0.2651

Configuration CC-38
Subtest A
Run 1716BP
Fig. B.45

α	C_l	$C_{d,wake}$	$C_{m,c_{sys}/4}$
9.1	1.70	0.02453	-0.2605
10.1	1.75	0.02500	-0.2601
11.2	1.83	0.02556	-0.2618
12.2	1.87	0.02616	-0.2570
13.2	2.00	0.02657	-0.2610
14.2	2.04	0.02773	-0.2589
15.2	2.10	0.03159	-0.2581
16.2	2.10	0.03385	-0.2545
17.2	2.11	0.03875	-0.2511
18.3	2.19	0.04581	-0.2542

Configuration CC-39
Subtest A
Run 1717BP
Fig. B.46

α	C_l	$C_{d,wake}$	$C_{m,c_{sys}/4}$
9.1	1.67	0.02469	-0.2521
10.1	1.75	0.02505	-0.2540
11.1	1.78	0.02568	-0.2530
12.2	1.82	0.02482	-0.2490
13.2	1.94	0.02606	-0.2531
15.2	2.01	0.02926	-0.2500
16.2	2.09	0.03190	-0.2484
17.3	2.12	0.03915	-0.2533
18.3	2.20	0.04474	-0.2561

Configuration CC-39
Subtest B
Run 1765BP
Fig. B.47

α	C_l	$C_{d,wake}$	$C_{m,c_{sys}/4}$
11.2	1.80	0.02499	-0.2478
12.2	1.90	0.02576	-0.2499
13.2	1.96	0.02517	-0.2499
14.2	1.99	0.02813	-0.2472
15.3	2.12	0.02667	-0.2522
16.3	2.10	0.02718	-0.2473
17.3	2.13	0.03262	-0.2485
18.3	2.19	0.03631	-0.2494

Configuration CC-39
Subtest C
Run 1766BP
Fig. B.48

α	C_l	$C_{d,wake}$	$C_{m,c_{sys}/4}$
9.1	1.72	0.02477	-0.2529
10.2	1.87	0.02593	-0.2591
11.2	1.82	0.02558	-0.2509
12.2	1.91	0.02534	-0.2520
13.2	1.97	0.02691	-0.2527
14.2	1.92	0.02631	-0.2437
15.2	2.07	0.02847	-0.2497
17.2	2.10	0.03130	-0.2459
18.3	2.18	0.03755	-0.2502

Configuration CC-39
Subtest D
Run 1767BP
Fig. B.49

α	C_l	$C_{d,wake}$	$C_{m,c_{sys}/4}$
9.1	1.72	0.02482	-0.2528
10.1	1.79	0.02559	-0.2534
11.2	1.86	0.02588	-0.2546
13.2	1.96	0.02581	-0.2519
14.2	1.97	0.02725	-0.2471
15.2	2.05	0.02672	-0.2495
16.3	2.10	0.03023	-0.2498
17.3	2.16	0.03313	-0.2521
18.3	2.18	0.03663	-0.2524

Configuration CC-40
Subtest A
Run 1718BP
Fig. B.50

α	C_l	$C_{d,wake}$	$C_{m,c_{sys}/4}$
9.1	1.74	0.02625	-0.2752
10.1	1.75	0.02533	-0.2717
12.1	1.87	0.02566	-0.2704
13.2	1.95	0.02494	-0.2704
14.2	2.03	0.02444	-0.2701
15.2	2.07	0.02729	-0.2679
16.2	2.14	0.02834	-0.2695
17.2	2.18	0.02931	-0.2690

Configuration CC-41
Subtest A
Run 1719BP
Fig. B.51

α	C_l	$C_{d,wake}$	$C_{m,c_{sys}/4}$
9.1	1.73	0.02478	-0.2686
10.1	1.74	0.02534	-0.2646
11.1	1.83	0.02517	-0.2668
12.2	1.91	0.02658	-0.2667
13.2	2.00	0.02594	-0.2676
14.2	2.03	0.02776	-0.2649
15.2	2.10	0.02825	-0.2657
16.3	2.15	0.03034	-0.2655
17.3	2.20	0.03218	-0.2653
18.3	2.22	0.03911	-0.2648

Configuration CC-42
Subtest A
Run 1720BP
Fig. B.52

α	C_l	$C_{d,wake}$	$C_{m,c_{sys}/4}$
9.1	1.67	0.02462	-0.2693
10.1	1.75	0.02545	-0.2677
11.1	1.80	0.02565	-0.2637
12.2	1.91	0.02600	-0.2662
13.2	1.94	0.02598	-0.2627
15.2	2.11	0.02896	-0.2663
16.3	2.20	0.02985	-0.2698
17.3	2.20	0.03636	-0.2637
18.3	2.27	0.04018	-0.2673

Configuration CC-43
Subtest A
Run 1721BP
Fig. B.53

α	C_l	$C_{d,wake}$	$C_{m,c_{sys}/4}$
9.1	1.70	0.02472	-0.2695
10.1	1.74	0.02444	-0.2700
11.1	1.79	0.02375	-0.2697
12.2	1.89	0.02475	-0.2671
13.2	1.92	0.02527	-0.2632
14.2	2.02	0.02530	-0.2635
15.2	2.07	0.02999	-0.2629
16.3	2.15	0.03245	-0.2647
17.2	2.16	0.03801	-0.2649
18.3	2.23	0.04559	-0.2658

Configuration CC-44
Subtest A
Run 1722BP
Fig. B.54

α	C_l	$C_{d,wake}$	$C_{m,c_{sys}/4}$
9.1	1.69	0.02330	-0.2675
10.1	1.71	0.02436	-0.2681
11.1	1.80	0.02461	-0.2698
12.1	1.85	0.02456	-0.2688
13.2	1.92	0.02639	-0.2662
14.2	2.02	0.02834	-0.2694
16.2	2.05	0.03220	-0.2679
17.2	2.13	0.04015	-0.2703
18.2	2.16	0.04688	-0.2668

Configuration CC-45
Subtest A
Run 1723BP
Fig. B.55

α	C_l	$C_{d,wake}$	$C_{m,c_{sys}/4}$
10.1	1.73	0.02277	-0.2451
11.1	1.76	0.02356	-0.2468
12.2	1.83	0.02371	-0.2481
13.2	1.86	0.02258	-0.2481
14.2	1.83	0.02669	-0.2420
15.2	1.93	0.02918	-0.2443
16.2	1.93	0.03118	-0.2426
17.2	2.02	0.03888	-0.2450
18.2	2.06	0.04730	-0.2458

Configuration CC-46
Subtest A
Run 1724BP
Fig. B.56

α	C_l	$C_{d,wake}$	$C_{m,c_{sys}/4}$
9.1	1.64	0.02328	-0.2427
12.2	1.79	0.02439	-0.2467
13.2	1.88	0.02556	-0.2484
14.2	1.89	0.02636	-0.2459
15.2	1.97	0.02854	-0.2493
16.2	2.00	0.03034	-0.2481
17.2	2.04	0.03613	-0.2474
18.2	2.08	0.04113	-0.2467

Configuration CC-47
Subtest A
Run 1725BP
Fig. B.57

α	C_l	$C_{d,wake}$	$C_{m,c_{sys}/4}$
9.1	1.65	0.02337	-0.2478
10.1	1.73	0.02387	-0.2511
11.1	1.75	0.02354	-0.2514
12.2	1.83	0.02429	-0.2529
13.2	1.84	0.02589	-0.2514
14.2	1.96	0.02660	-0.2555
15.2	1.94	0.02814	-0.2503
18.2	2.07	0.04417	-0.2507

Configuration CC-48
Subtest A
Run 1726BP
Fig. B.58

α	C_l	$C_{d,wake}$	$C_{m,c_{sys}/4}$
10.1	1.71	0.02280	-0.2485
11.1	1.76	0.02314	-0.2498
12.1	1.79	0.02323	-0.2472
13.2	1.88	0.02640	-0.2483
15.2	2.01	0.02933	-0.2466
16.2	2.01	0.03425	-0.2415
17.2	2.06	0.04415	-0.2420
18.3	2.11	0.04961	-0.2444

Configuration CC-49
Subtest A
Run 1727BP
Fig. B.59

α	C_l	$C_{d,wake}$	$C_{m,c_{sys}/4}$
9.1	1.67	0.02341	-0.2489
10.1	1.73	0.02369	-0.2536
11.1	1.78	0.02413	-0.2557
13.2	1.87	0.02421	-0.2521
14.2	1.93	0.02674	-0.2508
15.2	2.05	0.03008	-0.2564
16.2	2.06	0.03445	-0.2501
17.3	2.08	0.04581	-0.2464

Configuration CC-50
Subtest A
Run 1728BP
Fig. B.60

α	C_l	$C_{d,wake}$	$C_{m,c_{sys}/4}$
9.1	1.62	0.02364	-0.2474
10.1	1.75	0.02309	-0.2549
11.1	1.76	0.02363	-0.2529
12.1	1.77	0.02356	-0.2505
13.2	1.86	0.02541	-0.2507
14.2	1.92	0.02799	-0.2517
15.2	1.98	0.02874	-0.2511
16.2	2.05	0.03638	-0.2507
17.2	2.01	0.03824	-0.2417
18.2	2.09	0.04267	-0.2494

Configuration CC-51
Subtest A
Run 1729BP
Fig. B.61

α	C_l	$C_{d,wake}$	$C_{m,c_{sys}/4}$
10.1	1.76	0.02350	-0.2564
11.2	1.81	0.02185	-0.2570
12.2	1.86	0.02315	-0.2537
13.2	1.89	0.02639	-0.2521
14.2	1.99	0.02871	-0.2527
15.2	2.00	0.03230	-0.2483
16.2	1.97	0.03894	-0.2427
17.2	2.03	0.04469	-0.2444
18.3	2.13	0.05491	-0.2465

Configuration CC-52
Subtest A
Run 1730BP
Fig. B.62

α	C_l	$C_{d,wake}$	$C_{m,c_{sys}/4}$
10.1	1.78	0.02272	-0.2566
11.2	1.81	0.02400	-0.2541
12.2	1.91	0.02558	-0.2560
13.2	1.94	0.02505	-0.2527
14.2	2.02	0.02755	-0.2522
15.2	2.00	0.02995	-0.2464
17.3	2.14	0.03917	-0.2487
18.2	2.11	0.05251	-0.2433

Configuration CC-53
Subtest A
Run 1731BP
Fig. B.63

α	C_l	$C_{d,wake}$	$C_{m,c_{sys}/4}$
9.1	1.71	0.02300	-0.2573
10.1	1.73	0.02381	-0.2535
11.2	1.81	0.02327	-0.2568
13.2	1.94	0.02480	-0.2529
14.2	2.00	0.02679	-0.2519
15.2	2.04	0.02922	-0.2506
16.3	2.11	0.03449	-0.2525
17.3	2.17	0.03874	-0.2542
18.3	2.21	0.04795	-0.2525

Configuration CC-54
Subtest A
Run 1732BP
Fig. B.64

α	C_l	$C_{d,wake}$	$C_{m,c_{sys}/4}$
9.1	1.67	0.02384	-0.2465
10.1	1.68	0.02370	-0.2467
11.1	1.76	0.02367	-0.2486
12.2	1.81	0.02305	-0.2503
13.2	1.89	0.02499	-0.2499
14.2	1.91	0.02611	-0.2481
15.2	1.94	0.02697	-0.2464
16.2	1.95	0.02962	-0.2459
17.2	2.04	0.03369	-0.2489
18.2	2.06	0.04257	-0.2460

Configuration CC-55
Subtest A
Run 1733BP
Fig. B.65

α	C_l	$C_{d,wake}$	$C_{m,c_{sys}/4}$
9.1	1.64	0.02243	-0.2476
10.1	1.67	0.02321	-0.2476
11.2	1.80	0.02347	-0.2538
12.2	1.85	0.02348	-0.2540
13.2	1.87	0.02473	-0.2505
14.2	1.85	0.02377	-0.2463
15.2	1.95	0.02712	-0.2505
16.2	1.94	0.03210	-0.2452
17.2	2.07	0.03499	-0.2526
18.2	2.07	0.04238	-0.2490

Configuration CC-56
Subtest A
Run 1734BP
Fig. B.66

α	C_l	$C_{d,wake}$	$C_{m,c_{sys}/4}$
9.1	1.66	0.02419	-0.2517
10.1	1.72	0.02436	-0.2534
11.1	1.78	0.02281	-0.2560
12.2	1.82	0.02448	-0.2560
13.2	1.86	0.02511	-0.2543
14.2	1.91	0.02693	-0.2529
15.2	1.97	0.02750	-0.2557
17.2	2.02	0.03644	-0.2556
18.2	2.07	0.04122	-0.2550

Configuration CC-57
Subtest A
Run 1735BP
Fig. B.67

α	C_l	$C_{d,wake}$	$C_{m,c_{sys}/4}$
9.1	1.68	0.02268	-0.2545
10.1	1.70	0.02474	-0.2519
11.1	1.80	0.02417	-0.2581
12.1	1.81	0.02450	-0.2551
13.2	1.89	0.02448	-0.2547
14.2	1.98	0.02448	-0.2583
15.2	1.94	0.02610	-0.2466
16.2	2.04	0.03027	-0.2508
17.2	2.02	0.03704	-0.2533
18.2	2.13	0.04045	-0.2536

Configuration CC-58
Subtest A
Run 1736BP
Fig. B.68

α	C_l	$C_{d,wake}$	$C_{m,c_{sys}/4}$
9.1	1.70	0.02383	-0.2522
11.1	1.74	0.02463	-0.2522
12.2	1.80	0.02463	-0.2517
13.2	1.86	0.02428	-0.2508
14.2	1.93	0.02580	-0.2541
15.2	1.98	0.02650	-0.2540
16.2	2.01	0.02767	-0.2524
17.2	2.07	0.03671	-0.2528
18.2	2.17	0.03953	-0.2588

Configuration CC-59
Subtest A
Run 1737BP
Fig. B.69

α	C_l	$C_{d,wake}$	$C_{m,c_{sys}/4}$
9.1	1.66	0.02416	-0.2523
10.1	1.70	0.02393	-0.2523
11.1	1.82	0.02372	-0.2612
12.2	1.82	0.02347	-0.2553
13.2	1.88	0.02480	-0.2559
14.2	1.93	0.02638	-0.2543
15.2	1.99	0.02595	-0.2568
16.2	1.98	0.02828	-0.2551
17.2	2.13	0.03125	-0.2628
18.2	2.06	0.04229	-0.2545

Configuration CC-60
Subtest A
Run 1738BP
Fig. B.70

α	C_l	$C_{d,wake}$	$C_{m,c_{sys}/4}$
9.1	1.69	0.02390	-0.2547
10.1	1.75	0.02320	-0.2537
11.2	1.78	0.02370	-0.2517
12.2	1.87	0.02403	-0.2511
13.2	1.88	0.02471	-0.2468
14.2	1.95	0.02532	-0.2484
15.2	2.05	0.02692	-0.2473
16.2	2.06	0.03007	-0.2466
17.2	2.10	0.03501	-0.2452
18.3	2.16	0.04163	-0.2471

Configuration CC-61
Subtest A
Run 1739BP
Fig. B.71

α	C_l	$C_{d,wake}$	$C_{m,c_{sys}/4}$
9.1	1.69	0.02362	-0.2564
11.1	1.76	0.02342	-0.2544
12.2	1.85	0.02324	-0.2562
13.2	1.91	0.02383	-0.2547
14.2	2.00	0.02464	-0.2537
15.2	1.97	0.02611	-0.2513
16.2	2.05	0.02992	-0.2529
17.2	2.06	0.03706	-0.2468
18.3	2.15	0.04275	-0.2515

Configuration CC-62
Subtest A
Run 1740BP
Fig. B.72

α	C_l	$C_{d,wake}$	$C_{m,c_{sys}/4}$
9.1	1.69	0.02385	-0.2568
11.1	1.79	0.02399	-0.2583
12.2	1.89	0.02531	-0.2607
13.2	1.90	0.02559	-0.2547
14.2	1.97	0.02623	-0.2550
15.2	2.08	0.02793	-0.2601
16.2	2.09	0.03064	-0.2581
17.3	2.12	0.03393	-0.2534
18.3	2.16	0.04344	-0.2562

Configuration CC-63
Subtest A
Run 1741BP
Fig. B.73

α	C_l	$C_{d,wake}$	$C_{m,c_{sys}/4}$
9.1	1.60	0.02335	-0.2361
10.1	1.70	0.02288	-0.2432
11.1	1.71	0.02393	-0.2388
12.1	1.75	0.02460	-0.2390
13.2	1.82	0.02470	-0.2388
14.2	1.88	0.02579	-0.2399
15.2	1.91	0.02669	-0.2404
16.2	1.95	0.02823	-0.2392
17.2	1.96	0.03708	-0.2377
18.2	2.11	0.04162	-0.2456

Configuration CC-64
Subtest A
Run 1742BP
Fig. B.74

α	C_l	$C_{d,wake}$	$C_{m,c_{sys}/4}$
9.1	1.66	0.02323	-0.2449
10.1	1.74	0.02354	-0.2504
11.1	1.72	0.02441	-0.2454
12.2	1.84	0.02408	-0.2493
13.2	1.88	0.02532	-0.2490
14.2	1.88	0.02730	-0.2441
15.2	2.00	0.02809	-0.2504
16.2	2.04	0.03093	-0.2514
17.2	2.02	0.03418	-0.2477
18.3	2.17	0.04013	-0.2549

Configuration CC-65
Subtest A
Run 1743BP
Fig. B.75

α	C_l	$C_{d,wake}$	$C_{m,c_{sys}/4}$
9.1	1.66	0.02382	-0.2468
10.1	1.67	0.02324	-0.2475
11.1	1.73	0.02577	-0.2480
12.2	1.84	0.02513	-0.2532
13.2	1.85	0.02499	-0.2511
14.2	1.94	0.02730	-0.2531
16.2	2.04	0.03391	-0.2557
17.2	2.03	0.03836	-0.2524
18.2	2.05	0.04389	-0.2502

Configuration CC-66
Subtest A
Run 1744BP
Fig. B.76

α	C_l	$C_{d,wake}$	$C_{m,c_{sys}/4}$
9.1	1.67	0.02312	-0.2452
10.1	1.70	0.02413	-0.2459
11.1	1.78	0.02375	-0.2490
12.2	1.82	0.02429	-0.2489
13.2	1.86	0.02412	-0.2465
14.2	1.92	0.02552	-0.2475
15.2	1.99	0.02850	-0.2471
16.2	1.98	0.02987	-0.2431
17.2	2.04	0.03435	-0.2459
18.2	2.07	0.04551	-0.2470

Configuration CC-67
Subtest A
Run 1745BP
Fig. B.77

α	C_l	$C_{d,wake}$	$C_{m,c_{sys}/4}$
9.1	1.67	0.02319	-0.2500
10.1	1.73	0.02415	-0.2529
11.1	1.72	0.02345	-0.2492
12.2	1.80	0.02412	-0.2502
13.2	1.85	0.02404	-0.2498
14.2	1.96	0.02605	-0.2532
16.2	2.03	0.02995	-0.2538
17.2	2.04	0.03275	-0.2507
18.2	2.09	0.04128	-0.2533

Configuration CC-68
Subtest A
Run 1746BP
Fig. B.78

α	C_l	$C_{d,wake}$	$C_{m,c_{sys}/4}$
9.1	1.71	0.02358	-0.2539
10.1	1.75	0.02404	-0.2553
11.1	1.80	0.02437	-0.2582
12.2	1.86	0.02499	-0.2569
13.2	1.91	0.02545	-0.2577
14.2	1.99	0.02555	-0.2594
15.2	1.96	0.02843	-0.2556
18.2	2.08	0.04170	-0.2546

Configuration CC-69
Subtest A
Run 1747BP
Fig. B.79

α	C_l	$C_{d,wake}$	$C_{m,c_{sys}/4}$
9.1	1.71	0.02406	-0.2537
10.1	1.75	0.02375	-0.2536
11.1	1.76	0.02506	-0.2487
12.2	1.90	0.02518	-0.2536
13.2	1.94	0.02618	-0.2519
15.2	2.02	0.02883	-0.2489
16.2	2.06	0.03287	-0.2490
17.2	2.05	0.03327	-0.2470

Configuration CC-70
Subtest A
Run 1748BP
Fig. B.80

α	C_l	$C_{d,wake}$	$C_{m,c_{sys}/4}$
9.1	1.70	0.02499	-0.2537
10.1	1.74	0.02501	-0.2533
11.2	1.85	0.02478	-0.2571
12.2	1.86	0.02478	-0.2531
13.2	1.97	0.02691	-0.2558
14.2	2.00	0.02996	-0.2541
15.2	1.97	0.02928	-0.2477
17.2	2.07	0.03806	-0.2515
18.2	2.14	0.04237	-0.2547

Configuration CC-71
Subtest A
Run 1749BP
Fig. B.81

α	C_l	$C_{d,wake}$	$C_{m,c_{sys}/4}$
9.1	1.69	0.02525	-0.2560
10.1	1.77	0.02596	-0.2561
11.2	1.79	0.02601	-0.2535
12.2	1.93	0.02617	-0.2595
13.2	1.93	0.02679	-0.2548
14.2	1.98	0.02629	-0.2550
15.2	2.00	0.02956	-0.2528
16.2	2.05	0.03023	-0.2551
17.2	2.10	0.03499	-0.2555
18.2	2.17	0.04240	-0.2580

Configuration CC-72
Subtest A
Run 1750BP
Fig. B.82

α	C_l	$C_{d,wake}$	$C_{m,c_{sys}/4}$
9.1	1.60	0.02450	-0.2422
10.1	1.69	0.02475	-0.2470
12.2	1.82	0.02480	-0.2482
13.2	1.83	0.02428	-0.2456
14.2	1.86	0.02722	-0.2452
15.2	1.88	0.02779	-0.2435
16.2	1.95	0.03125	-0.2446
17.2	1.98	0.03470	-0.2436
18.2	2.07	0.04382	-0.2480

Configuration CC-73
Subtest A
Run 1751BP
Fig. B.83

α	C_l	$C_{d,wake}$	$C_{m,c_{sys}/4}$
9.1	1.66	0.02336	-0.2476
10.1	1.70	0.02442	-0.2485
11.1	1.77	0.02417	-0.2501
13.2	1.86	0.02525	-0.2486
14.2	1.89	0.02765	-0.2480
15.2	1.91	0.02972	-0.2457
16.2	1.93	0.03324	-0.2454
17.2	1.98	0.03654	-0.2446
18.2	1.96	0.04293	-0.2409

Configuration CC-74
Subtest A
Run 1752BP
Fig. B.84

α	C_l	$C_{d,wake}$	$C_{m,c_{sys}/4}$
9.1	1.62	0.02573	-0.2445
10.1	1.69	0.02433	-0.2495
11.1	1.76	0.02532	-0.2507
12.2	1.82	0.02512	-0.2504
13.2	1.83	0.02531	-0.2478
14.2	1.91	0.02660	-0.2508
15.2	1.94	0.03010	-0.2490
16.2	2.05	0.02986	-0.2536
17.2	2.00	0.03509	-0.2482
18.2	2.05	0.04039	-0.2484

Configuration CC-75
Subtest A
Run 1753BP
Fig. B.85

α	C_l	$C_{d,wake}$	$C_{m,c_{sys}/4}$
9.1	1.65	0.02431	-0.2414
10.1	1.73	0.02398	-0.2442
11.2	1.85	0.02431	-0.2505
12.2	1.80	0.02448	-0.2426
13.2	1.90	0.02581	-0.2476
14.2	1.95	0.02646	-0.2453
15.2	1.93	0.02962	-0.2423
16.2	1.97	0.03181	-0.2423
17.2	2.09	0.03429	-0.2455
18.2	2.06	0.04499	-0.2433

Configuration CC-76
Subtest A
Run 1754BP
Fig. B.86

α	C_l	$C_{d,wake}$	$C_{m,c_{sys}/4}$
9.1	1.67	0.02499	-0.2437
10.1	1.73	0.02460	-0.2439
11.2	1.77	0.02416	-0.2448
12.2	1.82	0.02504	-0.2437
13.2	1.91	0.02664	-0.2477
14.2	1.94	0.02974	-0.2473
17.2	2.07	0.03603	-0.2510
18.2	2.07	0.04150	-0.2465

Configuration CC-77
Subtest A
Run 1755BP
Fig. B.87

α	C_l	$C_{d,wake}$	$C_{m,c_{sys}/4}$
9.1	1.67	0.02382	-0.2434
10.1	1.71	0.02370	-0.2435
11.2	1.82	0.02567	-0.2468
12.2	1.79	0.02584	-0.2434
13.2	1.89	0.02641	-0.2469
14.2	1.93	0.02724	-0.2463
15.2	2.00	0.02886	-0.2496
16.2	1.98	0.03278	-0.2480
17.2	2.09	0.03589	-0.2538
18.2	2.05	0.05001	-0.2478

Configuration CC-78
Subtest A
Run 1756BP
Fig. B.88

α	C_l	$C_{d,wake}$	$C_{m,c_{sys}/4}$
9.1	1.67	0.02256	-0.2502
10.1	1.75	0.02378	-0.2519
11.2	1.81	0.02219	-0.2538
12.2	1.86	0.02483	-0.2535
13.2	1.90	0.02748	-0.2510
14.2	1.98	0.02770	-0.2534
15.2	1.98	0.03056	-0.2476
16.2	2.02	0.04485	-0.2498
17.2	2.06	0.04695	-0.2466
18.2	2.10	0.05767	-0.2497

Configuration CC-79
Subtest A
Run 1757BP
Fig. B.89

α	C_l	$C_{d,wake}$	$C_{m,c_{sys}/4}$
9.1	1.65	0.02315	-0.2519
10.1	1.76	0.02401	-0.2559
11.2	1.83	0.02535	-0.2586
12.2	1.83	0.02448	-0.2527
13.2	1.85	0.02661	-0.2478
14.2	1.97	0.02901	-0.2531
15.2	2.02	0.03538	-0.2530
16.2	2.05	0.03841	-0.2522
17.3	2.12	0.04733	-0.2523
18.3	2.13	0.05571	-0.2535

Configuration CC-80
Subtest A
Run 1758BP
Fig. B.90

α	C_l	$C_{d,wake}$	$C_{m,c_{sys}/4}$
9.1	1.67	0.02348	-0.2529
10.1	1.71	0.02459	-0.2508
12.2	1.81	0.02566	-0.2500
14.2	1.96	0.02642	-0.2423
15.2	2.07	0.02823	-0.2485
16.3	2.10	0.03214	-0.2472
17.2	2.06	0.03394	-0.2420
18.3	2.15	0.04175	-0.2464

Tabulated Well Separated Performance Data Tables

Configuration WS-1
Subtest C
Run 1872BP
Fig. B.91

α	C_l	$C_{d,wake}$	$C_{m,c_{sys}/4}$
6.0	1.20	0.01682	-0.2548
7.1	1.30	0.01506	-0.2582
8.1	1.40	0.01711	-0.2593
9.1	1.50	0.01631	-0.2624
10.1	1.59	0.01555	-0.2643
11.1	1.65	0.01520	-0.2628
12.2	1.68	0.01535	-0.2552
13.2	1.72	0.01479	-0.2501
14.2	1.69	0.01684	-0.2341
15.2	1.69	0.01526	-0.2230
16.2	1.65	0.01605	-0.2127
17.2	1.68	0.01663	-0.2032
18.2	1.65	0.01693	-0.1957
19.2	1.67	0.01728	-0.2050
20.2	1.66	0.01945	-0.2006
21.2	1.64	0.02038	-0.1846
22.2	1.65	0.02441	-0.1897
23.2	1.63	0.02584	-0.1853
24.2	1.59	0.03002	-0.1824
25.2	1.59	0.03559	-0.1770
26.2	1.59	0.04272	-0.1717
27.2	1.59	0.04800	-0.1730
26.3	1.58	0.04213	-0.1694
25.2	1.59	0.03868	-0.1750
24.2	1.62	0.03250	-0.1842
23.2	1.62	0.02810	-0.1908
22.2	1.66	0.02590	-0.2011
21.2	1.66	0.02021	-0.2078
20.2	1.72	0.01898	-0.2112
19.2	1.68	0.01848	-0.2140
18.2	1.73	0.01679	-0.2268
17.2	1.71	0.01704	-0.2180
16.2	1.73	0.01596	-0.2264
15.2	1.74	0.01494	-0.2357

Continued ...
Subtest C
Run 1872BP

α	C_l	$C_{d,wake}$	$C_{m,c_{sys}/4}$
14.2	1.76	0.01505	-0.2404
13.2	1.75	0.01534	-0.2535
12.2	1.74	0.01528	-0.2598
11.2	1.67	0.01600	-0.2611
10.1	1.60	0.01553	-0.2625
9.1	1.52	0.01597	-0.2611
8.1	1.41	0.01744	-0.2566
7.1	1.32	0.01810	-0.2555
6.1	1.21	0.01655	-0.2532
5.0	1.11	0.01629	-0.2519
4.0	1.00	0.01684	-0.2515
3.0	0.89	0.01727	-0.2485
2.0	0.82	0.02937	-0.2190
1.0	0.71	0.03122	-0.2153
-0.1	0.61	0.03310	-0.2115
-1.1	0.50	0.03638	-0.2065
-2.1	0.20	0.08630	-0.1093
-3.1	0.12	0.08906	-0.0953
-4.1	0.07	0.09271	-0.0857
-5.1	0.03	0.09538	-0.0784
-6.1	0.00	0.09798	-0.0734
-7.1	-0.03	0.09997	-0.0695
-6.1	0.00	0.09728	-0.0776
-5.1	0.03	0.09418	-0.0818
-4.1	0.07	0.09290	-0.0892
-3.1	0.12	0.08994	-0.0979
-2.1	0.19	0.08648	-0.1115
-1.1	0.29	0.08281	-0.1297
-0.1	0.42	0.07325	-0.1535
0.9	0.70	0.03097	-0.2196
2.0	0.80	0.02939	-0.2233
3.0	0.90	0.02878	-0.2274
4.0	1.00	0.02839	-0.2322
5.0	1.11	0.02639	-0.2383

Configuration WS-1
Subtest D
Run 1873BP
Fig. B.92

α	C_l	$C_{d,wake}$	$C_{m,c_{sys}/4}$
-0.0	0.46	0.06999	-0.1669
0.9	0.71	0.03019	-0.2282
2.0	0.81	0.02938	-0.2322
3.0	0.92	0.02837	-0.2365
4.0	1.01	0.02811	-0.2401
5.0	1.11	0.02637	-0.2454
6.0	1.21	0.01659	-0.2658
7.0	1.31	0.01716	-0.2664
8.1	1.41	0.01643	-0.2679
9.1	1.52	0.01638	-0.2706
10.1	1.60	0.01550	-0.2697
11.1	1.67	0.01574	-0.2690
12.2	1.71	0.01527	-0.2669
13.2	1.75	0.01488	-0.2558
14.2	1.70	0.01475	-0.2478
15.2	1.72	0.01513	-0.2367
16.2	1.71	0.01485	-0.2297
17.2	1.72	0.01527	-0.2216
18.2	1.68	0.01723	-0.2133
19.2	1.68	0.01723	-0.2194
20.2	1.66	0.02034	-0.2073
21.2	1.68	0.02066	-0.2056
22.2	1.64	0.02456	-0.2035
23.2	1.64	0.02762	-0.1964
24.2	1.62	0.02909	-0.1929
25.2	1.63	0.03833	-0.1882

Configuration WS-2
Subtest A
Run 1874BP
Fig. B.93

α	C_l	$C_{d,wake}$	$C_{m,c_{sys}/4}$
-0.1	0.55	0.06578	-0.2047
0.9	0.83	0.02953	-0.2836
1.9	0.93	0.02839	-0.2877
2.9	1.02	0.02760	-0.2899
4.0	1.13	0.02731	-0.2958
5.0	1.22	0.02608	-0.3044
6.0	1.32	0.01759	-0.3186
7.0	1.43	0.01753	-0.3221
8.0	1.52	0.01678	-0.3215
9.1	1.62	0.01587	-0.3242
10.1	1.68	0.01626	-0.3209
11.1	1.72	0.01475	-0.3145
12.1	1.73	0.01474	-0.3017
13.1	1.74	0.01389	-0.2884
14.1	1.71	0.01454	-0.2699
15.2	1.72	0.01487	-0.2592
16.2	1.70	0.01418	-0.2464
17.2	1.69	0.01497	-0.2374
18.2	1.67	0.01626	-0.2241
19.2	1.69	0.01594	-0.2190
20.2	1.63	0.01690	-0.2012
21.2	1.65	0.01799	-0.1942
22.2	1.65	0.01931	-0.1824
23.2	1.65	0.02184	-0.1754
24.2	1.63	0.02511	-0.1645
25.2	1.64	0.03120	-0.1631

Configuration WS-3
Subtest A
Run 1875BP
Fig. B.94

α	C_l	$C_{d,wake}$	$C_{m,c_{sys}/4}$
-0.1	0.76	0.03202	-0.2752
0.9	0.85	0.03091	-0.2810
1.9	0.95	0.02910	-0.2858
2.9	1.05	0.02808	-0.2911
4.0	1.15	0.02754	-0.2949
5.0	1.25	0.02551	-0.3021
6.0	1.34	0.01793	-0.3182
7.0	1.45	0.01698	-0.3198
8.1	1.55	0.01570	-0.3220
9.1	1.63	0.01535	-0.3223
10.1	1.68	0.01527	-0.3162
11.1	1.72	0.01459	-0.3096
12.1	1.75	0.01504	-0.3005
13.1	1.75	0.01462	-0.2890
14.2	1.76	0.01457	-0.2751
15.1	1.71	0.01504	-0.2592
16.2	1.72	0.01553	-0.2552
17.2	1.72	0.01564	-0.2485
18.2	1.68	0.01562	-0.2249
19.2	1.69	0.01585	-0.2165
20.2	1.65	0.01719	-0.2029
21.2	1.67	0.01732	-0.1942
22.2	1.63	0.02115	-0.1778
23.2	1.65	0.02578	-0.1814
24.2	1.65	0.02722	-0.1745
25.2	1.59	0.03179	-0.1679

Configuration WS-4
Subtest A
Run 1876BP
Fig. B.95

α	C_l	$C_{d,wake}$	$C_{m,c_{sys}/4}$
-0.1	0.61	0.06175	-0.2122
0.9	0.87	0.02989	-0.2795
1.9	0.97	0.02821	-0.2840
3.0	1.07	0.02760	-0.2883
4.0	1.17	0.02637	-0.2927
5.0	1.27	0.02458	-0.2984
6.0	1.35	0.01736	-0.3132
7.0	1.47	0.01717	-0.3168
8.1	1.55	0.01655	-0.3156
9.1	1.63	0.01563	-0.3152
10.1	1.69	0.01482	-0.3118
11.1	1.71	0.01503	-0.3016
12.1	1.72	0.01418	-0.2889
13.1	1.69	0.01439	-0.2710
14.2	1.71	0.01368	-0.2609
15.2	1.68	0.01507	-0.2470
16.2	1.71	0.01515	-0.2445
17.2	1.65	0.01557	-0.2279
18.2	1.68	0.01669	-0.2222
19.2	1.63	0.01528	-0.2057
20.2	1.64	0.01654	-0.1995
21.2	1.64	0.01896	-0.1870
22.2	1.63	0.02064	-0.1874
23.2	1.62	0.02783	-0.1674
24.2	1.61	0.02813	-0.1716
25.2	1.61	0.03326	-0.1672

Configuration WS-5
Subtest A
Run 1877BP
Fig. B.96

α	C_l	$C_{d,wake}$	$C_{m,c_{sys}/4}$
-0.1	0.58	0.06200	-0.2074
0.9	0.85	0.02929	-0.2756
1.9	0.95	0.02789	-0.2804
3.0	1.05	0.02746	-0.2842
4.0	1.14	0.02681	-0.2874
5.0	1.24	0.02630	-0.2934
6.0	1.34	0.01810	-0.3122
7.0	1.44	0.01695	-0.3122
8.1	1.54	0.01574	-0.3126
9.1	1.63	0.01575	-0.3143
10.1	1.67	0.01594	-0.3072
11.1	1.71	0.01480	-0.3003
12.1	1.67	0.01472	-0.2806
13.1	1.67	0.01456	-0.2660
14.2	1.68	0.01407	-0.2537
15.2	1.63	0.01493	-0.2365
16.2	1.66	0.01497	-0.2310
17.2	1.62	0.01604	-0.2156
18.2	1.65	0.01580	-0.2091
19.2	1.63	0.01613	-0.1943
20.2	1.62	0.01641	-0.1851
21.2	1.59	0.01814	-0.1763
22.2	1.62	0.02186	-0.1685
23.2	1.59	0.02558	-0.1583
24.2	1.60	0.03152	-0.1542
25.2	1.61	0.04736	-0.1572

Configuration WS-6
Subtest A
Run 1878BP
Fig. B.97

α	C_l	$C_{d,wake}$	$C_{m,c_{sys}/4}$
-0.1	0.78	0.03081	-0.2660
0.9	0.86	0.02985	-0.2714
1.9	0.96	0.02835	-0.2754
3.0	1.06	0.02675	-0.2792
4.0	1.16	0.02724	-0.2853
5.0	1.26	0.02627	-0.2903
6.0	1.35	0.01781	-0.3066
7.0	1.44	0.01710	-0.3066
8.1	1.54	0.01620	-0.3092
9.1	1.62	0.01550	-0.3083
10.1	1.64	0.01483	-0.2996
11.1	1.69	0.01546	-0.2927
12.1	1.66	0.01529	-0.2739
13.1	1.67	0.01441	-0.2611
14.2	1.64	0.01447	-0.2432
15.2	1.65	0.01476	-0.2378
16.2	1.64	0.01537	-0.2296
17.2	1.62	0.01595	-0.2201
18.2	1.61	0.01539	-0.2102
19.2	1.59	0.01585	-0.2100
20.2	1.58	0.01711	-0.1863
21.2	1.57	0.01961	-0.1837
22.2	1.59	0.02212	-0.1792
23.2	1.54	0.02664	-0.1681
24.2	1.56	0.03723	-0.1724
25.2	1.55	0.03633	-0.1753

Configuration WS-7
Subtest A
Run 1879BP
Fig. B.98

α	C_l	$C_{d,wake}$	$C_{m,c_{sys}/4}$
-0.1	0.76	0.03121	-0.2641
0.9	0.85	0.03014	-0.2680
1.9	0.95	0.02911	-0.2727
3.0	1.04	0.02791	-0.2753
4.0	1.14	0.02719	-0.2802
5.0	1.24	0.02697	-0.2872
6.0	1.33	0.01821	-0.3022
7.0	1.43	0.01730	-0.3035
8.1	1.53	0.01636	-0.3044
9.1	1.62	0.01590	-0.3055
10.1	1.66	0.01514	-0.2997
11.1	1.66	0.01545	-0.2863
12.1	1.67	0.01593	-0.2759
13.1	1.67	0.01539	-0.2586
14.2	1.64	0.01407	-0.2410
15.2	1.64	0.01521	-0.2299
16.2	1.63	0.01649	-0.2187
17.2	1.61	0.01613	-0.2055
18.2	1.62	0.01675	-0.2016
19.2	1.61	0.01530	-0.1834
20.2	1.56	0.01897	-0.1688
21.2	1.58	0.01865	-0.1650
22.2	1.56	0.02035	-0.1617
23.2	1.59	0.03047	-0.1670
24.2	1.51	0.03222	-0.1594
25.2	1.53	0.04293	-0.1538

Configuration WS-8
Subtest A
Run 1880BP
Fig. B.99

α	C_l	$C_{d,wake}$	$C_{m,c_{sys}/4}$
-0.1	0.55	0.06416	-0.1939
0.9	0.82	0.02947	-0.2609
2.0	0.92	0.02823	-0.2643
3.0	1.02	0.02719	-0.2680
4.0	1.11	0.02724	-0.2714
5.0	1.20	0.02631	-0.2769
6.0	1.30	0.01752	-0.2947
7.0	1.40	0.01715	-0.2953
8.1	1.50	0.01569	-0.2962
9.1	1.58	0.01529	-0.2970
10.1	1.64	0.01544	-0.2942
11.1	1.68	0.01499	-0.2879
12.1	1.66	0.01538	-0.2711
13.1	1.67	0.01513	-0.2583
14.2	1.67	0.01521	-0.2459
15.2	1.66	0.01524	-0.2334
16.2	1.65	0.01563	-0.2208
17.2	1.65	0.01566	-0.2122
18.2	1.64	0.01656	-0.1959
19.2	1.60	0.01792	-0.1811
20.2	1.61	0.01720	-0.1760
21.2	1.59	0.02126	-0.1662
22.2	1.61	0.02290	-0.1649
23.2	1.54	0.02958	-0.1462
24.2	1.53	0.04194	-0.1527
25.2	1.54	0.04428	-0.1571

Configuration WS-9
Subtest A
Run 1881BP
Fig. B.100

α	C_l	$C_{d,wake}$	$C_{m,c_{sys}/4}$
-0.1	0.77	0.03092	-0.2584
0.9	0.85	0.02949	-0.2626
2.0	0.95	0.02807	-0.2666
3.0	1.05	0.02770	-0.2704
4.0	1.14	0.02731	-0.2739
5.0	1.24	0.02614	-0.2802
6.0	1.33	0.01712	-0.2973
7.0	1.43	0.01678	-0.2983
8.1	1.52	0.01565	-0.2996
9.1	1.61	0.01570	-0.3007
10.1	1.63	0.01550	-0.2906
11.1	1.64	0.01532	-0.2775
12.1	1.65	0.01542	-0.2641
13.1	1.60	0.01481	-0.2430
14.2	1.63	0.01451	-0.2339
15.2	1.59	0.01553	-0.2166
16.2	1.60	0.01505	-0.2072
17.2	1.58	0.01513	-0.1949
18.2	1.56	0.01599	-0.1876
19.2	1.58	0.01701	-0.1766
20.2	1.55	0.02065	-0.1751
21.2	1.55	0.02990	-0.1654
22.2	1.53	0.02777	-0.1605
23.2	1.53	0.03442	-0.1576
24.2	1.49	0.04044	-0.1497
25.2	1.51	0.04578	-0.1497

Configuration WS-10
Subtest A
Run 1882BP
Fig. B.101

α	C_l	$C_{d,wake}$	$C_{m,c_{sys}/4}$
-0.1	0.79	0.03162	-0.2572
0.9	0.87	0.02952	-0.2613
2.0	0.97	0.02801	-0.2658
3.0	1.07	0.02675	-0.2685
4.0	1.16	0.02702	-0.2723
5.0	1.26	0.02656	-0.2777
6.0	1.35	0.01695	-0.2950
7.1	1.45	0.01671	-0.2960
8.1	1.53	0.01511	-0.2960
9.1	1.61	0.01518	-0.2956
10.1	1.64	0.01594	-0.2878
11.1	1.66	0.01518	-0.2770
12.1	1.62	0.01436	-0.2554
13.2	1.62	0.01459	-0.2402
14.2	1.62	0.01536	-0.2282
15.2	1.56	0.01484	-0.2085
16.2	1.58	0.01504	-0.2070
17.2	1.60	0.01569	-0.1984
18.2	1.55	0.01787	-0.1802
19.2	1.58	0.01811	-0.1732
20.2	1.55	0.02175	-0.1687
21.2	1.54	0.02634	-0.1544
22.2	1.51	0.02772	-0.1493
23.2	1.51	0.03298	-0.1494
24.2	1.52	0.03867	-0.1478
25.2	1.47	0.04497	-0.1379

Configuration WS-11
Subtest A
Run 1883BP
Fig. B.102

α	C_l	$C_{d,wake}$	$C_{m,c_{sys}/4}$
-0.1	0.76	0.03064	-0.2514
0.9	0.83	0.02935	-0.2551
2.0	0.93	0.02757	-0.2589
3.0	1.03	0.02737	-0.2628
4.0	1.12	0.02767	-0.2663
5.0	1.22	0.02641	-0.2729
6.0	1.31	0.01696	-0.2895
7.1	1.41	0.01625	-0.2906
8.1	1.50	0.01592	-0.2910
9.1	1.58	0.01560	-0.2911
10.1	1.61	0.01531	-0.2839
11.1	1.62	0.01555	-0.2728
12.1	1.66	0.01588	-0.2617
13.1	1.60	0.01503	-0.2455
14.2	1.65	0.01650	-0.2345
15.2	1.59	0.01629	-0.2153
16.2	1.60	0.01572	-0.2117
17.2	1.60	0.01587	-0.1985
18.2	1.58	0.01727	-0.1875
19.2	1.56	0.01866	-0.1707
20.2	1.56	0.02151	-0.1707
21.2	1.54	0.02514	-0.1652
22.2	1.53	0.03214	-0.1575
23.2	1.51	0.04090	-0.1460
24.2	1.50	0.04446	-0.1433
25.2	1.47	0.05628	-0.1300

Configuration WS-12
Subtest A
Run 1884BP
Fig. B.103

α	C_l	$C_{d,wake}$	$C_{m,c_{sys}/4}$
-0.1	0.76	0.03034	-0.2469
0.9	0.84	0.02983	-0.2514
2.0	0.95	0.02813	-0.2572
3.0	1.04	0.02745	-0.2576
4.0	1.13	0.02705	-0.2617
5.0	1.23	0.02624	-0.2670
6.0	1.32	0.01732	-0.2850
7.1	1.41	0.01635	-0.2857
8.1	1.51	0.01509	-0.2886
9.1	1.59	0.01551	-0.2882
10.1	1.64	0.01532	-0.2832
11.1	1.69	0.01484	-0.2776
12.2	1.68	0.01476	-0.2611
13.2	1.63	0.01451	-0.2393
14.2	1.64	0.01481	-0.2352
15.2	1.64	0.01516	-0.2236
16.2	1.64	0.01564	-0.2184
17.2	1.64	0.01657	-0.2116
18.2	1.60	0.01786	-0.1970
19.2	1.60	0.01786	-0.1765
20.2	1.60	0.02434	-0.1783
21.2	1.57	0.02798	-0.1609
22.2	1.56	0.03396	-0.1582
23.2	1.55	0.04082	-0.1477
24.2	1.56	0.04645	-0.1441
25.2	1.51	0.05271	-0.1313

Configuration WS-13
Subtest A
Run 1885BP
Fig. B.104

α	C_l	$C_{d,wake}$	$C_{m,c_{sys}/4}$
-0.0	0.80	0.03112	-0.2532
0.9	0.88	0.02898	-0.2576
2.0	0.98	0.02763	-0.2607
3.0	1.07	0.02686	-0.2633
4.0	1.17	0.02620	-0.2675
5.0	1.26	0.02592	-0.2742
6.0	1.35	0.01695	-0.2897
7.1	1.45	0.01651	-0.2904
8.1	1.54	0.01553	-0.2912
9.1	1.62	0.01436	-0.2911
10.1	1.69	0.01449	-0.2919
11.1	1.74	0.01474	-0.2871
12.2	1.81	0.01487	-0.2821
13.2	1.76	0.01415	-0.2663
14.2	1.79	0.01420	-0.2585
15.2	1.73	0.01546	-0.2557
16.2	1.77	0.01526	-0.2423
17.2	1.72	0.01652	-0.2410
18.2	1.73	0.01691	-0.2397
19.2	1.70	0.01868	-0.2306
20.2	1.71	0.01887	-0.2131
21.2	1.69	0.02185	-0.2197
22.2	1.69	0.02577	-0.2113
23.2	1.63	0.03036	-0.1984
24.2	1.65	0.03683	-0.1967
25.2	1.61	0.04339	-0.1824

Configuration WS-14
Subtest A
Run 1892BP
Fig. B.105

α	C_l	$C_{d,wake}$	$C_{m,c_{sys}/4}$
-0.0	0.82	0.02993	-0.2610
0.9	0.89	0.02871	-0.2623
2.0	0.99	0.02810	-0.2660
3.0	1.08	0.02683	-0.2682
4.0	1.18	0.02617	-0.2733
5.0	1.27	0.02053	-0.2808
6.0	1.35	0.01710	-0.2941
7.1	1.43	0.01582	-0.2910
8.1	1.42	0.01524	-0.2762
9.1	1.44	0.01533	-0.2644
10.1	1.39	0.01518	-0.2436
11.1	1.40	0.01454	-0.2308
12.1	1.38	0.01508	-0.2130
13.1	1.38	0.01470	-0.2007
14.1	1.38	0.01473	-0.1922
15.1	1.35	0.01575	-0.1773
16.2	1.35	0.01608	-0.1672
17.2	1.36	0.01672	-0.1602
18.2	1.31	0.01857	-0.1446
19.2	1.34	0.02128	-0.1402
20.2	1.30	0.02640	-0.1257
21.2	1.31	0.03195	-0.1192
22.2	1.31	0.03549	-0.1140
23.2	1.30	0.04443	-0.1074
24.2	1.32	0.04961	-0.1060
25.2	1.31	0.05740	-0.1014

Configuration WS-15
Subtest A
Run 1886BP
Fig. B.106

α	C_l	$C_{d,wake}$	$C_{m,c_{sys}/4}$
-0.0	0.79	0.04968	-0.2200
1.0	0.85	0.04573	-0.2230
2.0	0.93	0.04475	-0.2269
3.0	1.00	0.04329	-0.2274
4.0	1.08	0.04160	-0.2310
5.0	1.17	0.03939	-0.2362
6.1	1.25	0.03654	-0.2398
7.1	1.32	0.03496	-0.2435
8.1	1.40	0.03284	-0.2483
9.1	1.49	0.03000	-0.2522
10.1	1.55	0.02654	-0.2528
11.1	1.61	0.02341	-0.2495
12.1	1.64	0.02164	-0.2531
13.2	1.67	0.02217	-0.2434
14.2	1.68	0.02052	-0.2388
15.2	1.68	0.01983	-0.2406
16.2	1.67	0.02141	-0.2403
17.2	1.63	0.01613	-0.2402
18.2	1.64	0.01892	-0.2404
19.2	1.60	0.01981	-0.2305
20.2	1.61	0.02343	-0.2280
21.2	1.57	0.02547	-0.2225
22.2	1.58	0.03237	-0.2178
23.2	1.55	0.03460	-0.2100
24.2	1.54	0.04229	-0.2062
25.2	1.50	0.04998	-0.1929

Configuration WS-16
Subtest A
Run 1887BP
Fig. B.107

α	C_l	$C_{d,wake}$	$C_{m,c_{sys}/4}$
-0.0	0.80	0.04969	-0.2250
1.0	0.86	0.04665	-0.2293
2.0	0.94	0.04348	-0.2326
3.0	1.02	0.04206	-0.2351
4.0	1.11	0.04132	-0.2390
5.0	1.19	0.03927	-0.2437
6.1	1.27	0.03695	-0.2476
7.1	1.35	0.03478	-0.2522
8.1	1.43	0.03233	-0.2561
9.1	1.49	0.02907	-0.2570
10.1	1.56	0.02504	-0.2577
11.1	1.65	0.02361	-0.2608
12.1	1.68	0.02125	-0.2631
13.2	1.73	0.02076	-0.2583
14.2	1.72	0.01992	-0.2520
15.2	1.71	0.02032	-0.2516
16.2	1.69	0.01948	-0.2581
17.1	1.69	0.01637	-0.2636
18.1	1.69	0.01607	-0.2592
19.2	1.69	0.01747	-0.2508
20.2	1.64	0.02291	-0.2358
21.2	1.65	0.02506	-0.2453
22.2	1.65	0.03147	-0.2419
23.2	1.60	0.03751	-0.2309
24.2	1.62	0.04212	-0.2265
25.2	1.62	0.04838	-0.2228

Configuration WS-17
Subtest A
Run 1888BP
Fig. B.108

α	C_l	$C_{d,wake}$	$C_{m,c_{sys}/4}$
-0.0	0.77	0.05069	-0.2270
1.0	0.83	0.04696	-0.2296
2.0	0.91	0.04464	-0.2330
3.0	0.99	0.04418	-0.2363
4.0	1.08	0.04164	-0.2401
5.0	1.16	0.04008	-0.2441
6.0	1.25	0.03782	-0.2497
7.1	1.32	0.03484	-0.2528
8.1	1.41	0.03318	-0.2582
9.1	1.48	0.02927	-0.2593
10.1	1.57	0.02610	-0.2635
11.1	1.61	0.02338	-0.2593
12.2	1.64	0.02269	-0.2591
13.2	1.68	0.02046	-0.2531
14.2	1.66	0.02015	-0.2469
15.1	1.66	0.02160	-0.2427
16.2	1.67	0.01983	-0.2412
17.2	1.62	0.01631	-0.2393
18.2	1.63	0.01823	-0.2397
19.2	1.64	0.01987	-0.2295
20.2	1.58	0.02625	-0.2138
21.2	1.60	0.03192	-0.2165
22.2	1.56	0.03810	-0.2062
23.2	1.56	0.04269	-0.1950
24.2	1.55	0.04967	-0.1909
25.2	1.56	0.05043	-0.2009

Configuration WS-18
Subtest A
Run 1889BP
Fig. B.109

α	C_l	$C_{d,wake}$	$C_{m,c_{sys}/4}$
-0.0	0.78	0.05209	-0.2327
1.0	0.84	0.04913	-0.2366
2.0	0.92	0.04520	-0.2402
3.0	1.01	0.04414	-0.2443
4.0	1.09	0.04168	-0.2478
5.0	1.18	0.03945	-0.2534
6.0	1.26	0.03753	-0.2579
7.1	1.35	0.03442	-0.2632
8.1	1.41	0.03133	-0.2644
9.1	1.51	0.02965	-0.2709
10.1	1.56	0.02642	-0.2695
11.1	1.61	0.02394	-0.2670
12.1	1.64	0.02170	-0.2610
13.1	1.61	0.02035	-0.2493
14.2	1.62	0.02052	-0.2477
15.1	1.60	0.01992	-0.2378
16.1	1.60	0.01893	-0.2399
17.1	1.56	0.01586	-0.2335
18.1	1.57	0.01521	-0.2386
19.2	1.56	0.01893	-0.2263
20.2	1.51	0.02150	-0.1985
21.2	1.54	0.02709	-0.2016
22.2	1.49	0.03077	-0.1942
23.2	1.51	0.03562	-0.1954
24.2	1.50	0.04763	-0.1756
25.2	1.46	0.05345	-0.1753

Configuration WS-19
Subtest A
Run 1890BP
Fig. B.110

α	C_l	$C_{d,wake}$	$C_{m,c_{sys}/4}$
-0.1	0.75	0.05210	-0.2358
0.9	0.82	0.04909	-0.2400
2.0	0.90	0.04635	-0.2444
3.0	0.98	0.04464	-0.2481
4.0	1.07	0.04215	-0.2523
5.0	1.16	0.03993	-0.2574
6.0	1.24	0.03901	-0.2620
7.0	1.32	0.03561	-0.2663
8.1	1.41	0.03220	-0.2716
9.1	1.48	0.02864	-0.2744
10.1	1.55	0.02522	-0.2748
11.1	1.60	0.02409	-0.2728
12.1	1.62	0.02153	-0.2674
13.1	1.60	0.02047	-0.2540
14.2	1.61	0.02005	-0.2485
15.1	1.59	0.02058	-0.2431
16.1	1.56	0.01842	-0.2395
17.1	1.55	0.01432	-0.2420
18.1	1.56	0.01648	-0.2376
19.2	1.54	0.01827	-0.2269
20.2	1.51	0.01929	-0.2139
21.2	1.52	0.01797	-0.2133
22.2	1.49	0.02090	-0.1883
23.2	1.47	0.03469	-0.1937
24.1	1.47	0.03472	-0.2000
25.2	1.45	0.04351	-0.2017

Configuration WS-20
Subtest A
Run 1891BP
Fig. B.111

α	C_l	$C_{d,wake}$	$C_{m,c_{sys}/4}$
-0.1	0.74	0.05464	-0.2403
0.9	0.81	0.05134	-0.2459
2.0	0.90	0.04855	-0.2510
3.0	0.99	0.04555	-0.2552
4.0	1.07	0.04284	-0.2593
5.0	1.17	0.04091	-0.2641
6.0	1.26	0.03819	-0.2696
7.0	1.34	0.03586	-0.2748
8.1	1.44	0.03267	-0.2805
9.1	1.52	0.02969	-0.2842
10.1	1.56	0.02581	-0.2795
11.1	1.58	0.02373	-0.2733
12.1	1.60	0.02203	-0.2681
13.1	1.60	0.02064	-0.2592
14.1	1.59	0.02024	-0.2499
15.1	1.58	0.02011	-0.2432
16.1	1.56	0.01665	-0.2431
17.1	1.53	0.01501	-0.2397
18.1	1.54	0.01598	-0.2346
19.2	1.50	0.01587	-0.2166
20.2	1.51	0.01688	-0.2108
21.2	1.52	0.02168	-0.2038
22.2	1.49	0.02218	-0.1933
23.2	1.47	0.02592	-0.1761
24.2	1.45	0.03154	-0.1828
25.2	1.47	0.03828	-0.1684

Configuration WS-21
Subtest A
Run 1911BP
Fig. B.112

α	C_l	$C_{d,wake}$	$C_{m,c_{sys}/4}$
-0.1	0.72	0.03186	-0.2438
0.9	0.81	0.02976	-0.2496
2.0	0.90	0.02881	-0.2541
3.0	1.00	0.02843	-0.2595
4.0	1.10	0.02786	-0.2657
5.0	1.20	0.02062	-0.2802
6.0	1.31	0.01753	-0.2962
7.0	1.39	0.01629	-0.2960
8.1	1.42	0.01497	-0.2875
9.1	1.45	0.01538	-0.2783
10.1	1.42	0.01509	-0.2611
11.1	1.40	0.01499	-0.2467
12.1	1.43	0.01520	-0.2348
13.1	1.36	0.01464	-0.2130
14.1	1.38	0.01466	-0.2071
15.1	1.38	0.01624	-0.1902
16.2	1.33	0.01620	-0.1729
17.2	1.34	0.01775	-0.1662
18.2	1.32	0.01966	-0.1676
19.2	1.31	0.02136	-0.1575
20.2	1.28	0.02569	-0.1461
21.2	1.31	0.03010	-0.1425
22.2	1.26	0.03525	-0.1267
23.2	1.28	0.04274	-0.1261
24.2	1.28	0.04978	-0.1209
25.2	1.25	0.05538	-0.1100

Configuration WS-22
Subtest A
Run 1912BP
Fig. B.113

α	C_l	$C_{d,wake}$	$C_{m,c_{sys}/4}$
-0.1	0.75	0.03298	-0.2523
0.9	0.83	0.03033	-0.2570
2.0	0.93	0.02907	-0.2621
3.0	1.03	0.02855	-0.2684
4.0	1.13	0.02703	-0.2754
5.0	1.23	0.01950	-0.2905
6.0	1.33	0.01719	-0.3032
7.0	1.41	0.01611	-0.3038
8.1	1.47	0.01538	-0.3009
9.1	1.48	0.01504	-0.2877
10.1	1.47	0.01491	-0.2723
11.1	1.48	0.01444	-0.2603
12.1	1.46	0.01447	-0.2417
13.1	1.45	0.01371	-0.2251
14.1	1.42	0.01376	-0.2092
15.1	1.42	0.01440	-0.2012
16.1	1.41	0.01562	-0.1935
17.2	1.38	0.01530	-0.1824
18.2	1.38	0.01653	-0.1816
19.2	1.37	0.01965	-0.1734
20.1	1.33	0.01874	-0.1751
21.2	1.35	0.02142	-0.1728
22.2	1.33	0.02459	-0.1548
23.2	1.30	0.03424	-0.1577
24.2	1.31	0.04218	-0.1533
25.2	1.28	0.04356	-0.1469

Configuration WS-23
Subtest A
Run 1913BP
Fig. B.114

α	C_l	$C_{d,wake}$	$C_{m,c_{sys}/4}$
-0.1	0.73	0.03214	-0.2546
0.9	0.81	0.03052	-0.2595
2.0	0.91	0.02941	-0.2651
3.0	1.01	0.02810	-0.2704
4.0	1.11	0.02679	-0.2771
5.0	1.22	0.01728	-0.3050
6.0	1.31	0.01673	-0.3050
7.0	1.40	0.01624	-0.3067
8.0	1.46	0.01540	-0.3028
9.1	1.45	0.01533	-0.2876
10.1	1.47	0.01515	-0.2775
11.1	1.45	0.01392	-0.2597
12.1	1.42	0.01451	-0.2405
13.1	1.42	0.01391	-0.2267
14.1	1.40	0.01420	-0.2094
15.1	1.39	0.01450	-0.2022
16.1	1.39	0.01496	-0.1964
17.1	1.36	0.01477	-0.1843
18.1	1.36	0.01533	-0.1850
19.2	1.32	0.01720	-0.1680
20.2	1.33	0.01923	-0.1648
21.2	1.32	0.01815	-0.1565
22.2	1.31	0.01975	-0.1446
23.2	1.30	0.03046	-0.1461
24.1	1.28	0.03397	-0.1464
25.2	1.30	0.04115	-0.1488

Configuration WS-24
Subtest A
Run 1893BP
Fig. B.115

α	C_l	$C_{d,wake}$	$C_{m,c_{sys}/4}$
-0.0	0.59	0.07696	-0.1956
0.9	0.78	0.05715	-0.2382
2.0	1.01	0.02818	-0.2820
3.0	1.10	0.02615	-0.2853
4.0	1.19	0.02659	-0.2893
5.0	1.28	0.02602	-0.2934
6.0	1.34	0.01624	-0.3061
7.0	1.43	0.01605	-0.3069
8.1	1.44	0.01533	-0.2953
9.1	1.44	0.01460	-0.2807
10.1	1.44	0.01412	-0.2675
11.1	1.45	0.01448	-0.2507
12.1	1.42	0.01409	-0.2299
13.1	1.41	0.01340	-0.2154
14.1	1.40	0.01516	-0.2072
15.1	1.40	0.01511	-0.1901
16.1	1.36	0.01686	-0.1863
17.2	1.38	0.01718	-0.1786
18.2	1.33	0.02149	-0.1651
19.2	1.34	0.02236	-0.1637
20.2	1.30	0.02309	-0.1465
21.2	1.32	0.03074	-0.1359
22.2	1.29	0.03545	-0.1402
23.2	1.31	0.03807	-0.1227
24.2	1.28	0.04787	-0.1260
25.2	1.29	0.05086	-0.1243

Configuration WS-25
Subtest A
Run 1894BP
Fig. B.116

α	C_l	$C_{d,wake}$	$C_{m,c_{sys}/4}$
-0.1	0.56	0.07816	-0.1950
0.9	0.73	0.06055	-0.2280
1.9	0.99	0.02773	-0.2848
3.0	1.08	0.02646	-0.2875
4.0	1.17	0.02758	-0.2911
5.0	1.26	0.02665	-0.2966
6.0	1.33	0.01703	-0.3095
7.0	1.39	0.01653	-0.3060
8.0	1.40	0.01535	-0.2950
9.1	1.41	0.01465	-0.2813
10.1	1.40	0.01458	-0.2634
11.1	1.38	0.01460	-0.2442
12.1	1.37	0.01409	-0.2274
13.1	1.37	0.01380	-0.2149
14.1	1.35	0.01446	-0.2053
15.1	1.36	0.01510	-0.1938
16.1	1.32	0.01545	-0.1812
17.1	1.31	0.01660	-0.1863
18.2	1.31	0.01760	-0.1662
19.2	1.30	0.02099	-0.1520
20.2	1.33	0.01627	-0.1385
21.2	1.30	0.02733	-0.1441
22.2	1.28	0.03020	-0.1365
23.2	1.30	0.03899	-0.1301
24.2	1.25	0.04280	-0.1294
25.2	1.25	0.04774	-0.1146

Configuration WS-26
Subtest A
Run 1895BP
Fig. B.117

α	C_l	$C_{d,wake}$	$C_{m,c_{sys}/4}$
-0.1	0.55	0.07754	-0.1944
0.9	0.72	0.06124	-0.2312
1.9	0.99	0.02873	-0.2904
3.0	1.08	0.02653	-0.2926
4.0	1.17	0.02677	-0.2959
5.0	1.26	0.02679	-0.3000
6.0	1.32	0.01725	-0.3126
7.0	1.42	0.01693	-0.3131
8.0	1.43	0.01574	-0.3004
9.1	1.44	0.01419	-0.2910
10.1	1.47	0.01536	-0.2814
11.1	1.43	0.01487	-0.2558
12.1	1.40	0.01464	-0.2428
13.1	1.41	0.01433	-0.2229
14.1	1.38	0.01473	-0.2058
15.1	1.38	0.01451	-0.2026
16.1	1.36	0.01493	-0.1900
17.1	1.36	0.01436	-0.1756
18.2	1.34	0.01759	-0.1607
19.2	1.35	0.01594	-0.1671
20.2	1.30	0.02415	-0.1488
21.2	1.31	0.02519	-0.1468
22.2	1.30	0.03043	-0.1460
23.2	1.29	0.03333	-0.1372
24.2	1.27	0.04272	-0.1289
25.2	1.27	0.05205	-0.1138

Configuration WS-27
Subtest A
Run 1896BP
Fig. B.118

α	C_l	$C_{d,wake}$	$C_{m,c_{sys}/4}$
-0.1	0.52	0.07925	-0.1880
0.9	0.65	0.06586	-0.2148
1.9	0.96	0.02776	-0.2911
2.9	1.05	0.02710	-0.2928
4.0	1.15	0.02694	-0.2968
5.0	1.23	0.02676	-0.3014
6.0	1.31	0.01829	-0.3143
7.0	1.41	0.01724	-0.3177
8.0	1.48	0.01601	-0.3145
9.1	1.49	0.01539	-0.3027
10.1	1.48	0.01528	-0.2853
11.1	1.48	0.01484	-0.2710
12.1	1.47	0.01497	-0.2545
13.1	1.47	0.01420	-0.2389
14.1	1.43	0.01424	-0.2193
15.1	1.43	0.01481	-0.2104
16.1	1.44	0.01548	-0.2012
17.2	1.39	0.01691	-0.1827
18.2	1.40	0.01600	-0.1761
19.2	1.38	0.01620	-0.1740
20.2	1.38	0.01822	-0.1522
21.2	1.37	0.02531	-0.1397
22.2	1.35	0.03214	-0.1285
23.2	1.36	0.03388	-0.1167
24.2	1.34	0.04358	-0.1181
25.2	1.34	0.05491	-0.1151

Configuration WS-28
Subtest A
Run 1900BP
Fig. B.119

α	C_l	$C_{d,wake}$	$C_{m,c_{sys}/4}$
-0.0	0.59	0.07678	-0.1957
0.9	0.71	0.06235	-0.2160
2.0	0.97	0.02773	-0.2708
3.0	1.07	0.02688	-0.2731
4.0	1.15	0.02671	-0.2747
5.0	1.24	0.02747	-0.2797
6.0	1.31	0.02444	-0.2848
7.0	1.39	0.01652	-0.2953
8.1	1.45	0.01503	-0.2922
9.1	1.50	0.01608	-0.2856
10.1	1.45	0.01551	-0.2687
11.1	1.46	0.01518	-0.2533
12.1	1.44	0.01503	-0.2408
13.1	1.42	0.01432	-0.2216
14.1	1.40	0.01570	-0.2042
15.1	1.40	0.01552	-0.2034
16.1	1.39	0.01572	-0.1883
17.2	1.40	0.01683	-0.1866
18.2	1.37	0.01670	-0.1730
19.2	1.39	0.02214	-0.1653
20.2	1.34	0.02818	-0.1506
21.2	1.34	0.03225	-0.1364
22.2	1.30	0.04112	-0.1313
23.2	1.32	0.04415	-0.1264
24.2	1.29	0.05443	-0.1168
25.2	1.30	0.06134	-0.1164

Configuration WS-29
Subtest A
Run 1899BP
Fig. B.120

α	C_l	$C_{d,wake}$	$C_{m,c_{sys}/4}$
-0.1	0.59	0.07551	-0.1985
0.9	0.72	0.06179	-0.2216
2.0	0.98	0.02824	-0.2775
3.0	1.08	0.02675	-0.2795
4.0	1.17	0.02777	-0.2823
5.0	1.25	0.02633	-0.2856
6.0	1.33	0.01664	-0.2928
7.0	1.40	0.01673	-0.3011
8.1	1.44	0.01502	-0.2959
9.1	1.49	0.01453	-0.2896
10.1	1.43	0.01570	-0.2712
11.1	1.45	0.01498	-0.2619
12.1	1.46	0.01431	-0.2491
13.1	1.41	0.01506	-0.2225
14.1	1.43	0.01447	-0.2124
15.1	1.38	0.01523	-0.1992
16.1	1.40	0.01534	-0.1932
17.2	1.40	0.01550	-0.1771
18.2	1.36	0.01763	-0.1751
19.2	1.35	0.02295	-0.1509
20.2	1.35	0.02681	-0.1462
21.2	1.33	0.03635	-0.1444
22.2	1.34	0.04074	-0.1380
23.2	1.30	0.04423	-0.1270
24.2	1.31	0.05249	-0.1244
25.2	1.29	0.06056	-0.1168

Configuration WS-30
Subtest A
Run 1898BP
Fig. B.121

α	C_l	$C_{d,wake}$	$C_{m,c_{sys}/4}$
-0.0	0.60	0.07447	-0.2036
0.9	0.74	0.05753	-0.2283
1.9	0.99	0.02695	-0.2833
3.0	1.09	0.02684	-0.2855
4.0	1.18	0.02669	-0.2866
5.0	1.26	0.02667	-0.2901
6.0	1.32	0.01774	-0.3026
7.0	1.41	0.01684	-0.3039
8.1	1.46	0.01482	-0.2992
9.1	1.51	0.01594	-0.2935
10.1	1.45	0.01469	-0.2697
11.1	1.47	0.01469	-0.2585
12.1	1.45	0.01465	-0.2409
13.1	1.44	0.01481	-0.2251
14.1	1.39	0.01460	-0.2048
15.1	1.41	0.01420	-0.2014
16.1	1.39	0.01512	-0.1946
17.1	1.38	0.01456	-0.1909
18.2	1.36	0.01645	-0.1757
19.2	1.37	0.01728	-0.1753
20.2	1.33	0.02334	-0.1626
21.2	1.34	0.02390	-0.1337
22.2	1.31	0.03779	-0.1341
23.2	1.32	0.03655	-0.1349
24.2	1.32	0.04500	-0.1368
25.2	1.32	0.06043	-0.1285

Configuration WS-31
Subtest A
Run 1897BP
Fig. B.122

α	C_l	$C_{d,wake}$	$C_{m,c_{sys}/4}$
-0.1	0.57	0.07688	-0.1991
0.9	0.69	0.06088	-0.2241
1.9	0.96	0.02833	-0.2878
3.0	1.06	0.02715	-0.2912
4.0	1.15	0.02623	-0.2927
5.0	1.24	0.02680	-0.2965
6.0	1.30	0.01757	-0.3093
7.0	1.41	0.01689	-0.3140
8.0	1.52	0.01600	-0.3188
9.1	1.50	0.01506	-0.3025
10.1	1.53	0.01502	-0.2918
11.1	1.49	0.01443	-0.2715
12.1	1.49	0.01452	-0.2572
13.1	1.49	0.01429	-0.2424
14.1	1.46	0.01403	-0.2265
15.1	1.46	0.01421	-0.2195
16.2	1.44	0.01561	-0.2040
17.1	1.43	0.01610	-0.1977
18.2	1.41	0.01744	-0.1861
19.2	1.42	0.01852	-0.1735
20.2	1.38	0.01873	-0.1580
21.2	1.41	0.02558	-0.1519
22.2	1.36	0.03191	-0.1520
23.2	1.38	0.03436	-0.1352
24.2	1.34	0.04242	-0.1223
25.2	1.37	0.05886	-0.1352

Configuration WS-32
Subtest A
Run 1901BP
Fig. B.123

α	C_l	$C_{d,wake}$	$C_{m,c_{sys}/4}$
-0.0	0.78	0.03102	-0.2357
1.0	0.86	0.02941	-0.2398
2.0	0.95	0.02713	-0.2426
3.0	1.04	0.02746	-0.2454
4.0	1.12	0.02731	-0.2493
5.0	1.20	0.02562	-0.2514
6.0	1.28	0.01670	-0.2601
7.1	1.37	0.01532	-0.2717
8.1	1.44	0.01480	-0.2695
9.1	1.48	0.01463	-0.2611
10.1	1.48	0.01460	-0.2475
11.1	1.45	0.01459	-0.2298
12.1	1.46	0.01390	-0.2190
13.1	1.43	0.01403	-0.2036
14.2	1.43	0.01430	-0.1975
15.1	1.42	0.01464	-0.1897
16.2	1.40	0.01508	-0.1793
17.2	1.40	0.01648	-0.1713
18.2	1.38	0.01779	-0.1620
19.2	1.36	0.02065	-0.1493
20.2	1.36	0.02307	-0.1408
21.2	1.33	0.02642	-0.1302
22.2	1.35	0.03043	-0.1242
23.2	1.31	0.03481	-0.1115
24.2	1.31	0.03873	-0.1065
25.2	1.27	0.04627	-0.0959

Configuration WS-33
Subtest A
Run 1902BP
Fig. B.124

α	C_l	$C_{d,wake}$	$C_{m,c_{sys}/4}$
-0.0	0.81	0.03081	-0.2474
1.0	0.88	0.02851	-0.2501
2.0	0.98	0.02743	-0.2540
3.0	1.07	0.02673	-0.2561
4.0	1.15	0.02638	-0.2591
5.0	1.24	0.02583	-0.2643
6.0	1.32	0.01604	-0.2821
7.1	1.40	0.01539	-0.2803
8.1	1.45	0.01447	-0.2765
9.1	1.47	0.01405	-0.2655
10.1	1.46	0.01389	-0.2515
11.1	1.46	0.01387	-0.2374
12.1	1.42	0.01363	-0.2202
13.1	1.44	0.01389	-0.2098
14.1	1.43	0.01497	-0.1985
15.1	1.41	0.01498	-0.1902
16.2	1.38	0.01716	-0.1766
17.2	1.40	0.01820	-0.1737
18.2	1.36	0.01962	-0.1591
19.2	1.39	0.02322	-0.1557
20.2	1.35	0.02533	-0.1398
21.2	1.34	0.03023	-0.1359
22.2	1.33	0.03413	-0.1270
23.2	1.32	0.03782	-0.1185
24.2	1.30	0.04663	-0.1104
25.2	1.31	0.04995	-0.1090

Configuration WS-34
Subtest A
Run 1903BP
Fig. B.125

α	C_l	$C_{d,wake}$	$C_{m,c_{sys}/4}$
-0.0	0.81	0.03058	-0.2533
0.9	0.89	0.02901	-0.2571
2.0	0.98	0.02793	-0.2591
3.0	1.07	0.02725	-0.2619
4.0	1.16	0.02696	-0.2657
5.0	1.25	0.02483	-0.2718
6.0	1.33	0.01687	-0.2895
7.1	1.41	0.01541	-0.2888
8.1	1.46	0.01567	-0.2837
9.1	1.48	0.01490	-0.2720
10.1	1.47	0.01498	-0.2579
11.1	1.47	0.01490	-0.2459
12.1	1.44	0.01452	-0.2278
13.1	1.45	0.01452	-0.2160
14.1	1.41	0.01557	-0.2021
15.1	1.40	0.01509	-0.1918
16.2	1.42	0.01711	-0.1836
17.2	1.37	0.01804	-0.1705
18.2	1.38	0.01913	-0.1614
19.2	1.36	0.02340	-0.1503
20.2	1.35	0.02916	-0.1395
21.2	1.32	0.03205	-0.1254
22.2	1.33	0.04083	-0.1215
23.2	1.33	0.04393	-0.1144
24.2	1.29	0.05133	-0.1008
25.2	1.30	0.05722	-0.0967

Configuration WS-35
Subtest A
Run 1904BP
Fig. B.126

α	C_l	$C_{d,wake}$	$C_{m,c_{sys}/4}$
-0.1	0.79	0.03096	-0.2668
0.9	0.87	0.02928	-0.2713
2.0	0.96	0.02898	-0.2748
3.0	1.06	0.02812	-0.2784
4.0	1.16	0.02727	-0.2829
5.0	1.25	0.01936	-0.2935
6.0	1.33	0.01739	-0.3052
7.0	1.42	0.01703	-0.3052
8.1	1.47	0.01559	-0.2990
9.1	1.47	0.01536	-0.2862
10.1	1.48	0.01568	-0.2746
11.1	1.46	0.01555	-0.2576
12.1	1.47	0.01587	-0.2458
13.1	1.43	0.01491	-0.2269
14.1	1.42	0.01508	-0.2174
15.1	1.39	0.01587	-0.2029
16.1	1.41	0.01650	-0.1956
17.2	1.39	0.01745	-0.1830
18.2	1.36	0.01772	-0.1679
19.2	1.37	0.02167	-0.1605
20.2	1.33	0.02353	-0.1465
21.2	1.34	0.02939	-0.1397
22.2	1.31	0.03714	-0.1292
23.2	1.33	0.04303	-0.1241
24.2	1.29	0.04908	-0.1158
25.2	1.32	0.05482	-0.1113

Configuration WS-36
Subtest A
Run 1910BP
Fig. B.127

α	C_l	$C_{d,wake}$	$C_{m,c_{sys}/4}$
-0.0	0.60	0.07154	-0.1805
1.0	0.76	0.05458	-0.2135
2.0	0.97	0.02757	-0.2579
3.0	1.05	0.02677	-0.2580
4.0	1.13	0.02640	-0.2600
5.0	1.21	0.02610	-0.2622
6.0	1.29	0.01825	-0.2704
7.1	1.36	0.01514	-0.2772
8.1	1.42	0.01478	-0.2726
9.1	1.45	0.01357	-0.2635
10.1	1.45	0.01343	-0.2497
11.1	1.43	0.01356	-0.2332
12.1	1.43	0.01375	-0.2195
13.1	1.40	0.01406	-0.2037
14.2	1.41	0.01456	-0.1960
15.1	1.39	0.01542	-0.1877
16.2	1.39	0.01581	-0.1788
17.2	1.36	0.01776	-0.1648
18.2	1.35	0.01869	-0.1550
19.2	1.32	0.02120	-0.1410
20.2	1.33	0.02322	-0.1340
21.2	1.30	0.02714	-0.1206
22.2	1.31	0.03214	-0.1143
23.2	1.31	0.03411	-0.1073
24.2	1.27	0.04115	-0.0932
25.2	1.28	0.04697	-0.0875

Configuration WS-37
Subtest A
Run 1909BP
Fig. B.128

α	C_l	$C_{d,wake}$	$C_{m,c_{sys}/4}$
-0.0	0.60	0.06998	-0.1846
1.0	0.77	0.05390	-0.2192
2.0	0.99	0.02744	-0.2639
3.0	1.07	0.02679	-0.2652
4.0	1.16	0.02576	-0.2675
5.0	1.24	0.02565	-0.2694
6.0	1.30	0.01889	-0.2762
7.0	1.36	0.01408	-0.2808
8.1	1.44	0.01418	-0.2791
9.1	1.44	0.01398	-0.2668
10.1	1.43	0.01414	-0.2516
11.1	1.41	0.01361	-0.2343
12.1	1.41	0.01418	-0.2216
13.1	1.40	0.01329	-0.2077
14.1	1.39	0.01477	-0.1980
15.1	1.38	0.01420	-0.1917
16.1	1.34	0.01635	-0.1797
17.2	1.35	0.01785	-0.1716
18.2	1.31	0.01935	-0.1553
19.2	1.33	0.01965	-0.1509
20.2	1.32	0.02249	-0.1416
21.2	1.27	0.02774	-0.1258
22.2	1.28	0.03113	-0.1216
23.2	1.25	0.03783	-0.1070
24.2	1.27	0.04057	-0.1028
25.2	1.23	0.04807	-0.0895

Configuration WS-38
Subtest A
Run 1908BP
Fig. B.129

α	C_l	$C_{d,wake}$	$C_{m,c_{sys}/4}$
-0.0	0.59	0.07464	-0.1884
0.9	0.77	0.05332	-0.2240
2.0	1.00	0.02739	-0.2700
3.0	1.08	0.02759	-0.2713
4.0	1.17	0.02661	-0.2728
5.0	1.25	0.02603	-0.2766
6.0	1.31	0.01599	-0.2898
7.0	1.39	0.01492	-0.2906
8.1	1.45	0.01510	-0.2869
9.1	1.45	0.01409	-0.2717
10.1	1.44	0.01443	-0.2589
11.1	1.44	0.01373	-0.2445
12.1	1.42	0.01395	-0.2285
13.1	1.42	0.01434	-0.2128
14.1	1.40	0.01518	-0.2011
15.1	1.37	0.01552	-0.1901
16.2	1.39	0.01578	-0.1850
17.2	1.35	0.01622	-0.1731
18.2	1.35	0.01821	-0.1679
19.2	1.32	0.02279	-0.1572
20.2	1.32	0.02491	-0.1448
21.2	1.29	0.02700	-0.1390
22.2	1.30	0.03160	-0.1277
23.2	1.26	0.03748	-0.1192
24.2	1.28	0.04504	-0.1132
25.2	1.25	0.04912	-0.1024

Configuration WS-39
Subtest A
Run 1907BP
Fig. B.130

α	C_l	$C_{d,wake}$	$C_{m,c_{sys}/4}$
-0.0	0.56	0.07580	-0.1891
0.9	0.74	0.05581	-0.2257
2.0	0.99	0.02733	-0.2755
3.0	1.08	0.02723	-0.2778
4.0	1.16	0.02670	-0.2795
5.0	1.24	0.02595	-0.2831
6.0	1.31	0.01636	-0.2984
7.0	1.40	0.01453	-0.2992
8.1	1.44	0.01439	-0.2930
9.1	1.46	0.01463	-0.2819
10.1	1.44	0.01421	-0.2594
11.1	1.46	0.01348	-0.2465
12.1	1.41	0.01370	-0.2236
13.1	1.41	0.01372	-0.2184
14.1	1.40	0.01469	-0.2076
15.1	1.41	0.01471	-0.1873
16.2	1.37	0.01543	-0.1828
17.2	1.37	0.01794	-0.1702
18.2	1.37	0.02133	-0.1638
19.2	1.33	0.01998	-0.1679
20.2	1.34	0.02292	-0.1595
21.2	1.30	0.02714	-0.1479
22.2	1.30	0.03170	-0.1432
23.2	1.27	0.03724	-0.1304
24.2	1.28	0.03923	-0.1243
25.2	1.25	0.04988	-0.1150

Configuration WS-40
Subtest A
Run 1906BP
Fig. B.131

α	C_l	$C_{d,wake}$	$C_{m,c_{sys}/4}$
-0.1	0.56	0.07639	-0.1943
0.9	0.70	0.05794	-0.2201
2.0	0.99	0.02777	-0.2829
3.0	1.08	0.02761	-0.2855
4.0	1.16	0.02742	-0.2880
5.0	1.25	0.02619	-0.2917
6.0	1.31	0.01688	-0.3041
7.0	1.40	0.01615	-0.3049
8.1	1.47	0.01540	-0.3011
9.1	1.44	0.01527	-0.2835
10.1	1.46	0.01492	-0.2731
11.1	1.46	0.01468	-0.2581
12.1	1.41	0.01466	-0.2376
13.1	1.43	0.01454	-0.2196
14.1	1.40	0.01519	-0.2103
15.1	1.40	0.01580	-0.2012
16.1	1.38	0.01483	-0.1884
17.2	1.38	0.01852	-0.1785
18.2	1.35	0.02123	-0.1644
19.2	1.35	0.02332	-0.1572
20.2	1.32	0.02730	-0.1433
21.2	1.34	0.02969	-0.1398
22.2	1.30	0.03628	-0.1335
23.2	1.32	0.04115	-0.1243
24.2	1.28	0.04739	-0.1119
25.2	1.29	0.05291	-0.1093

Configuration WS-41
Subtest A
Run 1905BP
Fig. B.132

α	C_l	$C_{d,wake}$	$C_{m,c_{sys}/4}$
-0.1	0.56	0.07695	-0.1990
0.9	0.70	0.05825	-0.2243
1.9	0.98	0.02836	-0.2862
3.0	1.08	0.02780	-0.2886
4.0	1.17	0.02747	-0.2919
5.0	1.25	0.02668	-0.2969
6.0	1.33	0.01662	-0.3100
7.0	1.41	0.01680	-0.3096
8.0	1.49	0.01590	-0.3072
9.1	1.46	0.01599	-0.2883
10.1	1.45	0.01561	-0.2733
11.1	1.45	0.01526	-0.2584
12.1	1.42	0.01512	-0.2394
13.1	1.42	0.01552	-0.2258
14.1	1.39	0.01503	-0.2107
15.1	1.39	0.01602	-0.2008
16.2	1.39	0.01704	-0.1902
17.1	1.35	0.01732	-0.1746
18.2	1.35	0.01909	-0.1631
19.2	1.33	0.02239	-0.1484
20.2	1.34	0.02623	-0.1409
21.2	1.31	0.03064	-0.1279
22.2	1.31	0.03758	-0.1183
23.2	1.31	0.04130	-0.1126
24.2	1.27	0.05125	-0.0983
25.2	1.29	0.05613	-0.0995

Configuration WS-42
Subtest A
Run 1914BP
Fig. B.133

α	C_l	$C_{d,wake}$	$C_{m,c_{sys}/4}$
-0.0	0.70	0.03777	-0.2224
1.0	0.83	0.02983	-0.2412
2.0	0.92	0.02919	-0.2452
3.0	1.02	0.02790	-0.2492
4.0	1.11	0.02633	-0.2552
5.0	1.21	0.02514	-0.2619
6.0	1.30	0.01705	-0.2861
7.0	1.40	0.01697	-0.2886
8.1	1.48	0.01563	-0.2903
9.1	1.51	0.01523	-0.2829
10.1	1.52	0.01570	-0.2698
11.1	1.52	0.01543	-0.2637
12.1	1.53	0.01461	-0.2444
13.1	1.48	0.01451	-0.2258
14.1	1.46	0.01398	-0.2204
15.1	1.48	0.01535	-0.2102
16.2	1.44	0.01677	-0.1983
17.2	1.44	0.01547	-0.1927
18.1	1.40	0.01570	-0.1887
19.2	1.41	0.02138	-0.1821
20.2	1.40	0.01842	-0.1717
21.2	1.38	0.02407	-0.1742
22.2	1.37	0.02887	-0.1730
23.2	1.33	0.03428	-0.1631
24.2	1.35	0.03914	-0.1642
25.2	1.33	0.04606	-0.1516

Configuration WS-43
Subtest A
Run 1915BP
Fig. B.134

α	C_l	$C_{d,wake}$	$C_{m,c_{sys}/4}$
-0.1	0.74	0.03454	-0.2486
0.9	0.83	0.03088	-0.2550
2.0	0.93	0.03030	-0.2600
3.0	1.03	0.02867	-0.2659
4.0	1.13	0.02701	-0.2737
5.0	1.23	0.01738	-0.2992
6.0	1.34	0.01746	-0.3012
7.0	1.42	0.01629	-0.2998
8.1	1.50	0.01579	-0.2984
9.1	1.52	0.01610	-0.2890
10.1	1.51	0.01610	-0.2690
11.1	1.51	0.01532	-0.2591
12.1	1.51	0.01466	-0.2392
13.1	1.44	0.01452	-0.2184
14.2	1.45	0.01509	-0.2027
15.1	1.44	0.01608	-0.1994
16.2	1.46	0.01612	-0.1950
17.2	1.41	0.01736	-0.1823
18.2	1.42	0.01617	-0.1850
19.2	1.41	0.01906	-0.1620
20.2	1.36	0.02221	-0.1538
21.2	1.38	0.02547	-0.1584
22.2	1.34	0.02832	-0.1524
23.2	1.34	0.03222	-0.1467
24.2	1.32	0.03884	-0.1358
25.2	1.33	0.04262	-0.1285

Configuration WS-44
Subtest A
Run 1916BP
Fig. B.135

α	C_l	$C_{d,wake}$	$C_{m,c_{sys}/4}$
-0.1	0.79	0.03214	-0.2664
0.9	0.87	0.03001	-0.2706
2.0	0.96	0.02901	-0.2727
3.0	1.06	0.02727	-0.2767
4.0	1.16	0.02666	-0.2815
5.0	1.24	0.01775	-0.3047
6.0	1.34	0.01738	-0.3045
7.0	1.43	0.01727	-0.3044
8.1	1.47	0.01508	-0.2960
9.1	1.49	0.01498	-0.2843
10.1	1.46	0.01463	-0.2627
11.1	1.48	0.01497	-0.2481
12.1	1.45	0.01430	-0.2274
13.1	1.43	0.01385	-0.2097
14.1	1.44	0.01438	-0.2079
15.1	1.44	0.01432	-0.1941
16.2	1.39	0.01464	-0.1731
17.2	1.40	0.01723	-0.1714
18.2	1.38	0.01832	-0.1783
19.2	1.38	0.02065	-0.1551
20.2	1.36	0.02228	-0.1530
21.2	1.36	0.02161	-0.1486
22.2	1.31	0.03088	-0.1322
23.2	1.32	0.03397	-0.1234
24.2	1.30	0.04219	-0.1201
25.2	1.31	0.04845	-0.1180

Configuration WS-45
Subtest A
Run 1917BP
Fig. B.136

α	C_l	$C_{d,wake}$	$C_{m,c_{sys}/4}$
-0.0	0.65	0.05605	-0.2117
0.9	0.76	0.04187	-0.2288
2.0	0.95	0.02830	-0.2604
3.0	1.04	0.02726	-0.2635
4.0	1.13	0.02715	-0.2672
5.0	1.22	0.02616	-0.2718
6.0	1.32	0.01903	-0.2829
7.0	1.40	0.01670	-0.2950
8.1	1.47	0.01604	-0.2931
9.1	1.49	0.01507	-0.2853
10.1	1.51	0.01534	-0.2726
11.1	1.50	0.01452	-0.2586
12.1	1.50	0.01424	-0.2449
13.1	1.46	0.01460	-0.2269
14.1	1.46	0.01423	-0.2157
15.1	1.44	0.01507	-0.2101
16.1	1.43	0.01440	-0.1994
17.1	1.42	0.01569	-0.1973
18.2	1.41	0.01682	-0.1874
19.2	1.38	0.01692	-0.1746
20.2	1.37	0.02184	-0.1802
21.2	1.36	0.02901	-0.1784
22.2	1.34	0.03065	-0.1573
23.2	1.32	0.03390	-0.1601
24.2	1.34	0.04090	-0.1558
25.2	1.30	0.05053	-0.1458

Configuration WS-46
Subtest A
Run 1918BP
Fig. B.137

α	C_l	$C_{d,wake}$	$C_{m,c_{sys}/4}$
-0.0	0.36	0.04725	-0.1285
1.0	0.51	0.04883	-0.1591
2.0	1.05	0.01682	-0.2898
3.0	1.16	0.01691	-0.2911
4.0	1.27	0.01728	-0.2914
5.0	1.37	0.01772	-0.2906
6.1	1.46	0.01766	-0.2899
7.1	1.53	0.01610	-0.2863
8.1	1.57	0.01578	-0.2788
9.1	1.53	0.01605	-0.2585
10.1	1.53	0.01528	-0.2436
11.2	1.55	0.01536	-0.2276
12.2	1.49	0.01489	-0.2103
13.2	1.52	0.01492	-0.2014
14.2	1.50	0.01478	-0.1870
15.2	1.47	0.01542	-0.1752
16.2	1.47	0.01595	-0.1621
17.2	1.43	0.01850	-0.1597
18.2	1.44	0.01810	-0.1559
19.2	1.40	0.02170	-0.1483
20.2	1.41	0.02269	-0.1440
21.2	1.38	0.02769	-0.1335
22.2	1.40	0.03223	-0.1355
23.2	1.37	0.03744	-0.1228
24.2	1.38	0.04516	-0.1196
25.2	1.35	0.05046	-0.1145

Appendix D

Airfoil Coordinates

Unit chord coordinates for all models tested in the wind tunnel are included in this section. The chord length of the closely coupled model main element was 14.0-in long, flap one measured 3.5 in, and the chord of flap two was 3.0 in. Chord length of the main element of the main element in the well separated test was 11.5 in and the strut chord measured 7.85 in. Two sets of coordinates are presented for each airfoil. A set labeled "as designed" are the coordinates which were designed by Ragheb, et al. A second set labeled "as built" are the coordinates of the constructed model. Coordinates of the models were measured with a three-axis CMM.

MFF-089 Main Element (as designed)	
x	y
1.00000	0.00070
0.97627	0.01348
0.94536	0.03006
0.91361	0.04662
0.88028	0.06293
0.84066	0.08140
0.79583	0.10200
0.74972	0.12294
0.70488	0.14298
0.66311	0.16117
0.62412	0.17759
0.58848	0.19203
0.55595	0.20450
0.52550	0.21544
0.49714	0.22501
0.47094	0.23319
0.44659	0.24018
0.42414	0.24601
0.40320	0.25085
0.38374	0.25483
0.36567	0.25795
0.34861	0.26036
0.33267	0.26222
0.31781	0.26342
0.30374	0.26405
0.29036	0.26411
0.27750	0.26356
0.26495	0.26246
0.25267	0.26084
0.24054	0.25871
0.22856	0.25617
0.21675	0.25321
0.20517	0.24986
0.19381	0.24603
0.18256	0.24184
0.17160	0.23732
0.16089	0.23240
0.15044	0.22715
0.14031	0.22156
0.13040	0.21559
0.12081	0.20943
0.11159	0.20292
0.10266	0.19620
Continued ...	

Continued ...	
x	y
0.09413	0.18921
0.08595	0.18198
0.07813	0.17452
0.07064	0.16689
0.06356	0.15910
0.05681	0.15117
0.05053	0.14315
0.04463	0.13492
0.03905	0.12669
0.03393	0.11836
0.02917	0.10996
0.02478	0.10154
0.02078	0.09313
0.01715	0.08472
0.01388	0.07638
0.01105	0.06805
0.00851	0.05977
0.00632	0.05160
0.00451	0.04351
0.00300	0.03552
0.00180	0.02767
0.00095	0.01995
0.00037	0.01236
0.00003	0.00494
0.00001	-0.00233
0.00024	-0.00953
0.00073	-0.01666
0.00148	-0.02370
0.00252	-0.03064
0.00382	-0.03748
0.00538	-0.04420
0.00716	-0.05081
0.00919	-0.05726
0.01157	-0.06354
0.01419	-0.06969
0.01713	-0.07567
0.02040	-0.08149
0.02405	-0.08712
0.02810	-0.09259
0.03250	-0.09796
0.03727	-0.10320
0.04243	-0.10837
0.04792	-0.11345
0.05386	-0.11846
0.06010	-0.12345
0.06683	-0.12827
0.07393	-0.13312
Continued ...	

Continued ...	
x	y
0.08147	-0.13780
0.08954	-0.14236
0.09808	-0.14686
0.10712	-0.15124
0.11669	-0.15547
0.12681	-0.15952
0.13756	-0.16339
0.14890	-0.16708
0.16086	-0.17052
0.17353	-0.17368
0.18694	-0.17657
0.20107	-0.17918
0.21597	-0.18141
0.23167	-0.18331
0.24805	-0.18474
0.26535	-0.18566
0.28356	-0.18609
0.30274	-0.18597
0.32275	-0.18529
0.34370	-0.18391
0.36582	-0.18181
0.38900	-0.17899
0.41325	-0.17534
0.43891	-0.17077
0.46588	-0.16531
0.49408	-0.15884
0.52413	-0.15122
0.55558	-0.14250
0.58946	-0.13229
0.62620	-0.12054
0.66508	-0.10744
0.70769	-0.09238
0.75331	-0.07606
0.79646	-0.06084
0.83531	-0.04748
0.86856	-0.03635
0.89657	-0.02671
0.92108	-0.01799
0.94187	-0.01108
0.96077	-0.00592
0.97997	-0.00233
1.00000	-0.00070

MFF-089 Main Element (as built)	
x	y
0.99976	0.00000
0.99791	0.00421
0.99501	0.00596
0.99290	0.00714
0.99095	0.00823
0.98880	0.00949
0.98720	0.01037
0.98571	0.01122
0.98332	0.01254
0.98080	0.01392
0.97794	0.01548
0.97392	0.01768
0.97059	0.01957
0.96628	0.02193
0.96206	0.02454
0.95621	0.02768
0.95140	0.03025
0.94638	0.03290
0.93879	0.03689
0.93040	0.04124
0.92160	0.04582
0.91183	0.05077
0.89993	0.05677
0.88464	0.06415
0.86953	0.07131
0.85624	0.07754
0.84513	0.08270
0.83072	0.08934
0.81711	0.09559
0.80107	0.10292
0.78437	0.11051
0.76979	0.11710
0.75377	0.12431
0.74041	0.13032
0.72354	0.13783
0.70906	0.14425
0.69026	0.15243
0.67339	0.15973
0.65876	0.16598
0.64347	0.17243
0.62392	0.18053
0.60273	0.18882
0.57873	0.19824
Continued ...	

Continued ...	
x	y
0.55873	0.20599
0.54149	0.21233
0.52243	0.21908
0.50406	0.22531
0.48782	0.23056
0.47239	0.23532
0.45559	0.24012
0.43767	0.24494
0.41898	0.24963
0.40447	0.25294
0.38636	0.25670
0.36953	0.25976
0.35124	0.26247
0.33227	0.26457
0.31622	0.26574
0.30376	0.26621
0.28980	0.26620
0.27570	0.26555
0.26015	0.26398
0.24243	0.26116
0.22959	0.25845
0.21815	0.25557
0.20111	0.25048
0.15878	0.23280
0.15047	0.22852
0.14302	0.22439
0.13510	0.21973
0.12649	0.21426
0.11932	0.20943
0.11188	0.20413
0.10501	0.19885
0.09797	0.19316
0.08975	0.18605
0.08190	0.17866
0.07481	0.17166
0.06562	0.16168
0.05904	0.15421
0.05427	0.14931
0.04969	0.14330
0.04492	0.13662
0.04102	0.13087
0.03807	0.12627
0.03441	0.12031
0.03262	0.11723
0.02995	0.11249
0.02806	0.10897
0.02560	0.10421
Continued ...	

Continued ...	
x	y
0.02249	0.09778
0.02021	0.09277
0.01843	0.08863
0.01718	0.08559
0.01516	0.08042
0.01351	0.07592
0.01197	0.07145
0.00995	0.06498
0.00892	0.06136
0.00752	0.05617
0.00648	0.05192
0.00567	0.04842
0.00452	0.04292
0.00355	0.03745
0.00259	0.03143
0.00222	0.03021
0.00149	0.02461
0.00101	0.02016
0.00067	0.01620
0.00019	0.00815
0.00000	0.00000
0.00013	-0.00756
0.00068	-0.01556
0.00116	-0.02113
0.00166	-0.02561
0.00246	-0.03143
0.00347	-0.03735
0.00503	-0.04470
0.00664	-0.05100
0.00841	-0.05694
0.01035	-0.06264
0.01273	-0.06880
0.01739	-0.07871
0.02381	-0.08951
0.03128	-0.09955
0.03950	-0.10874
0.05073	-0.11929
0.06420	-0.12996
0.07431	-0.13691
0.08654	-0.14436
0.10065	-0.15190
0.11627	-0.15911
0.13784	-0.16742
0.15922	-0.17407
0.18816	-0.18101
0.22545	-0.18691
0.25852	-0.18965
Continued ...	

Continued ...	
x	y
0.29494	-0.19040
0.33158	-0.18905
0.37244	-0.18533
0.41509	-0.17921
0.45030	-0.17265
0.48748	-0.16441
0.51741	-0.15688
0.54613	-0.14897
0.57247	-0.14117
0.59207	-0.13508
0.62046	-0.12584
0.65220	-0.11500
0.68077	-0.10494
0.70162	-0.09748
0.72002	-0.09086
0.73226	-0.08645
0.75115	-0.07965
0.77011	-0.07287
0.78563	-0.06734
0.80443	-0.06068
0.82198	-0.05452
0.84028	-0.04811
0.85414	-0.04331
0.86802	-0.03851
0.87891	-0.03474
0.89010	-0.03087
0.89925	-0.02771
0.90641	-0.02522
0.91405	-0.02254
0.92130	-0.01996
0.92864	-0.01741
0.93421	-0.01554
0.94040	-0.01354
0.94469	-0.01222
0.94891	-0.01097
0.95262	-0.00991
0.95624	-0.00894
0.96022	-0.00793
0.96258	-0.00737
0.96574	-0.00666
0.96792	-0.00620
0.96982	-0.00582
0.97304	-0.00521
0.97566	-0.00476
0.97972	-0.00415
0.98274	-0.00380
0.98613	-0.00347
Continued ...	

Continued ...	
x	y
0.98800	-0.00333
0.99016	-0.00320
0.99256	-0.00312
0.99467	-0.00287
0.99766	-0.00238
1.00000	-0.00104

MFFS-026 Main Element (as designed)	
x	y
1.00000	0.00090
0.98744	0.00617
0.97159	0.01231
0.95362	0.01853
0.93299	0.02555
0.90978	0.03340
0.88427	0.04201
0.85707	0.05114
0.82875	0.06070
0.79960	0.07046
0.76972	0.08037
0.73978	0.09023
0.70990	0.09995
0.68068	0.10930
0.65192	0.11825
0.62376	0.12679
0.59647	0.13475
0.56966	0.14218
0.54364	0.14914
0.51877	0.15534
0.49460	0.16097
0.47162	0.16586
0.44943	0.17004
0.42819	0.17345
0.40728	0.17606
0.38665	0.17807
0.36627	0.17945
0.34624	0.18030
0.32660	0.18047
0.30721	0.18010
0.28832	0.17921
0.26989	0.17772
0.25189	0.17575
0.23458	0.17330
0.21782	0.17036
0.20176	0.16698
0.18632	0.16313
0.17155	0.15894
0.15751	0.15441
0.14417	0.14957
0.13159	0.14452
0.11977	0.13926
0.10871	0.13384
Continued ...	

Continued ...	
x	y
0.09839	0.12822
0.08873	0.12258
0.07982	0.11688
0.07158	0.11109
0.06393	0.10536
0.05690	0.09967
0.05046	0.09402
0.04456	0.08845
0.03919	0.08294
0.03428	0.07753
0.02981	0.07225
0.02579	0.06704
0.02216	0.06193
0.01883	0.05698
0.01585	0.05215
0.01323	0.04741
0.01093	0.04277
0.00878	0.03830
0.00699	0.03390
0.00543	0.02957
0.00401	0.02535
0.00287	0.02119
0.00191	0.01711
0.00117	0.01312
0.00063	0.00922
0.00023	0.00541
0.00001	0.00171
0.00002	-0.00192
0.00023	-0.00554
0.00058	-0.00917
0.00122	-0.01277
0.00205	-0.01635
0.00313	-0.01987
0.00452	-0.02331
0.00617	-0.02665
0.00825	-0.02977
0.01083	-0.03257
0.01382	-0.03505
0.01727	-0.03708
0.02104	-0.03883
0.02511	-0.04032
0.02947	-0.04158
0.03412	-0.04268
0.03908	-0.04362
0.04438	-0.04441
0.05005	-0.04505
0.05616	-0.04552
Continued ...	

Continued ...	
x	y
0.06273	-0.04588
0.06985	-0.04602
0.07760	-0.04599
0.08609	-0.04576
0.09545	-0.04533
0.10580	-0.04461
0.11739	-0.04356
0.13044	-0.04219
0.14519	-0.04040
0.16201	-0.03810
0.18124	-0.03524
0.20320	-0.03180
0.22795	-0.02781
0.25502	-0.02344
0.28348	-0.01891
0.31257	-0.01444
0.34205	-0.01009
0.37124	-0.00599
0.40020	-0.00222
0.42877	0.00120
0.45709	0.00416
0.48572	0.00674
0.51456	0.00909
0.54317	0.01109
0.57195	0.01270
0.60113	0.01402
0.63028	0.01509
0.65952	0.01584
0.68859	0.01630
0.71780	0.01639
0.74699	0.01630
0.77560	0.01588
0.80402	0.01515
0.83186	0.01417
0.85881	0.01296
0.88441	0.01150
0.90869	0.00982
0.93104	0.00802
0.95153	0.00599
0.97013	0.00391
0.98677	0.00158
1.00000	-0.00090

MFFS-026 Main Element (as built)	
x	y
0.99982	0.00000
0.99947	0.00496
0.99719	0.00649
0.99595	0.00700
0.99340	0.00800
0.99062	0.00905
0.98718	0.01031
0.98402	0.01147
0.97663	0.01412
0.96872	0.01691
0.95463	0.02182
0.93866	0.02731
0.91942	0.03387
0.89914	0.04070
0.87805	0.04774
0.85204	0.05643
0.82394	0.06578
0.79793	0.07443
0.76877	0.08403
0.73680	0.09452
0.70470	0.10490
0.67154	0.11534
0.63684	0.12603
0.59602	0.13793
0.56234	0.14719
0.52311	0.15720
0.48151	0.16666
0.44490	0.17343
0.40833	0.17835
0.36979	0.18156
0.32679	0.18257
0.29063	0.18142
0.25345	0.17796
0.21536	0.17161
0.19354	0.16657
0.17234	0.16063
0.14857	0.15263
0.12637	0.14363
0.10909	0.13535
0.09325	0.12653
0.07704	0.11608
0.06465	0.10687
0.05323	0.09726
Continued ...	

Continued ...	
x	y
0.04257	0.08704
0.03775	0.08189
0.03320	0.07668
0.02966	0.07237
0.02609	0.06770
0.02264	0.06289
0.02001	0.05894
0.01735	0.05468
0.01550	0.05154
0.01386	0.04857
0.01226	0.04548
0.01071	0.04231
0.00907	0.03865
0.00739	0.03458
0.00616	0.03128
0.00487	0.02749
0.00405	0.02487
0.00320	0.02186
0.00199	0.01673
0.00144	0.01389
0.00080	0.00982
0.00036	0.00609
0.00014	0.00333
0.00000	0.00000
0.00377	-0.02905
0.00519	-0.03218
0.00668	-0.03477
0.00879	-0.03778
0.01133	-0.04063
0.01547	-0.04413
0.01661	-0.04492
0.02043	-0.04716
0.02590	-0.04946
0.03308	-0.05165
0.04257	-0.05352
0.05662	-0.05512
0.07073	-0.05568
0.08699	-0.05544
0.10355	-0.05447
0.11891	-0.05303
0.13950	-0.05047
0.15906	-0.04763
0.17692	-0.04481
0.19744	-0.04147
0.21740	-0.03818
0.24000	-0.03438
0.25965	-0.03104
Continued ...	

Continued ...	
x	y
0.29213	-0.02563
0.32144	-0.02090
0.34687	-0.01701
0.37547	-0.01282
0.40790	-0.00838
0.44113	-0.00429
0.47784	-0.00024
0.51533	0.00333
0.53849	0.00520
0.56822	0.00741
0.59731	0.00920
0.62251	0.01025
0.64169	0.01092
0.65610	0.01130
0.67456	0.01175
0.69314	0.01212
0.71094	0.01238
0.73153	0.01252
0.74855	0.01253
0.76051	0.01249
0.77441	0.01232
0.79036	0.01206
0.80104	0.01180
0.81691	0.01135
0.83047	0.01091
0.84643	0.01031
0.86249	0.00968
0.87746	0.00901
0.89497	0.00813
0.90592	0.00749
0.91778	0.00669
0.92987	0.00576
0.94319	0.00462
0.95196	0.00377
0.95973	0.00297
0.96669	0.00223
0.97386	0.00145
0.98090	0.00061
0.98531	0.00015
0.98976	-0.00028
0.99160	-0.00044
0.99517	-0.00067
0.99772	-0.00041
1.00000	-0.00216

MFFS-026 Strut (as designed)	
x	y
1.00000	0.00130
0.98637	0.00601
0.96908	0.01154
0.94956	0.01736
0.92733	0.02389
0.90252	0.03130
0.87600	0.03919
0.84859	0.04745
0.81996	0.05615
0.78997	0.06526
0.75874	0.07481
0.72705	0.08436
0.69514	0.09386
0.66410	0.10299
0.63422	0.11155
0.60551	0.11959
0.57849	0.12680
0.55221	0.13352
0.52758	0.13952
0.50420	0.14483
0.48207	0.14944
0.46076	0.15343
0.44025	0.15687
0.42049	0.15968
0.40099	0.16197
0.38178	0.16386
0.36333	0.16531
0.34536	0.16622
0.32768	0.16671
0.31052	0.16682
0.29395	0.16651
0.27783	0.16580
0.26223	0.16474
0.24720	0.16332
0.23266	0.16154
0.21859	0.15947
0.20514	0.15717
0.19232	0.15457
0.17998	0.15168
0.16814	0.14857
0.15681	0.14524
0.14598	0.14171
0.13563	0.13804
Continued ...	

Continued ...	
x	y
0.12581	0.13422
0.11648	0.13023
0.10759	0.12608
0.09911	0.12182
0.09107	0.11750
0.08347	0.11306
0.07623	0.10856
0.06940	0.10404
0.06297	0.09945
0.05693	0.09479
0.05124	0.09006
0.04587	0.08528
0.04080	0.08050
0.03604	0.07571
0.03165	0.07086
0.02754	0.06595
0.02369	0.06105
0.02012	0.05613
0.01687	0.05116
0.01386	0.04616
0.01110	0.04117
0.00869	0.03611
0.00648	0.03103
0.00464	0.02588
0.00301	0.02069
0.00173	0.01544
0.00080	0.01010
0.00013	0.00469
0.00002	-0.00084
0.00022	-0.00617
0.00090	-0.01100
0.00183	-0.01543
0.00327	-0.01950
0.00504	-0.02324
0.00735	-0.02657
0.01012	-0.02949
0.01332	-0.03200
0.01683	-0.03418
0.02063	-0.03612
0.02467	-0.03789
0.02895	-0.03953
0.03349	-0.04103
0.03830	-0.04246
0.04340	-0.04378
0.04884	-0.04500
0.05464	-0.04615
0.06083	-0.04720
Continued ...	

Continued ...	
x	y
0.06749	-0.04815
0.07467	-0.04904
0.08242	-0.04987
0.09080	-0.05056
0.09996	-0.05111
0.11001	-0.05153
0.12109	-0.05180
0.13335	-0.05190
0.14695	-0.05179
0.16217	-0.05143
0.17907	-0.05083
0.19776	-0.04987
0.21855	-0.04850
0.24149	-0.04674
0.26642	-0.04454
0.29326	-0.04195
0.32130	-0.03899
0.35047	-0.03564
0.38022	-0.03199
0.41052	-0.02799
0.44115	-0.02377
0.47119	-0.01973
0.50119	-0.01600
0.53085	-0.01259
0.56047	-0.00949
0.58971	-0.00672
0.61892	-0.00432
0.64833	-0.00221
0.67791	-0.00042
0.70777	0.00113
0.73737	0.00242
0.76671	0.00336
0.79601	0.00403
0.82458	0.00445
0.85246	0.00452
0.87936	0.00442
0.90435	0.00403
0.92775	0.00344
0.94889	0.00259
0.96849	0.00153
0.98598	0.00027
1.00000	-0.00013

MFFS-026 Strut (as built)	
x	y
1	0
0.99903	0.00595
0.99675	0.00854
0.99263	0.01022
0.98990	0.01116
0.98536	0.01271
0.98208	0.01379
0.97687	0.01549
0.96809	0.01825
0.96004	0.02075
0.94763	0.02454
0.93869	0.02727
0.92764	0.03065
0.91522	0.03440
0.89976	0.03901
0.88113	0.04448
0.86744	0.04846
0.85310	0.05267
0.83917	0.05671
0.82286	0.06156
0.80532	0.06666
0.78599	0.07226
0.76728	0.07770
0.74110	0.08533
0.71737	0.09220
0.69220	0.09943
0.66310	0.10770
0.63341	0.11600
0.59304	0.12697
0.56390	0.13460
0.52686	0.14366
0.48851	0.15187
0.45217	0.15823
0.41983	0.16266
0.38491	0.16610
0.35605	0.16788
0.33132	0.16859
0.30531	0.16848
0.28894	0.16796
0.24073	0.16415
0.22413	0.16197
0.19633	0.15719
0.18555	0.15487
Continued ...	

Continued ...	
x	y
0.17117	0.15136
0.16083	0.14849
0.15251	0.14596
0.14709	0.14420
0.15313	0.14616
0.14124	0.14217
0.12055	0.13398
0.11256	0.13036
0.10192	0.12512
0.09564	0.12179
0.09034	0.11881
0.08193	0.11381
0.07826	0.11152
0.07293	0.10803
0.06847	0.10499
0.06551	0.10287
0.05767	0.09700
0.04853	0.08955
0.03908	0.08058
0.03374	0.07486
0.02720	0.06709
0.02057	0.05800
0.01512	0.04940
0.01160	0.04301
0.00702	0.03298
0.00210	0.01737
0.00071	0.00948
0.00026	0.00518
0.00001	0.00066
0.00000	0.00000
0.00014	-0.00516
0.00177	-0.01556
0.00311	-0.02009
0.00536	-0.02557
0.00860	-0.03121
0.01281	-0.03647
0.01785	-0.04113
0.02362	-0.04510
0.03042	-0.04870
0.03792	-0.05172
0.04454	-0.05384
0.05237	-0.05591
0.06022	-0.05762
0.06591	-0.05866
0.07789	-0.06047
0.09913	-0.06260
0.13031	-0.06385
Continued ...	

Continued ...	
x	y
0.16444	-0.06361
0.18775	-0.06279
0.22507	-0.06046
0.27031	-0.05637
0.31375	-0.05139
0.36682	-0.04460
0.43989	-0.03494
0.50198	-0.02687
0.56199	-0.01950
0.61144	-0.01410
0.65286	-0.01057
0.70125	-0.00717
0.74361	-0.00510
0.78355	-0.00382
0.81175	-0.00316
0.83374	-0.00278
0.85234	-0.00261
0.86286	-0.00256
0.87161	-0.00256
0.88226	-0.00259
0.89510	-0.00268
0.90482	-0.00276
0.91658	-0.00290
0.92795	-0.00308
0.93787	-0.00321
0.94485	-0.00336
0.95057	-0.00352
0.96074	-0.00378
0.96717	-0.00397
0.97587	-0.00417
0.98026	-0.00425
0.98373	-0.00427
0.99278	-0.00422
0.99546	-0.00409

Flap One (as designed)	
x	y
1.00000	0.00286
0.98702	0.00731
0.97129	0.01287
0.95418	0.01826
0.93462	0.02384
0.91266	0.02981
0.88822	0.03620
0.86153	0.04297
0.83297	0.05001
0.80297	0.05723
0.77195	0.06453
0.74022	0.07185
0.70805	0.07914
0.67563	0.08636
0.64311	0.09347
0.61067	0.10045
0.57846	0.10724
0.54667	0.11380
0.51555	0.12008
0.48537	0.12598
0.45642	0.13145
0.42901	0.13638
0.40335	0.14069
0.37936	0.14430
0.35677	0.14722
0.33532	0.14948
0.31488	0.15112
0.29538	0.15218
0.27677	0.15269
0.25900	0.15265
0.24202	0.15211
0.22579	0.15108
0.21029	0.14959
0.19550	0.14769
0.18140	0.14540
0.16800	0.14275
0.15527	0.13977
0.14321	0.13649
0.13179	0.13293
0.12100	0.12913
0.11081	0.12512
0.10122	0.12092
0.09220	0.11657
Continued ...	

Continued ...	
x	y
0.08374	0.11208
0.07582	0.10749
0.06842	0.10280
0.06151	0.09804
0.05509	0.09323
0.04912	0.08838
0.04358	0.08352
0.03847	0.07864
0.03374	0.07377
0.02940	0.06892
0.02542	0.06409
0.02179	0.05929
0.01848	0.05454
0.01549	0.04983
0.01281	0.04517
0.01041	0.04056
0.00828	0.03602
0.00642	0.03154
0.00482	0.02714
0.00346	0.02280
0.00233	0.01854
0.00144	0.01436
0.00076	0.01027
0.00030	0.00625
0.00005	0.00233
0.00002	-0.00151
0.00020	-0.00531
0.00060	-0.00909
0.00121	-0.01283
0.00206	-0.01651
0.00320	-0.02011
0.00469	-0.02359
0.00658	-0.02690
0.00889	-0.02998
0.01166	-0.03277
0.01483	-0.03526
0.01835	-0.03753
0.02215	-0.03964
0.02623	-0.04164
0.03061	-0.04352
0.03529	-0.04529
0.04030	-0.04697
0.04568	-0.04856
0.05145	-0.05007
0.05765	-0.05150
0.06435	-0.05284
0.07160	-0.05408
Continued ...	

Continued ...	
x	y
0.07948	-0.05523
0.08807	-0.05627
0.09748	-0.05719
0.10782	-0.05797
0.11922	-0.05858
0.13184	-0.05901
0.14581	-0.05920
0.16128	-0.05912
0.17836	-0.05872
0.19713	-0.05793
0.21758	-0.05674
0.23963	-0.05509
0.26307	-0.05299
0.28764	-0.05044
0.31289	-0.04749
0.33847	-0.04403
0.36488	-0.03990
0.39273	-0.03514
0.42159	-0.03013
0.45085	-0.02525
0.48020	-0.02061
0.50944	-0.01630
0.53859	-0.01232
0.56767	-0.00869
0.59668	-0.00540
0.62564	-0.00246
0.65454	0.00015
0.68334	0.00241
0.71198	0.00432
0.74037	0.00588
0.76839	0.00709
0.79587	0.00794
0.82261	0.00844
0.84837	0.00858
0.87289	0.00838
0.89595	0.00784
0.91739	0.00700
0.93713	0.00586
0.95525	0.00441
0.97185	0.00260
0.98719	0.00014
1.00000	-0.00286

Flap One (as built)	
x	y
0.99744	0
0.98761	0.00627
0.97655	0.01021
0.95586	0.01677
0.93885	0.02180
0.92151	0.02674
0.90839	0.03039
0.88829	0.03589
0.87347	0.03989
0.85451	0.04494
0.82929	0.05153
0.80074	0.05890
0.76624	0.06768
0.72483	0.07780
0.69167	0.08591
0.65162	0.09560
0.60908	0.10572
0.56221	0.11660
0.52725	0.12450
0.47971	0.13480
0.44900	0.14104
0.38442	0.15226
0.32259	0.15953
0.28561	0.16173
0.25490	0.16182
0.24485	0.16147
0.22616	0.16024
0.19962	0.15732
0.18273	0.15456
0.17059	0.15212
0.15796	0.14915
0.14499	0.14562
0.13151	0.14138
0.12416	0.13878
0.11180	0.13395
0.10075	0.12909
0.09176	0.12470
0.08048	0.11852
0.06656	0.10954
0.05781	0.10310
0.04760	0.09480
0.03881	0.08671
0.03250	0.08020
Continued ...	

Continued ...	
x	y
0.02572	0.07234
0.01958	0.06426
0.01092	0.04997
0.01157	0.05124
0.00626	0.03952
0.00371	0.03221
0.00137	0.02298
0.00032	0.01574
0.00000	0.00000
0.00558	-0.02018
0.01682	-0.03509
0.02866	-0.04376
0.03864	-0.04903
0.04566	-0.05209
0.06155	-0.05750
0.08242	-0.06244
0.10601	-0.06617
0.12336	-0.06794
0.14209	-0.06914
0.16115	-0.06959
0.17944	-0.06953
0.19414	-0.06915
0.21896	-0.06794
0.23921	-0.06661
0.26338	-0.06466
0.28269	-0.06287
0.30367	-0.06068
0.33576	-0.05695
0.36059	-0.05384
0.38486	-0.05067
0.41100	-0.04714
0.43330	-0.04405
0.46081	-0.04025
0.48410	-0.03709
0.51395	-0.03310
0.54122	-0.02962
0.57008	-0.02613
0.59915	-0.02294
0.62968	-0.02009
0.65846	-0.01795
0.68614	-0.01644
0.71209	-0.01547
0.73800	-0.01487
0.75167	-0.01461
0.77457	-0.01437
0.78526	-0.01433
0.80268	-0.01436
Continued ...	

Continued ...	
x	y
0.82249	-0.01460
0.83837	-0.01492
0.85500	-0.01544
0.88106	-0.01673
0.90094	-0.01817
0.91975	-0.01997
0.93776	-0.02207
0.94989	-0.02360
0.96479	-0.02503
0.98937	-0.02529
1.00000	-0.01366

Flap Two (as designed)	
x	y
1.00000	0.00333
0.98636	0.00630
0.96932	0.01045
0.95006	0.01492
0.92773	0.01989
0.90249	0.02551
0.87479	0.03168
0.84520	0.03832
0.81433	0.04527
0.78270	0.05240
0.75078	0.05959
0.71891	0.06674
0.68732	0.07377
0.65614	0.08062
0.62549	0.08724
0.59549	0.09358
0.56623	0.09959
0.53782	0.10521
0.51039	0.11038
0.48393	0.11504
0.45831	0.11916
0.43335	0.12276
0.40899	0.12586
0.38529	0.12847
0.36227	0.13058
0.33995	0.13217
0.31834	0.13325
0.29745	0.13384
0.27733	0.13395
0.25801	0.13359
0.23954	0.13279
0.22193	0.13157
0.20521	0.12995
0.18936	0.12797
0.17440	0.12566
0.16032	0.12306
0.14711	0.12021
0.13474	0.11715
0.12319	0.11390
0.11243	0.11049
0.10240	0.10695
0.09308	0.10330
0.08441	0.09956
Continued ...	

Continued ...	
x	y
0.07635	0.09575
0.06887	0.09189
0.06194	0.08797
0.05551	0.08402
0.04955	0.08003
0.04405	0.07599
0.03897	0.07192
0.03428	0.06782
0.02998	0.06369
0.02602	0.05955
0.02240	0.05540
0.01910	0.05124
0.01609	0.04709
0.01338	0.04296
0.01095	0.03884
0.00879	0.03475
0.00688	0.03069
0.00523	0.02666
0.00382	0.02267
0.00264	0.01873
0.00169	0.01484
0.00095	0.01102
0.00043	0.00725
0.00012	0.00355
0.00001	-0.00007
0.00010	-0.00365
0.00041	-0.00725
0.00095	-0.01084
0.00171	-0.01441
0.00275	-0.01795
0.00414	-0.02139
0.00594	-0.02471
0.00817	-0.02784
0.01077	-0.03081
0.01373	-0.03360
0.01703	-0.03624
0.02062	-0.03878
0.02449	-0.04126
0.02865	-0.04369
0.03312	-0.04606
0.03792	-0.04836
0.04309	-0.05061
0.04865	-0.05282
0.05464	-0.05497
0.06110	-0.05709
0.06808	-0.05916
0.07565	-0.06118
Continued ...	

Continued ...	
x	y
0.08387	-0.06314
0.09281	-0.06504
0.10255	-0.06686
0.11318	-0.06857
0.12480	-0.07016
0.13748	-0.07159
0.15132	-0.07283
0.16635	-0.07384
0.18261	-0.07458
0.20006	-0.07501
0.21863	-0.07507
0.23821	-0.07473
0.25864	-0.07397
0.27978	-0.07274
0.30146	-0.07103
0.32366	-0.06870
0.34696	-0.06561
0.37206	-0.06177
0.39935	-0.05734
0.42843	-0.05260
0.45837	-0.04777
0.48857	-0.04302
0.51878	-0.03842
0.54890	-0.03402
0.57889	-0.02984
0.60874	-0.02589
0.63843	-0.02219
0.66796	-0.01873
0.69728	-0.01553
0.72635	-0.01260
0.75507	-0.00994
0.78335	-0.00758
0.81101	-0.00553
0.83786	-0.00380
0.86366	-0.00241
0.88818	-0.00138
0.91118	-0.00070
0.93251	-0.00038
0.95211	-0.00042
0.97009	-0.00084
0.98652	-0.00180
1.00000	-0.00333

Flap Two (as built)	
x	y
1.00000	0.00000
0.99535	0.01100
0.98918	0.01514
0.98111	0.01755
0.97365	0.01943
0.96504	0.02150
0.95404	0.02404
0.94253	0.02664
0.91702	0.03242
0.89293	0.03787
0.86275	0.04477
0.83017	0.05221
0.80067	0.05894
0.76715	0.06649
0.73393	0.07362
0.69168	0.08282
0.65123	0.09154
0.61477	0.09924
0.57284	0.10789
0.52945	0.11656
0.48378	0.12519
0.45782	0.12978
0.42223	0.13548
0.38379	0.14065
0.35202	0.14387
0.32791	0.14553
0.29565	0.14666
0.27281	0.14667
0.24802	0.14586
0.22221	0.14409
0.20069	0.14177
0.16431	0.13592
0.13107	0.12790
0.10352	0.11904
0.07774	0.10801
0.06371	0.10053
0.05025	0.09182
0.04297	0.08625
0.03609	0.08015
0.02781	0.07159
0.02297	0.06581
0.01725	0.05806
0.01174	0.04924
Continued ...	

Continued ...	
x	y
0.00658	0.03868
0.00429	0.03273
0.00336	0.02992
0.00137	0.02222
0.00000	0.00000
0.00089	-0.00658
0.00184	-0.01108
0.00387	-0.01763
0.00569	-0.02189
0.00895	-0.02775
0.01204	-0.03212
0.01731	-0.03805
0.02431	-0.04407
0.03289	-0.04988
0.04009	-0.05382
0.04764	-0.05734
0.05496	-0.06028
0.06805	-0.06475
0.07857	-0.06774
0.09375	-0.07147
0.11363	-0.07535
0.12482	-0.07720
0.13504	-0.07867
0.14180	-0.07954
0.14871	-0.08032
0.16512	-0.08183
0.17922	-0.08279
0.19840	-0.08356
0.21520	-0.08377
0.24214	-0.08329
0.24729	-0.08309
0.27721	-0.08132
0.30047	-0.07922
0.31643	-0.07762
0.34109	-0.07483
0.36362	-0.07206
0.39870	-0.06741
0.42710	-0.06346
0.45843	-0.05911
0.48592	-0.05524
0.51530	-0.05118
0.54640	-0.04681
0.58194	-0.04199
0.61220	-0.03812
0.64348	-0.03443
0.66850	-0.03176
0.70331	-0.02858
Continued ...	

Continued ...	
x	y
0.74206	-0.02589
0.76777	-0.02452
0.79765	-0.02300
0.82122	-0.02199
0.84034	-0.02129
0.85516	-0.02085
0.87889	-0.02035
0.89613	-0.02014
0.90940	-0.02010
0.91677	-0.02015
0.92601	-0.02021
0.93096	-0.02026
0.94346	-0.02047
0.95298	-0.02052
0.96141	-0.02046
0.96590	-0.02037
0.97489	-0.01990
0.98224	-0.01920
0.98941	-0.01773
0.99488	-0.01476

Appendix E

Supporting 2-D CAD

Information presented in this appendix contains two-dimensional CAD drawings of the machined components used in experiments described in this thesis. Documentation is provided to assist future researchers in the event that a component needs to be remanufactured. CAD drawings are provided for the FPS, SFB, MFF-089 model, and the MFFS-026 model.

FPS CAD

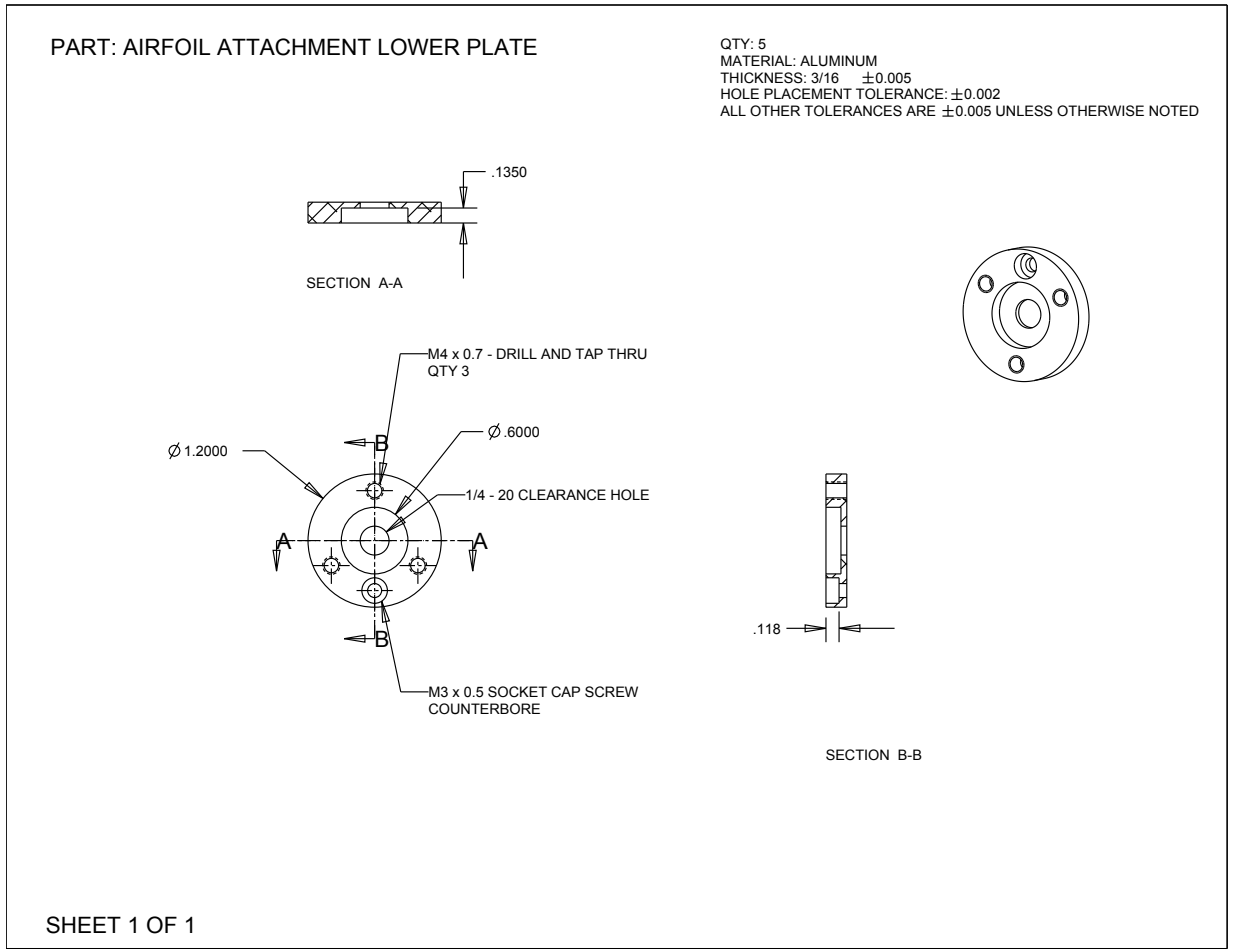

Figure E.1: Two-dimensional CAD drawing of airfoil attachment plate.

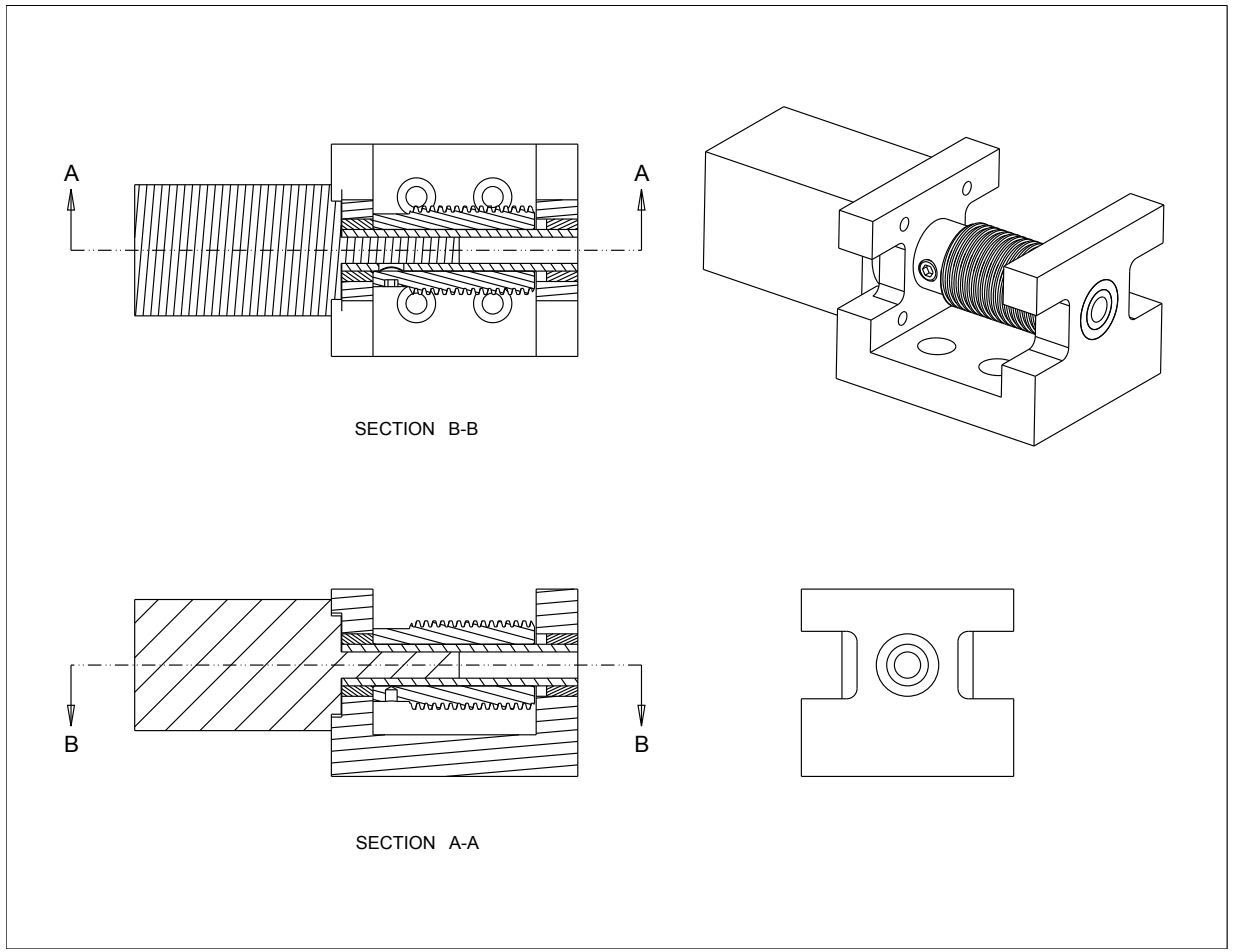

Figure E.2: Two-dimensional CAD drawing of alpha drive block.

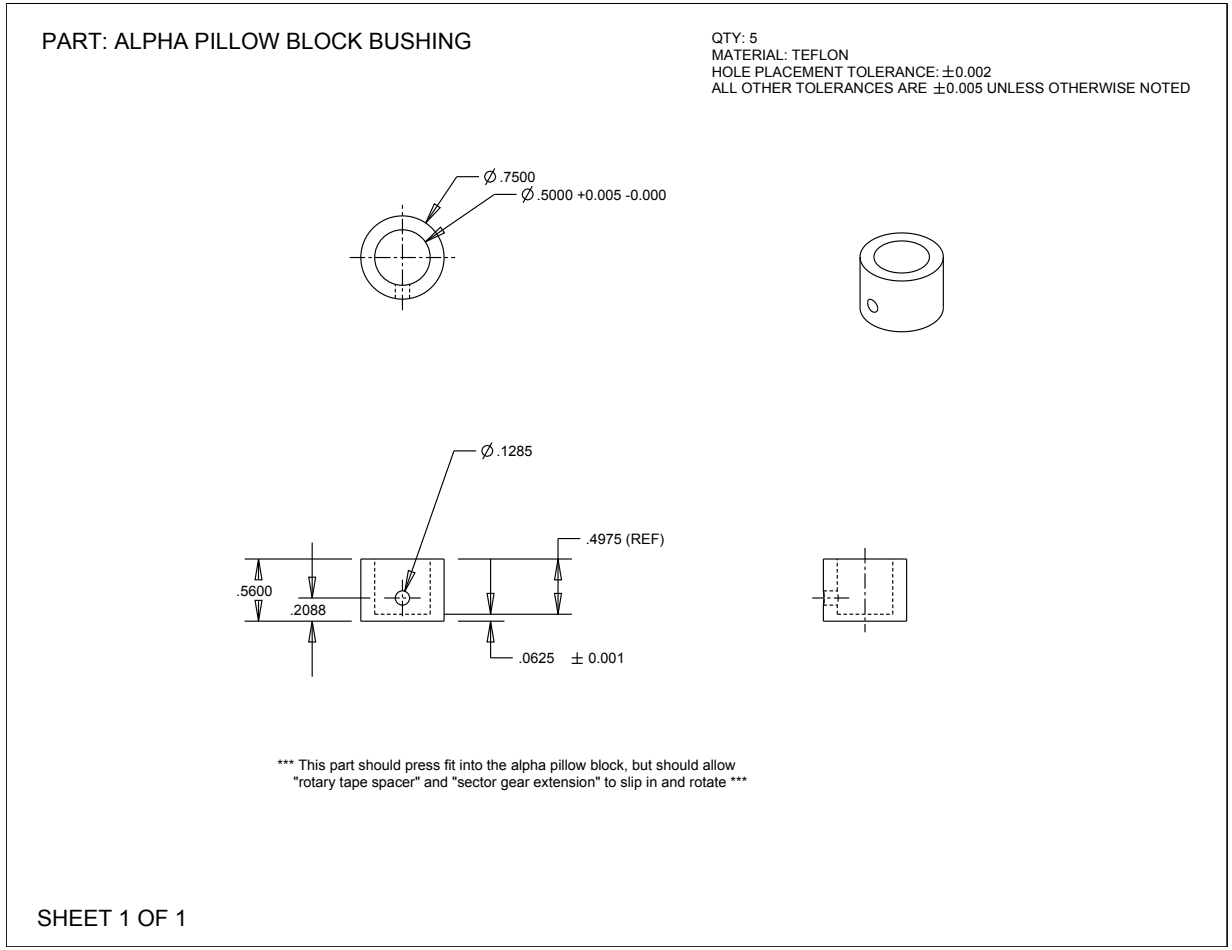

Figure E.3: Two-dimensional CAD drawing of pillow block bushing.

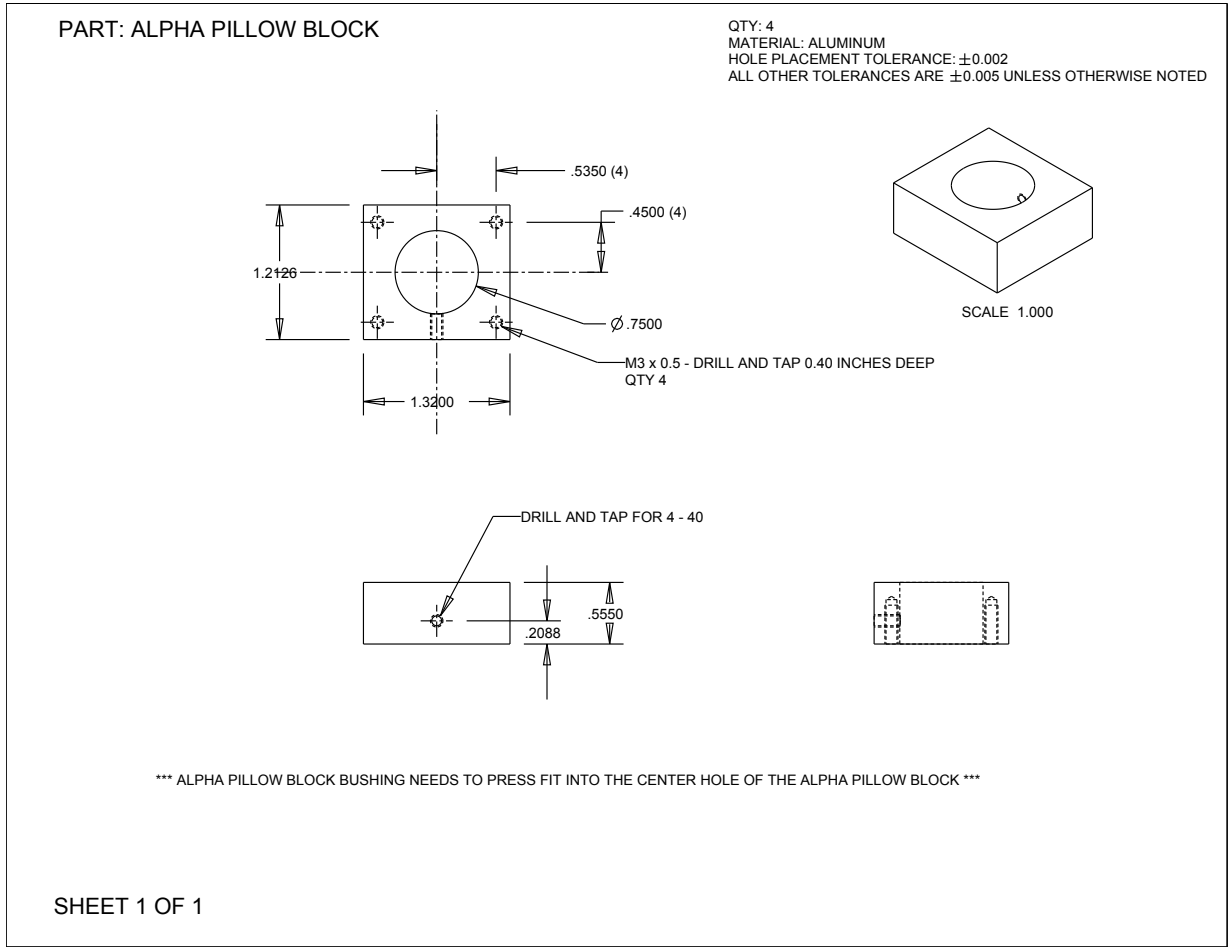

Figure E.4: Two-dimensional CAD drawing of pillow block.

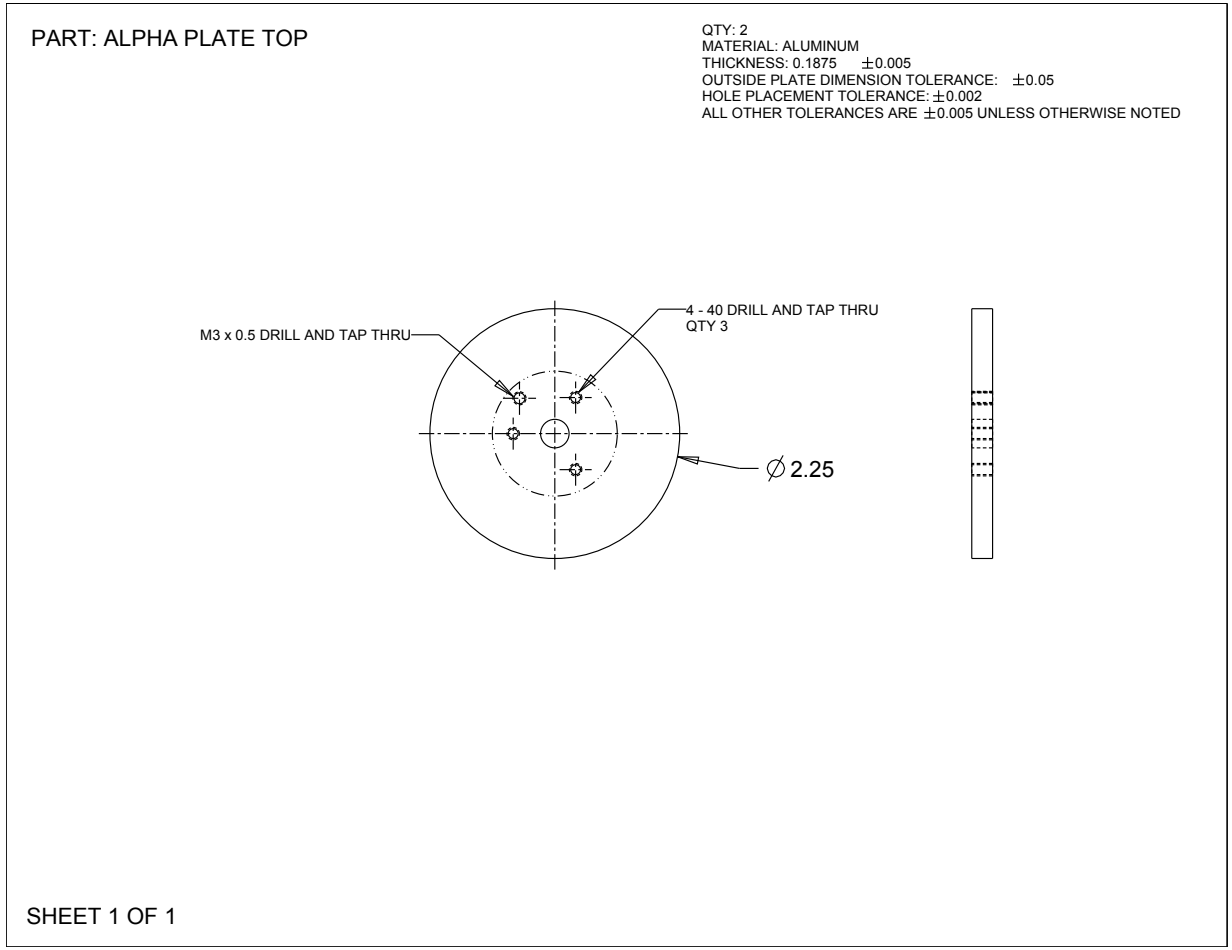

Figure E.5: Two-dimensional CAD drawing of alpha plate.

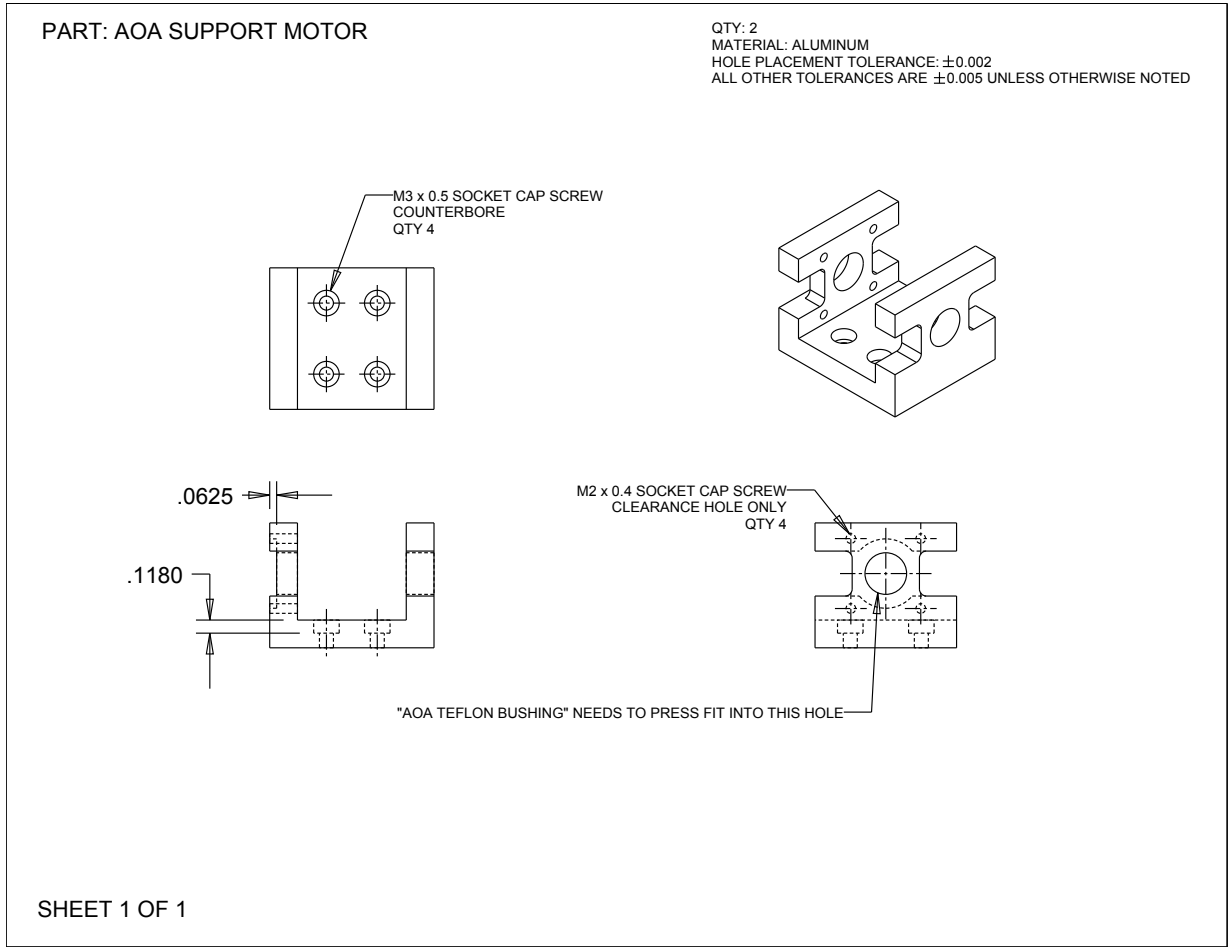

Figure E.6: Two-dimensional CAD drawing of motor mount.

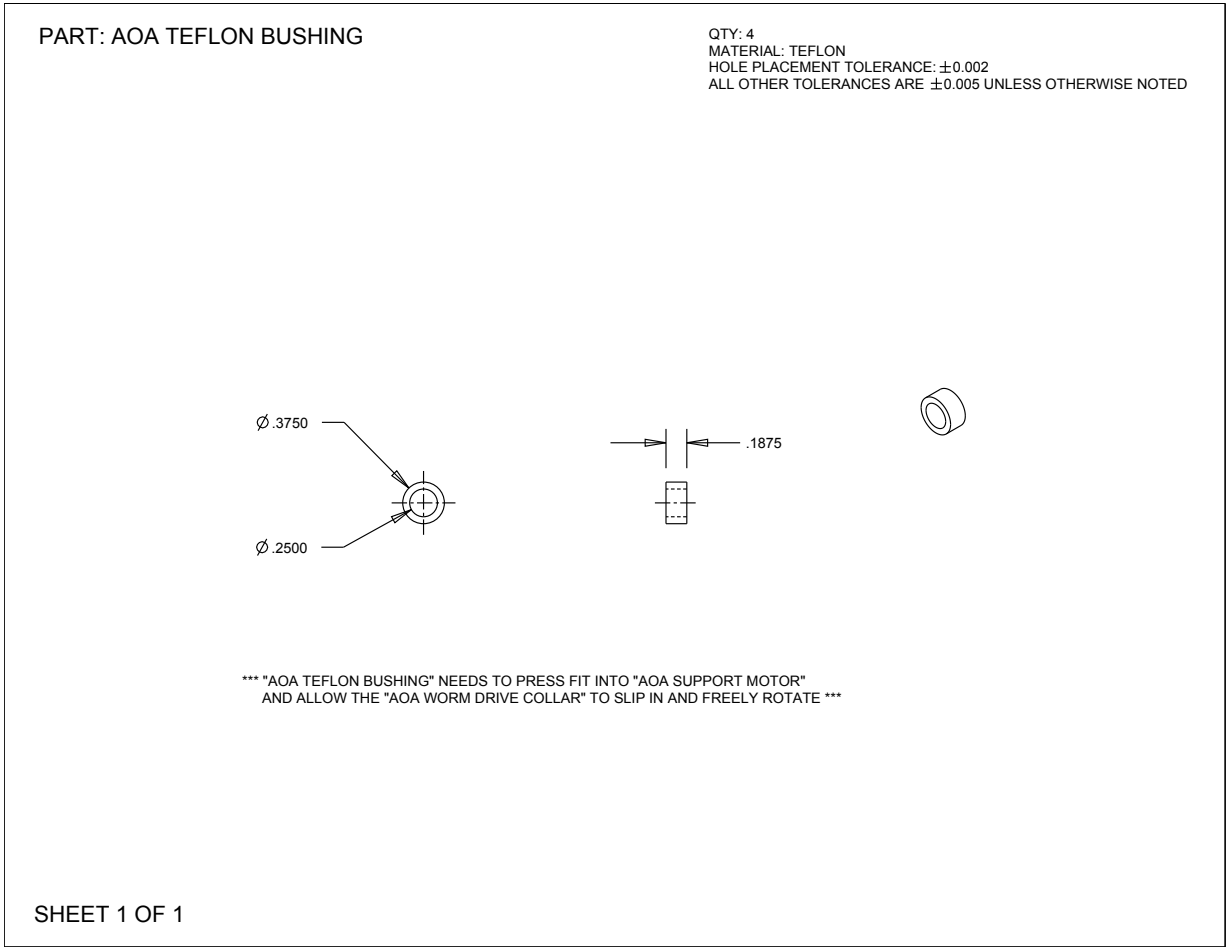

Figure E.7: Two-dimensional CAD drawing of motor bushing.

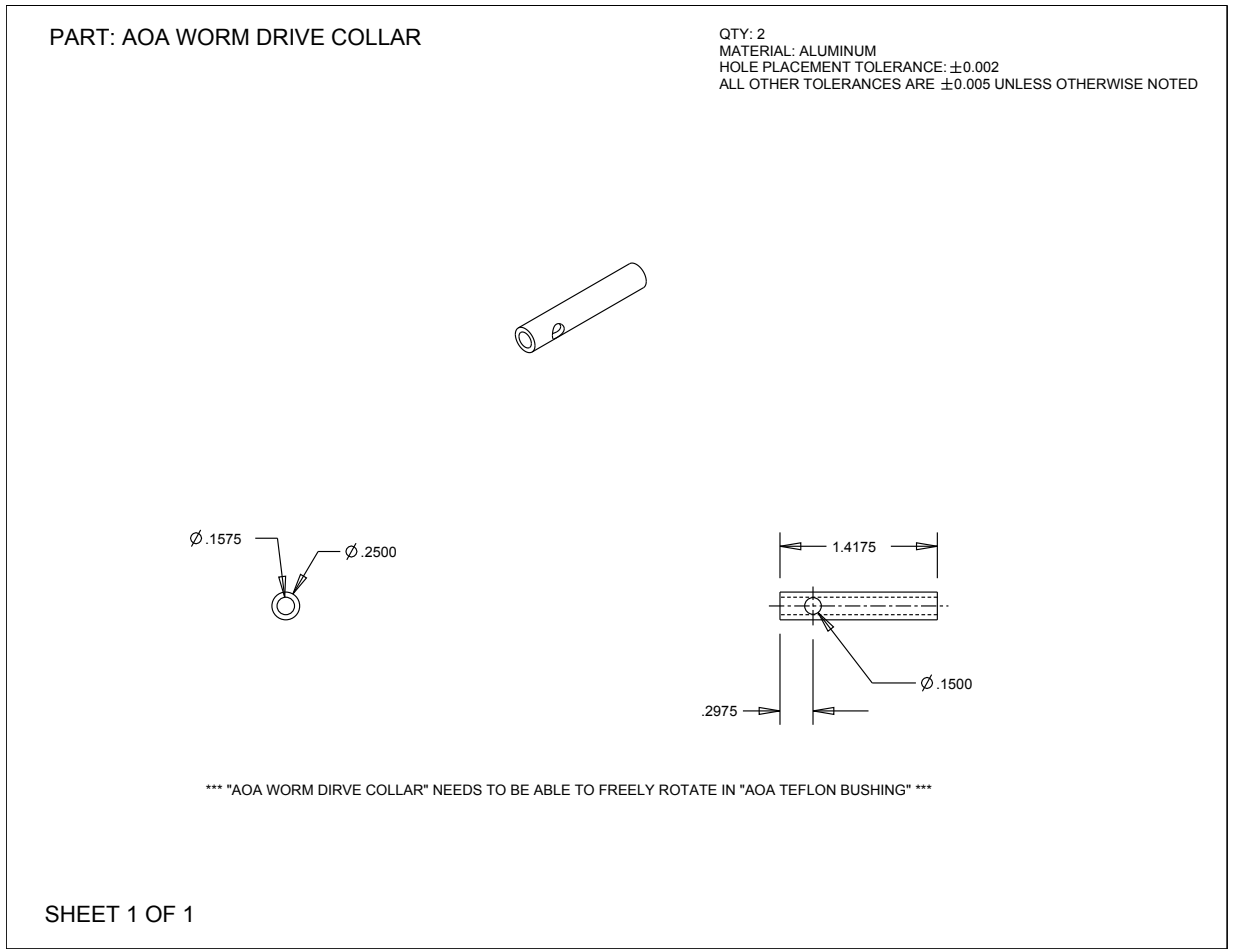

Figure E.8: Two-dimensional CAD drawing of worm collar.

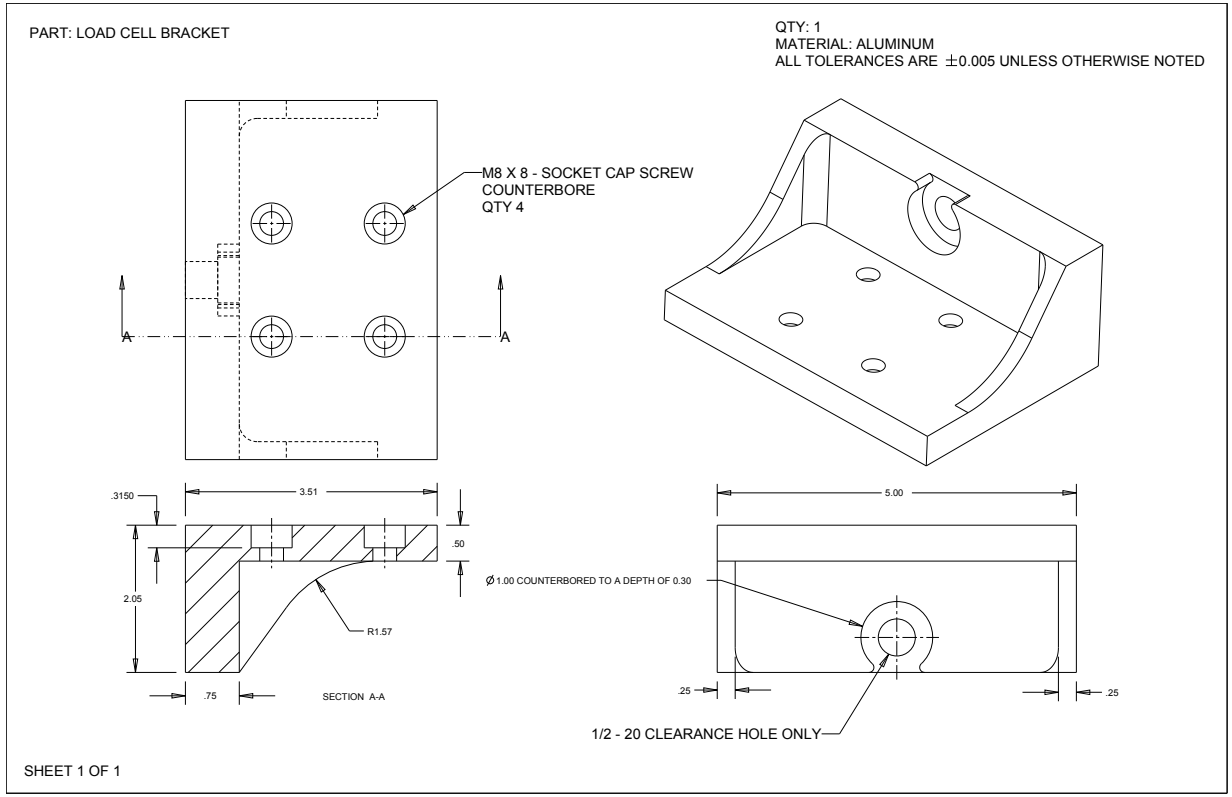

Figure E.9: Two-dimensional CAD drawing of load cell bracket.

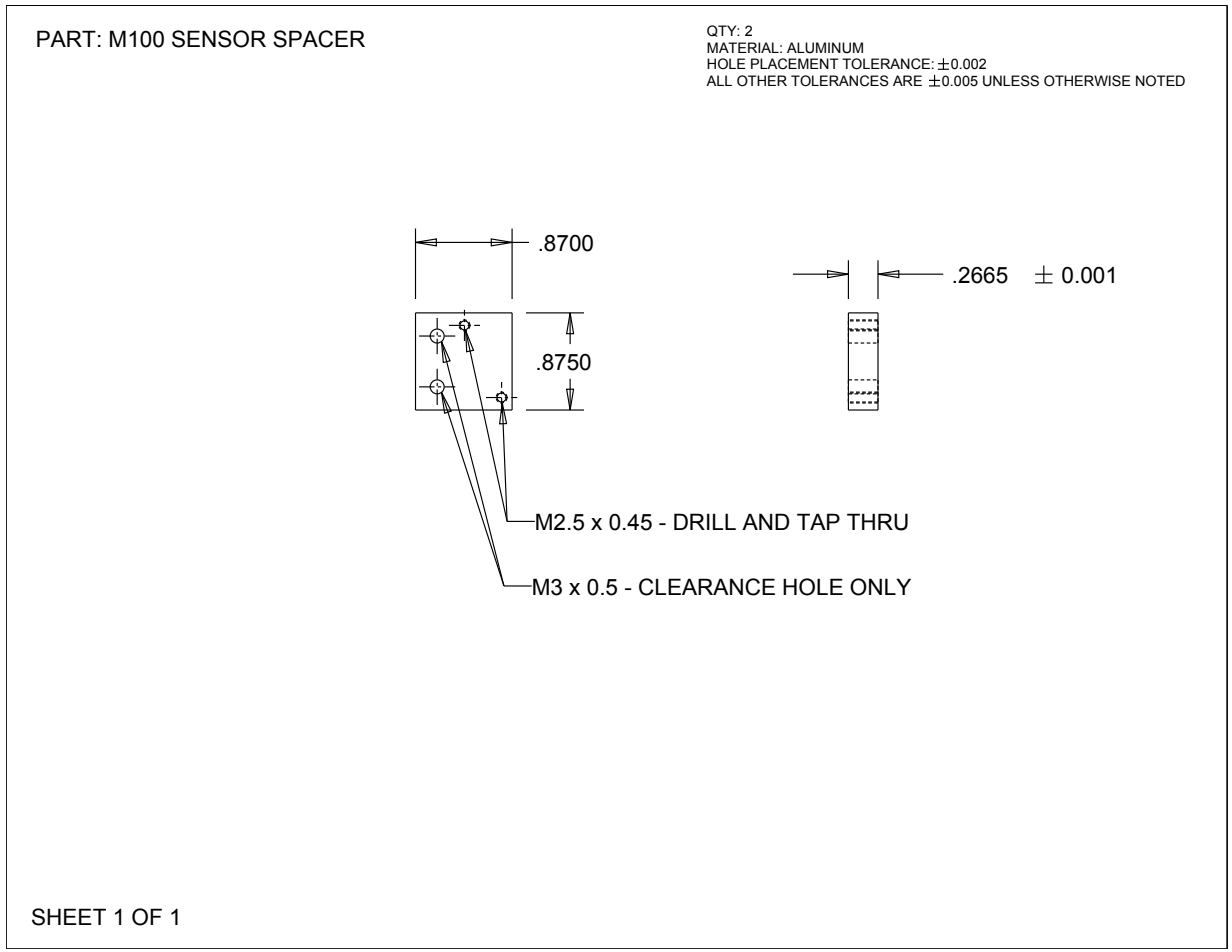

Figure E.10: Two-dimensional CAD drawing of encoder spacer.

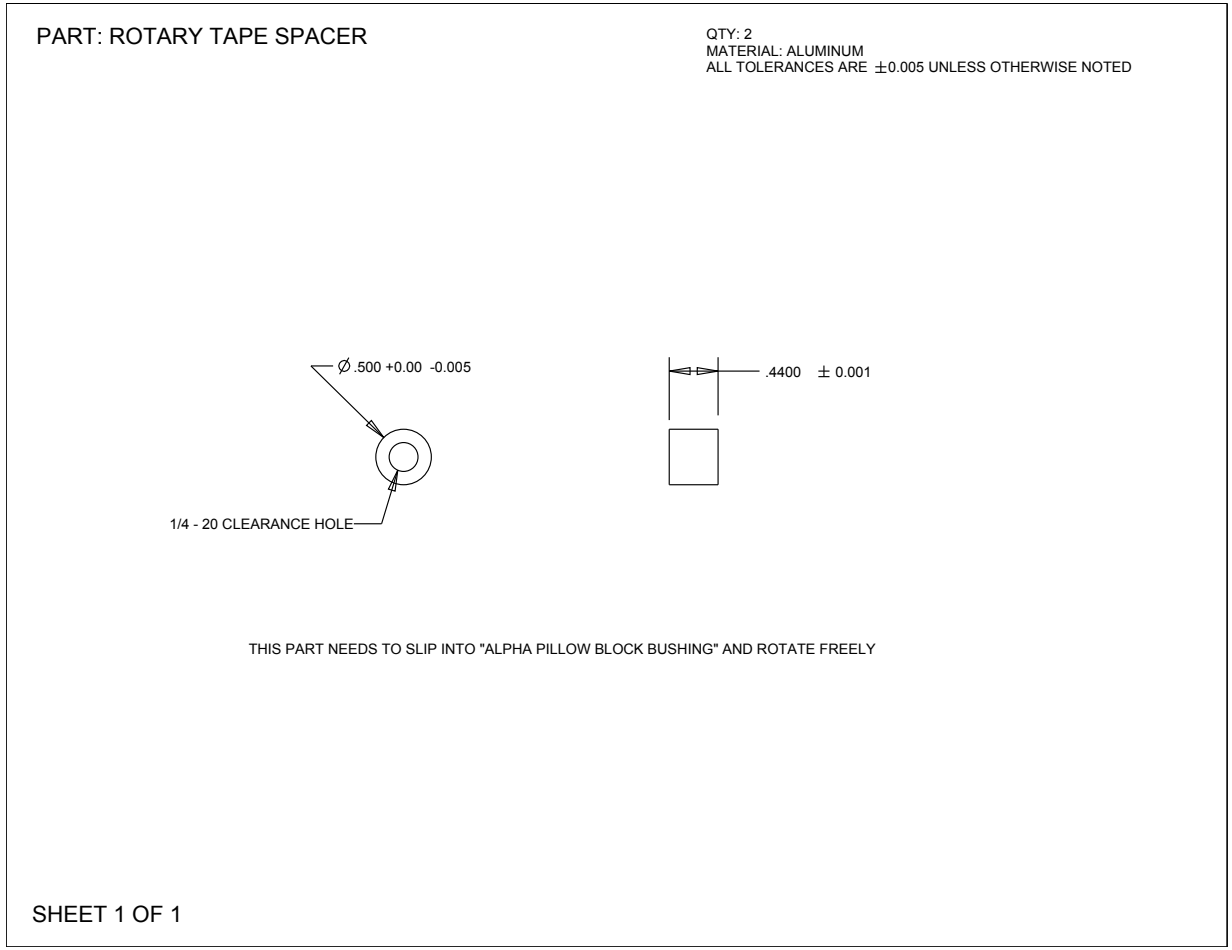

Figure E.11: Two-dimensional CAD drawing of rotary encoder spacer.

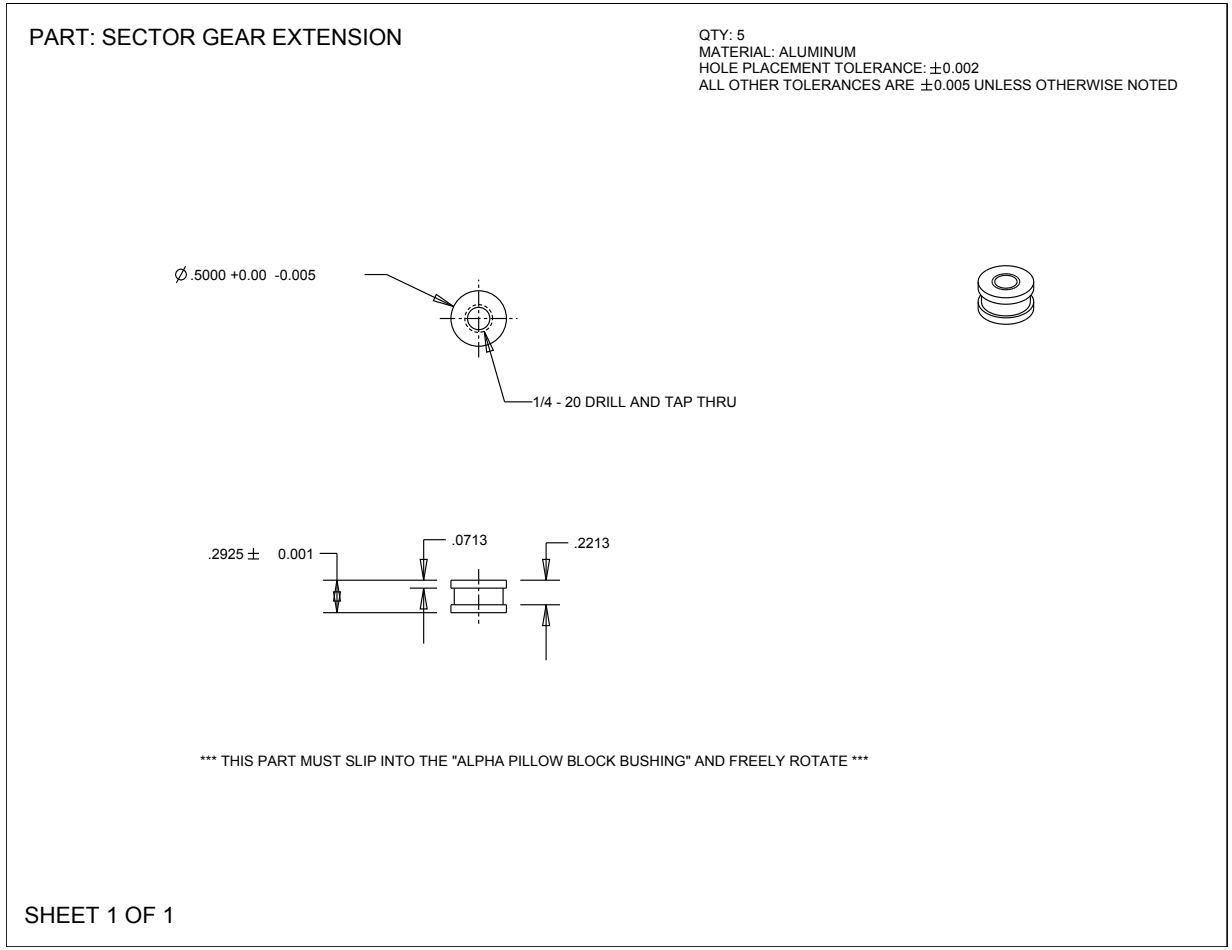

Figure E.12: Two-dimensional CAD drawing of sector gear extension.

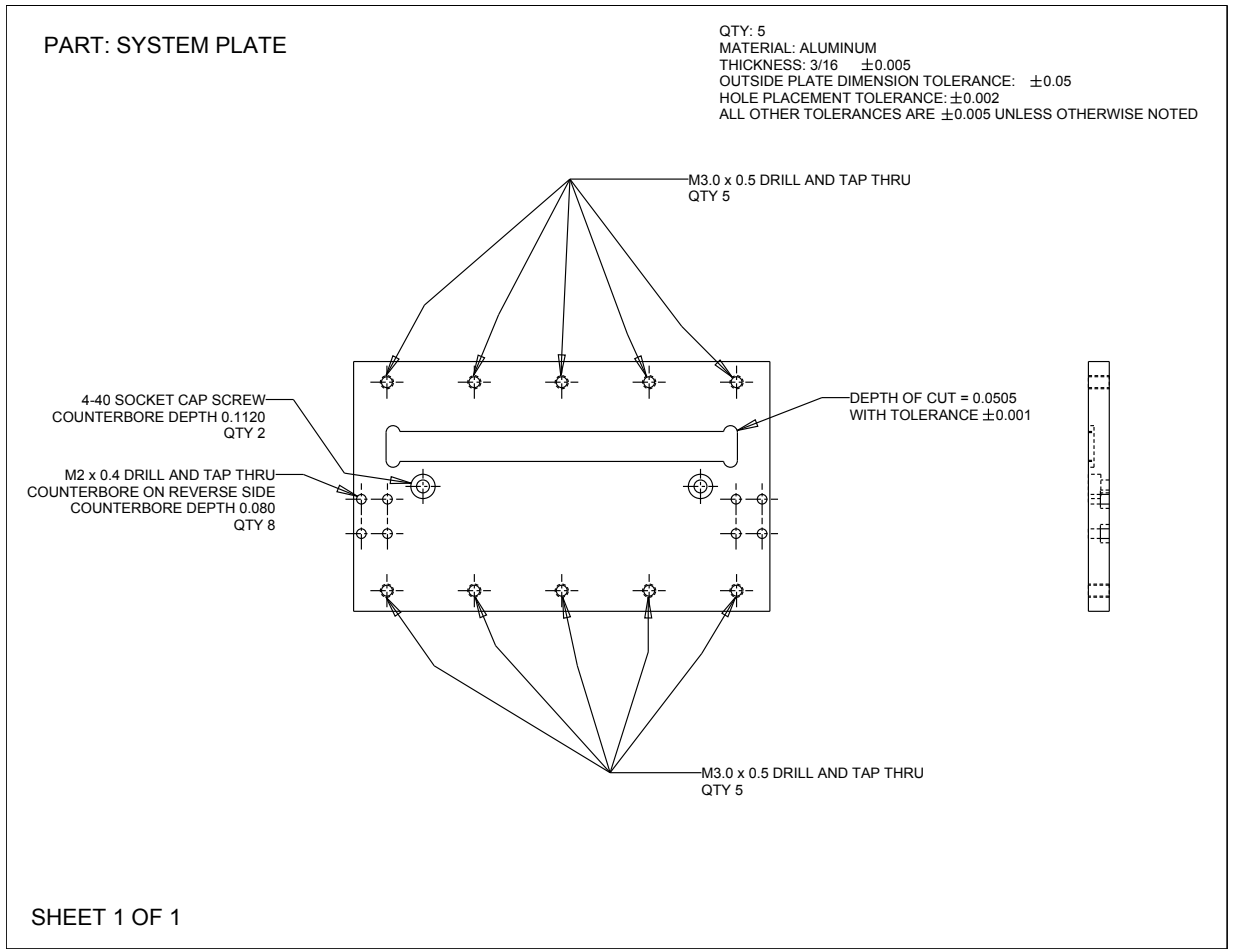

Figure E.13: Two-dimensional CAD drawing of system plate.

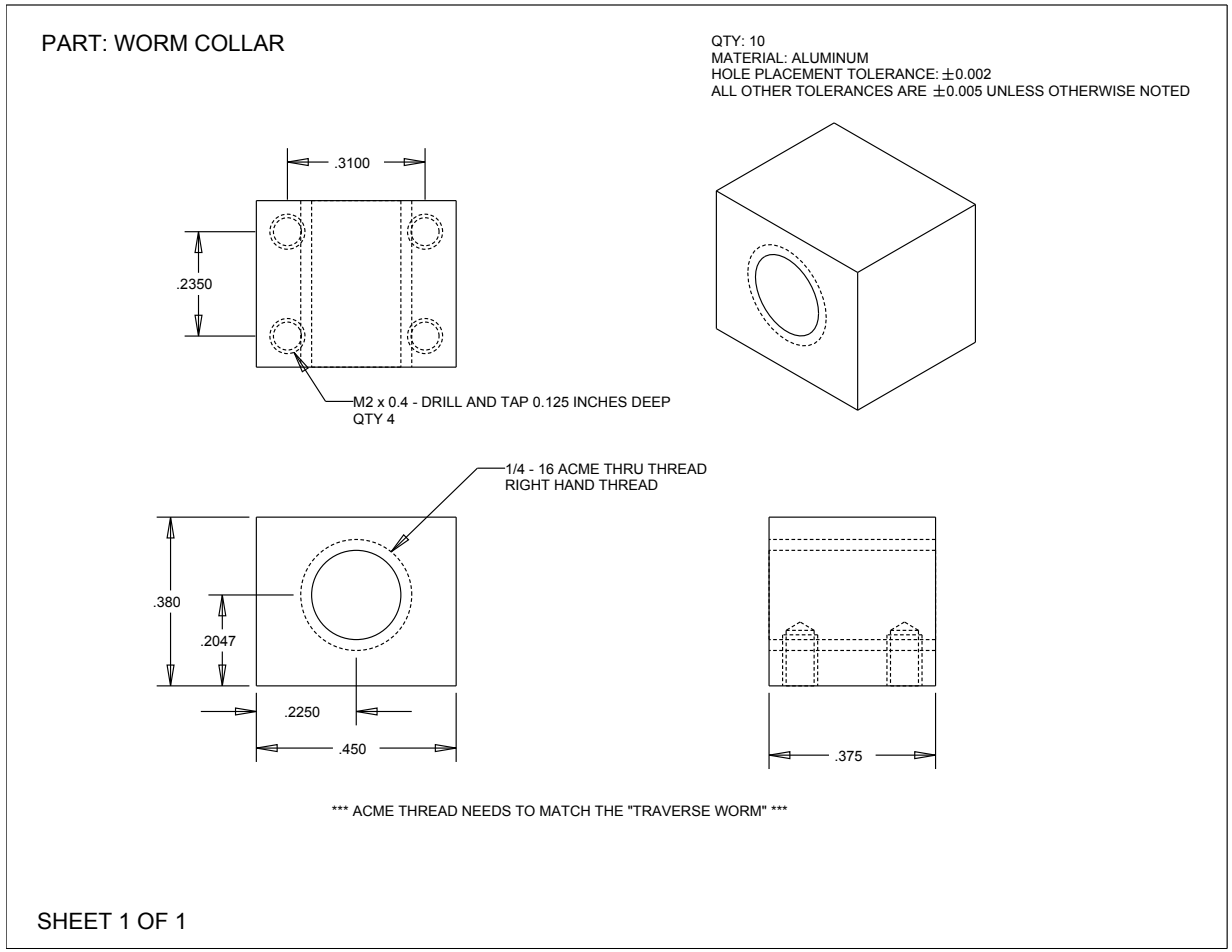

Figure E.14: Two-dimensional CAD drawing of worm collar.

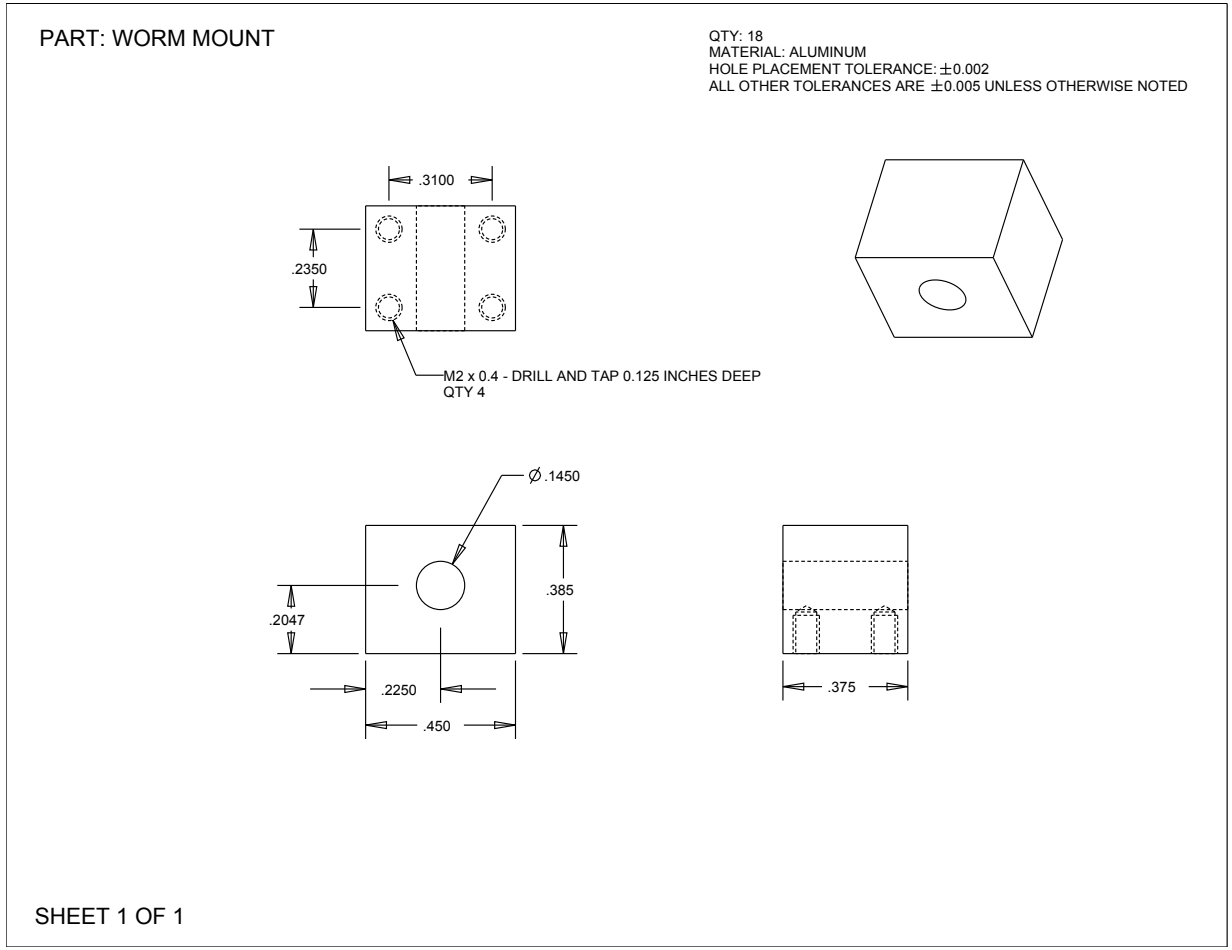

Figure E.15: Two-dimensional CAD drawing of worm mount.

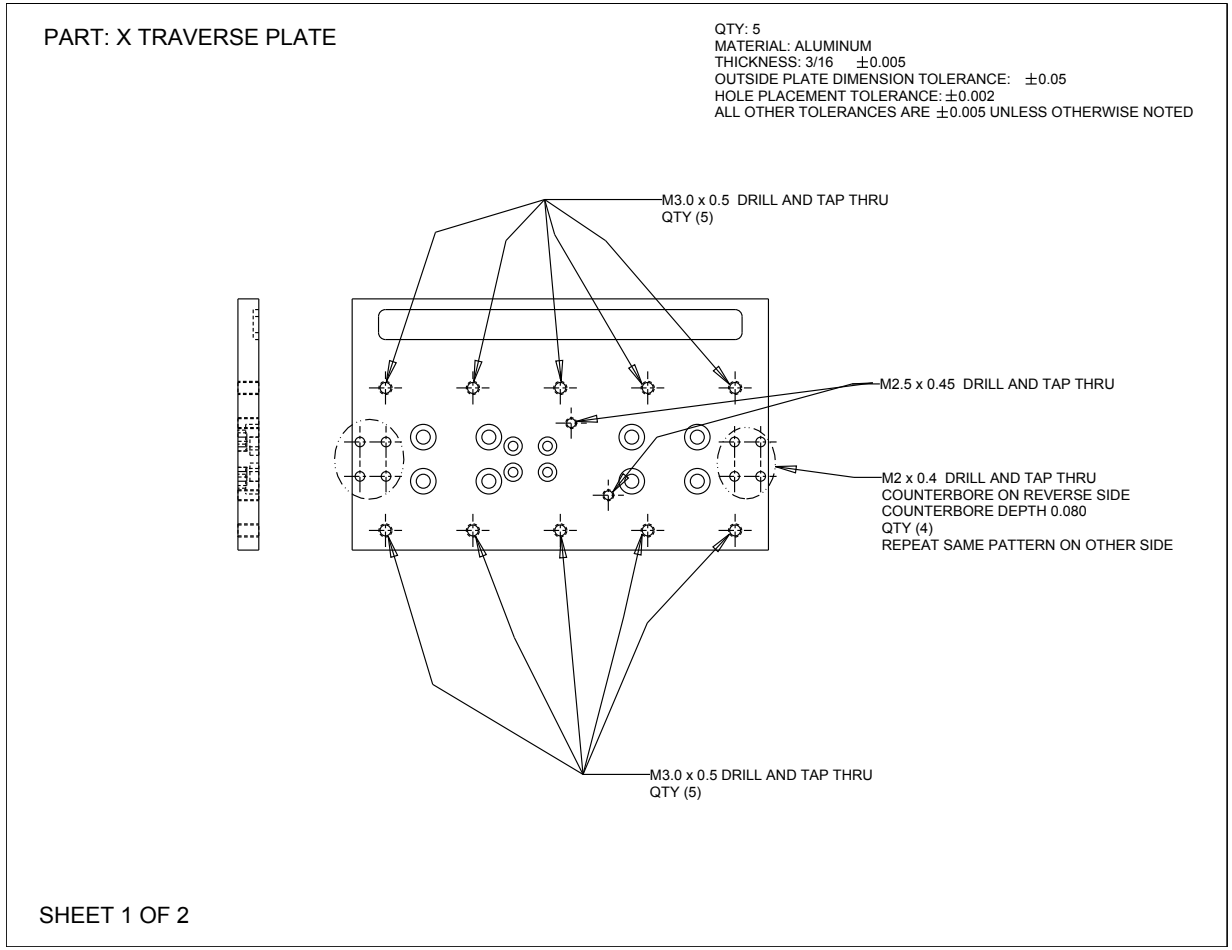

Figure E.16: Two-dimensional CAD drawing of x-traverse plate.

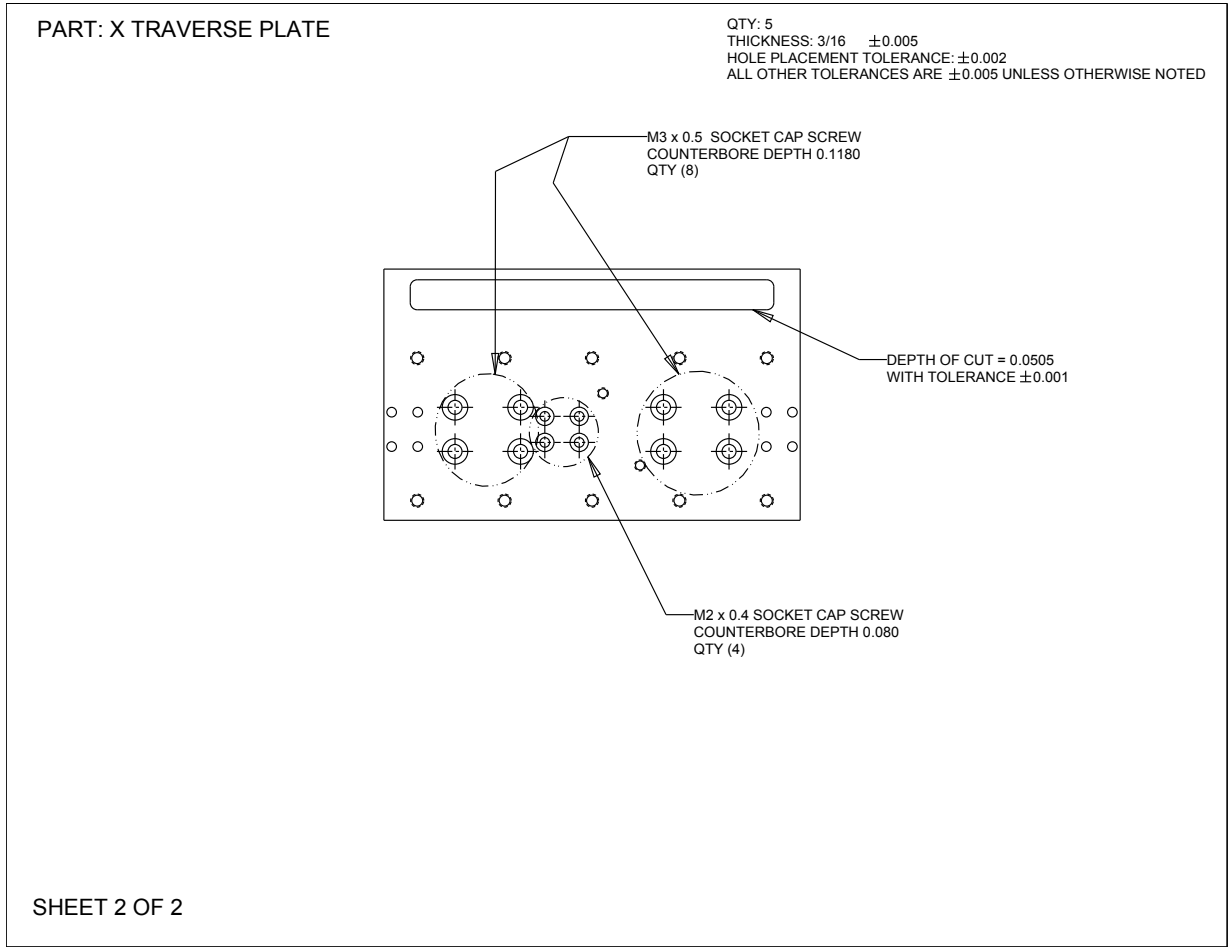

Figure E.16: Continued: Two-dimensional CAD drawing of x-traverse plate.

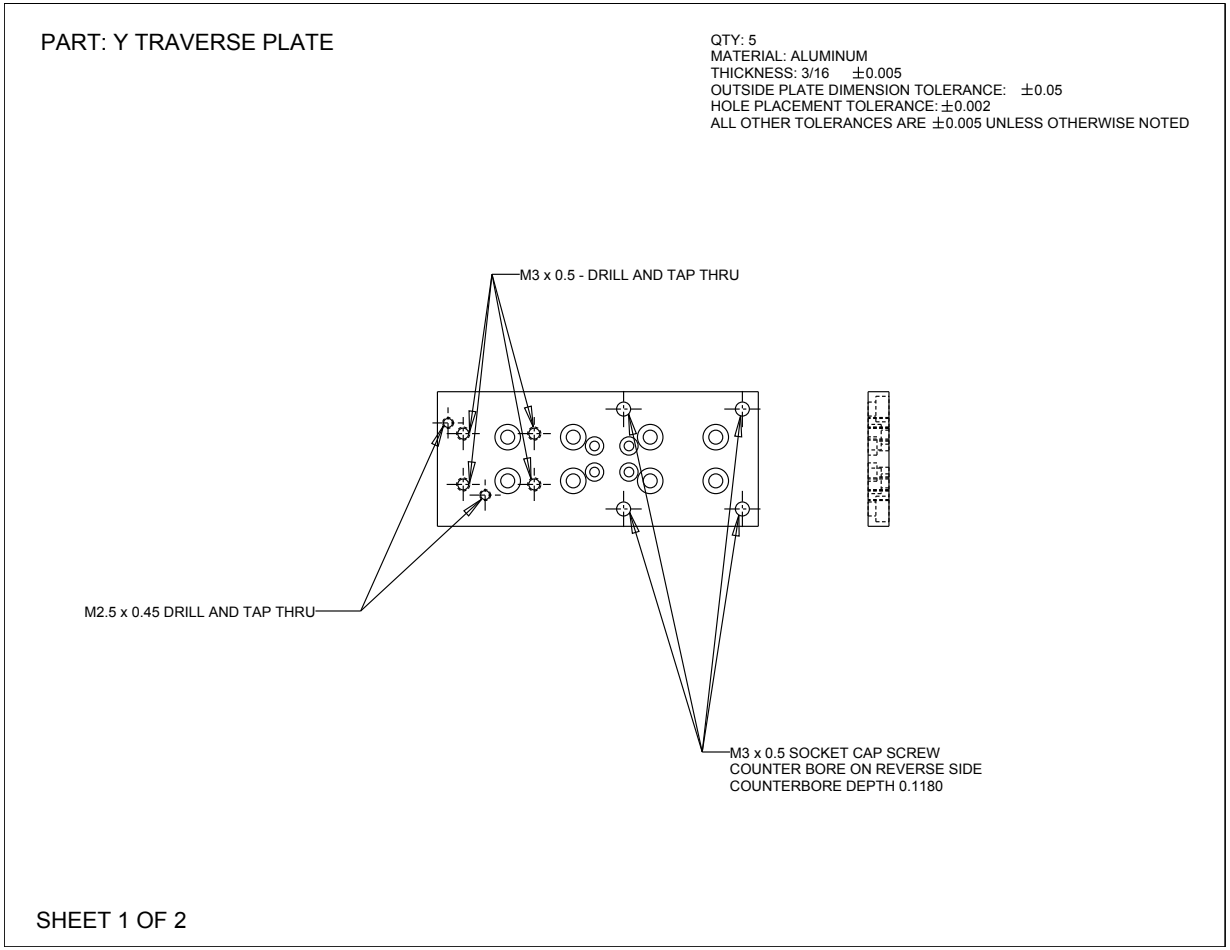

Figure E.17: Two-dimensional CAD drawing of y-traverse plate.

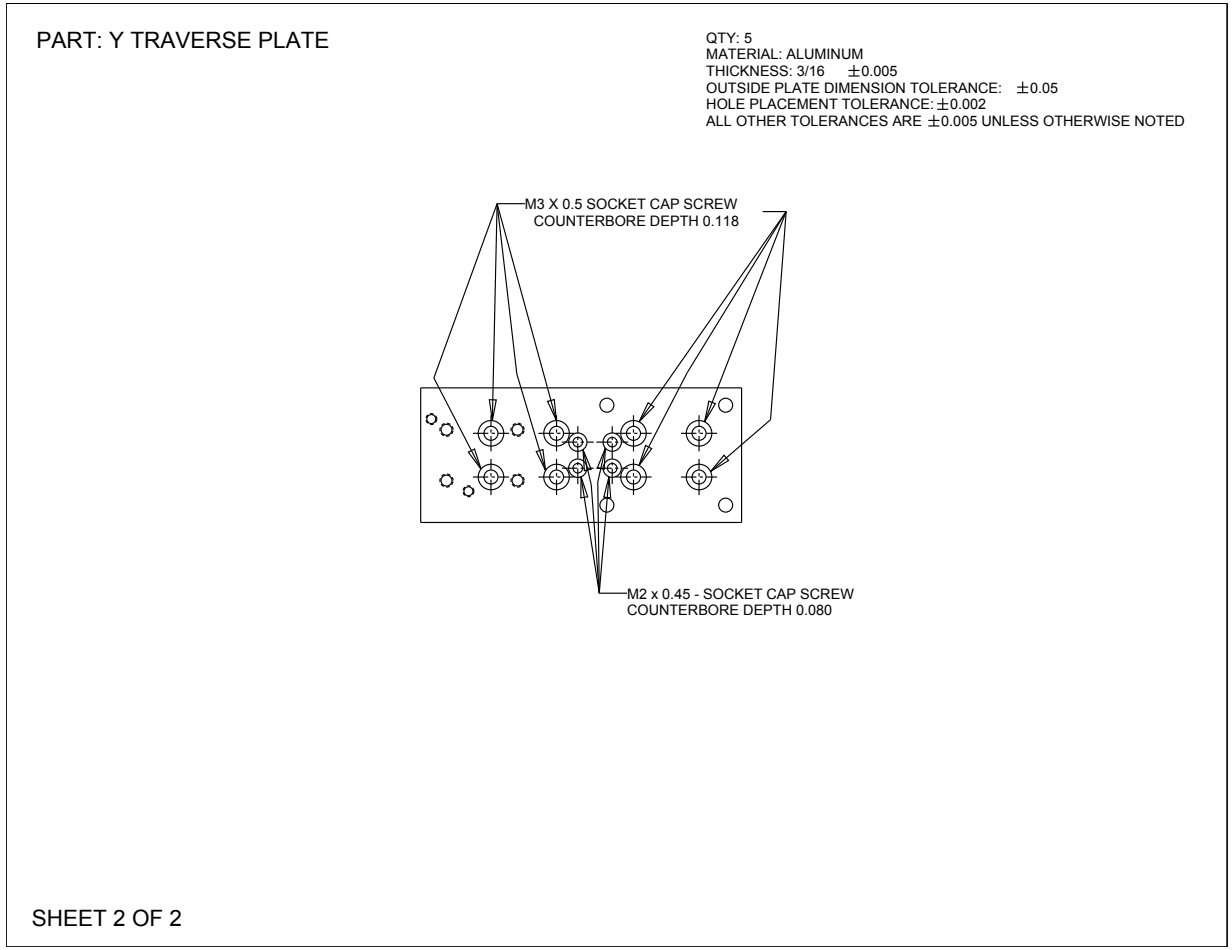

Figure E.17: Continued: Two-dimensional CAD drawing of y-traverse plate.

FPS: Future Models

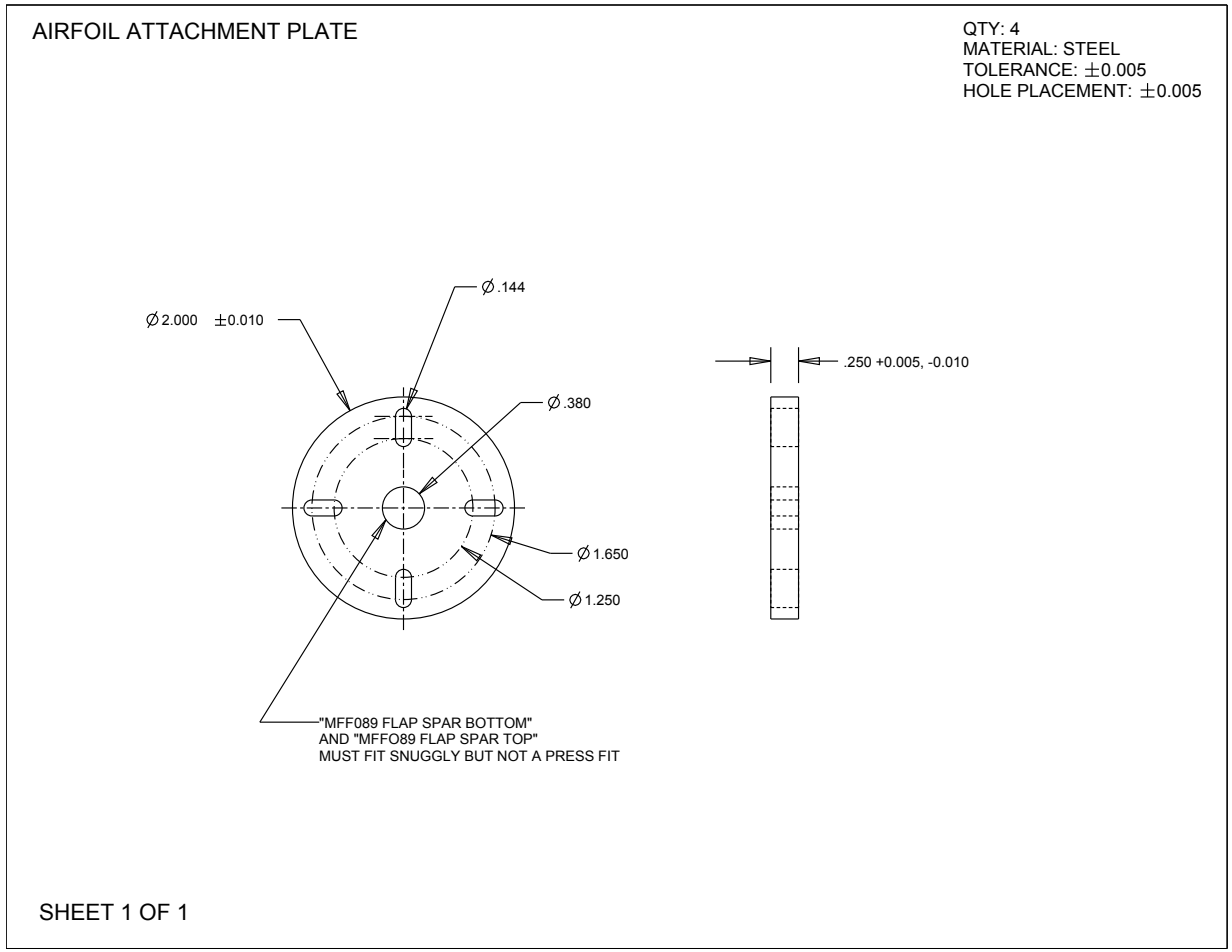

Figure E.18: Two-dimensional CAD drawing of airfoil attachment plate.

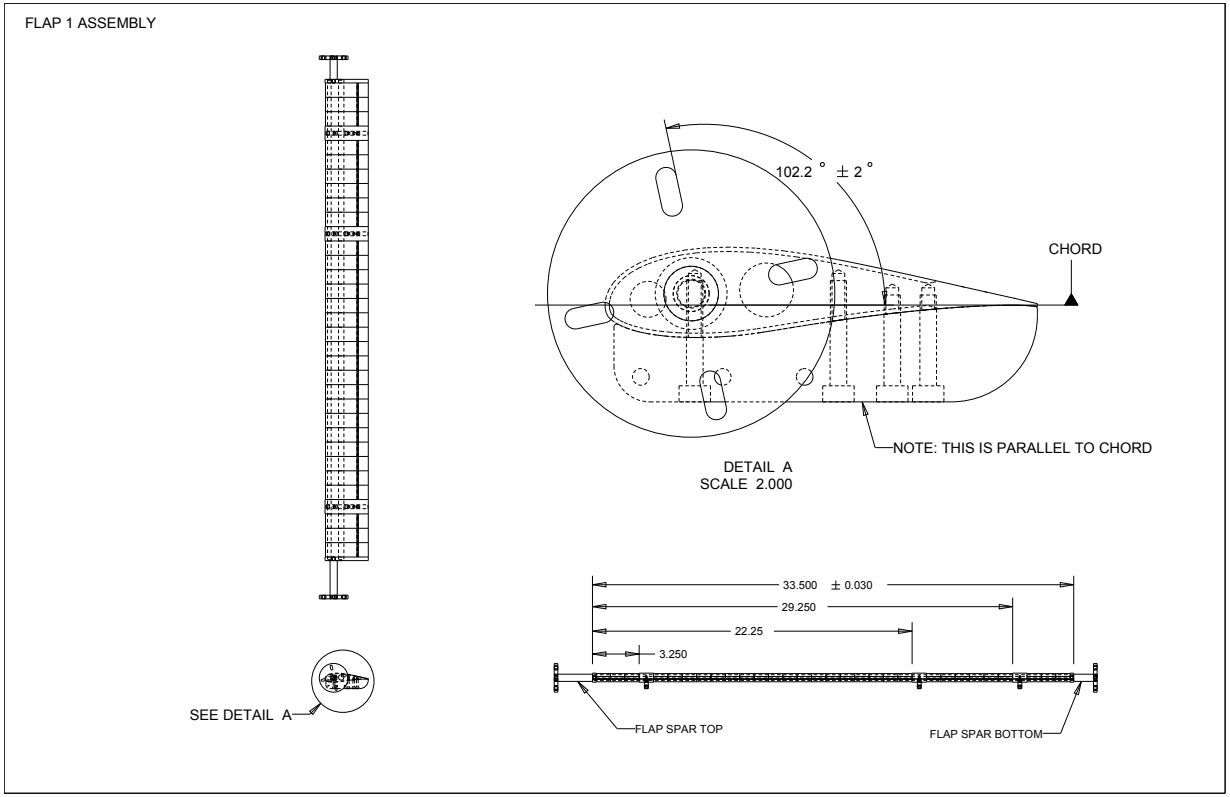

Figure E.19: Two-dimensional CAD drawing of flap one airfoil assembly.

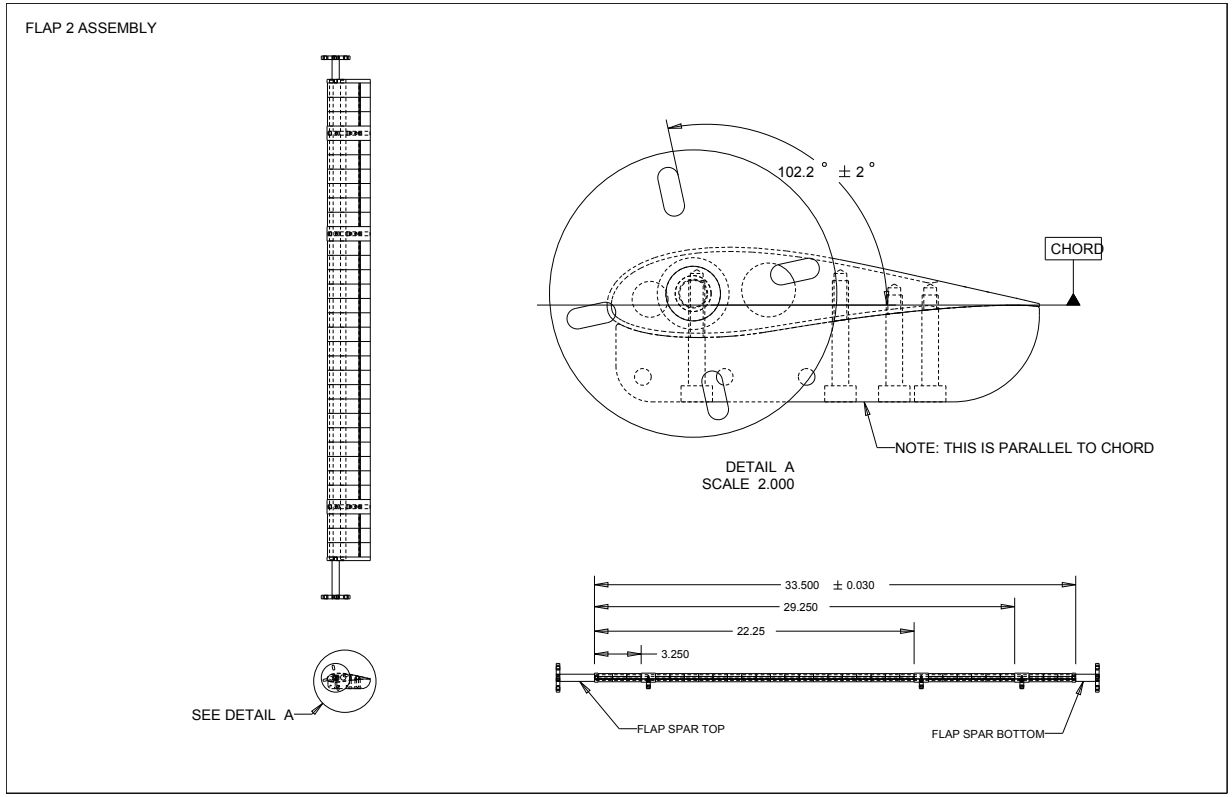

Figure E.20: Two-dimensional CAD drawing of flap two airfoil assembly.

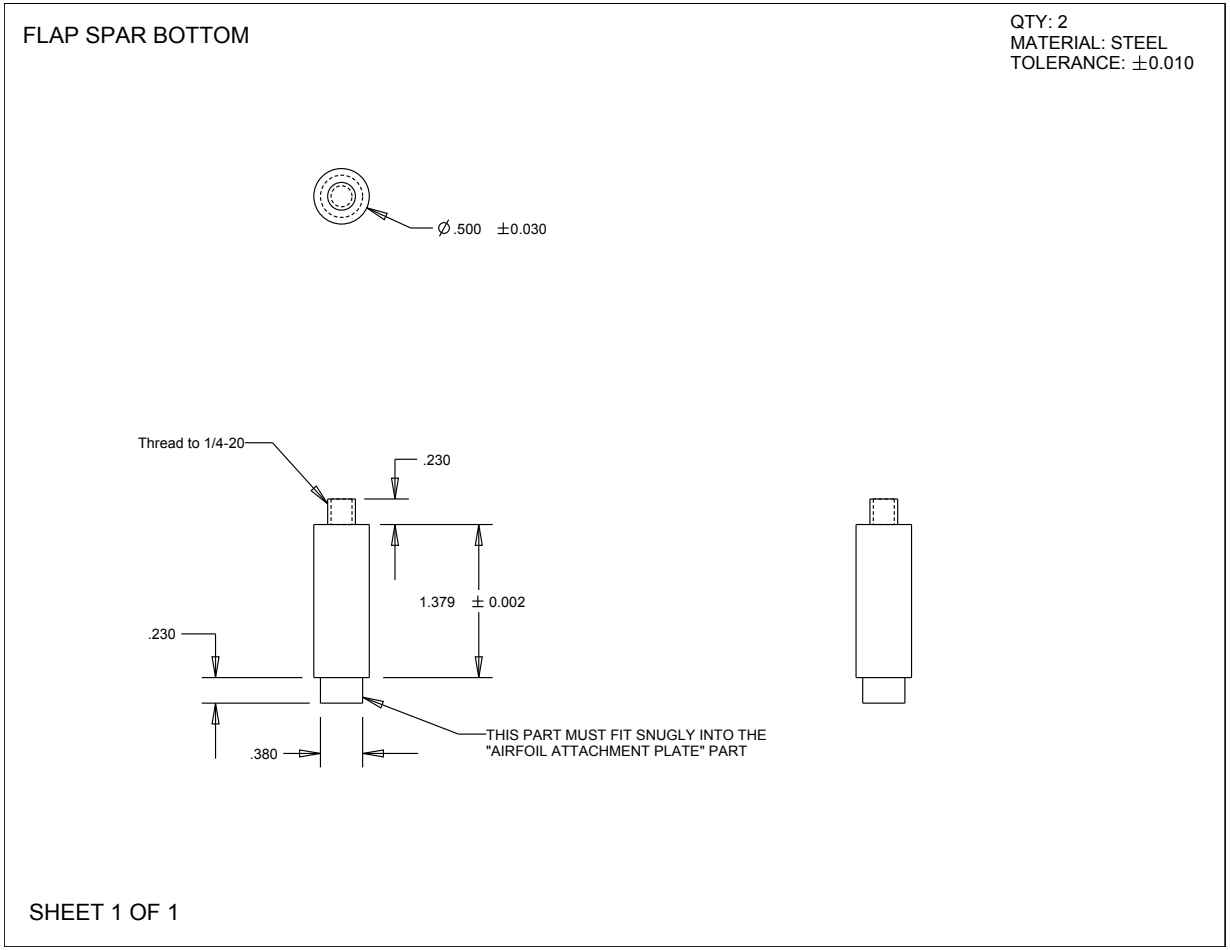

Figure E.21: Two-dimensional CAD drawing of constructed flap lower spar.

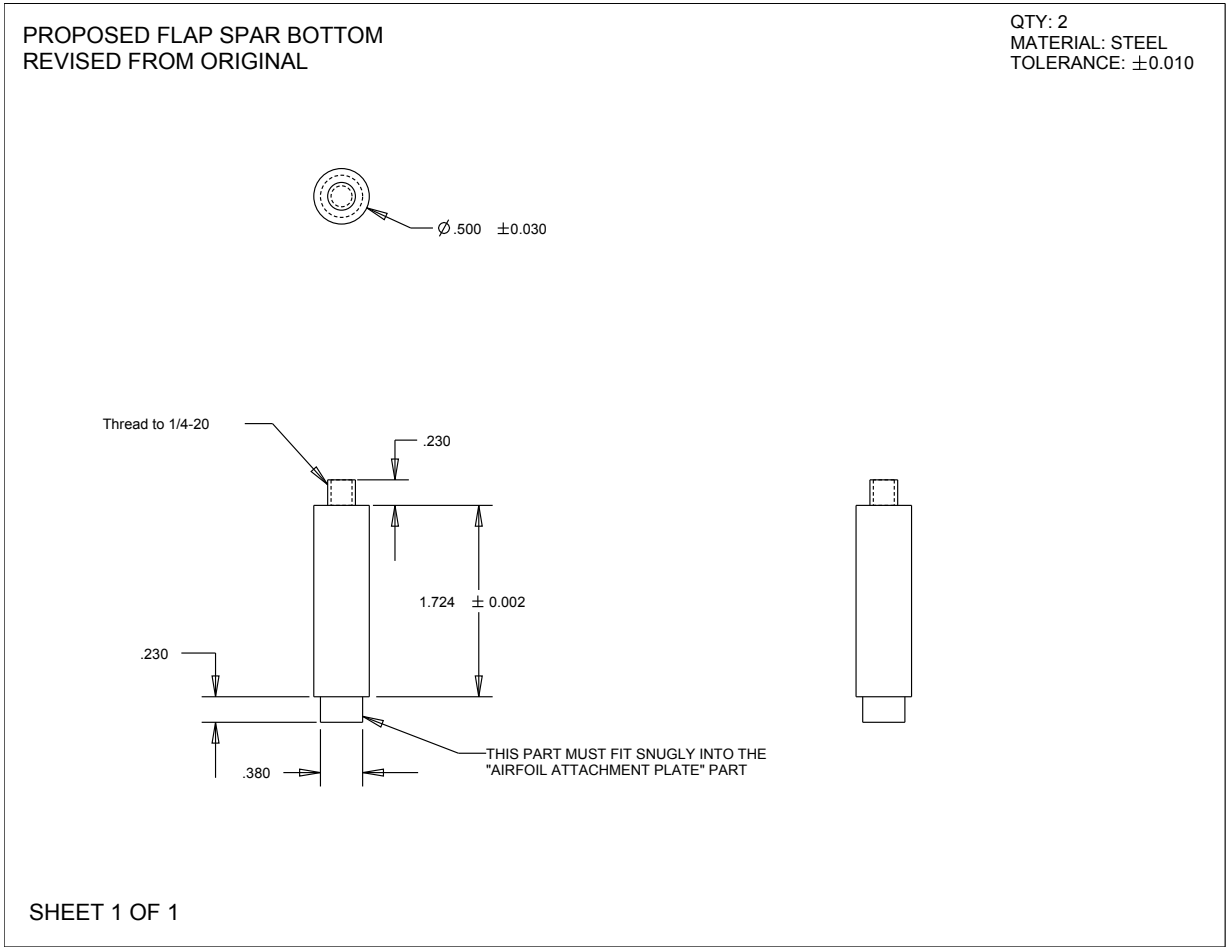

Figure E.22: Two-dimensional CAD drawing of proposed flap lower spar.

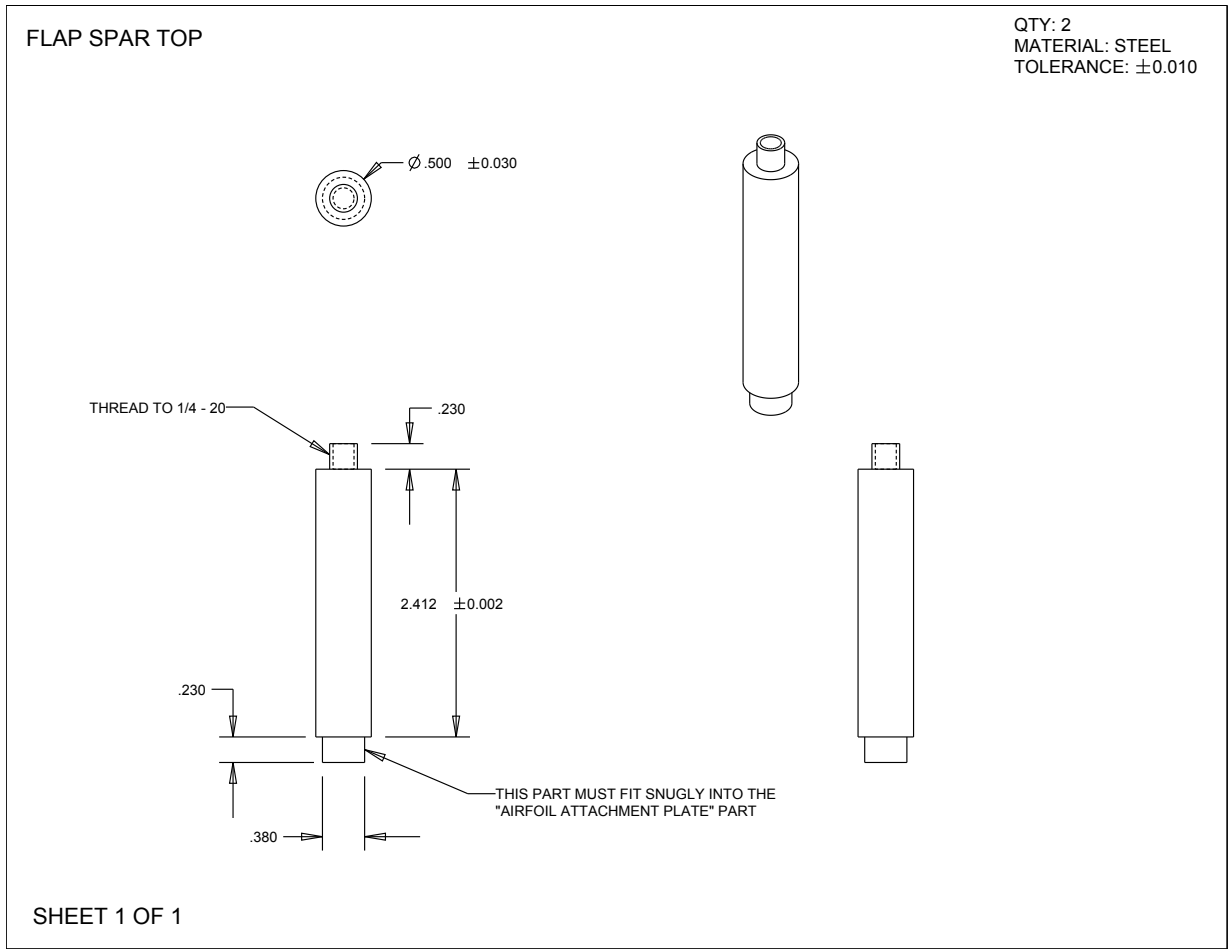

Figure E.23: Two-dimensional CAD drawing of constructed flap upper spar.

SFB CAD

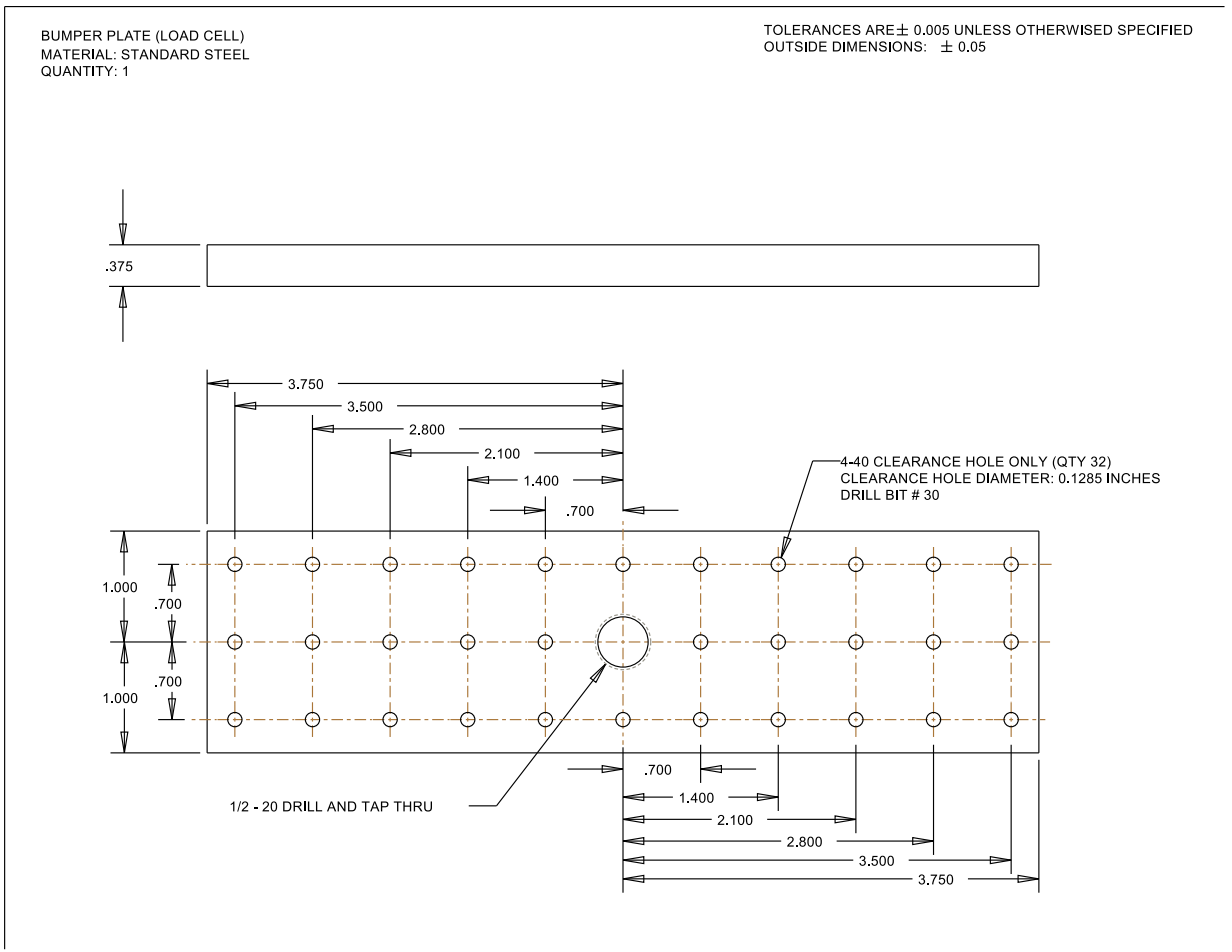

Figure E.24: Two-dimensional CAD drawing of bumper plate (load cell side).

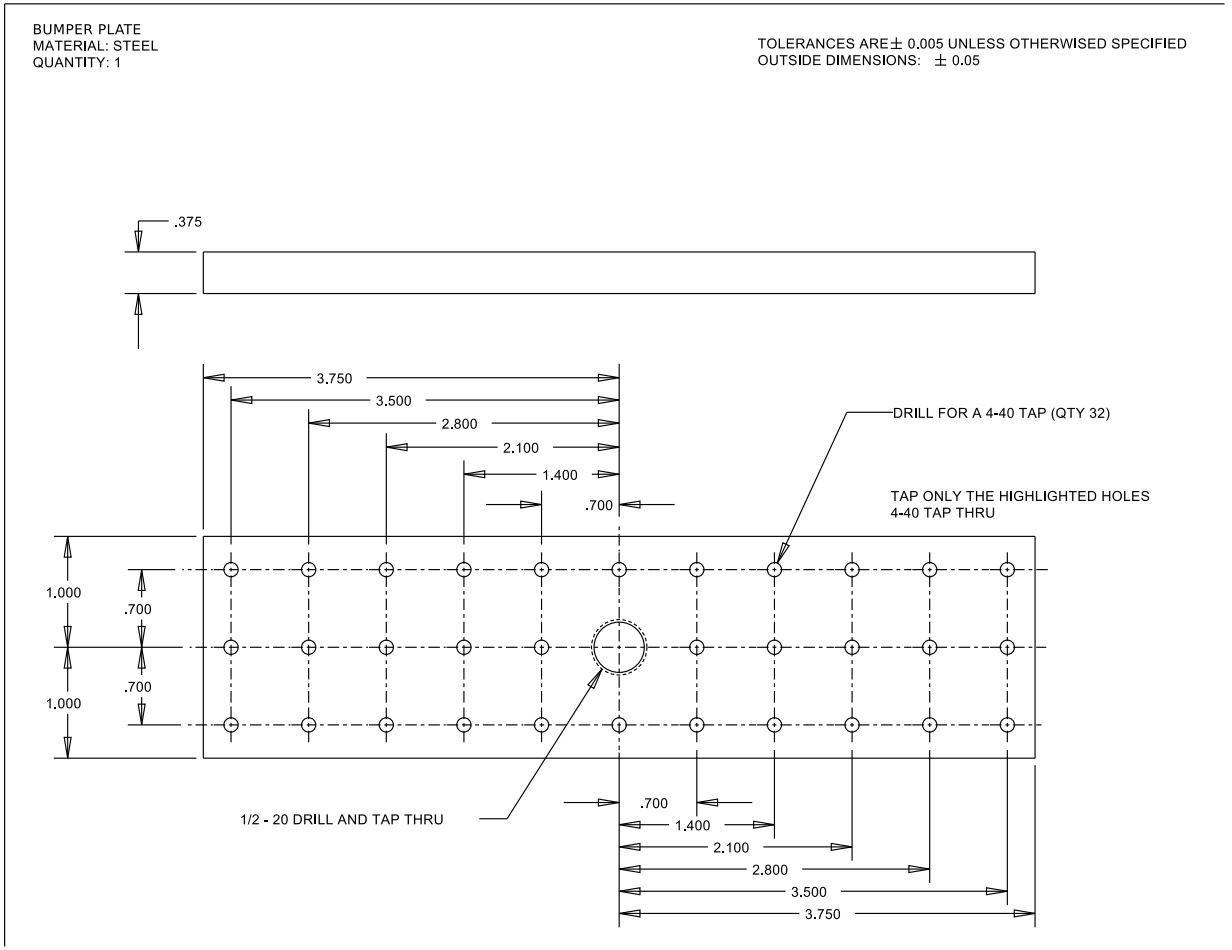

Figure E.25: Two-dimensional CAD drawing of bumper plate.

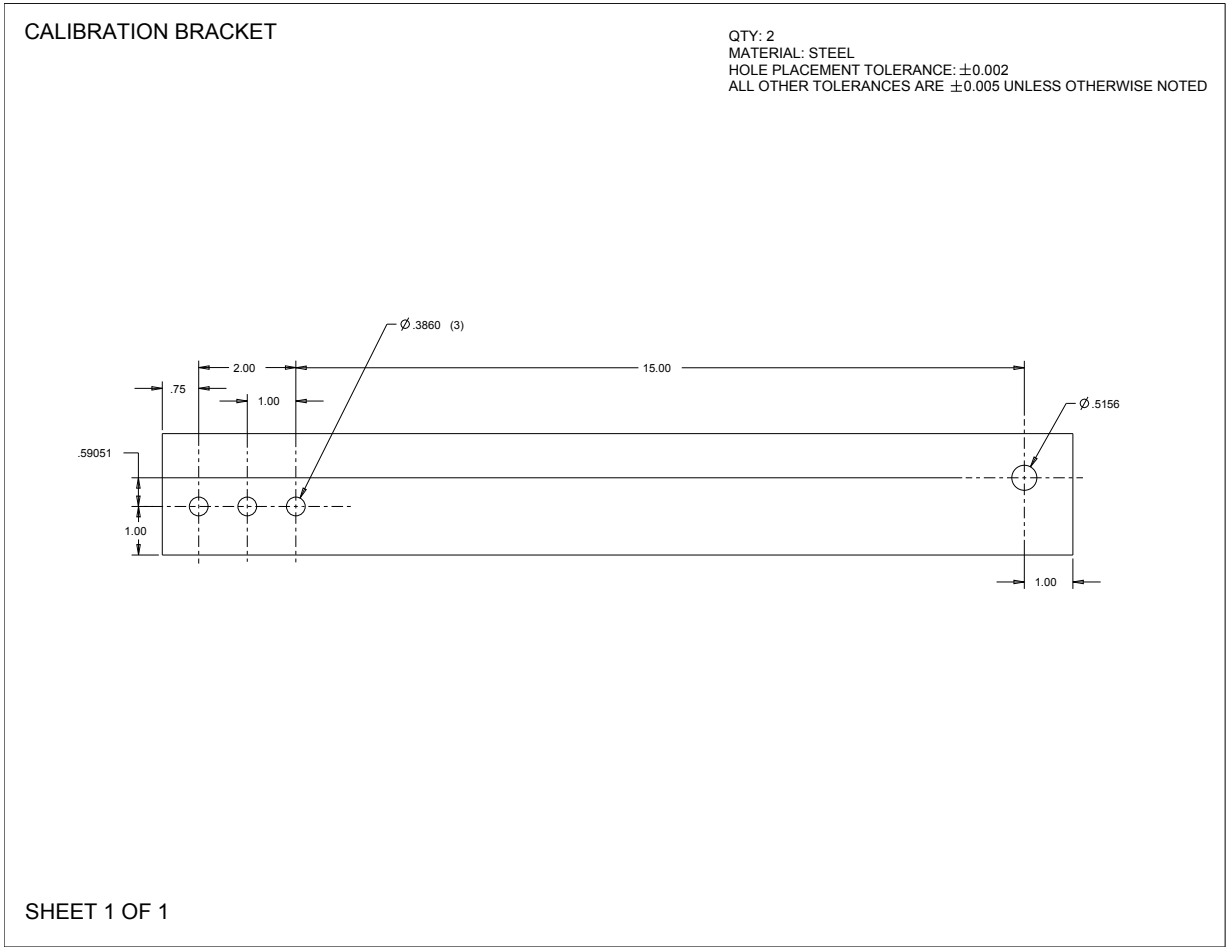

Figure E.26: Two-dimensional CAD drawing of calibration bracket.

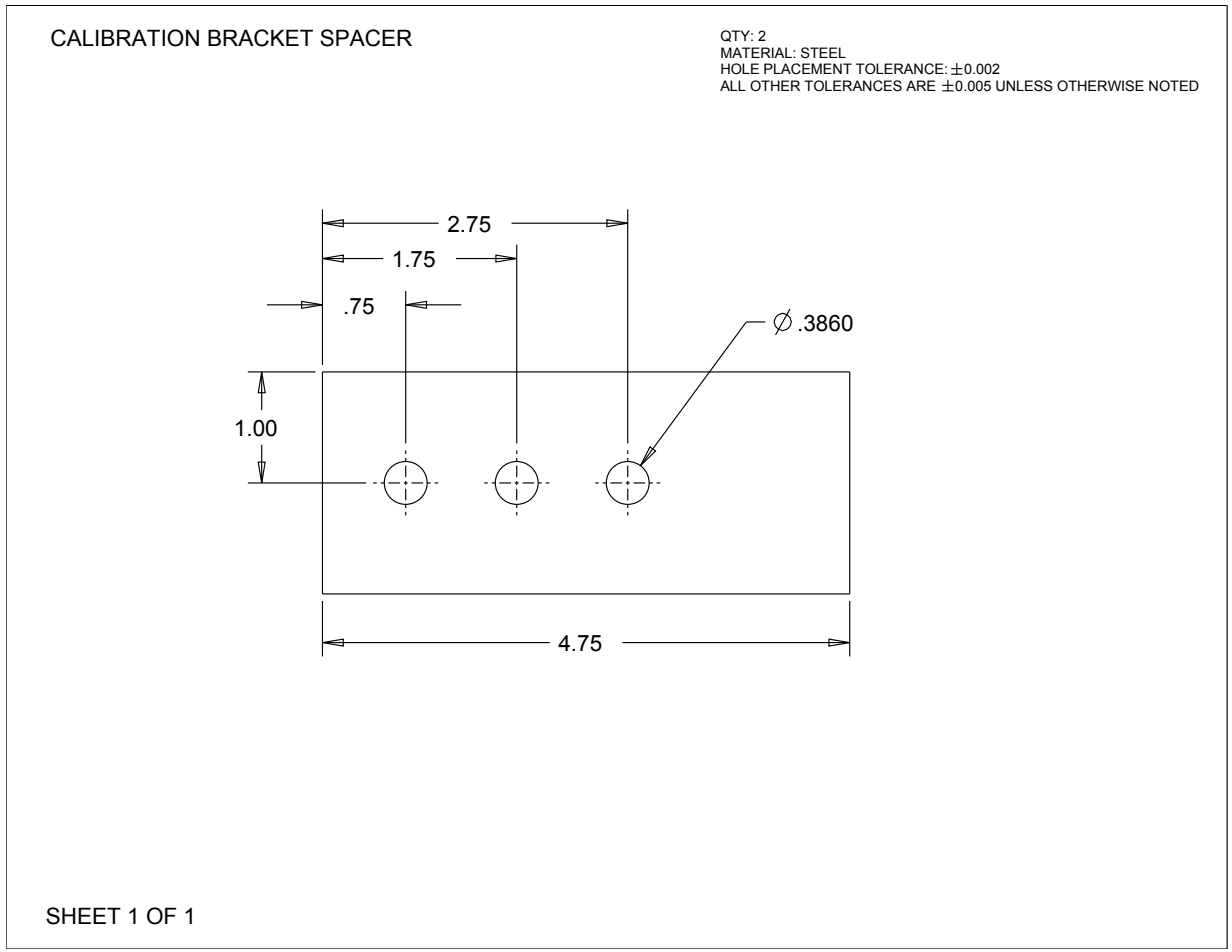

Figure E.27: Two-dimensional CAD drawing of calibration bracket spacer.

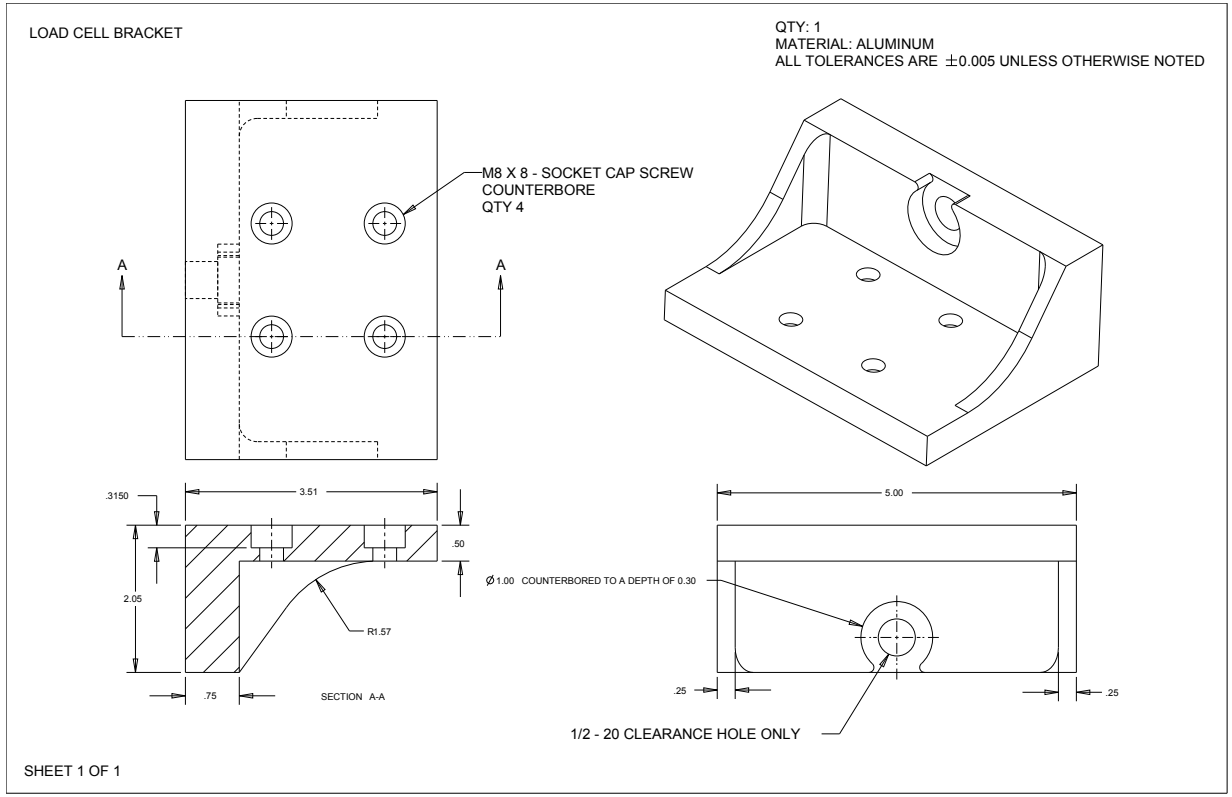

Figure E.28: Two-dimensional CAD drawing of load cell bracket.

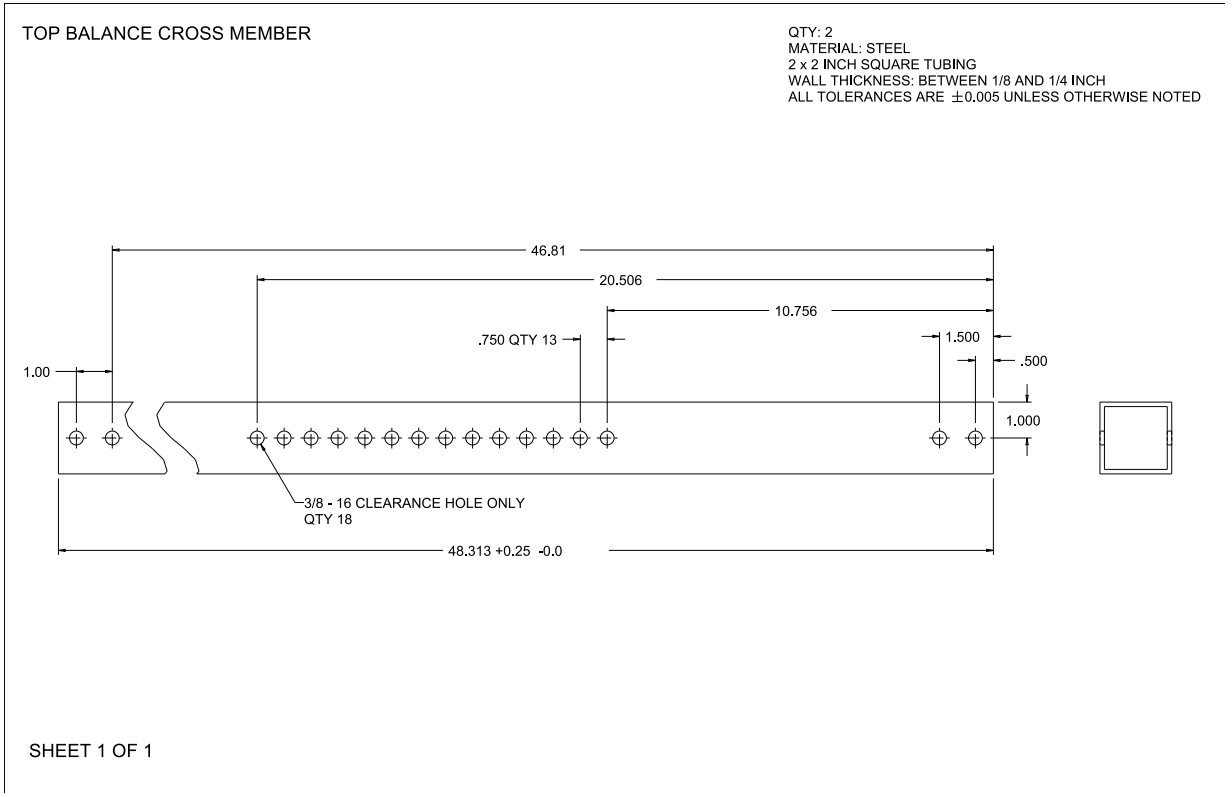

Figure E.29: Two-dimensional CAD drawing of top balance cross member.

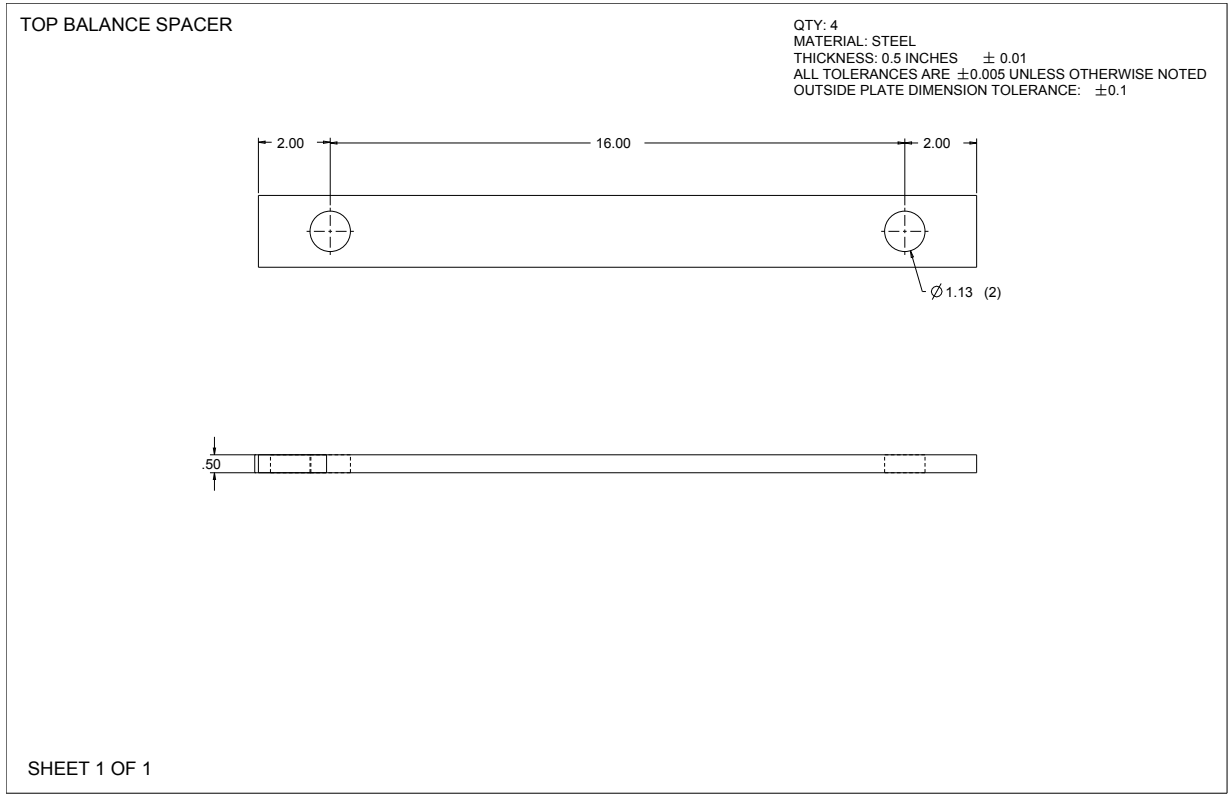

Figure E.30: Two-dimensional CAD drawing of top balance spacer.

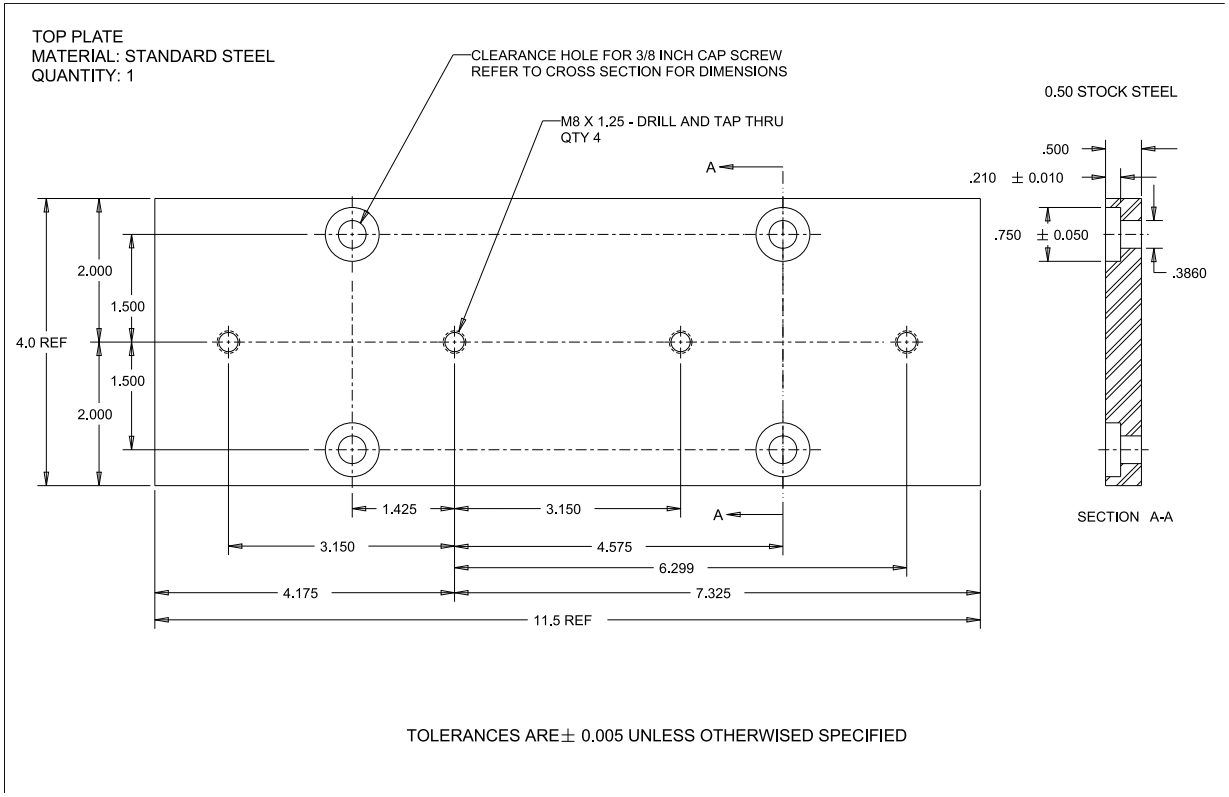

Figure E.31: Two-dimensional CAD drawing of top plate.

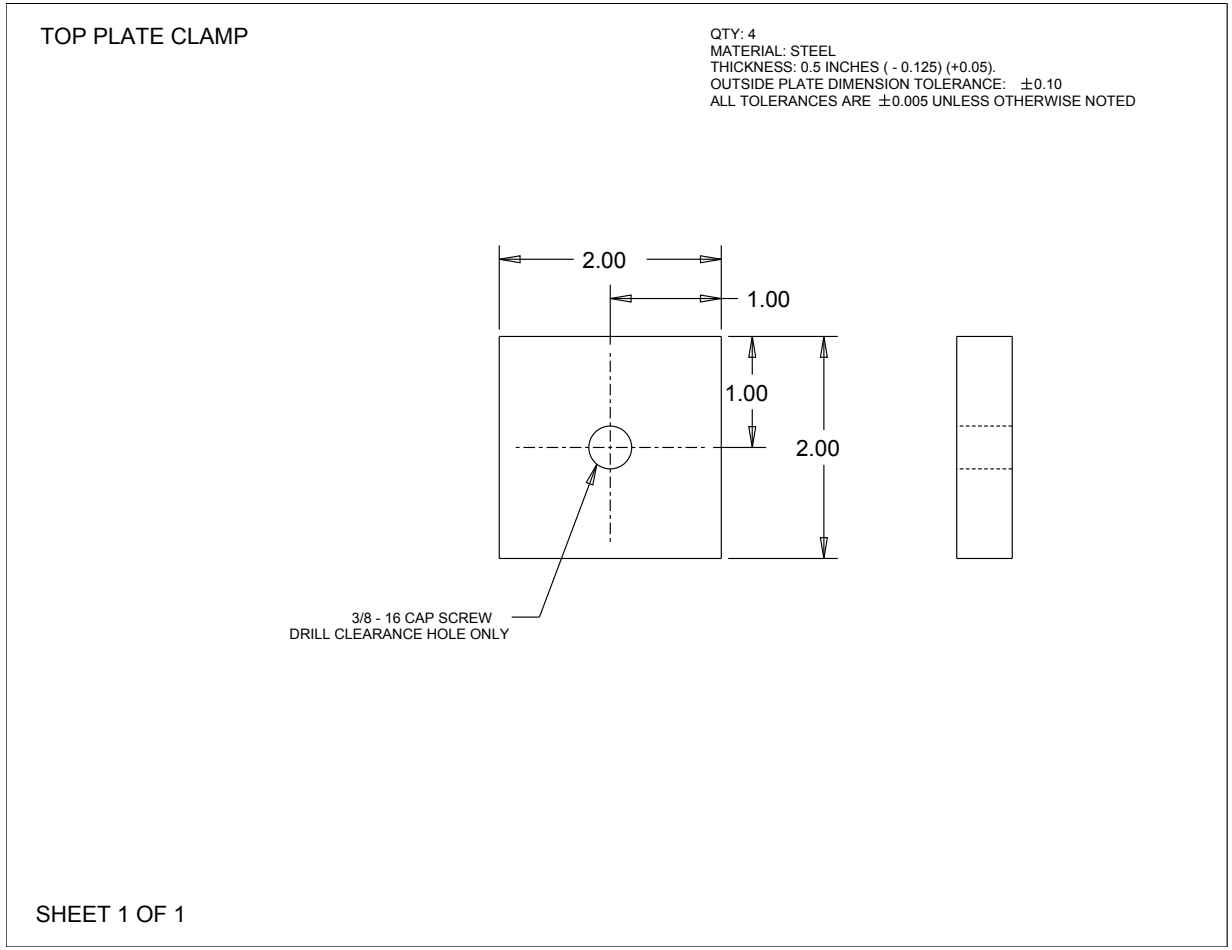

Figure E.32: Two-dimensional CAD drawing of top plate clamps.

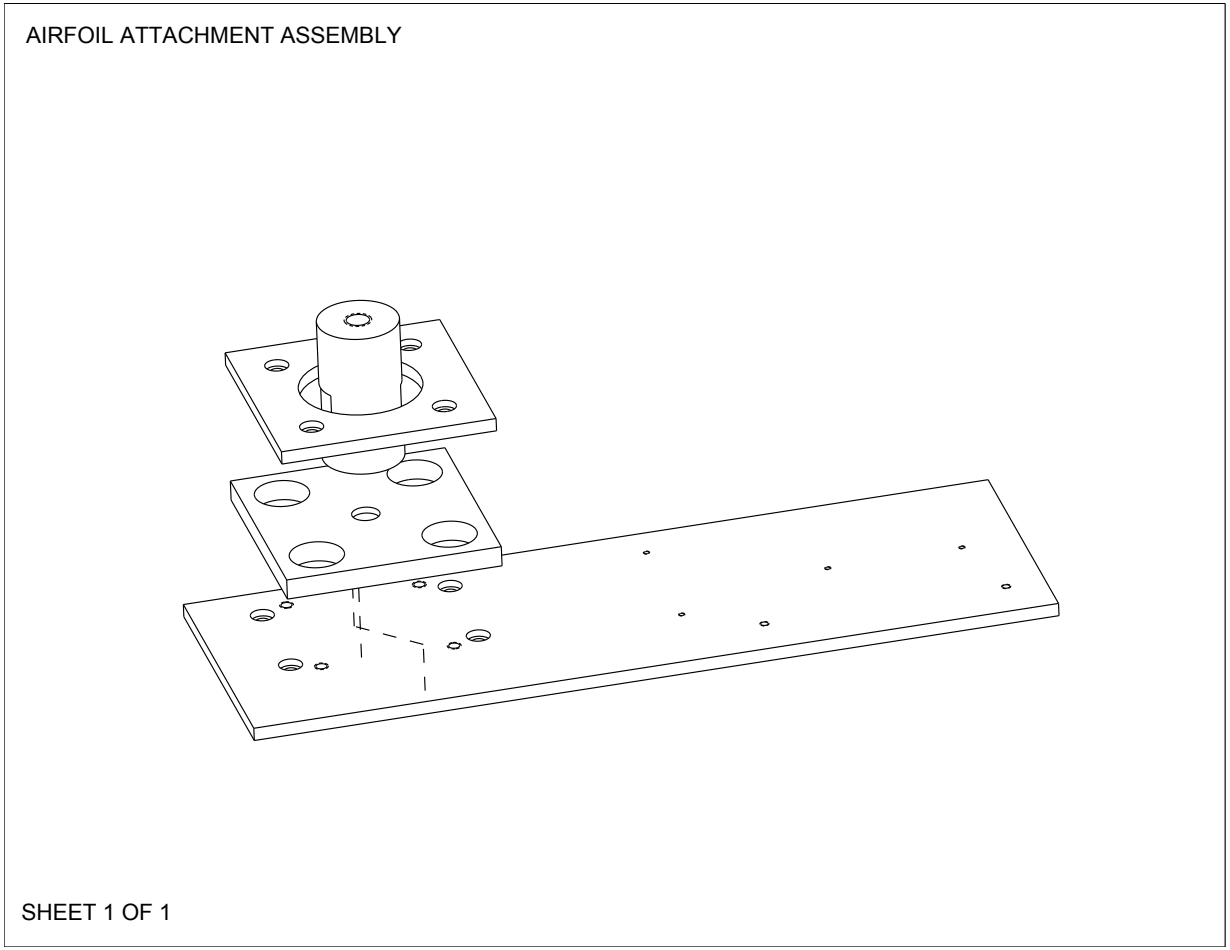

Figure E.33: Two-dimensional CAD drawing of MFF-089 airfoil SFB attachment assembly.

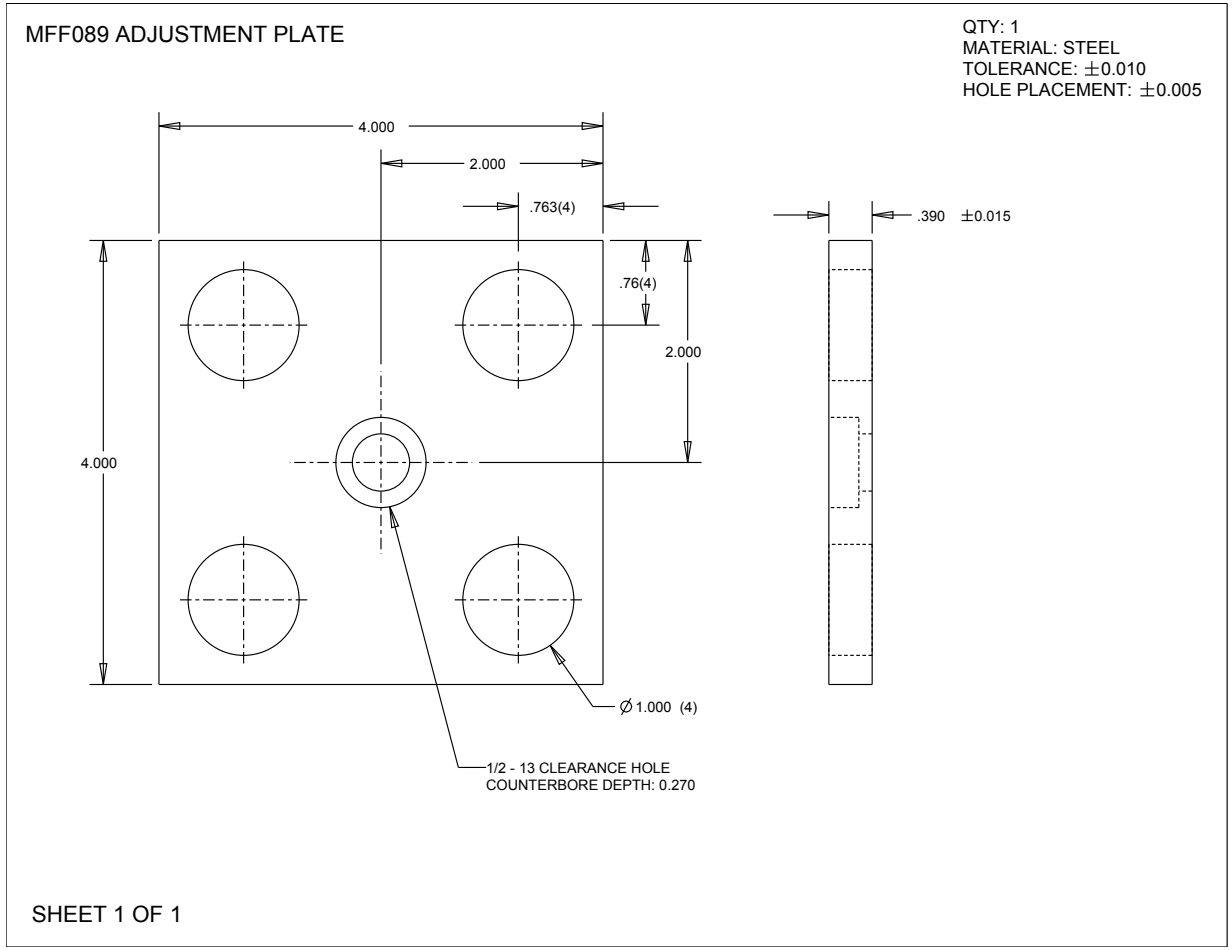

Figure E.34: Two-dimensional CAD drawing of MFF-089 attachment adjustment plate.

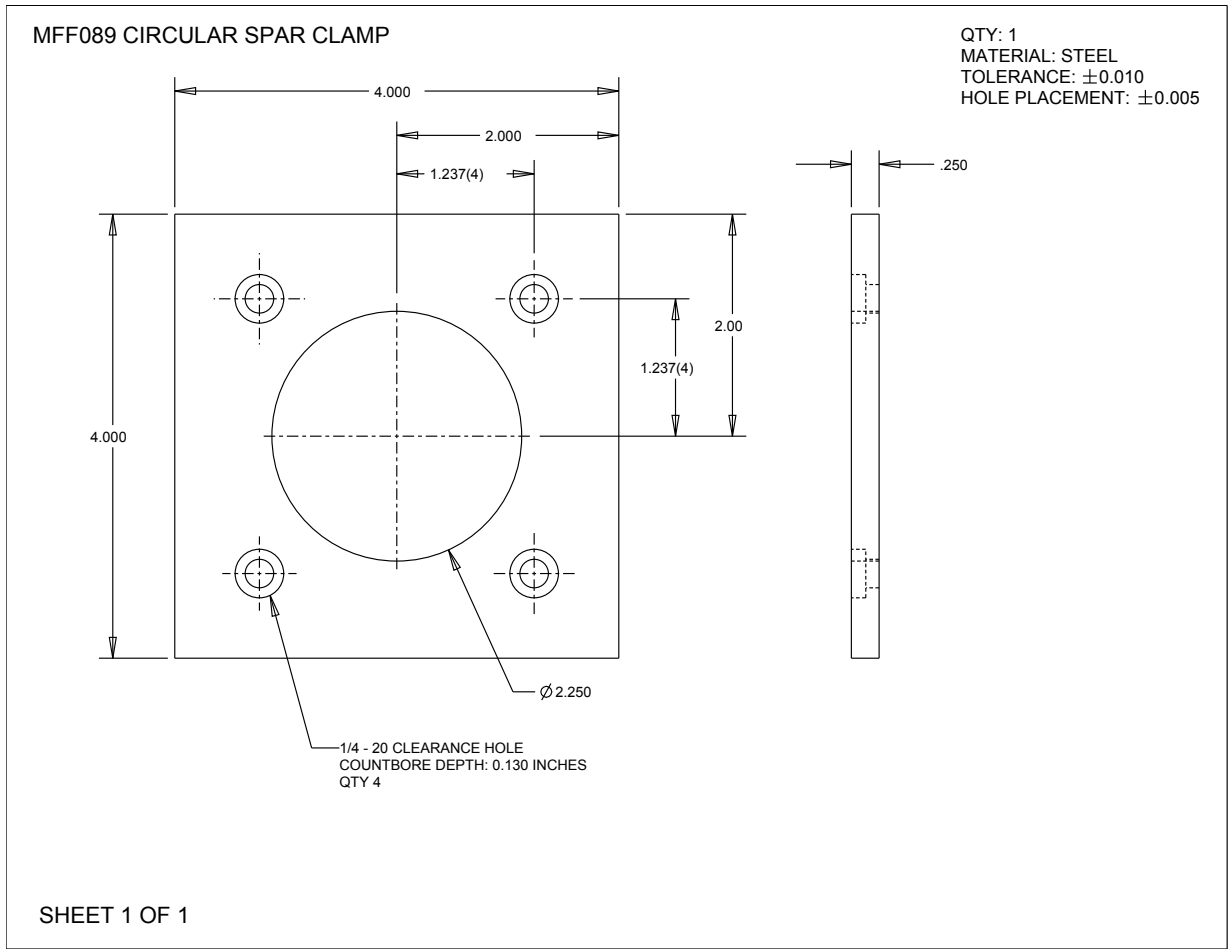

Figure E.35: Two-dimensional CAD drawing of MFF-089 circular spar clamp.

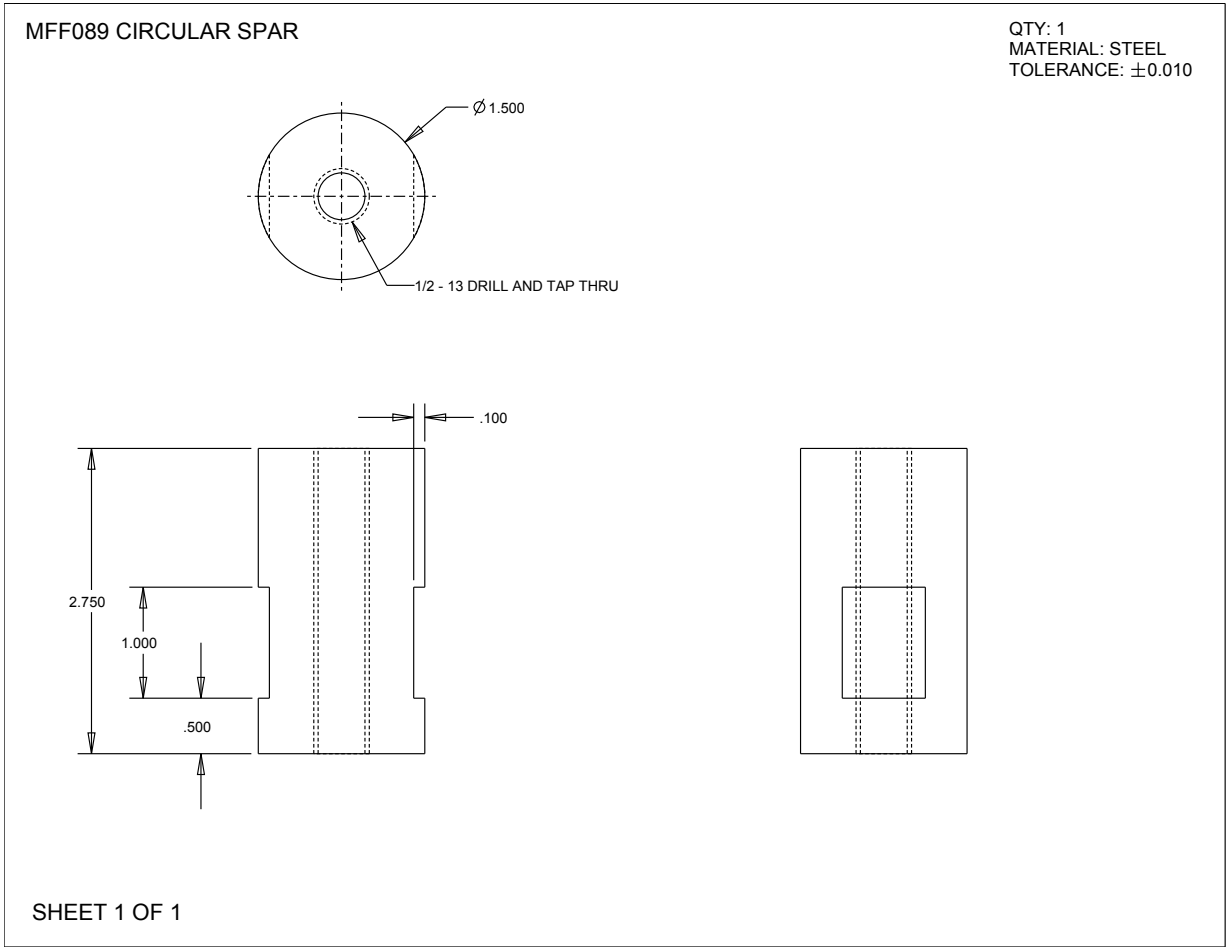

Figure E.36: Two-dimensional CAD drawing of MFF-089 circular spar.

MFF-089 Model CAD

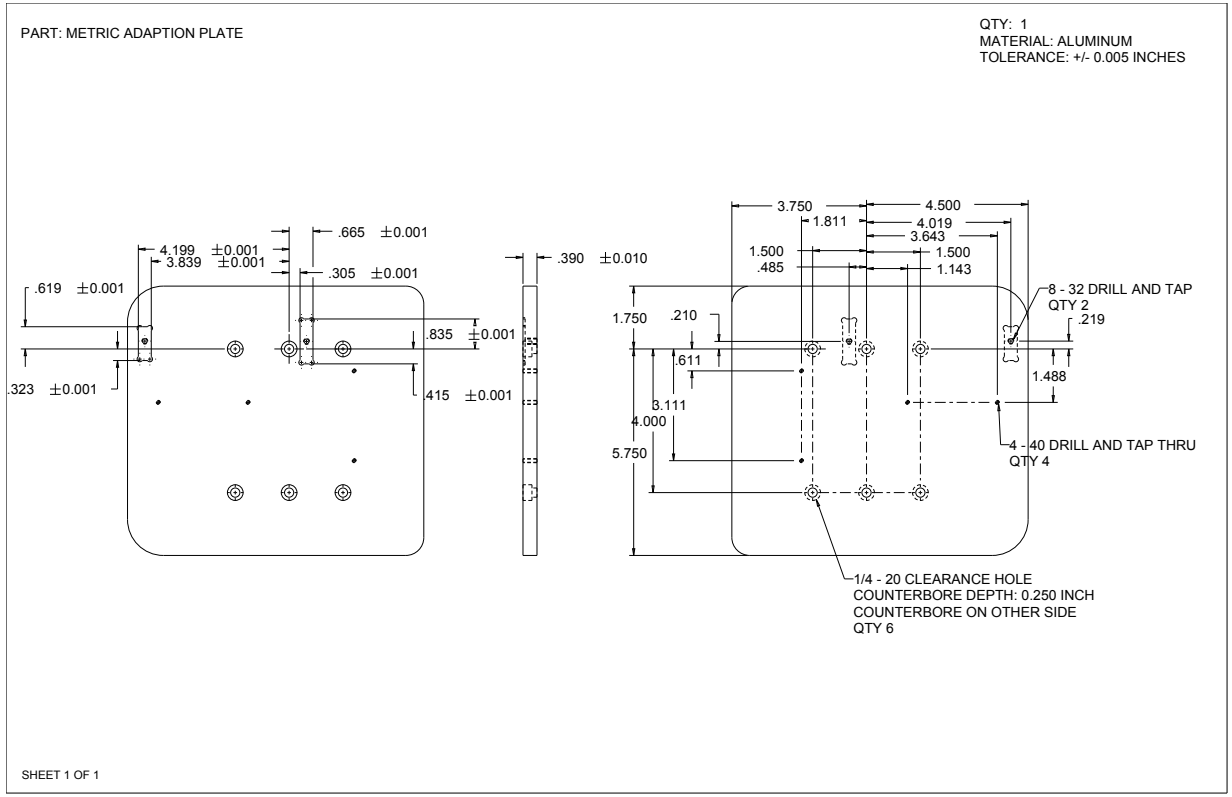

Figure E.37: Two-dimensional CAD drawing of metric adaption plate for closely coupled model.

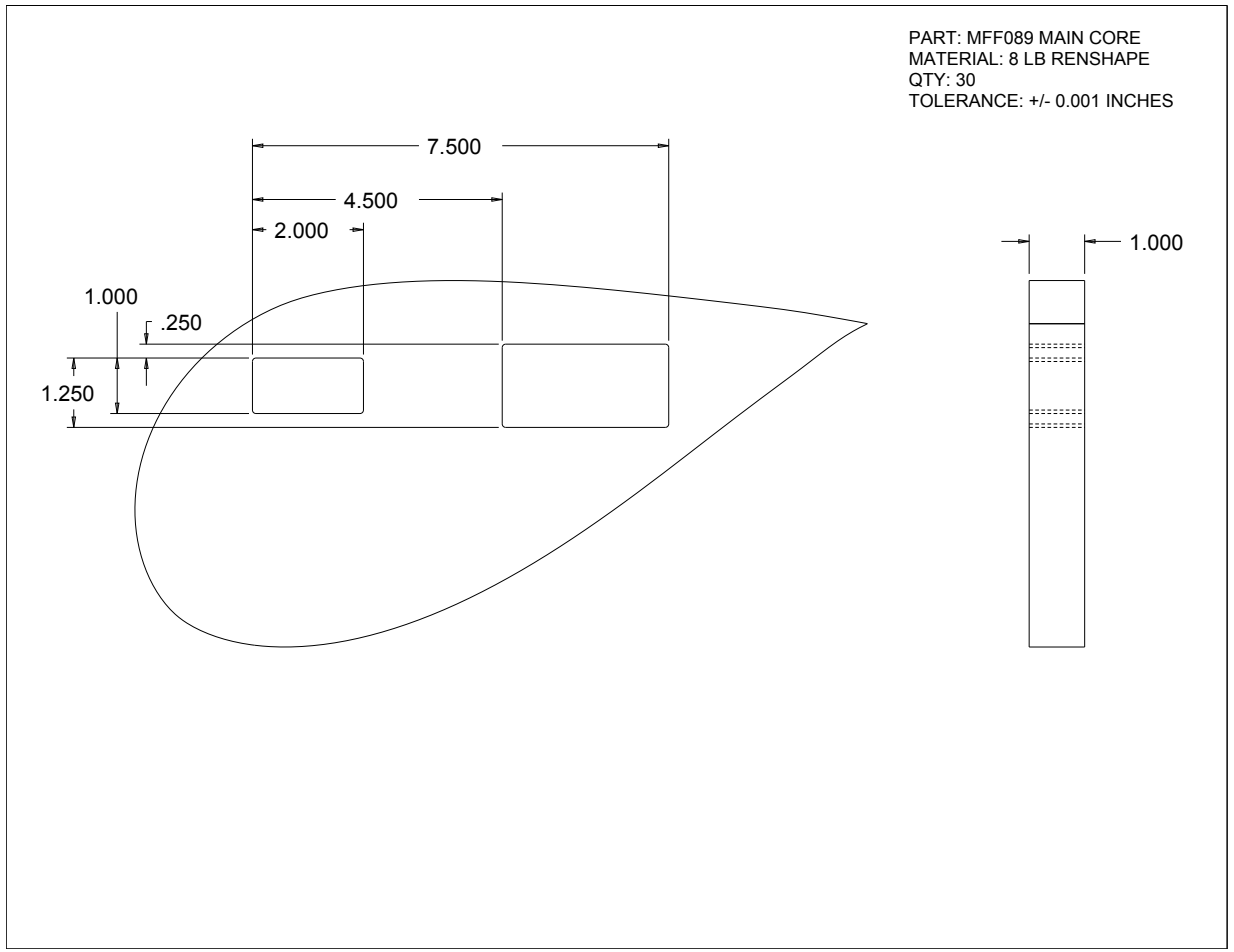

Figure E.38: Two-dimensional CAD drawing of main element foam core for closely coupled model.

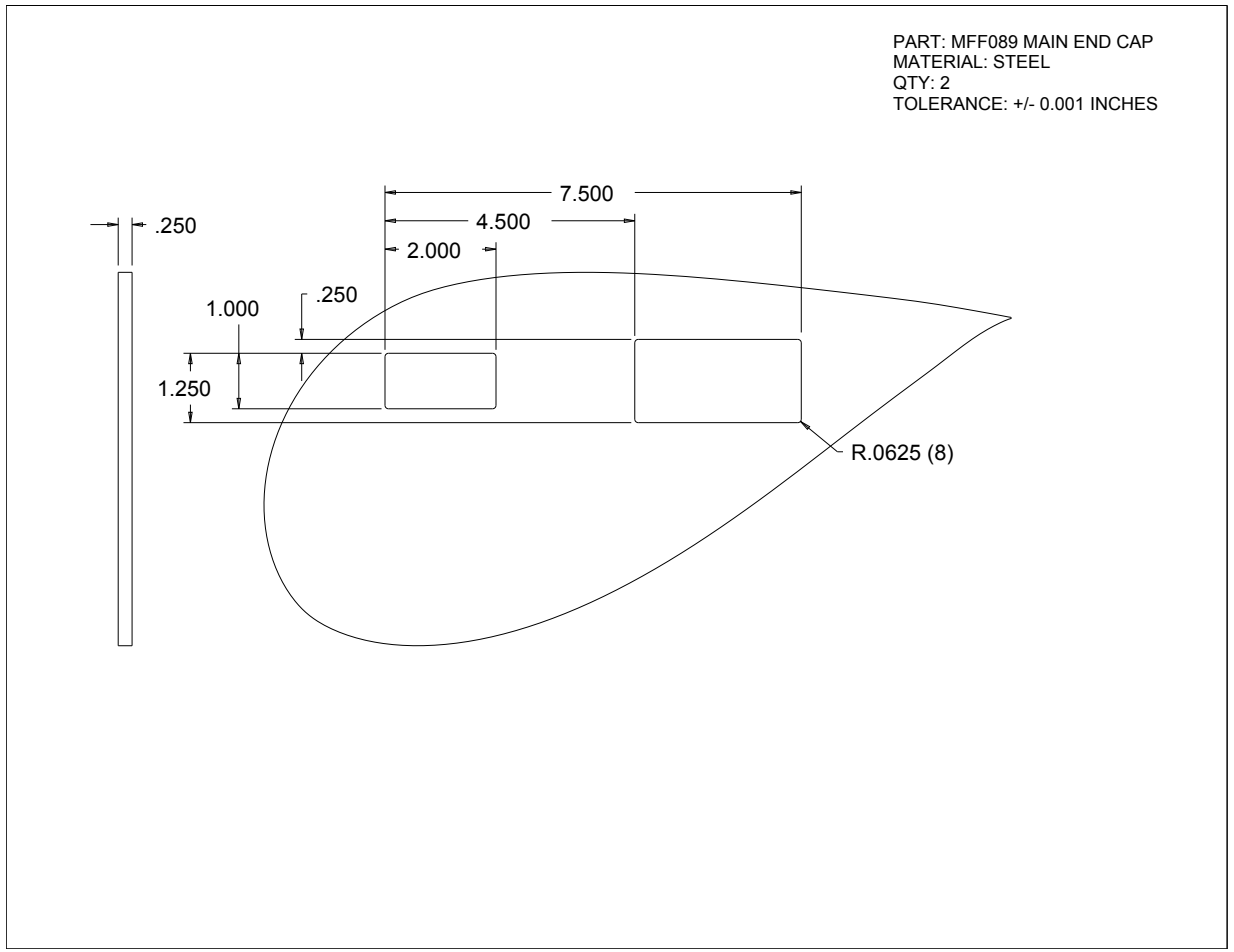

Figure E.39: Two-dimensional CAD drawing of main element end plate for closely coupled model.

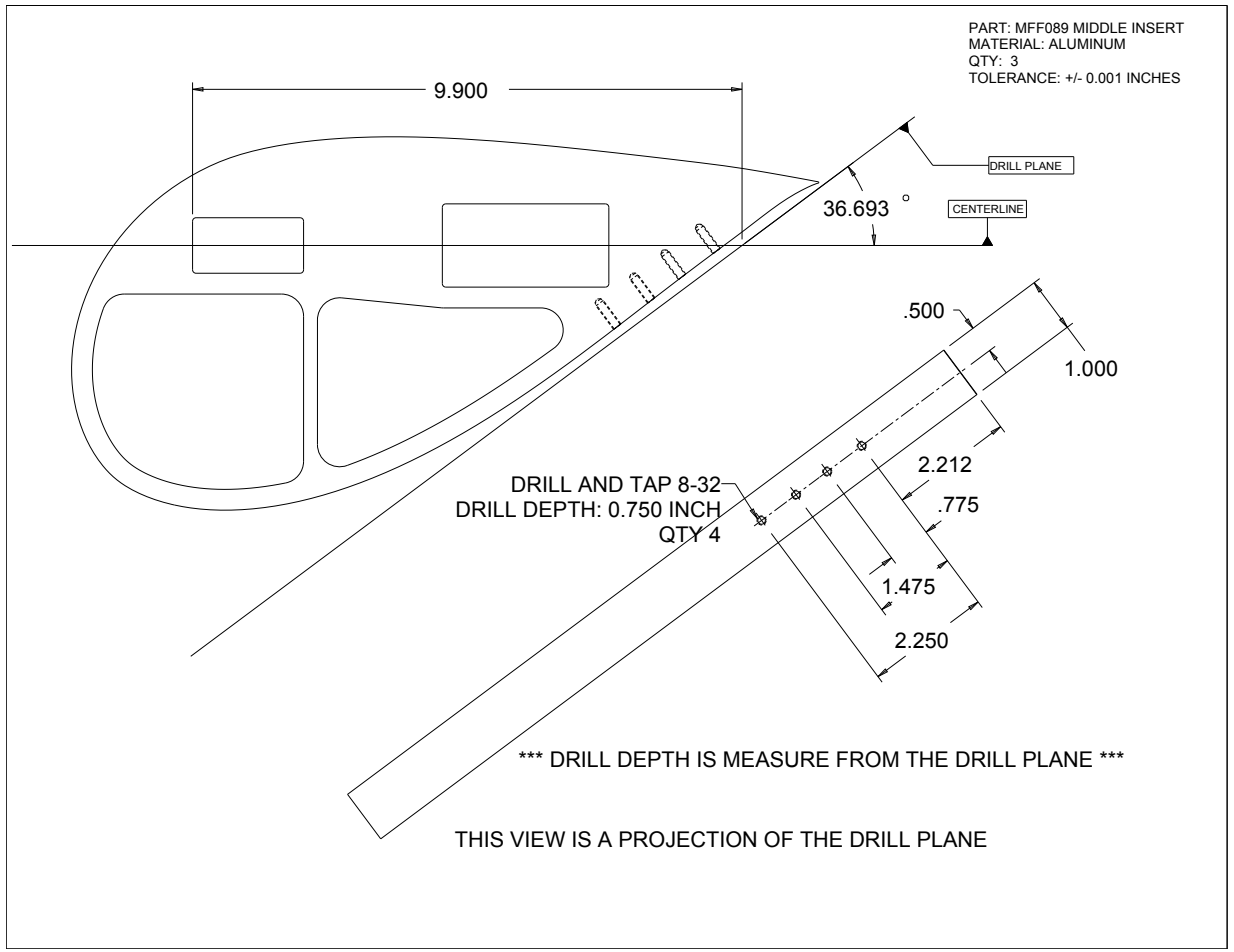

Figure E.40: Two-dimensional CAD drawing of main element insert for closely coupled model.

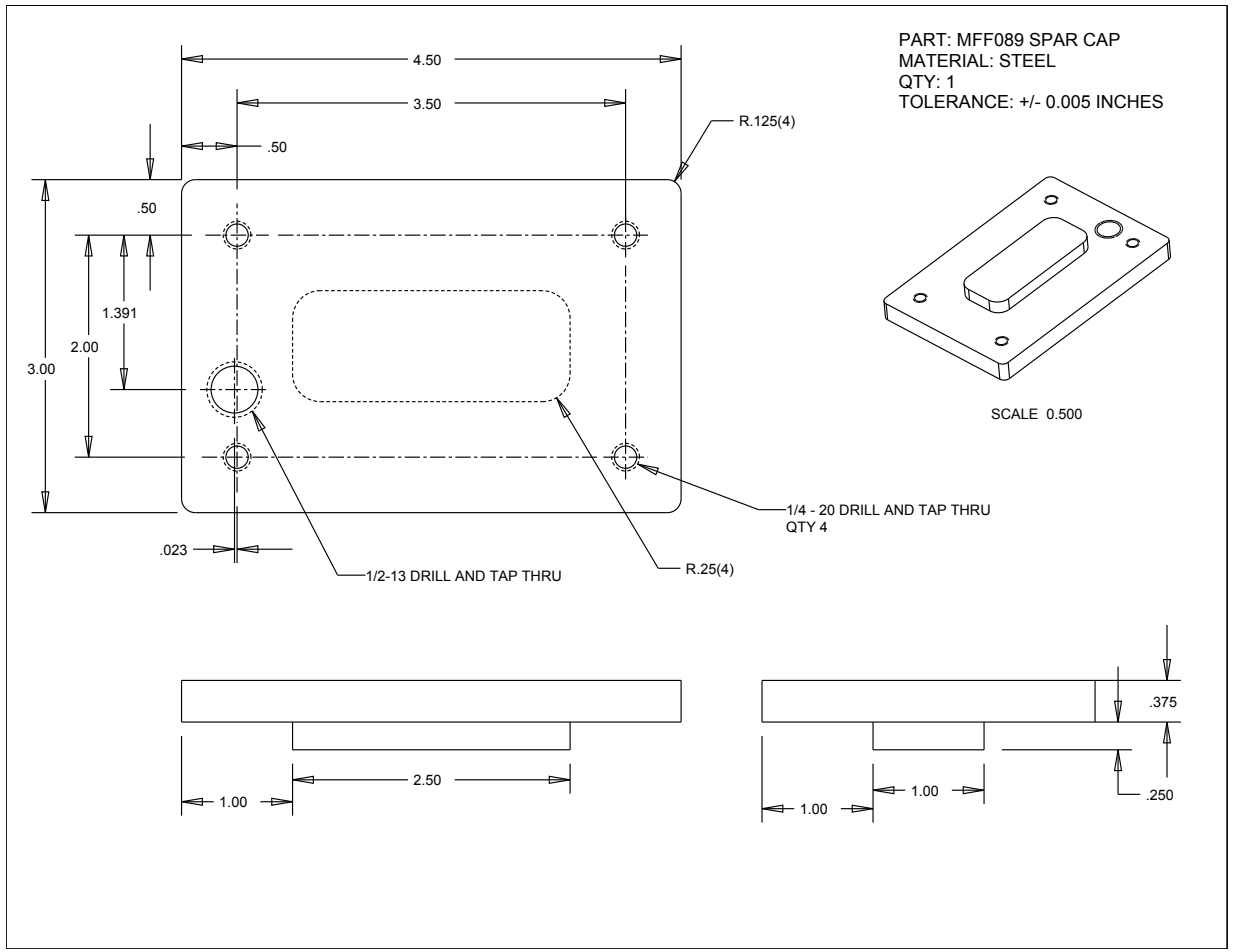

Figure E.41: Two-dimensional CAD drawing of main element spar cap for closely coupled model.

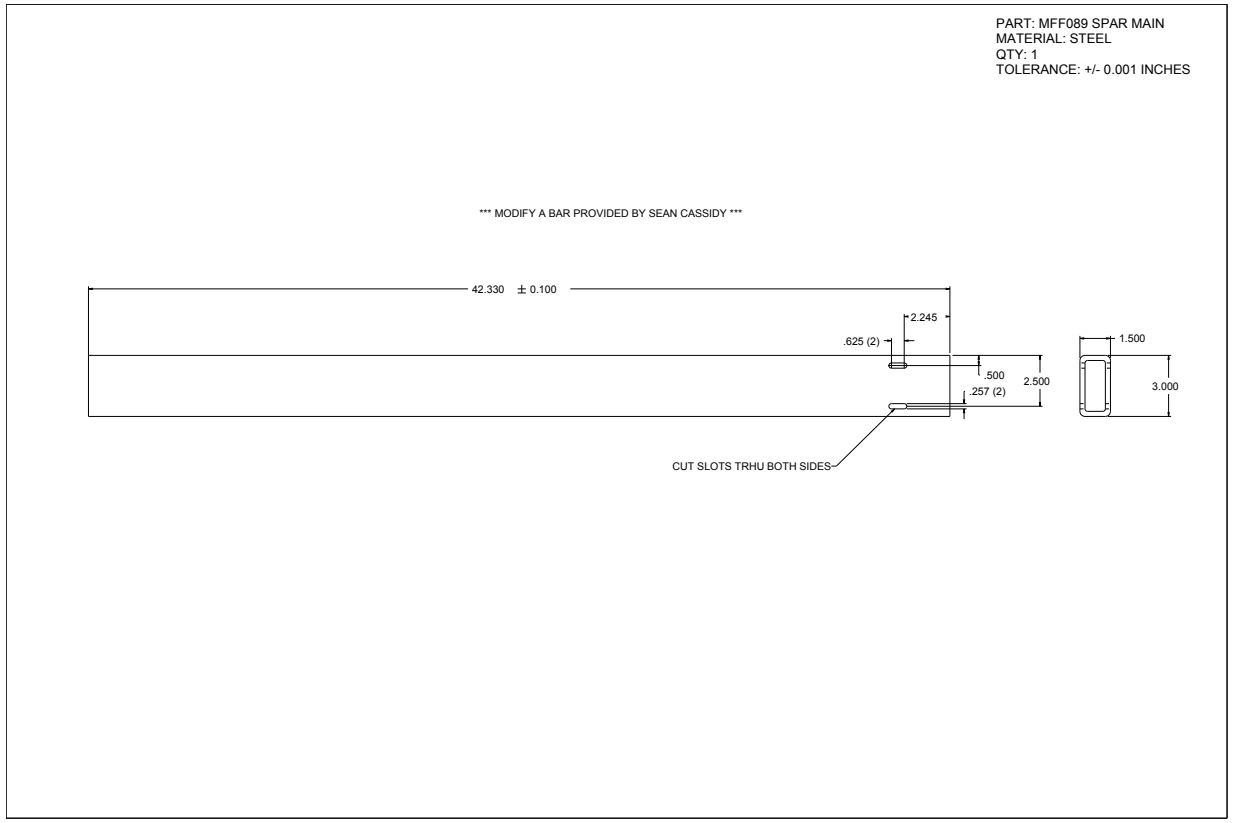

Figure E.42: Two-dimensional CAD drawing of main element spar for closely coupled model.

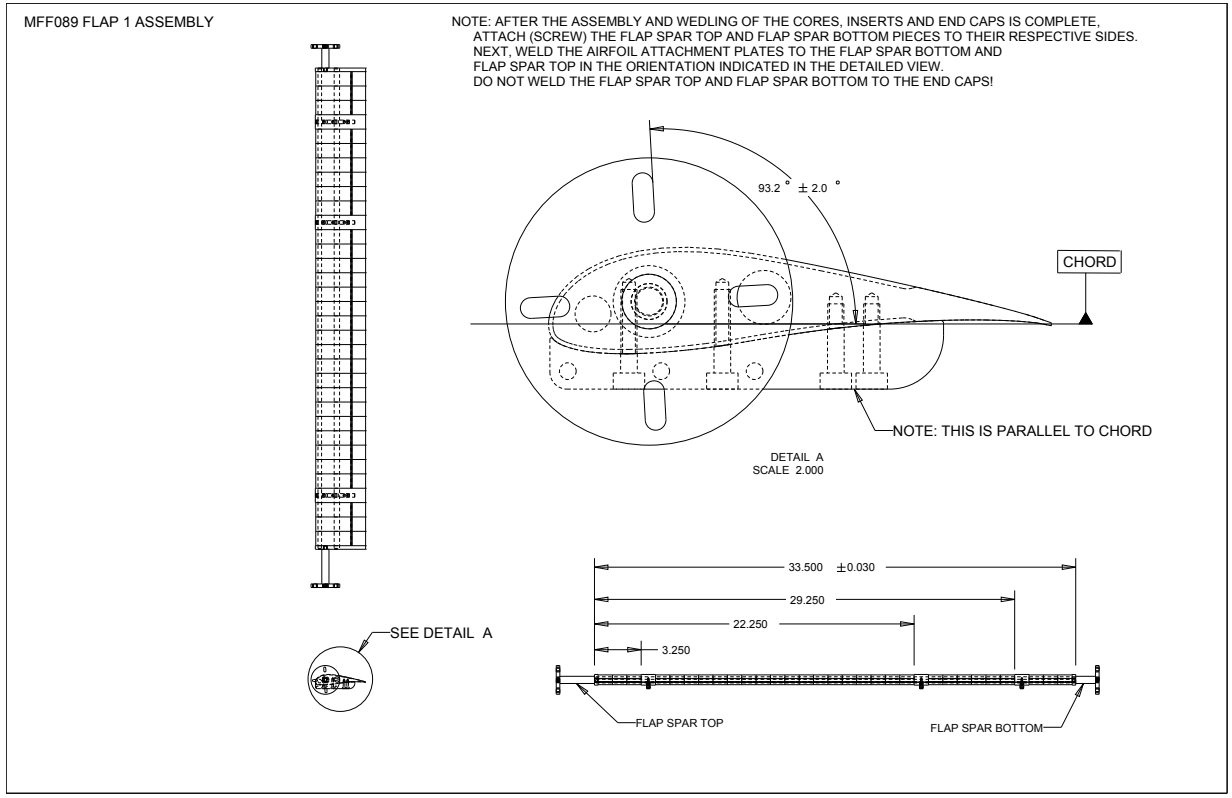

Figure E.43: Two-dimensional CAD drawing of flap 1 assembly.

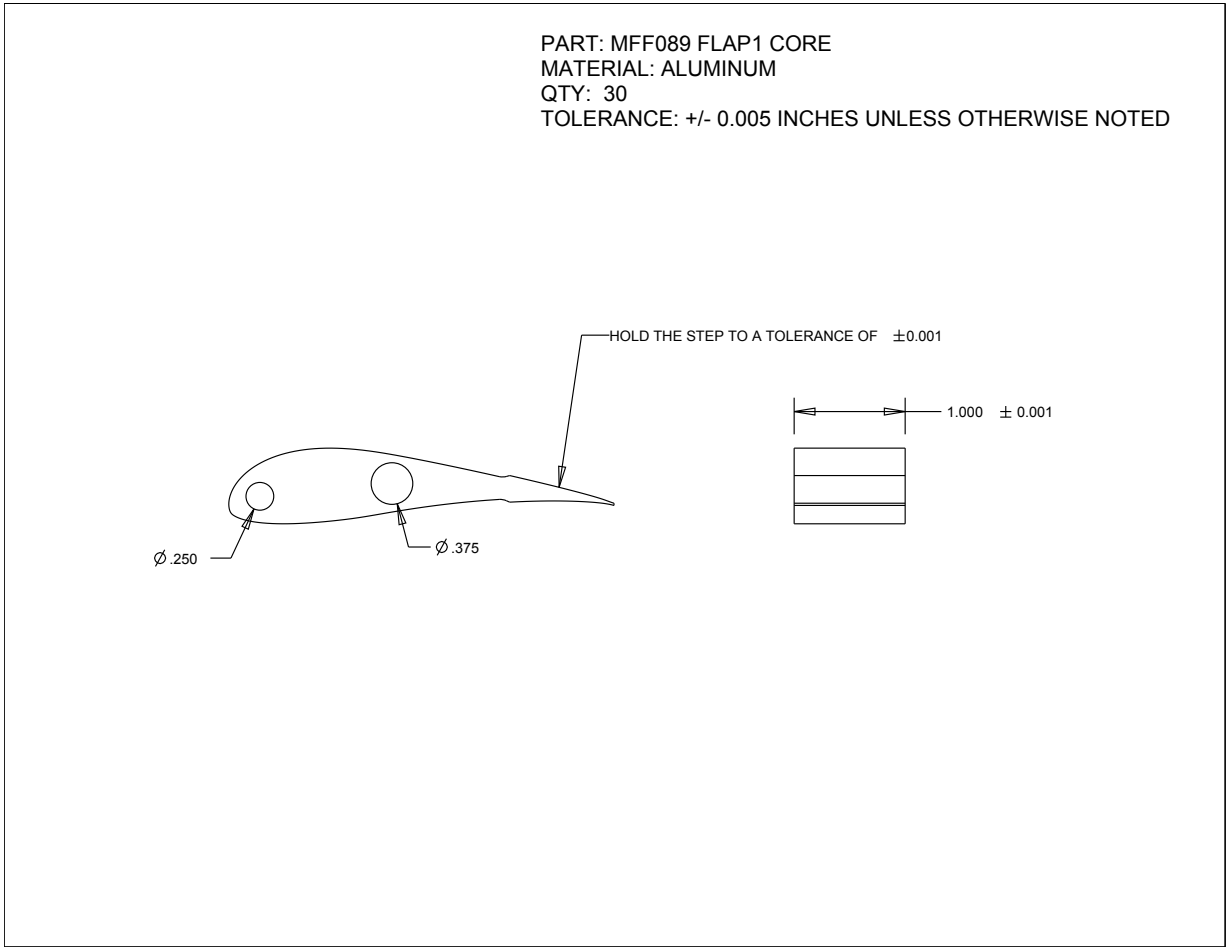

Figure E.44: Two-dimensional CAD drawing of flap 1 foam core.

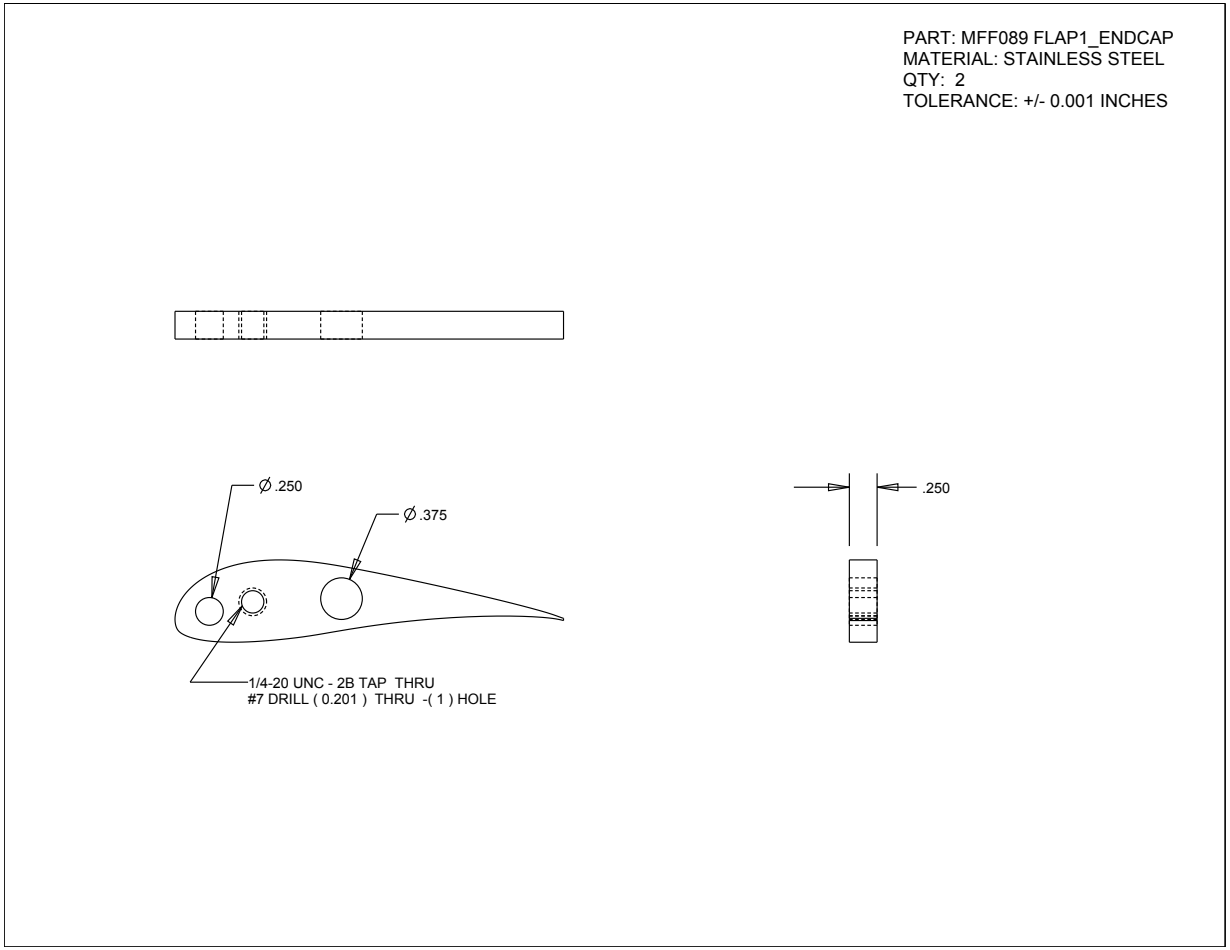

Figure E.45: Two-dimensional CAD drawing of flap 1 endcap.

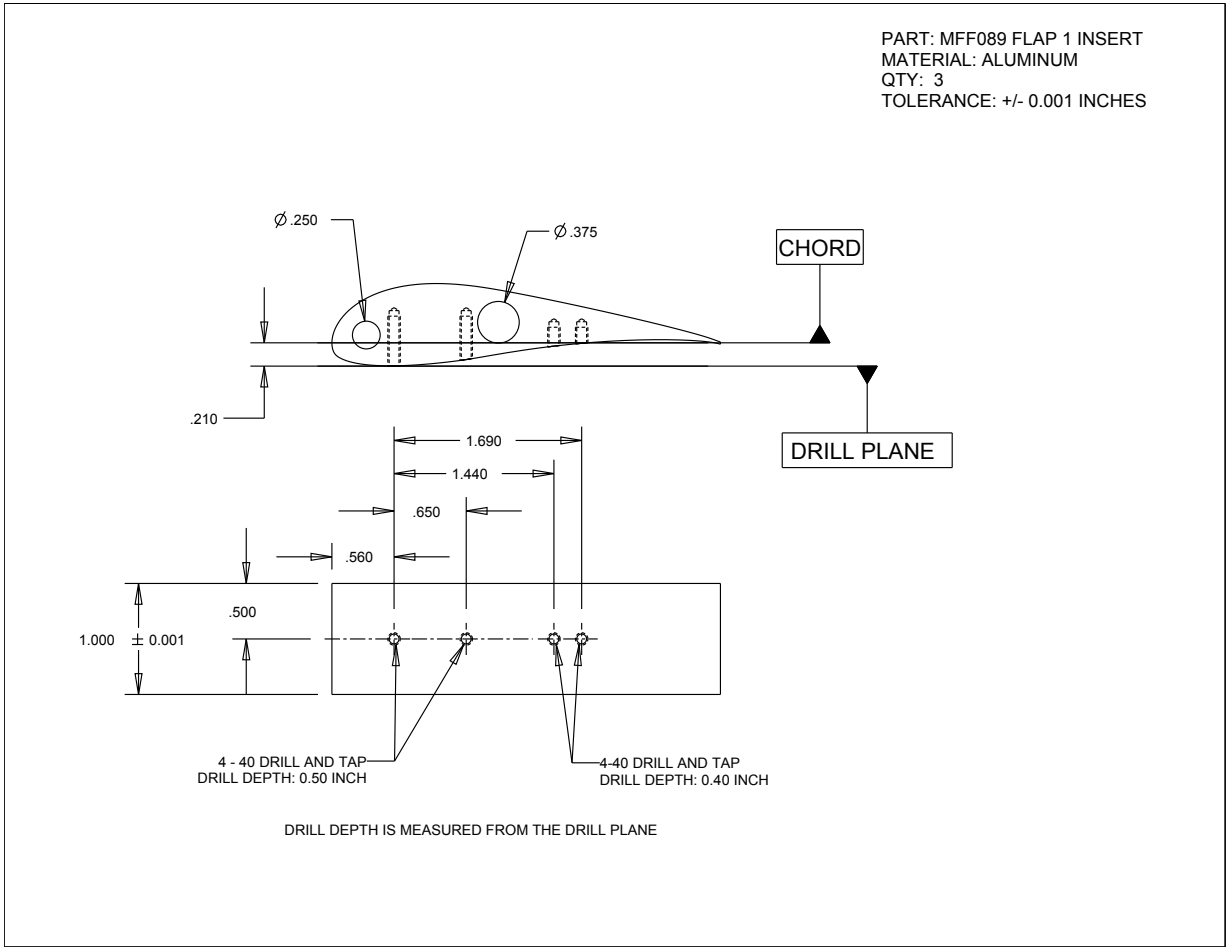

Figure E.46: Two-dimensional CAD drawing of flap 1 insert.

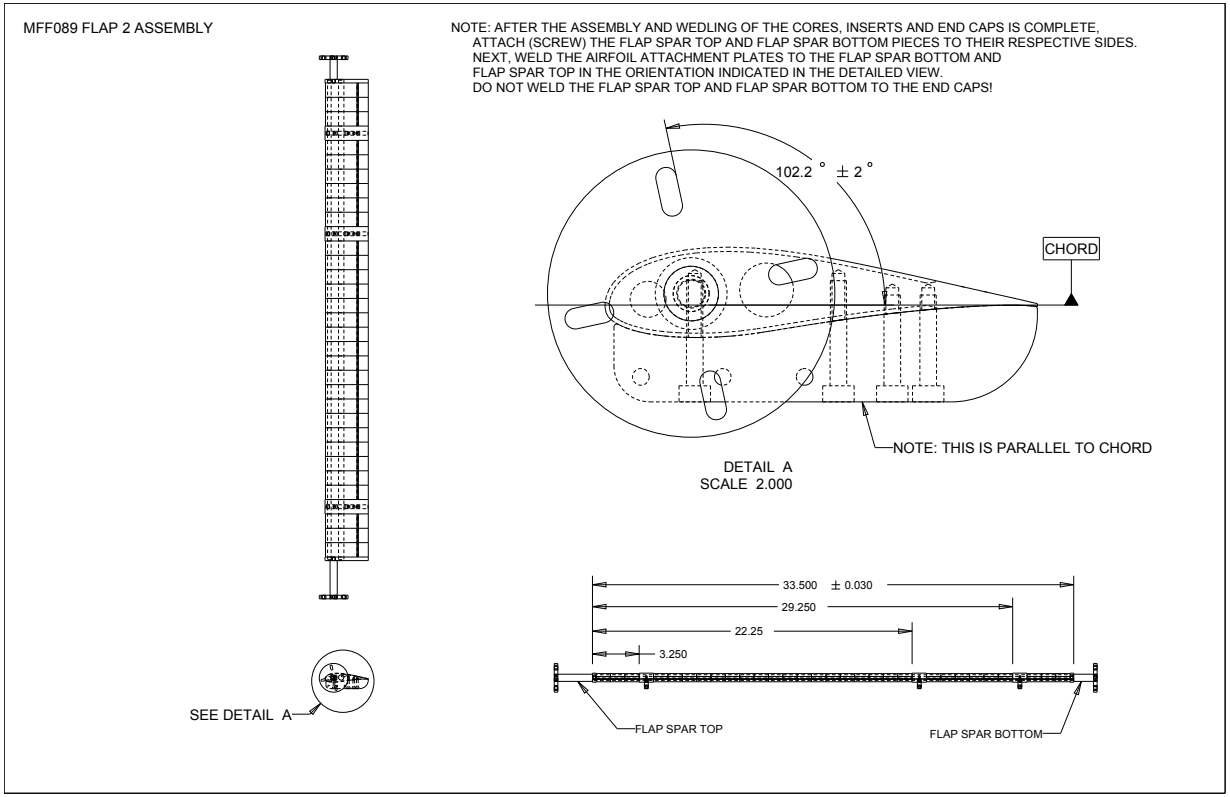

Figure E.47: Two-dimensional CAD drawing of flap 2 assembly.

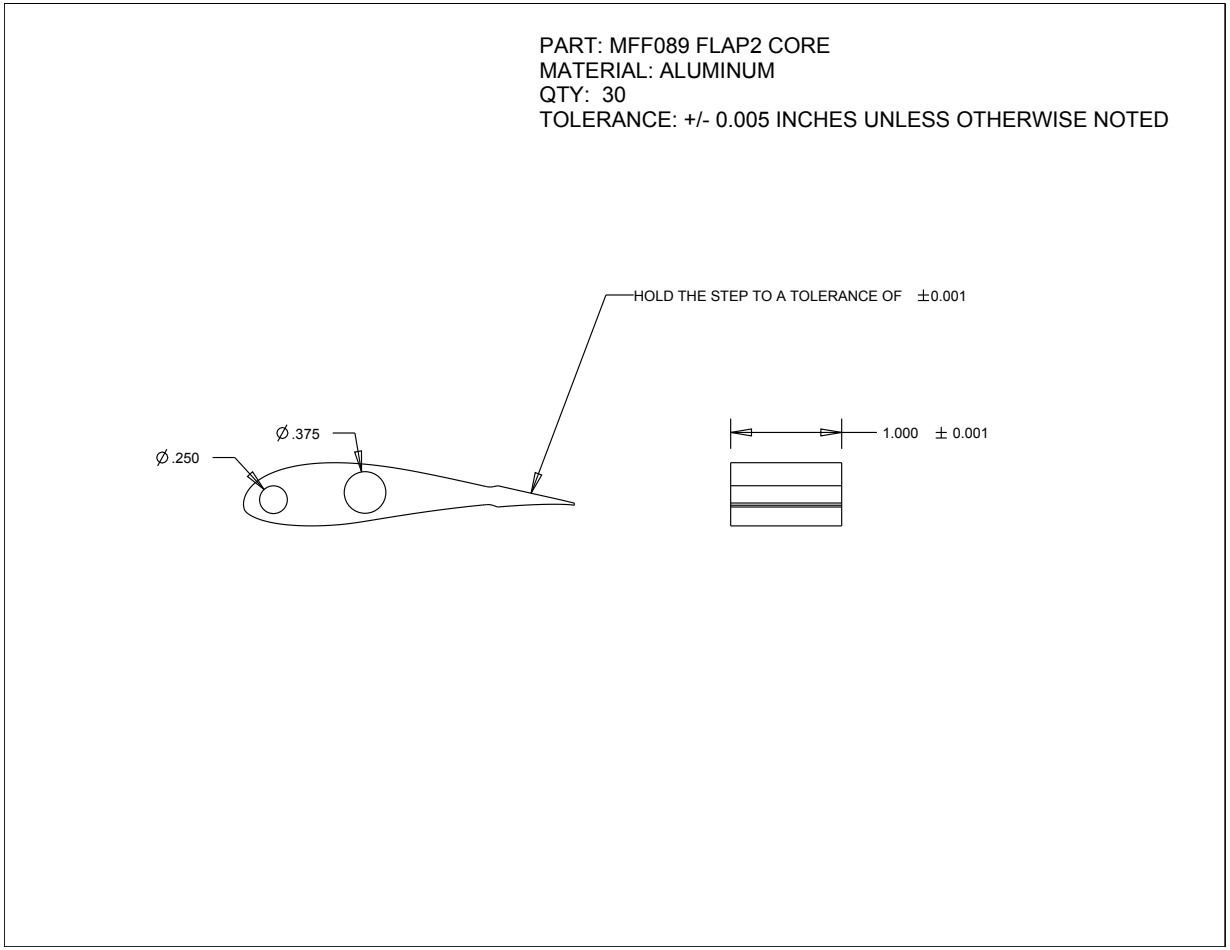

Figure E.48: Two-dimensional CAD drawing of flap 2 foam core.

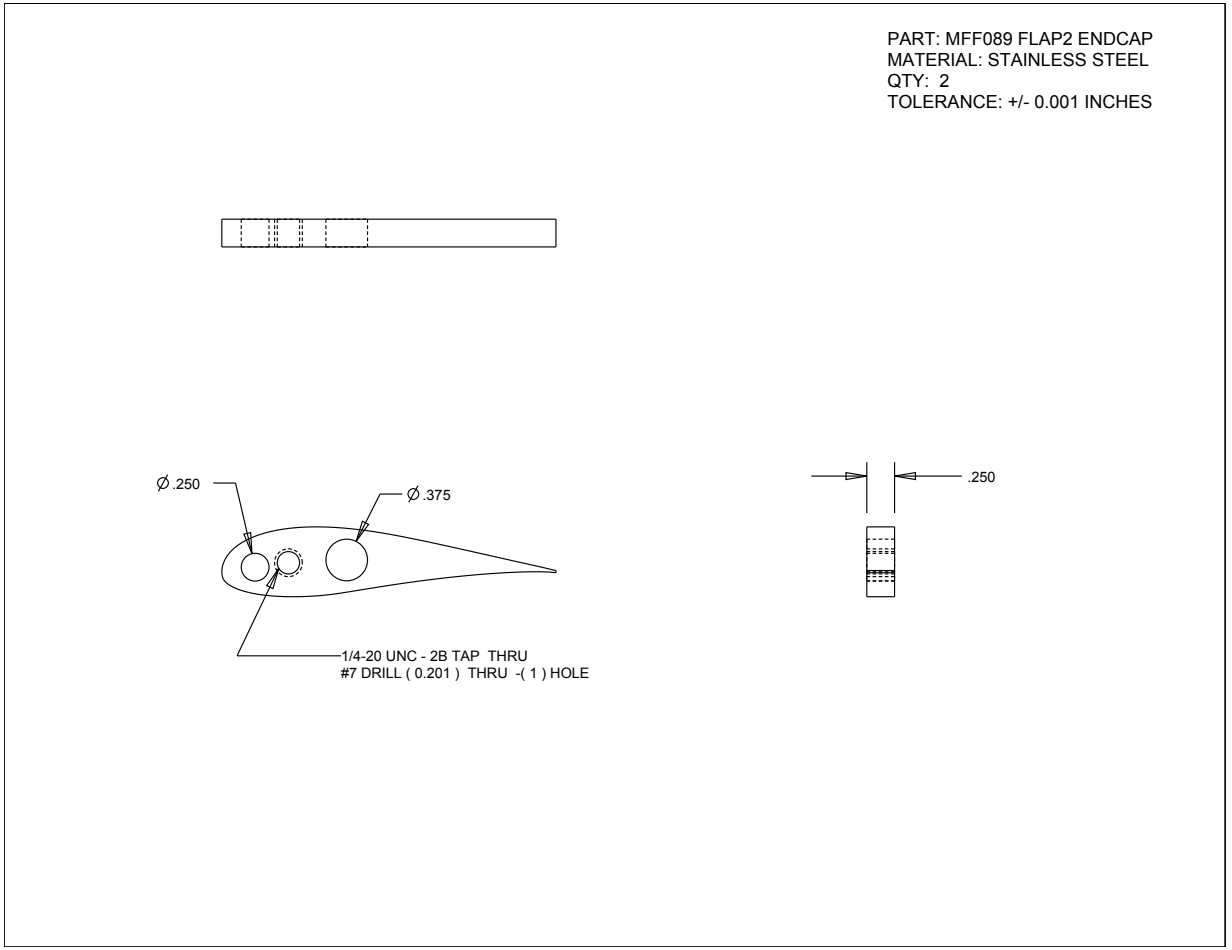

Figure E.49: Two-dimensional CAD drawing of flap 2 endcap.

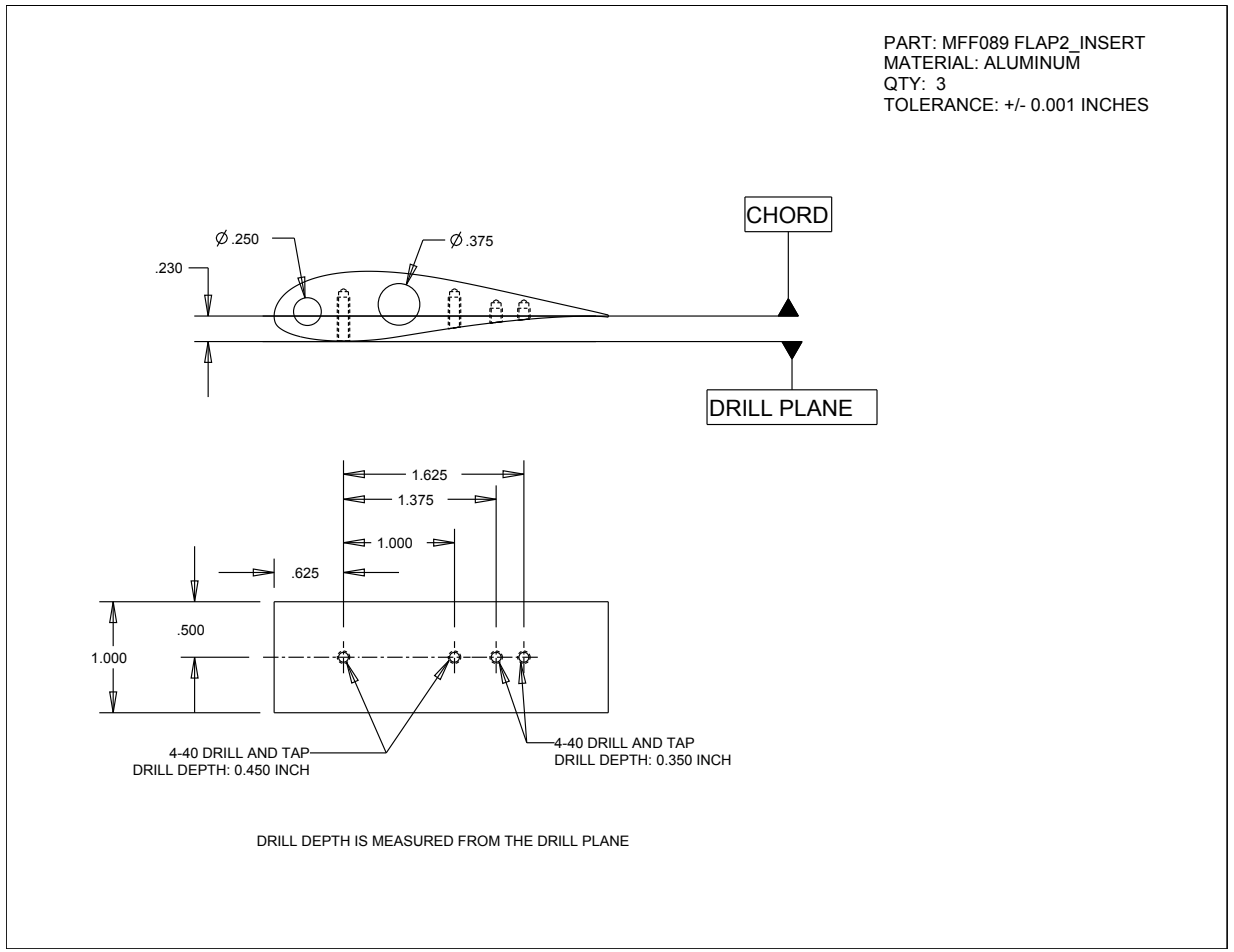

Figure E.50: Two-dimensional CAD drawing of flap 2 insert.

MFFS-026 Model CAD

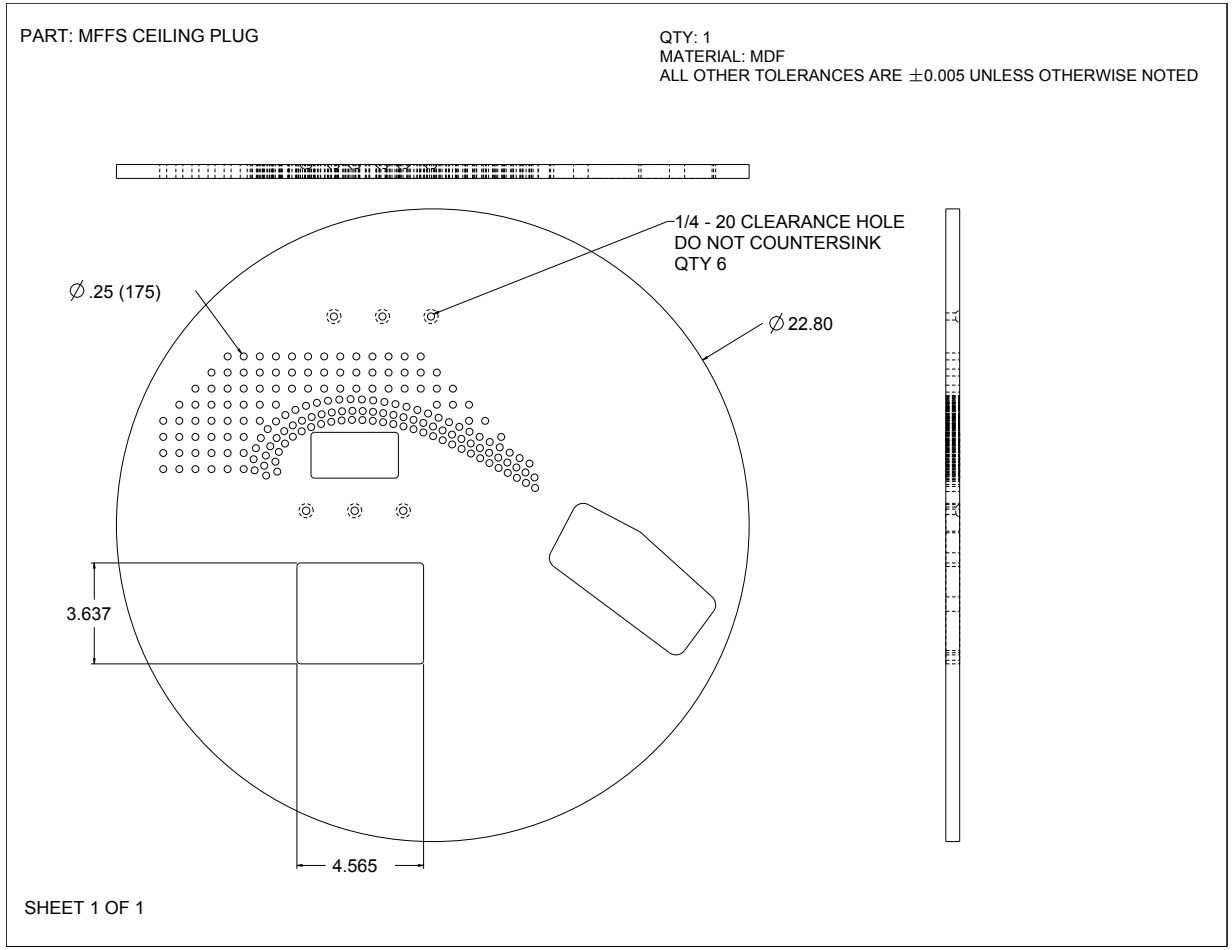

Figure E.51: Two-dimensional CAD drawing of ceiling plug for well separated model.

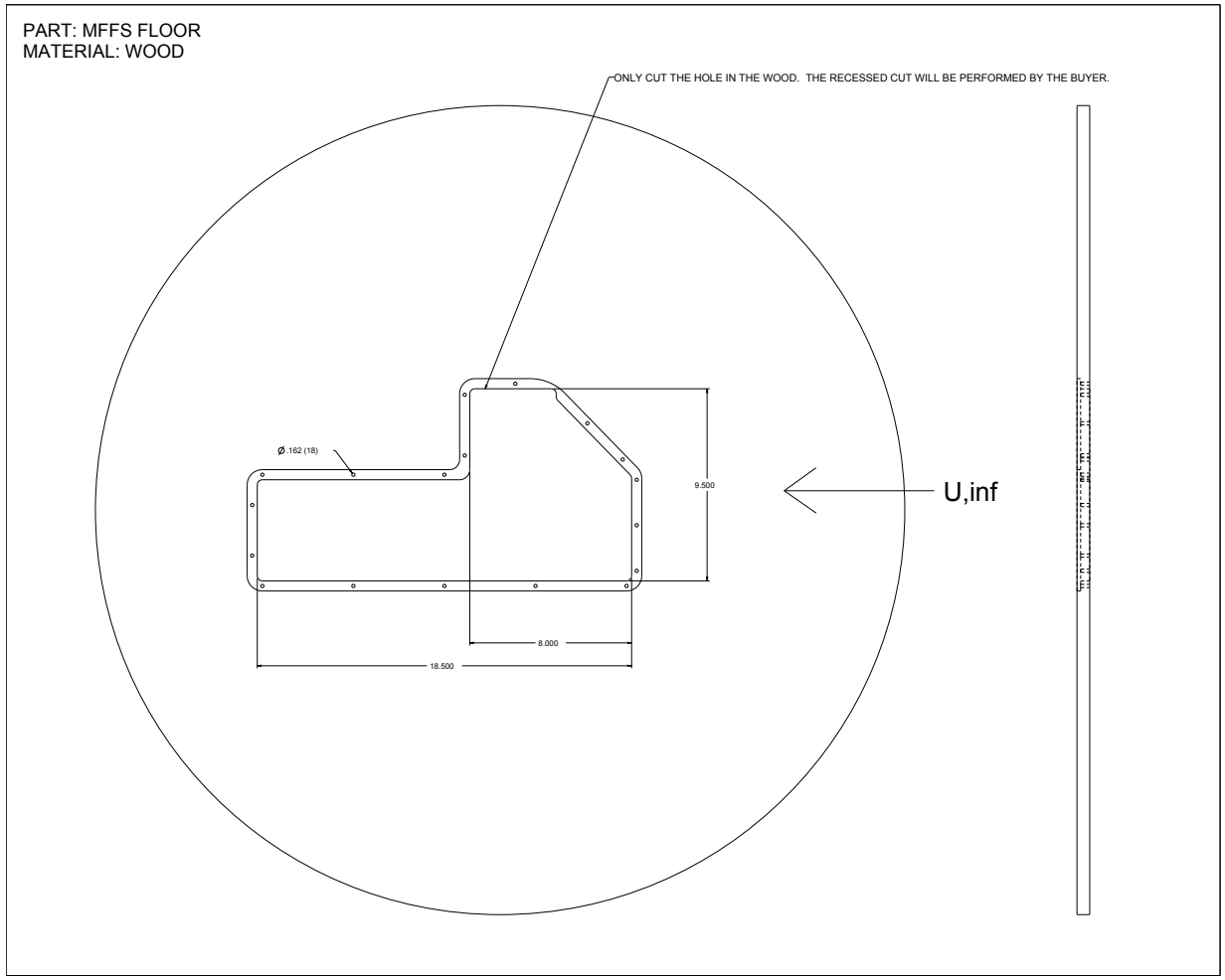

Figure E.52: Two-dimensional CAD drawing of wooden floor for well separated model.

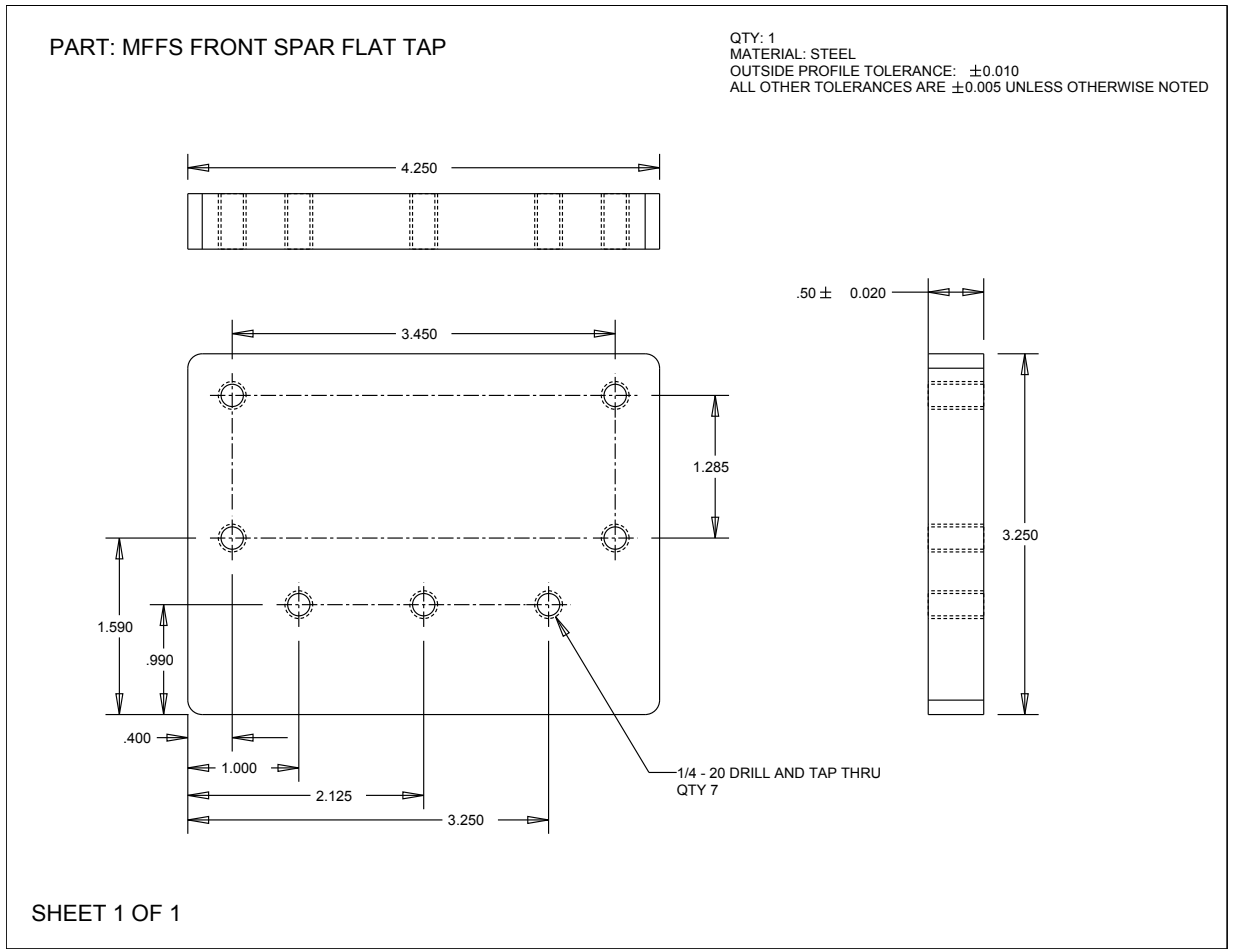

Figure E.53: Two-dimensional CAD drawing of top spar flat for well separated model.

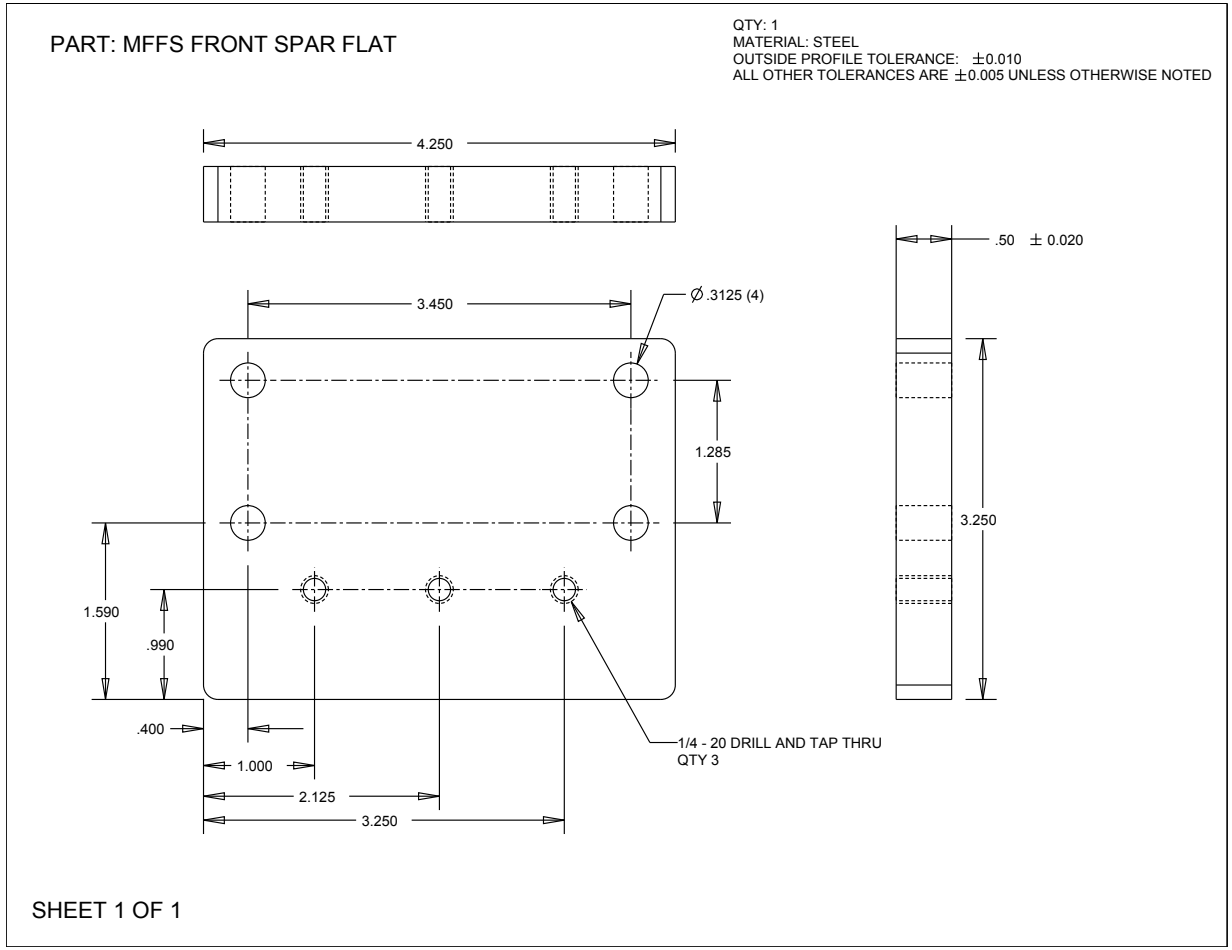

Figure E.54: Two-dimensional CAD drawing of front spar flat for well separated model.

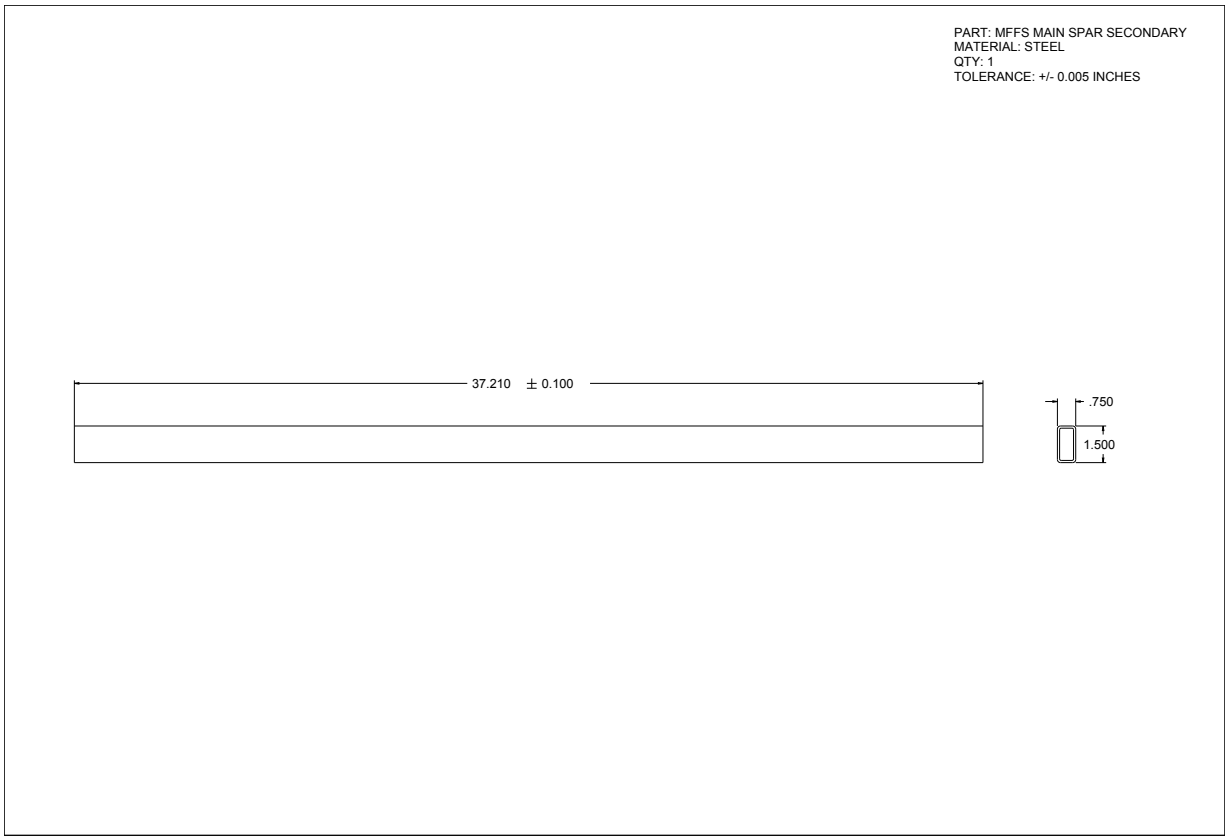

Figure E.55: Two-dimensional CAD drawing of secondary spar for well separated model.

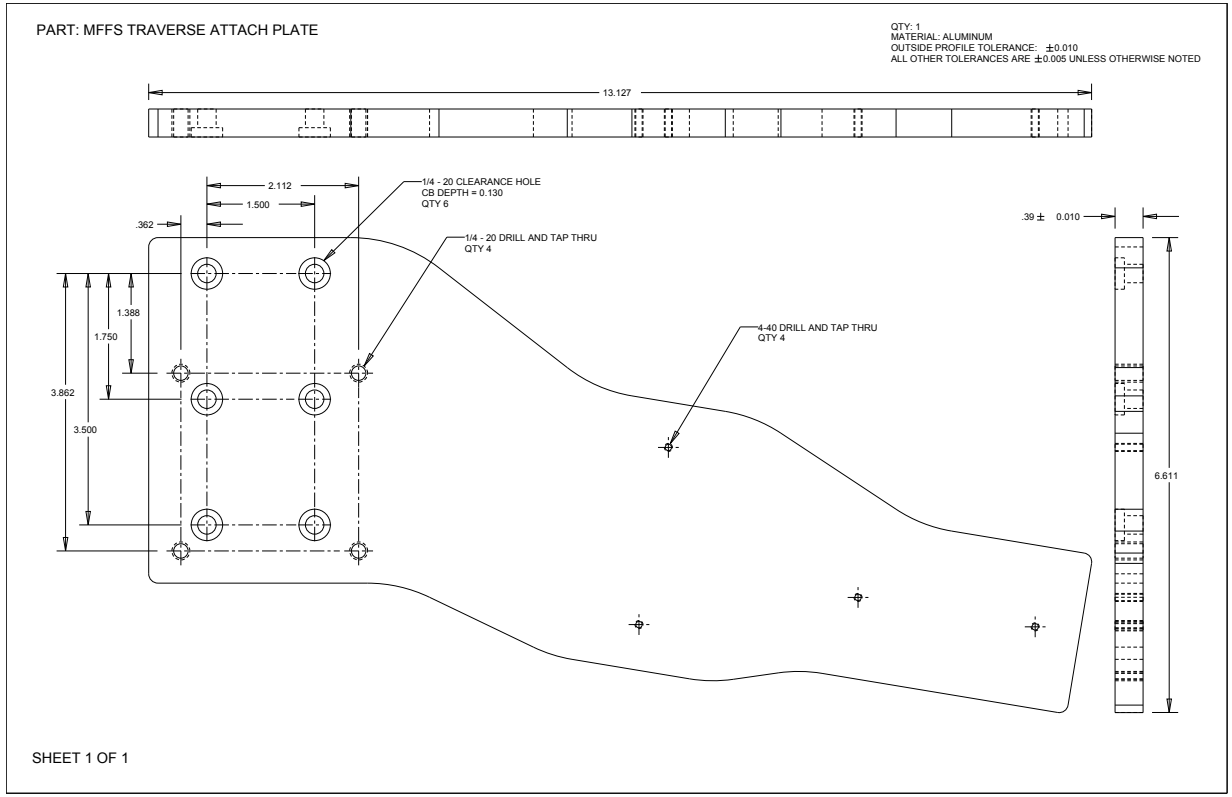

Figure E.56: Two-dimensional CAD drawing of traverse attachment plate for well separated model.

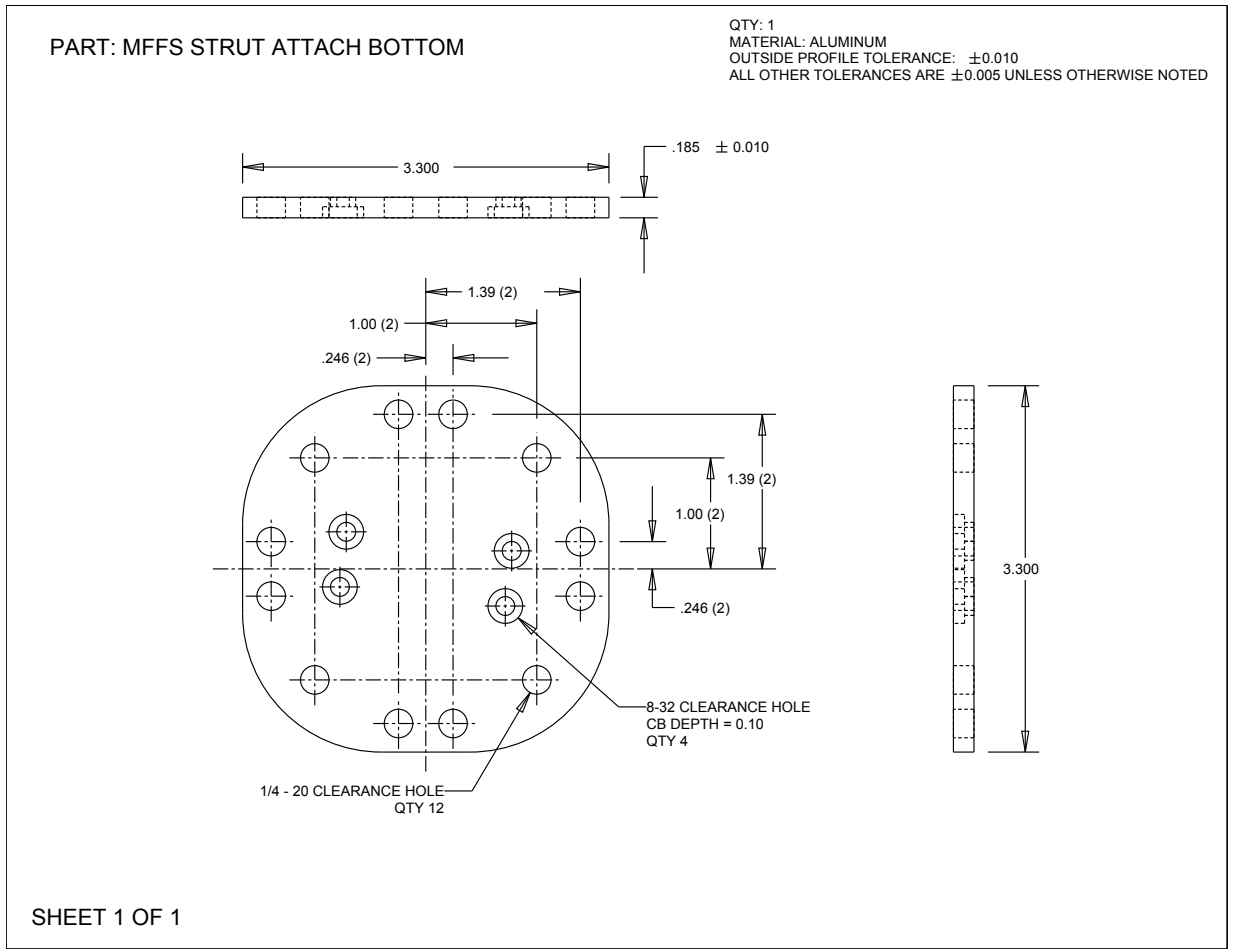

Figure E.57: Two-dimensional CAD drawing of bottom strut attachment plate for well separated model.

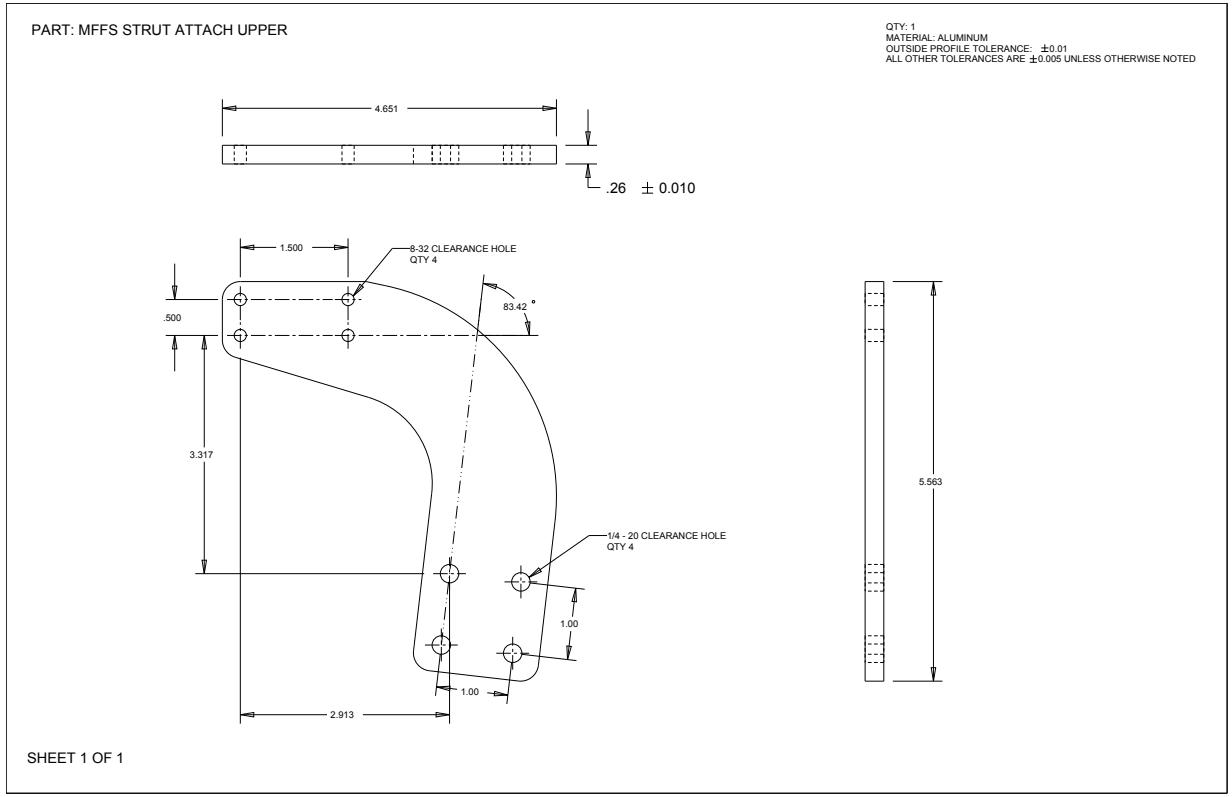

Figure E.58: Two-dimensional CAD drawing of top strut attachment plate for well separated model.

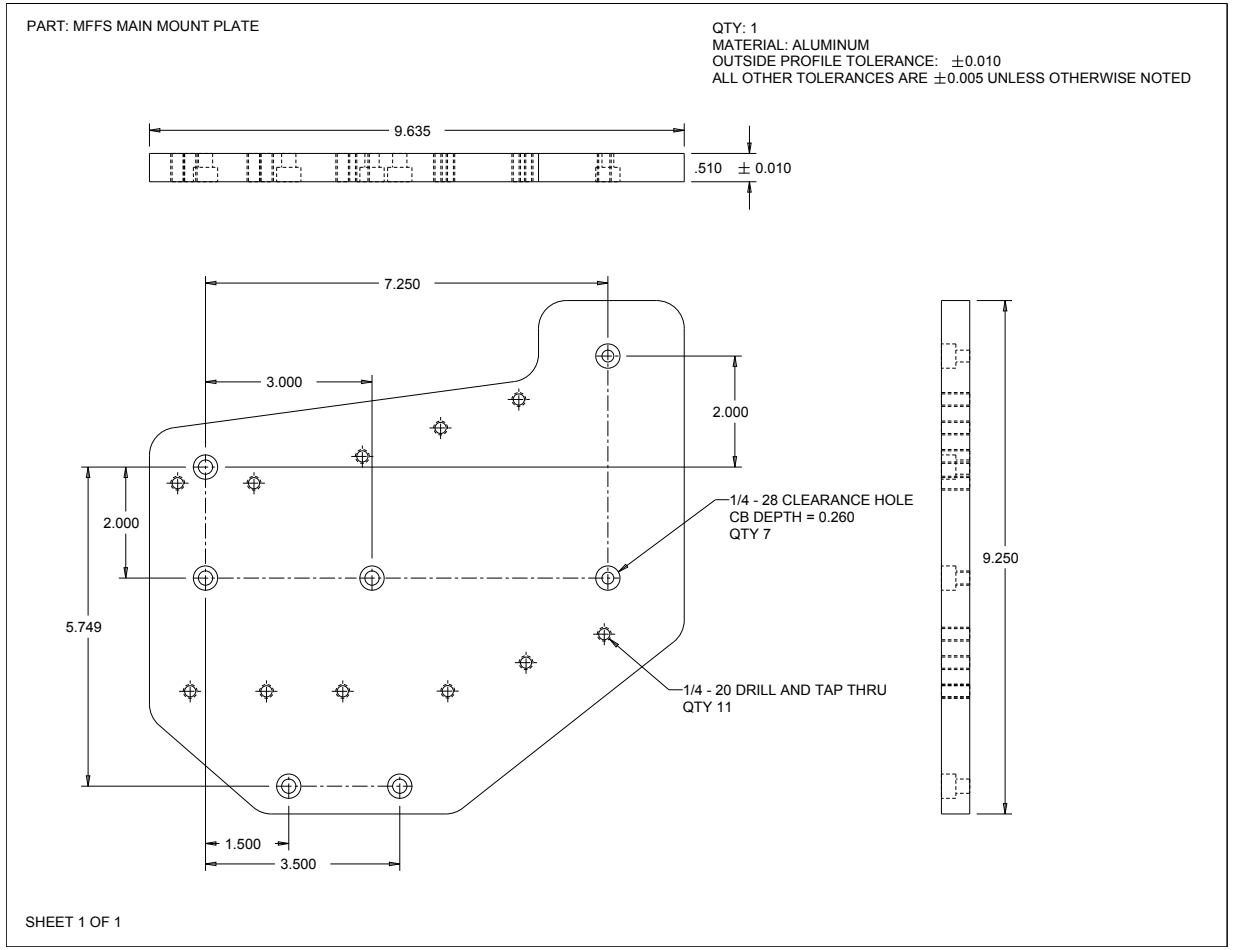

Figure E.59: Two-dimensional CAD drawing of main element mounting plate for well separated model.

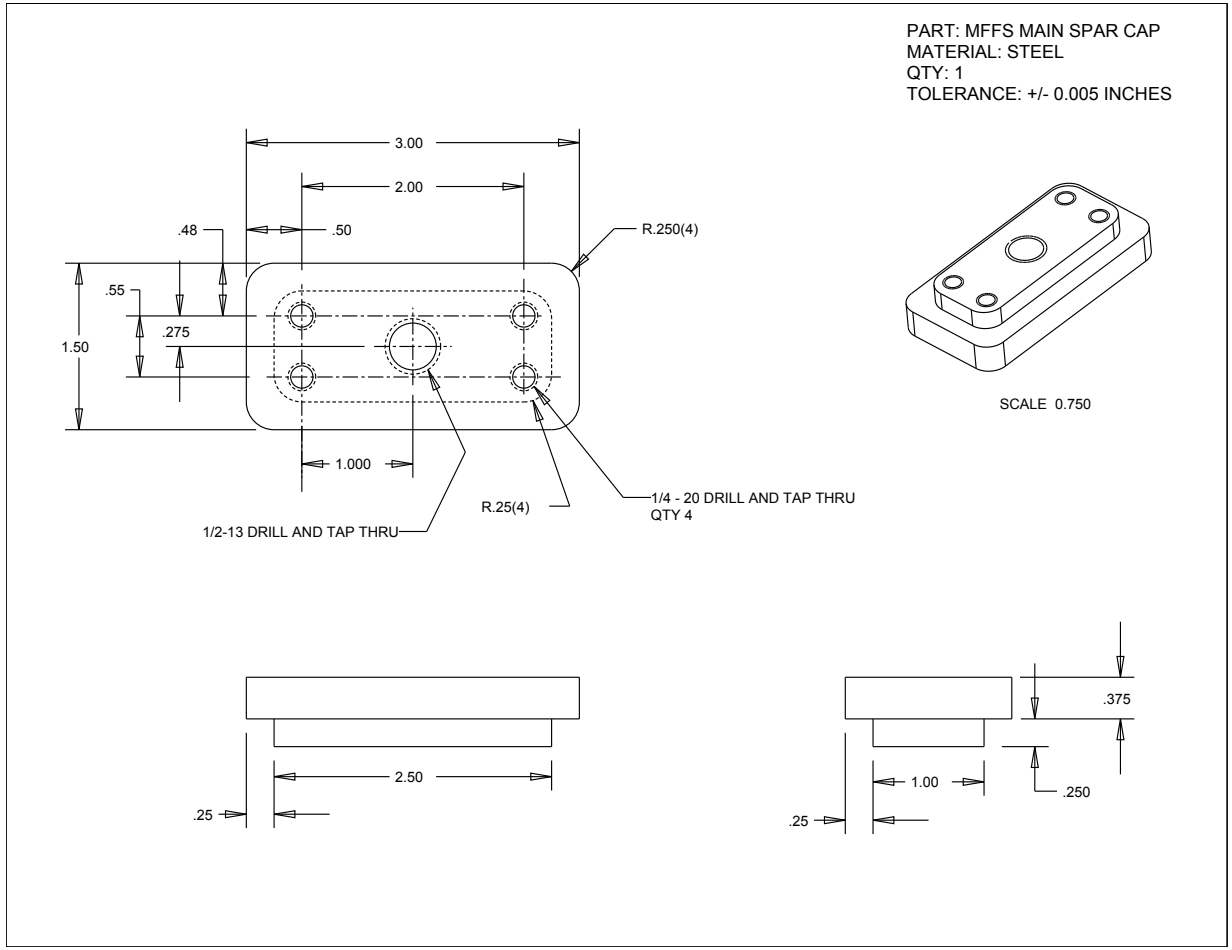

Figure E.60: Two-dimensional CAD drawing of main element spar cap for well separated model.

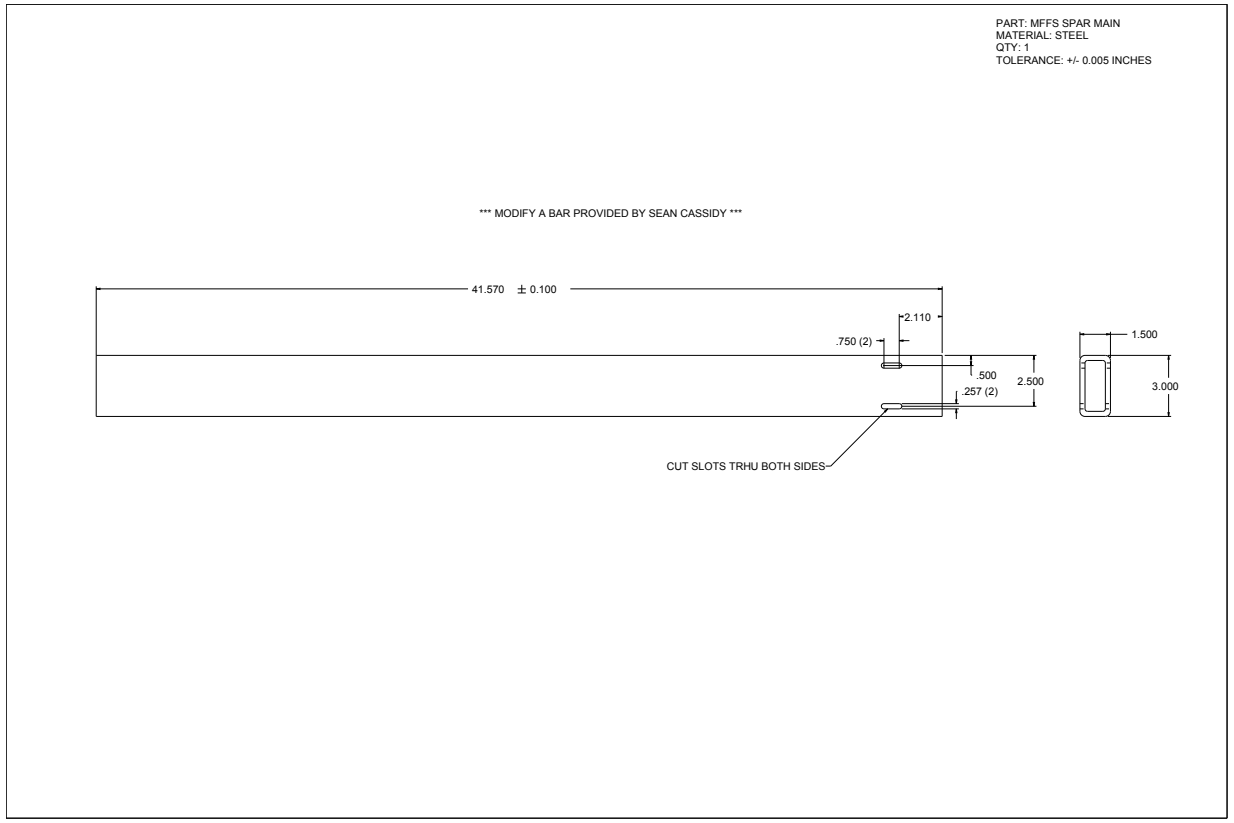

Figure E.61: Two-dimensional CAD drawing of main element spar for well separated model.

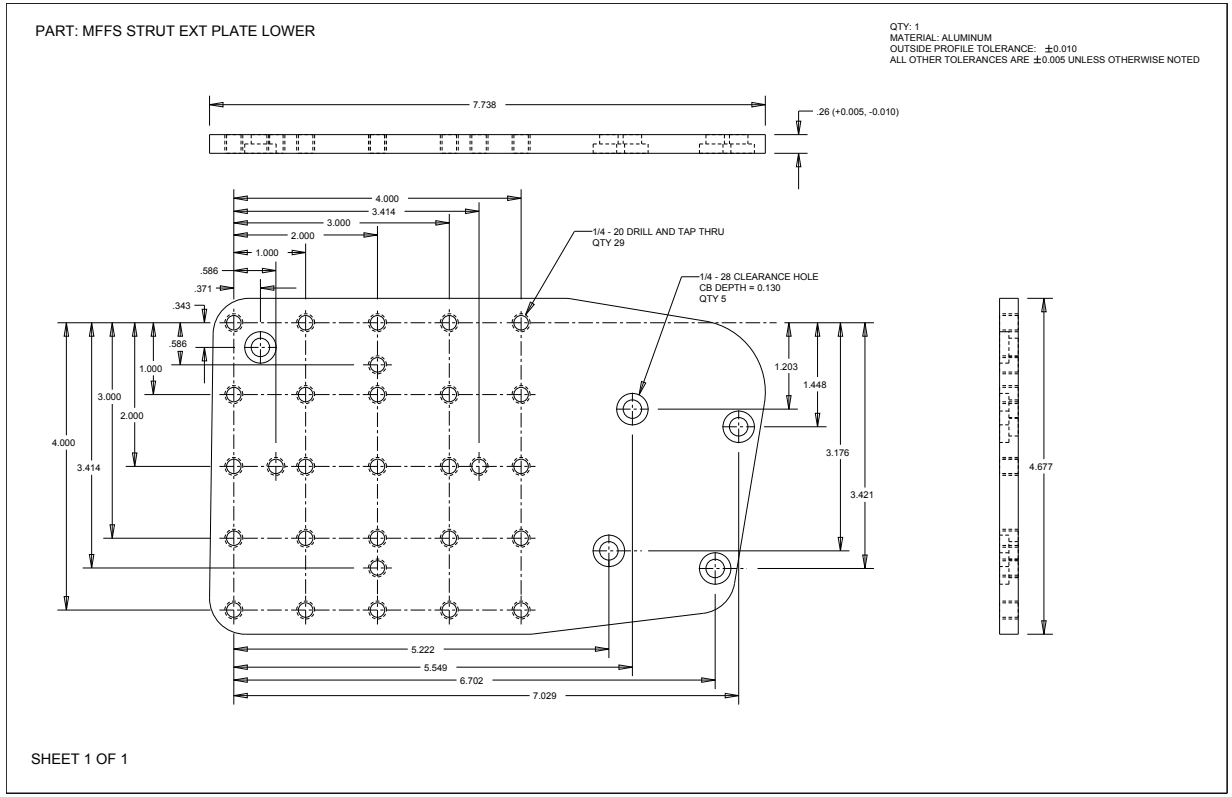

Figure E.62: Two-dimensional CAD drawing of strut lower extension plate for well separated model.

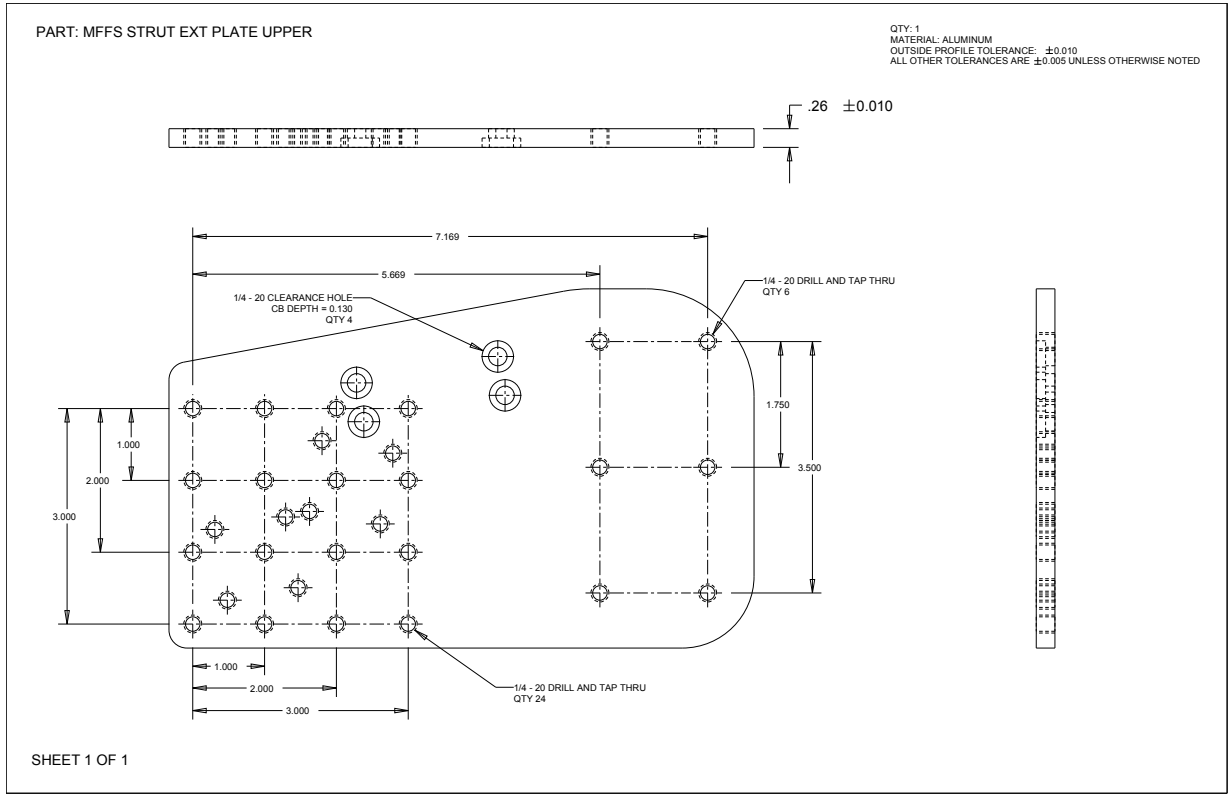

Figure E.63: Two-dimensional CAD drawing of strut upper extension plate for well separated model.

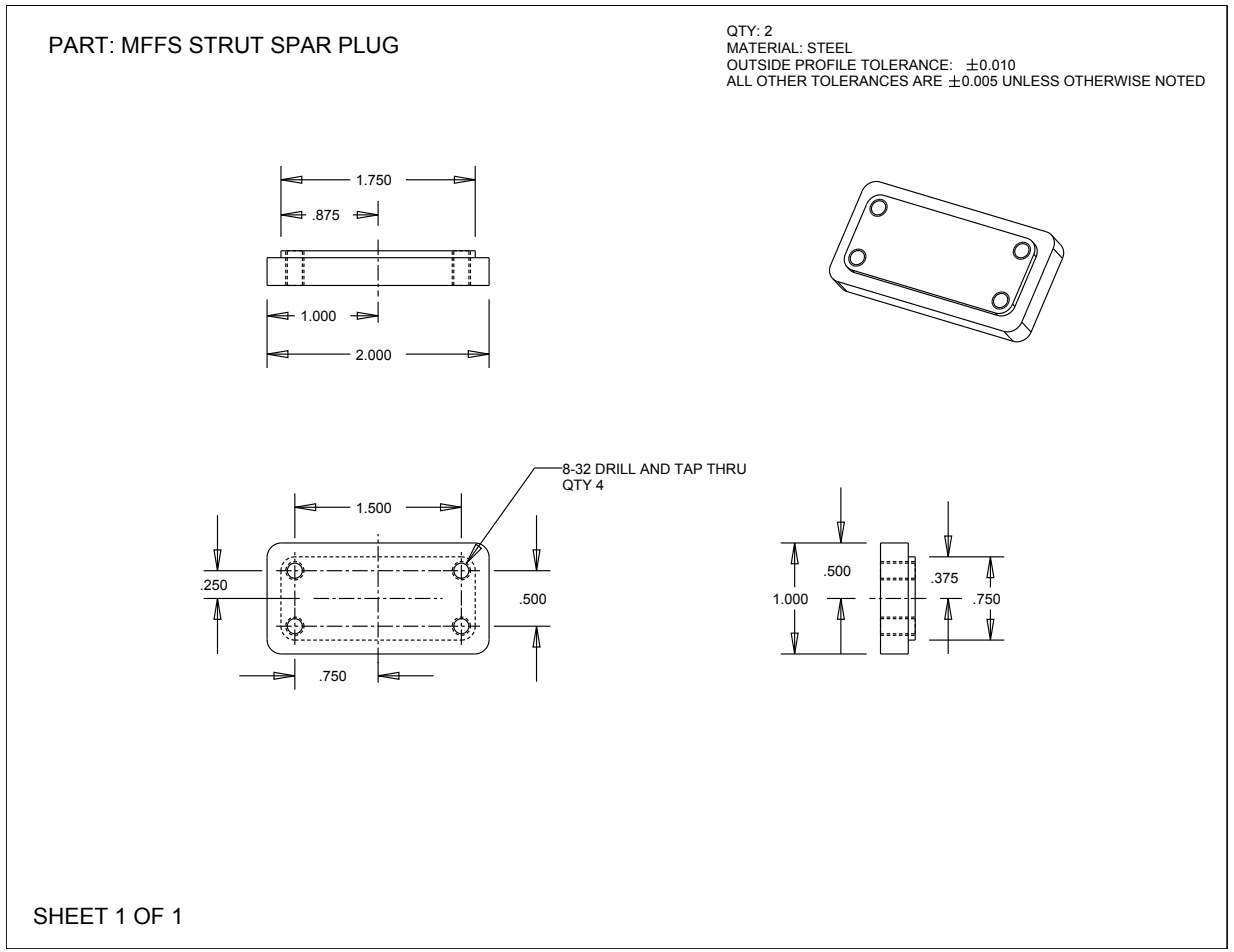

Figure E.64: Two-dimensional CAD drawing of strut spar plug for well separated model.

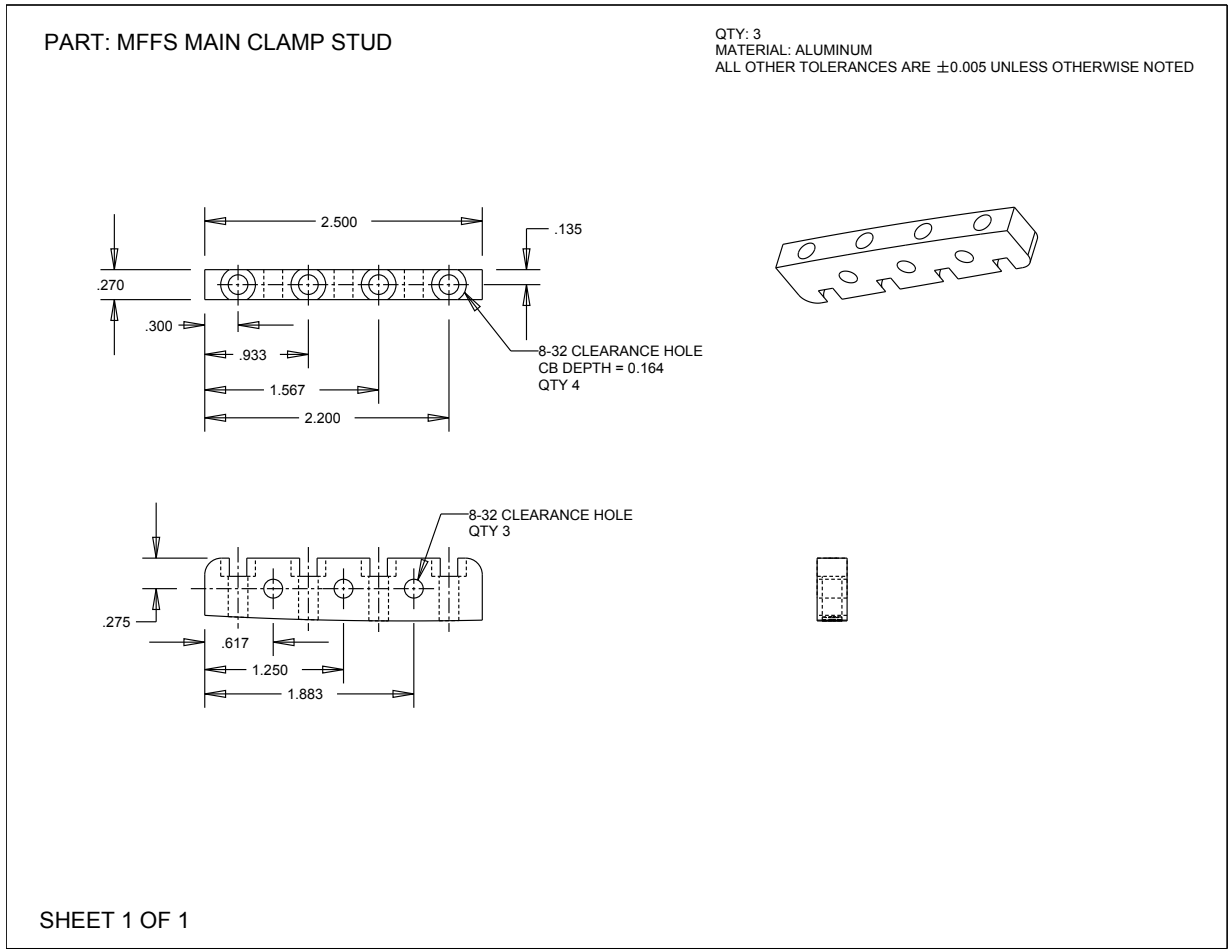

Figure E.65: Two-dimensional CAD drawing of main clamp stud for well separated model.

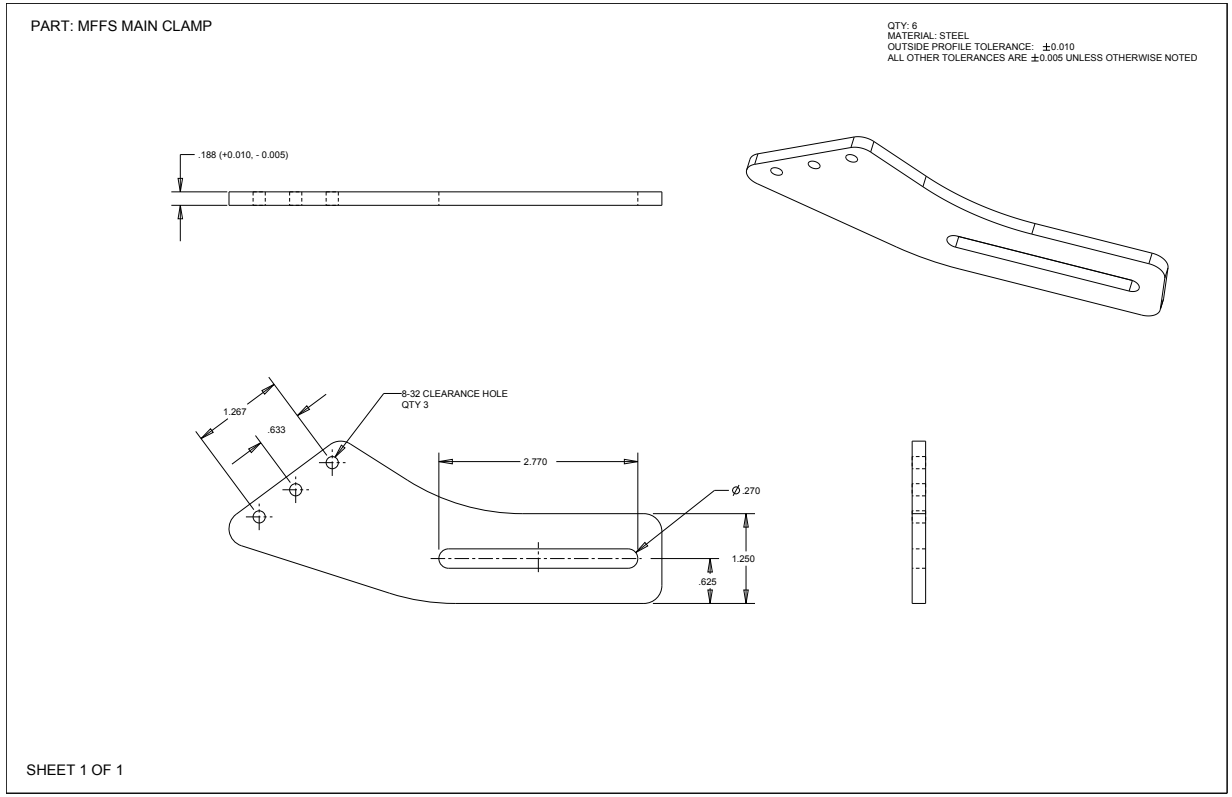

Figure E.66: Two-dimensional CAD drawing of main clamp for well separated model.

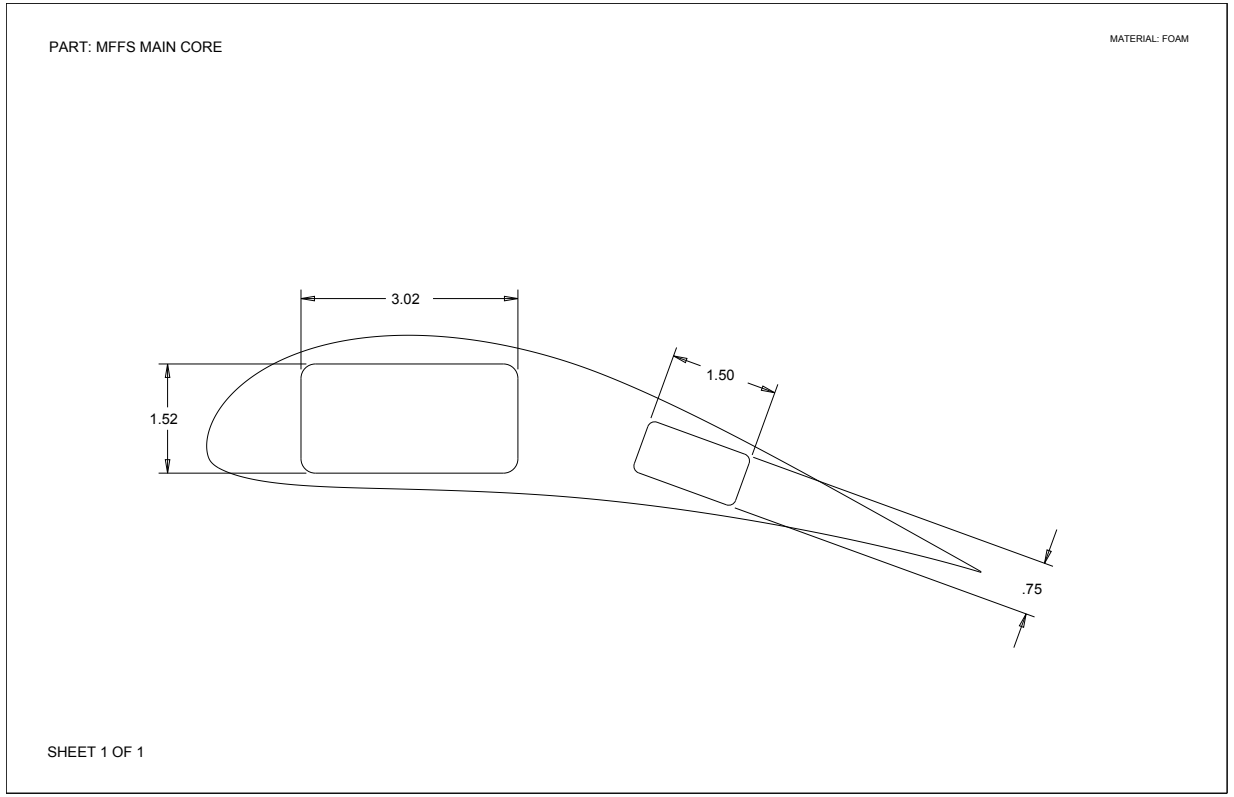

Figure E.67: Two-dimensional CAD drawing of main element foam core for well separated model.

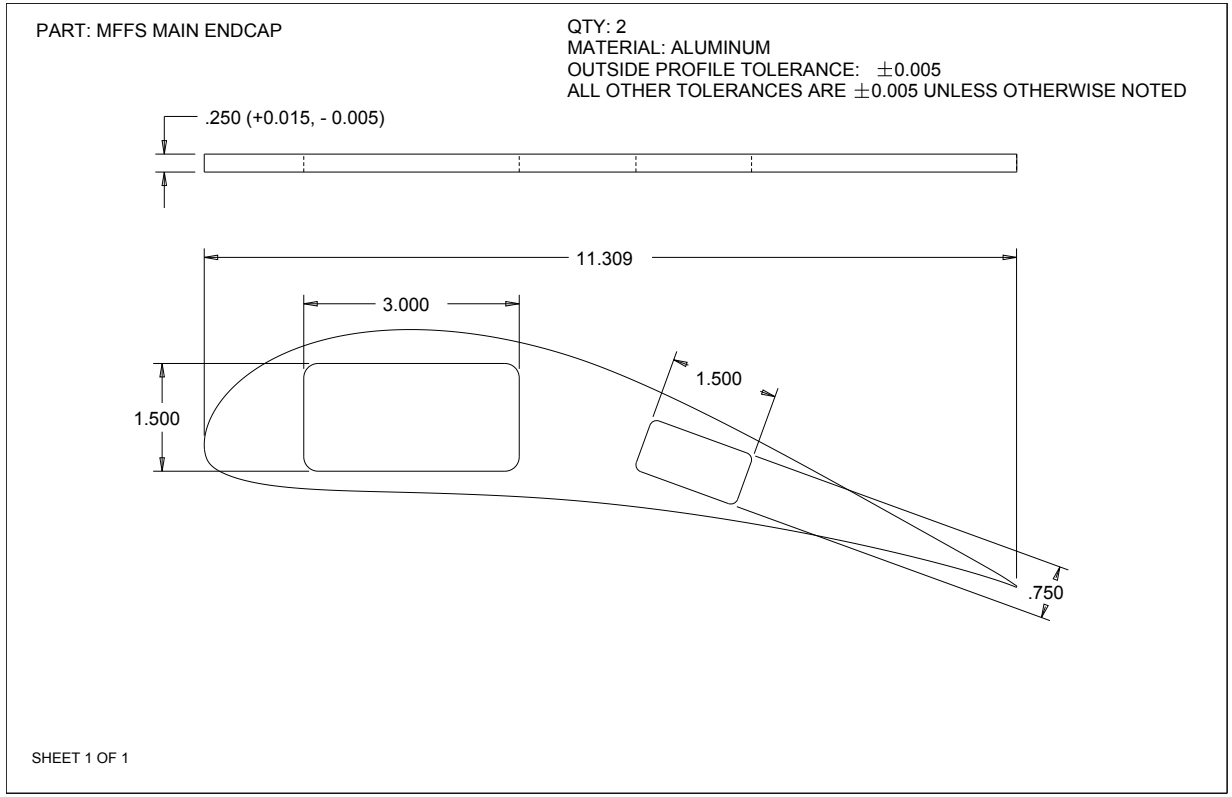

Figure E.68: Two-dimensional CAD drawing of main element endcap for well separated model.

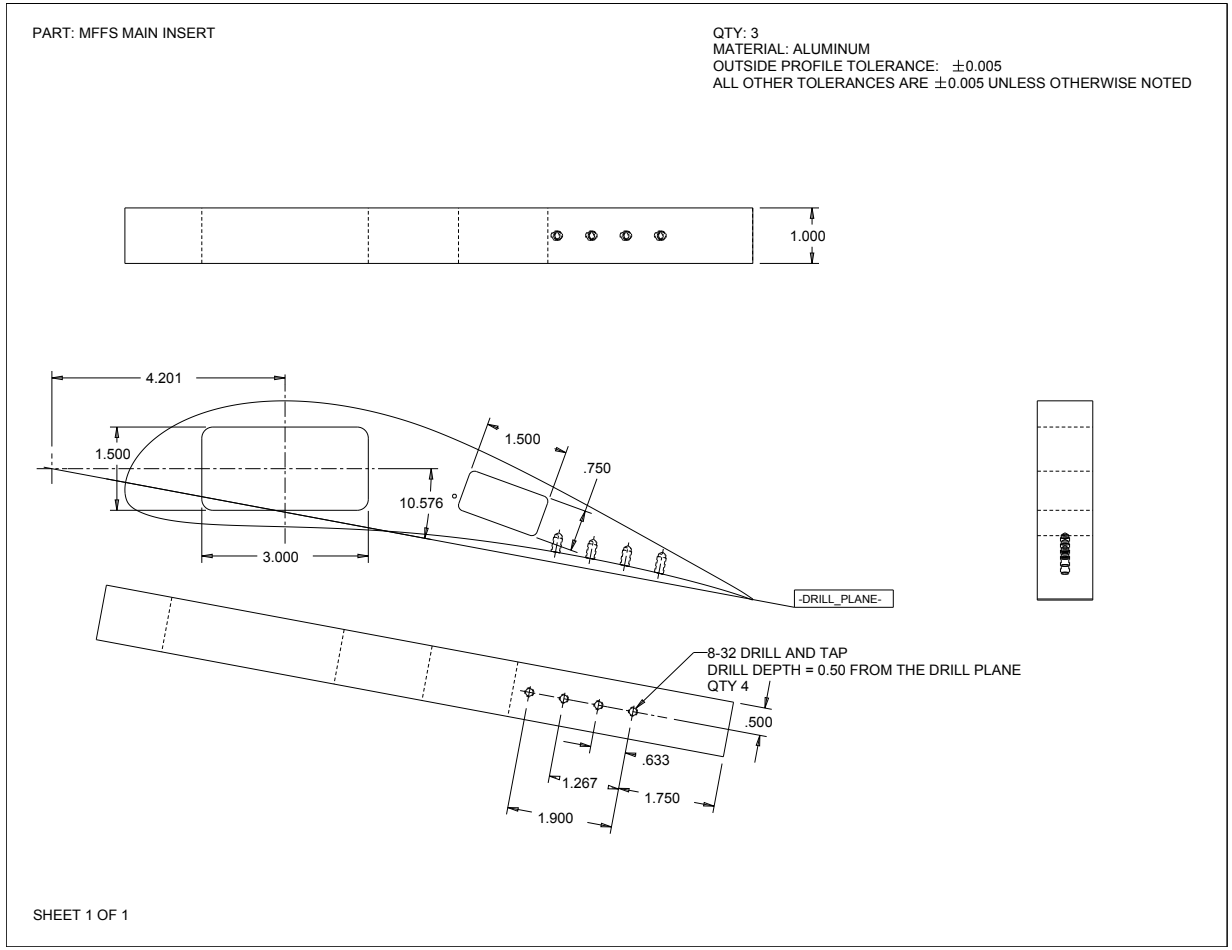

Figure E.69: Two-dimensional CAD drawing of main element insert for well separated model.

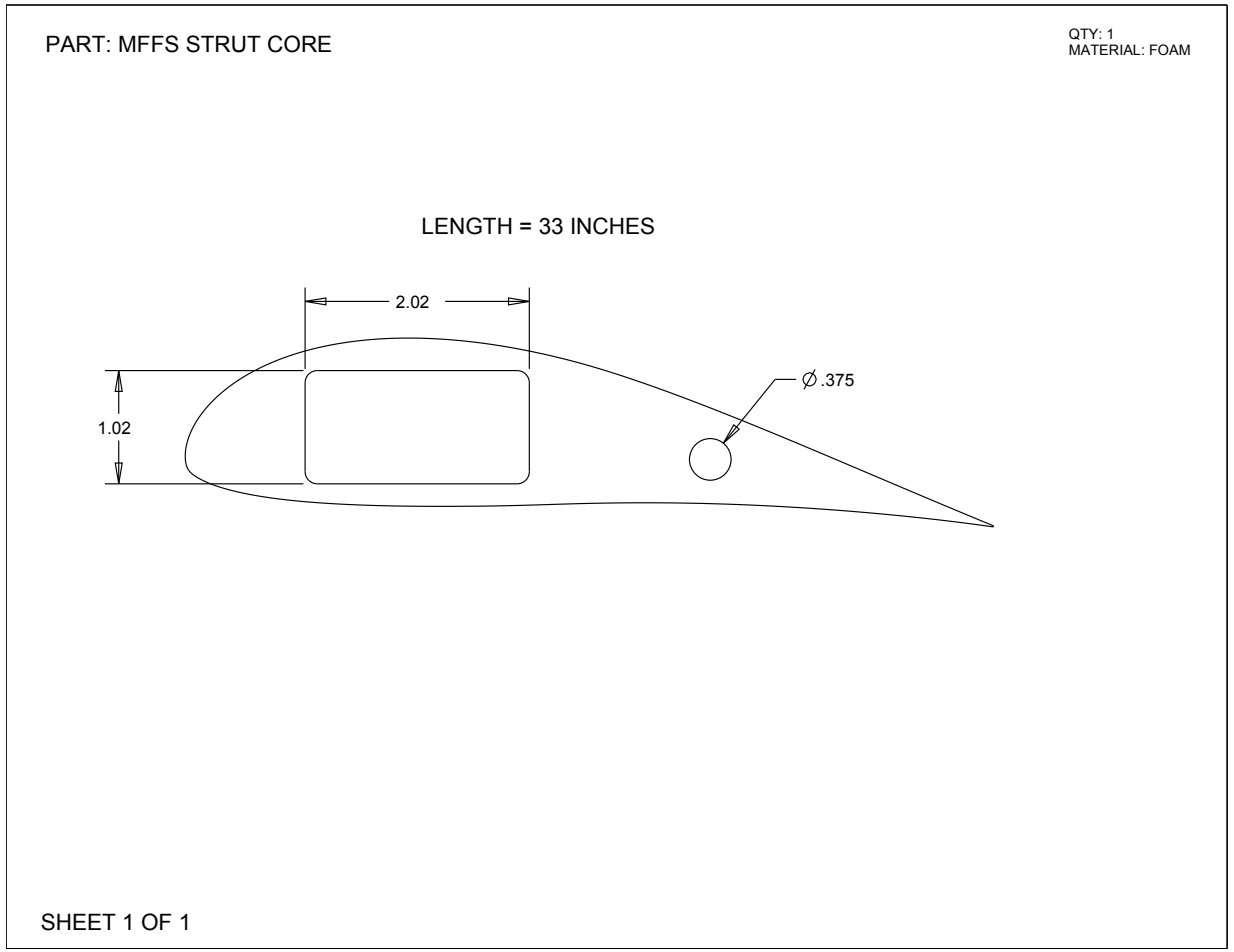

Figure E.70: Two-dimensional CAD drawing of strut foam core for well separated model.

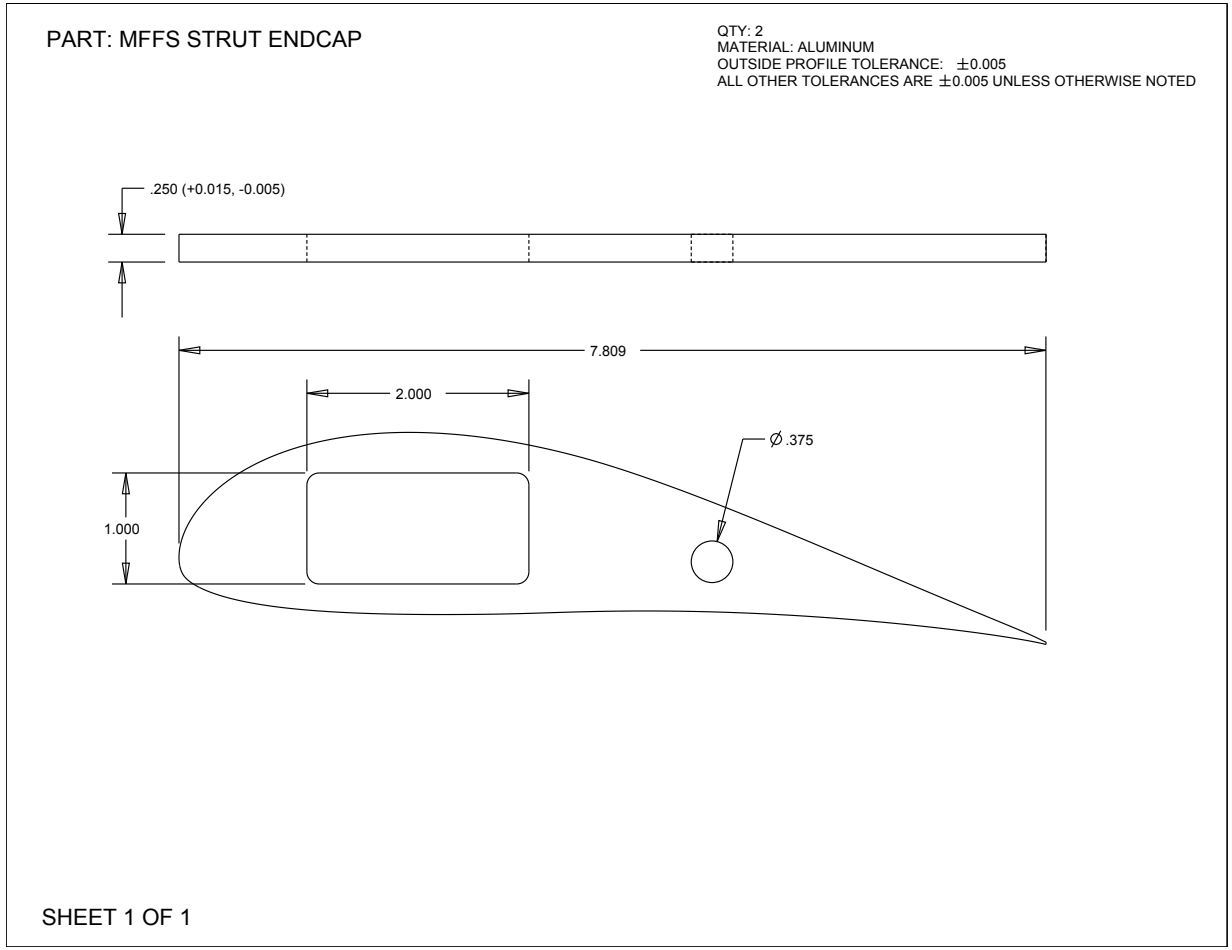

Figure E.71: Two-dimensional CAD drawing of strut endcap for well separated model.

References

[1] Wirz, R. E. and Johnson, P. M., "Aero-Structural Performance of Multiplane Wind Turbine Blades," AIAA 2011-3025, Applied Aerodynamics Conference, Honolulu HI, 2011.

[2] Pomeroy, B. W., Ananda, G. K., and Selig, M. S., "Wind Tunnel Measurement of Thick Airfoils for Wind Turbines," Confidential Report - UILU ENG 11-0505, Urbana IL, 2011.

[3] Abbott, I. H. and Miller, R. B., "Tests of a Highly Cambered Low-Drag Airfoil Section with a Lift-Control Flap," NASA Langley Research Center, NASA TR 74843, 1943.

[4] Jacobs, E. N., Abbott, I., and Davidson, M., "Preliminary Low-Drag-Airfoil and Flap Data from Tests at Large Reynolds Numbers and Low Turbulence," NACA-TM-74843, 1943.

[5] Smith, A. M. O., "High-Lift Aerodynamics," *Journal of Aircraft*, Vol. 12, No. 6, 1975, pp. 501–530.

[6] Liebeck, R. H., "On the Design of Subsonic Airfoils for High Lift," AIAA 76-406, AIAA Fluid and Plasma Dynamics Conference, San Diego CA, 1976.

[7] Liebeck, R. H., "Design of Subsonic Airfoils for High Lift," *Journal of Aircraft*, Vol. 15, No. 9, 1978, pp. 547–561.

[8] Klausmeyer, S. M. and Lin, J. C., "An Experimental Investigation of Skin Friction on a Multi-Element Airfoil," AIAA 94-1870, AIAA Applied Aerodynamics Conference, Colorado Springs CO, 1994.

[9] Valarezo, W. O., Dominik, C. H., and McGhee, R. J., "Multielement Airfoil Performance Due to Reynolds and Mach Number Variations," *Journal of Aircraft*, Vol. 30, No. 5, 1993, pp. 689–694.

[10] van Dam, C. P., "The Aerodynamics Design of Multi-Element High-Lift Systems for Transport Airplanes," *Progress in Aerospace Sciences*, Vol. 38, 2002, pp. 101–144.

[11] Ashby, D. L., "Experimental and Computational Investigation of Lift-Enhancing Tabs on a Multi-Element Airfoil," NASA Ames Research Center, NASA TR 110432, 1996.

[12] Myose, R., Papadakis, M., and Heron, I., "A Parametric Study on the Effect of Gurney Flaps on Single and Multielement Airfoils, Three-Dimensional Wings, and Reflection Plane Model," AIAA 97-0034, AIAA Aerospace Sciences Meeting, Reno NV, 1997.

[13] Biber, K. and Zumwalt, G. W., "Experimental Studies of a Two-Element Airfoil with Large Separation," AIAA 92-0267, AIAA Aerospace Sciences Meeting, Reno NV, 1992.

[14] Cerra, D. F. and Katz, J., "Design of a High-Lift, Thick Airfoil for Unmanned Aerial Vehicle Applications," *Journal of Aircraft*, Vol. 45, No. 5, 2008, pp. 1789–1793.

[15] Spaid, F. W., "High Reynolds Number, Multielement Airfoil Flowfield Measurements," *Journal of Aircraft*, Vol. 37, No. 3, 2000, pp. 499–507.

[16] Lin, J. C. and Doninik, C. J., "Parametric Investigation of a High-Lift Airfoil at High Reynolds Numbers," *Journal of Aircraft*, Vol. 34, No. 4, 1997, pp. 485–491.

[17] Coiro, D. P., Nicolosi, F., and Grasso, F., "Design and Testing of Multi-Element Airfoil for Short-Takeoff-and-Landing Ultralight Aircraft," *Journal of Aircraft*, Vol. 46, No. 5, 2009, pp. 1795–1807.

[18] Rogers, S. E., "Progress in High-Lift Aerodynamic Calculations," *Journal of Aircraft*, Vol. 31, No. 6, 1994, pp. 1244–1251.

[19] Nakayama, A., Kreplin, H., and Morgan, H., "Experimental Investigation of Flowfield About a Multi-element Airfoil," *AIAA Journal*, Vol. 28, No. 1, 1988, pp. 14–21.

[20] Chin, V. D., "Flowfield Measurements about a Multi-Element Airfoil at High Reynolds Numbers," AIAA 93-3137, AIAA Fluid Dynamics Conference, Orlando FL, 1993.

[21] Drela, M. and Giles, M. B., "Viscous-Inviscid Analysis of Transonic and Low Reynolds Number Airfoils," AIAA 86-1786, AIAA Applied Aerodynamics Conference, 1986.

[22] Drela, M., "Design and Optimization Method for Multi-Element Airfoils," AIAA 93-0969, AIAA Aerospace Design Conference, 1993.

[23] Bucci, G. S. and Sullivan, J. P., "An Experimental Simulation of High Lift Wake Flows at High Reynolds Number," AIAA 97-31787, AIAA Applied Aerodynamics Conference, 1997.

[24] Cebeci, T., Besnard, E., and Chen, H. H., "Calculation of Multielement Airfoil Flows, Including Flap Wells," AIAA 96-0056, AIAA Aerospace Sciences Meeting, Reno NV, 1996.

[25] Czerwiec, R. and Edwards, J. R., "Theory and Experiment of Multielement Airfoils - A Comparison," AIAA 2000-0985, AIAA Aerospace Sciences Meeting, Reno NV, 2000.

[26] Hoffenberg, R. and Sullivan, J., "Simulation of High-Lift Wake Behavior," AIAA 97-0718, AIAA Aerospace Sciences Meeting, Reno NV, 1997.

[27] Driver, D. M. and Mateer, G. G., "Wake Flow in Adverse Pressure Gradient," *International Journal of Heat and Fluid Flow*, Vol. 223, 2002, pp. 564–571.

[28] Hoffenberg, R. and Sullivan, J., "Measurement and Simulation of Wake Deceleration," AIAA 98-0522, AIAA Aerosciences Meeting, Reno NV, 1998.

[29] Schneider, S., Campbell, B., Bucci, G., and Sullivan, J., "An Experimental Simulation of Flap Flow on Multielement Airfoils at High Reynolds Number," AIAA 94-2613, AIAA Aerospace Ground Testing Conference, Colorado Springs CO, 1994.

[30] Hoffenberg, R., Sullivan, J., and Schneider, S., "Wake Measurements in a Strong Adverse Pressure Gradient," NASA CR 197272, 1995.

[31] Narsipur, S., Pomeroy, B. W., and Selig, M. S., "CFD Analysis of Multielement Airfoils for Wind Turbines," to be presented at 2012 AIAA Applied Aerodynamics Conference, New Orleans LA.

[32] Ragheb, A. M. and Selig, M. S., "Multi-Element-Airfoil-Configurations-for-Wind-Turbines," AIAA 2011-3971, AIAA Applied Aerodynamics Conference, 2011.

[33] Howe, G. D., "Optimization of 2-D Flap Geometry Using Matlab and Fun3D," AIAA 2011-823, AIAA Aerospace Sciences Meeting, Orlando FL, 2011.

[34] Noe, S. C., *Force Balance Measurements of Wind-Turbine Airfoil Performance with Simulated Leading-Edge Ice Accretions*, Master's thesis, University of Illinois at Urbana-Champaign, 1996.

[35] Jones, B. M., "Measurement of Profile Drag by the Pitot-Traverse Method," British Aeronautical Research Council R&M 1688, 1936.

[36] Schlichting, H., *Boundary-Layer Theory*, McGraw-Hill Book Company, 1979.

[37] Barlow, J. B., Rae, Jr., W. H., and Pope, A., *Low-Speed Wind Tunnel Testing*, Wiley-Interscience, 3rd ed., 1999.

[38] Garner, H. C., Rogers, E. W. E., Acum, W. E. A., and Maskell, E. C., "Subsonic Wind Tunnel Wall Corrections," AGARDograph 109, 1966.

[39] Thom, A., "Blockage Corrections in a High Speed Wind Tunnel," Aeronautical Research Committee R&M 2033, 1943.

[40] Maskell, E. C., "A Theory of the Blockage Effects on Bluff Bodies and Stalled Wings in a Closed Wind Tunnel," Aeronautical Research Committee TN 3400, 1965.

[41] Somers, D. M., "Design and Experimental Results for the S809 Airfoil," NREL SR-440-6918, Golden, CO, 1997.

[42] Ansell, P. J., *Flight Envelope Protection Using Flap Hinge Moment Measurement*, Master's thesis, University of Illinois at Urbana-Champaign, Urbana IL, 2010.

[43] Glauert, H., "Wind Tunnel Interference on Wings, Bodies, and Airscrews," Aeronautical Research Committee TN 1566, 1933.

[44] Klunker, E. B. and Harder, K. C., "On the Second-Order Tunnel Wall Construction Correction in Two-Dimensional Compressible Flow," TN 2350, 1951.

[45] Young, A. D. and Squire, H. B., "Blockage Corrections in a Closed Rectangular Tunnel," Aeronautical Research Committee R&M 1984, 1945.